

PRINCIPLES of COMPUTATIONAL MODELLING *in* NEUROSCIENCE

David Sterratt
Bruce Graham
Andrew Gillies
David Willshaw

CAMBRIDGE

CAMBRIDGE

www.cambridge.org/9780521877954

This page intentionally left blank

Principles of Computational Modelling in Neuroscience

The nervous system is made up of a large number of elements that interact in a complex fashion. To understand how such a complex system functions requires the construction and analysis of computational models at many different levels.

This book provides a step-by-step account of how to model the neuron and neural circuitry to understand the nervous system at many levels, from ion channels to networks. Starting with a simple model of the neuron as an electrical circuit, gradually more details are added to include the effects of neuronal morphology, synapses, ion channels and intracellular signalling. The principle of abstraction is explained through chapters on simplifying models, and how simplified models can be used in networks. This theme is continued in a final chapter on modelling the development of the nervous system.

Requiring an elementary background in neuroscience and some high school mathematics, this textbook provides an ideal basis for a course on computational neuroscience.

An associated website, providing sample codes and up-to-date links to external resources, can be found at www.compneuroprinciples.org.

David Sterratt is a Research Fellow in the School of Informatics at the University of Edinburgh. His computational neuroscience research interests include models of learning and forgetting, and the formation of connections within the developing nervous system.

Bruce Graham is a Reader in Computing Science in the School of Natural Sciences at the University of Stirling. Focusing on computational neuroscience, his research covers nervous system modelling at many levels.

Andrew Gillies works at Psymetrix Limited, Edinburgh. He has been actively involved in computational neuroscience research.

David Willshaw is Professor of Computational Neurobiology in the School of Informatics at the University of Edinburgh. His research focuses on the application of methods of computational neurobiology to an understanding of the development and functioning of the nervous system.

Principles of Computational Modelling in Neuroscience

David Sterratt

University of Edinburgh

Bruce Graham

University of Stirling

Andrew Gillies

Psymetrix Limited

David Willshaw

University of Edinburgh



CAMBRIDGE UNIVERSITY PRESS
Cambridge, New York, Melbourne, Madrid, Cape Town,
Singapore, São Paulo, Delhi, Tokyo, Mexico City
Cambridge University Press
The Edinburgh Building, Cambridge CB2 8RU, UK

Published in the United States of America by Cambridge University Press, New York

www.cambridge.org
Information on this title: www.cambridge.org/9780521877954

© D. Sterratt, B. Graham, A. Gillies and D. Willshaw 2011

This publication is in copyright. Subject to statutory exception and to the provisions of relevant collective licensing agreements, no reproduction of any part may take place without the written permission of Cambridge University Press.

First published 2011

Printed in the United Kingdom at the University Press, Cambridge

A catalogue record for this publication is available from the British Library

Library of Congress Cataloguing in Publication data
Principles of computational modelling in neuroscience / David Sterratt ... [et al.]
p. cm.

Includes bibliographical references and index.

ISBN 978-0-521-87795-4

1. Computational neuroscience. I. Sterratt, David, 1973-
QP357.5.P75 2011
612.801'13 - dc22 2011001055

ISBN 978-0-521-87795-4 Hardback

Cambridge University Press has no responsibility for the persistence or accuracy of URLs for external or third-party internet websites referred to in this publication, and does not guarantee that any content on such websites is, or will remain, accurate or appropriate.

Contents

<i>List of abbreviations</i>	<i>page</i> viii
<i>Preface</i>	x
<i>Acknowledgements</i>	xii
<hr/>	
Chapter 1 Introduction	1
1.1 What is this book about?	1
1.2 Overview of the book	9
<hr/>	
Chapter 2 The basis of electrical activity in the neuron	13
2.1 The neuronal membrane	14
2.2 Physical basis of ion movement in neurons	16
2.3 The resting membrane potential: the Nernst equation	22
2.4 Membrane ionic currents not at equilibrium: the Goldman–Hodgkin–Katz equations	26
2.5 The capacitive current	30
2.6 The equivalent electrical circuit of a patch of membrane	30
2.7 Modelling permeable properties in practice	35
2.8 The equivalent electrical circuit of a length of passive membrane	36
2.9 The cable equation	39
2.10 Summary	45
<hr/>	
Chapter 3 The Hodgkin–Huxley model of the action potential	47
3.1 The action potential	47
3.2 The development of the model	50
3.3 Simulating action potentials	60
3.4 The effect of temperature	65
3.5 Building models using the Hodgkin–Huxley formalism	66
3.6 Summary	71
<hr/>	
Chapter 4 Compartmental models	72
4.1 Modelling the spatially distributed neuron	72
4.2 Constructing a multi-compartmental model	73
4.3 Using real neuron morphology	77
4.4 Determining passive properties	83
4.5 Parameter estimation	87
4.6 Adding active channels	93
4.7 Summary	95

Chapter 5 Models of active ion channels	96
5.1 Ion channel structure and function	97
5.2 Ion channel nomenclature	99
5.3 Experimental techniques	103
5.4 Modelling ensembles of voltage-gated ion channels	105
5.5 Markov models of ion channels	110
5.6 Modelling ligand-gated channels	115
5.7 Modelling single channel data	118
5.8 The transition state theory approach to rate coefficients	124
5.9 Ion channel modelling in theory and practice	131
5.10 Summary	132
Chapter 6 Intracellular mechanisms	133
6.1 Ionic concentrations and electrical response	133
6.2 Intracellular signalling pathways	134
6.3 Modelling intracellular calcium	137
6.4 Transmembrane fluxes	138
6.5 Calcium stores	140
6.6 Calcium diffusion	143
6.7 Calcium buffering	151
6.8 Complex intracellular signalling pathways	159
6.9 Stochastic models	163
6.10 Spatial modelling	169
6.11 Summary	170
Chapter 7 The synapse	172
7.1 Synaptic input	172
7.2 The postsynaptic response	173
7.3 Presynaptic neurotransmitter release	179
7.4 Complete synaptic models	187
7.5 Long-lasting synaptic plasticity	189
7.6 Detailed modelling of synaptic components	191
7.7 Gap junctions	192
7.8 Summary	194
Chapter 8 Simplified models of neurons	196
8.1 Reduced compartmental models	198
8.2 Integrate-and-fire neurons	204
8.3 Making integrate-and-fire neurons more realistic	211
8.4 Spike-response model neurons	218
8.5 Rate-based models	220
8.6 Summary	224

Chapter 9	Networks of neurons	226
9.1	Network design and construction	227
9.2	Schematic networks: the associative memory	233
9.3	Networks of simplified spiking neurons	243
9.4	Networks of conductance-based neurons	251
9.5	Large-scale thalamocortical models	254
9.6	Modelling the neurophysiology of deep brain stimulation	259
9.7	Summary	265
Chapter 10	The development of the nervous system	267
10.1	The scope of developmental computational neuroscience	267
10.2	Development of nerve cell morphology	269
10.3	Development of cell physiology	279
10.4	Development of nerve cell patterning	280
10.5	Development of patterns of ocular dominance	284
10.6	Development of connections between nerve and muscle	286
10.7	Development of retinotopic maps	294
10.8	Summary	312
Chapter 11	Farewell	314
11.1	The development of computational modelling in neuroscience	314
11.2	The future of computational neuroscience	315
11.3	And finally...	318
Appendix A	Resources	319
A.1	Simulators	319
A.2	Databases	324
A.3	General-purpose mathematical software	326
Appendix B	Mathematical methods	328
B.1	Numerical integration methods	328
B.2	Dynamical systems theory	333
B.3	Common probability distributions	341
B.4	Parameter estimation	346
	<i>References</i>	351
	<i>Index</i>	382

Abbreviations

ADP	adenosine diphosphate
AHP	afterhyperpolarisation
AMPA	α -amino-3-hydroxy-5-methyl-4-isoxalone propionic acid
AMPAR	AMPA receptor
ATP	adenosine triphosphate
BAPTA	bis(aminophenoxy)ethanetetraacetic acid
BCM	Bienenstock–Cooper–Munro
BPAP	back-propagating action potential
cAMP	cyclic adenosine monophosphate
cDNA	cloned DNA
cGMP	cyclic guanosine monophosphate
CICR	calcium-induced calcium release
CNG	cyclic-nucleotide-gated channel family
CNS	central nervous system
CST	corticospinal tract
CV	coefficient of variation
DAG	diacylglycerol
DBS	deep brain stimulation
DCM	Dual Constraint model
DNA	deoxyribonucleic acid
DTI	diffusion tensor imaging
EBA	excess buffer approximation
EEG	electroencephalogram
EGTA	ethylene glycol tetraacetic acid
EM	electron microscope
EPP	endplate potential
EPSC	excitatory postsynaptic current
EPSP	excitatory postsynaptic potential
ER	endoplasmic reticulum
ES	evolution strategies
GABA	γ -aminobutyric acid
GHK	Goldman–Hodgkin–Katz
GPi	globus pallidus internal segment
HCN	hyperpolarisation-activated cyclic-nucleotide-gated channel family
HH model	Hodgkin–Huxley model
HVA	high-voltage-activated
IP ₃	inositol 1,4,5-triphosphate
IPSC	inhibitory postsynaptic current
ISI	interspike interval
IUPHAR	International Union of Pharmacology
KDE	kernel density estimation
LGN	lateral geniculate nucleus
LTD	long-term depression

LTP	long-term potentiation
LVA	low-voltage-activated
MAP	microtubule associated protein
MEPP	miniature endplate potential
mGluR	metabotropic glutamate receptor
MLE	maximum likelihood estimation
MPTP	1-methyl-4-phenyl-1,2,3,6-tetrahydropyridine
MRI	magnetic resonance imaging
mRNA	messenger RNA
NMDA	N-methyl-D-aspartic acid
ODE	ordinary differential equation
PDE	partial differential equation
PDF	probability density function
PIP ₂	phosphatidylinositol 4,5-bisphosphate
PLC	phospholipase C
PMCA	plasma membrane Ca ²⁺ -ATPase
PSC	postsynaptic current
PSD	postsynaptic density
RBA	rapid buffer approximation
RC	resistor-capacitor
RGC	retinal ganglion cell
RNA	ribonucleic acid
RRVP	readily releasable vesicle pool
SERCA	sarcoplasmic reticulum Ca ²⁺ -ATPase
SSA	Stochastic Simulation Algorithm
STDP	spike-timing-dependent plasticity
STN	subthalamic nucleus
TEA	tetraethylammonium
TPC	two-pore-channels family
TRP	transient receptor potential channel family
TTX	tetrodotoxin
VSD	voltage-sensitive domain

Preface

To understand the nervous system of even the simplest of animals requires an understanding of the nervous system at many different levels, over a wide range of both spatial and temporal scales. We need to know at least the properties of the nerve cell itself, of its specialist structures such as synapses, and how nerve cells become connected together and what the properties of networks of nerve cells are.

The complexity of nervous systems make it very difficult to theorise cogently about how such systems are put together and how they function. To aid our thought processes we can represent our theory as a computational model, in the form of a set of mathematical equations. The variables of the equations represent specific neurobiological quantities, such as the rate at which impulses are propagated along an axon or the frequency of opening of a specific type of ion channel. The equations themselves represent how these quantities interact according to the theory being expressed in the model. Solving these equations by analytical or simulation techniques enables us to show the behaviour of the model under the given circumstances and thus addresses the questions that the theory was designed to answer. Models of this type can be used as explanatory or predictive tools.

This field of research is known by a number of largely synonymous names, principally computational neuroscience, theoretical neuroscience or computational neurobiology. Most attempts to analyse computational models of the nervous system involve using the powerful computers now available to find numerical solutions to the complex sets of equations needed to construct an appropriate model.

To develop a computational model in neuroscience the researcher has to decide how to construct and apply a model that will link the neurobiological reality with a more abstract formulation that is analytical or computationally tractable. Guided by the neurobiology, decisions have to be taken about the level at which the model should be constructed, the nature and properties of the elements in the model and their number, and the ways in which these elements interact. Having done all this, the performance of the model has to be assessed in the context of the scientific question being addressed.

This book describes how to construct computational models of this type. It arose out of our experiences in teaching Masters-level courses to students with backgrounds from the physical, mathematical and computer sciences, as well as the biological sciences. In addition, we have given short computational modelling courses to biologists and to people trained in the quantitative sciences, at all levels from postgraduate to faculty members. Our students wanted to know the principles involved in designing computational models of the nervous system and its components, to enable them to develop their own models. They also wanted to know the mathematical basis in as far as it describes neurobiological processes. They wanted to have more than the basic recipes for running the simulation programs which now exist for modelling the nervous system at the various different levels.

This book is intended for anyone interested in how to design and use computational models of the nervous system. It is aimed at the postgraduate level and beyond. We have assumed a knowledge of basic concepts such as neurons, axons and synapses. The mathematics given in the book is necessary to understand the concepts introduced in mathematical terms. Therefore we have assumed some knowledge of mathematics, principally of functions such as logarithms and exponentials and of the techniques of differentiation and integration. The more technical mathematics have been put in text boxes and smaller points are given in the margins. For non-specialists, we have given verbal descriptions of the mathematical concepts we use.

Many of the models we discuss exist as open source simulation packages and we give links to these simulators. In many cases the original code is available.

Our intention is that several different types of people will be attracted to read this book and that these will include:

The experimental neuroscientist. We hope that the experimental neuroscientist will become interested in the computational approach to neuroscience.

A teacher of computational neuroscience. This book can be used as the basis of a hands-on course on computational neuroscience.

An interested student from the physical sciences. We hope that the book will motivate graduate students, post doctoral researchers or faculty members in other fields of the physical, mathematical or information sciences to enter the field of computational neuroscience.

Acknowledgements

There are many people who have inspired and helped us throughout the writing of this book. We are particularly grateful for the critical comments and suggestions from Fiona Williams, Jeff Wickens, Gordon Arbuthnott, Mark van Rossum, Matt Nolan, Matthias Hennig, Irina Erchova, Stephen Eglen and Ewa Henderson. We are grateful to our publishers at Cambridge University Press, particularly Gavin Swanson, with whom we discussed the initial project, and Martin Griffiths. Finally, we appreciate the great help, support and forbearance of our family members.

Chapter 1

Introduction

1.1 | What is this book about?

This book is about how to construct and use computational models of specific parts of the nervous system, such as a neuron, a part of a neuron or a network of neurons. It is designed to be read by people from a wide range of backgrounds from the biological, physical and computational sciences. The word ‘model’ can mean different things in different disciplines, and even researchers in the same field may disagree on the nuances of its meaning. For example, to biologists, the term ‘model’ can mean ‘animal model’; to physicists, the standard model is a step towards a complete theory of fundamental particles and interactions. We therefore start this chapter by attempting to clarify what we mean by computational models and modelling in the context of neuroscience. Before giving a brief chapter-by-chapter overview of the book, we also discuss what might be called the philosophy of modelling: general issues in computational modelling that recur throughout the book.

1.1.1 Theories and mathematical models

In our attempts to understand the natural world, we all come up with theories. Theories are possible explanations for how the phenomena under investigation arise, and from theories we can derive predictions about the results of new experiments. If the experimental results disagree with the **predictions**, the theory can be rejected, and if the results agree, the theory is validated – for the time being. Typically, the theory will contain **assumptions** which are about the properties of elements or mechanisms which have not yet been quantified, or even observed. In this case, a full test of the theory will also involve trying to find out if the assumptions are really correct.

In the first instance, a theory is described in words, or perhaps with a diagram. To derive predictions from the theory we can deploy verbal reasoning and further diagrams. Verbal reasoning and diagrams are crucial tools for theorising. However, as the following example from ecology demonstrates, it can be risky to rely on them alone.

Suppose we want to understand how populations of a species in an ecosystem grow or decline through time. We might theorise that ‘the larger the population, the more likely it will grow and therefore the faster it will

Mendel's Laws of Inheritance form a good example of a theory formulated on the basis of the interactions of elements whose existence was not known at the time. These elements are now known as genes.

increase in size'. From this theory we can derive the prediction, as did Malthus (1798), that the population will grow infinitely large, which is incorrect. The reasoning from theory to prediction is correct, but the prediction is wrong and so logic dictates that the theory is wrong. Clearly, in the real world, the resources consumed by members of the species are only replenished at a finite rate. We could add to the theory the stipulation that for large populations, the rate of growth slows down, being limited by finite resources. From this, we can make the reasonable prediction that the population will stabilise at a certain level at which there is zero growth.

We might go on to think about what would happen if there are two species, one of which is a predator and one of which is the predator's prey. Our theory might now state that: (1) the prey population grows in proportion to its size but declines as the predator population grows and eats it; and (2) the predator population grows in proportion to its size and the amount of the prey, but declines in the absence of prey. From this theory we would predict that the prey population grows initially. As the prey population grows, the predator population can grow faster. As the predator population grows, this limits the rate at which the prey population can grow. At some point, an equilibrium is reached when both predator and prey sizes are in balance.

Thinking about this a bit more, we might wonder whether there is a second possible prediction from the theory. Perhaps the predator population grows so quickly that it is able to make the prey population extinct. Once the prey has gone, the predator is also doomed to extinction. Now we are faced with the problem that there is one theory but two possible conclusions; the theory is logically inconsistent.

The problem has arisen for two reasons. Firstly, the theory was not clearly specified to start with. Exactly how does the rate of increase of the predator population depend on its size and the size of the prey population? How fast is the decline of the predator population? Secondly, the theory is now too complex for qualitative verbal reasoning to be able to turn it into a prediction.

The solution to this problem is to specify the theory more precisely, in the language of mathematics. In the equations corresponding to the theory, the relationships between predator and prey are made precisely and unambiguously. The equations can then be solved to produce one prediction. We call a theory that has been specified by sets of equations a **mathematical model**.

It so happens that all three of our verbal theories about population growth have been formalised in mathematical models, as shown in Box 1.1. Each model can be represented as one or more differential equations. To predict the time evolution of a quantity under particular circumstances, the equations of the model need to be solved. In the relatively simple cases of unlimited growth, and limited growth of one species, it is possible to solve these equations analytically to give equations for the solutions. These are shown in Figure 1.1a and Figure 1.1b, and validate the conclusions we came to verbally.

In the case of the predator and prey model, analytical solution of its differential equations is not possible and so the equations have to be solved

Box 1.1 Mathematical models

Mathematical models of population growth are classic examples of describing how particular variables in the system under investigation change over space and time according to the given theory.

According to the Malthusian, or exponential, growth model (Malthus, 1798), a population of size $P(t)$ grows in direct proportion to this size. This is expressed by an **ordinary differential equation** that describes the rate of change of P :

$$\frac{dP}{dt} = P/\tau$$

where the proportionality constant is expressed in terms of the time constant, τ , which determines how quickly the population grows. Integration of this equation with respect to time shows that at time t a population with initial size P_0 will have size $P(t)$, given as:

$$P(t) = P_0 \exp(t/\tau).$$

This model is unrealistic as it predicts unlimited growth (Figure 1.1a). A more complex model, commonly used in ecology, that does not have this defect (Verhulst, 1845), is one where the population growth rate dP/dt depends on the Verhulst, or **logistic function** of the population P :

$$\frac{dP}{dt} = P(1 - P/K)/\tau.$$

Here K is the maximum allowable size of the population. The solution to this equation (Figure 1.1b) is:

$$P(t) = \frac{KP_0 \exp(t/\tau)}{K + P_0(\exp(t/\tau) - 1)}.$$

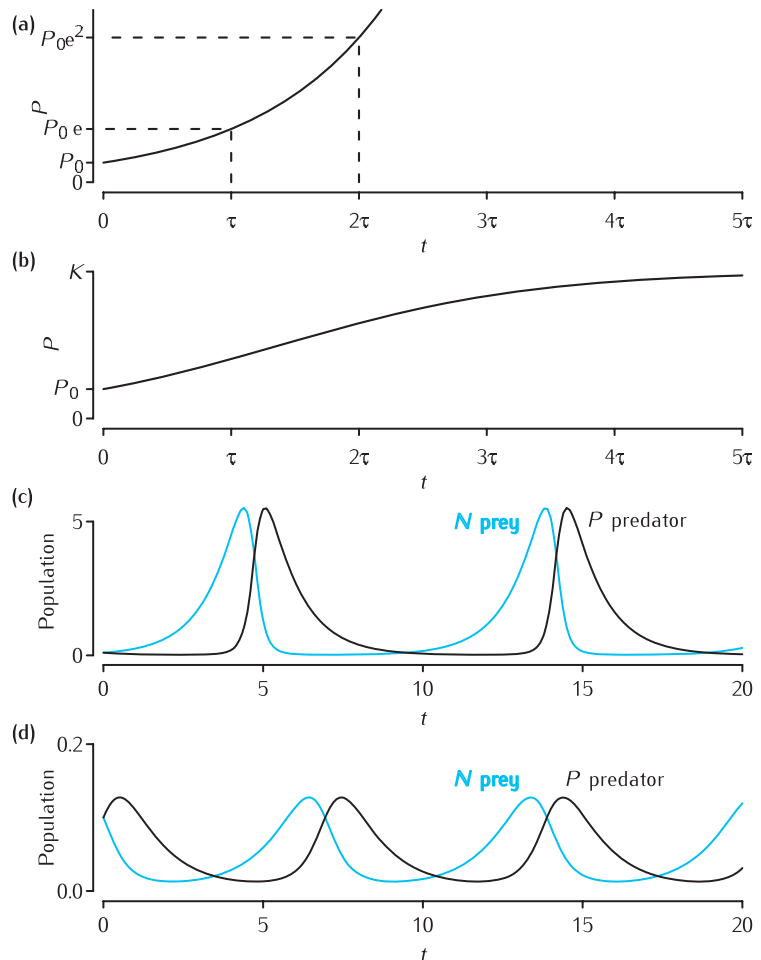
A more complicated situation is where there are two types of species and one is a predator of the other. For a prey population with size $N(t)$ and a predator population with size $P(t)$, it is assumed that (1) the prey population grows in a Malthusian fashion and declines in proportion to the rate at which predator and prey meet (assumed to be the product of the two population sizes, NP); (2) conversely, there is an increase in predator size in proportion to NP and an exponential decline in the absence of prey. This gives the following mathematical model:

$$\frac{dN}{dt} = N(a - bP) \quad \frac{dP}{dt} = P(cN - d).$$

The parameters a , b , c and d are constants. As shown in Figure 1.1c, these equations have periodic solutions in time, depending on the values of these parameters. The two population sizes are out of phase with each other, large prey populations co-occurring with small predator populations, and vice versa. In this model, proposed independently by Lotka (1925) and by Volterra (1926), predation is the only factor that limits growth of the prey population, but the equations can be modified to incorporate other factors. These types of models are used widely in the mathematical modelling of competitive systems found in, for example, ecology and epidemiology.

As can be seen in these three examples, even the simplest models contain parameters whose values are required if the model is to be understood; the number of these parameters can be large and the problem of how to specify their values has to be addressed.

Fig. 1.1 Behaviour of the mathematical models described in Box 1.1. (a) Malthusian, or exponential growth: with increasing time, t , the population size, P , grows increasingly rapidly and without bounds. (b) Logistic growth: the population increases with time, up to a maximum value of K . (c) Behaviour of the Lotka–Volterra model of predator–prey interactions, with parameters $a = b = c = d = 1$. The prey population is shown by the blue line and the predator population by the black line. Since the predator population is dependent on the supply of prey, the predator population size always lags behind the prey size, in a repeating fashion. (d) Behaviour of the Lotka–Volterra model with a second set of parameters: $a = 1$, $b = 20$, $c = 20$ and $d = 1$.



using numerical integration (Appendix B.1). In the past this would have been carried out laboriously by hand and brain, but nowadays, the computer is used. The resulting sizes of predator and prey populations over time are shown in Figure 1.1c. It turns out that neither of our guesses was correct. Instead of both species surviving in equilibrium or going extinct, the predator and prey populations oscillate over time. At the start of each cycle, the prey population grows. After a lag, the predator population starts to grow, due to the abundance of prey. This causes a sharp decrease in prey, which almost causes its extinction, but not quite. Thereafter, the predator population declines and the cycle repeats. In fact, this behaviour is observed approximately in some systems of predators and prey in ecosystems (Edelstein-Keshet, 1988).

In the restatement of the model’s behaviour in words, it might now seem obvious that oscillations would be predicted by the model. However, the step of putting the theory into equations was required in order to reach this understanding. We might disagree with the assumptions encoded in the mathematical model. However, this type of disagreement is better than the inconsistencies between predictions from a verbal theory.

The process of modelling described in this book almost always ends with the calculation of the numerical solution for quantities, such as neuronal membrane potentials. This we refer to as **computational modelling**. A particular mathematical model may have an analytical solution that allows exact calculation of quantities, or may require a numerical solution that approximates the true, unobtainable values.

1.1.2 Why do computational modelling?

As the predator-prey model shows, a well-constructed and useful model is one that can be used to increase our understanding of the phenomena under investigation and to predict reliably the behaviour of the system under the given circumstances. An excellent use of a computational model in neuroscience is Hodgkin and Huxley's simulation of the propagation of a nerve impulse (action potential) along an axon (Chapter 3).

Whilst ultimately a theory will be validated or rejected by experiment, computational modelling is now regarded widely as an essential part of the neuroscientist's toolbox. The reasons for this are:

- (1) Modelling is used as an aid to reasoning. Often the consequences derived from hypotheses involving a large number of interacting elements forming the neural subsystem under consideration can only be found by constructing a computational model. Also, experiments often only provide indirect measurements of the quantities of interest, and models are used to infer the behaviour of the interesting variables. An example of this is given in Box 1.2.
- (2) Modelling removes ambiguity from theories. Verbal theories can mean different things to different people, but formalising them in a mathematical model removes that ambiguity. Use of a mathematical model ensures that the assumptions of the model are explicit and logically consistent. The predictions of what behaviour results from a fully specified mathematical model are unambiguous and can be checked by solving again the equations representing the model.
- (3) The models that have been developed for many neurobiological systems, particularly at the cellular level, have reached a degree of sophistication such that they are accepted as being adequate representations of the neurobiology. Detailed compartmental models of neurons are one example (Chapter 4).
- (4) Advances in computer technology mean that the number of interacting elements, such as neurons, that can be simulated is very large and representative of the system being modelled.
- (5) In principle, testing hypotheses by computational modelling could supplement experiments in some cases. Though experiments are vital in developing a model and setting initial parameter values, it might be possible to use modelling to extend the effective range of experimentation.

Building a computational model of a neural system is not a simple task. Major problems are: deciding what type of model to use; at what level to model; what aspects of the system to model; and how to deal with parameters that have not or cannot be measured experimentally. At each stage of this book we try to provide possible answers to these questions as a guide

Box 1.2 Reasoning with models

An example in neuroscience where mathematical models have been key to reasoning about a system is chemical synaptic transmission. Though more direct experiments are becoming possible, much of what we know about the mechanisms underpinning synaptic transmission must be inferred from recordings of the postsynaptic response. Statistical models of neurotransmitter release are a vital tool.

In the 1950s, the **quantal hypothesis** was put forward by Del Castillo and Katz (1954a) as an aid to explaining data obtained from frog neuromuscular junctions. Release of acetylcholine at the nerve–muscle synapse results in an **endplate potential (EPP)** in the muscle. In the absence of presynaptic activity, spontaneous **miniature endplate potentials (MEPPs)** of relatively uniform size were recorded. The working hypothesis was that the EPPs evoked by a presynaptic action potential actually were made up by the sum of very many MEPPs, each of which contributed a discrete amount, or ‘quantum’, to the overall response. The proposed underlying model is that the mean amplitude of the evoked EPP, V_e , is given by:

$$V_e = npq,$$

where n quanta of acetylcholine are available to be released. Each can be released with a mean probability p , though individual release probabilities may vary across quanta, contributing an amount q , the **quantal amplitude**, to the evoked EPP (Figure 1.2a).

To test their hypothesis, Del Castillo and Katz (1954a) reduced synaptic transmission by lowering calcium and raising magnesium in their experimental preparation, allowing them to evoke and record small EPPs, putatively made up of only a few quanta. If the model is correct, then the mean number of quanta released per EPP, m , should be:

$$m = np.$$

Given that n is large and p is very small, the number released on a trial-by-trial basis should follow a Poisson distribution (Appendix B.3) such that the probability that x quanta are released on a given trial is (Figure 1.2b):

$$P(x) = (m^x/x!) \exp(-m).$$

This leads to two different ways of obtaining a value for m from the experimental data. Firstly, m is the mean amplitude of the evoked EPPs divided by the quantal amplitude, $m \equiv \bar{V}_e/q$, where q is the mean amplitude of recorded miniature EPPs. Secondly, the recording conditions result in many complete failures of release, due to the low release probability. In the Poisson model the probability of no release, $P(0)$, is $P(0) = \exp(-m)$, leading to $m = -\ln(P(0))$. $P(0)$ can be estimated as (number of failures)/(number of trials). If the model is correct, then these two ways of determining m should agree with each other:

$$m \equiv \bar{V}_e/q = \ln \frac{\text{trials}}{\text{failures}}.$$

Plots of the experimental data confirmed that this was the case (Figure 1.2c), lending strong support for the quantal hypothesis.

Such **quantal analysis** is still a major tool in analysing synaptic responses, particularly for identifying the pre- and postsynaptic loci of biophysical changes underpinning short- and long-term synaptic plasticity (Ran *et al.*, 2009; Redman, 1990). More complex and dynamic models are explored in Chapter 7.

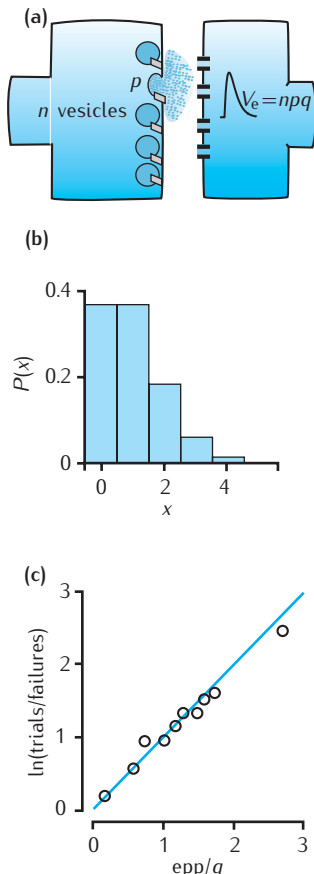


Fig. 1.2 (a) Quantal hypothesis of synaptic transmission. (b) Example Poisson distribution of the number of released quanta when $m = 1$. (c) Relationship between two estimates of the mean number of released quanta at a neuromuscular junction. Blue line shows where the estimates would be identical. Plotted from data in Table 1 of Del Castillo and Katz (1954a), following their Figure 6.

to the modelling process. Often, there is no single correct answer, but is a matter of skilled and informed judgement.

1.1.3 Levels of analysis

To understand the nervous system requires analysis at many different levels (Figure 1.3), from molecules to behaviour, and computational models exist at all levels. The nature of the scientific question that drives the modelling work will largely determine the level at which the model is to be constructed. For example, to model how ion channels open and close requires a model in which ion channels and their dynamics are represented; to model how information is stored in the cerebellar cortex through changes in synaptic strengths requires a model of the cerebellar circuitry involving interactions between nerve cells through modifiable synapses.

1.1.4 Levels of detail

Models that are constructed at the same level of analysis may be constructed to different levels of detail. For example, some models of the propagation of electrical activity along the axon assume that the electrical impulse can be represented as a square pulse train; in some others the form of the impulse is modelled more precisely as the voltage waveform generated by the opening and closing of sodium and potassium channels. The level of detail adopted also depends on the question being asked. An investigation into how the relative timing of the synaptic impulses arriving along different axons affects the excitability of a target neuron may only require knowledge of the impulse arrival times, and not the actual impulse waveform.

Whatever the level of detail represented in a given model, there is always a more detailed model that can be constructed, and so ultimately how detailed the model should be is a matter of judgement. The modeller is faced perpetually with the choice between a more realistic model with a large number of parameter values that have to be assigned by experiment or by other means, and a less realistic but more tractable model with few undetermined parameters. The choice of what level of detail is appropriate for the model is also a question of practical necessity when running the model on the computer; the more details there are in the model, the more computationally expensive the model is. More complicated models also require more effort, and lines of computer code, to construct.

As with experimental results, it should be possible to reproduce computational results from a model. The ultimate test of reproducibility is to read the description of a model in a scientific paper, and then redo the calculations, possibly by writing a new version of the computer code, to produce the same results. A weaker test is to download the original computer code of the model, and check that the code is correct, i.e. that it does what is described of it in the paper. The difficulty of both tests of reproducibility increases with the complexity of the model. Thus, a more detailed model is not necessarily a better model. Complicating the model needs to be justified as much as simplifying it, because it can sometimes come at the cost of understandability.

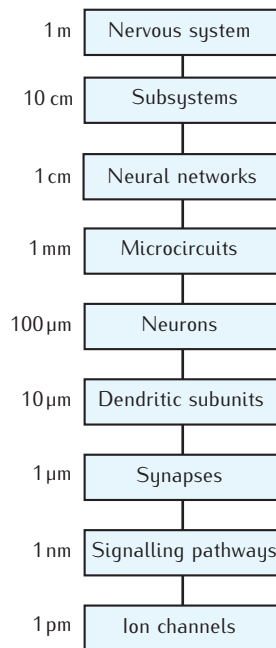


Fig. 1.3 To understand the nervous system requires an understanding at many different levels, at spatial scales ranging from metres to nanometres or smaller. At each of these levels there are detailed computational models for how the elements at that level function and interact, be they, for example, neurons, networks of neurons, synapses or molecules involved in signalling pathways.

In deciding how much detail to include in a model we could take guidance from Albert Einstein, who is reported as saying 'Make everything as simple as possible, but not simpler.'

1.1.5 Parameters

A key aspect of computational modelling is in determining values for model parameters. Often these will be estimates at best, or even complete guesses. Using the model to show how sensitive a solution is to the varying parameter values is a crucial use of the model.

Returning to the predator-prey model, Figure 1.1c shows the behaviour of only one of an infinitely large range of models described by the final equation in Box 1.1. This equation contains four **parameters**, a , b , c and d . A parameter is a constant in a mathematical model which takes a particular value when producing a numerical solution of the equations, and which can be adjusted between solutions. We might argue that this model only produced oscillations because of the set of parameter values used, and try to find a different set of parameter values that gives steady state behaviour. In Figure 1.1d the behaviour of the model with a different set of parameter values is shown; there are still oscillations in the predator and prey populations, though they are at a different frequency.

In order to determine whether or not there are parameter values for which there are no oscillations, we could try to search the **parameter space**, which in this case is made up of all possible values of a , b , c and d in combination. As each value can be any real number, there are an infinite number of combinations. To restrict the search, we could vary each parameter between, say, 0.1 and 10 in steps of 0.1, which gives 100 different values for each parameter. To search all possible combinations of the four parameters would therefore require 100^4 (100 million) numerical solutions to the equations. This is clearly a formidable task, even with the aid of computers.

In the case of this particular simple model, the mathematical method of stability analysis can be applied (Appendix B.2). This analysis shows that there are oscillations for *all* parameter settings.

Often the models we devise in neuroscience are considerably more complex than this one, and mathematical analysis is of less help. Furthermore, the equations in a mathematical model often contain a large number of parameters. While some of the values can be specified (for example, from experimental data), usually not all parameter values are known. In some cases, additional experiments can be run to determine some values, but many parameters will remain **free parameters** (i.e. not known in advance).

How to determine the values of free parameters is a general modelling issue, not exclusive to neuroscience. An essential part of the modeller's toolkit is a set of techniques that enable free parameter values to be estimated. Amongst these techniques are:

Optimisation techniques: automatic methods for finding the set of parameter values for which the model's output best fits known experimental data. This assumes that such data is available and that suitable measures of goodness of fit exist. Optimisation involves changing parameter values systematically so as to improve the fit between simulation and experiment. Issues such as the uniqueness of the fitted parameter values then also arise.

Sensitivity analysis: finding the parameter values that give stable solutions to the equations; that is, values that do not change rapidly as the parameter values are changed very slightly.

Constraint satisfaction: use of additional equations which express global constraints (such as, that the total amount of some quantity is conserved). This comes at the cost of introducing more assumptions into the model.

Educated guesswork: use of knowledge of likely values. For example, it is likely that the reversal potential of potassium is around -80 mV in many neurons in the central nervous system (CNS). In any case, results of any automatic parameter search should always be subject to a ‘sanity test’. For example, we ought to be suspicious if an optimisation procedure suggested that the reversal potential of potassium was hundreds of millivolts.

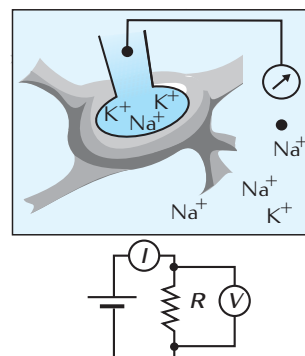
1.2 | Overview of the book

Most of this book is concerned with models designed to understand the electrophysiology of the nervous system in terms of the propagation of electrical activity in nerve cells. We describe a series of computational models, constructed at different levels of analysis and detail.

The level of analysis considered ranges from ion channels to networks of neurons, grouped around models of the nerve cell. Starting from a basic description of membrane biophysics (Chapter 2), a well-established model of the nerve cell is introduced (Chapter 3). In Chapters 4–7 the modelling of the nerve cell in more and more detail is described: modelling approaches in which neuronal morphology can be represented (Chapter 4); the modelling of ion channels (Chapter 5); or intracellular mechanisms (Chapter 6); and of the synapse (Chapter 7). We then look at issues surrounding the construction of simpler neuron models (Chapter 8). One of the reasons for simplifying is to enable networks of neurons to be modelled, which is the subject of Chapter 9.

Whilst all these models embody assumptions, the premises on which they are built (such as that electrical signalling is involved in the exchange of information between nerve cells) are largely accepted. This is not the case for mathematical models of the developing nervous system. In Chapter 10 we give a selective review of some models of neural development, to highlight the diversity of models and assumptions in this field of modelling.

Chapter 2, The basis of electrical activity in the neuron, describes the physical basis for the concepts used in modelling neural electrical activity. A semipermeable membrane, along with ionic pumps which maintain different concentrations of ions inside and outside the cell, results in an electrical potential across the membrane. This membrane can be modelled as an electrical circuit comprising a resistor, a capacitor and a battery in parallel. It is assumed that the resistance does not change; this is called a passive model. Whilst it is now known that the passive model is too simple a mathematical description of real neurons, this approach is useful in assessing how specific



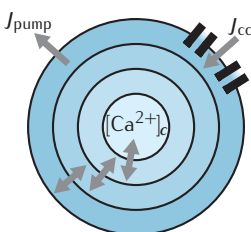
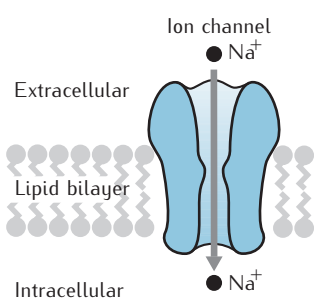
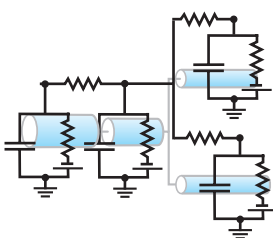
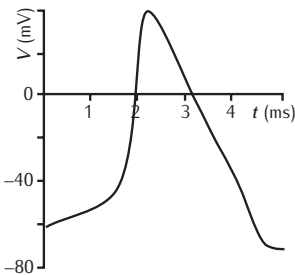
passive properties, such as those associated with membrane resistance, can affect the membrane potential over an extended piece of membrane.

Chapter 3, The Hodgkin–Huxley model of the action potential, describes in detail this landmark model for the generation of the nerve impulse in nerve membranes with active properties; i.e. the effects on membrane potential of the voltage-gated ion channels are now included in the model. This model is widely heralded as the first successful example of combining experimental and computational studies in neuroscience. In the late 1940s the newly invented voltage clamp technique was used by Hodgkin and Huxley to produce the experimental data required to construct a set of mathematical equations representing the movement of independent gating particles across the membrane thought to control the opening and closing of sodium and potassium channels. The efficacy of these particles was assumed to depend on the local membrane potential. These equations were then used to calculate the form of the action potentials in the squid giant axon. Whilst subsequent work has revealed complexities that Hodgkin and Huxley could not consider, today their formalism remains a useful and popular technique for modelling channel types.

Chapter 4, Compartmental models, shows how to model complex dendritic and axonal morphology using the multi-compartmental approach. The emphasis is on deriving the passive properties of neurons, although some of the issues surrounding active channels are discussed, in anticipation of a fuller treatment in Chapter 5. We discuss how to construct a compartmental model from a given morphology and how to deal with measurement errors in experimentally determined morphologies. Close attention is paid to modelling incomplete data, parameter fitting and parameter value searching.

Chapter 5, Models of active ion channels, examines the consequences of introducing into a model of the neuron the many types of active ion channel known in addition to the sodium and potassium voltage-gated ion channels studied in Chapter 3. There are two types of channel, those gated by voltage and those gated by ligands, such as calcium. In this chapter we present methods for modelling the kinetics of both types of channel. We do this by extending the formulation used by Hodgkin and Huxley of an ion channel in terms of independent gating particles. This formulation is the basis for the thermodynamic models, which provide functional forms for the rate coefficients determining the opening and closing of ion channels that are derived from basic physical principles. To improve on the fits to data offered by models with independent gating particles, the more flexible Markov model is then introduced, where it is assumed that a channel can exist in a number of different states ranging from fully open to fully closed.

Chapter 6, Intracellular mechanisms. Ion channel dynamics are influenced heavily by intracellular ionic signalling. Calcium plays a particularly important role and models for several different ways in which calcium is known to have an effect have been developed. We investigate models of signalling involving calcium: via the influx of calcium ions through voltage-gated channels; their release from second messenger and calcium-activated stores; intracellular diffusion; and buffering and extrusion by calcium pumps. Essential background material on the mathematics of



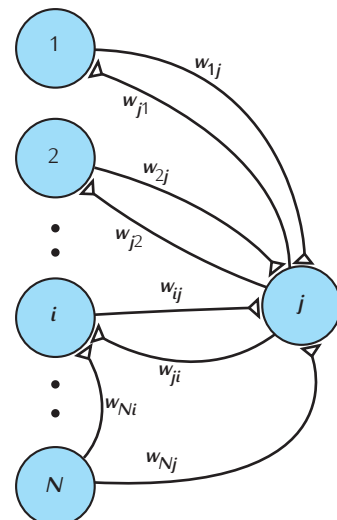
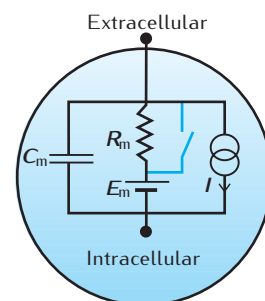
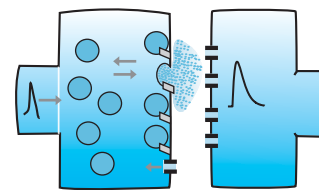
diffusion and electrodiffusion is included. We then review models for other intracellular signalling pathways which involve more complex enzymatic reactions and cascades. We introduce the well-mixed approach to modelling these pathways and explore its limitations. The elements of more complex stochastic and spatial techniques for modelling protein interactions are given, including use of the Monte Carlo scheme.

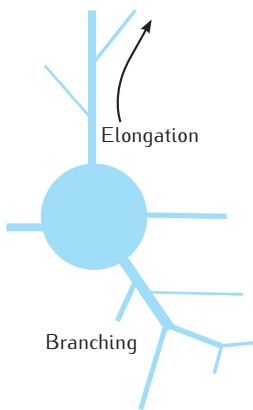
Chapter 7, The synapse, examines a range of models of chemical synapses. Different types of model are described, with different degrees of complexity. These range from electrical circuit-based schemes designed to replicate the change in electrical potential in response to synapse stimulation to more detailed kinetic schemes and to complex Monte Carlo models including vesicle recycling and release. Models with more complex dynamics are then considered. Simple static models that produce the same postsynaptic response for every presynaptic action potential are compared with more realistic models incorporating short-term dynamics producing facilitation and depression of the postsynaptic response. Different types of excitatory and inhibitory chemical synapses, including AMPA and NMDA, are considered. Models of electrical synapses are discussed.

Chapter 8, Simplified models of neurons, signals a change in emphasis. We examine the issues surrounding the construction of models of single neurons that are simpler than those described already. These simplified models are particularly useful for incorporating in networks since they are computationally more efficient, and in some cases they can be analysed mathematically. A spectrum of models is considered, including reduced compartmental models and models with a reduced number of gating variables. These simplifications make it easier to analyse the function of the model using the dynamical systems analysis approach. In the even simpler integrate-and-fire model, there are no gating variables, with action potentials being produced when the membrane potential crosses a threshold. At the simplest end of the spectrum, rate-based models communicate via firing rates rather than individual spikes. Various applications of these simplified models are given and parallels between these models and those developed in the field of neural networks are drawn.

Chapter 9, Networks of neurons. In order to construct models of networks of neurons, many simplifications will have to be made. How many neurons are to be in the modelled network? Should all the modelled neurons be of the same or different functional type? How should they be positioned and interconnected? These are some of the questions to be asked in this important process of simplification. To illustrate approaches to answering these questions, various example models are discussed, ranging from models where an individual neuron is represented as a two-state device to models in which model neurons of the complexity of detail discussed in Chapters 2–7 are coupled together. The advantages and disadvantages of these different types of model are discussed.

Chapter 10, The development of the nervous system. The emphasis in Chapters 2–9 has been on how to model the electrical and chemical properties of nerve cells and the distribution of these properties over the complex structures that make up the individual neurons of the nervous system and their connections. The existence of the correct neuroanatomy is





essential for the proper functioning of the nervous system, and here we discuss computational modelling work that addresses the development of this anatomy. There are many stages of neural development and computational models for each stage have been constructed. Amongst the issues that have been addressed are: how the nerve cells become positioned in 3D space; how they develop their characteristic physiology and morphology; and how they make the connections with each other. Models for development often contain fundamental assumptions that are as yet untested, such as that nerve connections are formed through correlated neural activity. This means that the main use of such models is in testing out the theory for neural development embodied in the model, rather than using an agreed theory as a springboard to test out other phenomena. To illustrate the approaches used in modelling neural development, we describe examples of models for the development of individual nerve cells and for the development of nerve connections. In this latter category we discuss the development of patterns of ocular dominance in visual cortex, the development of retinotopic maps of connections in the vertebrate visual system and a series of models for the development of connections between nerve and muscle.

Chapter 11, Farewell, summarises our views on the current state of computational neuroscience and its future as a tool within neuroscience research. Major efforts to standardise and improve both experimental data and model specifications and dissemination are progressing. These will ensure a rich and expanding future for computational modelling within neuroscience.

The appendices contain overviews and links to computational and mathematical resources. **Appendix A** provides information about neural simulators, databases and tools, most of which are open source. Links to these resources can be found on our website: compneuroprinciples.org. **Appendix B** provides a brief introduction to mathematical methods, including numerical integration of differential equations, dynamical systems analysis, common probability distributions and techniques for parameter estimation.

Some readers may find the material in Chapters 2 and 3 familiar to them already. In this case, at a first reading they may be skipped or just skimmed. However, for others, these chapters will provide a firm foundation for what follows. The remaining chapters, from Chapter 4 onwards, each deal with a specific topic and can be read individually.

Chapter 2

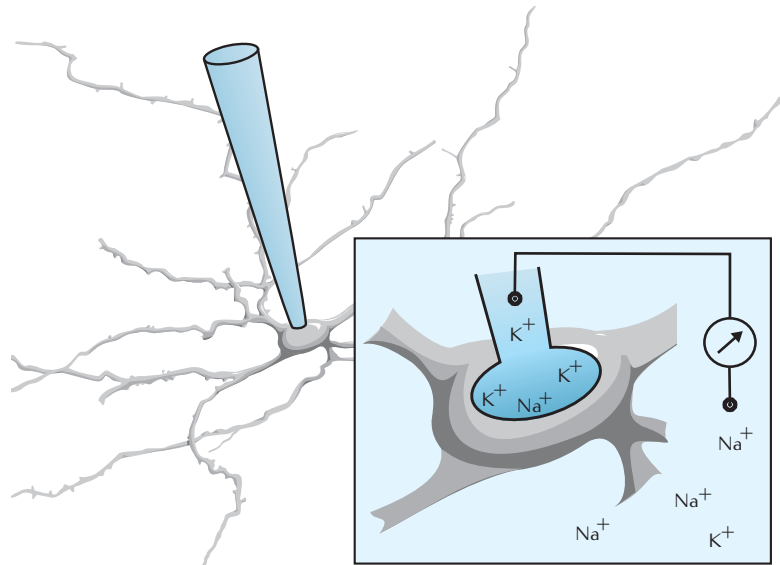
The basis of electrical activity in the neuron

The purpose of this chapter is to introduce the physical principles underlying models of the electrical activity of neurons. Starting with the neuronal cell membrane, we explore how its permeability to different ions and the maintenance by ionic pumps of concentration gradients across the membrane underpin the resting membrane potential. We show how the electrical activity of a small neuron can be represented by equivalent electrical circuits, and discuss the insights this approach gives into the time-dependent aspects of the membrane potential, as well as its limitations. It is shown that spatially extended neurons can be modelled approximately by joining together multiple compartments, each of which contains an equivalent electrical circuit. To model neurons with uniform properties, the cable equation is introduced. This gives insights into how the membrane potential varies over the spatial extent of a neuron.

A nerve cell, or neuron, can be studied at many different levels of analysis, but much of the computational modelling work in neuroscience is at the level of the electrical properties of neurons. In neurons, as in other cells, a measurement of the voltage across the membrane using an intracellular electrode (Figure 2.1) shows that there is an electrical potential difference across the cell membrane, called the **membrane potential**. In neurons the membrane potential is used to transmit and integrate signals, sometimes over large distances. The **resting membrane potential** is typically around -65 mV , meaning that the potential inside the cell is more negative than that outside.

For the purpose of understanding their electrical activity, neurons can be represented as an electrical circuit. The first part of this chapter explains why this is so in terms of basic physical processes such as diffusion and electric fields. Some of the material in this chapter does not appear directly in computational models of neurons, but the knowledge is useful for informing the decisions about what needs to be modelled and the way in which it is modelled. For example, changes in the concentrations of ions sometimes alter the electrical and signalling properties of the cell significantly, but sometimes they are so small that they can be ignored. This chapter will give the information necessary to make this decision.

Fig. 2.1 Differences in the intracellular and extracellular ion compositions and their separation by the cell membrane is the starting point for understanding the electrical properties of the neuron. The inset shows that for a typical neuron in the CNS, the concentration of sodium ions is greater outside the cell than inside it, and that the concentration of potassium ions is greater inside the cell than outside. Inserting an electrode into the cell allows the membrane potential to be measured.

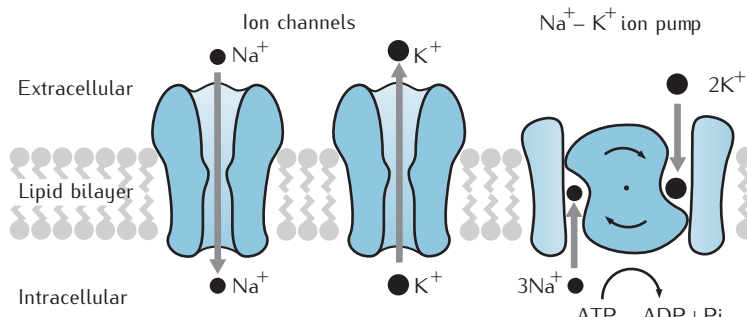


The second part of this chapter explores basic properties of electrical circuit models of neurons, starting with very small neurons and going on to (electrically) large neurons. Although these models are missing many of the details which are added in later chapters, they provide a number of useful concepts, and can be used to model some aspects of the electrical activity of neurons.

2.1 | The neuronal membrane

The electrical properties which underlie the membrane potential arise from the separation of intracellular and extracellular space by a cell membrane. The intracellular medium, **cytoplasm**, and the extracellular medium contain differing concentrations of various ions. Some key inorganic ions in nerve cells are positively charged **cations**, including sodium (Na^+), potassium (K^+), calcium (Ca^{2+}) and magnesium (Mg^{2+}), and negatively charged **anions** such as chloride (Cl^-). Within the cell, the charge carried by anions and cations is usually almost balanced, and the same is true of the extracellular space. Typically, there is a greater concentration of extracellular sodium than intracellular sodium, and conversely for potassium, as shown in Figure 2.1.

The key components of the membrane are shown in Figure 2.2. The bulk of the membrane is composed of the 5 nm thick **lipid bilayer**. It is made up of two layers of lipids, which have their hydrophilic ends pointing outwards and their hydrophobic ends pointing inwards. It is virtually impermeable to water molecules and ions. This impermeability can cause a net build-up of positive ions on one side of the membrane and negative ions on the other. This leads to an electrical field across the membrane, similar to that found between the plates of an ideal electrical capacitor (Table 2.1).



Ion channels are pores in the lipid bilayer, made of proteins, which can allow certain ions to flow through the membrane. A large body of biophysical work, starting with the work of Hodgkin and Huxley (1952d) described in Chapter 3 and summarised in Chapter 5, has shown that many types of ion channels, referred to as **active channels**, can exist in open states, where it is possible for ions to pass through the channel, and closed states, in which ions cannot permeate through the channel. Whether an active channel is in an open or closed state may depend on the membrane potential, ionic concentrations or the presence of bound ligands, such as neurotransmitters. In contrast, **passive channels** do not change their permeability in response to changes in the membrane potential. Sometimes a channel's dependence on the membrane potential is so mild as to be virtually passive.

Both passive channels and active channels in the open state exhibit **selective permeability** to different types of ion. Channels are often labelled by the ion to which they are most permeable. For example, potassium channels

Fig. 2.2 Constituents of the membrane. Three types of component play important electrical roles in a neuron's membrane. The lipid bilayer forms a virtually impermeable barrier for inorganic ions. The ion channel is a protein or cluster of proteins that form a pore through the membrane, allowing certain ions to pass through. The ionic pump, or ion exchanger, pumps or exchanges certain ion types across the membrane. This example shows the Na^+-K^+ pump which exchanges three Na^+ ions from inside with two K^+ ions from outside using the energy from the hydrolysis of ATP into ADP and a phosphate ion.

Table 2.1 Review of electrical circuit components. For each component, the circuit symbol, the mathematical symbol, the SI unit, and the abbreviated form of the SI unit are shown

Component	Symbols and units	Function
Battery		Pumps charge around a circuit E (volts, V)
Current source		Provides a specified current (which may vary with time) I (amps, A)
Resistor		Resists the flow of current in a circuit R (ohms, Ω)
Capacitor		Stores charge. Current flows onto (not through) a capacitor C (farad, F)

primarily allow potassium ions to pass through. There are many types of ion channel, each of which has a different permeability to each type of ion.

In this chapter, how to model the flow of ions through passive channels is considered. The opening and closing of active channels is a separate topic, which is covered in detail in Chapters 3 and 5; the concepts presented in this chapter are fundamental to describing the flow of ions through active channels in the open state. It will be shown how the combination of the selective permeability of ion channels and ionic concentration gradients lead to the membrane having properties that can be approximated by ideal resistors and batteries (Table 2.1). This approximation and a fuller account of the electrical properties arising from the permeable and impermeable aspects of the membrane are explored in Sections 2.3–2.5.

Ionic pumps are membrane-spanning protein structures that actively pump specific ions and molecules in and out of the cell. Particles moving freely in a region of space always move so that their concentration is uniform throughout the space. Thus, on the high concentration side of the membrane, ions tend to flow to the side with low concentration, thus diminishing the concentration gradient. Pumps counteract this by pumping ions against the concentration gradient. Each type of pump moves a different combination of ions. The sodium–potassium exchanger pushes K^+ into the cell and Na^+ out of the cell. For every two K^+ ions pumped into the cell, three Na^+ ions are pumped out. This requires energy, which is provided by the hydrolysis of one molecule of adenosine triphosphate (ATP), a molecule able to store and transport chemical energy within cells. In this case, there is a net loss of charge in the neuron, and the pump is said to be electrogenic. An example of a pump which is not electrogenic is the sodium–hydrogen exchanger, which pumps one H^+ ion out of the cell against its concentration gradient for every Na^+ ion it pumps in. In this pump, Na^+ flows down its concentration gradient, supplying the energy required to extrude the H^+ ion; there is no consumption of ATP. Other pumps, such as the sodium–calcium exchanger, are also driven by the Na^+ concentration gradient (Blaustein and Hodgkin, 1969). These pumps consume ATP indirectly as they increase the intracellular Na^+ concentration, giving the sodium–potassium exchanger more work to do.

In this chapter, ionic pumps are not considered explicitly; rather we assume steady concentration gradients of each ion type. The effects of ionic pumps are considered in more detail in Chapter 6.

2.2 | Physical basis of ion movement in neurons

The basis of electrical activity in neurons is movement of ions within the cytoplasm and through ion channels in the cell membrane. Before proceeding to fully fledged models of electrical activity, it is important to understand the physical principles which govern the movement of ions through channels and within neurites, the term we use for parts of axons or dendrites.

Firstly, the electric force on ions is introduced. We then look at how to describe the diffusion of ions in solution from regions of high to low

concentration in the absence of an electric field. This is a first step to understanding movement of ions through channels. We go on to look at electrical drift, caused by electric fields acting on ions which are concentrated uniformly within a region. This can be used to model the movement of ions longitudinally through the cytoplasm. When there are both electric fields and non-uniform ion concentrations, the movement of the ions is described by a combination of electrical drift and diffusion, termed **electrodiffusion**. This is the final step required to understand the passage of ions through channels. Finally, the relationship between the movement of ions and electrical current is described.

2.2.1 The electric force on ions

As ions are electrically charged they exert forces on and experience forces from other ions. The force acting on an ion is proportional to the ion's charge, q . The **electric field** at any point in space is defined as the force experienced by an object with a unit of positive charge. A positively charged ion in an electric field experiences a force acting in the direction of the electric field; a negatively charged ion experiences a force acting in exactly the opposite direction to the electric field (Figure 2.3). At any point in an electric field a charge has an electrical potential energy. The difference in the potential energy per unit charge between any two points in the field is called the **potential difference**, denoted V and measured in volts.

A simple example of an electric field is the one that can be created in a parallel plate capacitor (Figure 2.4). Two flat metal plates are arranged so they are facing each other, separated by an electrical insulator. One of the plates is connected to the positive terminal of a battery and the other to the negative terminal. The battery attracts electrons (which are negatively charged) into its positive terminal and pushes them out through its negative terminal. The plate connected to the negative terminal therefore has an excess of negative charge on it, and the plate connected to the positive terminal has an excess of positive charge. The separation of charges sets up an electric field between the plates of the capacitor.

Because of the relationship between electric field and potential, there is also a potential difference across the charged capacitor. The potential difference is equal to the **emf** of the battery. For example, a battery with an emf of 1.5 V creates a potential difference of 1.5 V between the plates of the capacitor.

The strength of the electric field set up through the separation of ions between the plates of the capacitor is proportional to the magnitude of the excess charge q on the plates. As the potential difference is proportional to the electric field, this means that the charge is proportional to the potential difference. The constant of proportionality is called the **capacitance** and is measured in **farads**. It is usually denoted by C and indicates how much charge can be stored on a particular capacitor for a given potential difference across it:

$$q = CV. \quad (2.1)$$

Capacitance depends on the electrical properties of the insulator and size and distance between the plates.

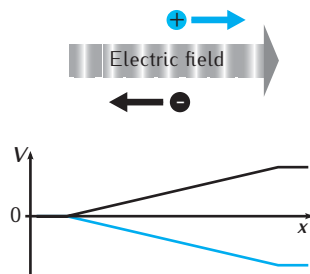


Fig. 2.3 The forces acting on both positively and negatively charged ions placed within an electric field. The potential difference V between the left-hand side of the field and points along the x axis is shown for the positively charged ion (in blue) and the negatively charged ion (in black).

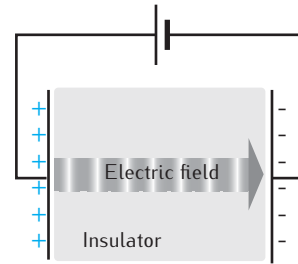


Fig. 2.4 A charged capacitor creates an electric field.

The capacitance of an ideal parallel plate capacitor is proportional to the area a of the plates and inversely proportional to the distance d between the plates:

$$C = \frac{a}{\epsilon d}$$

where ϵ is the permittivity of the insulator, a measure of how hard it is to form an electric field in the material.

Box 2.1 Voltage and current conventions in cells

By convention, the membrane potential, the potential difference across a cell membrane, is defined as the potential inside the cell minus the potential outside the cell. The convention for current flowing through the membrane is that it is defined to be *positive* when there is a flow of positive charge *out* of the cell, and to be *negative* when there is a net flow of positive charge *into* the cell.

According to these conventions, when the inside of the cell is more positively charged than the outside, the membrane potential is positive. Positive charges in the cell will be repelled by the other positive charges in the cell, and will therefore have a propensity to move out of the cell. Any movement of positive charge out of the cell is regarded as a positive current. It follows that a positive membrane potential tends to lead to a positive current flowing across the membrane. Thus, the voltage and current conventions fit with the notion that current flows from higher to lower voltages.

It is also possible to define the membrane potential as the potential outside minus the potential inside. This is an older convention and is not used in this book.

2.2.2 Diffusion

Individual freely moving particles, such as dissociated ions, suspended in a liquid or gas appear to move randomly, a phenomenon known as **Brownian motion**. However, in the behaviour of large groups of particles, statistical regularities can be observed. **Diffusion** is the net movement of particles from regions in which they are highly concentrated to regions in which they have low concentration. For example, when ink drips into a glass of water, initially a region of highly concentrated ink will form, but over time this will spread out until the water is uniformly coloured. As shown by Einstein (1905), **diffusion, a phenomenon exhibited by groups of particles, actually arises from the random movement of individual particles**. The rate of diffusion depends on characteristics of the diffusing particle and the medium in which it is diffusing. It also depends on temperature; the higher the temperature, the more vigorous the Brownian motion and the faster the diffusion.

In the ink example molecules diffuse in three dimensions, and the concentration of the molecule in a small region changes with time until the final steady state of uniform concentration is reached. In this chapter, we need to understand how molecules diffuse from one side of the membrane to the other through channels. The channels are barely wider than the diffusing molecules, and so can be thought of as being one-dimensional.

The concentration of an arbitrary molecule or ion X is denoted [X]. When [X] is different on the two sides of the membrane, molecules will diffuse through the channels down the concentration gradient, from the side with higher concentration to the side with lower concentration (Figure 2.5). **Flux** is the amount of X that flows through a cross-section of unit area per unit time. Typical units for flux are $\text{mol cm}^{-2} \text{s}^{-1}$, and its sign

Concentration is typically measured in moles per unit volume. One mole contains Avogadro's number (approximately 6.02×10^{23}) atoms or molecules. **Molarity** denotes the number of moles of a given substance per litre of solution (the units are mol L^{-1} , often shortened to M).

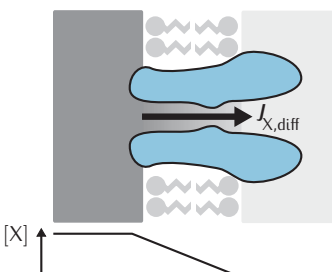


Fig. 2.5 Fick's first law in the context of an ion channel spanning a neuronal membrane.

depends on the direction in which the molecules are flowing. To fit in with our convention for current (Box 2.1), we define the flux as positive when the flow of molecules is out of the cell, and negative when the flow is inward. Fick (1855) provided an empirical description relating the molar flux, $J_{X,\text{diff}}$, arising from the diffusion of a molecule X, to its concentration gradient $d[X]/dx$ (here in one dimension):

$$J_{X,\text{diff}} = -D_X \frac{d[X]}{dx} \quad (2.2)$$

where D_X is defined as the **diffusion coefficient** of molecule X. The diffusion coefficient has units of $\text{cm}^2 \text{s}^{-1}$. This equation captures the notion that larger concentration gradients lead to larger fluxes. The negative sign indicates that the flux is in the opposite direction to that in which the concentration gradient increases; that is, molecules flow from high to low concentrations.

2.2.3 Electrical drift

Although they experience a force due to being in an electric field, ions on the surface of a membrane are not free to move across the insulator which separates them. In contrast, ions in the cytoplasm and within channels are able to move. Our starting point for thinking about how electric fields affect ion mobility is to consider a narrow cylindrical tube in which there is a solution containing positively and negatively charged ions such as K^+ and Cl^- . The concentration of both ions in the tube is assumed to be uniform, so there is no concentration gradient to drive diffusion of ions along the tube. Apart from lacking intracellular structures such as microtubules, the endoplasmic reticulum and mitochondria, this tube is analogous to a section of neurite.

Now suppose that electrodes connected to a battery are placed in the ends of the tube to give one end of the tube a higher electrical potential than the other, as shown in Figure 2.6. The K^+ ions will experience an electrical force pushing them down the potential gradient, and the Cl^- ions, because of their negative charge, will experience an electrical force in the opposite direction. If there were no other molecules present, both types of ion would accelerate up or down the neurite. But the presence of other molecules causes frequent collisions with the K^+ and Cl^- ions, preventing them from accelerating. The result is that both K^+ and Cl^- molecules travel at an average speed (**drift velocity**) that depends on the strength of the field. Assuming there is no concentration gradient of potassium or chloride, the flux is:

$$J_{X,\text{drift}} = -\frac{D_X F}{RT} z_X [X] \frac{dV}{dx} \quad (2.3)$$

where z_X is the ion's signed **valency** (the charge of the ion measured as a multiple of the elementary charge). The other constants are: R , the gas constant; T , the temperature in kelvins; and F , Faraday's constant, which is the charge per mole of monovalent ions.

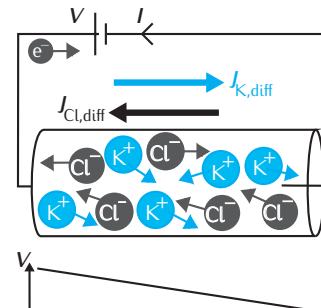


Fig. 2.6 Electrical drift. The cylinder represents a section of neurite containing positively charged potassium ions and negatively charged chloride ions. Under the influence of a potential difference between the ends, the potassium ions tend to drift towards the positive terminal and the chloride ions towards the negative terminal. In the wire the current is transported by electrons.

z_X is +2 for calcium ions, +1 for potassium ions and -1 for chloride ions.

$$R = 8.314 \text{ J K}^{-1} \text{ mol}^{-1}$$

$$F = 9.648 \times 10^4 \text{ C mol}^{-1}$$

The universal convention is to use the symbol R to denote both the gas constant and electrical resistance. However, what R is referring to is usually obvious from the context: when R refers to the universal gas constant, it is very often next to temperature T .

2.2.4 Electrodiffusion

Diffusion describes the movement of ions due to a concentration gradient alone, and electrical drift describes the movement of ions in response to a potential gradient alone. To complete the picture, we consider **electrodiffusion**, in which both voltage and concentration gradients are present, as is usually the case in ion channels. The total flux of an ion X, J_X , is simply the sum of the diffusion and drift fluxes from Equations 2.2 and 2.3:

$$J_X = J_{X,\text{diff}} + J_{X,\text{drift}} = -D_X \left(\frac{d[X]}{dx} + \frac{z_X F}{RT} [X] \frac{dV}{dx} \right). \quad (2.4)$$

This equation, developed by Nernst (1888) and Planck (1890), is called the **Nernst–Planck equation** and is a general description of how charged ions move in solution in electric fields. It is used to derive the expected relationships between the membrane potential and ionic current flowing through channels (Section 2.4).

2.2.5 Flux and current density

So far, movement of ions has been quantified using flux, the number of moles of an ion flowing through a cross-section of unit area. However, often we are interested in the flow of the charge carried by molecules rather than the flow of the molecules themselves. The amount of positive charge flowing per unit of time past a point in a conductor, such as an ion channel or neurite, is called **current** and is measured in amperes (denoted A). The **current density** is the amount of charge flowing per unit of time per unit of cross-sectional area. In this book, we denote current density with the symbol I , with typical units $\mu\text{A cm}^{-2}$.

The current density I_X due to a particular ion X is proportional to the molar flux of that ion and the charge that it carries. We can express this as:

$$I_X = F z_X J_X \quad (2.5)$$

where F is Faraday's constant and z_X is the ion's signed valency. As with the flux of an ion, the sign of the current depends on the direction in which the charged particles are flowing. As defined earlier, the flux of molecules or ions through channels is positive when they are flowing out of the cell. Thus, the current due to positively charged ions, such as Na^+ and K^+ , will be positive when they are flowing out of the cell, and negative when they flow into the cell, since z_X is positive for these ions. However, for negatively charged ions, such as Cl^- , when their flux is positive the current they carry is negative, and vice versa. A negative ion flowing into the cell has the same effect on the net charge balance as a positive ion flowing out of it.

The total current density flowing in a neurite or through a channel is the sum of the contributions from the individual ions. For example, the total ion flow due to sodium, potassium and chloride ions is:

$$I = I_{\text{Na}} + I_{\text{K}} + I_{\text{Cl}} = F z_{\text{Na}} J_{\text{Na}} + F z_{\text{K}} J_{\text{K}} + F z_{\text{Cl}} J_{\text{Cl}}. \quad (2.6)$$

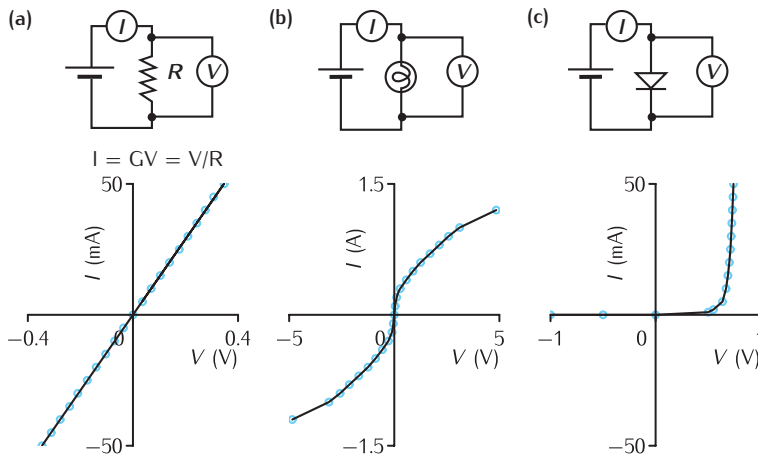


Fig. 2.7 *I*-*V* characteristics of a number of electrical devices. In a typical high-school experiment to determine the *I*-*V* characteristics of various components, the voltage *V* across the component is varied, and the current *I* flowing through the component is measured using an ammeter. *I* is then plotted against *V*. (a) The *I*-*V* characteristic of a 1 m length of wire, which shows that in the wire the current is proportional to the voltage. Thus the wire obeys Ohm's law in the range measured. The constant of proportionality is the conductance *G*, which is measured in siemens. The inverse of the conductance is resistance *R*, measured in ohms. Ohm's law is thus $I = V/R$. (b) The *I*-*V* characteristic of a filament light bulb. The current is not proportional to the voltage, at least in part due to the temperature effects of the bulb being hotter when more current flows through it. (c) The *I*-*V* characteristic of a silicon diode. The magnitude of the current is much greater when the voltage is positive than when it is negative. As it is easier for the current to flow in one direction than the other, the diode exhibits rectification. Data from unpublished A-level physics practical, undertaken by Sterrett, 1989.

2.2.6 *I*-*V* characteristics

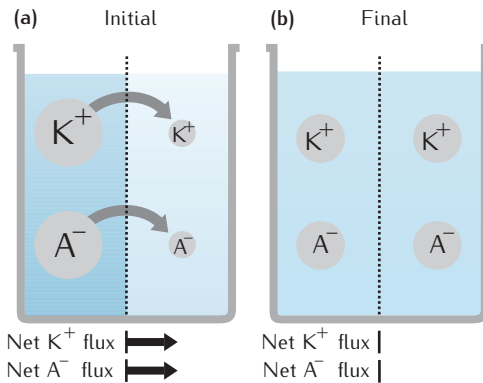
Returning to the case of electrodiffusion along a neurite (Section 2.2.4), Equations 2.3 and 2.6 show that the current flowing along the neurite, referred to as the **axial current**, should be proportional to the voltage between the ends of the neurite. Thus the axial current is expected to obey **Ohm's law** (Figure 2.7a), which states that, at a fixed temperature, the current *I* flowing through a conductor is proportional to the potential difference *V* between the ends of the conductor. The constant of proportionality *G* is the **conductance** of the conductor in question, and its reciprocal *R* is known as the **resistance**. In electronics, an ideal resistor obeys Ohm's law, so we can use the symbol for a resistor to represent the electrical properties along a section of neurite.

It is worth emphasising that Ohm's law does not apply to all conductors. Conductors that obey Ohm's law are called **ohmic**, whereas those that do not are **non-ohmic**. Determining whether an electrical component is ohmic or not can be done by applying a range of known potential differences across it and measuring the current flowing through it in each case. The resulting plot of current versus potential is known as an ***I*-*V* characteristic**. The *I*-*V* characteristic of a component that obeys Ohm's law is a straight line passing through the origin, as demonstrated by the *I*-*V* characteristic of a wire shown in Figure 2.7a. The *I*-*V* characteristic of a filament light bulb, shown in Figure 2.7b, demonstrates that in some components, the current is not proportional to the voltage, with the resistance going up as the voltage increases. The filament may in fact be an ohmic conductor, but this could be masked in this experiment by the increase in the filament's temperature as the amount of current flowing through it increases.

An example of a truly non-ohmic electrical component is the diode, where, in the range tested, current can flow in one direction only (Figure 2.7c). This is an example of **rectification**, the property of allowing current to flow more freely in one direction than another.

While the flow of current along a neurite is approximately ohmic, the flow of ions through channels in the membrane is not. The reason for this difference is that there is a diffusive flow of ions across the membrane due to

Fig. 2.8 Setup of a thought experiment to explore the effects of diffusion across the membrane. In this experiment a container is divided by a membrane that is permeable to both K^+ , a cation, and anions, A^- . The grey arrows indicate the diffusion flux of both types of ion. (a) Initially, the concentrations of both K^+ and A^- are greater than their concentrations on the right-hand side. Both molecules start to diffuse through the membrane down their concentration gradients, to the right. (b) Eventually the system reaches an equilibrium.



the concentration difference, as well as the electrical drift due to the potential difference. We explore this in more detail in Section 2.4.

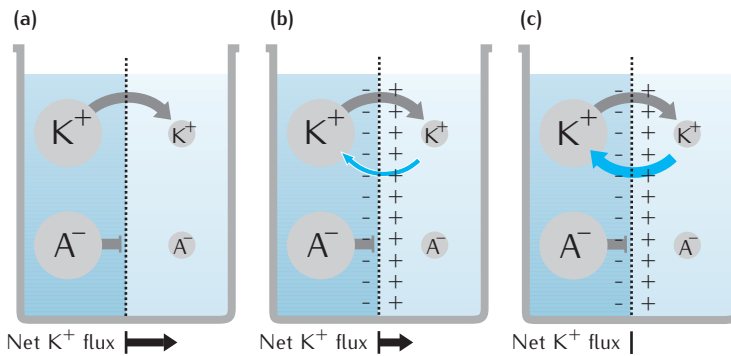
2.3 | The resting membrane potential: the Nernst equation

The ion channels which span the lipid bilayer confer upon the neuronal cell membrane the property of permeability to multiple types of ion. The first step towards understanding the origin of the resting membrane potential is to consider diffusion and electrical drift of ions through the membrane in a sequence of thought experiments.

The initial setup of the first thought experiment, shown in Figure 2.8a, is a container divided into two compartments by a membrane. The left-hand half represents the inside of a cell and the right-hand half the outside. Into the left (intracellular) half we place a high concentration of a potassium solution, consisting of equal numbers of potassium ions, K^+ , and anions, A^- . Into the right (extracellular) half we place a low concentration of the same solution. If the membrane is permeable to both types of ions, both populations of ions will diffuse from the half with a high concentration to the half with a low concentration. This will continue until both halves have the same concentration, as seen in Figure 2.8b. This diffusion is driven by the concentration gradient; as we have seen, where there is a concentration gradient, particles or ions move down the gradient.

In the second thought experiment, we suppose that the membrane is permeable only to K^+ ions and *not* to the anions (Figure 2.9a). In this situation only K^+ ions can diffuse down their concentration gradient (from left to right in this figure). Once this begins to happen, it creates an excess of positively charged ions on the right-hand surface of the membrane and an excess of negatively charged anions on the left-hand surface. As when the plates of a capacitor are charged, this creates an electric field, and hence a potential difference across the membrane (Figure 2.9b).

The electric field influences the potassium ions, causing an electrical drift of the ions back across the membrane opposite to their direction of diffusion (from right to left in the figure). The potential difference across the



membrane grows until it provides an electric field that generates a net electrical drift that is equal and opposite to the net flux resulting from diffusion. Potassium ions will flow across the membrane either by diffusion in one direction or by electrical drift in the other direction until there is no net movement of ions. The system is then at equilibrium, with equal numbers of positive ions flowing rightwards due to diffusion and leftwards due to the electrical drift. At equilibrium, we can measure a stable potential difference across the membrane (Figure 2.9c). This potential difference, called the **equilibrium potential** for that ion, depends on the concentrations on either side of the membrane. Larger concentration gradients lead to larger diffusion fluxes (Fick's first law, Equation 2.2).

In the late nineteenth century, Nernst (1888) formulated the **Nernst equation** to calculate the equilibrium potential resulting from permeability to a single ion:

$$E_X = \frac{RT}{z_X F} \ln \frac{[X]_{\text{out}}}{[X]_{\text{in}}} \quad (2.7)$$

where X is the membrane-permeable ion and $[X]_{\text{in}}$, $[X]_{\text{out}}$ are the intracellular and extracellular concentrations of X, and E_X is the equilibrium potential, also called the **Nernst potential**, for that ion. As shown in Box 2.2, the Nernst equation can be derived from the Nernst–Planck equation.

As an example, consider the equilibrium potential for K^+ . Suppose the intracellular and extracellular concentrations are similar to that of the squid giant axon (400 mM and 20 mM, respectively) and the recording temperature is 6.3 °C (279.3 K). Substituting these values into the Nernst equation:

$$E_K = \frac{RT}{z_K F} \ln \frac{[K^+]_{\text{out}}}{[K^+]_{\text{in}}} = \frac{(8.314)(279.3)}{(+1)(9.648 \times 10^4)} \ln \frac{20}{400} = -72.1 \text{ mV.} \quad (2.8)$$

Table 2.2 shows the intracellular and extracellular concentrations of various important ions in the squid giant axon and the equilibrium potentials calculated for them at a temperature of 6.3 °C.

Since Na^+ ions are positively charged, and their concentration is greater outside than inside, the sodium equilibrium potential is positive. On the other hand, K^+ ions have a greater concentration inside than outside and so have a negative equilibrium potential. Like Na^+ , Cl^- ions are more concentrated outside than inside, but because they are negatively charged their equilibrium potential is negative.

Fig. 2.9 The emergence of a voltage across a semipermeable membrane. The grey arrows indicate the net diffusion flux of the potassium ions and the blue arrows the flow due to the induced electric field.

(a) Initially, K^+ ions begin to move down their concentration gradient (from the more concentrated left side to the right side with lower concentration). The anions cannot cross the membrane. (b) This movement creates an electrical potential across the membrane. (c) The potential creates an electric field that opposes the movement of ions down their concentration gradient, so there is no net movement of ions; the system attains equilibrium.

The squid giant axon is an accessible preparation used by Hodgkin and Huxley to develop the first model of the action potential (Chapter 3).

Table 2.2 The concentrations of various ions in the squid giant axon and outside the axon, in the animal's blood (Hodgkin, 1964). Equilibrium potentials are derived from these values using the Nernst equation, assuming a temperature of 6.3°C. For calcium, the amount of free intracellular calcium is shown (Baker *et al.*, 1971). There is actually a much greater total concentration of intracellular calcium (0.4 mM), but the vast bulk of it is bound to other molecules

Ion	K ⁺	Na ⁺	Cl ⁻	Ca ²⁺
Concentration inside (mM)	400	50	40	10 ⁻⁴
Concentration outside (mM)	20	440	560	10
Equilibrium potential (mV)	-72	52	-64	139

This thought experiment demonstrates that the lipid bilayer forming the cell membrane acts as a capacitor, with the surfaces of the thin insulating membrane being the plates of the capacitor. Direct measurements of the specific **membrane capacitance** of various types of neurons range between 0.7 $\mu\text{F cm}^{-2}$ and 1.3 $\mu\text{F cm}^{-2}$, and the specific capacitance can be treated as a 'biological constant' of 0.9 $\mu\text{F cm}^{-2}$ (Gentet *et al.*, 2000), which is often rounded up to 1 $\mu\text{F cm}^{-2}$.

So far, we have neglected the fact that in the final resting state of our second thought experiment, the concentration of K⁺ ions on either side will differ from the initial concentration, as some ions have passed through the membrane. We might ask if this change in concentration is significant in neurons. We can use the definition of capacitance, $q = CV$ (Equation 2.1), to compute the number of ions required to charge the membrane to its resting potential. This computation, carried out in Box 2.3, shows that in large neurites, the total number of ions required to charge the membrane is usually a tiny fraction of the total number of ions in the cytoplasm, and therefore changes the concentration by a very small amount. The intracellular and extracellular concentrations can therefore be treated as constants.

Box 2.2 | Derivation of the Nernst equation

The Nernst equation is derived by assuming diffusion in one dimension along a line that starts at $x = 0$ and ends at $x = X$. For there to be no flow of current, the flux is zero throughout, so from Equation 2.4, the Nernst–Planck equation, it follows that:

$$\frac{1}{[X]} \frac{d[X]}{dx} = -\frac{z_x F}{RT} \frac{dV}{dx}.$$

Integrating, we obtain:

$$\int_{E_m}^0 -dV = \int_{[X]_{in}}^{[X]_{out}} \frac{RT}{z_x F [X]} d[X].$$

Evaluating the integrals gives:

$$E_m = \frac{RT}{z_x F} \ln \frac{[X]_{out}}{[X]_{in}}$$

which is the Nernst equation, Equation 2.7.

Box 2.3 | How many ions charge the membrane?

We consider a cylindrical section of squid giant axon 500 µm in diameter and 1 µm long at a resting potential of -70 mV . Its surface area is $500\pi\text{ }\mu\text{m}^2$, and so its total capacitance is $500\pi \times 10^{-8}\text{ }\mu\text{F}$ ($1\text{ }\mu\text{F cm}^{-2}$ is the same as $10^{-8}\text{ }\mu\text{F}\mu\text{m}^{-2}$). As charge is the product of voltage and capacitance (Equation 2.1), the charge on the membrane is therefore $500\pi \times 10^{-8} \times 70 \times 10^{-3}\text{ }\mu\text{C}$. Dividing by Faraday's constant gives the number of moles of monovalent ions that charge the membrane: 1.139×10^{-17} . The volume of the axonal section is $\pi(500/2)^2\text{ }\mu\text{m}^3$, which is the same as $\pi(500/2)^2 \times 10^{-15}$ litres. Therefore, if the concentration of potassium ions in the volume is 400 mM (Table 2.2), the number of moles of potassium is $\pi(500/2)^2 \times 10^{-15} \times 400 \times 10^{-3} = 7.85 \times 10^{-11}$. Thus, there are roughly 6.9×10^6 times as many ions in the cytoplasm than on the membrane, and so in this case the potassium ions charging and discharging the membrane have a negligible effect on the concentration of ions in the cytoplasm.

In contrast, the head of a dendritic spine on a hippocampal CA1 cell can be modelled as a cylinder with a diameter of around 0.4 µm and a length of 0.2 µm. Therefore its surface area is $0.08\pi\text{ }\mu\text{m}^2$ and its total capacitance is $C = 0.08\pi \times 10^{-8}\text{ }\mu\text{F} = 0.08\pi \times 10^{-14}\text{ F}$. The number of moles of calcium ions required to change the membrane potential by ΔV is $\Delta VC/(zF)$ where $z = 2$ since calcium ions are doubly charged. If $\Delta V = 10\text{ mV}$, this is $10 \times 10^{-3} \times 0.08\pi \times 10^{-14}/(2 \times 9.468 \times 10^4) = 1.3 \times 10^{-22}$ moles. Multiplying by Avogadro's number (6.0221×10^{23} molecules per mole), this is 80 ions. The resting concentration of calcium ions in a spine head is around 70 nM (Sabatini *et al.*, 2002), so the number of moles of calcium in the spine head is $\pi(0.4/2)^2 \times 0.2 \times 10^{-15} \times 70 \times 10^{-9} = 1.8 \times 10^{-24}$ moles. Multiplying by Avogadro's number the product is just about 1 ion. Thus the influx of calcium ions required to change the membrane potential by 10 mV increases the number of ions in the spine head from around 1 to around 80. This change in concentration cannot be neglected.

However, in small neurites, such as the spines found on dendrites of many neurons, the number of ions required to change the membrane potential by a few millivolts can change the intracellular concentration of the ion significantly. This is particularly true of calcium ions, which have a very low free intracellular concentration. In such situations, ionic concentrations cannot be treated as constants, and have to be modelled explicitly. Another reason for modelling Ca^{2+} is its critical role in intracellular signalling pathways. Modelling ionic concentrations and signalling pathways will be dealt with in Chapter 6.

What is the physiological significance of equilibrium potentials? In squid, the resting membrane potential is -65 mV , approximately the same as the potassium and chloride equilibrium potentials. Although originally it was thought that the resting membrane potential might be due to potassium, precise intracellular recordings of the resting membrane potential show that the two potentials differ. This suggests that other ions also contribute towards

the resting membrane potential. In order to predict the resting membrane potential, a membrane permeable to more than one type of ion must be considered.

2.4 Membrane ionic currents not at equilibrium: the Goldman–Hodgkin–Katz equations

To understand the situation when a membrane is permeable to more than one type of ion, we continue our thought experiment using a container divided by a semipermeable membrane (Figure 2.10a). The solutions on either side of the membrane now contain two types of membrane-permeable ions, K^+ and Na^+ , as well as membrane-impermeable anions, which are omitted from the diagram for clarity. Initially, there is a high concentration of K^+ and a very low concentration of Na^+ on the left, similar to the situation inside a typical neuron. On the right (outside) there are low concentrations of K^+ and Na^+ (Figure 2.10a).

In this example the concentrations have been arranged so the concentration difference of K^+ is greater than the concentration difference of Na^+ . Thus, according to Fick's first law, the flux of K^+ flowing from left to right down the K^+ concentration gradient is bigger than the flux of Na^+ from right to left flowing down its concentration gradient. This causes a net movement of positive charge from left to right, and positive charge builds up on the right-hand side of the membrane (Figure 2.10b). This in turn creates an electric field which causes electrical drift of both Na^+ and K^+ to the left. This reduces the net K^+ flux to the right and increases the net Na^+ flux to the left. Eventually, the membrane potential grows enough to make the K^+ flux and the Na^+ flux equal in magnitude but opposite in direction. When the net flow of charge is zero, the charge on either side of the membrane is constant, so the membrane potential is steady.

While there is no net flow of charge across the membrane in this state, there is net flow of Na^+ and K^+ , and over time this would cause the concentration gradients to run down. As it is the concentration differences that are responsible for the potential difference across the membrane, the membrane potential would reduce to zero. In living cells, ionic pumps counteract this effect. In this chapter pumps are modelled implicitly by assuming that they maintain the concentrations through time. It is also possible to model pumps explicitly (Section 6.4).

From the thought experiment, we can deduce qualitatively that the resting membrane potential should lie between the sodium and potassium equilibrium potentials calculated using Equation 2.7, the Nernst equation, from their intracellular and extracellular concentrations. Because there is not enough positive charge on the right to prevent the flow of K^+ from left to right, the resting potential must be greater than the potassium equilibrium potential. Likewise, because there is not enough positive charge on the left to prevent the flow of sodium from right to left, the resting potential must be less than the sodium equilibrium potential.

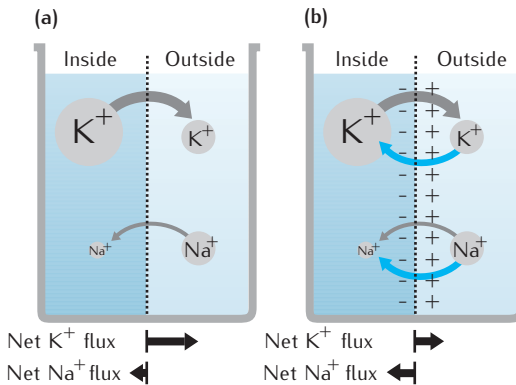


Fig. 2.10 The diffusion and electrical drift of two ions with different concentration ratios either side of a semipermeable membrane. The arrows have the same significance as in Figure 2.9, and anions have been omitted from the diagram for clarity. (a) Initially, K^+ ions diffuse from the left to right side, and Na^+ ions from the right to left side, as each ion flows down its concentration gradient. (b) This results in an electrical potential across the membrane. The potential arises in a similar manner as in Figure 2.9. However, here it is influenced both by ions and their diffusion. At equilibrium, there is still a flow of ions across the membrane; the electrical effect of the movement of one sodium ion (right to left) is neutralised by the effect of the movement of one potassium ion (left to right).

To make a quantitative prediction of the resting membrane potential, we make use of the theory of current flow through the membrane devised by Goldman (1943) and Hodgkin and Katz (1949). By making a number of assumptions, they were able to derive a formula, referred to as the **Goldman-Hodgkin-Katz (GHK) current equation**, which predicts the current I_X mediated by a single ionic species X flowing across a membrane when the membrane potential is V . The GHK current equation and the assumptions from which it was derived are shown in Box 2.4, and the corresponding $I-V$ curves are shown in Figure 2.11.

There are a number of properties worth noting from these curves.

- (1) No current flows when the voltage is equal to the equilibrium potential for the ion. This is because at this potential, current flow due to electrical drift and diffusion are equal and opposite. For the concentrations of ions shown in Table 2.2, the equilibrium potential of potassium is -72 mV , and the equilibrium potential of calcium is $+139\text{ mV}$.
- (2) The current changes direction (reverses) at the equilibrium potential. The current is negative (positive charge inwards) when the membrane voltage is below the equilibrium potential and positive above it. For this reason, the equilibrium potential of an ion is also known as its **reversal potential**.
- (3) The individual ions do not obey Ohm's law since the current is not proportional to the voltage.
- (4) A consequence of this is that the $I-V$ characteristics display rectification, defined in Section 2.2.6. The potassium characteristic favours outward currents, and is described as **outward rectifying** (Figure 2.11a). The calcium characteristic favours inward currents and is described as **inward rectifying** (Figure 2.11b). The rectification effect for calcium is particularly pronounced. The GHK current equation shows that when the extracellular concentration is greater than the intracellular concentration, the characteristic is inward rectifying, and when the converse is true, it is outward rectifying.

We can now calculate the $I-V$ characteristic of a membrane permeable to more than one ion type. Assuming that ions flow through the membrane independently, the total current flowing across the membrane is the sum of the ionic currents (Equation 2.6) predicted by the GHK current equations.

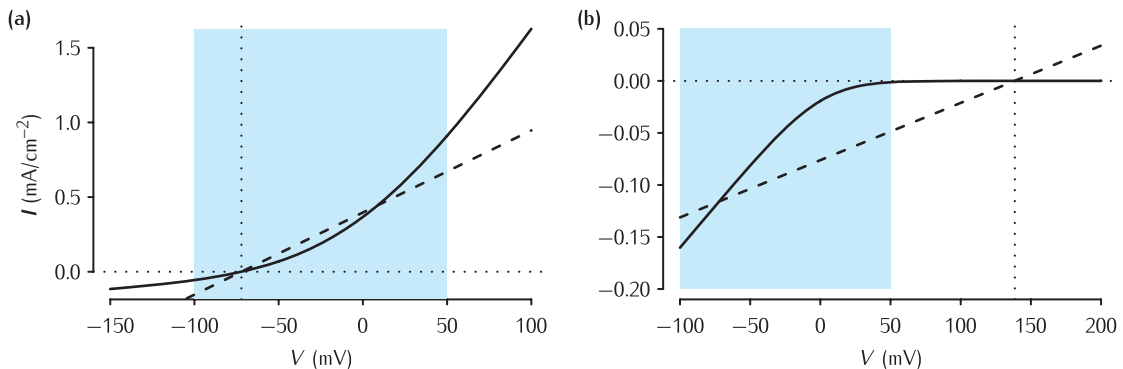


Fig. 2.11 The I - V characteristics for (a) K^+ and (b) Ca^{2+} ions. The solid line shows the I - V relationship given by the GHK current equation. The vertical dotted lines show the voltage at which no current flows (i.e. the equilibrium potential). The dashed line shows a linear approximation to the GHK I - V characteristic that also yields no current at the equilibrium potential. The shaded regions illustrate the range of voltage within which a neuron usually operates. The concentration values are taken from squid axon (Hodgkin, 1964; Baker *et al.*, 1971), with current densities calculated at 6.3°C .

We can therefore calculate the total current flowing across the membrane for a given value of the membrane potential. The resulting characteristic is broadly similar to the characteristics for the individual ions, in that the current is negative at low potentials and then increases as the membrane potential is raised. We recall that the reversal potential is defined as the membrane potential at which the current reverses direction. The reversal potential for more than one ion type lies between the equilibrium potentials of the individual ions.

The GHK current equation can be used to calculate the reversal potential. As we have seen, there is one GHK current equation for every ion to which the membrane is permeable. By setting the **membrane current** I to zero and solving this equation for voltage, we obtain the **Goldman–Hodgkin–Katz voltage equation** for the reversal potential when there is more than one type of ion. For a membrane permeable to Na^+ , K^+ and Cl^- , it reads:

$$E_m = \frac{RT}{F} \ln \frac{P_{\text{K}}[\text{K}^+]_{\text{out}} + P_{\text{Na}}[\text{Na}^+]_{\text{out}} + P_{\text{Cl}}[\text{Cl}^-]_{\text{in}}}{P_{\text{K}}[\text{K}^+]_{\text{in}} + P_{\text{Na}}[\text{Na}^+]_{\text{in}} + P_{\text{Cl}}[\text{Cl}^-]_{\text{out}}} \quad (2.9)$$

where P_{K} , P_{Na} , and P_{Cl} are the membrane permeabilities to K^+ , Na^+ and Cl^- respectively (membrane permeability is described in Box 2.4). The pattern of this equation is followed for other sets of monovalent ions, with the numerator containing the *external* concentrations of the *positively charged ions* and the *internal* concentrations of the *negatively charged ions*.

As the permeabilities occur in the numerator and the denominator, it is sufficient to know only relative permeabilities to compute the voltage at equilibrium. The relative permeabilities of the membrane of the squid giant axon to K^+ , Na^+ and Cl^- ions are 1.0, 0.03 and 0.1 respectively. With these values, and the concentrations from Table 2.2, the resting membrane potential of the squid giant axon predicted by the GHK voltage equation is -60 mV at 6.3°C .

Equation 2.9, the GHK voltage equation, looks similar to the Nernst equation. Indeed, it reduces to the equivalent Nernst equation when the permeability of two of the ions is zero. However, this equation also demonstrates that the membrane potential with two ion types is not the sum of the individual equilibrium potentials.

Box 2.4 | The GHK equations

Goldman (1943) and Hodgkin and Katz (1949) developed a formalism for describing the currents through and voltages across semipermeable membranes. This formalism models the diffusion of ions through a uniformly permeable membrane, predating the notion of channels or pores through the membrane. It is assumed that ions cross the membrane independently (the **independence principle**) and that the electric field within the membrane is constant. The flux or movement of ions within the membrane is governed by the internal concentration gradient and the electric field arising from the potential difference, calculated by the Nernst–Plank equation.

From these assumptions, the Goldman–Hodgkin–Katz current equation can be derived (Johnston and Wu, 1995):

$$I_X = P_X z_X F \frac{z_X F V}{RT} \left(\frac{[X]_{\text{in}} - [X]_{\text{out}} e^{-z_X F V / RT}}{1 - e^{-z_X F V / RT}} \right).$$

This equation predicts the net flow I_X per unit area of membrane, measured in cm^{-2} of an arbitrary ion type X with valency z_X . P_X is the **permeability** of the membrane to ion X, with units of cm s^{-1} . It characterises the ability of an ion X to diffuse through the membrane and is defined by the empirical relationship between molar flux J and the concentration difference across the membrane:

$$J_X = -P_X ([X]_{\text{in}} - [X]_{\text{out}}).$$

In the GHK model of the membrane, permeability is proportional to the diffusion coefficient, D_X , defined in Fick's first law (Equation 2.2). Hille (2001) discusses the relationship in more detail.

The GHK equation predates the notion of membrane channels and treats the membrane as homogeneous. In active membranes we can interpret the diffusion coefficient, D_X , as variable – an increase in the number of open channels in the membrane will increase the membrane permeability. Because of the assumption of a constant electric field in the membrane, the GHK equations are sometimes referred to as the **constant-field equations**.

2.4.1 An electrical circuit approximation of the GHK current equation

It is often sufficient to use a simpler equation in place of the GHK current equation. In the potassium characteristic shown in Figure 2.11a, the straight line that gives zero current at the equilibrium potential (-72mV) is a close approximation of the I – V characteristic for membrane potentials between about -100mV and 50mV , the voltage range within which cells normally operate. The equation describing this line is:

$$I_X = g_X (V - E_X) \quad (2.10)$$

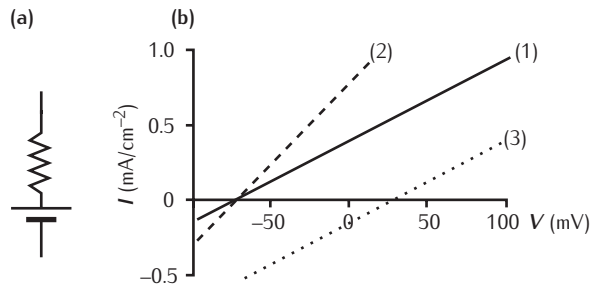
where X is the ion of interest, E_X its equilibrium potential, and g_X is the gradient of the line with the units of conductance per unit area, often mS cm^{-2} . The term in brackets ($V - E_X$) is called the **driving force**. When the membrane potential is at the equilibrium potential for X, the driving force is zero.

Fig. 2.12 Interpretation of the approximation of the GHK current equation. (a) The approximation can be viewed as a resistor, or conductance, in series with a battery. (b) The graph shows three different I - V characteristics from this circuit given different conductances and battery voltages.

(1) $g_x = 5.5 \text{ mS cm}^{-2}$, $E_x = -72 \text{ mV}$; this line is the same as the K^+ approximation in Figure 2.11a;

(2) $g_x = 11.0 \text{ mS cm}^{-2}$, $E_x = -72 \text{ mV}$;

(3) $g_x = 5.5 \text{ mS cm}^{-2}$, $E_x = 28 \text{ mV}$.



In some cases, such as for calcium in Figure 2.11b, the GHK I - V characteristic rectifies too much for a linear approximation to be valid.

Making this linear approximation is similar to assuming Ohm's law, $I = GV$, where conductance G is a constant. Since the straight line does not necessarily pass through the origin, the correspondence is not exact and this form of linear I - V relation is called **quasi-ohmic**. There is still a useful interpretation of this approximation in terms of electrical components. The I - V characteristic is the same as for a battery with **electromotive force** equal to the equilibrium potential in series with a resistor of resistance $1/g_x$ (Figure 2.12).

2.5 | The capacitive current

We now have equations that describe how the net flow of current I through the different types of channels depends on the membrane potential V . In order to complete the description of the system, we need to know how the current affects the voltage.

All the current passing through the membrane either charges or discharges the membrane capacitance. So the rate of change of charge on the membrane dq/dt is the same as the net current flowing through the membrane: $I = dq/dt$. By differentiating Equation 2.1 for the charge stored on a capacitor with respect to time, we obtain a differential equation that links V and I :

$$\frac{dV}{dt} = \frac{I}{C} = \frac{1}{C} \frac{dq}{dt} \quad (2.11)$$

This shows that the rate of change of the membrane potential is proportional to the current flowing across the membrane. The change in voltage over time, during the charging or discharging of the membrane, is inversely proportional to the capacitance – it takes longer to charge up a bigger capacitor.

2.6 | The equivalent electrical circuit of a patch of membrane

We have seen how we can represent the permeable and impermeable properties of the membrane as electrical components. Figure 2.13 shows how these

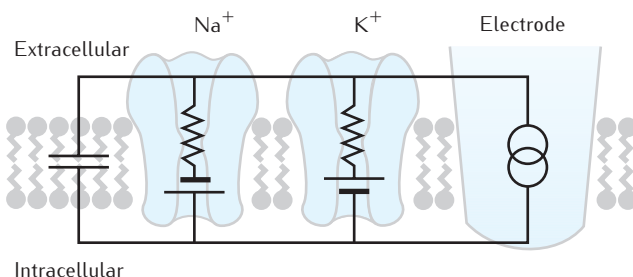


Fig. 2.13 The equivalent electrical circuit of a patch of membrane.

components fit together to form an **equivalent electrical circuit** of a small patch of membrane. It comprises the membrane capacitance in parallel with one resistor and battery in series for each type of ion channel. There is also a current source that represents an electrode that is delivering a constant amount of current. It is said to be in **current clamp mode**. The amount of current injected is denoted by I_e , and in electrophysiological applications is usually measured in nanoamps (nA).

For the remainder of this chapter, we consider a membrane that contains passive ion channels, with constant permeability or conductance. In general, ion channels are active, so their permeability changes in response to changes in membrane potential. It is useful to consider passive membranes as a first step towards understanding the behaviour of active membranes. In addition, for small deviations of the membrane potential from the resting potential, active channels can be treated as passive channels.

2.6.1 Simplification of the equivalent electrical circuit

We can simplify the electrical circuit representing a patch of passive membrane, such as the circuit shown in Figure 2.13, by lumping together all of the channel properties. Figure 2.14a shows this simplified circuit. In place of the two resistor/battery pairs in Figure 2.13, there is one pair with a resistance, which we call the specific membrane resistance R_m , measured in Ωcm^2 , and a membrane battery with an electromotive force of E_m .

We can derive these values from the conductances and reversal potentials of the individual ions using **Thévenin's theorem**. For channels X, Y and Z combined, the equivalent electromotive force and membrane resistance are:

$$E_m = \frac{g_X E_X + g_Y E_Y + g_Z E_Z}{g_X + g_Y + g_Z} \quad (2.12)$$

$$\frac{1}{R_m} = g_m = g_X + g_Y + g_Z.$$

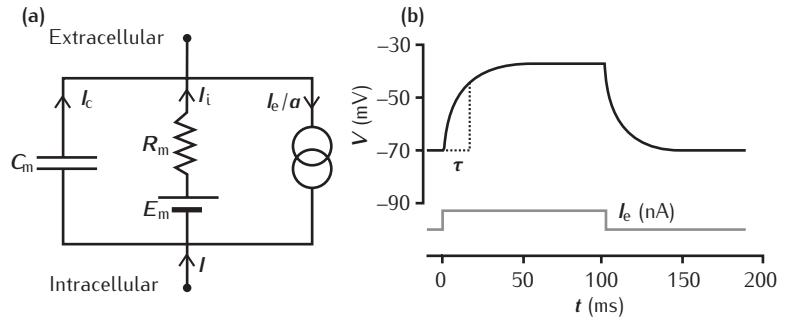
Note that Equation 2.12 is the ohmic equivalent of the GHK voltage equation Equation 2.9.

A summary of key passive quantities and their typical units is given in Table 2.3. It is usual to quote the parameters of the membrane as **intensive quantities**. To avoid adding extra symbols, we use intensive quantities in our electrical circuits and equations. Supposing that the area of our patch of membrane is a , its membrane resistance is proportional to the specific

Thévenin's theorem states that any combination of voltage sources and resistances across two terminals can be replaced by a single voltage source and a single series resistor. The voltage is the open circuit voltage E at the terminals and the resistance is E divided by the current with the terminals short circuited.

An **intensive quantity** is a physical quantity whose value does not depend on the amount or dimensions of the property being measured. An example of an intensive quantity is the specific membrane capacitance, the capacitance per unit area of membrane.

Fig. 2.14 (a) The electrical circuit representing a passive patch of membrane. (b) The behaviour of the membrane potential in an RC circuit in response to an injected current pulse, shown below.



Kirchhoff's current law is based on the principle of conservation of electrical charge. It states that at any point in an electrical circuit, the sum of currents flowing toward that point is equal to the sum of currents flowing away from that point.

membrane resistance divided by the area: R_m/a . Since conductance is the inverse of resistance, the membrane conductance of the patch is proportional to area: $g_m a$; its membrane capacitance is proportional to the specific membrane capacitance: $C_m a$. Current (for example, current crossing the membrane) is given by the current density I which has units $\mu\text{A cm}^{-2}$ multiplied by the area: Ia .

2.6.2 The RC circuit

The simplified circuit shown in Figure 2.14a is well known in electronics, where it is called an RC circuit, since its main elements are a resistor R and a capacitor C . In order to find out how the membrane potential changes when current is injected into the circuit, we need to know how current varies with voltage. By **Kirchhoff's current law**, the sum of the current Ia flowing through the membrane and the injected current I_e is equal to the sum of the capacitive current $I_c a$ and the ionic current $I_i a$:

$$\begin{aligned} Ia + I_e &= I_c a + I_i a \\ I + I_e/a &= I_c + I_i \end{aligned} \quad (2.13)$$

The ionic current flowing through the resistor and battery is given by the quasi-ohmic relation in Equation 2.10:

$$\begin{aligned} I_i a &= \frac{V - E_m}{R_m/a} \\ I_i &= \frac{V - E_m}{R_m} \end{aligned} \quad (2.14)$$

Finally, the capacitive current is given by the membrane capacitance multiplied by the rate of change of voltage (Section 2.5):

$$I_c = C_m \frac{dV}{dt}. \quad (2.15)$$

If this circuit is isolated, i.e. the membrane current Ia is zero, substituting for I_i , and I_c in Equation 2.13 for this RC circuit gives:

$$C_m \frac{dV}{dt} = \frac{E_m - V}{R_m} + \frac{I_e}{a}. \quad (2.16)$$

This is a first order **ordinary differential equation** (ODE) for the membrane potential V . It specifies how, at every instant in time, the rate of

change of the membrane potential is related to the membrane potential itself and the current injected. For any particular form of injected current pulse and initial membrane potential, it determines the time course of the membrane potential.

2.6.3 Behaviour of the RC circuit

Solving the differential equation is the process of using this equation to calculate how the membrane potential varies over time. We can solve Equation 2.16 using numerical methods. Appropriate numerical methods are programmed into neural simulation computer software, such as **NEURON** or **GENESIS**, so it is not strictly necessary to know the numerical methods in depth. However, a basic understanding of numerical methods is useful and we present an overview in Appendix B. Figure 2.14b shows the result of solving the equation numerically when the injected current is a square pulse of magnitude I_e and duration t_e . On the rising edge of the pulse the membrane potential starts to rise steeply. This rise away from the resting potential is referred to as **depolarisation**, because the amount of positive and negative charge on the membrane is reducing. As the pulse continues, the rise in voltage becomes less steep and the voltage gets closer and closer to a limiting value. On the falling edge of the pulse the membrane potential starts to fall quite steeply. The rate of fall decreases as the membrane potential gets close to its original value. As the charge on the membrane is building back up to resting levels, this phase is called **repolarisation**. By injecting negative current, it is possible to reduce the membrane potential below its resting level, which is referred to as **hyperpolarisation**.

Generally, it is difficult, and often not possible, to solve differential equations analytically. However, Equation 2.16 is sufficiently simple to allow an analytical solution. We assume that the membrane is initially at rest, so that $V = E_m$ at time $t = 0$. We then integrate Equation 2.16 to predict the response of the membrane potential during the current pulse, giving:

$$V = E_m + \frac{R_m I_e}{a} \left(1 - \exp \left(-\frac{t}{R_m C_m} \right) \right). \quad (2.17)$$

This is an inverted decaying exponential that approaches the steady state value $E_m + R_m I_e / a$ as time t gets very large. Defining V_0 as the value the membrane potential has reached at the end of the current pulse at $t = t_e$, the response of the membrane is given by:

$$V = E_m + (V_0 - E_m) \exp \left(-\frac{t - t_e}{R_m C_m} \right), \quad (2.18)$$

which is a decaying exponential.

In both rising and falling responses, the denominator inside the exponential is the product of the membrane resistance and membrane capacitance $R_m C_m$. This factor has the units of time, and it characterises the length of time taken for the membrane potential to get to $1/e$ (about one-third) of the way from the final value. For this reason the product $R_m C_m$ is defined as the **membrane time constant** τ . It is a measure of how long the membrane ‘remembers’ its original value. Typical values of τ for neurons range between

NEURON and **GENESIS** are two well known open source neural simulators which allow numerical solutions to the differential equations describing the spatiotemporal variation in the neuron membrane potential to be obtained. These simulators can be applied to a single neuron or a network of interconnected neurons. Appendix A.1 contains a comprehensive list of neural simulators.

Solving an equation analytically means that an expression for how the membrane potential (in this case) depends on position and time can be derived as a function of the various parameters of the system. The alternative is to solve the equation numerically.

Table 2.3 Passive quantities

Quantity	Description	Typical units	Relationships
d	Diameter of neurite	μm	
l	Length of compartment	μm	
R_m	Specific membrane resistance	$\Omega \text{ cm}^2$	
C_m	Specific membrane capacitance	$\mu\text{F cm}^{-2}$	
R_a	Specific axial resistance (resistivity)	$\Omega \text{ cm}$	
r_m	Membrane resistance per inverse unit length	$\Omega \text{ cm}$	$r_m = \frac{R_m}{\pi d}$
c_m	Membrane capacitance per unit length	$\mu\text{F cm}^{-1}$	$c_m = C_m \pi d$
r_a	Axial resistance per unit length	Ω/cm^{-1}	$r_a = \frac{4R_a}{\pi d^2}$
V	Membrane potential	mV	
E_m	Leakage reversal potential due to different ions	mV	
I	Membrane current density	$\mu\text{A cm}^{-2}$	
I_e	Injected current	nA	
I_c	Capacitive current	nA	
I_i	Ionic current	nA	

The units of R_m and R_a can often seem counter-intuitive. It can sometimes be more convenient to consider their inverse quantities, specific membrane conductance and specific intracellular conductance. These have units of S cm^{-2} and S cm^{-1} respectively. The quantities r_m , r_a , and c_m are useful alternatives to their specific counterparts. They express key electrical properties of a neurite of specific diameter and can clarify the equations representing a specific cable or neurite of arbitrary length.

1 and 20 ms. It is possible to measure the membrane time constant for use in a model RC type circuit. The assumptions that are made when doing this and the effects of measurement accuracy are discussed in Chapter 4.

Another important quantity that characterises the response of neurons to injected current is the **input resistance**, defined as the change in the steady state membrane potential divided by the injected current causing it (Koch, 1999). To determine the input resistance of any cell in which current is injected, the resting membrane potential is first measured. Next, a small amount of current I_e is injected, and the membrane potential is allowed to reach a steady state V_∞ . The input resistance is then given by:

$$R_{in} = \frac{V_\infty - E_m}{I_e}. \quad (2.19)$$

For a single RC circuit representation of a cell, the input resistance can be calculated from the properties of the cell. From Equation 2.16, by setting $dV/dt = 0$ the steady state membrane potential can be shown to be $V_\infty = E_m + (R_m/a)I_e$. By substituting this value of V_∞ into Equation 2.19, it can be seen that the input resistance $R_{in} = R_m/a$. This is a quasi-ohmic current-voltage relation where the constant of proportionality is the input resistance, given by R_m/a .

The input resistance measures the response to a steady state input. A more general concept is the **input impedance**, which measures the amplitude and phase lag of the membrane potential in response to a sinusoidal

injection current of a particular frequency. The input impedance of the RC circuit can be computed, and shows that the RC circuit acts as a low-pass filter, reducing the amplitude of high-frequency components of the input signal. The topic of input impedance and the frequency-response of neurons is covered in depth by Koch (1999).

2.7 Modelling permeable properties in practice

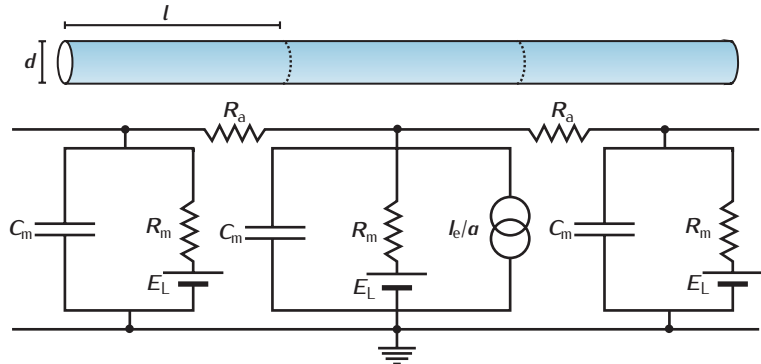
Both the approximations expressed by the GHK current equations and quasi-ohmic electrical circuit approximation are used in models. However, neither should be considered a perfect representation of currents through the membrane. The GHK equations were originally used to describe ion permeability through a uniform membrane, whereas today they are used primarily to describe the movement of ions through channels. Assumptions on which the equations are based, such as the independence of movement of ions through the membrane (the independence principle; Box 2.4 and Chapter 5) and of constant electric fields, are generally not valid within the restricted space of a single channel. It is therefore not surprising that experiments reveal that the flux through channels saturates at large ionic concentrations, rather than increasing without limit as the GHK equations would predict (Hille, 2001).

There are a number of models of the passage of ions through ion channels, which are more detailed than the GHK and quasi-ohmic descriptions (Hille, 2001), but these more detailed descriptions are not generally used in computational models of the electrical activity of neurons. We might ask how we can justify using a more inaccurate description when more accurate ones exist. In answer, modelling itself is the process of making approximations or simplifications in order to understand particular aspects of the system under investigation. A theme that will be visited many times in this book is: what simplifications or approximations are appropriate? The answer depends on the question that the model is designed to address. For certain questions, the level of abstraction offered by the quasi-ohmic approximation has proved extremely valuable, as we see in Chapter 3. Similarly, the GHK equation is used in many modelling and theoretical approaches to membrane permeability.

When choosing which of these approximations is most appropriate, there are a number of issues to consider. Most ion types do not have a strongly rectifying I - V characteristic in the region of typical membrane potentials, and so the quasi-ohmic approximation can be useful. However, if the I - V characteristic is very strongly rectifying (as in the example of calcium), the GHK current equation may give a better fit. Even with fairly weak rectification, the GHK can fit the data better than the quasi-ohmic approximation (Sah *et al.*, 1988).

We might want to model how changes in intracellular concentration affect the I - V characteristic. In this case, the GHK equations may be a more useful tool. This often applies to calcium, since its intracellular concentration is so low that relatively small influxes can change its concentration by an order of magnitude. Moreover, we may need to consider modelling imperfect

Fig. 2.15 A length of passive membrane described by a compartmental model.



(and more realistic) ion selective channels which have permeabilities to more than one ion. All ion selective channels allow some level of permeability to certain other ions, and so the GHK voltage equation can be used to calculate the reversal potential of these channels.

2.8 | The equivalent electrical circuit of a length of passive membrane

So far, we have looked at the properties of a patch of membrane or small neuron. This is appropriate when considering an area of membrane over which the membrane potential is effectively constant, or **isopotential**. However, most neurons cannot be considered isopotential throughout, which leads to axial current flowing along the neurites. For example, during the propagation of action potentials, different parts of the axon are at different potentials. Similarly, dendrites cannot generally be treated as isopotential. This is evident from changes in the form of the excitatory postsynaptic potentials (EPSPs) as they move down a dendrite.

Fortunately, it is quite easy to extend the model of a patch of membrane to spatially extended neurites. In this chapter, we consider only an unbranched neurite, and in Chapter 4 we look at branched structures. Because of the similarity to an electrical cable, we often refer to this unbranched neurite as a cable.

2.8.1 The compartmental model

The basic concept is to split up the neurite into cylindrical **compartments** (Figure 2.15). Each compartment has a length l and a diameter d , making its surface area $a = \pi dl$. Within each compartment, current can flow onto the membrane capacitance or through the membrane resistance. This is described by the RC circuit for a patch of membrane, encountered in the last section. Additionally, current can flow longitudinally through the cytoplasm and the extracellular media. This is modelled by axial resistances that link the compartments.

Since it is usually assumed that the intracellular resistance is much greater than the extracellular resistance, it may be acceptable to consider the extracellular component of this resistance to be effectively zero (implying that the main longitudinal contribution is intracellular resistivity). We may then

model the extracellular medium as electrical ground, and it acts in an isopotential manner (as shown in Figure 2.15). For many research questions, such as modelling intracellular potentials, this assumption is valid. However, in any case it is straightforward to incorporate the non-zero extracellular resistance. In Chapter 9 the approach is extended to networks of resistances to model the field potentials in extended regions of extracellular space (Box 9.1).

We assume here a circuit as given in Figure 2.15, with the extracellular medium modelled as ground. The axial resistance of a compartment is proportional to its length l and inversely proportional to the cylinder's cross-sectional area $\pi d^2/4$. The **axial resistivity**, also known as the specific **axial resistance**, R_a , has units $\Omega \text{ cm}$ and gives the resistivity properties of the intracellular medium. The axial resistance of the cylindrical compartment is then $4R_a l / \pi d^2$. Compartments with longer lengths have larger axial resistance and those with larger cross-sectional areas have reduced resistances.

We can describe the electrical circuit representing the cable with one equation per compartment. We number the compartments in sequence using the subscript j . For example, V_j denotes the membrane potential in the j th compartment and $I_{e,j}$ is the current injected into the j th compartment. Following the procedure used in the previous section, we can use Kirchhoff's current law, the quasi-ohmic relation and the equation for the capacitive current (Equations 2.13 to 2.16) to derive our circuit equations. The main difference from the previous treatment is that, rather than the compartment being isolated, the membrane current $I_{j,a}$ is now able to spread both leftwards and rightwards within the cytoplasm, i.e. the membrane current is equal to the sum of the leftwards and rightwards axial currents, each given by Ohm's law:

$$I_{j,a} = \frac{V_{j+1} - V_j}{4R_a l / \pi d^2} + \frac{V_{j-1} - V_j}{4R_a l / \pi d^2}. \quad (2.20)$$

In this case, we are assuming all compartments have the same cylindrical dimensions. Substituting for this membrane current into Equation 2.13:

$$\begin{aligned} I_{c,j}a + I_{i,j}a &= I_{j,a} + I_{e,j} \\ I_{c,j}a + I_{i,j}a &= \frac{V_{j+1} - V_j}{4R_a l / \pi d^2} + \frac{V_{j-1} - V_j}{4R_a l / \pi d^2} + I_{e,j}. \end{aligned} \quad (2.21)$$

This leads to an equation that is similar to Equation 2.16 for a patch of membrane, but now has two extra terms, describing the current flowing along the axial resistances into the two neighbouring compartments $j-1$ and $j+1$:

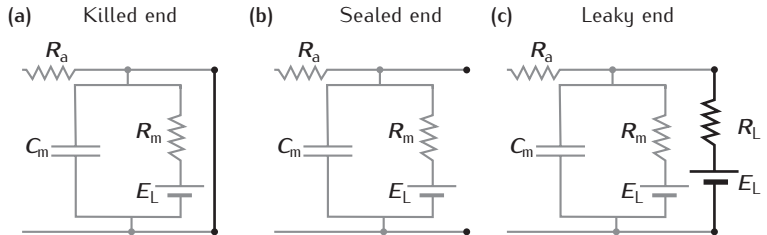
$$\pi d l C_m \frac{dV_j}{dt} = \frac{E_m - V_j}{R_m / \pi d l} + \frac{V_{j+1} - V_j}{4R_a l / \pi d^2} + \frac{V_{j-1} - V_j}{4R_a l / \pi d^2} + I_{e,j}. \quad (2.22)$$

We have used the surface area of the cylinder $\pi d l$ as the area a . Dividing through by this area gives a somewhat less complicated-looking equation:

$$C_m \frac{dV_j}{dt} = \frac{E_m - V_j}{R_m} + \frac{d}{4R_a} \left(\frac{V_{j+1} - V_j}{l^2} + \frac{V_{j-1} - V_j}{l^2} \right) + \frac{I_{e,j}}{\pi d l}. \quad (2.23)$$

This equation is the fundamental equation of a compartmental model.

Fig. 2.16 Circuit illustration of three types of cable terminal conditions.



2.8.2 Boundary conditions

The equations above assume that each compartment j has two neighbouring compartments $j - 1$ and $j + 1$, but this is not true in the compartments corresponding to the ends of neurites. Special treatment is needed for these compartments, which depends on the condition of the end of the neurite being modelled.

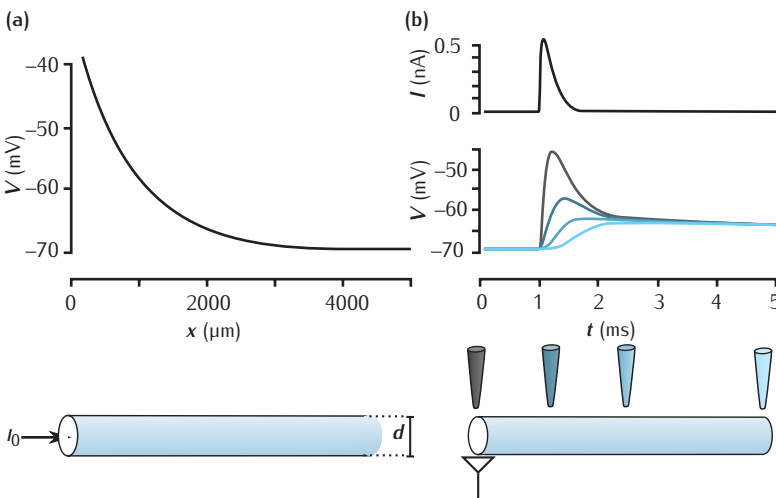
The simplest case is that of a **killed end**, in which the end of the neurite has been cut. This can arise in some preparations such as dissociated cells, and it means that the intracellular and extracellular media are directly connected at the end of the neurite. Thus the membrane potential at the end of the neurite is equal to the extracellular potential. To model this, in the equation for the membrane potential, V_0 in the first compartment is set to 0, as illustrated in Figure 2.16a. This allows Equation 2.23 to be used. The condition $V_0 = 0$ is called a **boundary condition** as it specifies the behaviour of the system at one of its edges. This type of boundary condition, where the value of a quantity at the boundary is specified, is called a **Dirichlet** boundary condition.

If the end of the neurite is intact, a different boundary condition is required. Here, because the membrane surface area at the tip of the neurite is very small, its resistance is very high. In this **sealed end** boundary condition, illustrated in electric circuit form in Figure 2.16b, we assume that the resistance is so high that a negligible amount of current flows out through the end. Since the axial current is proportional to the gradient of the membrane potential along the neurite, zero current flowing through the end implies that the gradient of the membrane potential at the end is zero. For reasons made clear in Appendix B.1 in the compartmental framework, this boundary condition is modelled by setting $V_{-1} = V_1$. This leads to a modified version of Equation 2.23 for compartment 0. This type of boundary condition, where the spatial derivative of a quantity at the boundary is specified, is called a **Neumann** boundary condition.

It can also be assumed that there is a **leaky end**; in other words, that the resistance at the end of the cable has a finite absolute value R_L (Figure 2.16c). In this case, the boundary condition is derived by equating the axial current, which depends on the spatial gradient of the membrane potential, to the current flowing through the end, $(V - E_m)/R_L$.

2.8.3 Behaviour of the membrane potential in a compartmental model

As with the patch of membrane, we can use a simulation software package, such as NEURON or GENESIS, to solve these equations numerically. The



membrane potential is now going to vary over space and time, the spatial variations being from compartment to compartment.

Before looking at examples of the spatiotemporal evolution of the membrane potential, consider the steady state behaviour. If current is injected for long enough, the membrane potential in each compartment will stabilise. Figure 2.17a shows the simulated steady state membrane potential along a cable in response to continuous current injection at a point ($x = 0 \mu\text{m}$). The membrane potential is highest nearest to the point of current injection. The injected current flows down the cable, gradually leaking out through the membrane resistances. This results in the membrane potential decaying further away from the site of injection.

An example of the time-dependent behaviour of the membrane potential is shown in Figure 2.17b. To simulate synaptic input, a pulse of current is injected at time zero at a ‘synapse’ at one end of the cable, and the membrane potential is measured at different points along the cable. The membrane potential close to the point of injection peaks quickly and has greater amplitude than the membrane potential measured further away from the synapse. After about 2 ms, the membrane potential measured at the different points converges and decays slowly. This example demonstrates that the further away a synaptic input is from some point on a neuron, the lower the amplitude of the EPSP measured at that point is expected to be. Thus, in less idealised neurons, synaptic inputs to distal parts of the dendritic tree are expected to be attenuated more on their way to the soma, or cell body, than inputs to the proximal dendritic tree.

Fig. 2.17 (a) Steady state membrane potential as a function of distance in a semi-infinite cable in response to current injection at one end ($x = 0 \mu\text{m}$). The parameters are $d = 1 \mu\text{m}$, $R_a = 35.4 \Omega \text{ cm}$, $R_m = 10 \text{ k}\Omega \text{ cm}^2$, which, from Equation 2.26, gives the length constant $\lambda = 840 \mu\text{m}$. (b) Top: a simulated excitatory postsynaptic current (EPSC). Below: the membrane potential measured at different points along a cable in response to the EPSC evoked at the left-hand end of the cable. The colour of each trace corresponds to the locations of the electrodes. The neurite is 500 μm long and other parameters are the same as the semi-infinite cable shown in (a).

2.9 | The cable equation

We saw in Section 2.6 that it is possible to solve analytically the equation representing a single membrane compartment. This gave us an equation from which it is easy to see the basis for the time course of the membrane

potential, and the important concept of the membrane time constant. In the preceding section, extra compartments were added to allow spatially extended neurites to be described, but this has come at the expense of being able to solve the equations analytically. Although modern computers can numerically integrate the equations of the compartmental model at very high spatial resolutions by using many compartments, looking at analytical solutions can give a deeper understanding of the behaviour of the system.

In this section, we introduce the **cable equation**, which allows the spatiotemporal evolution of the membrane potential to be solved analytically. As shown in more detail in Box 2.5, the cable equation is derived from the equations of a compartmental model (Equation 2.23) by effectively splitting a neurite into an infinite number of infinitesimally small compartments. The cable equation is a **partial differential equation** (PDE) with the form:

$$C_m \frac{\partial V}{\partial t} = \frac{E_m - V}{R_m} + \frac{d}{4R_a} \frac{\partial^2 V}{\partial x^2} + \frac{I_e}{\pi d}. \quad (2.24)$$

In the cable equation the membrane potential is a function of distance x along a continuous cable, and time $V(x, t)$, and $I_e(x, t)$ is the current injected per unit length at position x .

The cable equation is very similar to the equation of a single compartment (Equation 2.16), except that the derivative dV/dt has been replaced by the partial derivative $\partial V/\partial t$ and there is an extra term $d/4R_a \partial^2 V/\partial x^2$. The extra term is the net density of current flowing along the length of the cable into point x .

2.9.1 Steady state behaviour of the membrane potential

The simplest situation to examine is the steady state case, in which a constant current is injected into the cable; this situation often arises in experiments. In the steady state, when the system has settled and the voltage no longer changes through time, the derivative $\partial V/\partial t$ in Equation 2.24 is zero. This equation then turns into a second order, ordinary differential equation, which is considerably easier to solve.

Semi-infinite cable

We start by considering a semi-infinite cable which was simulated approximately in Figure 2.17. It has one sealed end from which it extends an infinite distance, and current with an absolute value of I_e is injected into the cable at the sealed end. Although this is unrealistic, it gives us an initial feel for how voltage changes over large distances from a single injection site. The analytical solution to Equation 2.24, along with the sealed end boundary conditions (Box 2.5), shows that, in agreement with the numerical solution of the discrete cable equation shown in Figure 2.17a, the steady state membrane potential is a decaying exponential function of distance along the neurite:

$$V(x) = E_m + R_\infty I_e e^{-x/\lambda}. \quad (2.25)$$

The quantity λ is called the **length constant** of the cable and R_∞ is the input resistance (defined in Section 2.6.3) of a semi-infinite cable.

Box 2.5 | Derivation of the cable equation

To derive the cable equation from the discrete equations for the compartmental model (Equation 2.23) we set the compartment length l to the small quantity δx . A compartment indexed by j is at a position $x = j\delta x$ along the cable, and therefore the membrane potentials in compartments $j - 1$, j and $j + 1$ can be written:

$$V_j = V(x, t) \quad V_{j-1} = V(x - \delta x, t) \quad V_{j+1} = V(x + \delta x, t).$$

Also, we define the current injected per unit length as $I_e(x, t) = I_{e,j}/\delta x$. This allows Equation 2.23 to be rewritten as:

$$\begin{aligned} C_m \frac{\partial V(x, t)}{\partial t} &= \frac{E_m - V(x, t)}{R_m} \\ &+ \frac{d}{4R_a} \left[\frac{1}{\delta x} \left(\frac{V(x + \delta x, t) - V(x, t)}{\delta x} - \frac{V(x, t) - V(x - \delta x, t)}{\delta x} \right) \right] + \frac{I_e(x, t)}{\pi d}. \end{aligned} \quad (\text{a})$$

The derivative of V with respect to t is now a partial derivative to signify that the membrane potential is a function of more than one variable.

The length δx of each compartment can be made arbitrarily small, so that eventually there is an infinite number of infinitesimally short compartments. In the limit as δx goes to 0, the term in square brackets in the equation above becomes the same as the definition of the second partial derivative of distance:

$$\frac{\partial^2 V(x, t)}{\partial x^2} = \lim_{\delta x \rightarrow 0} \frac{1}{\delta x} \left(\frac{V(x + \delta x, t) - V(x, t)}{\delta x} - \frac{V(x, t) - V(x - \delta x, t)}{\delta x} \right).$$

Substituting this definition into Equation (a) leads to Equation 2.24, the cable equation.

In the case of discrete cables, the sealed end boundary condition is that:

$$\frac{d}{4R_a} \frac{V_1 - V_0}{\delta x^2} = \frac{I_{e,1}}{\pi d \delta x} + \frac{E_m - V_1}{\pi d \delta x R_L}.$$

In the limit of $\delta x \rightarrow 0$, at the $x = 0$ end of the cable, this is:

$$-\frac{d}{4R_a} \frac{\partial V}{\partial x} = \frac{I_e(0, t)}{\pi d} + \frac{E_m - V(0, t)}{\pi d R_L}.$$

At the $x = l$ end of the cable, this is

$$\frac{d}{4R_a} \frac{\partial V}{\partial x} = \frac{I_e(l, t)}{\pi d} + \frac{E_m - V(l, t)}{\pi d R_L},$$

assuming a sealed end means that the axial current at the sealed end is zero, and therefore that the gradient of the voltage at the end is also zero.

The value of λ determines the shape of the exponential voltage decay along the length of the cable. It is determined by the specific membrane resistance, the axial resistivity and the diameter of the cable:

$$\lambda = \sqrt{\frac{R_m d}{4R_a}} = \sqrt{\frac{r_m}{r_a}}. \quad (2.26)$$

In Equation 2.26 we have introduced two diameter-specific constants, r_m and r_a , defined in Table 2.3. These are convenient quantities that express the key passive electrical properties of a specific cable of arbitrary length. They are often used to simplify the equations representing a neurite of specific diameter.

This equation shows that the smaller the membrane resistance is relative to the axial resistance, the smaller the length constant will be. The leakier the membrane is (smaller r_m), the more current is lost earlier in its journey along the neurite. Just as the membrane time constant sets the temporal scale of a neurite, so the length constant sets the spatial scale.

The input resistance of a semi-infinite cable R_∞ is determined by the specific membrane resistance, the axial resistivity, and the diameter:

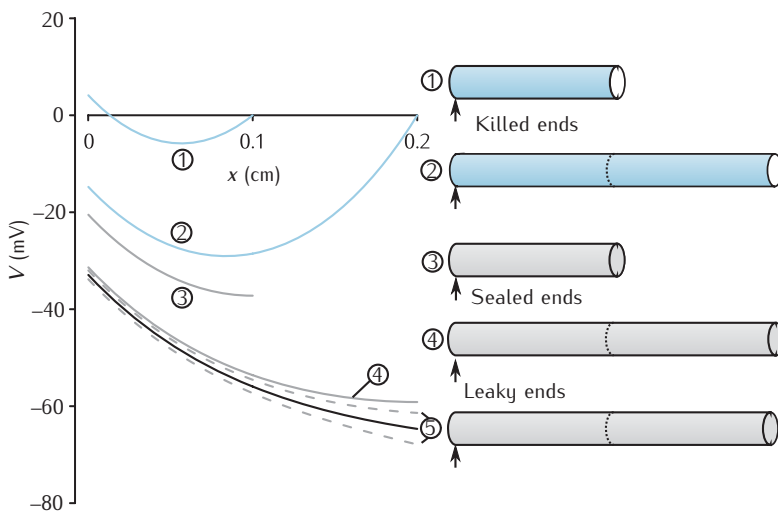
$$R_\infty = \frac{R_m}{\pi d \lambda} = \sqrt{\frac{4R_m R_a}{\pi^2 d^3}} = \sqrt{r_m r_a}. \quad (2.27)$$

This tells us that we should expect the input resistance of thinner neurites to be higher than that of thicker ones. This means that a given injection current will have a greater effect on the membrane potential of a thinner neurite. As we will see, this general idea also applies with time-varying input and in branching dendrites.

Finite cable

The situation of a cable of finite length is more complicated than the infinite cable as the boundary conditions of the cable at the far end (sealed, killed or leaky) come into play. It is possible to solve the cable equation analytically with a constant current injection applied to a finite cable. This will give an expression for the membrane potential as a function of distance along the cable that also depends on the injection current I_e and the type of end condition of the cable. The end condition is represented by a resistance R_L at the end of the cable. For a sealed end, the end resistance is considered to be so large that R_L is effectively infinite. For leaky end conditions, R_L is assumed to be finite. A killed end is a short circuit where the intracellular and extracellular media meet and there is zero potential difference at the end of the axon. The analytical solution to the finite cable equation in these cases is given in Box 2.6.

Examples of how different end conditions alter the change in voltage over the length of the axon are plotted in Figure 2.18. The solid black line shows the membrane potential in a semi-infinite cable, and serves as a reference. The two solid grey lines show the membrane potential in two cables with sealed ends but of different lengths, one of length $l = 1000 \mu\text{m}$ and the other $l = 2000 \mu\text{m}$. Given that the displacement of the membrane potential from its resting value of -70 mV is proportional to the input resistance, Figure 2.18 shows that the shorter cable has a higher input resistance than both the longer one and the semi-infinite cable. This makes sense since the shorter cable offers fewer paths to the extracellular medium than the longer one. The membrane potential of the longer cable is quite close to that of the semi-infinite cable. As the cable gets longer, the difference between the two will become negligible. Note that the gradient of the membrane potential at the end of a sealed end cable is zero. Since the gradient of the curve is proportional to the current flowing along the axon, a zero gradient means that there is no axial current flowing at the end of the cable, which has an infinitely large resistance.



The two blue lines show what happens under a killed end condition. The membrane potential at the far end of the cable is equal to the extracellular membrane potential (0 mV). This is because the circuit is effectively ‘short circuited’ by a zero end resistance.

The two dotted grey lines show what happens when there is a leaky end to the cable. Here, there is a finite resistance R_L at the cable end. The upper dotted line shows the situation when R_L is greater than R_∞ and the lower line shows R_L being less than R_∞ . The importance of this situation will become apparent in Chapter 4, where we consider simplifying branched dendrites.

2.9.2 Time-dependent behaviour of the membrane potential

So far we have ignored time in our study of the cable equation. It is possible to solve the cable equation to give mathematical expressions for the time course of the membrane potential at different points along a passive cable in response to pulses of current or continuous input. At any point along the dendrite, the time course of the membrane potential will be given by:

$$V(x, t) = C_0(x)e^{-t/\tau_0} + C_1(x)e^{-t/\tau_1} + C_2(x)e^{-t/\tau_2} + \dots \quad (2.28)$$

where the coefficients $C_n(x)$ depend on distance along the cable, τ_0 is the membrane time constant and τ_1 , τ_2 , and so on, are time constants with successively smaller values (Rall, 1969). A method for determining multiple time constants experimentally is described in Chapter 4.

Figure 2.17b shows the simulation of the membrane potential at different points along a cable following synaptic input at one end. After about 2 ms, in this simulation, the membrane potential at all points has equalised, and the membrane potential decays exponentially to its resting value. The time constant of this final decay is the membrane time constant, τ_0 , as this is the

Fig. 2.18 The membrane potential as a function of distance for different lengths of cable with different end terminal resistances when current of 0.5 nA is injected at one end (shown by arrows). The passive cable properties are $R_m = 6000 \Omega \text{ cm}^2$, $R_a = 35.4 \Omega \text{ cm}$, and $d = 2.5 \mu\text{m}$. From Equation 2.26, the length constant $\lambda = 1029 \mu\text{m}$. The black line shows the membrane potential in a semi-infinite cable. The solid grey lines (3, 4) refer to cables with sealed ends, one of length 1000 μm (approximately one length constant) and one of length 2000 μm (approximately two length constants). The solid blue lines (1, 2) refer to cables with one killed end. The dotted grey lines (5) refer to cables with leaky ends; see text for details.

Box 2.6 | Solutions to the cable equation

It is often useful to express the length along the neurite or cable in relation to the length constant. We denote this normalised length as X , defined as $X = x/\lambda$. The quantity X is dimensionless and it leads to clearer formulae. For example, the steady state membrane potential along a semi-infinite cable (compare with Equation 2.25) becomes:

$$V(X) = E_m + R_\infty I_e e^{-X}$$

For clarity, we look at the finite cable solutions for the sealed end and leaky end boundary conditions. As we are not dealing with the killed end case, we do not present it here.

Given a resistance R_L at the end of a leaky cable and injection current I_e , the membrane potential as a function of length X is given by:

$$V(X) = E_m + R_\infty I_e \frac{R_L/R_\infty \cosh(L-X) + \sinh(L-X)}{R_L/R_\infty \sinh L + \cosh L}, \quad (\text{a})$$

where R_∞ is the input resistance of a semi-infinite cable with the same diameter, membrane resistance and cytoplasmic resistivity (Equation 2.27) and L is the length of the cable measured in terms of the length constant λ , the true length of the cable being $l = L\lambda$. The **hyperbolic functions** sinh and cosh are the hyperbolic sine and hyperbolic cosine, defined as:

$$\sinh x = \frac{e^x - e^{-x}}{2} \quad \cosh x = \frac{e^x + e^{-x}}{2}.$$

According to the definition of input resistance (Equation 2.19), the input resistance of the leaky cable is:

$$R_{in} = \frac{V(0) - E_m}{I_e} = R_\infty \frac{R_L/R_\infty \cosh L + \sinh L}{R_L/R_\infty \sinh L + \cosh L}$$

In the case of a sealed end, where $R_L = \infty$, the membrane potential as a function of length in Equation (a) simplifies to:

$$V(X) = E_m + R_\infty I_e \frac{\cosh(L-X)}{\sinh L} \quad (\text{b})$$

and the input resistance simplifies to:

$$R_{in} = R_\infty \frac{\cosh L}{\sinh L} = R_\infty \coth L,$$

where the function coth is the hyperbolic cotangent, defined as:

$$\coth x = \frac{\cosh x}{\sinh x} = \frac{e^x + e^{-x}}{e^x - e^{-x}}.$$

longest time constant ($\tau_0 > \tau_1$, etc.). The contributions of the faster time constants, τ_1 , τ_2 , etc., become smaller as t becomes large.

The solutions of the time-dependent cable equation are not just of descriptive value, but have also been decisive in resolving interpretations of data (Box 2.7). In Chapter 4, we see how the smaller time constants can be used to infer the length constant of a dendrite.

Box 2.7 Eccles, Rall and the charging time constant of motor neurons

A dispute between Eccles and Rall – described in detail in Segev *et al.* (1995) – over how to interpret the charging curves of motor neurons demonstrates the importance of time-dependent solutions to the cable equation. Recall that when a current is injected into a small passive neuron, the membrane potential responds by shifting to a new steady state value. The time course of the approach to the new potential varies exponentially with the membrane time constant. Coombs *et al.* (1956) injected current into motor neurons and recorded the membrane potential as a function of time (thick black line in Figure 2.19). These data could be fitted by an exponential function with a time constant of 2.5 ms (Figure 2.19, dashed curve). Under the implicit assumption that a spatially extended motor neuron has the equivalent electrical behaviour to a neuron composed of a soma only, Coombs *et al.* concluded that the membrane time constant was 2.5 ms.

Rall showed that this method of analysing the data gives an answer for the membrane time constant that is too small by a factor of two (Rall, 1957). In Figure 2.19, the blue line shows Rall's solution of the full time-dependent cable equation for a 'ball and stick' model of the motor neuron, a soma with a single dendrite attached to it, in which the membrane time constant is 5 ms. This solution can be seen to be very similar to the charging curve of a lone soma with a membrane time constant of 2.5 ms. For comparison, the charging curve of a lone soma with a membrane time constant of 5 ms is shown in black.

The Eccles group was effectively using the lone soma model to analyse data from a soma and dendrites. They therefore had to fit the experimental data (dashed line) with a curve with a shorter time constant instead of fitting the curve generated from the ball and stick model with a longer time constant (black line); this procedure therefore gave the wrong result.

The expression for the charging curve of the ball and stick model is $V/V_0 = \frac{1}{6}(1 - \exp(-t/\tau)) + \frac{5}{6} \operatorname{erf} \sqrt{t/\tau}$, where the function 'erf' is the **error function**, defined below. The factors $\frac{1}{6}$ and $\frac{5}{6}$ derive from Rall's assumption that in the steady state, one-sixth of the current injected flows out through the soma and the remaining five-sixths through the dendrites.

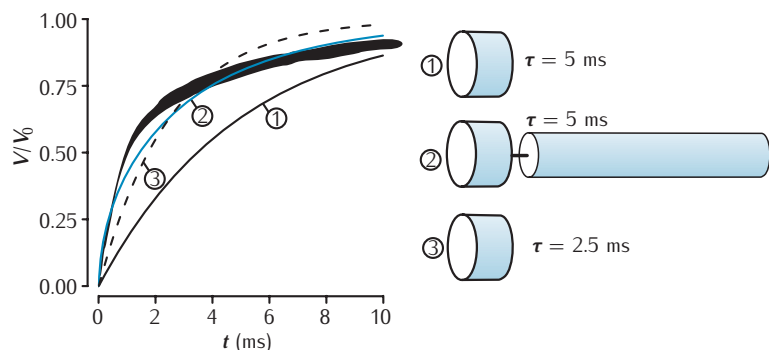
The error function $\operatorname{erf} x$ is the area under the Gaussian $\frac{2}{\sqrt{\pi}} \exp(u^2)$ between 0 and x :

$$\operatorname{erf} x = \frac{2}{\sqrt{\pi}} \int_0^x \exp(u^2) du.$$

2.10 | Summary

This chapter has touched on some of the primary electrical properties of neurons that provide a basis for the development of neuronal models. The physical properties of certain cell components, such as lipid membranes,

Fig. 2.19 Membrane charging curves in three models. The thick black line shows the original data of Coombs *et al.* (1956). The solid black curve (1) shows the membrane charging curve of a point neuron with a membrane time constant of 5 ms. The blue curve (2) shows the charging curve of a 'ball and stick' neuron in which the membrane time constant is 5 ms. The dashed black curve (3) shows the charging curve of a point neuron which has a membrane time constant of 2.5 ms. It can be seen that the charging curve of the ball and stick neuron is similar to the curve of the point neuron with a membrane time constant a factor of two smaller. All membrane potentials are shown relative to the resting potential, and as a fraction of the steady state displacement of the membrane potential from rest V_0 .



intracellular and extracellular solutions and passive membrane channels, are drawn together to build an electrical circuit model of the neurite. This RC circuit model is an approximation of the passive electrical properties and is based on assumptions such as linear I - V characteristics for ions traversing the membrane, i.e. passive membrane channels acting as electrical resistors. The Goldman–Hodgkin–Katz theory of current flow through the membrane provides an alternative model that demonstrates that the linear assumptions made in the electrical model are inappropriate for ions such as Ca^{2+} . Models of multiple channel types will generally involve combinations of these approaches (Chapter 5).

Modelling the membrane potential along a length of a neurite can be achieved by connecting together individual electrical circuits, or compartments. This is a fundamental modelling approach used for simulating the electrical properties over complex neuronal morphologies (Chapter 4). Treating a length of neurite as a cable also provides a useful analogy for understanding the influence that specific passive properties, such as R_m and R_a , have on the membrane potential over the length of the cable.

Chapter 3

The Hodgkin–Huxley model of the action potential

This chapter presents the first quantitative model of active membrane properties, the **Hodgkin–Huxley model**. This was used to calculate the form of the action potentials in the squid giant axon. Our step-by-step account of the construction of the model shows how Hodgkin and Huxley used the **voltage clamp** to produce the experimental data required to construct mathematical descriptions of how the sodium, potassium and leak currents depend on the membrane potential. Simulations of the model produce action potentials similar to experimentally recorded ones and account for the threshold and refractory effects observed experimentally. While subsequent experiments have uncovered limitations in the Hodgkin–Huxley model descriptions of the currents carried by different ions, the **Hodgkin–Huxley formalism** is a useful and popular technique for modelling channel types.

3.1 | The action potential

In the previous chapter we described the basis of the membrane resting potential and the propagation of signals down a passive neurite. We now explain a widespread feature of signalling in the nervous system: the **action potential**.

Intracellular recordings (Figure 3.1) demonstrate that action potentials are characterised by a sharp increase in the membrane potential (**depolarisation** of the membrane) followed by a somewhat less sharp decrease towards the resting potential (**repolarisation**). This may be followed by an afterhyperpolarisation phase in which the membrane potential falls below the resting potential before recovering gradually to the resting potential. The main difference between the propagation of action potentials and passive propagation of signals is that action potentials are **regenerative**, so their magnitude does not decay during propagation.

Hodgkin and Huxley (partly in collaboration with Katz) were the first to describe the active mechanisms quantitatively (Hodgkin *et al.*, 1952; Hodgkin and Huxley, 1952a, b, c, d). Their work proceeded in three main stages:

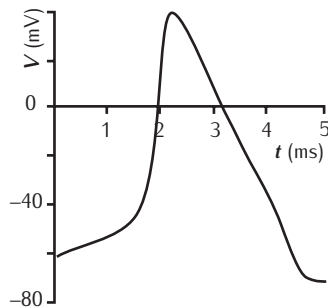


Fig. 3.1 The squid giant axon action potential. Simulated action potential in the squid giant axon at 6.3°C.

- (1) They recorded intracellularly from the squid giant axon. They used a voltage clamp amplifier in space clamp configuration (Box 3.1) to look at how current flow depends on voltage. By changing the extracellular concentration of sodium, they were able to infer how much of the current was carried by sodium ions and how much by other ions, principally potassium.
- (2) They fitted these results to a mathematical model. Part of the model is the theoretically motivated framework developed in Chapter 2. Another part is based on the idea of ion-selective voltage-dependent gates controlled by multiple gating particles. The remainder of the model is determined by fitting curves to experimental data. The model is expressed in terms of a set of equations which are collectively called the **Hodgkin–Huxley model**, or **HH model** for short.
- (3) They solved the equations defining the model to describe the behaviour of the membrane potential under various conditions. This involved solving the equations numerically. The simulated action potentials were very similar to the recorded ones. The threshold, propagation speed and refractory properties of the simulated action potentials also matched those of the recorded action potentials.

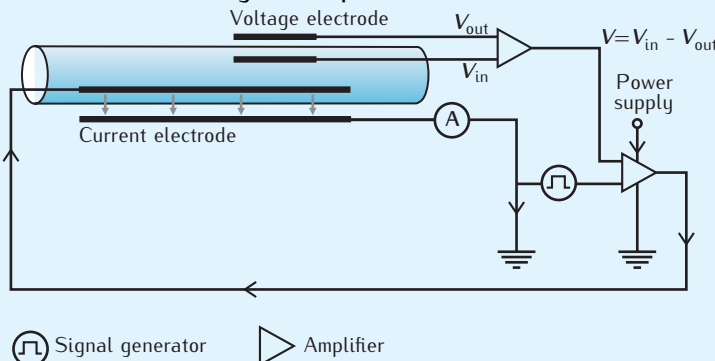
Their work earned them a Nobel prize in 1963, shared with Eccles for his work on synaptic transmission.

Hodgkin and Huxley were not able to deduce the molecular mechanisms underlying the active properties of the membrane, which was what they had set out to do (Box 3.3). Nevertheless, their ideas were the starting point for the biophysical understanding of the structures now known as ion channels, the basics of which are outlined in Chapter 5. Hille (2001) provides a comprehensive treatment of the structure and function of ion channels.

The HH model characterises two types of active channel present in the squid giant axon, namely a sodium channel and a potassium channel belonging to the family of potassium delayed rectifier channels. Work since 1952 in preparations from many different species has uncovered a large number of other types of active channel. Despite the age and limited scope of the HH model, a whole chapter of this book is devoted to it as a good deal of Hodgkin and Huxley's methodology is still used today:

- (1) Voltage clamp experiments are carried out to determine the kinetics of a particular type of channel, though now the methods of recording and isolating currents flowing through particular channel types are more advanced.
- (2) A model of a channel type is constructed by fitting equations, often of the same mathematical form, to the recordings. Modern methods of fitting equation parameters to data are covered later on, in Section 4.5.
- (3) Models of axons, dendrites or entire neurons are constructed by incorporating models of individual channel types in the compartmental models introduced in Chapter 2. Once the equations for the models are solved, albeit using fast computers rather than by hand, action potentials and other behaviours of the membrane potential can be simulated.

Box 3.1 | The voltage clamp



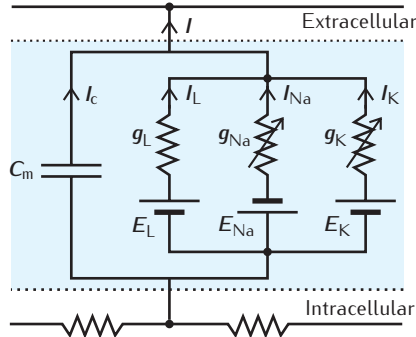
The next great experimental advance after intracellular recording was the voltage clamp. This was developed by Cole and Marmont in the 1940s at the University of Chicago (Marmont, 1949; Cole, 1968). Hodgkin, who was already working on a similar idea, learnt about the technique from Cole in 1947. The basic idea is to clamp the membrane potential to a steady value or to a time-varying profile, determined by the experimenter (see figure above). As with a current clamp (Chapter 2), an electrode is used to inject current I_e into the cell. At the same time, a voltage electrode records the membrane potential. The apparatus adjusts the injected current continually so that it is just enough to counteract deviations of the recorded membrane potential from the desired voltage value. This ensures that the membrane potential remains at the desired steady value or follows the required time-varying profile.

Hodgkin and Huxley used a **space clamp** configuration, where the electrodes are long, thin wires that short circuit the electrical resistance of the cytoplasm and the extracellular space. This ensures that the potential is uniform over a large region of membrane and that therefore there is no axial current in the region. There is no contribution to the membrane current from the axial current. In this configuration, the membrane current is identical to the electrode current, so the membrane current can be measured exactly as the amount of electrode current to be supplied to keep the membrane at the desired value.

To understand the utility of the voltage clamp, we recall that the membrane current I comprises a capacitive and an ionic current (Equation 3.1). When the voltage clamp is used to set the membrane potential to a constant value, no capacitive current flows as the rate of change in membrane potential, dV/dt , is zero. The voltage clamp current is then equal to the ionic current. Therefore, measuring the voltage clamp current means that the ionic current is being measured directly.

In this chapter, we focus on the second (modelling) and third (simulation) parts of the procedure. In Section 3.2, we begin with a step-by-step description of how Hodgkin and Huxley used a mixture of physical intuition and curve-fitting to produce their mathematical model. In Section 3.3, we look

Fig. 3.2 The Hodgkin–Huxley equivalent electrical circuit.



at simulations of nerve action potentials using the model, and compare these with the experimental recordings. In Section 3.4 we consider how Hodgkin and Huxley corrected for temperature. Finally, in Section 3.5, we consider the simplifications inherent in the HH model and how to use the Hodgkin–Huxley formalism to build models of ion channels.

3.2 | The development of the model

The starting point of the HH model is the equivalent electrical circuit of a compartment shown in Figure 3.2. There are three types of ionic current in the circuit: a **sodium current**, I_{Na} , a **potassium current**, I_K , and a current that Hodgkin and Huxley dubbed the **leak current**, I_L , which is mostly made up of chloride ions. The key difference between this circuit and the one presented in Chapter 2 is that the sodium and potassium conductances depend on voltage, as indicated by the arrow through their resistors. Since their properties change with the voltage across them, they are **active** rather than **passive** elements.

The equation that corresponds to the equivalent electrical circuit is:

$$I = I_c + I_i = C_m \frac{dV}{dt} + I_i, \quad (3.1)$$

where the **membrane current** I and the **capacitive current** I_c are as defined in Chapter 2. The total **ionic current** I_i is the sum of sodium, potassium and leak currents:

$$I_i = I_{\text{Na}} + I_K + I_L. \quad (3.2)$$

The magnitude of each type of ionic current is calculated from the product of the ion's driving force and the membrane conductance for that ion:

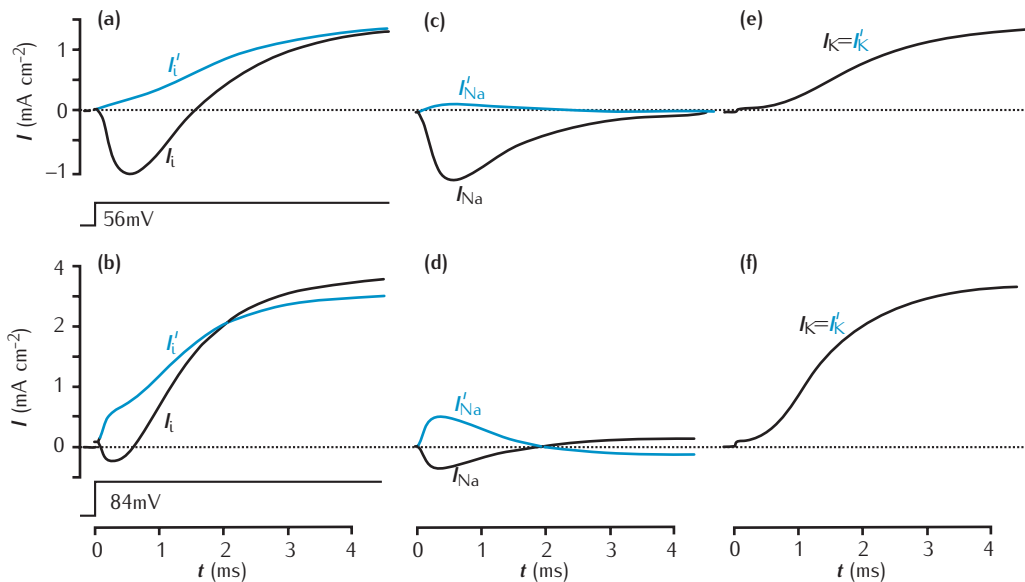
$$I_{\text{Na}} = g_{\text{Na}}(V - E_{\text{Na}}), \quad (3.3)$$

$$I_K = g_K(V - E_K), \quad (3.4)$$

$$I_L = \bar{g}_L(V - E_L), \quad (3.5)$$

where the sodium, potassium and leak conductances are g_{Na} , g_K and \bar{g}_L respectively, and E_{Na} , E_K and E_L are the corresponding equilibrium potentials. The bar on the leakage conductance \bar{g}_L indicates that it is a constant, in contrast with the sodium and potassium conductances which depend on the recent history of the membrane potential.

As defined in Section 2.4.1, the **driving force** of an ion is the difference between the membrane potential and the equilibrium potential of that ion. Hence, the sodium driving force is $V - E_{\text{Na}}$.



3.2.1 The potassium current

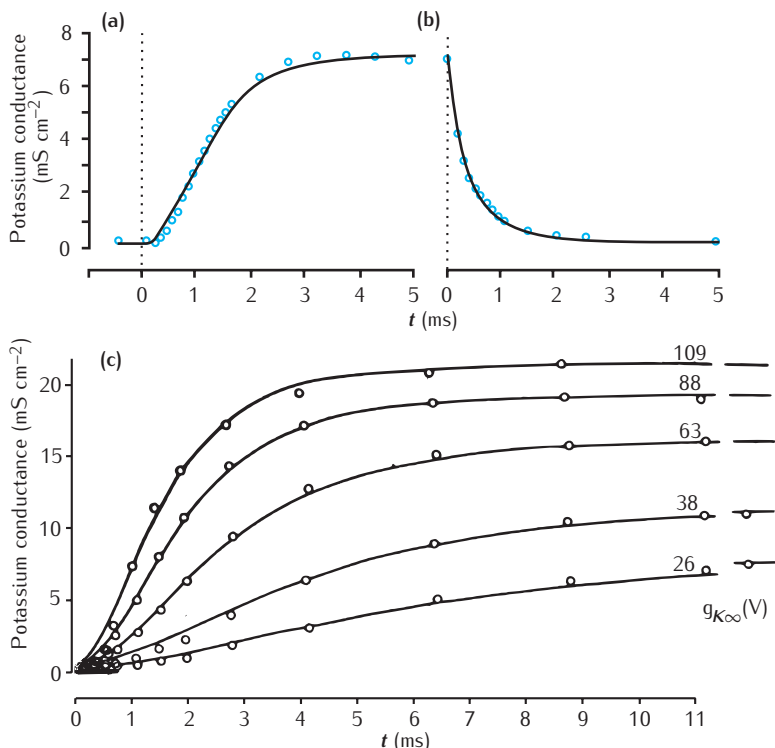
Hodgkin and Huxley measured the potassium conductance for a number of voltage clamp holding potentials. After first isolating the potassium current (Box 3.2 and Figure 3.3), they calculated the conductance using Equation 3.4. The form of the curves at each holding potential is similar to the example of the response to a holding potential of 25 mV above rest, shown in Figure 3.4a. Upon depolarisation, the conductance rises to a constant value. This rise in conductance is referred to as **activation**. The conductance stays at this peak value until the voltage is stepped back down to rest, where the conductance then decays exponentially (Figure 3.4b). The fall in conductance is called **deactivation**.

Box 3.2 | The ion substitution method

In order to fit the parameters of their model, Hodgkin and Huxley needed to isolate the current carried by each type of ion. To do this they used the **ion substitution method**. They lowered the extracellular sodium concentration by replacing a proportion of the sodium ions in the standard extracellular solution (sea water) with impermeant choline ions. The currents recorded under voltage clamp conditions in sea water and in choline water were carried by sodium ions, potassium ions and other ions. On the assumption that the independence principle holds (Box 2.4), the currents carried by sodium ions in sea water and choline water differ, but the other ionic flows will remain the same. Therefore, the difference between currents recorded in sodium water and choline water can be used to infer the sodium current (Figure 3.3). Having isolated the sodium current and calculated the leak current by other methods, the potassium current can be deduced by subtracting the sodium and leak currents from the total current.

Fig. 3.3 The sodium current separated from the other currents using the ion substitution method (Box 3.2). (a) The ionic current in sea water (I_i) and in choline water (I'_i) in response to a voltage clamp of 56 mV (sea water) or 60 mV (choline water) above resting potential. (b) The same traces as (a), but in response to a voltage clamp of 84 mV (sea water) and 88 mV (choline water) above resting potential. (c,d) The sodium currents in sea water (I_{Na}) and in choline water (I'_{Na}) inferred from pairs of ionic currents in (a) and (b). (e,f) The potassium current in sea water (I_K) and in choline water (I'_K) inferred from the pairs of ionic currents in (a) and (b), as described in the text. These two currents are, in fact, identical. The recording temperature was 8.5 °C. Adapted from Hodgkin and Huxley (1952a), with permission from John Wiley & Sons Ltd.

Fig. 3.4 Time course of the potassium conductance in a voltage clamp with (a) a step from resting potential to 25 mV above resting potential and (b) return to resting potential. The open circles represent data points derived from experiment. The solid lines are fits to the data (see text). (c) Time course of potassium conductance in response to voltage clamp steps to varying holding potentials; the voltage of the holding potential relative to rest is shown on each curve. Note that the activation of the conductance in response to a holding potential of 26 mV is slower than the activation in response to almost the same holding potential in (a). This is due to a difference in recording temperatures: 21 °C in (a) and (b), compared to 6 °C in (c). Adapted from Hodgkin and Huxley (1952d), with permission from John Wiley & Sons Ltd.



The family of conductance activation curves (Figure 3.4c) show that there are two features of the curve that depend on the level of the voltage clamp holding potential:

- (1) The value that the conductance reaches over time, $g_{K\infty}$, increases as the holding potential is increased. It approaches a maximum at high holding potentials. This implied that there was a **maximum potassium conductance** per unit area of membrane, which Hodgkin and Huxley denoted \bar{g}_K and were able to estimate.
- (2) The speed at which the limiting conductance is approached becomes faster at higher depolarising holding potentials.

The conductance curves show that the limiting conductance and the rate at which this limit is approached depends on the membrane voltage. Hodgkin and Huxley considered a number of models for describing this voltage dependence (Box 3.3). They settled on the idea of the membrane containing a number of **gates** which can be either closed to the passage of all ions or open to the passage of potassium ions. Each gate is controlled by a number of independent **gating particles**, each of which can be in either an open or closed position. For potassium ions to flow through a gate, *all* of the gating particles in the gate have to be in the open position.

The movement of gating particles between their closed and open positions is controlled by the membrane potential. The **gating variable** n is the probability of a single potassium gating particle being in the open state. As the gating particles are assumed to act independently of each other, the probability of the entire gate being open is equal to n^x , where x is the number

Box 3.3 Gating particles

Hodgkin and Huxley's goal had been to deduce the molecular mechanisms underlying the permeability changes evident in their experimental data. Reflecting on this later, Hodgkin (1976) wrote:

although we had obtained much new information the overall conclusion was basically a disappointment As soon as we began to think about molecular mechanisms it became clear that the electrical data would by itself yield only very general information about the class of system likely to be involved. So we settled for the more pedestrian aim of finding a simple set of mathematical equations which might plausibly represent the movement of electrically charged gating particles.

Their initial hypothesis was that sodium ions were carried across the membrane by negatively charged carrier particles or dipoles. At rest these would be held by electrostatic forces. Consequently, they would not carry sodium ions in this state and, on depolarisation, they could carry sodium into the membrane. However, Hodgkin and Huxley's data pointed to a voltage-dependent gate. They settled on deriving a set of equations that would represent the theoretical movement of charged gating particles acting independently in a voltage-dependent manner.

In the contemporary view, the idea of gating particles can be taken to imply the notion of gated channels, but the hypothesis of ion pores or channels was not established at that time. Thus, though Hodgkin and Huxley proposed charged gating particles, it is perhaps tenuous to suggest that they predicted the structure of gated channels. Nevertheless, there is a correspondence between the choice of the fourth power for potassium conductance and the four subunits of the tetrameric potassium channel (Section 5.1).

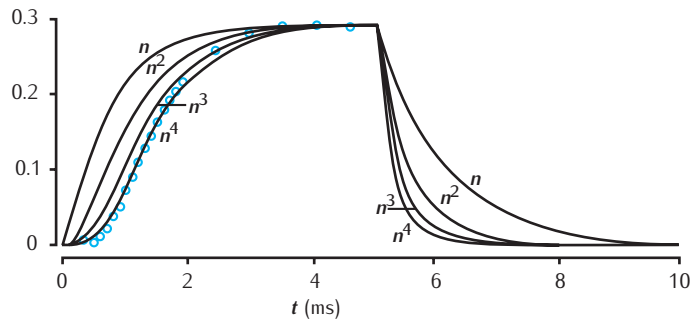
of gating particles in the gate. Although, as described in Chapter 5, gating particles do not act independently, this assumption serves reasonably well in the case of potassium conductance in the squid giant axon. When there are large numbers of particles present, the large numbers ensure the proportion of particles being in the open position is very close to the probability n of an individual channel being in the open position, and the expected proportion of gates open is also the same as the probability of an individual gate being open, n^x .

The conductance of the membrane is given by the maximum conductance multiplied by the probability of a gate being open. For example, if each gate is controlled by four gating particles, as Hodgkin and Huxley's experiments suggested, the relationship between the potassium conductance g_K and gating particle open probability n is:

$$g_K = \bar{g}_K n^4. \quad (3.6)$$

If each potassium gate were dependent solely on a single theoretical gating particle, the conductance would be $\bar{g}_K n$.

Fig. 3.5 A family of curves showing the time course of n raised to various powers. From top to bottom curves with n raised to the power 1, 2, 3 and 4 are shown. The parameters are as in Figure 3.4: $\tau_n(V_0) = 1.1 \text{ ms}$, $\tau_n(V_1) = 0.75 \text{ ms}$, $g_{K\infty}(V_0) = 0.09 \text{ mS cm}^{-2}$ and $g_{K\infty}(V_1) = 7.06 \text{ mS cm}^{-2}$. To compare the curves, the time course of n raised to the powers 2, 3 and 4 have initial and final values of n given by $(g_{K\infty}/\bar{g}_K)^{1/2}$, $(g_{K\infty}/\bar{g}_K)^{1/3}$, and $(g_{K\infty}/\bar{g}_K)^{1/4}$. The circular data points shown are the same as in Figure 3.4. Adapted from Hodgkin and Huxley (1952d), with permission from John Wiley & Sons Ltd.



The movement of a gating particle between its closed (C) and open (O) positions can be expressed as a reversible chemical reaction:



The fraction of gating particles that are in the O state is n , and the fraction in the C state is $1 - n$. The variables α_n and β_n are **rate coefficients** which depend on the membrane potential; sometimes they are written $\alpha_n(V)$ and $\beta_n(V)$ to highlight their dependence on voltage. Just as rate laws govern the evolution of concentrations in chemical reactions, there is a **rate law** or **first order kinetic equation** corresponding to Equation 3.7, which specifies how the gating variable n changes over time:

$$\frac{dn}{dt} = \alpha_n(1 - n) - \beta_n n. \quad (3.8)$$

The time course of the response of the gating variable n to a step change in membrane potential to a particular voltage V_1 can be determined by integrating Equation 3.8. A solution for the response of n to a voltage step is shown in Figure 3.5, along with the time courses of n raised to various powers. The curve for n looks roughly like the conductance curve shown in Figure 3.4. The main difference is that the theoretical time course of n is not S-shaped like the experimental curve; it has no initial inflection. As Figure 3.5 shows, when the time course of n in response to a positive voltage step is squared, cubed or raised to the power four, the resulting rising curve does have an inflection. The decaying part of the curve retains its decaying exponential shape. Hodgkin and Huxley found that raising n to the power four could give a better fit than cubing or squaring, suggesting that each gate contains four gating particles.

The general form of the time course for $n(t)$ in response to a voltage step is:

$$n(t) = n_\infty(V_1) - (n_\infty(V_1) - n_0) \exp(-t/\tau_n(V_1)), \quad (3.9)$$

where n_0 is the value of n at the start of the step, defined to be at time zero; the variables $n_\infty(V)$ and $\tau_n(V)$ are related to the rate coefficients $\alpha_n(V)$ and $\beta_n(V)$ by:

$$n_\infty = \frac{\alpha_n}{\alpha_n + \beta_n} \quad \text{and} \quad \tau_n = \frac{1}{\alpha_n + \beta_n}, \quad (3.10)$$

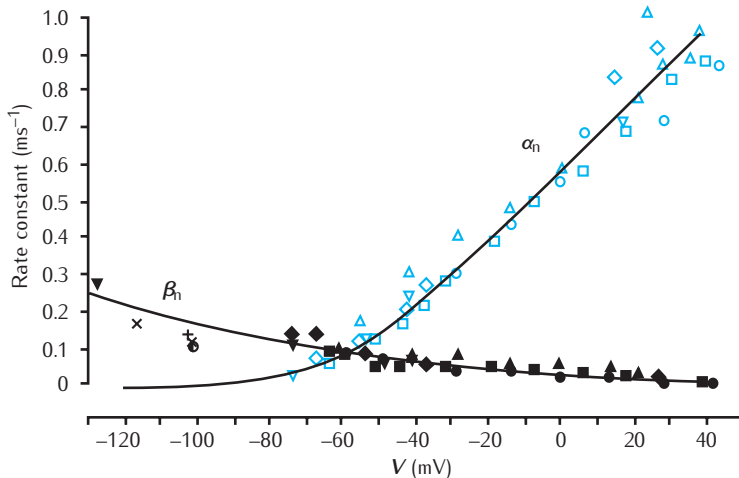


Fig. 3.6 Potassium rate coefficients α_n and β_n as a function of membrane potential. Blue symbols refer to measurements of α_n and black symbols to β_n . The shapes of the symbols identify the axon in which the value was recorded. Adapted from Hodgkin and Huxley (1952d), with permission from John Wiley & Sons Ltd.

where n_∞ is the limiting probability of a gating particle being open if the membrane potential is steady as t approaches infinity and τ_n is a time constant. When the membrane potential is clamped to V_1 , the rate coefficients will immediately move to new values $\alpha_n(V_1)$ and $\beta_n(V_1)$. This means that, with the membrane potential set at V_1 , over time n will approach the limiting value $n_\infty(V_1)$ at a rate determined by $\tau_n(V_1)$. The variables n_∞ and τ_n allow Equation 3.8 to be rewritten as:

$$\frac{dn}{dt} = \frac{n_\infty - n}{\tau_n}. \quad (3.11)$$

The final step in modelling the potassium current is to determine how the rate coefficients α_n and β_n in the kinetic equation of n (Equation 3.8) depend on the membrane potential. In using experimental data to determine these parameters, it is convenient to use the alternative quantities n_∞ and τ_n (Equation 3.10). The value of n_∞ at a specific voltage V may be determined experimentally by recording the maximum conductance attained at that voltage step, called $g_{K\infty}(V)$. Using Equation 3.6, the value of n_∞ at voltage V is then given by:

$$n_\infty(V) = \left(\frac{g_{K\infty}(V)}{\bar{g}_K} \right)^{\frac{1}{4}}. \quad (3.12)$$

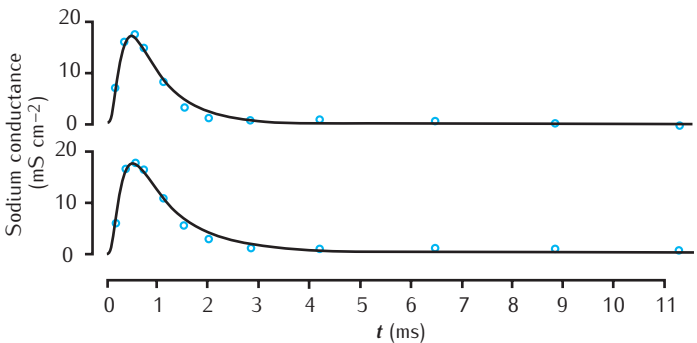
The value for τ_n at a particular membrane potential is obtained by adjusting it so as to give the best match predicted time course of n given in Equation 3.9 and the data (Figure 3.4).

This process provides values for n_∞ and τ_n at various voltages. Hodgkin and Huxley converted them to the values for α_n and β_n using the inverse formulae to Equation 3.10:

$$\alpha_n = \frac{n_\infty}{\tau_n} \quad \text{and} \quad \beta_n = \frac{1 - n_\infty}{\tau_n}. \quad (3.13)$$

These experimental data points are shown in Figure 3.6, along with plots of the final fitted functions for α_n and β_n ; see also Figure 3.10 for the equivalent

Fig. 3.7 Time course of the sodium conductance in a voltage clamp with a step change in voltage from resting potential to 76 mV and 88 mV above resting potential. The open circles represent data points derived from experiment. The solid lines are fits to the data (see text). Adapted from Hodgkin and Huxley (1952d), with permission from John Wiley & Sons Ltd.



n_∞ and τ_n plots. The equations for the functions $\alpha_n(V)$ and $\beta_n(V)$ are given in the summary of the entire set of equations describing the potassium ionic current through the membrane:

$$\begin{aligned} I_K &= \bar{g}_K n^4 (V - E_K), \\ \frac{dn}{dt} &= \alpha_n(1-n) - \beta_n n, \\ \alpha_n &= 0.01 \frac{V + 55}{1 - \exp(-(V + 55)/10)}, \\ \beta_n &= 0.125 \exp(-(V + 65)/80). \end{aligned} \quad (3.14)$$

3.2.2 The sodium ionic current

In a similar manner to the procedure used for potassium conductance, Hodgkin and Huxley isolated the sodium current and calculated the sodium conductance curves over a range of voltage clamp steps. The time course of the sodium conductance is illustrated in Figure 3.7. The most notable difference from the potassium conductance is that the sodium conductance reaches a peak and then decays back to rest, even while the clamped voltage remains in a sustained depolarising step. This reduction in conductance is termed **inactivation**, in contrast to deactivation (Section 3.2.1) when the reduction in conductance is due to termination of a voltage step. The time course of the conductance during inactivation differs from the time course during deactivation, and this suggested that two distinct processes can act to reduce the conductance.

The inactivation of the sodium conductance meant that Hodgkin and Huxley could not use the description they used for potassium, where there was just one gating variable, n . In order to quantify the inactivation process, Hodgkin and Huxley applied a range of voltage clamp experiments and protocols (Box 3.4 and Figures 3.8 and 3.9). They introduced a gating type variable, called b , to represent the level of inactivation. It could either be in the state of ‘not inactivated’ or the state of ‘inactivated’. The rate of transition between these states is voltage dependent and governed by a first order kinetic equation similar to n :

$$\frac{db}{dt} = \alpha_b(1-b) - \beta_b b. \quad (3.15)$$

As with the n gating particle, the voltage-dependent rate coefficients α_h and β_h can be reexpressed in terms of a limiting value b_∞ and a time constant τ_h . Hodgkin and Huxley's experiments suggested that sodium conductance was proportional to the inactivation variable b .

Hodgkin and Huxley completed their model of sodium conductance by introducing another gating particle which, like n , may be viewed as the proportion of theoretical gating particles that are in an open state, determining sodium conductance activation. They called this sodium activation particle m . As with n and b , the time course of m was governed by a first order kinetic equation with voltage-dependent forward and backward rates α_m and β_m :

$$\frac{dm}{dt} = \alpha_m(1-m) - \beta_m m. \quad (3.16)$$

As with potassium (Figure 3.5), the activation curve of the sodium conductance is inflected. The inflection was modelled satisfactorily by using three independent m gating particles, making the sodium conductance:

$$g_{Na} = \bar{g}_{Na} m^3 b. \quad (3.17)$$

This enabled a good fit to be made to experimental recordings by adjusting m_∞ and τ_m for different holding potentials and \bar{g}_{Na} for all holding potentials. As with the gating variable n , Hodgkin and Huxley converted the limiting values and time constants of the m and b variables into rate coefficients (α_m , β_m and α_h , β_h) and plotted each as a function of voltage. They then found a fit to each rate coefficient that matched their experimental data. The final model of the sodium current is given by the following set of equations:

$$\begin{aligned} I_{Na} &= \bar{g}_{Na} m^3 b(V - E_{Na}), \\ \frac{dm}{dt} &= \alpha_m(1-m) - \beta_m m, \quad \frac{db}{dt} = \alpha_h(1-b) - \beta_h b, \\ \alpha_m &= 0.1 \frac{V + 40}{1 - \exp(-(V + 40)/10)}, \quad \alpha_h = 0.07 \exp(-(V + 65)/20), \\ \beta_m &= 4 \exp(-(V + 65)/18), \quad \beta_h = \frac{1}{\exp(-(V + 35)/10) + 1}. \end{aligned} \quad (3.18)$$

3.2.3 The leak current

Hodgkin and Huxley's evidence suggested that while potassium is a major part of the non-sodium ionic current, other ions besides sodium might carry current across the membrane. At the potassium equilibrium potential, they found that some non-sodium current still flows. This current could not be due to potassium ions since the driving force $V - E_K$ was zero. Hodgkin and Huxley proposed that it was due to a mixture of ions, and they dubbed it the leak current I_L . They assumed this was a resting background current that was not dependent on voltage. Using a quasi-ohmic current–voltage relationship they derived E_L and \bar{g}_L from their experimental results. Both the leakage conductance and equilibrium potential are due largely to the permeability

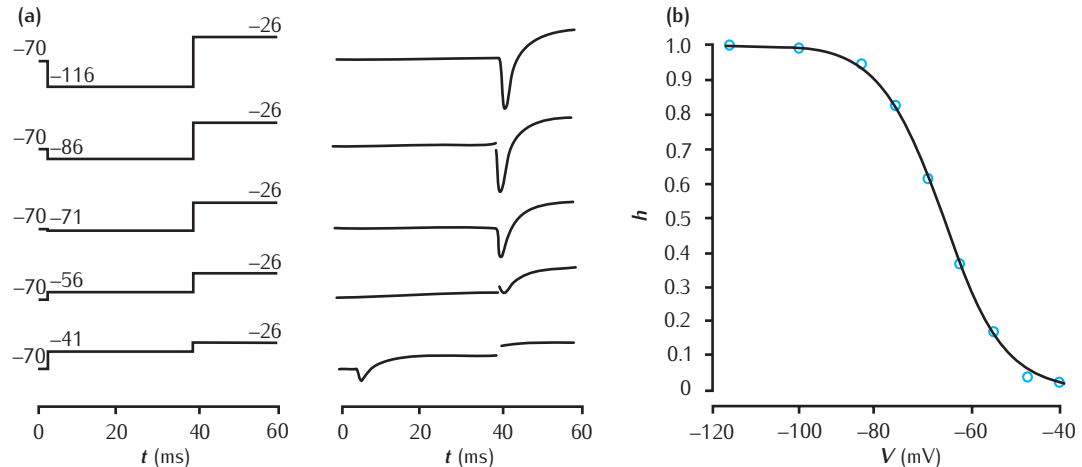


Fig. 3.8 (a) Two-pulse protocol used to calculate the influence of membrane potential on the inactivation of sodium in the squid giant axon. From a rest holding potential, the membrane is shifted to a test potential and then stepped to a fixed potential (-26 mV). The sodium current recorded in response to the final step (right) is influenced by the level of inactivation resulting from the test potential. (b) The level of inactivation as a function of the test potential (recorded current relative to the maximum current). Adapted from Hodgkin and Huxley (1952c), with permission from John Wiley & Sons Ltd.

of the membrane to chloride ions. The leak current is modelled by:

$$I_L = \bar{g}_L(V - E_L). \quad (3.19)$$

Although the leak conductance \bar{g}_L in the Hodgkin–Huxley circuit and the membrane resistance R_m in the passive circuit (Chapter 2) appear similar, they have different meanings. In the HH model, the resting membrane potential differs from the electromotive force of the leak battery and the resting membrane resistance is not equal to the inverse of the leak conductance. Instead, the resting membrane potential and the resting membrane resistance are determined by the sodium, potassium and leak resting conductances. We return to this difference in Section 4.4.

3.2.4 The complete model

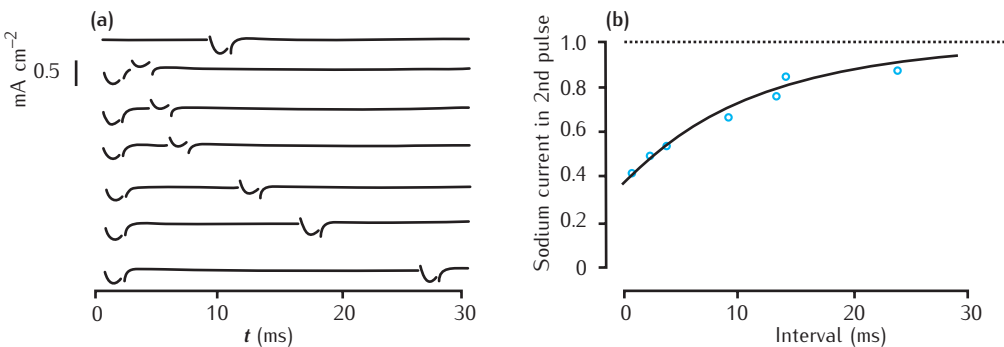
In the final paper of the series, Hodgkin and Huxley (1952d) inserted their expressions for the three ionic currents (Equations 3.3–3.5) into the membrane equation (Equation 3.1) to give a description of how the membrane potential in a small region of squid giant axon changes over time:

$$C_m \frac{dV}{dt} = -\bar{g}_L(V - E_L) - \bar{g}_{Na}m^3 h(V - E_{Na}) - \bar{g}_K n^4(V - E_K) + I, \quad (3.20)$$

where I is the **local circuit current**, the net contribution of the axial current from neighbouring regions of the axon. In a continuous cable model of the axon, this contribution is the second derivative of the membrane potential with respect to space (Equation 2.24). When Equation 3.20 is put together with the differential equations for the gating variables n , m and h and the expressions for the rate coefficients (Equations 3.14 and 3.18), the resulting set of four differential equations forms the HH model. It is summarised in Box 3.5.

Equation 3.20 could equally well relate to a compartment in a compartmental model, as described in Section 2.8. In this case, the local circuit current depends on the membrane potential in the neighbouring compartments (Equations 2.20).

The system can be simplified by imposing the space clamp condition (Box 3.1) so that the membrane potential is constant over the membrane.



This means that there is no local current and the system reduces to a much simpler first order ordinary differential equation (Box 3.5).

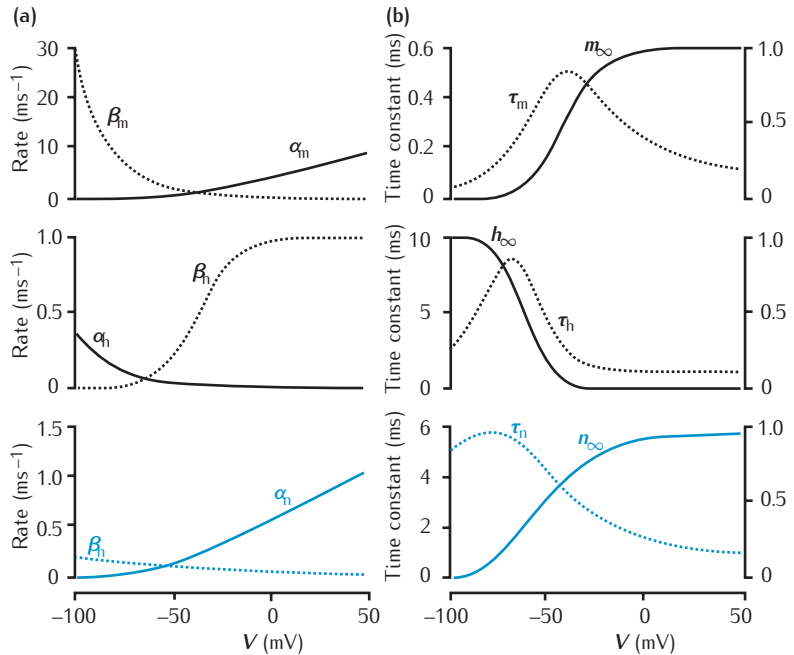
Box 3.4 | Fitting inactivation kinetics

In order to quantify inactivation, Hodgkin and Huxley applied a voltage clamp protocol using two pulses. The first pulse was a long (30 ms) **conditioning pulse**. This was set to a range of different voltages, and its purpose was to give the sodium conductance enough time to inactivate fully at that holding potential. The second pulse was a **test pulse**, which was set to the same value each time. Figure 3.8a shows that the response to the conditioning pulse was similar to the response to a prolonged pulse: the sodium conductance rises to a peak with a height that increases with membrane depolarisation and then decays. The response to the test pulse is similar, but the height of the test pulse depends on the level of the conditioning pulse. The higher the conditioning pulse, the smaller the current amplitude at the test pulse. At a conditioning pulse depolarisation of -41 mV above resting potential, there is virtually no response to the test pulse. Conversely, when the membrane is hyperpolarised to beyond -116 mV below resting potential, the amplitude of the current at the pulse reaches a limiting value. This allowed Hodgkin and Huxley to isolate the amount of inactivated conductance at different voltages. By performing a large number of these experiments over a range of conditioning voltages, they were able to fit the data to produce the voltage-dependent inactivation function h_∞ (Figure 3.8b).

To measure the time constant τ_h of inactivation, a different form of the two-pulse experiment was used (Figure 3.9b). A short depolarising pulse is followed by an interval in which the membrane is clamped to a **recovery potential** and then by a depolarising pulse identical to the first. The peak sodium conductance in both test pulses is measured. The ratio gives a measure of how much the sodium conductance has recovered from inactivation during the time the membrane has been held at the recovery potential. Plotting the ratio against the time of the recovery pulse gives the exponential curve shown in Figure 3.9b, from which the time constant of recovery from inactivation τ_h can be obtained at that particular recovery potential. Over a range of recovery potentials, the voltage dependence of τ_h can be assessed.

Fig. 3.9 (a) The membrane currents associated with two square waves applied in succession to the squid giant axon (square wave amplitude 44 mV and duration 1.8 ms). The interval between the two pulses is varied, allowing the recovery from inactivation to be plotted as a function of interval. (b) The ratio of the amplitude of the current in the second pulse to the amplitude of the current in the first pulse is plotted against the interval between the pulses. Adapted from Hodgkin and Huxley (1952c), with permission from John Wiley & Sons Ltd.

Fig. 3.10 Voltage dependence of rate coefficients and limiting values and time constants for the Hodgkin–Huxley gating variables. (a) Graphs of forward rate variables α_m , α_h and α_n (solid lines) and backward rate variables β_m , β_h and β_n (dashed lines) for the m , h and n gating particles. (b) The equivalent graphs for m_∞ , h_∞ and n_∞ (solid lines) and τ_m , τ_h and τ_n (dotted lines).



3.3 | Simulating action potentials

In order to predict how the membrane potential changes over time, the complete system of coupled non-linear differential equations comprising the HH model (Box 3.5) have to be solved. Hodgkin and Huxley used numerical integration methods (Appendix B.1). It took them three weeks' work on a hand-operated calculator. Nowadays, it takes a matter of milliseconds for fast computers to solve the many coupled differential equations in a compartmental formulation of the HH model.

In this section we look at the action potentials that these equations predict, both under space clamp conditions and under free propagation conditions. This will lead us to comparisons with experimental recordings and a brief review of the insights that this model provided. It is worth noting that the recordings in this section were all made at 6.3 °C, and the equations and simulations all apply to this temperature. Hodgkin and Huxley discovered that temperature has a strong influence on the rate coefficients of the gating variables, but were able to correct for this, as will be discussed in Section 3.4.

3.3.1 Space clamped action potentials

In one set of experiments under space clamp (but not voltage clamp) conditions, Hodgkin and Huxley depolarised the membrane potential to varying levels by charging the membrane quickly with a brief current clamp pulse. Small depolarisations led to the membrane potential decaying back to its resting value, but when the membrane was depolarised above a threshold of around 10 mV above resting potential, action potentials were initiated

Box 3.5 | Summary of the Hodgkin–Huxley model

The equation for the membrane current is derived by summing up the various currents in the membrane, including spatial spread of current from local circuits:

$$C_m \frac{\partial V}{\partial t} = -\bar{g}_L(V - E_L) - \bar{g}_{Na}m^3h(V - E_{Na}) - \bar{g}_K n^4(V - E_K) + \frac{d}{4R_a} \frac{\partial^2 V}{\partial x^2}.$$

Under space clamp conditions, i.e. no axial current:

$$C_m \frac{dV}{dt} = -\bar{g}_L(V - E_L) - \bar{g}_{Na}m^3h(V - E_{Na}) - \bar{g}_K n^4(V - E_K).$$

Sodium activation and inactivation gating variables:

$$\begin{aligned} \frac{dm}{dt} &= \alpha_m(1-m) - \beta_m m, & \frac{dh}{dt} &= \alpha_h(1-h) - \beta_h h, \\ \alpha_m &= 0.1 \frac{V + 40}{1 - \exp(-(V + 40)/10)}, & \alpha_h &= 0.07 \exp(-(V + 65)/20), \\ \beta_m &= 4 \exp(-(V + 65)/18), & \beta_h &= \frac{1}{\exp(-(V + 35)/10) + 1}. \end{aligned}$$

Potassium activation gating variable:

$$\begin{aligned} \frac{dn}{dt} &= \alpha_n(1-n) - \beta_n n, \\ \alpha_n &= 0.01 \frac{V + 55}{1 - \exp(-(V + 55)/10)}, \\ \beta_n &= 0.125 \exp(-(V + 65)/80). \end{aligned}$$

Parameter values (from Hodgkin and Huxley, 1952d):

$$\begin{array}{ll} C_m = 1.0 \text{ } \mu\text{F cm}^{-2} & \\ E_{Na} = 50 \text{ mV} & \bar{g}_{Na} = 120 \text{ mS cm}^{-2} \\ E_K = -77 \text{ mV} & \bar{g}_K = 36 \text{ mS cm}^{-2} \\ E_L = -54.4 \text{ mV} & \bar{g}_L = 0.3 \text{ mS cm}^{-2} \end{array}$$

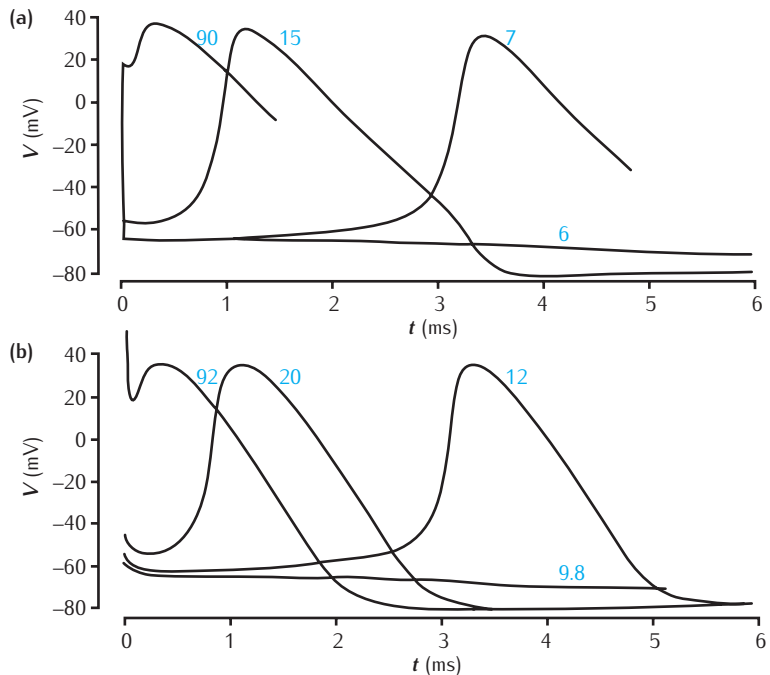
See Figure 3.10 for plots of the voltage dependence of the gating particle rate coefficients.

(Figure 3.11). Hodgkin and Huxley referred to these action potentials induced under space clamp conditions as **membrane action potentials**.

To simulate the different depolarisations in experiments, they integrated the equations of their space clamped model with different initial conditions for the membrane potential. Because the current pulse that caused the initial depolarisation was short, it was safe to assume that initially n , m and h were at their resting levels.

The numerical solutions were remarkably similar to the experimental results (Figure 3.11). Just as in the experimental recordings, super-threshold depolarisations led to action potentials and sub-threshold ones did not, though the threshold depolarisation was about 6 mV above rest instead of 10 mV. The time courses of the observed and calculated action potentials were very similar, although the peaks of the calculated action potentials were too sharp and there was a kink in the falling part of the action potential curve.

Fig. 3.11 Simulated and experimental membrane action potentials. (a) Solutions of the Hodgkin–Huxley equations for isopotential membrane for initial depolarisations of 90, 15, 7 and 6 mV above resting potential at 6.3°C. (b) Experimental recordings with a similar set of initial depolarisations at 6.3°C. Adapted from Hodgkin and Huxley (1952d), with permission from John Wiley & Sons Ltd.



Besides reproducing the action potential, the HH model offers insights into the mechanisms underlying it, which experiments alone were not able to do. Figure 3.12 shows how the sodium and potassium conductances and the gating variables change during a membrane action potential. At the start of the recording, the membrane has been depolarised to above the threshold. This causes activation of the sodium current, as reflected in the increase in m and g_{Na} . Recall that the dependence of m on the membrane potential is roughly sigmoidal (Figure 3.10). As the membrane potential reaches the sharply rising part of this sigmoid curve, the g_{Na} activation increases greatly. As the sodium reversal potential is much higher than the resting potential, the voltage increases further, causing the sodium conductance to increase still further. This snowball effect produces a sharp rise in the membrane potential.

The slower potassium conductance g_K , the n gating variable, starts to activate soon after the sharp depolarisation of the membrane. The potassium conductance allows current to flow out of the neuron because of the low potassium reversal potential. The outward current flow starts to repolarise the cell, taking the membrane potential back down towards rest. It is the delay in its activation and repolarising action that leads to this type of potassium current being referred to as the **delayed rectifier** current.

The repolarisation of the membrane is also assisted by the inactivating sodium variable h , which decreases as the membrane depolarises, causing the inactivation of g_{Na} and reduction of the sodium current flow into the cell. The membrane potential quickly swoops back down to its resting level, overshooting somewhat to hyperpolarise the neuron. This causes the rapid deactivation of the sodium current (m reduces) and its **deinactivation**,

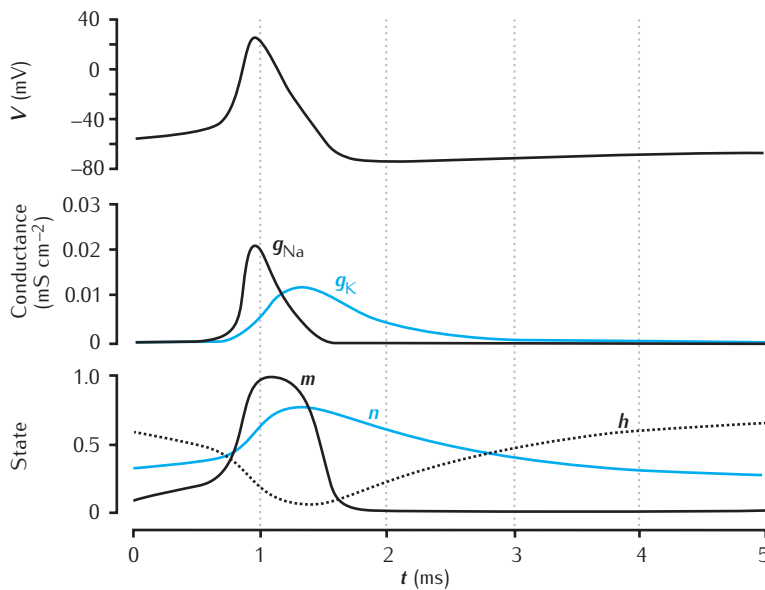


Fig. 3.12 The time courses of membrane potential, conductances and gating variables during an action potential.

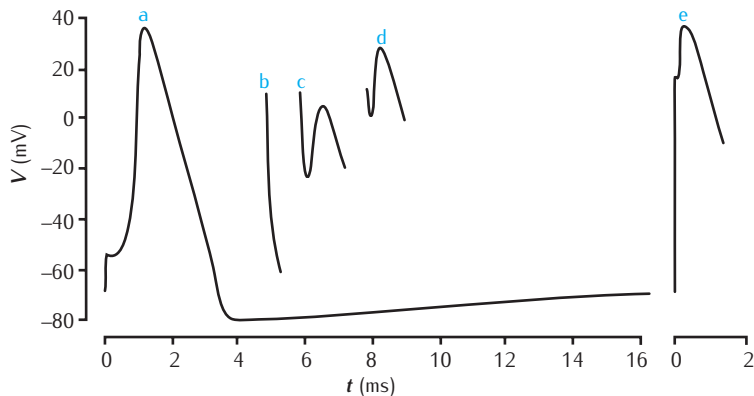
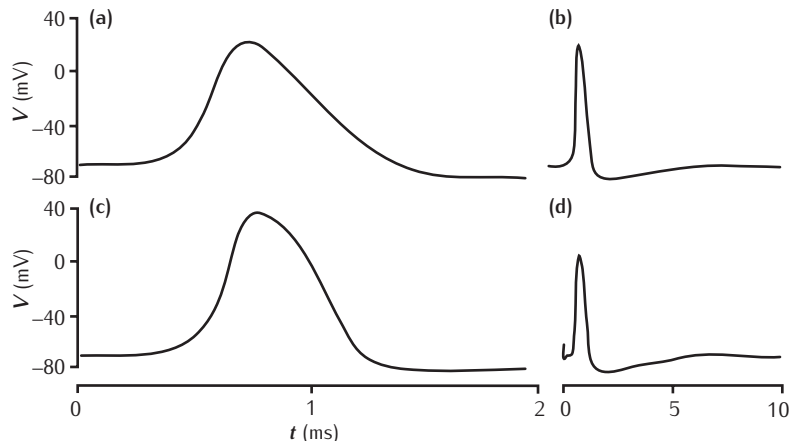


Fig. 3.13 Refractory properties of the HH model. Upper curves are calculated membrane action potentials at 6.3°C . Curve a is the response to a fast current pulse that delivers 15 nC cm^{-2} . Curves b to d are the responses to a charge of 90 nC cm^{-2} delivered at different times after the initial pulse. Adapted from Hodgkin and Huxley (1952d), with permission from John Wiley & Sons Ltd.

whereby the inactivation is released (h increases). In this phase, the potassium conductance also deactivates. Eventually all the state variables return to their resting states and the membrane potential returns to its resting level.

The HH model also explains the **refractory period** of the axon. During the **absolute refractory period** after an action potential, it is impossible to generate a new action potential by injecting current. Thereafter, during the **relative refractory period**, the threshold is higher than when the membrane is at rest, and action potentials initiated in this period have a lower peak voltage. From Figure 3.12, the gating variables take a long time, relative to the duration of an action potential, to recover to their resting values. It should be harder to generate an action potential during this period for two reasons. Firstly, the inactivation of the sodium conductance (low value of h) means that any increase in m due to increasing voltage will not increase the sodium conductance as much as it would when h is at its higher resting value

Fig. 3.14 Calculated and recorded propagating action potentials. (a) Time course of action potential calculated from the Hodgkin–Huxley equations. The conduction velocity was 18.8 m s^{-1} and the temperature 18.5°C . (b) Same action potential at a slower timescale. (c) Action potential recorded from squid giant axon at 18.5°C on same time scale as simulation in (a). (d) Action potential recorded from a different squid giant axon at 19.2°C at a slower timescale. Adapted from Hodgkin and Huxley (1952d), with permission from John Wiley & Sons Ltd.



(Figure 3.10). Secondly, the prolonged activation of the potassium conductance means that any inward sodium current has to counteract a more considerable outward potassium current than in the resting state. Hodgkin and Huxley's simulations (Figure 3.13) confirmed this view, and were in broad agreement with their experiments.

Hodgkin and Huxley had to assume that the membrane potential propagated at a constant velocity so that they could convert the partial differential equation into a second order ordinary differential equation, giving a soluble set of equations.

3.3.2 Propagating action potentials

The propagated action potential calculated by Hodgkin and Huxley was also remarkably similar to the experimentally recorded action potential (Figure 3.14). The value of the velocity they calculated was 18.8 m s^{-1} , close to the experimental value of 21.2 m s^{-1} at 18.5°C .

Figure 3.15 shows the capacitive, local and ionic currents flowing at different points on the membrane at a particular instant when an action potential is propagating from left to right. At the far right, local circuit currents are flowing in from the left because of the greater membrane potential there. These local circuit currents charge the membrane capacitance, leading to a rise in the membrane potential. Further to the left, the membrane is sufficiently depolarised to open sodium channels, allowing sodium ions to flow into the cell. Further left still, the sodium ionic current makes a dominant contribution to charging the membrane, leading to the opening of more sodium channels and the rapid rise in the membrane potential that characterises the initial phase of the action potential. To the left of this, the potassium conductance is activated, due to the prolonged depolarisation. Although sodium ions are flowing into the cell here, the net ionic current is outward. This outward current, along with a small local circuit contribution, discharges the membrane capacitance, leading to a decrease in the membrane potential. At the far left, in the falling part of the action potential, only potassium flows as sodium channels have inactivated. The final **afterhyperpolarisation** potential is not shown fully for reasons of space and because the current is very small. In this part, sodium is deactivating and potassium is deactivating. This leads to a small inward current that brings the membrane potential back up to its resting potential.

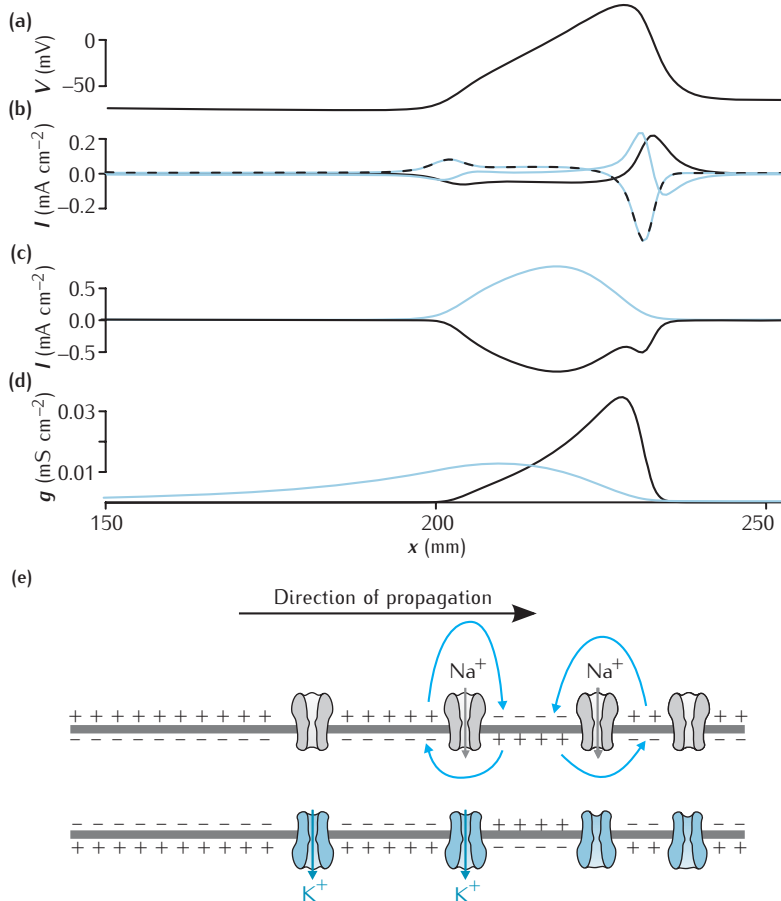


Fig. 3.15 Currents flowing during a propagating action potential. (a) The voltage along an axon at one instant in time during a propagating action potential. (b) The axial current (blue line), the ionic current (dashed black-blue line) and the capacitive current (black line) at the same points. (c) The sodium (black) and potassium (blue) contributions to the ionic current. The leak current is not shown. (d) The sodium (black) and potassium (blue) conductances. (e) Representation of the state of ion channels, the membrane and local circuit current along the axon during a propagating action potential.

3.4 | The effect of temperature

Hodgkin *et al.* (1952) found that the temperature of the preparation affects the time course of voltage clamp recordings strongly: the rates of activation and inactivation increase with increasing temperature. In common with many biological and chemical processes, the rates increase roughly exponentially with the temperature. The **Q_{10} temperature coefficient**, a measure of the increase in rate for a 10°C temperature change, is used to quantify this temperature dependence:

$$Q_{10} = \frac{\text{rate at } T + 10^\circ\text{C}}{\text{rate at } T}. \quad (3.21)$$

If the values of the HH voltage-dependent rate coefficients α and β at a temperature T_1 are $\alpha(V, T_1)$ and $\beta(V, T_1)$, then their values at a second temperature T_2 are:

$$\alpha(V, T_2) = \alpha(V, T_1) Q_{10}^{\frac{T_2-T_1}{10}} \quad \text{and} \quad \beta(V, T_2) = \beta(V, T_1) Q_{10}^{\frac{T_2-T_1}{10}}. \quad (3.22)$$

In the alternative form of the kinetic equations for the gating variables (see, for example, Equation 3.11), this adjustment due to temperature can

be achieved by decreasing the time constants τ_n , τ_m and τ_h by a factor of $Q_{10}^{(T_2-T_1)/10}$ and leaving the steady state values of the gating variables n_∞ , m_∞ and h_∞ unchanged.

Hodgkin *et al.* (1952) estimated, from recordings, a Q_{10} of about 3 for the time constants of the ionic currents. This is typical for the rate coefficients of ion channels (Hille, 2001). In fact, the principles of transition state theory, outlined in Section 5.8.1, show that the Q_{10} itself is expected to depend on temperature: the Q_{10} at 6 °C is not expected to be the same as the Q_{10} measured at 36 °C. Transition state theory also allows temperature to be incorporated into the equations for the rate coefficients explicitly, rather than as a correction factor.

As well as the rate coefficients, the maximum channel conductances also increase with temperature, albeit not as strongly. If the maximum conductance for an ion type X is $\bar{g}_X(T_1)$ at temperature T_1 , at temperature T_2 it will be given by:

$$\bar{g}_X(T_2) = \bar{g}_X(T_1) Q_{10}^{\frac{T_2-T_1}{10}}. \quad (3.23)$$

The Q_{10} is typically around 1.2 to 1.5 for conductances (Hodgkin *et al.*, 1952; Rodriguez *et al.*, 1998; Hille, 2001).

Assuming that reaction rate increases exponentially with temperature is equivalent to assuming that the effect is multiplicative. If the rate coefficient increases by a factor Q for a 1 °C increase in temperature, for a 2 °C increase it is $Q \times Q$; for a 10 °C increase it is $Q_{10} \equiv Q^{10}$ and for an increase from T_1 to T_2 it is $Q^{(T_2-T_1)}$ or $Q_{10}^{(T_2-T_1)/10}$.

3.5 Building models using the Hodgkin–Huxley formalism

The set of equations that make up the HH model (Box 3.5) were constructed to explain the generation and propagation of action potentials specifically in the squid giant axon. How relevant is the HH model to other preparations? While the parameters and equations for the rate coefficients present in the HH model are particular to squid giant axon, the general idea of gates comprising independent gating particles is used widely to describe other types of channel. In this section, we explore the model assumptions and highlight the constraints imposed by the Hodgkin–Huxley formalism. Moreover, we outline the types of experimental data that are required in order to construct this type of model of ion channels.

3.5.1 Model approximations

The HH model contains a number of approximations of what is now known about the behaviour of channels. Each of these will induce an error in the model, but the approximations are not so gross as to destroy the explanatory power of the model.

Each channel type is permeable to only one type of ion

Implicit in the HH model is the notion that channels are selective for only one type of ion. In fact, all ion channels are somewhat permeable to ions other than the dominant permeant ion (Section 2.1). Voltage-gated sodium channels in squid giant axon are about 8% as permeable to potassium as they are to sodium, and potassium channels are typically around 1% as permeable to sodium as they are to potassium (Hille, 2001).

The independence principle

As it is assumed that each type of current does not depend on the concentrations of other types of ion, these equations imply that the independence principle holds (Box 2.4). Hodgkin and Huxley (1952a) verified, to the limit of the resolving power of their experiments, that the independence principle holds for the sodium current. However, improved experimental techniques have revealed that this principle of independence does not hold exactly in general (Section 2.7).

The linear instantaneous *I*-*V* characteristic

One of the key elements of the HH model is that all the ionic currents that flow through open gates have a linear, quasi-ohmic dependence on the membrane potential (Equations 3.3–3.5), for example:

$$I_{\text{Na}} = g_{\text{Na}}(V - E_{\text{Na}}). \quad (3.3)$$

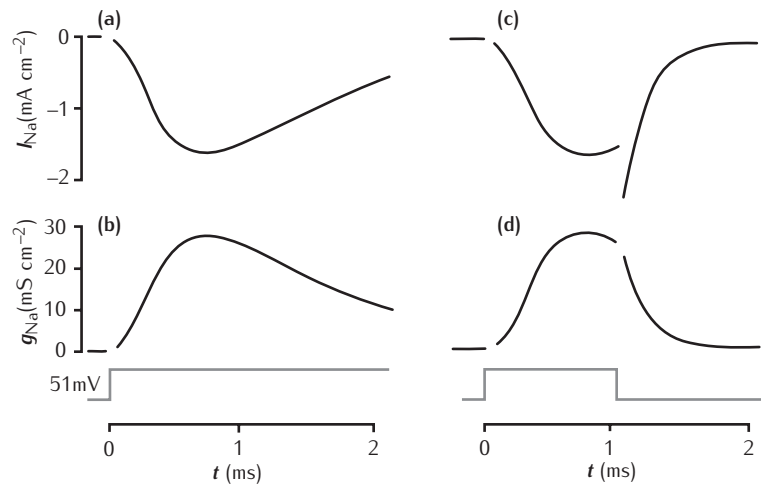
As described in Chapter 2, this relation is an approximation of the non-linear Goldman–Hodgkin–Katz current equation, which itself is derived theoretically from assumptions such as there being a constant electric field in the membrane.

Hodgkin and Huxley (1952b) did not take these assumptions for granted, and carried out experiments to check the validity of Equation 3.3, and the corresponding equation for potassium. Testing this relation appears to be a matter of measuring an *I*-*V* characteristic, but in fact it is more complicated, since, as seen earlier in the chapter, the conductance g_{Na} changes over time, and the desired measurements are values of current and voltage at a *fixed* value of the conductance. It was not possible for Hodgkin and Huxley to fix the conductance, but they made use of their observation that it is *rate of change* of an ionic conductance that depends directly on voltage, not the ionic conductance itself. Therefore, in a voltage clamp experiment, if the voltage is changed quickly, the conductance has little chance to change, and the values of current and voltage just before and after the voltage step can be used to acquire two pairs of current and voltage measurements. If this procedure is repeated with the same starting voltage level and a range of second voltages, an *I*-*V* characteristic can be obtained.

As explained in more detail in Box 3.6, Hodgkin and Huxley obtained such *I*-*V* characteristics in squid giant axon and found that the quasi-ohmic *I*-*V* characteristics given in Equations 3.3–3.5 were appropriate for this membrane. They referred to this type of *I*-*V* characteristic as the **instantaneous *I*-*V* characteristic**, since the conductance is given no time to change between the voltage steps. In contrast, if the voltage clamp current is allowed time to reach a steady state after setting the voltage clamp holding potential, the *I*-*V* characteristic measured is called the **steady state *I*-*V* characteristic**. In contrast to the instantaneous *I*-*V* characteristic, this is non-linear in the squid giant axon. With the advent of single channel recording (Chapter 5), it is possible to measure the *I*-*V* characteristic of an open channel directly in the open and closed states, as for example do Schrempf *et al.* (1995).

A potentially more accurate way to model the *I*-*V* characteristics would be to use the GHK current equation (Box 2.4). For example, the sodium

Fig. 3.16 Sodium current and sodium conductance under two different voltage clamp conditions. (a) The sodium current measured in response to a voltage clamp step at $t = 0$ of 51 mV above resting potential. (b) The conductance calculated from the current using Equation 3.3. (c) The current measured in response to a voltage step of the same amplitude, but which only lasted for 1.1 ms before returning to resting potential. The current is discontinuous at the end of the voltage step. The gap in the record is due to the capacitive surge being filtered out. (d) The conductance calculated from recording (c) and the value of the membrane potential. Although there is still a gap in the curve due to the capacitive surge, the conductance appears to be continuous at the point where the current was discontinuous. Adapted from Hodgkin and Huxley (1952b), with permission from John Wiley & Sons Ltd.



current would be given by:

$$I_{\text{Na}}(t) = \rho_{\text{Na}}(t) \frac{F^2 V(t)}{RT} \left(\frac{[\text{Na}^+]_{\text{in}} - [\text{Na}^+]_{\text{out}} e^{-FV(t)/RT}}{1 - e^{-FV(t)/RT}} \right), \quad (3.24)$$

where $\rho_{\text{Na}}(t)$ is the permeability to sodium at time t . This equation could be rearranged to determine the permeability over time from voltage clamp recordings, and then a gating particle model for the permeability (for example, of the form $\rho_{\text{Na}} = \bar{\rho}_{\text{Na}} m^3 h$) could be derived. Sometimes it is desirable to use this form of the model, particularly where the I - V characteristic is non-linear and better fitted by the GHK equation. This is particularly the case for ions whose concentration differences across the membrane are large, such as in the case of calcium (Figure 2.11b).

The independence of gating particles

Alternative interpretations and fits of the voltage clamp data have been proposed. For example, Hoyt (1963, 1968) suggested that activation and inactivation are coupled. This was later confirmed through experiments that removed the inactivation in squid giant axon using the enzyme pronase (Bezanilla and Armstrong, 1977). Subsequent isolation of the inactivation time course revealed a lag in its onset that did not conform to the independent particle hypothesis. Inactivation now appears to be voltage *independent* and coupled to sodium activation. Consequently, more accurate models of sodium activation and inactivation require a more complex set of coupled equations (Goldman and Schauf, 1972). Unrestricted kinetic schemes, described in Section 5.5.3, provide a way to model dependencies such as this.

Gating current is not considered

In the HH model, the only currents supposed to flow across the membrane are the ionic currents. However, there is another source of current across the membrane, the movement of charges in channel proteins as they open and close. This **gating current**, described in more detail in Section 5.3.4, is very small in comparison to the ionic currents, so small in fact that it took

Box 3.6 Verifying the quasi-ohmic I - V characteristic

To verify that the instantaneous I - V characteristics of the sodium and potassium currents were quasi-ohmic, Hodgkin and Huxley (1952a) made a series of recordings using a two-step voltage clamp protocol. In every recording, the first step was of the same duration, and depolarised the membrane to the same level. This caused sodium and potassium channels to open. The second step was to a different voltage in each experiment in the series. The ion substitution method allowed the sodium and potassium currents to be separated.

Figure 3.16c shows one such recording of the sodium current. At the end of the step, the current increases discontinuously and then decays to zero. There is a small gap due to the capacitive surge. The current just after the discontinuous leap (I_2) depends on the voltage of the second step (V_2). When I_2 was plotted against V_2 , a linear relationship passing through the sodium equilibrium potential E_{Na} was seen. The gradient of the straight line was the conductance at the time of the start of the second voltage step.

This justified the calculation of the conductance from the current and driving force according to Equation 3.3. Figure 3.16d shows the conductance so calculated. In contrast to the current, it is continuous at the end of the voltage step, apart from the gap due to the capacitive surge.

many years to be able to measure it in isolation from the ionic currents. Adding it to the HH model would make very little difference to the model's behaviour, and would not change the explanation provided by the model for the action potential. However, the gating current can be used to probe the detailed kinetics of ion channels. Thus, ignoring the gating current is a good example of a kind of simplification that is appropriate for one question, but if asking a different question, may be something to model with great accuracy.

3.5.2 Fitting the Hodgkin–Huxley formalism to data

The Hodgkin–Huxley formalism for a channel comprises

- (1) an instantaneous I - V characteristic, e.g. quasi-ohmic or GHK equation;
- (2) one or more gating variables (such as m and h) and the powers to which those gating variables are raised;
- (3) expressions for the forward and backward rate coefficients for these variables as a function of voltage.

The data required for all the quantities are voltage clamp recordings using various protocols of holding potential of the current passing through the channel type in question. This requires that the channel be isolated by some method, such as the ion substitution method (Box 3.2), channel blockers, Section 5.3.2, or expression in oocytes, Section 5.3.3. The data required for each is now discussed.

Linear *I*–*V* characteristic

For greatest accuracy, the instantaneous *I*–*V* characteristic should be measured. Even the GHK equation might not be able to capture some features of the characteristic. Also, the reversal potential may differ significantly from the equilibrium potential of the dominant permeant ion if there are other ions to which the channel is significantly permeable. However, in practice, the quasi-ohmic approximation is often used with a measured reversal potential as equilibrium potential. When the intracellular and extracellular concentration differences are great, such as in the case of calcium, the GHK equation may be used.

Gating variables

If the channel displays no inactivation, only one gating variable is required, but if there is inactivation, an extra variable will be needed. The gating variable is raised to the power of the number of activation particles needed to capture the inflection in conductance activation, which then determines the voltage-dependent rate coefficient functions α_n , β_n of Equation 3.7.

Coefficients for each gating variable

The voltage dependence of the forward and backward reaction coefficients α and β for each gating particle need to be determined. The basis for this is the data from voltage clamp experiments with different holding potentials.

These can be obtained using the types of methods described in this chapter to determine plots of steady state activation and inactivation and time constants against voltage. With modern parameter estimation techniques (Section 4.5), it is sometimes possible to short circuit these methods. Instead, the parameters of a model can be adjusted to make the behaviour of the model as similar as possible to recordings under voltage clamp conditions.

The steady state variables, for instance n_∞ and τ_n in the case of potassium, need not be converted into rate coefficients such as α_n and β_n , since the kinetics of the gating variable can be specified using n_∞ and τ_n (Equation 3.11). This approach is taken, for example, by Connor *et al.* (1977) in their model of the A-type potassium current (Box 5.2). Hodgkin and Huxley fit smooth functions to their data points, but some modellers (Connor and Stevens, 1971c) connect their data points with straight lines in order to make a piecewise linear approximation of the underlying function.

If functions are to be fitted, the question arises of what form they should take. The functions used by Hodgkin and Huxley (1952d) took three different forms, each of which corresponds to a model of how the gating particles moved in the membrane (Section 5.8.3). From the point of view of modelling the behaviour of the membrane potential at a particular temperature, it does not really matter which two quantities are fitted to data or what functional forms are used, as long as they describe the data well. However, from the point of view of understanding the biophysics of channels, more physically principled fitting functions (Section 5.8) are better than arbitrary functions. This can include temperature dependence, rather than having to bolt this on using the value of Q_{10} .

3.6 | Summary

In their model, Hodgkin and Huxley introduced active elements into the passive membrane equation. These active currents are specified through the concept of membrane-bound gated channels, or gates, each gate comprising a number of independent gating particles. While the Hodgkin–Huxley formalism does not relate directly to the physical structure of channels, it does provide a framework within which to describe experimental data. In particular, the use of kinetic reaction equations allows the system to be fitted to voltage-dependent characteristics of the active membrane currents through the voltage dependence of the kinetic rate coefficients. Putative functions for the kinetic rate coefficients are fitted to experimental voltage clamp data. The resulting quantitative model not only replicates the voltage clamp experiments to which it is tuned, but also reproduces the main features of the action potential.

In this chapter we have been considering the squid giant axon only. Furthermore, we have focused on single stretches of axon and have not included features such as branch points, varicosities and axon tapering in the model. These extensions may be added to the models using the multi-compartmental model approach. As seen previously, a single equivalent electrical circuit representing an isopotential patch of membrane can be connected to other membrane circuits in various ways to form an approximation of membrane area and discontinuities. This approach is introduced and discussed in Chapter 4.

Representing more complex neurons requires a model to contain more than sodium and potassium conductances. This can be achieved by including in the equivalent electrical circuit any number of transmembrane conductances in series with a voltage source representing new ionic currents. The voltage dependence of conductances may be characterised by the Hodgkin–Huxley formalism if the independent gating particle approach is deemed accurate enough. However, as will be seen in Chapter 5, the Hodgkin–Huxley formalism cannot explain some behaviours of ion channels, and more complex models are required. Conductances may also exhibit more than voltage dependence; for example, ligand-gated channels and channels dependent on ionic concentrations. These variations are discussed in Chapters 5 and 7.

Chapter 4

Compartmental models

In this chapter, we show how to model complex dendritic and axonal morphology using the **multi-compartmental** approach. We discuss how to represent an axon or a dendrite as a number of compartments derived from the real neurite's morphology. We discuss issues with measurement errors in experimentally determined morphologies and how to deal with them. Under certain assumptions, complex morphologies can be simplified for efficient modelling. We then consider how to match compartmental model output to physiological recordings and determine model parameters. We discuss in detail the techniques required for determining passive parameters, such as membrane resistance and capacitance over a distributed morphology. The extra problems that arise when modelling active membrane are also considered. **Parameter estimation** procedures are introduced.

4.1 Modelling the spatially distributed neuron

The basis of modelling the electrical properties of a neuron is the RC electrical circuit representation of passive membrane, consisting of a capacitor, leak resistor and a leak battery (Figure 2.14). Active membrane channels may be added by, for example, following the Hodgkin-Huxley approach. Further frameworks for modelling the myriad of ion channels found in neuronal membrane are covered in Chapter 5. If we are interested in voltage changes in more than just an isolated patch of membrane, we must consider how voltage spreads along the membrane. This can be modelled with multiple connected RC circuits. This approach is used widely and often referred to as multi-compartmental modelling or, more simply, **compartmental modelling**.

In Section 4.2 we start with how to construct a compartmental model using simple geometric objects such as cylinders to represent sections of neuronal membrane. In Section 4.3, we discuss approaches for using real neuronal morphology as the basis of the model. The relationship between a real neuron, its approximated morphology and overall equivalent electrical circuit, or compartmental model, is illustrated in Figure 4.1.

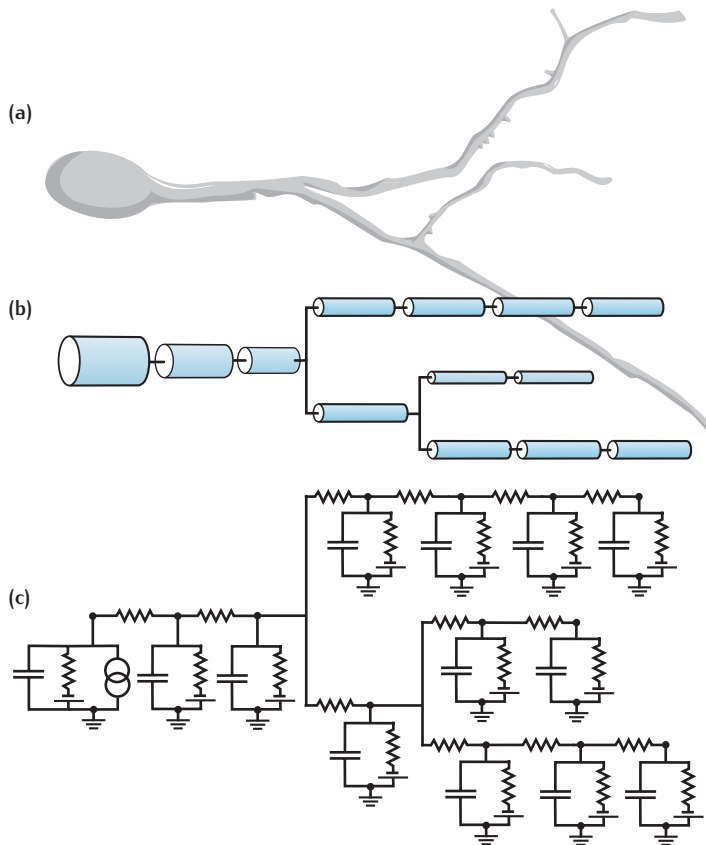


Fig. 4.1 A diagram of the development of a multi-compartmental model. (a) The cell morphology is represented by (b) a set of connected cylinders. An electrical circuit consisting of (c) interconnected RC circuits is then built from the geometrical properties of the cylinders, together with the membrane properties of the cell.

In Sections 4.4 and 4.5 we consider in detail how to estimate the passive cellular properties, membrane resistance, capacitance and intracellular resistance over the spatial extent of a neuron. Finally, in Section 4.6, we look at how models of active ion channels may be added, and the issues that arise with the additional complexity this brings to a compartmental model.

As additional ion channels and/or compartments are added to a compartmental model, a single model can quickly and easily become very complex. It is not unusual for such models to be described mathematically by hundreds, if not thousands, of coupled differential equations. This is not a problem for modern-day computers to solve numerically (see Appendix B.1 for an introduction to numerical integration techniques), but can be a problem for the modeller. How to select and constrain the many parameters in such systems, how to construct useful and informative simulations and how to analyse vast quantities of measurable variables are all issues to be tackled.

4.2 | Constructing a multi-compartmental model

As introduced in Section 2.8, the spatial extent of a neuron can be incorporated into a model of its electrical properties by assuming that the neuron is made up of many patches of isopotential membrane that are connected by

Box 4.1 Variations in compartment properties

Membrane and morphological properties are likely to vary along the length of a neurite. This can include changes in membrane capacitance and resistance, ion channel densities, axial resistivity and diameter. In the compartmental approach, changes in membrane properties are easily handled as all cross-membrane currents are calculated on a per compartment basis. This necessitates specifying capacitance, membrane resistance and ion channel densities uniquely for each compartment.

However, changes in diameter and axial resistivity affect intracellular current flow between adjacent compartments. This requires averaging values for these parameters between compartments, slightly complicating the resulting voltage equation. For variations in diameter, when calculating the voltage in compartment j , we calculate the cross-sectional area between, say, compartments j and $j + 1$ using the average diameter: $\pi((d_{j+1} + d_j)/2)^2/4$. To get the term coupling this compartment with compartment $j + 1$, this area is divided by the surface area of compartment j multiplied by its length, resulting in:

$$\frac{(d_{j+1} + d_j)^2}{16d_j R_a l^2} (V_{j+1} - V_j).$$

A full treatment of how to deal with such variations is given in Mascagni and Sherman (1998).

resistors that model longitudinal current flow in the intracellular medium. This forms a discrete approximation, since the actual current flow may change continuously in space as well as time. At any point in the neuron, the sum of axial currents flowing into the point is equal to the sum of the capacitive, ionic and electrode transmembrane currents at that point. The continuous cable equation (Section 2.9) along the length of a uniform cylinder of diameter d , with the membrane containing a variety of ion channels, is described by the partial differential equation:

$$C_m \frac{\partial V}{\partial t} = - \sum_k I_{i,k}(x) + \frac{d}{4R_a} \frac{\partial^2 V}{\partial x^2} + \frac{I_e(x)}{\pi d}, \quad (4.1)$$

where the left-hand side is the capacitive current and the terms on the right-hand side are the sum of all ionic currents, the axial current and an electrode current, respectively.

A compartmental approximation to this equation is:

$$C_m \frac{dV_j}{dt} = - \sum_k I_{i,k,j} + \frac{d}{4R_a} \frac{V_{j+1} - V_j}{l^2} + \frac{d}{4R_a} \frac{V_{j-1} - V_j}{l^2} + \frac{I_{e,j}}{\pi d l}, \quad (4.2)$$

Note that compartments adjacent to branch points in a dendrite or axon will have at least three neighbours, rather than two.

which determines how the voltage V_j in compartment j changes through time; d , l are the compartment diameter and length, respectively, and $j + 1$ and $j - 1$ are the adjoining compartments. This equation becomes a little more complicated if the diameter d varies along the length of the cable (Box 4.1).

The general approach is to represent quasi-isopotential sections of neurite (small pieces of dendrite, axon or soma) by simple geometric objects, such as spheres or cylinders, which we term **compartments**. This allows easy calculation of compartment surface areas and cross-sectional areas, which are needed for calculation of current flow through the membrane and between compartments.

The fundamental problem with constructing a compartmental model is to choose how closely to capture the actual morphology of the real neuron being modelled. Using realistic morphology is necessary, for example, if the aim is to explore the effects of synaptic inputs at specific spatial locations on the neuron. However, increasing morphological accuracy means more compartments and greater model complexity. A simplified geometry may be sufficient if the main interest is in the electrical responsiveness of the soma or axon initial segment, with the dendrites acting as an electrical load on the soma.

4.2.1 Mapping morphology to simple geometric objects

Typically, the morphology of a target cell is based on using simple geometric objects such as spheres, ellipsoids and cylinders to represent the anatomical structures observed. A cell body is usually represented by either a sphere or spheroid and modelled as a single RC circuit. The soma surface area α_s is calculated from the geometry and is used to calculate the electrical properties of the circuit, e.g. the soma membrane capacitance is given by $C_m \alpha_s$. Axonal and dendritic processes are typically represented as collections of connected cylinders. Diameters of processes can vary greatly along their length, particularly in dendrites. A rule for deciding when unbranched dendrites should be represented by more than one cylinder with different diameters has to be devised. For example, the point at which the real diameter changes by a preset amount (e.g. $0.1\text{ }\mu\text{m}$) along the dendrite can be chosen as a suitable criterion (Figure 4.2).

There may not necessarily be a one-to-one correspondence between the representation of morphology with simple geometric shapes and the final electrical circuit. A single long dendrite may be represented adequately by a single cylinder, but to model the voltage variations along the dendrite it should be represented by multiple compartments. Choosing the number and size of compartments is considered below. In addition, there may be more morphological information available from the real neuron than is required to specify the relationships between geometric elements. Three-dimensional spatial information specifying the relative positions and orientations of each element may also have been recorded in the reconstruction procedure. Although this may not be required in models that do not represent spatial aspects of a cell's environment, this information can be useful in certain situations; for example, in modelling the input to cells with processes in different cortical layers.

Simulation packages designed specifically for building compartmental neuron models (such as NEURON; Carnevale and Hines, 2006) often provide cylinders as the only geometrical object used to represent different morphologies. This means, for example, that a spherical soma or bouton must be translated to a cylinder with equivalent surface area (Figure 4.1). If the soma

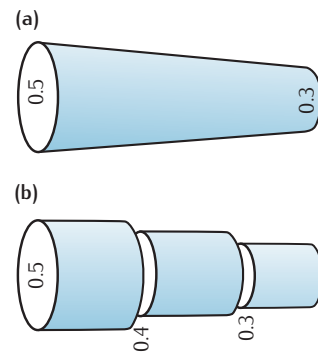


Fig. 4.2 (a) An unbranched tapered dendrite can be split into individual cylinders with (b) progressively smaller diameters.

or bouton is represented by a single RC circuit (i.e. a single electrical compartment), representing it as a cylinder makes no electrical difference. Some simulation packages allow representations that reflect the division between morphology and electrical compartments. This facility makes it straightforward to change the number of compartments electrically representing a single cylindrical branch without changing the geometric representation of the morphology. The spatial accuracy is then conveniently abstracted from the actual representation of the morphology.

4.2.2 Compartment size

Once the morphology has been represented as a set of cylindrical sections, they must be divided into electrical compartments. In compartmental modelling, the choice of compartment size is an important parameter in the model. It is assumed that each compartment is effectively isopotential. This will only be strictly the case if the size of the compartment is infinitely small. Compartmental models used in computer simulations must have a finite number of compartments (Figure 4.3), and generally a certain amount of error is tolerated in the simulation resulting from the inaccurate isopotential assumption in models with finite-sized compartments. Using a small compartment size reduces the error but increases the number of compartments needed to represent the morphology, and consequently the overall required computation for simulations. Box 4.2 gives an example of the error that can be introduced by a finite compartment size.

A general and often quoted rule of thumb is to make the compartment size no longer than 10% of the length constant λ . However, this length constant applies only to the spatial decay of steady state signals. Transient signals, such as synaptic potentials, may decrease much more than this over distance due to the low-pass filtering effects of the axial resistance and membrane capacitance. A length constant that captures the decay of signals of a high frequency, f , is (Carnevale and Hines, 2006):

$$\lambda_f \equiv \frac{1}{2} \sqrt{\frac{d}{\pi f R_a C_m}}. \quad (4.3)$$

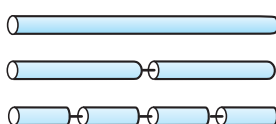


Fig. 4.3 An unbranched section of dendrite can be split into different numbers of compartments.

Carnevale and Hines (2006) give the rationale behind this length constant. This yields an alternative rule of thumb, which is to make the compartment size no more than 10% of λ_f , where f is chosen to be high enough that the transmembrane current is largely capacitive. Carnevale and Hines (2006) suggest frequencies of the order 50–100 Hz are reasonable to meet this criterion for a neuronal membrane. This is likely to give a smaller compartment size than using the steady state length constant. In either case, we need good estimates of the passive membrane properties to be able to use these rules of thumb. In Section 4.4 we deal with how such estimates can be obtained.

Other issues may influence the choice of compartment size. The choice depends on the desired spatial accuracy needed for the particular situation we wish to simulate. If we need to know the value of a parameter, such as voltage, that varies over the cell morphology, to a specific spatial accuracy, then we must design a model with a sufficient number of compartments to

Box 4.2 | Errors due to a finite compartment size

An isopotential patch of membrane represented by a single RC circuit is assumed to have infinitesimally small dimensions. However, in compartmental modelling a *finite* cylindrical compartment with dimensions of length l and diameter d is used. Ideally, this finite-sized compartment should be represented as a cable (i.e. represented by an infinite number of connected RC circuits). What difference do we observe in the electrical properties as a consequence of representing this finite cylindrical compartment by a single RC circuit compared to representing it with a finite cable? Carrying out this assessment enables us to choose the dimensions of a finite compartment (l , d) that yield an acceptably small difference.

In a sealed end cable of finite size the input resistance is given by:

$$R_{in} = \frac{R_m}{a} L \coth L.$$

This is derived by substituting R_∞ from Equation 2.27 into Equation (b) in Box 2.6. L is the length of the cable measured in terms of the length constant λ , with the true length of the cable being $l = L\lambda$. a is the surface area of the cylindrical cable excluding ends, $a = \pi dl$. Assuming this finite compartment is isopotential, i.e. that the voltage is constant over the entire compartment, and setting R_a to 0, the input resistance is given solely by the membrane resistance:

$$R_{in} = \frac{R_m}{a}.$$

This assumption implies that $L \coth L$ is equal to 1, which is only strictly the case for infinitesimally small lengths.

Suppose we choose a cylindrical compartment of a length l 20% of the length constant λ . Under sealed end conditions, the input resistance of a cable of this length is given by:

$$R_{in} = \frac{R_m}{a} 0.2 \coth 0.2 = 1.0133 \frac{R_m}{a},$$

i.e. the input resistance to the cable is 1% higher than it would be if it were modelled with an isopotential compartment, where $R_{in} = R_m/a$. Choosing smaller compartment lengths reduces this electrical difference.

meet that accuracy. For example, if we want to plot the voltage every 5 µm along a branch, modelling lengths greater than 5 µm with a single isopotential compartment would not provide the precision required.

4.3 | Using real neuron morphology

Compartmental models can be based on reconstructions of real cells. Morphological data are obtained from a stained neuron. For example, biocytin or neurobiotin can be added to the pipette when recording from a cell in a slice. Dye injection at the end of a recording session has the advantage of producing a stained neuron with associated recorded physiological properties.

Similarly, introduction of fluorescent dyes, either directly or via transgenic approaches, can be used to visualise neurons before artifacts of slice fixation are introduced. The classic fast Golgi method can be used to obtain a larger sample of stained cells. There are many published examples of these approaches (Ramón y Cajal, 1911; Kita and Armstrong, 1991; Chalfie *et al.*, 1994).

When the reconstruction of large neurons or processes, such as entire dendrites and axons, involves more than a single slice, careful alignment of processes must be made. Commercial computer-aided microscope packages, such as Neurolucida, can be useful in aiding the reconstruction process. In addition, new *in vitro* automatic and high throughput morphology analysis techniques are under active development (Wu *et al.*, 2004; Evers *et al.*, 2005; Wearne *et al.*, 2005; Rodriguez *et al.*, 2008). Here, rather than focus on any particular technique, we outline some of the general issues involved when extracting morphological data for modelling and in the process of using this data to construct compartmental models.

4.3.1 Morphological errors

It is important to consider how some of the artifacts that may result from reconstruction procedures affect the morphological data. Ideally, these can be dealt with by introducing compensatory factors into the final model of the cell.

Many fixation procedures lead to shrinkage or distortion of the slice and, consequently, the reconstructed neuron. Some fixation procedures, particularly methods used for electron micrograph preparation, may minimise the overall level of shrinkage to a level where it does not significantly affect the measured morphology (Larkman and Mason, 1990). Shrinkage factors can have a serious impact on the overall surface area of the cell. For example, if we measure the diameter of a cylindrical slice of dendrite as 0.5 µm but the real value is 0.6 µm, then there is an error in the surface area of 16% and in the cross-sectional area of 30%. These errors can then have a serious impact on the calculated passive properties (Steuber *et al.*, 2004).

It is possible to quantify the amount of shrinkage and apply these correction factors to the final data. This can be done by measuring the overall slice shrinkage and assuming that cells shrink in a uniformly similar manner; note that shrinkage in the slice depth (Z-axis) is generally more pronounced than in the X-Y plane. Alternatively, to judge the individual level of cell shrinkage, data from visualisation of the cell during the recording episode (e.g. using images of the soma or via fluorescent dyes) can be compared to the image of the cell as seen in the fixed slice. Calibration with high voltage electron microscopy can also prove useful. Ideally, if electrophysiological recordings have been taken from the target neuron, these too can be useful to assess the quality of cell preservation. Poor physiological data may be an indication of cell degeneration or damage, and so reconstruction of morphologies whose associated recordings indicate damage can be avoided.

Reconstruction methods using light microscopy often do not include small processes and spines. For example, spines can be too small to resolve accurately using light microscopy, or may be occluded behind their attached process. However, image analysis techniques are being developed

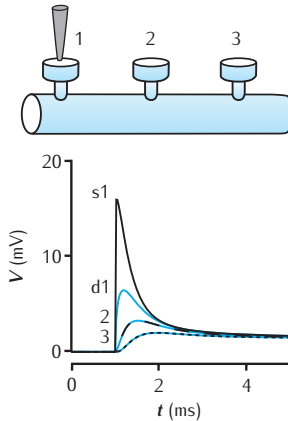


Fig. 4.4 Voltage response to a single synaptic EPSP at a spine on a dendrite. There are three spines 100 µm apart on a 1000 µm long dendrite of 2 µm diameter. EPSP occurs at spine 1. Black lines show the voltage at each spine head. Blue lines are the voltage response in the dendrite at the base of each spine. Dendrite modelled with 1006 compartments (1000 for main dendrite plus 2 for each spine); passive membrane throughout with $R_m = 28 \text{ k}\Omega \text{ cm}^2$, $R_a = 150 \Omega \text{ cm}$, $C_m = 1 \mu\text{F cm}^{-2}$; spine head: diameter 0.5 µm, length 0.5 µm; spine neck: diameter 0.2 µm, length 0.5 µm. For a similar circuit see Woolf *et al.* (1991).

to overcome these limitations (Rodriguez *et al.*, 2008). Electron microscope (EM) reconstruction procedures (e.g. high voltage EM) can yield more complete morphological sections, although the procedure can be time consuming and the equipment expensive. Despite being slow and laborious, reconstruction from EM sections can yield high accuracy, particularly in representing small processes. However, in compiling 3D images from EM sections, there can be significant differences in morphological structures when followed from section to section. For example, distortions, such as crimping, can arise during the sectioning process. The level of distortion can also depend on section thickness. Resolving these discontinuities can be difficult. Improving the resolution in the Z-axis is achievable with multiple EM images at different specimen angles (Auer, 2000).

4.3.2 Incorporating spines

For many neurons, dendritic spines are a conspicuous part of the morphology. Their functional role is the subject of a large body of experimental and modelling work (Shepherd, 1996). To include all possible spines in a detailed compartmental model of such a cell is computationally very expensive and is likely to involve many assumptions about the size, shape and location of the spines.

If the aim of the model is to explore local dendritic interactions between individual synapses, where the voltage transient or calcium influx at particular synapses is to be tracked, then it is crucial to include explicitly at least the spines on which the synapses occur. As shown in Figure 4.4, the voltage transient in an active spine head has much greater amplitude than the subsequent transient in the attached dendrite. However, transmission from the dendrite into a spine is not attenuated, and nearby spines will see a very similar transient to that in the adjacent dendrite. In Section 6.6.4 and Box 6.4 we show that longitudinal diffusion of calcium from a spine head usually has a much shorter length constant than the membrane voltage. Thus concentration transients are also highly local to the spine head.

Spines and small processes can have a significant impact on the overall surface area of the cell. For example, spines can account for half of the surface area of a typical pyramidal cell (Larkman *et al.*, 1991). It is possible to include their general effects on the electrical properties of the cell using data about their size, number and distribution. This can be done by adjusting the membrane surface area appropriately and keeping the ratio of length to diameter-squared to a constant value (Figure 4.5). The axial resistance of a cylindrical compartment of length l and diameter d is:

$$r_a l = \frac{4R_a l}{\pi d^2}. \quad (4.4)$$

Preserving the ratio of the length to diameter-squared ensures that the axial resistance remains constant (Stratford *et al.*, 1989). Alternatively, the values of specific electrical properties R_m and C_m can be adjusted (Holmes and Rall, 1992c) to account for the missing membrane. If preserving cell geometry is required, for visualisation or formation of network connections in 3D space, for example, then this method is to be preferred.

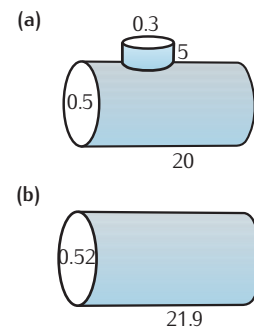


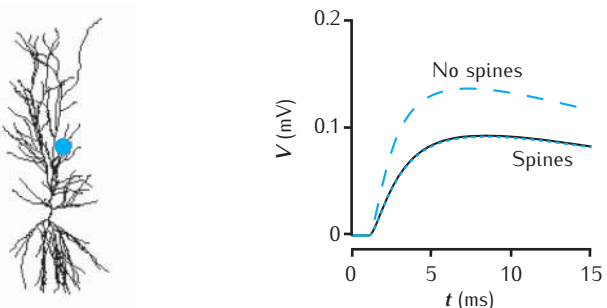
Fig. 4.5 (a) A dendritic cylinder with an attached spine can be represented as a single cylinder with an enlarged surface area. (b) The axial resistance is identical in the two dendritic cylinders as the ratio of length to diameter squared in the cylinders is kept the same.

R_m and C_m can be modified in a specific compartment to absorb the additional spine surface area a_{spine} while leaving the compartment dimensions, l and d , unchanged. Compartment specific values are respectively given as:

$$R_m \frac{\pi dl}{\pi dl + a_{spine}},$$

$$C_m \frac{\pi dl + a_{spine}}{\pi dl}.$$

Fig. 4.6 Somatic voltage response to a single synaptic EPSP on a spine at a distance of 500 µm in the apical dendrites of a CA1 pyramidal cell model (blue dot on cell image). The voltage amplitude is reduced (black line) when 20 000 inactive spines are evenly distributed in the dendrites, compared to when no spines are included (blue dashed line). The somatic voltage response is corrected if R_m is decreased and C_m is increased in proportion with the additional membrane area due to spines (blue dotted line). The CA1 pyramidal cell is n5038804, as used in Migliore *et al.* (2005); model has 455 compartments (with no spines); passive membrane throughout with $R_m = 28 \text{ k}\Omega \text{ cm}^2$, $R_a = 150 \Omega \text{ cm}$, $C_m = 1 \mu\text{F cm}^{-2}$; spine head: diameter 0.5 µm, length 0.5 µm; spine neck: diameter 0.2 µm, length 0.5 µm; 20 000 spines increase the total membrane area by 1.4 and reduce the somatic voltage response by around 30%. For a similar comparison see Holmes and Rall (1992b).



If the main aim of the model is to explore the somatic voltage response to synaptic input, then adjusting dendritic lengths and diameters to include spine membrane, or adjusting cellular membrane resistance and capacitance, may provide a reasonable and computationally efficient approximation to the contribution of spines. If such an adjustment is not made, then the quantitative contribution of a synaptic EPSP will be overestimated at the soma (Figure 4.6).

4.3.3 Simplifying the morphology

Although neural simulators, such as NEURON, can simulate large multi-compartmental models efficiently, there are situations in which simpler models are desirable; for example, if we want to run large numbers of simulations to explore the effects of changes in specific parameter values. Here, we focus on simplifications of the neuron morphology which lead to electrically identical compartmental models with a reduced complexity and number of compartments. More drastic approaches to simplifying neuron models and their consequences are discussed in Chapter 8.

Rall (1964) discovered that passive dendrites are equivalent electrically to a single cylinder, provided that they obey the following rules:

- (1) Specific membrane resistance (R_m) and specific axial resistance (R_a) must be the same in all branches.
- (2) All terminal branches must end with the same boundary conditions (for example, a sealed end).
- (3) The end of each terminal branch must be the same total electrotonic distance from the origin at the base of the tree.
- (4) For every parent branch, the relationship between the parent branch diameter (d_1) and its two child branch diameters (d_2 and d_3) is given by:

$$d_1^{3/2} = d_2^{3/2} + d_3^{3/2}. \quad (4.5)$$

This is known as the '3/2' diameter rule.

Before using this equivalent cylinder simplification, it is important to assess if these conditions apply to the morphological structures being examined. Applying this simplification to neurons whose morphologies or electrical properties do not meet the required assumptions can lead to erroneous results (Holmes and Rall, 1992a). At first glance, conditions (3) and (4) above may appear to be too restrictive. Some dendritic trees conform to the 3/2 diameter rule, such as the cat motor neuron (Rall, 1977) and cat lateral

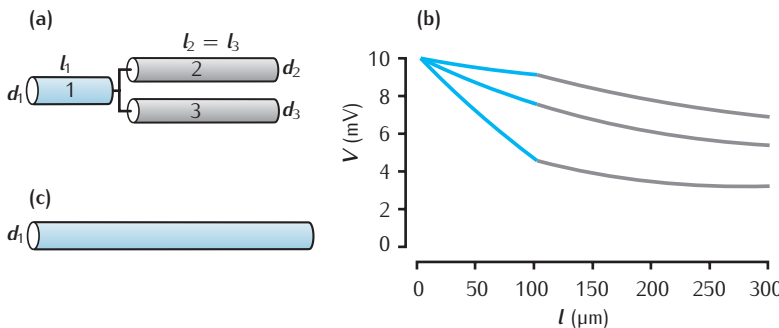


Fig. 4.7 (a) A simple example of a branching tree. (b) Curves showing the voltage at any point along the tree illustrated in (a), in response to a constant injected current at the left-hand end of the tree, for three different diameters of cylinder 1. The centre line shows the voltage along the tree for $d_1 = 0.8 \mu\text{m}$, which satisfies the 3/2 rule (blue indicates voltage along cylinder 1, grey along cylinder 2). The upper and lower curves illustrate the voltage along the tree where cylinder 1 diameters do not satisfy the 3/2 rule ($d_1 = 1.6 \mu\text{m}$ and $d_1 = 0.4 \mu\text{m}$ respectively). $R_m = 6000 \Omega \text{ cm}^2$, $R_a = 150 \Omega \text{ cm}$ and $E_L = 0 \text{ mV}$. (c) An equivalent cylinder for the tree in (a), with diameter $d_1 = 0.8 \mu\text{m}$ and length $l = 352 \mu\text{m}$. l is calculated from the electrotonic length, L , of the tree using $L = l/\lambda$.

geniculate nucleus relay cells (Bloomfield *et al.*, 1987). Other trees, such as apical trunks of cortical pyramidal neurons, violate the 3/2 assumption (Hillman, 1979). Note that these conditions do not imply that the tree must be symmetrical. For example, it is possible to have two branches from a parent with different lengths, provided the total electrotonic distance from the origin at the base of the tree to the ends of each terminal branch is the same. This can be the case when the longer branch has a larger diameter.

Using a model that has been simplified by using equivalent cylinders can significantly reduce the number of parameters and allow a clearer understanding of its responses. This was done for the cat motor neuron (Rall, 1977). Furthermore, the simplification is still useful with the addition of active membrane properties.

To demonstrate empirically how a tree satisfying the above conditions can act electrically as a single cylinder, we now investigate the small symmetrical tree in Figure 4.7a. It is assumed that the morphology is completely specified except for the diameter of the parent cylinder 1. We first assume all the conditions mentioned above are met, including that the diameter of cylinder 1 satisfies the 3/2 rule. By plotting the voltage along the length of the entire tree in response to a constant injected current at the left-hand end of the tree (central line, Figure 4.7b), we see that it decreases smoothly as if it were from a single cylinder – there is no abrupt change in the gradient at the tree branch point. Compare this with the situation where the diameter of cylinder 1 is set to a value which is half of what would satisfy the 3/2 rule ($d_1 = 0.4 \mu\text{m}$). The plot of voltage along the tree shows an abrupt change in the gradient at the branch point (lower line in Figure 4.7b). Similarly, if the diameter of cylinder 1 is greater than the value required for the 3/2 rule ($d_1 = 1.6 \mu\text{m}$) there is still an abrupt change in the gradient of the voltage plot (upper line, Figure 4.7b). Only where all the conditions are met does the voltage change smoothly, consistent with a single equivalent cylinder.

The equivalent cylinder can be constructed with the same diameter and length constant as the parent, and length given by the total electrotonic length of the tree. It can also be shown that the surface area of the tree and the surface area of such an equivalent cylinder are the same. Box 4.3 provides a demonstration, using the cable equation, of how these four conditions allow the construction of an equivalent cylinder.

Further limitations to using this simplification arise when modelling inputs over the dendritic tree. Representing a branching dendritic tree by a

Box 4.3 Equivalent cylinder for complex trees

To demonstrate the existence of an equivalent cylinder for an appropriate branching tree, we consider the small symmetrical tree shown in Figure 4.7a and assume that it meets all four conditions for cylinder equivalence (Section 4.3.3). Following Box 2.6, we use the dimensionless quantity L to measure cable branch lengths: L is the branch length l in terms of the length constant λ , $L = l/\lambda$. The resistance at the end of cable 1, R_{L1} , can be calculated from the input resistances of the two child branches, R_{in2} and R_{in3} :

$$\frac{1}{R_{L1}} = \frac{1}{R_{in2}} + \frac{1}{R_{in3}}. \quad (\text{a})$$

As the child branches have sealed ends, their input resistances are given by:

$$R_{in2} = R_{\infty 2} \coth L_2 \quad R_{in3} = R_{\infty 3} \coth L_3, \quad (\text{b})$$

where $R_{\infty 2}$ and $R_{\infty 3}$ are the input resistances of semi-infinite cables with the same electrical properties as the tree and with diameters d_2 and d_3 respectively (Box 2.6). The end of each terminal branch has the same total electrotonic length from the origin at the base of the tree (condition 3). In our example tree $L_1 + L_2 = L_1 + L_3$, and we define $L_D = L_2 = L_3$.

Using $1/R_\infty = \sqrt{\pi^2/4R_m R_a} d^{3/2}$, derived from Equation 2.27, and applying the 3/2 rule (condition 4), results in a relationship between the semi-infinite input resistances of the parent and child branches:

$$\frac{1}{R_{\infty 1}} = \frac{1}{R_{\infty 2}} + \frac{1}{R_{\infty 3}}. \quad (\text{c})$$

Substituting for R_{in2} and R_{in3} from Equations (b) into Equation (a):

$$\frac{1}{R_{L1}} = \frac{1}{\coth L_D} \left(\frac{1}{R_{\infty 2}} + \frac{1}{R_{\infty 3}} \right),$$

then using Equation (c), the resistance at the end of cylinder 1 is:

$$R_{L1} = R_{\infty 1} \coth L_D.$$

Therefore, the resistance at the end of the parent cylinder is equivalent to the input resistance of a single cylinder with the same diameter as the parent and length $l = L_D \lambda_1$.

Thus the entire tree can be described by a single cylinder of diameter d_1 , length constant λ_1 and length $l = (L_1 + L_D)\lambda_1$.

single cylinder limits the spatial distribution of inputs that can be modelled. Input at a single location on the equivalent cylinder corresponds to the sum of individual inputs, each with an identical voltage time course, simultaneously arriving at all electrotonically equivalent dendritic locations on the corresponding tree. For a fuller discussion of the class of trees that have mathematically equivalent cylinders and the use of this simplification, see Rall *et al.* (1992).

4.4 Determining passive properties

Passive RC circuit properties play a major role in a neuron's physiology. Values for capacitance (C_m), intracellular (axial) resistance (R_a) and membrane resistance (R_m) are required in building any RC circuit representation of a neuron. Assuming that C_m , R_a and R_m are constant over the cell morphology, the passive electrical behaviour of a compartment labelled j , with neighbours $j + 1$ and $j - 1$, is described by the equation (Equation 2.23 in Section 2.8.1):

$$C_m \frac{dV_j}{dt} = \frac{E_m - V_j}{R_m} + \frac{d}{4R_a} \left(\frac{V_{j+1} - V_j}{l^2} + \frac{V_{j-1} - V_j}{l^2} \right) + \frac{I_{e,j}}{\pi dl}, \quad (4.6)$$

which determines how the voltage in compartment j , V_j , changes through time; d , l are the compartment diameter and length, respectively.

By exploiting experimental situations in which a cell's membrane resistance can be considered constant, the passive RC circuit model can be used to set the values of these parameters. For example, in many cells, small voltage changes from the membrane resting potential (or lower potentials) demonstrate a passive nature. Data from cells under these passive conditions can be combined with the model to calculate the passive properties. Even the value of R_m , which generally results from a combination of channel resistances, can be useful as a constraint in later active models such that the total membrane resistance must equate to this passive R_m within the voltage range in which it was calculated.

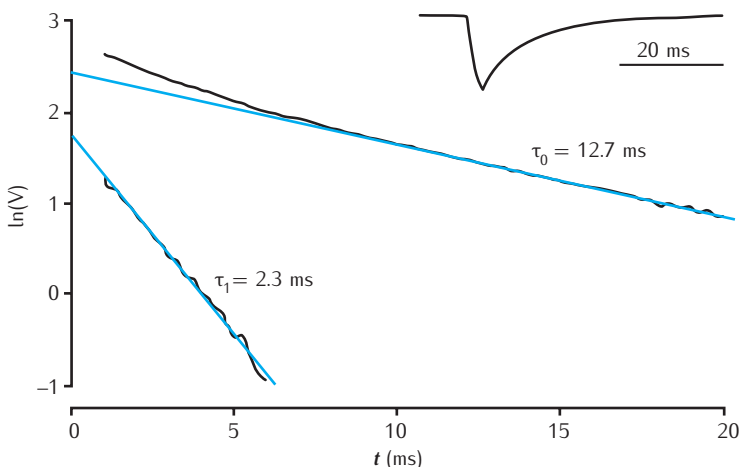
4.4.1 Matching model and neuron physiology

Measuring the three specific passive membrane parameters (C_m , R_a and R_m) directly with experimental techniques is often impractical. However, an electrical model of a passive cell can be used as a tool to estimate these properties. A careful reconstruction of the morphology can be turned into an electrical model consisting of connected passive RC circuits (Figure 4.1). With appropriately chosen values of C_m , R_a and R_m , this model should faithfully reproduce easily recordable passive electrophysiological properties from that cell. This technique of building a model from both morphological and physiological data from the same cell and the general procedure of selecting passive properties that reproduce recorded physiology has proved useful in estimating the capacitance and passive resistive properties of a variety of cells (Lux *et al.*, 1970; Clements and Redman, 1989; Rall *et al.*, 1992; Major *et al.*, 1994; Stuart and Spruston, 1998; Thurbon *et al.*, 1998).

In this process it is important to choose appropriate passive physiological properties that we wish the model to match or reproduce. Primarily, we need to ensure that they are effectively passive, i.e. that a model with a constant R_m can reproduce the phenomena. Not only does this restrict experiments to those involving small voltage changes, but also there should be experimental verification that the recorded responses are indeed passive. Similarly, we need to ensure that the passive properties we are modelling require C_m , R_a and R_m for their generation.

Injected current pulses can be used to assess whether the cell has a passive membrane resistance, R_m (Thurbon *et al.*, 1998). Averaged voltage transients produced with, for example, -0.5 nA current pulses can be compared to transients produced with -1.0 nA pulses. If the voltage transient arising from the larger amplitude pulse is twice that of the first, then the response is linear and the membrane resistance can be treated as being passive.

Fig. 4.8 A plot of the natural logarithm of voltage following a brief hyperpolarisation of a guinea pig motor neuron (black lines). The transient shown in the insert is an average of 50 responses in the same cell. A straight line fit of the later portion of the transient is used to calculate τ_0 (upper blue line). Subtracting this first exponential allows a second time constant τ_1 (lower blue line) to be estimated from the straight line fit to the remainder of the earlier portion of the transient. Adapted from Nitzan *et al.* (1990), with permission from The American Physiological Society.



We can only expect to estimate values of these parameters from observed physiology if these parameters are relevant to that physiology. For example, we cannot expect to determine realistic values of specific membrane capacitance by only comparing maximum stable voltage offsets induced by small current injection. Solutions to the membrane equation when the voltage is not changing do not depend on membrane capacitance (Box 2.6). Responses from periods during which the membrane potential is changing, e.g. transient responses, can give more information about electrotonic architecture than steady state responses as transient behaviour involves charging (or discharging) membrane capacitance.

In the following, we consider different approaches to estimating these passive parameters. This includes recording and comparing the membrane time constants and their coefficients. Directly comparing experimental and simulated membrane transients that arise from small and brief current injections is also a common approach. Such transients are dependent on all three passive parameters.

Time constants

Passive transients in the membrane potential can be described as a sum of exponentials, each with a time constant and amplitude coefficient (Equation 2.28 and Box 2.7):

$$V(t) = c_0 e^{-t/\tau_0} + c_1 e^{-t/\tau_1} + c_2 e^{-t/\tau_2} + \dots \quad (4.7)$$

By convention, the time constant τ_0 and associated amplitude coefficient c_0 account for the slowest response component; i.e. τ_0 is the largest time constant. Time constants and amplitude coefficients derived from experimental data can be used to estimate the passive properties (C_m , R_a , R_m) by demonstrating that a model with these properties and equivalent morphology generates the same transients with the same time constants.

Multiple time constants (τ_0 , τ_1 , etc.) and amplitude coefficients (c_0 , c_1 , etc.) can be derived from experimental data. Essentially, the voltage decay waveform is plotted with a logarithmic voltage axis, which enables straight

line regression to be applied to the final decay phase (Figure 4.8). This obtains an estimate of the apparent time constant τ_0 and amplitude constant c_0 of the slowest response component. The response due to this first exponential component is subtracted from the original response and the process is repeated for successively smaller time constants. For a full description of the approach see Rall (1969). This method is a good way of estimating the slowest time constant, τ_0 . However it is less reliable for estimating the remaining, faster time constants (Holmes *et al.*, 1992).

Voltage-clamp time constants

Voltage-clamp time constants can be recorded and compared with a model under simulated voltage clamp conditions (Rall, 1969). Voltage clamp techniques can ameliorate certain types of noise; for example, control of the voltage in the dendrites can limit the role of active channels in random synaptic events. Realistic modelling of a voltage clamp can require the values of additional model parameters that may not be easy to determine (Major *et al.*, 1993a, b; Major, 1993).

Input resistance

The steady state input resistance can be measured from the steady state voltage response to small current steps and compared to a theoretical input resistance calculated from the model. In a single sealed end cable, the input resistance is related to both the membrane and axial (cytoplasmic) resistances (Figure 4.9a; Box 2.6). In a more realistic branching dendritic tree, the relationship between these resistances is more complex. The input resistance to any non-terminal cylindrical branch can be calculated by treating that branch as a cable with a leaky end (Figure 4.9b). The resistance R_L at the leaky end is calculated from the input resistances of connected branches. For example, if the distal end of a branch connects to two child branches, then the resistance R_L for this branch can be calculated from the input resistances of the child branches, R_{in1} and R_{in2} , by:

$$\frac{1}{R_L} = \frac{1}{R_{in1}} + \frac{1}{R_{in2}}. \quad (4.8)$$

Assuming sealed ends at all terminal branches, we can use an algorithm to calculate the input resistance to any tree and consequently for the complete model cell itself (Box 4.4).

Note that R_{in} is significantly less sensitive to changes in intracellular resistance compared to membrane resistance (Nitzan *et al.*, 1990). This is important to consider when comparing the computed and physiologically recorded value of R_{in} . The same value of R_{in} can be calculated from models with very different intracellular resistances and only small differences in their membrane resistances.

Direct comparison of transients

Transients recorded from the cell – for example, the voltage decay after a brief current injection – can be compared directly to simulated transients generated from the model under the same simulated experimental conditions. Short current pulses used in the generation of transients have an

(a) Sealed end



$$R_{in} = R_\infty \coth(L)$$

(b) Leaky end

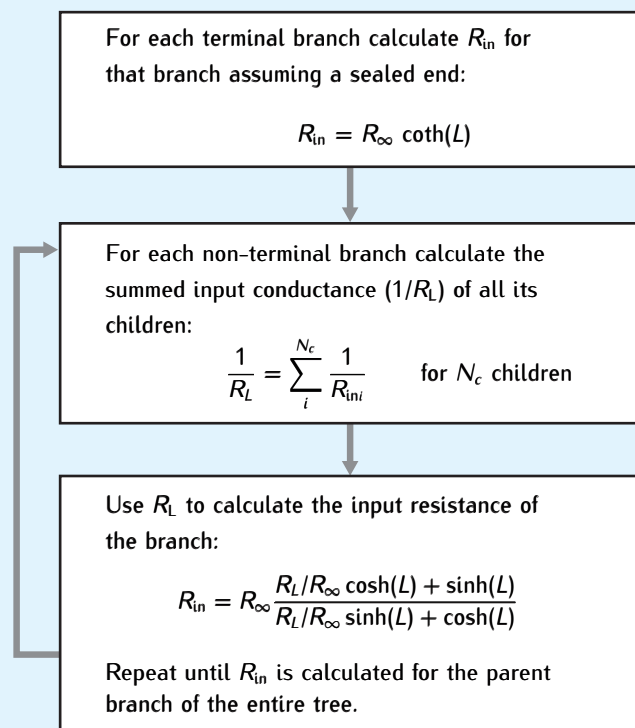


$$R_{in} = R_\infty \frac{R_L / R_\infty \cosh(L) + \sinh(L)}{R_L / R_\infty \sinh(L) + \cosh(L)}$$

Fig. 4.9 (a) Input resistance to a sealed end cable. Recall from Chapter 2 that $L = l/\lambda$ and $R_\infty = R_m/\pi d\lambda$. (b) The input resistance to the first branch of a tree can be calculated from a leaky end cable, where the leak resistance at the end is calculated from the combined input resistances of child branches.

Box 4.4 Input resistance in a branching tree

We can use an algorithmic approach to calculate the input resistance at the base of any complex branching tree by using the cable equation and different boundary conditions depending on the type of branch. Terminal branches are assumed to have a sealed end, and internal branches have leaky ends (with the leak calculated from the input resistances of connected branches):



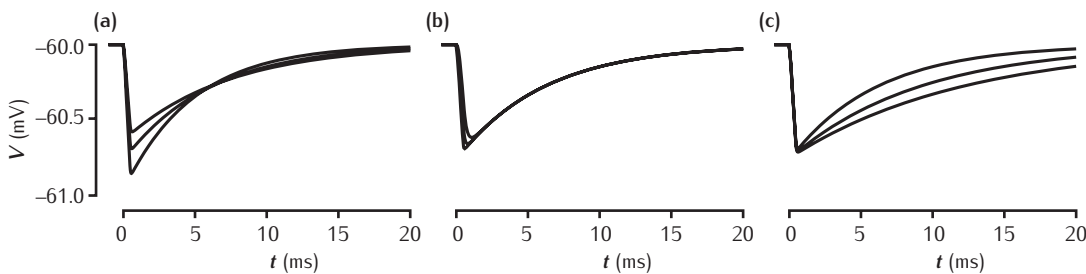
The input resistance of an entire model cell with N_t branches emerging from the soma is then given by:

$$\frac{1}{R_{in}} = \frac{1}{R_{soma}} + \sum_{i=1}^{N_t} \frac{1}{R_{in_i}}$$

R_{soma} is the input resistance of the soma compartment, generally given by R_m/a_{soma} where a_{soma} is the surface area of the soma compartment.

advantage over longer ones as they reduce the time during which the membrane potential deviates from its resting level, thereby lessening the risk of activating slow voltage-dependent conductances. The term **direct fitting** was coined by Clements and Redman (1989) in their procedure for optimising the values of passive parameters to fit a transient directly.

This direct approach avoids the errors that may be introduced when determining electrophysiological properties such as R_{in} , τ_0 and c_0 . These errors are passed into the estimation of R_m , C_m , R_a . Direct fitting has only one parameter estimation process, which is selecting values of R_m , C_m and R_a .



that minimise the differences between simulated and experimental voltage traces.

To ensure that transients do not engage active channels it is important to test that their form does not change over time when repeatedly producing transients. Large numbers of transients generated by the same stimulation protocol can be pooled and averaged to give a prototype target transient for the model to reproduce. This not only reduces noise but, with sufficiently large numbers of recorded samples, it is possible to place approximate bounds around the averaged target transient within which an individual transient will fall, say, 95% of the time. We can have confidence in a fit if it remains within these bands; otherwise the fit can be rejected (Major *et al.*, 1994).

The interval of time over which the comparison between model and recorded transients is made is critical. Immediately at the end of the stimulus, the recorded experimental transient is likely to include electrode artifacts (Section 4.5.1). Starting the comparison too soon so as to include these may lead to the selection of passive parameter values which are tainted by electrical properties of the electrode. Starting too late will reduce the information contained within the transient. If we wish to estimate the three passive properties of the RC circuit using the comparison, we need to ensure there is sufficient data in the time interval to constrain each parameter. Figure 4.10 illustrates areas of voltage transients affected by the passive properties. The early rise of the transient is affected significantly by both C_m and R_a (Figure 4.10a, b). R_m has a dominant influence on the decay phase (Figure 4.10c). Estimating the three passive parameters by only examining the late decay phase would not constrain the minimisation sufficiently nor generate useful estimates of R_a and C_m .

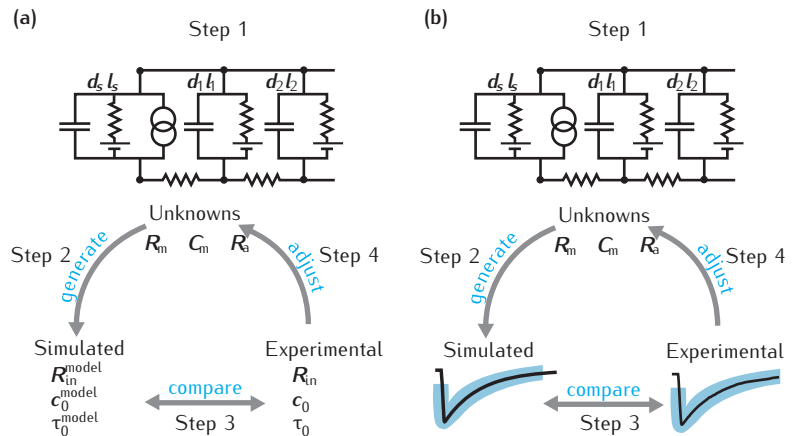
Fig. 4.10 Changes in RC circuit passive properties affect the shape of a simulated transient generated from stimulating a single cable with a brief $480 \mu\text{s}$ current pulse of -0.5nA . (a) C_m varied, with values $0.8, 1.0, 1.2 \mu\text{F cm}^{-2}$. (b) R_a varied, with values of $32.4, 97.2, 194.4 \Omega \text{cm}$. (c) R_m varied, with values of $6, 9, 12 \text{k}\Omega \text{cm}^2$. The standard passive circuit parameters are $C_m = 1.0 \mu\text{F cm}^{-2}$, $R_a = 32.4 \Omega \text{cm}$, $R_m = 6 \text{k}\Omega \text{cm}^2$.

4.5 Parameter estimation

Parameter estimation is the process of finding parameter values that best fit a mathematical model to experimental data. The number of parameters and, consequently, the number of degrees of freedom in even a simple model may be large (Rall, 1990). As every parameter in the model must be assigned a value, the more parameters that can be directly given experimentally measured values, the fewer need to be estimated. For example, with a good morphological reconstruction, the passive model requires only the three specific passive parameters, C_m , R_m and R_a to be estimated.

Fig. 4.11 Steps involved in parameter estimation for an example passive model.

(a) Example steps using derived physiological data (input resistance R_{in} , time constant τ_0 and coefficient c_0). (b) The same steps with direct comparison of transients.



The first task in parameter estimation is to devise a measure of how well the model fits the data. This is often termed a **fitness measure** or **error measure**. A typical error measure is the sum-of-squared difference between the membrane potential produced by the model and that recorded experimentally, over some fixed time window. The smaller the error, the better the fit. The main task is the estimation procedure itself, which attempts to discover a set of parameters that minimise the error measure (or maximise the fitness). Such a set may or may not be unique. The final task is to test the robustness of the model and its estimated parameter values by comparing model output against experimental data that was not used to determine the error during parameter estimation. A robust model will produce a close match to this new experimental data as well. This whole process proceeds in a step-by-step manner to achieve reasonable values for unknown parameters:

Step 1 Fix the known parameters, such as those specifying the cell morphology, and make educated guesses for the remaining unknown parameter values.

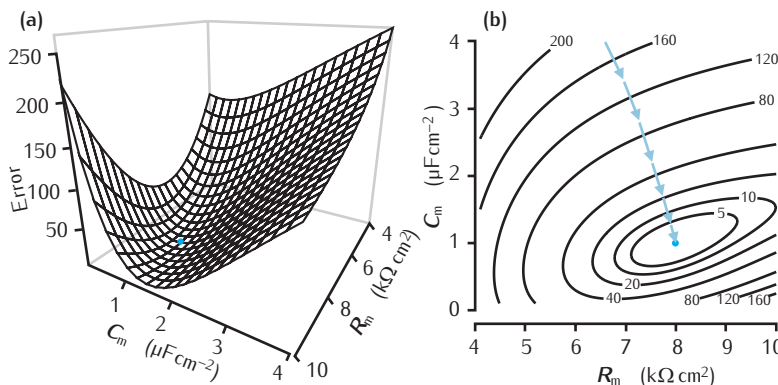
Step 2 Use the model to simulate experiments, such as the transient response, producing model data.

Step 3 Compare the model data with experimental data by calculating the value of the error measure.

Step 4 Adjust one or more unknown parameter values and repeat from Step 2 until the simulated data sufficiently matches the experimental data, i.e. minimises the error measure.

Step 5 Use the model to simulate new experiments not used in the steps above and compare the resulting model data with the new experimental data to verify that the chosen parameter values are robust.

The process of parameter estimation is illustrated in Figure 4.11, where the task is to estimate values for the passive parameters C_m , R_m and R_a . In the example in Figure 4.11a, R_{in} , τ_0 and c_0 have been produced from the model, and it is the difference between these simulated and the experimentally recorded values that we would like to be reduced. Our error measure is defined as the sum of the squared differences between simulated and



experimental data:

$$\text{error} = w_1(R_{\text{in}} - R_{\text{in}}^{\text{model}})^2 + w_2(\tau_0 - \tau_0^{\text{model}})^2 + w_3(c_0 - c_0^{\text{model}})^2, \quad (4.9)$$

where we are using the superscript ‘model’ to indicate simulated observables; the w_i are weights that can be used to scale the components of the error measure, but are all set to 1 in this example. In Figure 4.11b, we are doing direct fitting, so now the error measure is the difference between the simulated and recorded membrane potential transient at a (possibly large) number of discrete time points.

For every set of estimated values for R_m , C_m and R_a , we can produce a simulated output and then calculate the error. Plotting the error against different sets of parameter values defines a surface in a space with one dimension for each unknown parameter and one dimension for the value of the error. An example with two unknowns is shown in Figure 4.12. Although visualising high dimensions is difficult, an error surface provides a convenient concept in parameter estimation. The task of finding parameter values that lead to a minimum error translates to moving around this surface in order to find the minimum.

There are many **optimisation algorithms** designed to adjust parameter values iteratively until the error has reached a minimum. One of the simplest approaches is **gradient descent**. At any point on the surface, the direction and slope of the steepest way down can be calculated. In each iteration of the gradient descent algorithm, the parameter values are moved a small distance in the direction of the steepest descent and so the error decreases (Figure 4.12b).

One of the problems with complex error surfaces (e.g. surfaces containing multiple hills and valleys) is the possibility that algorithms that follow the gradient end up trapped in local minima rather than finding the global or overall minimum (Figure 4.13). Parameter spaces and error surfaces for multi-compartmental models are generally complex, with multiple local minima likely (Vanier and Bower, 1999). Searching for parameter values therefore requires algorithms and approaches that reduce the possibility of choosing parameter values that result in a local minimum error rather than the global minimum. One popular approach, called **simulated annealing** (Vanier and Bower, 1999), involves adding noise to the error estimates so the solution may manage to avoid, or jump out of, local minima. The

Fig. 4.12 (a) An error surface generated from direct comparison of transients in a single compartment RC circuit model. For convenience of visualisation the error surface is plotted over only two unknown variables, R_m and C_m . The minimum is indicated by a blue point ($C_m = 1 \mu\text{F cm}^{-2}$, $R_m = 8 \text{k}\Omega \text{cm}^2$). (b) A contour plot of the same surface demonstrating a single minimum. The arrows illustrate a gradient descent approach to finding the minimum.

An important aspect of defining a good error measure is that all values that contribute to the measure are of similar magnitude. This can usually be achieved by using suitable units for each quantity. If it is decided that one component of the error measure is qualitatively more important, then this can be reflected by weighting the components individually.

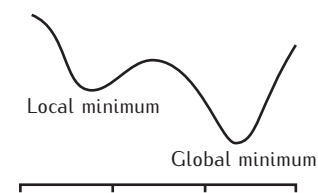


Fig. 4.13 One-dimensional plot of an error surface showing one local and one global minimum.

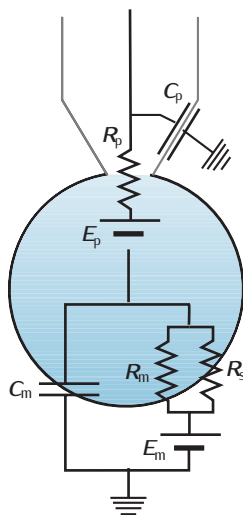


Fig. 4.14 A simple electrical circuit representing either an intracellular sharp or whole cell pipette electrode attached to a soma. The electrode is modelled as a tip potential E_p and resistance R_p in parallel with pipette wall capacitance C_p . For small diameter sharp electrodes, R_p is on the order of 10s to 100s of megohms, whereas for larger bore whole cell electrodes it is around 10 M Ω (Major *et al.*, 1994). C_p is typically on the order of 10 pF. An intracellular sharp electrode may introduce a shunt resistance R_s on the order of 100 M Ω . With a tight-seal whole cell electrode, R_s is on the order of 10 G Ω (Li *et al.*, 2004).

amount of noise is controlled by the so-called *temperature* parameter, which is decreased as the optimisation proceeds, so that the algorithm will settle on a final, hopefully global, solution.

Further discussion of error measures and optimisation procedures for parameter estimation is given in Appendix B.4.

4.5.1 Assumptions and accuracy of estimates

By following these model construction and parameter estimation approaches, estimates for the underlying passive properties of specific cells can be made. Confidence in these estimates is less easily obtained. This should be based not only on how small the error measure is in, for example, the comparison of transients, but also by comparing the model against new experimental data (Step 5), verifying model assumptions and an assessment of the main sources of possible error.

We have already encountered many of the assumptions on which the passive RC circuit model is built (Chapters 2 and 3), and they are summarised in Box 4.5. Ensuring these assumptions are reasonable is the first step in gaining confidence in the final passive parameter values attained. For some of the assumptions, such as that the resistance and capacitive membrane properties are passive, this is possible experimentally. For example, it is important to verify that the experimental protocol does not activate or inactivate voltage-dependent currents. Other assumptions, such as the uniformity of specific passive properties over the cell morphology, are harder to verify.

Furthermore, the presence of recording/stimulus electrodes can introduce artifacts (Box 4.6). In particular, sharp electrodes can lead to a shunt, or change in membrane resistance, at the electrode site (Figure 4.14). For example, the entry of calcium ions through a membrane puncture can activate calcium-dependent channels which are selective for potassium ions. **Whole cell patch electrodes** with seal resistances above 5 G Ω can minimise the risk of shunts. Li *et al.* (2004) have carried out a detailed comparison of the

Box 4.5 Key assumptions of the RC circuit representation of the passive membrane

- (1) The membrane is passive, its properties being described by fixed resistance and capacitance only.
- (2) Specific membrane resistance, capacitance and cytoplasmic resistivity are uniform throughout the morphology.
- (3) There is no depletion or accumulation of the ion pools on either side of the membrane.
- (4) The cytoplasm provides only ohmic resistance.
- (5) Voltage dependence within the cytoplasm is one-dimensional, with no radial or angular dependence.
- (6) The extracellular medium is isopotential.

See Rall (1977) for a review of the assumptions for a passive RC circuit multi-compartmental model, and some of their justifications.

Box 4.6 Modelling the electrode

The voltage and current recordings needed to determine passive cell physiology will be obtained using an intracellular **sharp electrode** (Purves, 1981) or a **whole-cell patch electrode** (Hamill *et al.*, 1981). High-quality recordings require the removal of the contributions of the electrical properties of the electrode and the rest of the recording apparatus from the recorded signals. This is done as a recording is made by appropriate circuitry in the recording apparatus. This circuitry subtracts signals from the recorded signal based on a simple model of the electrode as an RC circuit (Figure 4.14).

Passing current through the electrode results in a large voltage drop across the electrode tip due to the tip resistance, which is in series with the cell's membrane resistance. The measured voltage is the sum of the tip voltage and membrane voltage. The membrane voltage is obtained at the recording apparatus by subtracting a signal proportional to the injected current (which models the tip voltage) from the recorded voltage, a process known as **bridge balance**. This works well provided that the tip resistance is constant and the electrode time constant is much faster than the membrane time constant. These assumptions may be more or less reasonable in different recording setups.

The wall of the glass electrode contributes a capacitance that needs to be removed as well. Similarly to the electrode resistance, **capacitance compensation** is obtained by circuitry that feeds the output of the preamplifier through a capacitor and adds it to the preamplifier input, thus effectively adding in a capacitive current that is the inverse of the current lost through the capacitance of the electrode.

High-quality recordings rely on accurate calibration of the bridge balance and capacitance compensation (Park *et al.*, 1983; Wilson and Park, 1989), and the validity of the underlying assumptions forming the electrode 'model'. Even so, care still needs to be taken when analysing the slow measurements used for determining passive membrane properties (Section 4.5.1). The situation is worse when recording faster synaptic signals and action potentials. Particularly demanding are **dynamic clamp** experiments (Figure 4.15) in which rapidly changing currents, mimicking, say, synaptic signals, are injected into the cell and the resulting voltage transients are recorded. Serious artifacts can be introduced into the recording due to flaws in this simple electrode model (Brette *et al.*, 2008). Techniques based on better electrode models are being developed (Brette *et al.*, 2008).

artifacts introduced by sharp and whole cell electrodes in the same experimental preparation.

The model can be extended to include a membrane shunt in the soma that represents the change in membrane resistance in this compartment (Figure 4.14). This extension to the model allows the possibility of changes in membrane resistance at the soma to be captured at the expense of introducing an additional free parameter, the **soma shunt conductance**, g_{shunt} . This

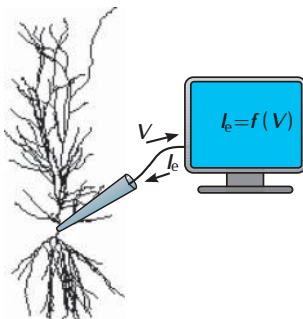


Fig. 4.15 The dynamic clamp experimental setup (Sharp *et al.*, 1993; Economo *et al.*, 2010). In real time, the recorded membrane voltage V is input to a computational model, which generates the injected current I_e . This current may represent a synaptic or ion channel current. Its calculation could involve voltage-gated channel kinetics, or the response of an entire compartmental model cell. This is an important use for the neural computational models described in this book.

The axial resistance in a passive model consisting of a single cylindrical compartment, diameter d_s and length l_s is:

$$\frac{4R_a l_s}{\pi d_s^2}.$$

With both R_a and d_s as unknown parameters, there is an infinite number of combinations of R_a and d_s that yield the same axial resistance.

additional parameter can be included in the general parameter estimation process, optimising now over four parameters.

It is possible to assess if an obvious soma shunt conductance is exhibited in the recorded transients. In this approach, a reference model is constructed, with realistic values of R_m , R_a and C_m . Perturbations of interest, such as a soma shunt, can be introduced into the reference model. Parameters of a model with no shunt (i.e. the three passive parameters) are then optimised to match the transients generated by the reference model. In other words, a simulated scenario is constructed where we optimise three parameters of a model to make it mimic, as best it can, the data generated from a model using four parameters. Examining the residual left after the reference transient is subtracted from the optimised model transient can prove useful in identifying cells with specific non-uniformities (Major and Evans, 1994; Thurbon *et al.*, 1998).

The electrode itself can also be responsible for sources of error in the final parameters. The combined capacitive properties of a patch pipette and amplifier can alter the early phase of transients. Subtracting extracellular controls from the response does not eliminate the introduced pipette aberrations (Major and Evans, 1994). Building a model of the pipette is one approach to quantifying its effect (Major *et al.*, 1994). In turn, this introduces additional electrode-specific parameters into the model, with values that can often be difficult to obtain. Alternatively, carefully selecting the times over which model and experimental transients are matched can avoid these errors. In particular, deciding on an appropriate post-stimulus start time for the comparison is crucial (Major *et al.*, 1994). Optimising parameters to fit transients too soon after the stimulus may yield values that are contaminated by the electrode artifacts. Starting the comparison too late will fail to sufficiently constrain the passive properties (Figure 4.10).

4.5.2 Uniqueness of estimates

Increasing the number of unknown parameters to estimate increases the possibility of non-unique solutions. In the passive model example, if any of the parameters defining the model morphology, such as soma diameter, are also unknown, an infinite number of combinations of the parameter values R_m , R_a , C_m and the unknown soma diameter d_s can generate identical simulated data. There is no unique set of parameter values that can be selected to underlie the passive physiology. In general, with unknowns in the model morphology it is very difficult to calculate unique parameter values from experimental data recorded with electrodes. Typically, multi-compartmental models with more than a handful of unknown parameters can result in parameter estimation being an under-determined problem.

There are a number of approaches to assess whether chosen parameter values are unique. The error minimisation procedure can be performed many times, each starting from different initial sets of parameters. If the final attained parameters and error values are sufficiently similar in each case, it is less likely that multiple combinations of parameter values that produce the same target physiology exist. However, this is not a guarantee of uniqueness. Furthermore, the usefulness of this approach critically depends on how the different starting conditions are selected.

There may be multiple sets of parameter values which generate identical model transients in response to one stimulation protocol, but generate different responses under other protocols. This type of non-uniqueness is particularly problematic for an unknown soma shunt (Major *et al.*, 1994). Consequently, it is important to keep aside, or have access to, experimental data not used in the parameter estimation procedure. This data can then be used to test the model and assess whether the chosen parameter values act appropriately in different situations.

It may be possible to place confidence bounds on the individual parameters by progressively increasing (and decreasing) each parameter value until the fit is rejected, using bands placed on experimental transients as described in Section 4.4.1. The model can also be subject to a thorough sensitivity analysis to determine the consequences of the choices made for parameter values. For example, varying specific parameter values, while keeping all other values fixed, and comparing the model outputs with a known experimental result can be used to identify parameters that strongly determine the particular model physiology or behaviour.

4.6 Adding active channels

In this section we introduce some of the issues involved in incorporating active channels into compartmental models. Chapter 5 explores models of individual active channels and reviews different channel types and classes.

4.6.1 Ion channel distributions

For electrotonically extensive compartmental models, the location of different types of ion channels has a critical effect on neuronal function (Gillies and Willshaw, 2006). It is possible to determine ion channel densities using patch clamp and blocking experiments at different locations in the dendrites (Hoffman *et al.*, 1997). In practice, this information is not always known and the densities of channels in each compartment are free parameters in the model. In models with many compartments, this can lead to an unmanageably large number of parameters; at least one conductance density parameter per channel type per compartment. Thus one of the immediate consequences of adding active channels is the explosion in the number of parameters in the model and a significant increase in the number of degrees of freedom (Rall, 1990).

One approach to reducing the number of degrees of freedom is to parameterise channel densities throughout a dendrite in terms of distribution functions (Migliore and Shepherd, 2002). The simplest of these would be a uniform distribution where a single maximum conductance density parameter is used in all compartments of the tree (Figure 4.16a). Linear distributions, where the conductance density changes with a linear gradient as a function of distance from the soma, is an example of a slightly more complex distribution function (Figure 4.16b). Knowledge of the particular cell and channel composition is crucial to guide the simplifications. For example, separate distributions may be required within different neuron dendritic processes

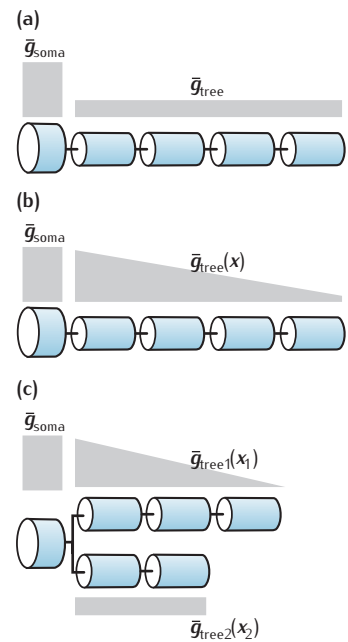


Fig. 4.16 Schematic of different channel distribution functions. (a) Uniform distribution in the tree with an independent soma channel distribution. (b) Linear distribution in the tree specified as a function of distance x from the soma. (c) Two trees with different distribution functions.

(Figure 4.16c), such as oblique branches as opposed to the apical trunk in hippocampal pyramidal cells (Poirazi *et al.*, 2003).

4.6.2 Ion channel models

The amount of work involved in developing ion channel models and fitting their parameters with targeted physiology often leads to using ion channel models and parameters not derived from the cell or cell type from which physiological data is actually being recorded. Inclusion of channel models and kinetics from channel libraries or published data is common practice in building multi-compartmental models (see Appendix A for resources). With appropriate adjustments, these models can provide a useful first approximation to an active channel and can reduce the number of potential free parameters in the compartmental model. The channel kinetics may have to be adjusted to match the temperature at which the model cell is being simulated. For example, a Q_{10} factor may be used (Chapter 3). A channel model with parameter values set to replicate observed channel behaviour at 20 °C will not be appropriate for a cell model being simulated at any other temperature. Two channels, where one has kinetic parameters set at 20 °C and the other at 30 °C, cannot both be added to the same model without adjustment for temperature.

4.6.3 Parameter estimation in active models

Provided there is sufficient experimental data and computational resources, the parameter estimation techniques already described in Section 4.5 can be used to give values to unknown parameters in models with complex channel compositions and distributions. The computational time needed for iterative optimisation algorithms to find solutions increases with large numbers of parameters, as does the probability of finding non-optimal solutions (Vanier and Bower, 1999). Nevertheless, by making appropriate model simplifications to reduce the number of free parameters and incorporating appropriate physiological data in the error measure so it constrains the parameters sufficiently, parameter estimation can prove more effective and robust than attempting to select parameters by hand.

As in the passive case, the choice of the physiology from which to calculate an error measure is crucial. With the increased complexity introduced by active channels, a wider set of experimental data under a range of stimulus conditions is required to produce a useful error measure. Ideally, experiments should be constructed that provide information about each free parameter. Where possible, it is useful to divide the parameter fitting task into separate problems. For example, selecting a kinetic model (Chapter 5) and associated parameter values for a particular ion channel type can often be done independently of the full compartmental model.

With appropriate and sufficient experimental data available to estimate free parameter values, it is possible to effectively select for individual compartment's multiple channel maximum conductances in a model with complex morphology. For example, voltage-sensitive dye recordings allow measurement of the voltage along a dendrite. Given sufficient spatio-temporal resolution and appropriate stimulus protocols, this data can provide target voltage recordings with which to match model responses from every spatial

compartment (Huys *et al.*, 2006). If the types of ion channels and their kinetics are known, under certain situations an optimal solution can be shown to exist, and conductance values for multiple channels at each compartment can easily be estimated.

However, even with this level of voltage data to constrain the conductance parameters, it can be difficult to assign unique maximum conductances to channels with very similar kinetic profiles where the experimental protocol does not or cannot separate the channel contributions to the response. In situations like this, it may be useful to include physiological responses in the presence of particular channel blockers in the set of physiological responses from which the estimation error is calculated. Accordingly, this may add additional parameters for modelling the quantitative effect of the channel blocker; e.g. dose-response data.

4.7 | Summary

The complex morphology of a neuron can be captured in a model by using the compartmental approach in which the neuron is approximated as a set of isopotential compartments of membrane connected by resistors. Compartments are often represented by cylinders, with lengths and diameters derived from reconstructed morphologies, or as stereotypical approximations of real dendrites and axons.

A multi-compartmental model with a complex morphology comes with a huge number of free parameters. The active and passive properties of the membrane of each compartment need to be specified. Choosing values for capacitance, membrane and axial resistances and ion channel conductances is often an underdetermined problem where multiple combinations of parameter values lead to the same observed physiology.

A significant part of the process of building multi-compartmental models is using appropriate approaches to reduce the number of free parameters. This can involve simplifying the morphology or assuming easily parameterised distributions of ion channels; e.g. a particular ion channel type may have the same conductance density throughout the neuron.

Parameter estimation techniques can be used to choose values for free parameters. These techniques select combinations of parameter values that specifically reduce an error measure reflecting the difference between model and experimentally recorded data. As multi-compartmental models can have complex error surfaces with the possibility of local minima, estimation techniques that avoid these may be required. An assessment of the final parameter values selected should also be made by, for example, reproducing experimental data not used in the estimation procedure.

Models of active ion channels

There are many types of active ion channel beyond the squid giant axon sodium and potassium voltage-gated ion channels studied in Chapter 3, including channels gated by ligands such as calcium. The aim of this chapter is to present methods for modelling the kinetics of voltage-gated and ligand-gated ion channels at a level suitable for inclusion in compartmental models. The chapter will show how the basic formulation used by Hodgkin and Huxley of independent gating particles can be extended to describe many types of ion channel. This formulation is the foundation for **thermodynamic models**, which provide functional forms for the rate coefficients derived from basic physical principles. To improve on the fits to data offered by models with independent gating particles, the more flexible **Markov models** are introduced. When and how to interpret kinetic schemes probabilistically to model the stochastic behaviour of single ion channels will be considered. Experimental techniques for characterising channels are outlined and an overview of the biophysics of channels relevant to modelling channels is given.

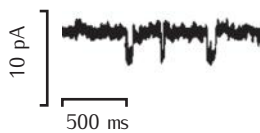


Fig. 5.1 Single channel recording of the current passing through an acetylcholine-activated channel recorded from frog muscle in the presence of acetylcholine (Neher and Sakmann, 1976). Though there is some noise, the current can be seen to flip between two different levels. Reprinted by permission from Macmillan Publishers Ltd: *Nature* 260, 779–802, © 1976.

Over 100 types of ion channel are known. Each type of channel has a distinct response to the membrane potential, intracellular ligands, such as calcium, and extracellular ligands, such as neurotransmitters. The membrane of a single neuron may contain a dozen or more different types, with the density of each type depending on its location in the membrane. The distribution of ion channels over a neuron affects many aspects of neuronal function, including the shape of the action potential, the duration of the refractory period, how synaptic inputs are integrated and the influx of calcium into the cell. When channels are malformed due to genetic mutations, diseases such as epilepsy, chronic pain, migraine and deafness can result (Jentsch, 2000; Catterall *et al.*, 2008).

Models of neurons containing multiple channel types are an invaluable aid to understanding how combinations of ion channels can affect the time course of the membrane potential. For example, later on in this chapter, it will be shown that the addition of just one type of channel to a Hodgkin-Huxley (HH) model neuron can have profound effects on its firing properties, effects that could not be predicted by verbal reasoning alone.

In order to build neuron models with multiple channel types, models of individual constituent channel types must be constructed. In Chapter 3 it was shown how voltage clamp currents of squid giant axon sodium and potassium channels could be reproduced approximately by a model in which the channel opening and closing is controlled by a set of independent gating particles. In this chapter, it will be shown how this method can be extended to different types of voltage- and ligand-gated channels.

Independent gating particle models are sufficiently accurate to explore many questions about neuronal electrical activity but, even with optimal parameter tuning, there are discrepancies between their behaviour and the behaviour of certain types of channel. An improved fit to the data can be achieved by using Markov models, which are not constrained by the idea of independent gating particles and consider the state of the entire channel, rather than constituent gating particles.

A further modification to channel models is required in order to explain voltage clamp recordings from single channels made using the patch clamp technique, pioneered by Neher and Sakmann (1976). Rather than being smoothly varying, single channel currents switch randomly between zero and a fixed amplitude (Figure 5.1). This chapter will show how probabilistic Markov models can be used to understand single channel data and will introduce a method for simulating a single channel stochastically. It will also consider under what circumstances this type of simulation is necessary.

The principal thrust of this chapter is how to construct models of the dependence of ion channel conductance on the membrane potential and concentrations of intracellular ligands. The chapter will also touch on the considerable understanding of the structure and function of ion channels at the level of the movement of molecules within channel proteins, which has culminated in the derivation of the 3D structure of ion channels (Figure 5.2) from X-ray crystallography (Doyle *et al.*, 1998). While much of this understanding is more detailed than needed for modelling the electrical behaviour of neurons, modelling studies can be informed by the concepts of ion channel structure and function. In this chapter, the theory of chemical reaction rates is applied to channel gating to produce thermodynamic models of channels, which naturally incorporate temperature and voltage dependence. Incorporating physical theory into channel models is desirable as it is likely to make them more accurate. A basic understanding of ion channel structure and function is also important when interpreting the data on which channel models are based.

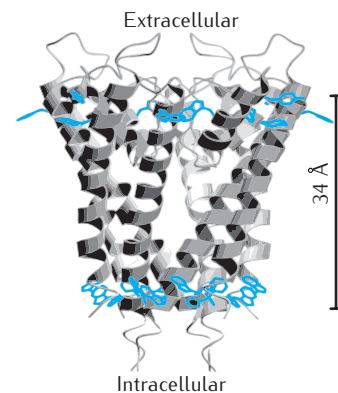


Fig. 5.2 Structure of a potassium channel (the KcsA channel) from the soil bacterium *Streptomyces lividans*, determined by X-ray crystallography by Doyle *et al.* (1998). The *kcsA* gene was identified, expressed and characterised electrophysiologically by Schrempf *et al.* (1995). The KcsA channel is blocked by caesium ions, giving rise to its name. From Doyle *et al.* (1998). Reprinted with permission from AAAS.

5.1 | Ion channel structure and function

A vast range of biochemical, biophysical and molecular biological techniques have contributed to the huge gain in knowledge of channel structure and function since Hodgkin and Huxley's seminal work. This section provides a very brief outline of our current understanding; Hille (2001) and more recent review papers such as Tombola *et al.* (2006) provide a comprehensive account.

Box 5.1 | The IUPHAR scheme for naming channels

The International Union of Pharmacology (IUPHAR) has formalised a naming system for ion channel proteins in the voltage-gated-like superfamily based on both structural protein motifs and primary functional characteristics (Yu *et al.*, 2005).

Under this scheme, channels are organised and named based on prominent functional characteristics and structural relationships. Where there is a principal permeating ion, the name begins with the chemical symbol of the ion. This is followed by the principal physiological regulator or classifier, often written as a subscript. For example, if voltage is the principal regulator of the channel, the subscript is 'v', as in Na_v or Ca_v . Where calcium concentration is the principal channel regulator the subscript is 'Ca', as in K_{Ca} . Examples of other structural classifications are the potassium channel families K_{ir} and K_{2P} . Two numbers separated by a dot follow the subscript, the first representing gene subfamily and the second the specific channel isoform (e.g. $\text{K}_v3.1$).

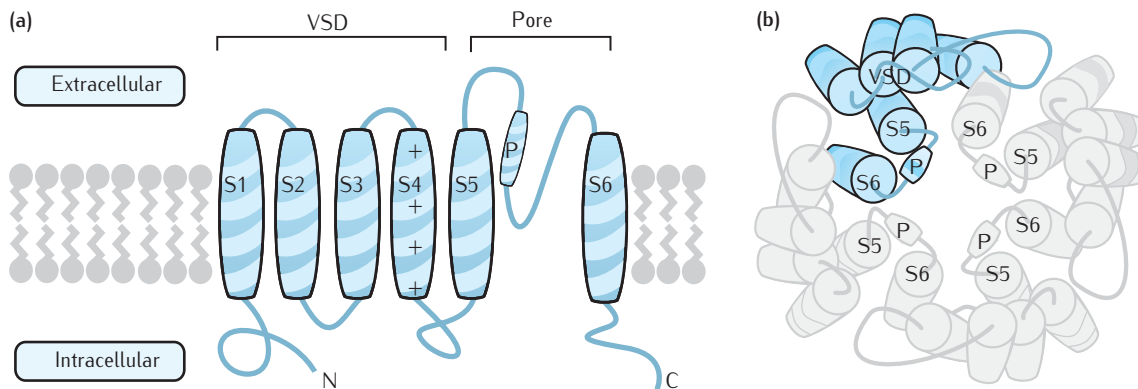
Where there is no principal permeating ion in a channel family, the family can be identified by the gating regulator or classifier alone. Examples are the cyclic-nucleotide-gated channel family (CNG), the hyperpolarisation-activated cyclic-nucleotide-gated channel family (HCN), the transient receptor potential channel family (TRP) and the two-pore-channels family (TPC).

In the HH model, there are four independent gating particles for the potassium conductance. This happens to correspond to the four subunits of the tetrameric, delayed rectifier potassium channel. However, this type of correspondence is not true of all independent gating particles models. For example, in the HH model of the sodium channel there are three activating particles, but the sodium channel has one principal subunit that contains four sets of voltage-sensitive domains and pore-forming domains.

Each ion channel is constructed from one or more protein subunits. Those that form the pore within the membrane are called **principal subunits**. There may be one principal subunit (e.g. in Na^+ and Ca^{2+} channels), or more than one (e.g. in voltage-gated K^+ channels). Ion channels with more than one principal subunit are called **multimers**; if the subunits are all identical, they are **homomers**, and if not, they are **heteromers**. Multimeric channel structures were presaged by Hodgkin and Huxley's idea (Chapter 3) of channels as gates containing multiple gating particles. However, there is not generally a direct correspondence between the model gating particles and channel subunits. As the number of known channel proteins has increased, systematic naming schemes for them, such as the IUPHAR naming scheme (Box 5.1), have been developed.

An ion channel may also have **auxiliary subunits** attached to the principal subunits or to other auxiliary subunits. The auxiliary subunits may be in the membrane or the cytoplasm and can modulate, or even change drastically, the function of the primary subunits. For example, when the $\text{K}_v1.5$ type of principal subunit is expressed in oocytes alone (Section 5.3.3) or with the $\text{K}_v\beta 2$ auxiliary subunit, the resulting channels are non-inactivating. However, when expressed with the $\text{K}_v\beta 1$ subunit the channels are inactivating (Heinemann *et al.*, 1996).

The secondary structure of one of the four principal subunits of a voltage-gated potassium channel is shown in Figure 5.3a. The polypeptide chain is arranged into segments organised into α -helices and connecting



loops. Figure 5.3b shows the 3D arrangement of the four principal subunits in a closed conformation of the channel protein. The S5 and S6 segments form the lining of the pore, and the S1–S4 segments form a voltage-sensitive domain (VSD). The 3D structure of a number of channels has been elucidated, including the weakly voltage-gated KcsA potassium channel shown in Figure 5.2 (Doyle *et al.*, 1998), a potassium channel from the bacterium *Aeropyrum pernix* (Jiang *et al.*, 2003) and the eukaryotic *Shaker K_v1.2* voltage-gated potassium channel (Long *et al.*, 2005).

As seen in Chapter 3, Hodgkin and Huxley proposed a voltage-sensing mechanism consisting of the movement of charged particles within the membrane. Such a mechanism has been broadly confirmed in the S4 segment of the voltage-gated potassium channel VSD. A number of positively charged residues within the S4 segment (called **gating charges**) experience the electric force due to the membrane potential. The resultant movements of the gating charges lead to other segments in the channel moving. The precise nature of the movement is currently not known, and may depend on the type of channel. This shift leads to a change in the pore confirmation through an interaction of the S4–S5 link with the *neighbouring* subunit's S6 segment. It is hypothesised that a hinge in the S6 helical segment forms the basis of the gate, allowing ions to flow in the open state, and limiting flow in the closed state. Evidence for this comes both from mutations in the S6 helical segment and data from X-ray crystallography (Tombola *et al.*, 2006).

The changes in conformation of channel proteins over periods of nanoseconds during gating and permeation of ions through the pore can be modelled using molecular dynamics simulations at an atomic level (see Roux *et al.* (2004) for a review). This type of model is much more detailed than is needed to understand how the distribution of different channel types throughout the cellular membrane leads to the electrical activity characteristic of different neurons.

Fig. 5.3 (a) Secondary structure of one subunit of a voltage-gated potassium channel (based on Tombola *et al.*, 2006). A number of segments of the polypeptide chain are arranged to form α -helices, which are connected together by loops. Six of these α -helices span the membrane and are labelled S1–S6, and there is also a P α -helix, in the loop that joins the S5 and S6 transmembrane segments. The S4 segment contains a number of charged residues and, along with segments S1–S3, makes up the voltage-sensing domain (VSD) of the subunit. Segments S5, S6 and P make up the pore region. Both the N-terminal and C-terminal of the polypeptide project into the cytoplasm. (b) The tertiary structure of the principal subunits in a closed conformation of the channel viewed from above. The four subunits (one of which is highlighted) can be seen to form a central pore, lined by the S5, S6 and P segments of each subunit.

5.2 Ion channel nomenclature

In the early 1980s the genes of ion channels began to be sequenced. With the completion of the human genome, genes for over 140 channels have been

Fig. 5.4 The superfamily of mammalian voltage-gated-like ion channels, organised as a phylogenetic tree constructed from the similarities between the amino acid sequences of the pore regions of the channels. There are 143 members of the superfamily, organised into a number of family groups: Na_v , Ca_v , K_v , K_{Ca} CNG/HCN, $\text{K}_{2\text{P}}/\text{K}_{\text{ir}}$, TRP and TPC. Although the $\text{K}_{\text{Ca}2}$ and $\text{K}_{\text{Ca}3}$ subfamilies are purely ligand-gated, because of the structural similarity of the pore, they still belong to the voltage-gated superfamily. Adapted from Yu *et al.* (2005), with permission from the American Society for Pharmacology and Experimental Therapeutics.

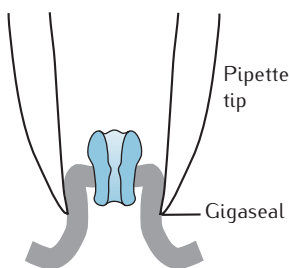
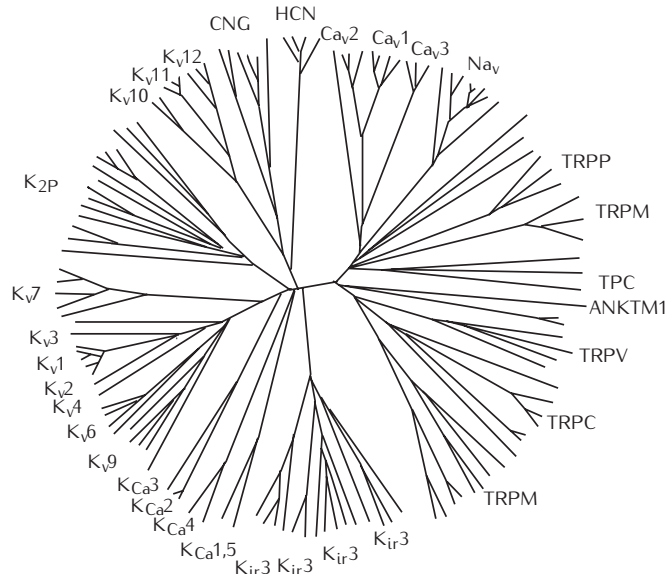


Fig. 5.5 The patch clamp technique. A fire-polished glass electrode with a tip of less than 5 μm in diameter has been placed on the surface of a cell and suction has been applied so that a very tight gigaseal has been formed between the electrode and the membrane surrounding a single channel. The electrode has then been withdrawn from the cell membrane, ripping the small patch of membrane away from the cell, to form an 'inside-out' patch.

discovered. Each channel gene is named according to the scheme used for the organism in which it occurs. The prefix of the gene gives some information about the type of channel to which it refers; for example, genes beginning with KCN are for potassium channels. This **gene nomenclature** is set by organism-specific committees; for example, The Human Genome Organisation Gene Nomenclature Committee is responsible for the naming of human genes.

Family trees of ion channels can be made by grouping the amino acid sequences corresponding to each gene (Figure 5.4). Within each family, channels with the same principal permeant ion are grouped together, and there are subgroups of channels which are voltage-gated or ligand-gated. The phylogenetic tree also reflects the similarities in the channel structures such as the number of transmembrane segments.

This structure is reflected in the system of naming cation channels adopted by the IUPHAR, sometimes referred to as the **clone nomenclature** (Hille, 2001). The scheme incorporates the ion selectivity and the principal activator, as well as the degree of sequence similarity (Box 5.1). Because of its functional relevance, the IUPHAR scheme is in common use among biophysicists and increasingly by electrophysiologists. The gene nomenclature does not reflect as much of the function and structure as the IUPHAR scheme, particularly in the case of potassium channels (Gutman *et al.*, 2005). Nevertheless, even the IUPHAR scheme has quirks, such as including in the calcium-activated potassium family, $\text{K}_{\text{Ca}}5.1$, a type of potassium channel whose gating is dependent on intracellular Na^+ and Cl^- but not Ca^{2+} .

A number of gene families of ion channels, excluding channels activated by extracellular ligands such as synaptic channels, are shown in Table 5.1. Apart from the chloride channels, all the families belong to the superfamily of voltage-gated-like channels, which has at least 143 members (Yu *et al.*, 2005). The superfamily is called voltage-gated-*like* because while most of

Table 5.1 Families of channel genes and their corresponding proteins

Human gene prefix	IUPHAR protein prefix	Ion selectivity	Activators
SCN	Na _v	Na ⁺	V↑
CACN	Ca _v	Ca ²⁺	V↑
KCN	K _v	K ⁺	V↑
KCNA	K _v 1	K ⁺	V↑
KCNB	K _v 2	K ⁺	V↑
KCNC	K _v 3	K ⁺	V↑
KCND	K _v 4	K ⁺	V↑
KCNQ	K _v 7	K ⁺	V↑
KCNMA	K _{Ca} 1	K ⁺	Ca ²⁺ , V↑
KCNN	K _{Ca} 2	K ⁺	Ca ²⁺ ↑
KCNJ	K _{ir}	K ⁺	G-proteins, V↑
KCNK	K _{2P}	K ⁺	Leak, various modulators
HCN	HCN	K ⁺ , Na ⁺	V↓
CNG	CNG	Ca ²⁺ , K ⁺ , Na ⁺	cAMP, cGMP
TRP	TRP	Ca ²⁺ , Na ⁺	Heat, second messengers
CLCN	–	Cl [–]	V↓, pH
CLCA	–	Cl [–]	Ca ²⁺

Data from IUPHAR *Compendium of Voltage-Gated Ion Channels* (Catterall *et al.*, 2005a, b; Gutman *et al.*, 2005; Wei *et al.*, 2005; Kubo *et al.*, 2005; Goldstein *et al.*, 2005; Hofmann *et al.*, 2005; Clapham *et al.*, 2005; Jentsch *et al.*, 2005).

its channels are voltage-gated, some are gated by intracellular ligands, second messengers or stimuli such as heat. For example, CNG channels, activated by the cyclic nucleotides cAMP (cyclic adenosine monophosphate) and cGMP (cyclic guanosine monophosphate), are expressed in rod and cone photoreceptor neurons and the cilia of olfactory neurons (Hofmann *et al.*, 2005). Similarly, members of the TRP family are involved in heat or chemical sensing.

Heterologous expression of the cloned DNA of a channel (Section 5.3.3) allows the physiological characteristics of channel proteins to be determined. The currents recorded under voltage clamp conditions can be matched to the existing gamut of currents which have been measured using other techniques such as channel blocking, and given ad hoc names such as the A-type current I_A or the T-type current I_{CaT} . This **ad hoc nomenclature** for channels is sometimes still used when the combination of genes expressed in a preparation is not known. However, as use of the IUPHAR system by neurophysiologists and modellers becomes more prevalent (see, for example, Maurice *et al.*, 2004), terms such as ‘Ca_v3.1-like’ (instead of I_{CaT}) are also now used when the presence of a particular channel protein is not known. The currents that are associated with some well-known voltage- and ligand-gated channel proteins are shown in Table 5.2.

The presence of the gene which encodes a particular channel protein, as opposed to current, can be determined using knockout studies (Stocker,

Table 5.2 Summary of important currents, their corresponding channel types and sample parameters.

Current	Channel proteins	Other names	Activation			Inactivation			Note
			$V_{1/2}$ (mV)	σ (mV)	τ (ms)	$V_{1/2}$ (mV)	σ (mV)	τ (ms)	
I_{Na}	Na _v 1.1–1.3,1.6		-30	6	0.2	-67	-7	5	a
I_{NaP}	Na _v 1.1–1.3,1.6		-52	5	0.2	-49	-10	1500	b
I_{CaL}	Ca _v 1.1–1.4	HVA _L	9	6	0.5	4	2	400	c
I_{CaN}	Ca _v 2.2	HVA _m	-15	9	0.5	-13	-19	100	d
I_{CaR}	Ca _v 2.3	HVA _m	3	8	0.5	-39	-9	20	e
I_{CaT}	Ca _v 3.1–3.3	LVA	-32	7	0.5	-70	-7	10	f
I_{PO}	K _v 3.1	Fast rectifier	-5	9	10	—	—	—	g
I_{DR}	K _v 2.2, K _v 3.2...	Delayed rectifier	-5	14	2	-68	-27	90	h
I_A	K _v 1.4,3.4,4.1,4.2...		-1	15	0.2	-56	-8	5	i
I_M	K _v 7.1–7.5	Muscarinic	-45	4	8	—	—	—	j
I_D	K _v 1.1–1.2		-63	9	1	-87	-8	500	k
I_h	HCN1–4	Hyperpolarisation-activated	-75	-6	1000	—	—	—	l
I_C	K _{Ca} 1.1	BK, maxi-K(Ca), fAHP	V & Ca ²⁺ -dep	—	—	—	—	—	m
I_{AHP}	K _{Ca} 2.1–2.3	SK1–3, mAHP	0.7 μM	40	—	—	—	—	n
I_{sAHP}	K _{Ca} ?	Slow AHP	0.08 μM	200	—	—	—	—	o

Parameters are for voltage-dependent activation and inactivation in one model of a channel; other models have significantly different parameters. $K_{0.5}$ (Section 5.6) is given for calcium dependent K⁺ channels. Time constants are adjusted to 37 °C using Q_{10} .

Notes:

- ^a Rat hippocampal CA1 pyramidal cells (Magee and Johnston, 1995; Hoffman *et al.*, 1997).
- ^b Rat entorhinal cortex layer II cells (Magistretti and Alonso, 1999). The same subtypes can underlie both I_{Na} and I_{NaP} due to modulation by G-proteins; auxiliary subunits can slow down the inactivation of some Na_v subtypes (Köhling, 2002).
- ^c Activation kinetics from rat CA1 cells *in vitro* (Jaffe *et al.*, 1994; Magee and Johnston, 1995). Inactivation kinetics from cultured chick dorsal root ganglion neurons (Fox *et al.*, 1987). Calcium-dependent inactivation can also be modelled (Gillies and Willshaw, 2006).
- ^d Rat neocortical pyramidal neurons (Brown *et al.*, 1993).
- ^e CA1 cells in rat hippocampus (Jaffe *et al.*, 1994; Magee and Johnston, 1995).
- ^f CA1 cells in rat hippocampus (Jaffe *et al.*, 1994; Magee and Johnston, 1995).
- ^g Gillies and Willshaw (2006), based on rat subthalamic nucleus (Wigmore and Lacey, 2000).
- ^h Guinea pig hippocampal CA1 cells (Sah *et al.*, 1988).
- ⁱ Rat hippocampal CA1 pyramidal cells; underlying channel protein probably K_v4.2 (Hoffman *et al.*, 1997). Expression of different auxiliary subunits can convert DR currents into A-type currents (Heinemann *et al.*, 1996).
- ^j Guinea pig hippocampal CA1 pyramidal cells (Halliwell and Adams, 1982); modelled by Borg-Graham (1989). See Jentsch (2000) for identification of channel proteins.
- ^k Rat hippocampal CA1 pyramidal neurons (Storm, 1988); modelled by Borg-Graham (1999). See Metz *et al.* (2007) for identification of channel proteins.
- ^l Guinea pig thalamic relay cells *in vitro*; $E_h = -43$ mV (Huguenard and McCormick, 1992).
- ^m Rat muscle (Moczydlowski and Latorre, 1983) and guinea pig hippocampal CA3 cells (Brown and Griffith, 1983). Inactivation sometimes modelled (Borg-Graham, 1999; Section 5.6).
- ⁿ Rat K_{Ca}2.2 expressed in *Xenopus* oocytes (Hirschberg *et al.*, 1998). Model in Section 5.6.
- ^o Borg-Graham (1999) based on various data. Channel proteins underlying I_{sAHP} are unknown (Section 5.6).

2004). In many instances, one channel gene can give rise to many different channel proteins, due to alternate splicing of RNA and RNA editing (Hille, 2001). Also, these channel types refer only to the sequences of the principal subunits; as covered in Section 5.1, the coexpression of auxiliary subunits modifies the behaviour of the principal subunits, sometimes dramatically. There is even more channel diversity than the plethora of gene sequences suggests.

5.3 | Experimental techniques

5.3.1 Single channel recordings

A major advance in our understanding of channels came with the development of the **patch clamp technique** (Neher and Sakmann, 1976), where a fine glass pipette is pressed against the side of a cell (Figure 5.5). The rim of the pipette forms a high-resistance seal around a small patch of the membrane, so that most of the current flowing through the patch of membrane has to flow through the pipette. Seals with resistances of the order of giga-ohms can be made, and have been dubbed **gigaseals** (Hamill *et al.*, 1981). This allows for much less noisy recordings and makes it possible to record from very small patches of membrane.

In the low-noise recordings from some patches, the current can be observed to switch back and forth between zero and up to a few picoamperes (Figure 5.6). This is interpreted as being caused by the opening and closing of a single channel. The times of opening and closing are apparently random, though order can be seen in the statistics extracted from the recordings. For example, repeating the same voltage clamp experiment a number of times leads to an **ensemble** of recordings, which can be aligned in time, and then averaged (Figure 5.6). This average reflects the probability of a channel being open at any time. The **macroscopic** currents (for example, those recorded by Hodgkin and Huxley), appear smooth as they are an ensemble average over a large population of **microscopic** currents due to stochastic channel events.

Neher and Sakmann received a Nobel prize for their work in 1991. The methods of forming high-resistance seals between the glass pipette and the membrane proved fundamental to resolving single channel currents from background noise.

5.3.2 Channel isolation by blockers

Hodgkin and Huxley (1952d) succeeded in isolating three currents with distinct kinetics (the sodium, potassium delayed rectifier and leak currents). Since then, many more currents with distinct kinetics have been isolated. The process was expedited by the discovery of **channel blockers**, pharmacological compounds which prevent certain types of current flowing. First to be discovered was tetrodotoxin (TTX), which is isolated from the Japanese puffer fish and blocks Na^+ channels involved in generating action potentials (Narahashi *et al.*, 1964). Likewise tetraethylammonium (TEA) was found to block some types of K^+ channel (Hagiwara and Saito, 1959). Subsequently, many more compounds affecting ion channel behaviour have been discovered (Hille, 2001). Appendix A provides links to the comprehensive lists of blockers for various channel subtypes that can be found online in the *IUPHAR Compendium of Voltage-gated Ion Channels* (Catterall and Gutman, 2005) and the *Guide to Receptors and Channels* (Alexander *et al.*, 2008).

The puffer fish is a delicacy in Japan. Sushi chefs are specially trained to prepare the fish so as to remove the organs which contain most of the toxin.

Fig. 5.6 Single channel recordings of two types of voltage-gated calcium channel in guinea pig ventricular cells (Nilius *et al.*, 1985), with 110 mM Ba²⁺ in the pipette. (a) The single channel currents seen on seven occasions in response to a voltage step to a test potential of 10 mV (top). The bottom trace shows the average of 294 such responses. It resembles the Hodgkin–Huxley sodium current. This channel, named L-type for its long-lasting current by Nilius *et al.* (1985), belongs to the Ca_v1 family of mammalian calcium channels. (b) Single channel and ensemble responses to a voltage step to the lower potential of –20 mV. The ensemble-averaged current inactivates more quickly. This channel, named T-type because of its transient nature by Nilius *et al.* (1985), belongs to the Ca_v3 family of mammalian channels. Reprinted by permission from Macmillan Publishers Ltd: *Nature* 316, 443–446, © 1985.

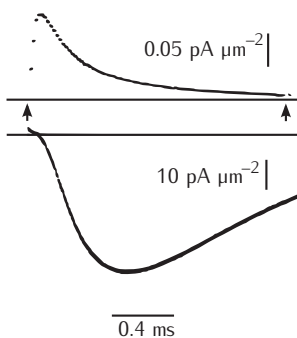
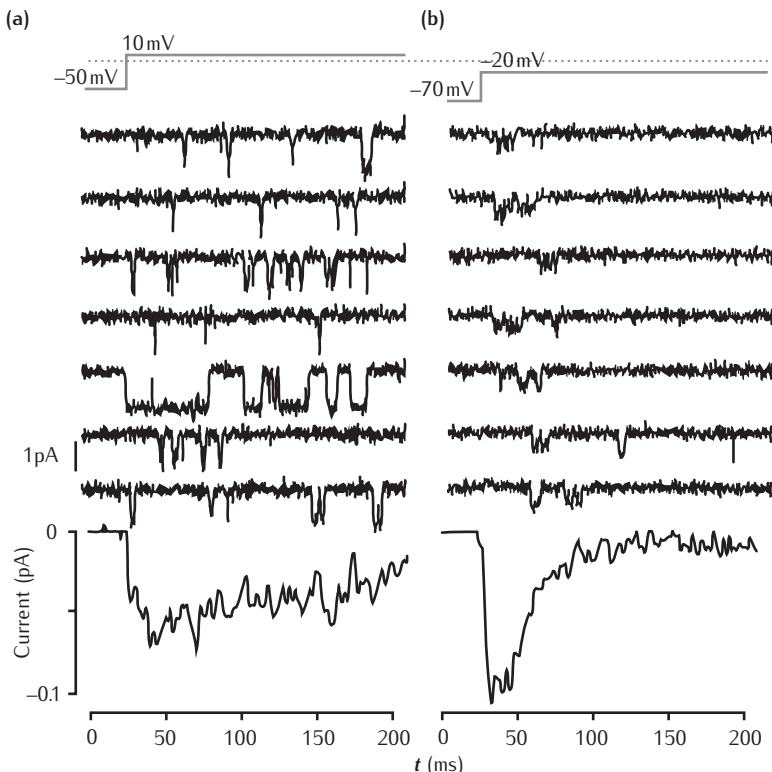


Fig. 5.7 Gating current (above) and ionic current (below) in squid giant axon sodium channels, measured by Armstrong and Bezanilla (1973). Reprinted by permission from Macmillan Publishers Ltd: *Nature* 242, 459–461, © 1973.

5.3.3 Channel isolation by mRNA transfection

Since the 1980s the molecular biological method of **heterologous expression** has been used to isolate channels. Heterologous expression occurs when the cloned DNA (cDNA) or messenger RNA (mRNA) of a protein is expressed in a cell which does not normally express that protein (Hille, 2001). Sumikawa *et al.* (1981) were the first to apply the method to ion channels, by transfecting oocytes of the amphibian *Xenopus laevis* with the mRNA of acetylcholine receptors and demonstrating the presence of acetylcholine channels in the oocyte by the binding of bungarotoxin. Subsequent voltage clamp experiments demonstrated the expression of functional acetylcholine channel proteins in the membrane (Mishina *et al.*, 1984). This approach has been extended to mammalian cell lines such as CHO (Chinese hamster ovary), HEK (human embryonic kidney) and COS (monkey kidney) (Hille, 2001). Thus channel properties can be explored in isolation from the original cell.

While heterologous expression gives a clean preparation, there are also potential pitfalls, as the function of ion channels can be modulated significantly by a host of factors that might not be present in the cell line, such as intracellular ligands or auxiliary subunits (Hille, 2001).

5.3.4 Gating current

The movement of the gating charges as the channel protein changes conformation leads to an electric current called the **gating current**, often referred

to as I_g (Hille, 2001). Gating currents tend to be much smaller than the ionic currents flowing through the membrane. In order to measure gating current, the ionic current is reduced, either by replacing permeant ions with impermeant ones or by using channel blockers, though the channel blocker itself may interfere with the gating mechanism. Other methods have to be employed to eliminate leak and capacitive currents. Figure 5.7 shows recordings by Armstrong and Bezanilla (1973) of the gating current and the sodium ionic current in response to a voltage step. The gating current is outward since the positively charged residues on the membrane protein are moving outwards. It also peaks before the ionic current peaks.

Gating currents are a useful tool for the development of kinetic models of channel activation. The measurement of gating current confirmed the idea of charged gating particles predicted by the HH model. However, gating current measurements in squid giant axon have shown that the HH model is not correct at the finer level of detail (Section 5.5.3).

5.4 Modelling ensembles of voltage-gated ion channels

5.4.1 Gating particle models

Before the detailed structure and function of ion channels outlined in Section 5.1 was known, electrophysiological experiments indicated the existence of different types of channel. Various blocking and subtraction protocols led to the isolation of specific currents which displayed particular characteristics.

The A-type current

To take one example, the potassium A-type current, often denoted I_A , has distinct kinetics from the potassium delayed rectifier current, denoted I_{DR} or I_K or $I_{K,DR}$, originally discovered by Hodgkin and Huxley. Connor and Stevens (1971a, c) isolated the current by using ion substitution and by the differences in current flow during different voltage clamp protocols in the somata of cells of marine gastropods. The A-type current has also been characterised in mammalian hippocampal CA1 and CA3 pyramidal cells using TTX to block sodium channels (Figure 5.8).

In contrast to the delayed rectifier current, the A-type current is inactivating, and has a lower activation threshold. It has been modelled using independent gating particles by a number of authors (Connor and Stevens, 1971b; Connor *et al.*, 1977; Hoffman *et al.*, 1997; Poirazi *et al.*, 2003). In the model of Connor *et al.* (1977), the A-type current in the crustacean *Cancer magister* (Box 5.2) depends on three independent activating gating particles and one inactivating particle. In contrast, Connor and Stevens (1971b) found that raising the activating gating variable to the fourth power rather than the third power gave the best fit to the A-type current they recorded from the somata of marine gastropods.

The significance of the A-type current is illustrated clearly in simulations of two neurons, one containing sodium and potassium conductances

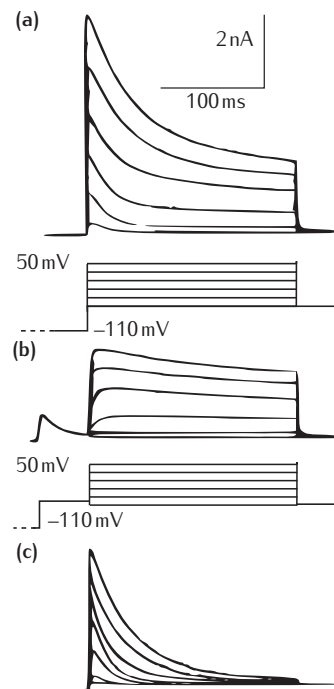
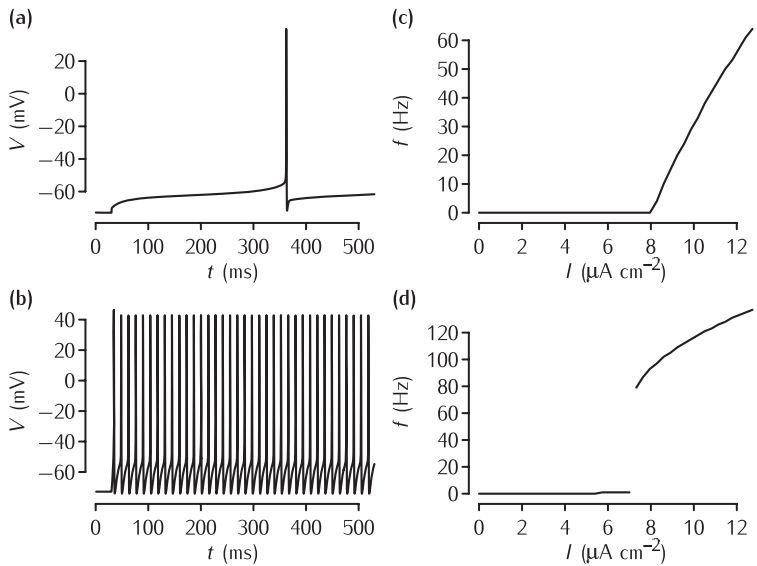


Fig. 5.8 Recordings of two types of potassium channel revealed by different voltage clamp protocols in hippocampal CA1 cells. (a) Family of voltage clamp current recordings from CA1 cells subjected to the voltage step protocol shown underneath. (b) The voltage was clamped as in (a), except that there was a delay of 50 ms before the step to the depolarising voltage. (c) Subtraction of trace in (b) from trace in (a) reveals a transient outward current known as the A-type current. Adapted from Klee *et al.* (1995), with permission from The American Physiological Society.

Fig. 5.9 The effect of the A-type current on neuronal firing in simulations. (a) The time course of the membrane potential in the model described in Box 5.2 in response to current injection of $8.21 \mu\text{A cm}^{-2}$ that is just suprathreshold. The delay from the start of the current injection to the neuron firing is over 300 ms. (b) The response of the model to a just suprathreshold input ($7.83 \mu\text{A cm}^{-2}$) when the A-type current is removed. The spiking rate is much faster. In order to maintain a resting potential similar to the neuron with the A-type current, the leak equilibrium potential E_L is set to -72.8 mV in this simulation. (c) A plot of firing rate f versus input current I in the model with the A-type conductance shown in (a). Note the gradual increase of the firing rate just above the threshold, the defining characteristic of Type I neurons. (d) The f - I plot of the neuron with no A-type conductance shown in (b). Note the abrupt increase in firing rate, the defining characteristic of Type II neurons.



modelled using the Hodgkin–Huxley equations, and the other containing an A-type conductance in addition to the sodium and potassium conductances (Figure 5.9a, b). In response to sustained current injection, the model containing the A-type conductance gives rise to action potentials that are delayed compared to the action potentials in the pure HH model. This is because the A-type potassium channel is open as the membrane potential increases towards the spiking threshold, slowing the rise of the membrane potential. However, eventually the A-type current inactivates, reducing the pull on the membrane potential towards the potassium equilibrium potential and allowing the cell to fire.

Another important difference caused by the insertion of the A-type channels is apparent from plots of firing frequency versus sustained current injection (Figure 5.9c, d). Both types of model exhibit a threshold level of current below which the neuron is quiescent. In the model with the A-type conductance, the firing frequency just above the threshold is very close to zero and increases gradually. By contrast, in the HH model, as soon as the threshold is crossed, the model starts firing at a non-zero frequency. Hodgkin (1948) had noticed the two different types of f - I curve in axons from the crustacean *Carcinus maenas*. According to his classification, neurons which produce the continuous curve (Figure 5.9c) are **Type I** neurons and those which produce the curve with the abrupt change at threshold (Figure 5.9d) are **Type II** neurons. In Chapter 8 reduced models of neurons will be introduced to gain understanding of the features of the models that give rise to Type I and Type II firing patterns.

5.4.2 Thermodynamic models

In Box 5.2 there are effectively five different forms of function to fit the dependence on voltage of the rate coefficients $\alpha_m(V)$, $\beta_m(V)$ and so on: three for the Hodgkin–Huxley sodium and potassium channels (Figure 5.10), and two for the A-type potassium channel. All these forms satisfy the critical requirement of fitting the data well. However, it is desirable to base the form

Box 5.2 Model of potassium A-type current

In their model of the conductances in axons from the crab *Cancer magister*, Connor *et al.* (1977) added an A-type potassium conductance g_A with an associated equilibrium potential E_A to a current equation which includes modified versions of the Hodgkin–Huxley sodium and potassium delayed rectifier conductances:

$$C_m \frac{dV}{dt} = -g_{Na}(V - E_{Na}) - g_K(V - E_K) - g_A(V - E_A) - g_L(V - E_L).$$

The A-type conductance was derived from the experiments of Connor *et al.* (1977) at 18°C and was modelled using independent gating particles: three activating particles a and an inactivating particle b . The kinetic equations (Section 3.2.1) written in terms of the steady state activation curves $a_\infty(V)$ and $b_\infty(V)$ and the relaxation time constants $\tau_a(V)$ and $\tau_b(V)$ are:

$$\begin{aligned} I_A &= g_A(V - E_A), & g_A &= \bar{g}_A a^3 b, \\ a_\infty &= \left(\frac{0.0761 \exp\left(\frac{V+99.22}{31.84}\right)}{1 + \exp\left(\frac{V+6.17}{28.93}\right)} \right)^{\frac{1}{3}}, & \tau_a &= 0.3632 + \frac{1.158}{1 + \exp\left(\frac{V+60.96}{20.12}\right)}, \\ b_\infty &= \frac{1}{\left(1 + \exp\left(\frac{V+58.3}{14.54}\right)\right)^4}, & \tau_b &= 1.24 + \frac{2.678}{1 + \exp\left(\frac{V-55}{16.027}\right)}. \end{aligned}$$

The Hodgkin–Huxley sodium and potassium delayed rectifier conductances are modified by shifting the steady state equilibrium curves of m , h and n , multiplying the rate coefficients by a Q_{10} -derived factor of 3.8 to adjust the temperature from 6.3°C to 18°C, and slowing down the n variable by a factor of 2:

$$\begin{aligned} g_{Na} &= \bar{g}_{Na} m^3 h, & g_K &= \bar{g}_K n^4, \\ \alpha_m &= 3.8 \frac{-0.1(V + 34.7)}{\exp(-(V + 34.7)/10) - 1}, & \beta_m &= 3.8 \times 4 \exp(-(V + 59.7)/18), \\ \alpha_h &= 3.8 \times 0.07 \exp(-(V + 53)/20), & \beta_h &= 3.8 \frac{1}{\exp(-(V + 23)/10) + 1}, \\ \alpha_n &= \frac{3.8}{2} \frac{-0.01(V + 50.7)}{\exp(-(V + 50.7)/10) - 1}, & \beta_n &= \frac{3.8}{2} 0.125 \exp(-(V + 60.7)/80). \end{aligned}$$

The remaining parameters of the model are:

$$\begin{array}{lll} C_m = 1 \mu\text{F cm}^{-2} & E_{Na} = 50 \text{ mV} & \bar{g}_{Na} = 120.0 \text{ mS cm}^{-2} \\ E_K = -77 \text{ mV} & \bar{g}_K = 20.0 \text{ mS cm}^{-2} & \\ E_A = -80 \text{ mV} & \bar{g}_A = 47.7 \text{ mS cm}^{-2} & \\ E_L = -22 \text{ mV} & g_L = 0.3 \text{ mS cm}^{-2} & \end{array}$$

In all the equations described here, the voltage is 5 mV lower than the values of Connor *et al.* (1977), to match the parameters used in Chapter 3.

This approach of adapting a model from a different organism contrasts with that taken in the earlier model of *Anisodoris* (Connor and Stevens, 1971b), where many of the values for the steady state variables are piecewise linear fits to recorded data. The two models give similar results.

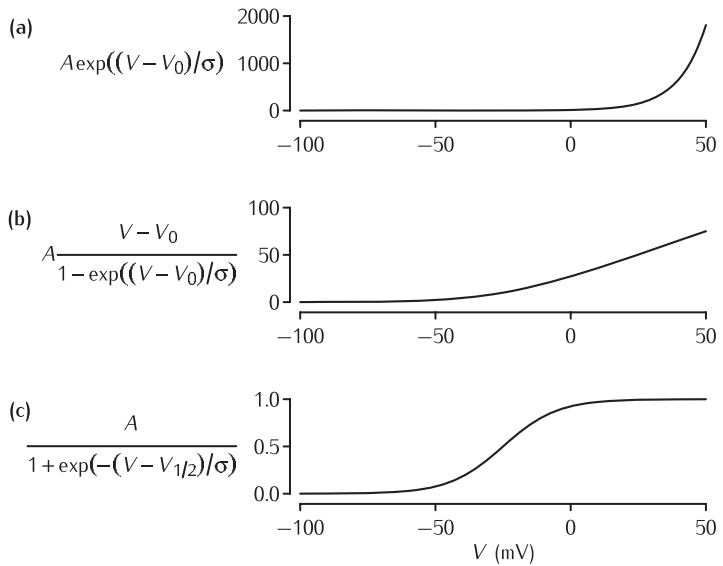
Fig. 5.10 In the HH model (Box 3.5), the voltage-dependent rate coefficients are described by three different types of equation.

(a) The rate coefficients β_m , α_h and β_n are described by exponential functions of the voltage V . A , V_0 and σ are constants. This fits the empirical rate coefficients α_m and α_n at low membrane potentials, but overestimates the rates at higher membrane potentials.

(b) Linear-exponential functions produce lower rate coefficients at higher voltages and fit the data well. However, it gives rate coefficients that are too high for the gating variable h at high voltages, where β_h saturates.

(c) β_h can be described by a rate coefficient with a sigmoidal function where $V_{1/2}$ is the half-activation voltage and where σ is the inverse slope.

The sigmoid curve is similar to Hodgkin and Huxley's fit to n_∞ (Figure 3.10) using the functions for α_n and β_n from Equation 3.13.



of these functions as much as possible on the biophysical theory of channels, since fitting to the most principled function is likely to minimise errors due to fitting.

In thermodynamic models (Borg-Graham, 1989; Destexhe and Huguenard, 2000), the rate coefficients are given by functions derived from the **transition state theory** (or energy barrier model) of chemical reactions, to be discussed in Section 5.8. For a gating particle represented by a gating variable x , the steady state activation is given by a sigmoid curve:

$$x_\infty = \frac{1}{1 + \exp(-(V - V_{1/2})/\sigma)}, \quad (5.1)$$

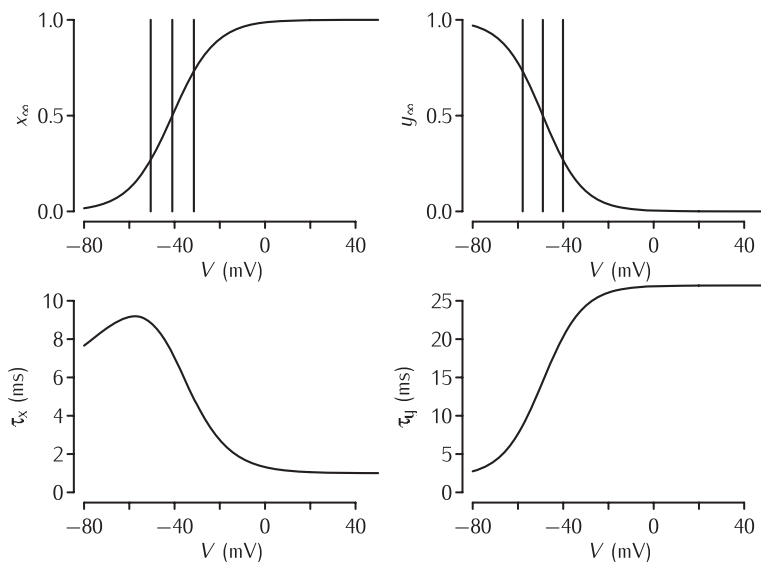
where $V_{1/2}$ is the half-activation voltage and σ is the inverse slope, as shown in Figure 5.11. The corresponding time constant is:

$$\tau_x = \frac{1}{\alpha'_x(V) + \beta'_x(V)} + \tau_0, \quad (5.2)$$

where τ_0 is a rate-limiting factor and the expressions for α'_x and β'_x are exponentials that depend on $V_{1/2}$ and σ , a maximum rate parameter K and a parameter δ , which controls the skew of the τ curve:

$$\begin{aligned} \alpha'_x(V) &= K \exp\left(\frac{\delta(V - V_{1/2})}{\sigma}\right) \\ \beta'_x(V) &= K \exp\left(\frac{-(1 - \delta)(V - V_{1/2})}{\sigma}\right). \end{aligned} \quad (5.3)$$

Figure 5.11 shows plots of the time constant as a function of voltage.



The term τ_0 is in fact an addition to the basic transition state theory account. However, if it is set to zero, the effective time constant $\tau_x = \alpha_x/(\alpha_x + \beta_x)$ can go to zero. In practice, transitions tend not to happen this quickly (Patlak, 1991), and it is evident from the equations for τ_x that the rate-limiting factor τ_0 leads to a minimum time constant.

The steady state value x_∞ and time constant τ_x can be converted into equations for the rate coefficients α_x and β_x (Equation 3.10), giving:

$$\begin{aligned}\alpha_x(V) &= \frac{\alpha'_x(V)}{\tau_0(\alpha'_x(V) + \beta'_x(V)) + 1} \\ \beta_x(V) &= \frac{\beta'_x(V)}{\tau_0(\alpha'_x(V) + \beta'_x(V)) + 1}.\end{aligned}\quad (5.4)$$

Fig. 5.11 Plots of the steady states x_∞ and y_∞ of the activation and inactivation and of the corresponding time constants τ_x and τ_y of a thermodynamic model of the A-type current due to Borg-Graham (1999). The curves for the steady states and time constants are derived from Equations 5.1 and 5.2, respectively. In the steady state curves, the middle vertical line indicates the half-activation voltage, $V_{1/2}$, and the two flanking lines indicate $V_{1/2} - \sigma$ and $V_{1/2} + \sigma$. The parameters for the activation (x) curves are $V_{1/2} = -41$ mV, $\sigma = 9.54$ mV, $K = 8 \times 10^2$ ms $^{-1}$, $\delta = 0.85$, $\tau_0 = 1$ ms. The parameters for the inactivation (y) curves are $V_{1/2} = -49$ mV, $\sigma = -8.90$ mV, $K = 4 \times 10^2$ ms $^{-1}$, $\delta = 1$, $\tau_0 = 2$ ms. The sign of σ determines whether the curve has a positive or negative slope.

Calcium channels

Similar principles apply to modelling calcium channels, such as the T- and L-types, voltage clamp recordings of which are shown in Figure 5.6. The only difference is that because of the inward rectifying nature of the I - V relationship for calcium due to low intracellular concentration of calcium, the GHK current equation (Box 2.4) is often used in modelling calcium channels. For the non-inactivating L-type channel, the permeability can be modelled with two activating particles m , and the inactivating T-type channel can be modelled with two activating particles m and one inactivating particle h (Borg-Graham, 1999). In both cases $1/K$ is small compared to τ_0 , so the time constants τ_m and τ_h are effectively independent of voltage. Table 5.2 shows typical values of $V_{1/2}$, σ and τ_0 for these channels. There is evidence that the L-type channels require calcium to inactivate. This could be modelled using an extra calcium-dependent inactivation variable (Section 5.6).

Other types of voltage-gated channels

There are many more types of current, some of which are listed in Table 5.2. They can be characterised broadly according to whether they are activated by voltage or calcium or both, in the case of I_C , and whether they display fast or slow activation and inactivation.

The half activation voltage and the slope of these curves varies between currents. The values of these quantities listed in Table 5.2 are only indicative as there can be substantial variations between different preparations; for example, variations in temperature (Section 3.4), expression of auxiliary sub-units (Section 5.1), or which modulators are present inside and outside the cell. Table 5.2 also lists the principal channel proteins which are proposed to underlie each type of current. In some cases, the same protein appears to be responsible for different currents; for example, $\text{Na}_v 1.1$ appears to underlie I_{Na} and the persistent sodium current I_{NaP} . This may be possible because of the differences in auxiliary subunit expression.

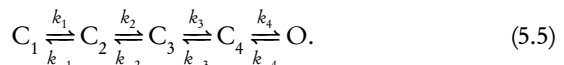
5.5 | Markov models of ion channels

In the channel models covered so far, the gating variables, such as n , m and h in the HH model, represent the probability of one of a number of gating particles being in an open position; the probability of the entire gate (or channel) being open is the product of these variables raised to a power, indicating that the gating particles act independently. This section introduces **Markov models** of ion channels in which the probability of the entire ion channel being in one of a number of possible states is represented, and one or more of these states may correspond to the ion channel being open. This allows data to be fitted more accurately, though at the expense of having a greater number of parameters to fit. Ideally, each state would correspond to one channel protein conformation, but in practice even complex Markov models are approximations of the actual dynamics of the channel.

Markov models are fundamentally probabilistic models in which the state changes are random. This makes them an appropriate framework in which to model the microscopic currents due to the opening and closing of single ion channels or ensembles of a small number of ion channels. However, when large numbers of channels are present, the recorded currents are smooth because the fluctuations of individual channels are averaged out, and it is approximately correct to interpret Markov models deterministically. In this section the deterministic interpretation of Markov models will be introduced. The techniques required for the stochastic interpretation of Markov models are introduced in Section 5.7.

5.5.1 Kinetic schemes

The states and possible transitions between them in a Markov model are represented by a **kinetic scheme**. An example of a kinetic scheme is:



The term ‘kinetic scheme’ is often used interchangeably with Markov model, especially when interpreting Markov models deterministically (Cannon and D’Alessandro, 2006).

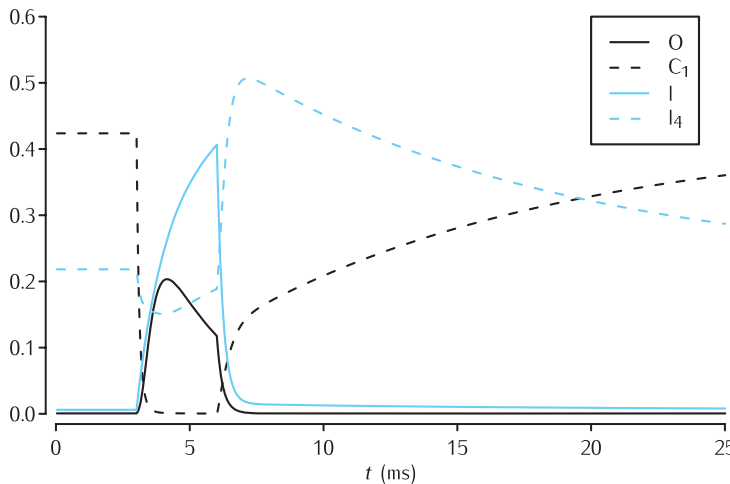


Fig. 5.12 Time evolution of a selection of the state variables in the Vandenberg and Bezanilla (1991) model of the sodium channel in response to a 3 ms long voltage pulse from -65 mV to -20 mV , and back to -65 mV . See Scheme 5.9 for the significance of the state variables shown. In the interests of clarity, only the evolution of the state variables I , O , I_4 and C_1 are shown.

The symbols C_1 , C_2 , C_3 and C_4 represent four different closed states of the channel, and there is one open state O . Each pair of reversible reaction arrows represents a possible transition between states of a single channel, with the rate coefficients k_1 , k_{-1} , k_2 , ..., which may depend on voltage or ligand concentration, specifying the speeds of the transitions. When the scheme is interpreted deterministically, the fractions of channels C_1 , C_2 , C_3 , C_4 and O in each state are the relevant variables. Their dynamics are described by the following set of coupled ODEs:

$$\begin{aligned}\frac{dC_1}{dt} &= k_{-1}C_2 - k_1C_1 \\ \frac{dC_2}{dt} &= k_1C_1 + k_{-2}C_3 - (k_{-1} + k_2)C_2 \\ \frac{dC_3}{dt} &= k_2C_2 + k_{-3}C_4 - (k_{-2} + k_3)C_3 \\ \frac{dC_4}{dt} &= k_3C_3 + k_{-4}O - (k_{-3} + k_4)C_4 \\ O &= 1 - (C_1 + C_2 + C_3 + C_4).\end{aligned}\quad (5.6)$$

We follow the convention of using upright type to denote a state (e.g. C_2) and italic type to denote the fraction of channels in that state (e.g. C_2).

An example of the time evolution of a selection of the gating variables in a complex scheme for a sodium channel (Vandenberg and Bezanilla, 1991; Section 5.5.3) is shown in Figure 5.12.

Any kinetic scheme can be interpreted deterministically and converted to a set of coupled ODEs (Stevens, 1978) by following the pattern exemplified above. The number of equations required is always one fewer than the number of states. This is because the fraction of channels in one state can be obtained by subtracting the fractions of all of the other channels from 1, as in the equation for O in Equation 5.6.

Some channels exhibit multiple open states (Hille, 2001). This can be modelled by associating each state j of a channel with the conductance γ_j of a single channel in state j . If the **state variable** representing the fraction of

Scheme 5.5, with four closed states, can be made to be equivalent to an independent gating particle scheme with four gating particles by setting the rate coefficients as follows:

$$\begin{aligned} k_1 &= 4\alpha_n & k_{-1} &= \beta_n \\ k_2 &= 3\alpha_n & k_{-2} &= 2\beta_n \\ k_3 &= 2\alpha_n & k_{-3} &= 3\beta_n \\ k_4 &= \alpha_n & k_{-4} &= 4\beta_n. \end{aligned}$$

The coefficients α_n and β_n are forward and backward rate coefficients, such as the ones defined in Chapter 3 (Equation 3.14).

channels in a state j in a patch containing N single channels is denoted by x_j , then the expected number of channels in each state X_j is equal to Nx_j . The total conductance of the patch is then:

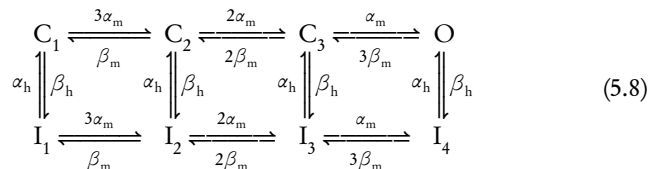
$$g(t) = \sum_{j=1}^N \gamma_j X_j(t). \quad (5.7)$$

In the deterministic, macroscopic interpretation of the kinetic scheme, the variables X_j are continuous. This equation can also be used for stochastic, microscopic simulations, where the number of channels X_j is a discrete variable that represents the actual (not expected) number of channels in each state.

5.5.2 Independent gating models as kinetic schemes

By linking the rate coefficients appropriately, Scheme 5.5 can be made to be equivalent to an independent gating particle model with four gating particles, such as the HH model for the potassium delayed rectifier. With this set of linked parameters, C_1 is the state in which all four gating particles are in their closed positions. A transition to C_2 , where exactly one of the four gating particles is in the open position, occurs when *any* one of the four particles moves to the open position. There are thus four routes out of C_1 , so the forward rate coefficient is four times the rate coefficient of the reaction of a single gating particle, i.e. $4\alpha_n$. A transition back from state C_2 to state C_1 requires that the one gating particle in the open position moves to its closed position, governed by the rate coefficient β_n ; a transition to C_3 , where two of the four gating particles are open, occurs when any one of the three closed gating particles are open. The forward rate coefficient from C_2 to C_3 is therefore $3\alpha_n$. In state C_4 only one of the gating particles is closed. Its transition to the open position, with rate coefficient α_n , leads to the open state O.

The Hodgkin–Huxley sodium channel can be represented by an eight-state diagram:



where I_1 – I_4 are inactivated states. In all the inactivation states, the inactivating particle is in the closed position, and there are 0, 1, 2 or 3 activation particles in the open position.

There might appear to be little to be gained by writing independent gating particle models as full kinetic schemes since both the number of state variables and the number of equations to be solved increase. However, the independent gating model can serve as a starting point for unrestricted

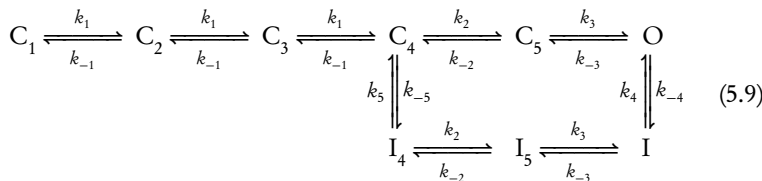
kinetic schemes. To model the data accurately, changes can be made to some of the rate coefficients.

5.5.3 Unrestricted kinetic schemes

By not restricting the parameters of kinetic schemes to correspond to those in independent gating particle models, a better fit to data can be obtained. For example, studies of the squid giant axon sodium channel subsequent to Hodgkin and Huxley revealed significant inaccuracies in their model (Patlak, 1991):

- (1) The measured deactivation time constant is slower than in the HH model. In the model, the time constant of the tail current following a voltage step is $\tau_m/3$ (Chapter 3), but experiments show that the time constant should be τ_m .
- (2) The gating current is not as predicted by the HH model. The model predicts the gating current is proportional to the rate of movement of gating particles dm/dt . Thus, at the start of a voltage clamp step, the gating current should rise instantaneously, and then decay with an exponential time course. However, the measured time course of gating current displays a continuous rising time course (Figure 5.7).
- (3) When inactivation is removed by the enzyme pronase in the cytoplasm, the mean open dwell times recorded from single channels (Section 5.7) are six times longer than would be expected from the value predicted from the Hodgkin–Huxley value of $1/\beta_m$ (Bezanilla and Armstrong, 1977).
- (4) There is a delay before inactivation sets in, which suggests that inactivation of the channel depends on activation.

In order to account for these discrepancies, Markov kinetic schemes which are not equivalent to independent gating particles have been devised. In contrast to the Hodgkin–Huxley scheme for the sodium channel (Scheme 5.8), the inactivated state or states can only be reached from the open state or one of the closed states. For example, in the scheme of Vandenberg and Bezanilla (1991), based on gating current, single channel recordings and macroscopic ionic recordings, there are five closed states, three inactivated states and one open state:



The deactivation kinetics of the HH model and the Vandenberg and Bezanilla (1991) model are shown in Figure 5.13. The membrane is clamped to a depolarising voltage long enough to activate sodium channels, but not long enough to inactivate them much. Then the membrane is clamped back down to a testing potential. The tail currents that result illustrate the slower

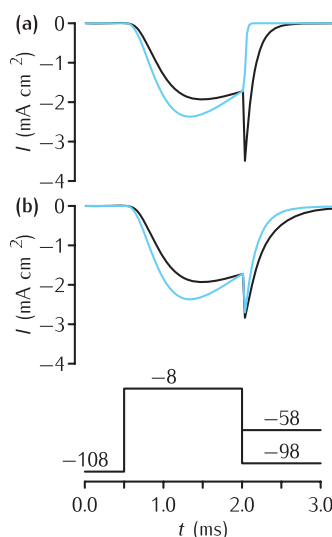


Fig. 5.13 Tail currents in the Vandenberg and Bezanilla (1991) model (VB, black traces) and the Hodgkin and Huxley (1952d) model (HH, blue traces) of the sodium current in squid giant axon in response to the voltage clamp protocol shown at the base, where the final testing potential could be (a) -98 mV or (b) -58 mV . During the testing potential, the tail currents show a noticeably slower rate of decay in the VB model than in the HH model. To assist comparison, the conductance in the VB model was scaled so as to make the current just before the tail current the same as in the HH model. Also, a quasi-ohmic I – V characteristic with the same E_{Na} as the HH model was used rather than the GHK I – V characteristic used in the VB model. This does not affect the time constants of the currents, since the voltage during each step is constant.

deactivation kinetics of the Vandenberg and Bezanilla (1991) model, in line with the experimental observations.

5.5.4 Independent gating particles versus unrestricted kinetic schemes

Although we refer to unrestricted schemes here, thermodynamics does impose some restrictions on the rate coefficients (Box 5.8).

Biophysicists have characterised the voltage-dependent behaviour of a number of ion channels precisely using Markov kinetic schemes (for example, Vandenberg and Bezanilla, 1991; Rodriguez *et al.*, 1998; Irvine *et al.*, 1999). Despite this, the approach formulated over fifty years ago by Hodgkin and Huxley of modelling channel kinetics with independent gating particles is still widespread in the computational neuroscience community and even some biophysicists (Patlak, 1991) regard them as the gold standard of channel kinetics. This is because independent gating particle models require less data to fit than kinetic schemes due to their relatively small number of parameters. Furthermore, independent gating particle models are sufficient to explain a large number of electrophysiological data, such as the origin of the action potential and spike adaptation due to A-type potassium channels.

Nevertheless, Markov kinetic schemes can describe the data more accurately than independent gating models, and could be especially important in understanding particular phenomena, such as repetitive firing (Bean, 2007). If a Markov kinetic scheme has been derived for the channel in question under comparable experimental conditions, most probably it will be a better choice than using the Hodgkin–Huxley formalism or a thermodynamic model. This applies especially in simulations where the time course needs to have sub-millisecond precision. However, care must be taken that the experimental conditions under which the channel recording was performed are a sufficiently close match to the cell being modelled. Much work on characterisation of ion channels is carried out using heterologous expression in transfected cell lines (Section 5.3.3), in which the biochemical environment is likely to be different from the cell under study. This may have a strong effect on some channel parameters; for example, half activation voltages $V_{1/2}$. Ideally, characteristics of the channel such as the activation and inactivation curves should be measured in the cell to be modelled. Examples of studies where experiment and modelling using kinetic schemes have been combined include Maurice *et al.* (2004) and Magistretti *et al.* (2006).

Another approach is to have two versions of the model, one with an independent gating model and one with a kinetic scheme model of the same channel. Comparing the behaviour of both models will give an indication of the functional importance of the ion channel description.

If a Markov kinetic scheme model is not available, is it worth doing the extra experiments needed to create it compared with doing the experiments required to constrain the parameters of independent gating particle models and thermodynamic models? There is no straightforward answer to this question, but before expending effort to make one part of a neuronal model very accurate, the accuracy (or inaccuracy) of the entire model should be considered. For example, it may be more important to put effort into determining the distribution of channel conductances over an entire cell rather than getting the kinetics of one channel as accurate as possible.

Neuroinformatics techniques that combine experiments with online data analysis are currently in development, and offer the hope of speeding up the time-consuming work of constructing full kinetic schemes (Section 5.7.4).

5.6 Modelling ligand-gated channels

In contrast to voltage-gated channels, some channels are activated by intracellular or extracellular ligands. Examples of extracellular ligands are the neurotransmitters acetylcholine, glutamate and glycine. Channels which have receptors on the extracellular membrane surface for these ligands perform the postsynaptic function of fast chemical synapses, which are discussed in Chapter 7. Among the intracellular ligands are second messengers such as cyclic nucleotides and calcium ions. The focus in this section will be on calcium-dependent potassium channels, but similar techniques can be applied to other intracellular ligands – for example, modulation of I_h by cyclic AMP (Wang *et al.*, 2002).

Calcium-activated potassium channels are responsible for the afterhyperpolarisation that can occur after a burst of spikes since calcium channels activated during the burst allow calcium into the cell, which in turn activates the K_{Ca} channels (Stocker, 2004). There are three main Ca^{2+} -dependent potassium currents (for review, see Sah and Faber, 2002):

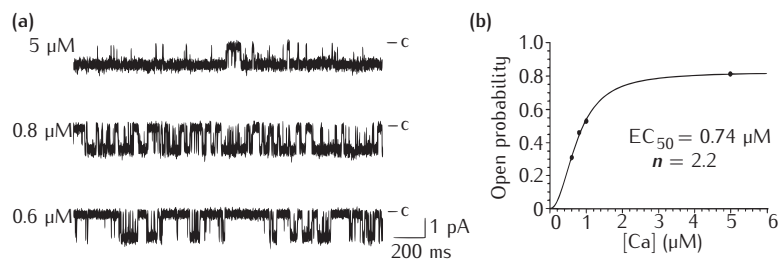
- (1) I_C , also known as $I_{K(C)}$. This current depends on voltage and calcium concentration, and is due to $K_{Ca}1.1$ channel proteins. It is responsible for the fast afterhyperpolarisation (fAHP).
- (2) I_{AHP} , also known as $I_{K(AHP)}$. This current depends only on calcium concentration and is due to channels in the $K_{Ca}2$ subfamily. It is responsible for the medium afterhyperpolarisation (mAHP).
- (3) I_{sAHP} , also known as I_{K-slow} and, confusingly, I_{AHP} . This also only depends on calcium concentration. It is currently not known what underlies this current (Stocker, 2004). Possibilities include an as-yet undiscovered member of the $K_{Ca}2$ family, colocalisation of $Ca_v1.3$ channels and $K_{Ca}2.1$ channels (Lima and Marrion, 2007) or modulation by auxiliary subunits (Sah and Faber, 2002). I_{sAHP} is responsible for slow afterhyperpolarisations (sAHP), which lead to spike train adaptation.

A prerequisite for incorporating ligand-gated ion channels into a model neuron is knowledge of the concentration of the ligand in the submembrane region. Intracellular ion concentrations do not feature explicitly in the equivalent electrical circuit models of the membrane considered in previous chapters, but models which include the influx, efflux, accumulation and diffusion of ligands such as Ca^{2+} will be described in detail in Chapter 6. For now, it is assumed that the time course of the Ca^{2+} concentration in the vicinity of a Ca^{2+} -gated ion channel is known.

Calcium activated potassium channels

In channels in the $K_{Ca}2$ subfamily, the open probability depends principally on intracellular calcium concentration (Figure 5.14). This dependence can be

Fig. 5.14 Behaviour of $K_{Ca}2.1$ small conductance calcium-dependent potassium channels (Hirschberg *et al.*, 1998), also known as SK channels. (a) Single channel current recordings from an inside-out patch voltage clamped at -80 mV with different calcium concentrations. The channel is more likely to be open when the Ca^{2+} concentration is greater. (b) Probability of the channel opening as a function of calcium concentration (circles) and a Hill function fit to it (line). © The Rockefeller University Press. *The Journal of General Physiology*, 1998, 111: 565–581.



fitted using the **Hill equation**:

$$\text{Prob(channel open)} \propto \frac{[\text{Ca}^{2+}]^n}{K_{0.5}^n + [\text{Ca}^{2+}]^n}, \quad (5.10)$$

where $K_{0.5}$ is the half maximal effective concentration of intracellular Ca^{2+} , sometimes referred to as EC_{50} , which is the concentration at which the open probability is $1/2$, and n is the **Hill coefficient**.

This can be incorporated into a model by introducing an activation variable whose steady state reflects the open probability. For example, Gillies and Willshaw (2006) use experimental data (Hirschberg *et al.*, 1998; Figure 5.14) to model the small conductance calcium-dependent potassium channel $K_{Ca}2.1$, which underlies I_{AHP} . The model is defined as:

$$g_{sKCa} = \bar{g}_{sKCa} w, \quad \frac{dw}{dt} = -\frac{w - w_\infty}{\tau_w}, \quad w_\infty = 0.81 \frac{[\text{Ca}^{2+}]^n}{K_{0.5}^n + [\text{Ca}^{2+}]^n} \quad (5.11)$$

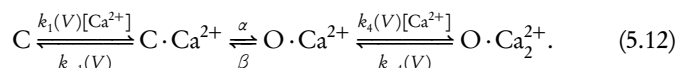
$$K_{0.5} = 0.74 \mu\text{M}, \quad n = 2.2, \quad \tau_w = 40 \text{ ms}$$

where $K_{0.5}$ is the EC_{50} . A similar approach can be taken for the slow AHP current I_{sAHP} (Yamanda *et al.*, 1998; Borg-Graham, 1999).

Calcium and voltage activated potassium channels

The gating of potassium channels in the $K_{Ca}1$ family, also known as I_C , $I_{K(C)}$, Slo1, BK or maxi K^+ , depends on the intracellular calcium concentration and membrane potential (Moczydlowski and Latorre, 1983; Cui *et al.*, 1997). This has been modelled using a number of kinetic schemes, most of which have only open and closed states (Moczydlowski and Latorre, 1983; Cui *et al.*, 1997), though inactivating states are sometimes included on physiological grounds (Borg-Graham, 1999).

A model that has been used in a number of studies (for example, Jaffe *et al.*, 1994; Migliore *et al.*, 1995) is the one derived by Moczydlowski and Latorre (1983) from their single channel recordings of $K_{Ca}1$ channels from rat muscle incorporated into planar lipid bilayers. The channel is described by a four-state kinetic scheme with two open states and two closed states:



The closed state can move to a closed state with one bound Ca^{2+} ion. From this state it can go to an open state, and thence to an open state with two bound Ca^{2+} ions. While the transition between the open and closed states

The Hill equation was originally devised to describe the binding of oxygen to haemoglobin and is an approximate mathematical description of the fraction of binding sites on a receptor that are occupied by a ligand. The Hill coefficient is a measure of the cooperativity of the binding. It is not equivalent to the number of binding sites, providing only a minimum estimate (Weiss, 1997). See also the Michaelis-Menton equation for enzymatic reactions in Section 6.2.2.

Box 5.3 | The Moczydłowski and Latorre (1983) model

Since it is assumed that the calcium binding transitions are fast compared to the change in conformation in Scheme 5.12, the fractions of channels in the two closed states are at equilibrium, as are the fractions of channels in the two open states. Thus the ratios between the two types of closed states and the two types of open states are:

$$\frac{[C \cdot \text{Ca}^{2+}]}{[C]} = \frac{k_1[\text{Ca}^{2+}]}{k_{-1}} \quad \text{and} \quad \frac{[O \cdot \text{Ca}_2^{2+}]}{[O \cdot \text{Ca}^{2+}]} = \frac{k_4[\text{Ca}^{2+}]}{k_{-4}}. \quad (\text{a})$$

We define the total fraction of channels in the closed state C and the open state O as:

$$C = [C] + [C \cdot \text{Ca}^{2+}] \quad \text{and} \quad O = [O \cdot \text{Ca}^{2+}] + [O \cdot \text{Ca}_2^{2+}].$$

Along with Equations (a), this allows us to state the relationship between the fraction of channels in the closed and open states, and the fractions in the states on either side of the conformational transition:

$$C = \left(1 + \frac{k_{-1}}{k_1[\text{Ca}^{2+}]}\right) [C \cdot \text{Ca}^{2+}] \quad \text{and} \quad O = \left(1 + \frac{k_4[\text{Ca}^{2+}]}{k_{-4}}\right) [O \cdot \text{Ca}^{2+}] \quad (\text{b})$$

The first order ODE that describes the dynamics of the aggregated open and closed states is:

$$\frac{dO}{dt} = \alpha[C \cdot \text{Ca}^{2+}] - \beta[O \cdot \text{Ca}^{2+}].$$

By substituting in the expressions in Equations (b) for $[C \cdot \text{Ca}^{2+}]$ and $[O \cdot \text{Ca}^{2+}]$, this ODE can be written as:

$$\frac{dO}{dt} = aC - bO = a(1 - O) - bO,$$

where

$$a = \alpha \left(1 + \frac{k_{-1}}{k_1[\text{Ca}^{2+}]}\right)^{-1} \quad \text{and} \quad b = \beta \left(1 + \frac{k_4[\text{Ca}^{2+}]}{k_{-4}}\right)^{-1}.$$

To complete the model, the ratios of the forward and backward rate constants are required. Moczydłowski and Latorre (1983) found that the ratios could be described by:

$$\frac{k_{-1}(V)}{k_1(V)} = K_1 \exp(-2\delta_1 FV/RT) \quad \text{and} \quad \frac{k_{-4}(V)}{k_4(V)} = K_4 \exp(-2\delta_4 FV/RT),$$

where F is Faraday's constant, R is the molar gas constant, K_1 and K_4 are constants with the units of concentration, and δ_1 and δ_4 are parameters related to the movement of gating charge (Section 5.8). The model parameters varied from channel to channel. For one channel these were $K_1 = 0.18 \text{ mM}$, $\delta_1 = 0.84$, $K_4 = 0.011 \text{ mM}$, $\delta_4 = 1.0$, $\alpha = 480 \text{ s}^{-1}$ and $\beta = 280 \text{ s}^{-1}$.

is independent of voltage, the calcium binding steps are voltage-dependent. Under the assumption that the calcium binding steps are much faster than the step between the closed and open states, the expression for the fraction of channels in either of the open states reduces to a first order ODE (Box 5.3).

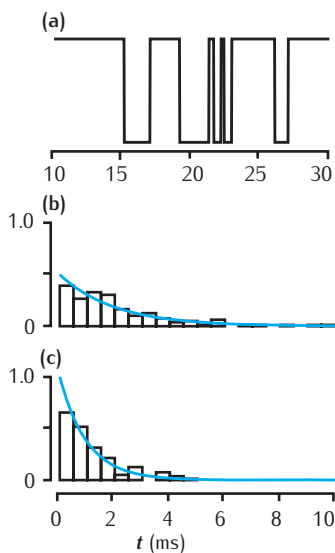


Fig. 5.15 Features of a two-state kinetic scheme.
(a) Simulated sample of the time course of channel conductance of the kinetic scheme described in Scheme 5.13. The parameters are $\alpha = 1 \text{ ms}^{-1}$ and $\beta = 0.5 \text{ ms}^{-1}$.
(b) Histogram of the open times in a simulation and the theoretical prediction of $0.5e^{-0.5t}$ from Equation 5.14. (c) Histogram of the simulated closed times and the theoretical prediction e^{-t} .

5.7 Modelling single channel data

Markov models of channels were introduced in Section 5.5, but only their deterministic interpretation was considered. In this section the underlying probabilistic basis of Markov models is outlined. This provides tools for analysing single channel data and for simulating Markov models.

5.7.1 Markov models for single channels

Markov models all obey the **Markov property**: the probability of a state transition depends only on the state the channel is in and the probabilities of transitions leading from that state, not on the previous history of transitions. This can be illustrated by considering a very simple kinetic scheme in which the channel can be in an open state (O) or a closed state (C):



where α and β are transition probabilities which can depend on voltage or ligand concentration, analogous to the rate coefficients in the deterministic interpretation. With the channel in the closed state, in an infinitesimally small length of time Δt it has a probability of $\alpha\Delta t$ of moving to the open state; if it is in the open state, it has a probability of $\beta\Delta t$ of moving back to the closed state. This scheme can be simulated exactly using the algorithm to be described in Section 5.7.2 to produce conductance changes such as those shown in Figure 5.15a. Each simulation run of the scheme produces a sequence of random switches between the C and O states.

A key statistic of single channels is the distribution of times for which they dwell in open or closed conductance states. Histograms of the channel open and closed times can be plotted, as shown in Figures 5.15b and 5.15c for the most basic two-state scheme (Scheme 5.13). By considering the time steps Δt to be infinitesimally small, the transition from one state to another acts as a Poisson process, in which the inter-event intervals are distributed exponentially:

$$\begin{aligned} \text{Prob(in closed state for time } t) &= \alpha \exp(-\alpha t) \\ \text{Prob(in open state for time } t) &= \beta \exp(-\beta t). \end{aligned} \quad (5.14)$$

The mean closed time is $1/\alpha$, meaning that the higher the forward reaction rate α the shorter the time during which the channel will stay in the closed state. Similarly, the mean open time is $1/\beta$.

Open and closed time histograms extracted from experimental recordings of single channel currents do not tend to have this simple exponential structure. For example, the closed time distribution of calcium channels in bovine chromaffin cells (Figure 5.16) is fitted more closely by a double exponential than by a single exponential (Fenwick *et al.*, 1982). As each exponential has a characteristic time constant, this indicates that there are at least three timescales in the system. Since each transition is associated with a time constant, this means that a kinetic scheme with at least three states is required to model the data. The data shown in Figure 5.16 can be modelled

by a three-state scheme with two closed states (C_1 and C_2) and one open state (O):



In this case it is possible to determine the four transition probabilities from the time constant of the open time distribution, the fast and slow time constants of the closed time distribution and the ratio of the fast and slow components of the closed time distribution.

5.7.2 Simulating a single channel

Within a single compartment of a compartmental model there is generally a population of more than one ion channel of the same type. The simulation of each ion channel can be considered individually. This is less efficient than the method of the Stochastic Simulation Algorithm (SSA) (Section 6.9). However, it makes the principle of stochastic simulation clear, so will be considered in this section.

As an example, consider the five-state potassium channel scheme (Scheme 5.5) with the rate coefficients given by the HH model. In this kinetic description, transitions between states depend only on the membrane potential. The method described in this section is efficient, but only works when the membrane potential is steady, as it is under voltage clamp conditions.

In order to simulate an individual potassium channel using this scheme, an initial state for the channel must be chosen. It is usual to select a state consistent with the system having been at rest initially. The probability that the channel is in each of the five states can then be calculated. For example, the probability of being in state C_1 given initial voltage V_0 is:

$$P_{C_1} = (1 - n_\infty(V_0))^4 = \left(1 - \frac{\alpha_n(V_0)}{\alpha_n(V_0) + \beta_n(V_0)}\right)^4. \quad (5.16)$$

C_4 is the state in which all four of the particles are closed. As described in Chapter 3, the probability of a particle being in the closed state is given by $1 - n_\infty(V_0)$. Consequently, the probability that all four of the particles are in the closed state is $(1 - n_\infty(V_0))^4$. The probability of being in state C_2 , where exactly one of the four particles is in the open state with the remainder closed is:

$$P_{C_2} = \binom{4}{3} (1 - n_\infty(V_0))^3 n_\infty(V_0), \quad (5.17)$$

where $\binom{4}{3}$ is the number of possible combinations in which any three of the four particles can be in the closed state. In a similar manner, the probabilities of the particle being in states C_3 , C_4 and O respectively, given the initial

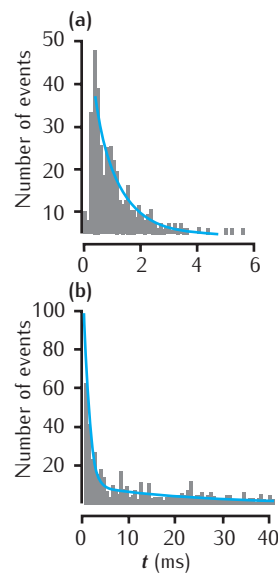


Fig. 5.16 Distributions of open and closed times of single Ca^{2+} channels from bovine chromaffin cells recorded by Fenwick *et al.* (1982). The distribution of open times is fitted by a single exponential with a time constant of 0.81 ms, but the distribution of closed times is fitted by two exponentials with time constants of 1.05 ms and 25.5 ms. Adapted from Fenwick *et al.* (1982), with permission from John Wiley & Sons Ltd.

$\binom{n}{k}$ is the number of combinations each of size k that can be drawn from an unordered set of n elements. This is given by:

$$\binom{n}{k} = \frac{n!}{k!(n-k)!}.$$

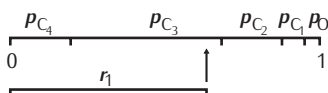


Fig. 5.17 The initial probabilities of each state of the kinetic model can be used to divide a unit line. The example uses the five-state Hodgkin and Huxley channel model given in Scheme 5.5 with initial voltage $V_0 = -60$.

voltage V_0 are given by:

$$\begin{aligned} P_{C_3} &= \binom{4}{2} (1 - n_\infty(V_0))^2 n_\infty(V_0)^2 \\ P_{C_4} &= \binom{4}{1} (1 - n_\infty(V_0)) n_\infty(V_0)^3 \\ P_O &= n_\infty(V_0)^4. \end{aligned} \quad (5.18)$$

The initial state for the simulation is selected stochastically by assigning to each probability a section of a line running from 0 to 1 (Figure 5.17), drawing a random number r_1 between 0 and 1 from a uniform distribution, and selecting the initial state according to where r_1 lies on the line.

The next step in the simulation is to determine how long the system resides in a state, given the membrane potential V . Suppose the channel is in state C_1 . As state transitions act as a Poisson process (Section 5.7.1), the probability that the system remains in state C_1 for duration τ is given by:

$$P_{C_1}(\tau) = 4\alpha_n \exp(-4\alpha_n \tau), \quad (5.19)$$

where $4\alpha_n$ is the rate at which state C_1 makes the transition to state C_2 at voltage V (the V dependency has been omitted from α_n for clarity). By converting this distribution into a cumulative distribution, another random number r_2 , between 0 and 1, can be used to calculate the duration:

$$\tau = -\frac{\ln(r_2)}{4\alpha_n}. \quad (5.20)$$

Similar probabilities for the other states can be calculated:

$$\begin{aligned} P_{C_2}(\tau) &= (3\alpha_n + \beta_n) \exp(-(3\alpha_n + \beta_n)\tau) \\ P_{C_3}(\tau) &= (2\alpha_n + 2\beta_n) \exp(-(2\alpha_n + 2\beta_n)\tau) \\ P_{C_4}(\tau) &= (\alpha_n + 3\beta_n) \exp(-(\alpha_n + 3\beta_n)\tau) \\ P_O(\tau) &= 4\beta_n \exp(-4\beta_n\tau) \end{aligned} \quad (5.21)$$

and the random duration calculated by replacing $4\alpha_n$ in Equation 5.20 with the appropriate rate.

Finally, once the system has resided in this state for the calculated duration, its next state must be chosen. In this example, in states C_1 and O there is no choice to be made, and transitions from those states can only go to one place. For the intermediate states, transition probabilities are used to select stochastically the next state. The probability of the transitions from state C_2 to C_1 or C_3 are given by:

$$\begin{aligned} P_{C_2, C_1} &= \frac{\beta_n}{\beta_n + 3\alpha_n} \\ P_{C_2, C_3} &= \frac{3\alpha_n}{\beta_n + 3\alpha_n}. \end{aligned} \quad (5.22)$$

Clearly, the sum of transition probabilities away from any state add to 1. To choose the new state stochastically, we can use the technique for selecting the initial state illustrated in Figure 5.17.

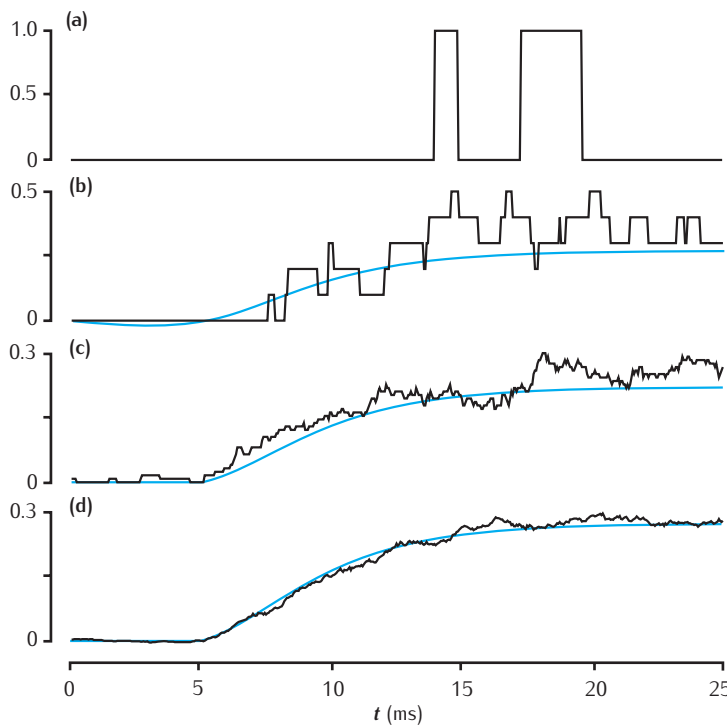


Fig. 5.18 Simulations of varying numbers of the stochastic potassium channel described in Scheme 5.5 during a voltage step from -60 mV to -30 mV at $t = 5\text{ ms}$. The conductance of a single channel is normalised to $1/N$, where N is the number of channels in the simulation.
 (a) Simulation of a single channel. (b) 10 channels. (c) 100 channels. (d) 1000 channels. The smooth blue line in (b)–(d) is the plot of n^4 , the Hodgkin and Huxley potassium gating variable, for the same voltage step.

5.7.3 Ensemble versus stochastic simulation

As seen in Figure 5.6, when the microscopic single channel records are aligned in time and averaged, the result looks like data from macroscopic patches of membrane. A similar effect appears when multiple channels in parallel are simulated (Figure 5.18): the more channels contribute to the current, the smoother the current. As the number of channels increases, the current tends towards what would be predicted by interpreting the kinetic scheme as the deterministic evolution of the fraction of channels in each state.

An important modelling question is: when is it appropriate to model multiple single channels stochastically, and when to model the average properties of an ensemble of channels? The answer depends strongly on the size of the compartment in which the channels are situated. For a given density of channels and probability of channels being open, the expected specific membrane conductance does not depend on the area of the compartment, but the size of fluctuations in the specific membrane conductance is inversely proportional to the square root of the area of the compartment (Box 5.4). It is sometimes possible to predict the fluctuations in voltage arising from fluctuations in conductance, though this is not straightforward, as the fluctuations in the membrane potential depend on a number of factors, including the membrane time constant, channel kinetics and the difference between the membrane potential and the reversal potential of the current of interest (Chow and White, 1996). However, the larger fluctuations in conductance present in compartments with smaller areas will tend to lead to larger fluctuations in voltage (Koch, 1999). If the fluctuations in voltage are small

Box 5.4 Magnitude of specific conductance fluctuations

Consider a compartment of area a , in which there is a density ρ (number of channels per unit area) of a particular channel type with a single channel conductance of γ . At a particular point in time, the probability of an individual channel being open is m .

The number of channels in the compartment is $N = \rho a$. The number of channels expected to be open is Nm . Therefore the expected specific membrane conductance due to this type of channel is:

$$\frac{Nm\gamma}{a} = \rho m\gamma.$$

Thus the expected specific conductance is independent of the area of the compartment. Assuming that channels open and close independently, the standard deviation in the number of channels open is, according to binomial statistics, $\sqrt{Nm(1-m)}$. Therefore the standard deviation in the specific conductance is:

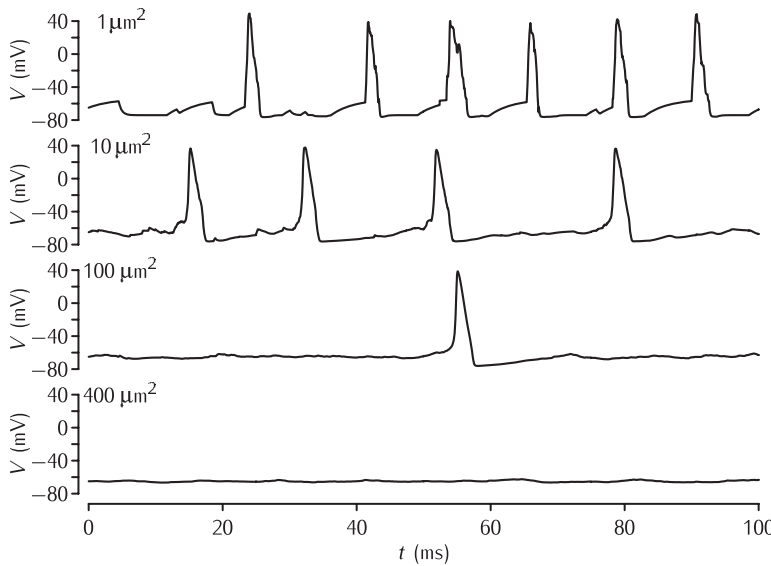
$$\frac{\sqrt{Nm(1-m)}\gamma}{a} = \frac{\sqrt{\rho m(1-m)}\gamma}{\sqrt{a}}.$$

Thus the fluctuation of the specific membrane conductance is inversely proportional to the square root of the area of the compartment.

compared to the maximum slope of the activation curves of all channels in the system, the noise due to stochastic opening and closing of channels is unlikely to play a large part in neuronal function. Nevertheless, even small fluctuations could be important if the cell is driven to just below its firing threshold, as small fluctuations in voltage could cause the membrane potential to exceed this threshold and fire an action potential (Strassberg and DeFelice, 1993; Chow and White, 1996).

Simulations of a stochastic version of the HH model in small patches of membrane, based on those of Chow and White (1996) and displayed in Figure 5.19, show that in squid giant axon patches of area less than $1 \mu\text{m}^2$, the opening of single channels has an appreciable effect on the membrane potential. In the simulations, no current is applied, yet when the area of the membrane is small enough, random fluctuations in the number of sodium and potassium channels open are sufficient to push the membrane potential above threshold. The action potentials generated are jagged compared to the smooth action potentials produced in the deterministic HH model. As the area of the membrane increases, and the total membrane capacitance of the patch becomes large compared to the conductance of a single channel, the membrane potential behaves more and more like it would do with deterministic channels.

With increasing amounts of computing power, simulating multiple stochastic channels is becoming more feasible, boosting the arguments in favour of stochastic simulation. Some simulator packages make it fairly straightforward to simulate the same kinetic scheme either deterministically or stochastically (Appendix A.1). In detailed models of neurons, especially those with narrow branches with compartments containing 100s rather than



1000s of channels, it may be worth running the initial simulations deterministically, and then running a number of simulations with stochastic dynamics in order to assess how important the effect of stochastic channel opening and closing is in the system.

Fig. 5.19 Simulations of patches of membrane of various sizes with stochastic Na^+ and K^+ channels. The density of Na^+ and K^+ channels is 60 channels per μm^2 and 18 channels per μm^2 respectively, and the single channel conductance of both types of channel $\gamma = 2\text{pS}$. The Markov kinetic scheme versions of the Hodgkin–Huxley potassium and sodium channel models were used (Schemes 5.5 and 5.8). The leak conductance and capacitance is modelled as in the standard HH model. No current is applied; the action potentials are due to the random opening of a number of channels taking the membrane potential to above threshold.

5.7.4 Fitting kinetic schemes

The chief difficulty with Markov models is the number of parameters compared to the amount of data. When transitions are voltage-dependent, the transition probabilities in Markov models are often parameterised using principles of transition state theory (Section 5.8), requiring at least four parameters per reversible transition, and leading to models with large numbers of parameters. Even using multiple sources of data, such as single channel recordings, macroscopic currents and gating currents, more than one kinetic scheme can often be used to fit the same data.

Fitting kinetic schemes is a complex subject in its own right, and traditionally the preserve of biophysics rather than computational neuroscience. Channel models are constructed by obtaining various statistics of the channel data, such as open and closed time histograms and activation curves, and then using these statistics to inform model construction. More than one kinetic scheme may be tried to fit an ion channel, and knowledge of channel structure can also be incorporated into the kinetic schemes. This type of fitting process is dealt with comprehensively elsewhere – see for example, Johnston and Wu (1995) or Sakmann and Neher (1995). Appendix A.2.4 gives details of the DC analysis programs and the QuB package, which use different algorithms (Colquhoun *et al.*, 1996; Qin *et al.*, 1996) to fit kinetic schemes to single channel data.

An alternative approach is to treat the problem of fitting ion channels as an **inverse problem** (Cannon and D'Alessandro, 2006). The likelihood of a particular experimental recording being generated by a hypothetical kinetic scheme is computed for various sets of parameters, and parameter estimation techniques (Section 4.5) are used to find the most likely set of parameters.

Box 5.5 Q_{10} and the Arrhenius equation

Equation 5.23 can be used to derive the **Arrhenius equation** (Arrhenius, 1889), which describes the ratio of rate coefficients $k(T_1)$ and $k(T_2)$ at temperatures T_1 and T_2 respectively:

$$\log\left(\frac{k(T_2)}{k(T_1)}\right) = \frac{E_a}{R} \left(\frac{1}{T_1} - \frac{1}{T_2} \right).$$

As described in Section 3.4, the Q_{10} measured at a temperature T is defined as the ratio $k(T+10)/k(T)$. By substituting $T_1 = T$ and $T_2 = T + 10$ into the Arrhenius equation, a relationship for the Q_{10} in terms of the activation energy E_a can be derived:

$$\log(Q_{10}) = \frac{E_a}{R} \frac{10}{T(T+10)}.$$

This equation can be used to estimate the activation energy from the Q_{10} . It also shows that, assuming that the activation energy is independent of temperature, the Q_{10} depends on temperature. However, this dependence is insignificant for the ranges considered in mammalian biology. For example, the Q_{10} of a reaction calculated from rates at 5°C and 15°C (278 K and 288 K), is expected to differ from the Q_{10} calculated at 27°C and 37°C (300 K and 310 K) by a factor of 1.000017.

Time-varying voltage clamp commands, such as simulated action potentials, can be incorporated easily into this framework, and in fact help to constrain parameters more than voltage steps do (Cannon and D'Alessandro, 2006). In the future, it is likely that these techniques will become more widely used.

Clearly, schemes with more states have the potential to be more accurate, though the larger number of parameters makes it harder to constrain the scheme (Section 4.6). This raises the question of how accurate kinetic schemes should be. Here the requirements of biophysicists and computational neuroscientists may differ. For example, currents due to transitions between open and closed states which have very fast time constants are of relevance to understanding channel structure, but will tend to be filtered out electrically because of the membrane time constant, and are therefore of less interest to computational neuroscientists.

5.8 The transition state theory approach to rate coefficients

This section describes **transition state theory** and shows how it can be applied to derive equations for the voltage-dependence of rate coefficients, commonly used in Markov models built by biophysicists. The section will also show how the thermodynamic models of ion channels introduced in Section 5.4.2 can be derived from transition state theory.

Box 5.6 Gibbs free energy

In thermodynamics, the ability of a system in a particular state to do work depends not only on its potential energy, but also on how disordered that state is. The degree of disorder associated with the state is quantified by **entropy**, S . Entropy reduces the ability of the state to donate energy to do work. This is expressed in the definition of **Gibbs free energy** G , which is a measure of how much energy there is available to do useful work:

$$G = H - TS,$$

where H is the potential energy, also called **heat energy** or **enthalpy** in the context of chemical reactions.

To apply the concept of Gibbs free energy to channel transitions, the activation energy E_a is replaced by the difference in Gibbs free energy ΔG_μ between the starting state and the transition state, the activated complex, of the μ th reaction, which in turn depends on the potential energy and entropy differences:

$$\Delta G_\mu = \Delta H_\mu - T\Delta S_\mu.$$

Along with the $k_B T/h$ dependence of the constant of proportionality, this leads to the Eyring equation (Equation 5.24).

If the transition state is more ordered than the base state (i.e. ΔS_μ is negative), this can allow for a negative potential energy difference ΔH_μ , and hence for the reaction rate to decrease with increasing temperature, giving a Q_{10} less than one, as measured in some chemical reactions (Eyring, 1935).

5.8.1 Transition state theory

Transition state theory describes how the rate of a chemical reaction depends on temperature. The key concept, put forward by Arrhenius (1889), is that during the conversion of reactants into products, there is an intermediate step in which the reactants form an activated complex. Forming the activated complex requires work to be done, and the energy for this work comes from thermal fluctuations. Once the activated complex is formed, it is converted into the products, releasing some energy. There is thus an **energy barrier** between the initial and final states of the system. Arrhenius postulated that the reaction rate coefficient k is given by:

$$k \propto \exp\left(-\frac{E_a}{RT}\right), \quad (5.23)$$

where E_a is the **activation energy** required to surmount the energy barrier.

The activation energy depends on the reaction in question. According to Equation 5.23, the larger the activation energy, the slower the reaction. The rate coefficient also depends on temperature: the higher the temperature the faster the reaction; the larger the activation energy, the stronger the dependence on temperature. This control of temperature dependence suggests a link between the activation energy and the Q_{10} , which is expanded on in Box 5.5.

Temperature T is always measured in kelvins in these equations. The units of the activation energy E_a are J mol^{-1} and the gas constant $R = 8.314 \text{ J K}^{-1} \text{ mol}^{-1}$.

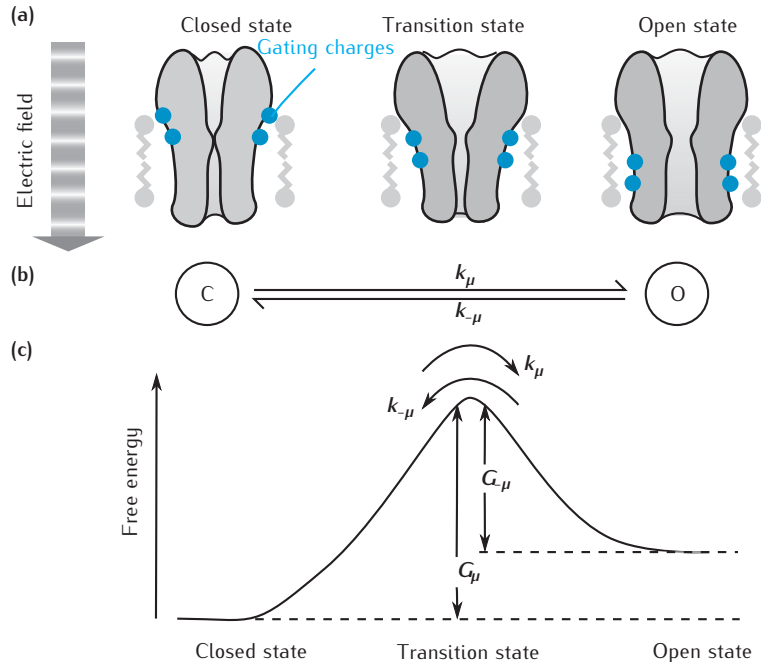
Fig. 5.20 The application of transition state theory to determining rate constants.

(a) Representation of a hypothetical channel protein with two stable states: a closed state and an open state. While changing conformation between these states, the channel passes through a **transition state**. In each state, the gating charges (in blue) have a different position in the electric field.

(b) Representation of the channel as a Markov scheme. The transition state does not feature in the scheme. The forward reaction, indexed by μ , has a rate constant k_μ and the backward reaction, indexed by $-\mu$, has a rate constant $k_{-\mu}$.

(c) The curve shows the free energy as a function of the progress of the channel protein between the closed and open states. In the forward reaction, the size of the free energy barrier that the reaction or channel has to surmount is ΔG_μ . In the backwards reaction the free energy barrier is $\Delta G_{-\mu}$. Both ΔG_μ and $\Delta G_{-\mu}$ depend on the voltage, as described in the text.

Boltzmann's constant
 $k_B = 1.3807 \times 10^{-23} \text{ J K}^{-1}$.
 Planck's constant
 $h = 6.6261 \times 10^{-34} \text{ J s}$.



The Arrhenius formula can be applied to a transition between channel states by (1) associating the reactants with the initial state of the channel; (2) associating the activated complex with a transitional, high-energy conformation of the ion channel; and (3) associating the product with the final conformation of the channel (Figure 5.20). As in the chemical reaction, each state has a certain level of energy.

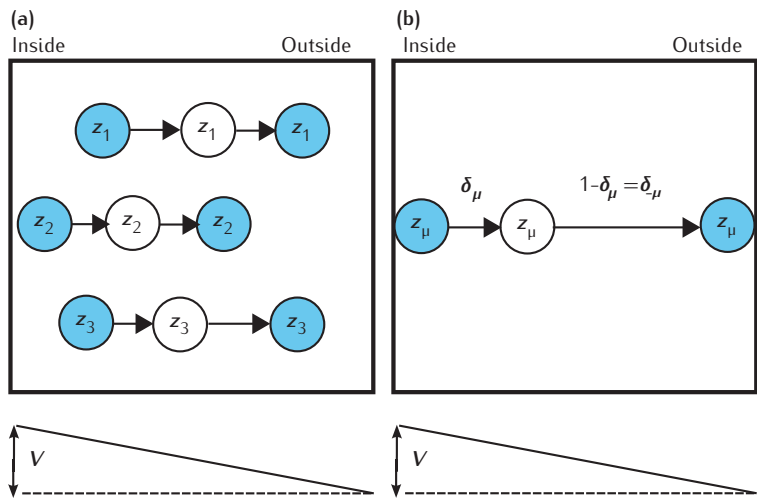
To describe the full range of temperature dependence of chemical reactions and channel transitions, an extension to the concept of Arrhenius activation energy using the concepts of Gibbs free energy and entropy from chemical thermodynamics (Box 5.6) is necessary. This is embodied in the **Eyring equation** (Eyring, 1935; Pollak and Talkner, 2005), here presented for a reaction indexed by μ :

$$k_\mu = \frac{k_B T}{h} \exp\left(-\frac{\Delta G_\mu}{RT}\right) = \frac{k_B T}{h} \exp\left(\frac{\Delta S_\mu}{R}\right) \exp\left(-\frac{\Delta H_\mu}{RT}\right), \quad (5.24)$$

where k_B is the Boltzmann constant and h is Planck's constant; ΔG_μ , ΔH_μ and ΔS_μ are respectively the differences in Gibbs free energy, potential energy and entropy between the base and transition states.

5.8.2 Voltage-dependent transition state theory

Although Equation 5.24 describes how the rate coefficient depends on temperature, it does not depend on the membrane potential explicitly. In fact, the membrane potential is in the equation implicitly, because as well as depending on the conformation (Figure 5.20a) of the ion channel in each state, the potential energy difference ΔH_μ depends on the membrane potential (Borg-Graham, 1989). This is because the gating charges move when the channel protein changes conformation (Section 5.1), and movement of



charges in an electric field requires work or releases energy, the amount of which depends on the electrical potential difference between the initial and final positions.

The movement of all of the gating charges of the channel proteins from state 1 through the transition state to state 2 can be reduced to movement of an **equivalent gating charge** z_μ from one side to the other of the membrane, with the transition state occurring at a fractional distance δ_μ through the membrane (Figure 5.21 and Box 5.7). If the potential energy difference between state 1 and the transition state when the membrane potential is zero is given by $\Delta H_\mu^{(0)}$, the potential energy difference when the membrane potential is V is given by:

$$\Delta H_\mu(V) = \Delta H_\mu^{(0)} - \delta_\mu z_\mu FV, \quad (5.25)$$

where z_μ is the effective valency of the equivalent gating charge and δ_μ is a number between 0 and 1 representing the distance travelled by the equivalent charge when the channel is in the activated state as a fraction of the total distance between the start and finish states (Figure 5.21). Since the channel protein can move back to its original conformation, taking the gating charge back to its original position, the potential energy change of the reverse reaction, labelled $-\mu$, is:

$$\Delta H_{-\mu}(V) = \Delta H_{-\mu}^{(0)} + (1 - \delta_\mu) z_\mu FV. \quad (5.26)$$

Substituting these expressions into Equation 5.24 gives a physically principled expression for the rate coefficient that depends on membrane potential and temperature:

$$k_\mu = \frac{k_B T}{h} \exp\left(\frac{\Delta S_\mu}{R}\right) \exp\left(-\frac{\Delta H_\mu^{(0)} - \delta_\mu z_\mu FV}{RT}\right) \quad (5.27)$$

$$k_{-\mu} = \frac{k_B T}{h} \exp\left(\frac{\Delta S_{-\mu}}{R}\right) \exp\left(-\frac{\Delta H_{-\mu}^{(0)} - (1 - \delta_\mu) z_\mu FV}{RT}\right). \quad (5.28)$$

Fig. 5.21 The gating charges in a channel. (a) Each channel, represented by the box, contains a number of charged regions, each of which contains a number of units of charge. There are three charges, with valencies z_1 , z_2 and z_3 , represented here by the circles. In state 1 the charges are at the left-hand positions. During a gating event, they move to the transitional positions, and then to the right-hand positions. (b) The multiple charges can be considered as an equivalent gating charge that moves from the inside to the outside of the membrane. The potential energy of these particles in their resting positions is the same as a charge with valency z_μ at the inside of the membrane. The difference in energy between state 1 and the transitional state is the same as when the equivalent charge has moved a fractional distance δ_μ through the membrane, i.e. $-z_\mu \delta_\mu V$. In the reverse direction the gating particle has to move a fractional distance $\delta_{-\mu} = 1 - \delta_\mu$ through the membrane. The energy of the gating charge in the field therefore contributes $z_\mu (1 - \delta_\mu) V$ to the enthalpy.

Box 5.7 Equivalent gating charge

Suppose there are a number of gating charges, indexed by j , on the protein that moves in reaction μ . The total energy required to move from state 1 to the transition state is:

$$FV \sum_j z_{\mu j} \delta_{\mu j},$$

where $\delta_{\mu j}$ is the fractional distance through the membrane that each charge travels. In the reverse direction, the total energy needed to move the gating charges from their positions in state 2 to their transition state positions is:

$$FV \sum_j z_{\mu j} \delta_{-\mu j}.$$

The equivalent gating charge z_μ is defined as:

$$z_\mu = \sum_j z_{\mu j} \delta_{\mu j} + \sum_j z_{\mu j} \delta_{-\mu j}.$$

In state 1, this equivalent gating charge is on the outside edge and in state 2 it is on the inside. The fractional distance that an equivalent charge would move through the membrane to get from state 1 (outside) to the transition state is:

$$\delta_\mu = \frac{\sum_j z_{\mu j} \delta_{\mu j}}{z_\mu},$$

and the fractional distance from the position of the equivalent charge in state 2 to its position in the transition state is:

$$\delta_{-\mu} = 1 - \delta_\mu.$$

Thus the forward and backward rates of each transition can be described by six parameters: ΔS_μ , $\Delta S_{-\mu}$, ΔH_μ , $\Delta H_{-\mu}$, z_μ and δ_μ .

In order to determine the potential energy and entropy components, experiments at different temperatures must be undertaken. A number of researchers have done this and produced Markov kinetic schemes where the enthalpy and entropy of every transition is known (Rodriguez *et al.*, 1998; Irvine *et al.*, 1999).

5.8.3 The thermodynamic formalism

When rate coefficients derived from transition state theory are used in independent gating models, the result is the thermodynamic formalism described in Section 5.4.2. This can be shown by considering an ensemble interpretation of the two-state system:



By using the expressions for k_1 and k_{-1} from Equations 5.27 and 5.28, the sigmoidal dependence of O_∞ on V as in Equation 5.1 is obtained:

$$O_\infty = \frac{1}{1 + \exp(-(V - V_{1/2})/\sigma)}, \quad (5.30)$$

where the inverse slope σ depends on the molar gas constant R , the temperature T the Faraday constant F and the effective valency of the gating charges z :

$$\sigma = \frac{RT}{zF}, \quad (5.31)$$

and where the half-activation voltage $V_{1/2}$ also depends on temperature:

$$V_{1/2} = \frac{\Delta H_1^{(0)} - \Delta H_{-1}^{(0)}}{zF} - \frac{\Delta S_1^{(0)} - \Delta S_{-1}^{(0)}}{zF} T. \quad (5.32)$$

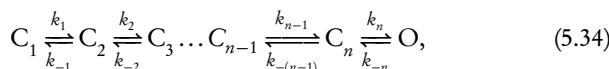
The constant of proportionality K in Equations 5.3 for $\alpha'_x(V)$ and $\beta'_x(V)$ is related to the thermodynamic parameters according to:

$$K = \frac{k_B T}{h} \exp\left(\frac{\delta_1 \Delta S_{-1}^0 + \delta_{-1} \Delta S_1^0}{R}\right) \exp\left(-\frac{\delta_1 \Delta H_{-1}^0 + \delta_{-1} \Delta H_1^0}{RT}\right) \quad (5.33)$$

where $\delta_{-1} = 1 - \delta_1$.

This corresponds to the thermodynamic models presented in Section 5.4.2 when the rate-limiting factor τ_0 is zero. There is an exponential temperature-dependence, which can be approximated by the Q_{10} (Box 5.5), built into this in the third factor. This is a theoretical basis for the Q_{10} factor applied to the gating variable time constants in thermodynamic models.

This derivation does not include the rate-limiting factor τ_0 . When this factor is non-zero, the exponential temperature dependence is no longer predicted to hold exactly. A more principled means of incorporating rate limiting is to use a model of the gating particle with more states. For example, the rate-limiting linear-exponential form for the rate coefficients used by Hodgkin and Huxley (Figure 5.10) can be obtained from a multi-well model (Tsien and Noble, 1969; Hille, 2001):



where the transitions between the initial closed state and the open state are voltage-independent. This approach can also be used to obtain other forms of rate coefficient, such as the sigmoidal form used by Hodgkin and Huxley (Figure 5.10), which can be obtained from the kinetic scheme:



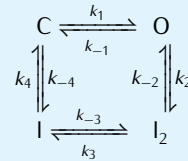
where all the rate coefficients use the thermodynamic formalism, but with k_2 being a voltage-independent coefficient. In principle, more accurate temperature dependencies could be generated by finding the thermodynamic

According to the Boltzmann distribution, at equilibrium the fraction of particles in a state i is proportional to $\exp(-G_i/kT)$ where G_i is the free energy of the i th state. Equation 5.1 can also be derived from the Boltzmann distribution.

The multi-well model (Scheme 5.34) is also a representation of the constant-field Nernst–Planck equation for electrodiffusion (Section 2.2.4) and corresponds to the idea that the gating charges permeate the membrane in the same way in which ions move through channels.

Box 5.8 | Microscopic reversibility

One important constraint on kinetic schemes which contain loops (Scheme 5.9 for instance) is that of **microscopic reversibility**, also known as **detailed balances** (Hille, 2001). The principle is that the sum of the energy differences in the loop must be zero. For example, in the hypothetical scheme:



the enthalpy and the entropy differences around the circuit must all sum to zero:

$$\Delta H_1 - \Delta H_{-1} + \Delta H_2 - \Delta H_{-2} + \Delta H_3 - \Delta H_{-3} + \Delta H_4 - \Delta H_{-4} = 0$$

$$\Delta S_1 - \Delta S_{-1} + \Delta S_2 - \Delta S_{-2} + \Delta S_3 - \Delta S_{-3} + \Delta S_4 - \Delta S_{-4} = 0.$$

From this it is possible to conclude that the product of the reaction coefficients going round the loop one way must equal the product in the other direction:

$$k_1 k_2 k_3 k_4 = k_{-1} k_{-2} k_{-3} k_{-4}.$$

With an enthalpy that depends linearly on the membrane potential (Equations 5.25 and 5.26), microscopic reversibility implies that the sum of effective gating charges around the loop is zero:

$$z_1 + z_2 + z_3 + z_4 = 0.$$

parameters of each reaction rather than by applying a Q_{10} correction to the rate generated by the entire scheme.

5.8.4 Higher order models

The potential energy differences between the various states may also be affected by processes such as deformation of the electric field within the membrane that depend on higher powers of V (Hill and Chen, 1972; Stevens, 1978; Destexhe and Huguenard, 2000). These can be incorporated by adding terms to the expression for the potential energy:

$$\Delta H_{-\mu}(V) = \Delta H_{-\mu}^{(0)} - (1 - \delta_\mu) z_\mu F V + b_\mu V^2 + c_\mu V^3, \quad (5.36)$$

where b_μ and c_μ are per-reaction constants. Using non-linear terms of voltage in the exponent (Equation 5.36) can improve the fit of thermodynamic models to data (Destexhe and Huguenard, 2000).

5.9 | Ion channel modelling in theory and practice

This chapter has concentrated on the theory of modelling ion channels. It has been shown how ion channel models of varying levels of complexity can be used to describe voltage- and ligand-gated ion channel types. Ideally, in order to construct a realistic model of a neuron, the computational neuroscientist should follow Hodgkin and Huxley by characterising the behaviour of each type of channel in the neuron at the temperature of interest, and producing, at least, an independent gating model of the channel.

In the real world, this does not tend to happen because the effort involved is prohibitive compared to the rewards. When faced with building a model containing a dozen channel types, rather than running experiments, typically the computational neuroscientist searches the literature for data from which to construct a model. The data is not necessarily from the neuron type, brain area or even species in question, and quite probably has been recorded at a temperature that differs from the model temperature. With the advent of databases of models such as ModelDB (Appendix A.2) it is possible to search for channel models which have already been implemented in simulation code. While differing temperatures can be corrected for, it is not possible to correct for the mismatch in the preparations and species. This means that the vast majority of compartmental models are incorrect in some details. However, even compartmental models with inexact models of channels are of utility, as they give insights into the types of behaviours possible from a neuron, and they force assumptions in arguments to be made explicit.

In fact, the situation is even more complicated. Various studies have shown that the distribution of channels varies from neuron to neuron, even when the neurons are of the same type (Marder and Prinz, 2002). However, the overall behaviour of the neurons is conserved between different members of the class. For example, in a relatively simple model of the crab stomatogastric ganglion cell with five conductances, Goldman *et al.* (2001) explored the behaviour of the model with combinations of the density of three of the conductances (a calcium conductance, a calcium-dependent potassium conductance and the A-type potassium conductance). This gave a 3D grid of parameter values, and the behaviour of the cell – quiescent, tonically firing or bursting – was determined at each grid point. The simulations showed that many possible combinations of ion channel can give rise to the same behaviours. In order to preserve given behaviours, channel densities are regulated dynamically (see Turrigiano and Nelson, 2004 for review). It may be that from the point of view of understanding cellular function, it is more important to understand these regulatory mechanisms than to model ion channels at the greatest level of detail.

5.10 | Summary

This chapter has described the types of models of voltage- and ligand-gated channels often used in computational studies of the electrical and chemical activity of neurons. Three broad formalisms have been used:

- (1) The Hodgkin–Huxley formalism, which has independent gating particles, and no constraints on the voltage dependence of the rate coefficients.
- (2) The thermodynamic formalism, which has independent gating particles, but where the rate coefficients are constrained by transition state theory.
- (3) Markov kinetic schemes with rate coefficients constrained by transition state theory.

As with many aspects of neuronal modelling, there is a range of options of varying levels of detail available to the modeller. How to decide which type of model to develop can be hard. The fundamental choices to make are:

- Is there enough experimental data to model at the desired level of detail?
- Is the Hodgkin–Huxley or a thermodynamic formalism good enough, or is a Markov kinetic scheme required?
- Does the model need to be stochastic, or will a deterministic model suffice?

While building detailed channel models can be tempting, they should be considered in the context of the entire cell model and the question that is being addressed.

This chapter has discussed the modelling of calcium-dependent channels. How to model the calcium signals that activate these channels is covered in Chapter 6. Modelling of synapses, the postsynaptic side of which are channels activated by extracellular ligands, will be covered in Chapter 7.

Chapter 6

Intracellular mechanisms

Intracellular ionic signalling plays a crucial role in channel dynamics and, ultimately, in the behaviour of the whole cell. In this chapter we investigate ways of modelling intracellular signalling systems. We focus on calcium, as it plays an extensive role in many cell functions. Included are models of **intracellular buffering** systems, **ionic pumps**, and calcium dependent processes. This leads us to outline other **intracellular signalling pathways** involving more complex enzymatic reactions and cascades. We introduce the well-mixed approach to modelling these pathways and explore its limitations. When small numbers of molecules are involved, stochastic approaches are necessary. Movement of molecules through diffusion must be considered in spatially inhomogeneous systems.

6.1 Ionic concentrations and electrical response

Most work in computational neuroscience involves the construction and application of computational models for the electrical response of neurons in experimental and behavioural conditions. So far, we have presented the fundamental components and techniques of such models. Already we have seen that differences in particular ionic concentrations between the inside and outside of a cell are the basis of the electrical response. For many purposes our electrical models do not require knowledge of precise ionic concentrations. They appear only implicitly in the equilibrium potentials of ionic species such as sodium and potassium, calculated from the Nernst equation assuming fixed intra- and extracellular concentrations (Chapter 2). The relative ionic concentrations, and hence the equilibrium potentials, are assumed to remain constant during the course of the electrical activity our models seek to reproduce. This is often a reasonable assumption for sodium and potassium, but is less reasonable for calcium where significant changes in intracellular calcium concentration relative to the extracellular concentration are likely. In this case, calcium concentration should be tracked over time to allow recalculation of the calcium equilibrium potential during the course of a simulation. In addition, certain potassium channels are

dependent on calcium as well as on voltage (Chapter 5), again requiring knowledge of the intracellular calcium concentration to enable the calculation of the channel conductance. If we are to accurately model the electrical response of a neuron, knowledge of ionic concentrations is needed in addition to ionic conductances.

Calcium also plays a crucial role in a multitude of **intracellular signalling pathways** (Berridge *et al.*, 2003). It acts as a **second messenger** in the cell, triggering processes such as (Hille, 2001):

- initiating the biochemical cascades that lead to the changes in receptor insertion in the membrane, which underlie synaptic plasticity;
- muscle contraction;
- secretion of neurotransmitter at nerve terminals;
- gene expression.

Of particular relevance to neuronal modelling is the involvement of calcium in pathways leading to long-term changes in synaptic strength (Berridge, 1998). Modelling intracellular signalling has long been the domain of systems biology, but is gaining increasing attention in computational neuroscience as we seek to understand the temporal and spatial characteristics of synaptic **long-term potentiation (LTP)** and **depression (LTD)** in different neuronal types and different synaptic pathways (Bhalla, 2004a; Ajay and Bhalla, 2005). This work is crucial to our understanding of learning and memory in the nervous system. Models of synaptic plasticity are considered in Section 6.8.2 and Section 7.5.

This chapter deals mainly with modelling intracellular calcium. The techniques are also applicable to other molecular species. For further information, see one of the excellent treatments of modelling intracellular calcium (De Schutter and Smolen, 1998; Koch, 1999; Bormann *et al.*, 2001; Smith, 2001).

6.2 | Intracellular signalling pathways

The cell cytoplasm is a complex milieu of molecules and organelles, which move by diffusion and active transport mechanisms, and may interact through chemical reactions. So far in this book we have treated the opening and closing of ion channels due to voltage changes or ligand binding as simple chemical reactions described by kinetic schemes. Within the cell, molecules may react in complex ways to create new molecular products. The propensity of reactions to occur depends on the concentrations of the particular molecular species involved, which may vary with location as molecules diffuse through the intracellular space. The combination of chemical reactions and molecular diffusion results in what is often called a **reaction-diffusion system**. Such systems are particularly important in neural development, involving extracellular as well as intracellular chemical gradients (Chapter 10). Specific sequences of reactions leading from a cause (such as transmitter release in the synaptic cleft) to an end effect (such as phosphorylation of

AMPA receptors that changes the strength of a synapse) are known as intracellular signalling pathways.

Much of the work on modelling intracellular signalling is based on the assumption of a **well-mixed system** in which the diffusion of the participant molecules is much faster than any reaction time course. We can then ignore diffusion and concentrate solely on modelling the reaction kinetics. Typical signalling pathways involve both binding and enzymatic reactions (Bhalla, 1998, 2001; Blackwell and Hellgren Kotaleski, 2002; Blackwell, 2005).

6.2.1 Binding reactions

In the simplest **binding reaction**, molecule A binds to molecule B to form complex AB:



Molecules A and B are the substrates and AB is the product. The reaction rate depends on the concentrations of all reacting species. The forward reaction rate coefficient k^+ has units of per unit concentration per unit time; the backward rate coefficient k^- is per unit time.

If the well-mixed system is sufficiently large such that the molecular species are present in abundance, then the **law of mass action** applies and the rate equation is equivalent to a set of coupled differential equations that describe the rate of change in concentration of the different molecular species. For this binding reaction, the rate of change of species A, and equivalently of species B, is:

$$\frac{d[A]}{dt} = -k^+[A][B] + k^-[AB]. \quad (6.2)$$

The time evolution of the product [AB] is the negative of this expression, given by:

$$\frac{d[AB]}{dt} = -k^-[AB] + k^+[A][B]. \quad (6.3)$$

For a closed system in which the mass does not change, given initial concentrations for the substrates and assuming no initial product, the concentrations of A and B can be calculated from the product concentration (Blackwell, 2005):

$$\begin{aligned} [A]_t &= [A]_0 - [AB]_t \\ [B]_t &= [B]_0 - [AB]_t, \end{aligned} \quad (6.4)$$

where t denotes time and $[A]_0$, $[B]_0$ are the initial concentrations of A and B.

At equilibrium, when the concentrations have attained the values $[A]_\infty$, $[B]_\infty$ and $[AB]_\infty$, the relative concentration of substrates to product is given by the dissociation constant:

$$K_d = [A]_\infty[B]_\infty/[AB]_\infty = k^-/k^+, \quad (6.5)$$

which has units of concentration.

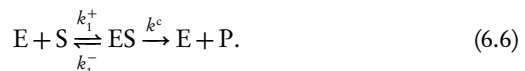
The law of mass action assumes that molecules move by diffusion and they interact through random collisions.

According to this law, the rate of action is proportional to the product of the concentrations of the reactants.

More complex binding reactions will involve more than two molecular species and may require more than a single molecule of a particular species to generate the product. Such reactions may be broken down into a sequence of simple binding reactions involving the reaction of only a single molecule of each of two species.

6.2.2 Enzymatic reactions

Enzymatic reactions are two-step reactions in which the action of one molecule, the enzyme E, results in a substrate S being converted into a product P via a reversible reaction that produces a complex ES. E itself is not consumed. This sort of reaction was described by Michaelis and Menten (1913) as the reaction sequence:



Note that the second reaction step leading to product P is assumed to be irreversible and typically the substrate is in excess, so the reaction sequence is limited by the amount of enzyme. Assuming the law of mass action applies, the production of complex ES and product P are described by the differential equations:

$$\begin{aligned} \frac{d[ES]}{dt} &= k_1^+[E][S] - (k_1^- + k^c)[ES] \\ \frac{d[P]}{dt} &= k^c[ES]. \end{aligned} \quad (6.7)$$

If the complex ES is in equilibrium with enzyme and substrate, then the dissociation constant is:

$$K_m = [E]_\infty[S]_\infty/[ES]_\infty = (k_1^- + k^c)/k_1^+. \quad (6.8)$$

If the reactions are sufficiently fast that it can be assumed that all species are effectively in equilibrium, then at all times we have:

$$k_1^+[E][S] - (k_1^- + k^c)[ES] = 0. \quad (6.9)$$

Substituting in $[E] = [E]_{\text{tot}} - [ES]$, where $[E]_{\text{tot}}$ is the total enzyme concentration, and rearranging leads to:

$$[ES] = \frac{[E]_{\text{tot}}[S]}{K_m + [S]}. \quad (6.10)$$

Thus the flux, in units of concentration per time, of substrate S going to product P is:

$$J_{\text{enz}} = \frac{d[P]}{dt} = V_{\max} \frac{[S]}{K_m + [S]}, \quad (6.11)$$

where $V_{\max} = k^c[E]_{\text{tot}}$ is the maximum velocity in units of concentration per time, and K_m , in units of concentration, determines the half-maximal production rate (Figure 6.1). This steady state approximation to the full enzymatic reaction sequence is often referred to as **Michaelis–Menten kinetics**, and Equation 6.11, which results from the approximation, is known as

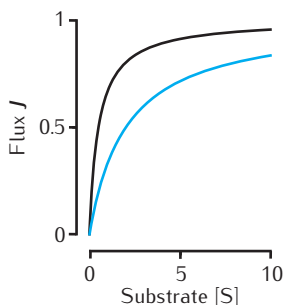


Fig. 6.1 Two examples of the enzymatic flux J as a function of the substrate concentration $[S]$ for Michaelis–Menten kinetics (Equation 6.11). Arbitrary units are used and $V_{\max} = 1$. Black line: $K_m = 0.5$. Blue line: $K_m = 2$. Note that half-maximal flux occurs when $[S] = K_m$.

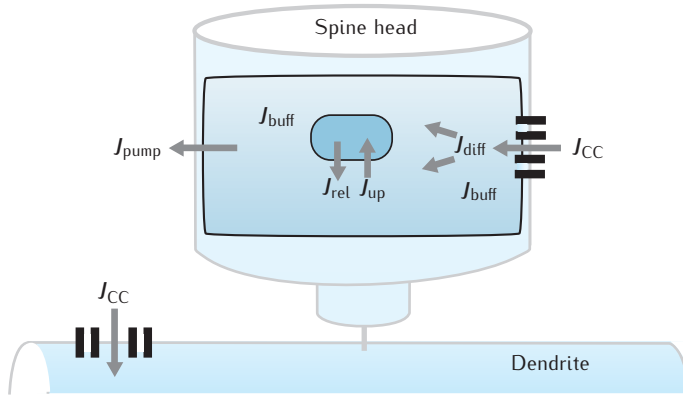


Fig. 6.2 Intracellular calcium concentration is determined by a variety of fluxes, including diffusion (J_{diff}), buffering (J_{buff}), entry through voltage- and ligand-gated calcium ion channels (J_{CC}), extrusion by membrane-bound ionic pumps (J_{pump}), uptake (J_{up}) and release (J_{rel}) from intracellular stores.

the **Michaelis–Menten function**. It is used extensively later in this chapter to model, for example, ionic pump fluxes (Section 6.4.3).

One of the features of Michaelis–Menten kinetics is that for low concentrations of S, the rate of production of P is approximately a linear function of S. This feature is not shared by more complex molecular pathways. For example, if the production of P involves the binding of a number n of identical molecules of S simultaneously, the rate of reaction is given by the Hill equation (Section 5.6):

$$\frac{d[P]}{dt} = V_{\max} \frac{[S]^n}{K_m^n + [S]^n}, \quad (6.12)$$

where n is the Hill coefficient.

Binding and enzymatic reactions, in combination with diffusion, are the basic building blocks for modelling intracellular signalling pathways. In Sections 6.3–6.7 they are used to develop a model for the dynamics of intracellular calcium. We then consider examples of more complex signalling pathways (Section 6.8), before addressing the problems that arise when the assumption of mass action kinetics is not reasonable (Section 6.9).

6.3 Modelling intracellular calcium

The calcium concentration in a cellular compartment is highly dynamic and is determined by influx of calcium through voltage-gated channels, release of calcium from second messenger- and calcium-activated internal stores, diffusion in the intracellular space, buffering by mobile and fixed buffers, and extrusion by calcium pumps (Figure 6.2). The change in calcium concentration with time is determined by the sum of these various fluxes:

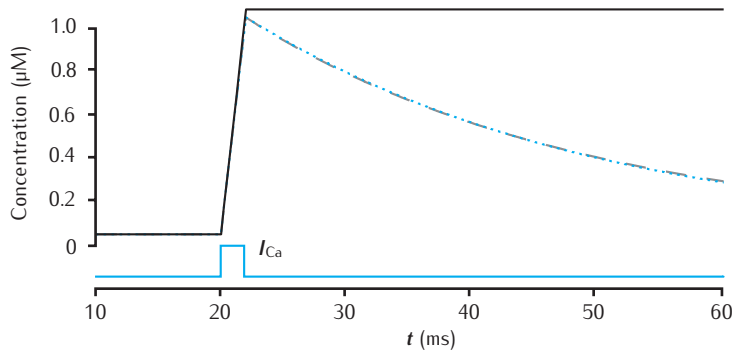
$$\frac{d[\text{Ca}^{2+}]}{dt} = J_{\text{diff}} - J_{\text{buff}} + J_{\text{cc}} - J_{\text{pump}} - J_{\text{up}} + J_{\text{rel}} - J_{\text{leak}} \quad (6.13)$$

It is possible, and sometimes desirable, to model explicitly many or all of these mechanisms. Through a series of models of increasing complexity, we now explore the effects of these different components on the dynamics

Here, each flux J specifies the rate of change of the number of molecules of calcium per unit volume, i.e. the rate of change of concentration (with typical units of $\mu\text{M s}^{-1}$). This is derived by multiplying the rate of movement of molecules across a unit surface area by the total surface area across which the movement is occurring, and dividing by the volume into which the molecules are being diluted.

J_{leak} represents a background leak flux (e.g. influx through voltage-gated calcium channels at rest) that ensures the total flux is zero at rest.

Fig. 6.3 Calcium transients in a single cylindrical compartment, 1 μm in diameter and 1 μm in length (similar in size to a spine head). Initial concentration is 0.05 μM . Influx is due to a calcium current of 5 $\mu\text{A cm}^{-2}$, starting at 20 ms for 2 ms, across the radial surface. Black line: accumulation of calcium with no decay or extrusion. Blue line: simple decay with $\tau_{\text{dec}} = 27$ ms. Dashed line: instantaneous pump with $V_{\text{pump}} = 4 \times 10^{-6} \mu\text{Ms}^{-1}$, equivalent to $10^{-11} \text{ mol cm}^{-2} \text{ s}^{-1}$ through the surface area of this compartment, $K_{\text{pump}} = 10 \mu\text{M}$, $J_{\text{leak}} = 0.0199 \times 10^{-6} \mu\text{Ms}^{-1}$.



of intracellular calcium. We highlight when it is reasonable to make simplifications and when it is not.

6.4 Transmembrane fluxes

Firstly, we examine the intracellular calcium dynamics that result from transmembrane fluxes into and out of a small cellular compartment, such as a spine head or short section of dendrite. Entry into the compartment is through voltage- or ligand-gated calcium channels in the cell membrane. Resting calcium levels are restored by extrusion of calcium back across the membrane by ionic pumps and by uptake into internal stores. The compartment is assumed to be well-mixed, meaning that the calcium concentration is uniform throughout.

The expression for the flux J_{cc} arises from the need to change the amount of charge passing into the compartment per unit time into the number of calcium ions carrying that charge. Faraday's constant gives the amount of charge carried by a mole of monovalent ions: 96 490 coulombs per mole. Since calcium is divalent, we multiply this by two then divide the current I_{Ca} by the result to get the number of moles flowing per unit area and per unit time. Multiplying this by the total surface area and dividing by the compartment volume gives the rate of change in concentration, i.e. the flux.

6.4.1 Ionic calcium currents

The flux that results from an ionic calcium current I_{Ca} , in units of current per unit area, is given by:

$$J_{\text{cc}} = -\frac{\alpha I_{\text{Ca}}}{2Fv}, \quad (6.14)$$

where α is the surface area across which the current flows, v is the volume of the intracellular compartment and F is Faraday's constant. The current results in a certain number of calcium ions entering the cellular compartment per unit time. The presence of the volume v in this equation turns this influx of calcium into a change in the calcium concentration in the compartment.

The rise in intracellular calcium due to a short calcium current pulse, such as might arise due to transmitter release activating NMDA channels at a synapse, or due to a back-propagating action potential activating voltage-gated calcium channels in the dendritic membrane, is illustrated in Figure 6.3. This short-lasting flux sees a rapid rise in the intracellular calcium concentration to a fixed level, since there are no mechanisms in this model to return the calcium to its resting level.

6.4.2 Calcium decay

Other fluxes, such as those due to membrane-bound pumps and buffering, act to restore calcium to its resting level following such an influx. A simple

model captures the phenomenon that the calcium concentration will always return to its resting value. This model describes calcium decay by a single time constant τ_{dec} (Traub and Llinás, 1977), giving:

$$\frac{d[\text{Ca}^{2+}]}{dt} = J_{\text{cc}} - \frac{[\text{Ca}^{2+}] - [\text{Ca}^{2+}]_{\text{res}}}{\tau_{\text{dec}}}, \quad (6.15)$$

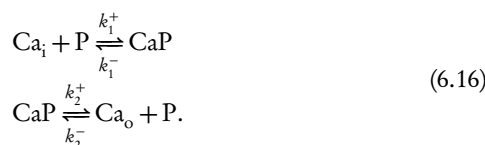
where $[\text{Ca}^{2+}]_{\text{res}}$ is the resting level. An example of such calcium decay is shown in Figure 6.3 (blue line).

This model is consistent with the calcium transients in cellular compartments imaged with fluorescent dyes. Clearance of calcium from small compartments, such as spine heads, may be quite rapid, with a time constant as small as 12 ms (Sabatini *et al.*, 2002). More complex models include the fluxes that remove calcium from a cellular compartment, such as pumps, buffering and diffusion. The sum of these fluxes may be approximated by this single exponential decay model.

6.4.3 Calcium extrusion

Membrane-bound pumps contribute to restoring resting levels of calcium by extruding calcium ions back through the membrane, moving them against their concentration gradient. Two pumps act to remove calcium from a cell. The calcium-ATPase pump (known as PMCA) is a high-affinity, low-capacity mechanism that can switch on rapidly following calcium entry through voltage-gated channels, and so plays a major role shaping dynamic changes in intracellular calcium. This pump is also responsible for uptake of calcium into intracellular stores (Section 6.5). The sodium-calcium exchanger acts as a low-affinity, high-capacity calcium pump that is largely responsible for maintaining resting calcium levels.

Complex pump models have been attempted, particularly of the sodium-calcium exchanger (Gabbiani *et al.*, 1994; De Schutter and Smolen, 1998). A relatively simple approach is to treat extrusion explicitly as a chemical reaction pathway. This involves the intracellular binding and extracellular unbinding of calcium to membrane-bound pump molecules P (Migliore *et al.*, 1995; Carnevale and Hines, 2006). Ca_i and Ca_o denote intracellular and extracellular calcium, respectively:



A high-affinity pump has a low dissociation constant K_m so that it reaches its half-maximal pump rate at a low calcium concentration. High capacity means that the maximum pump velocity V_{max} is large.

The external calcium concentration is typically much higher than intracellular calcium. Thus relative changes in external calcium during electrical activity are very small. If we assume extracellular calcium is effectively constant, the value of k_2^- can be set to zero. Then the pump flux can be modelled as an instantaneous function of the intracellular calcium concentration, described by a modified Michaelis-Menten relationship (e.g. Jaffe *et al.*, 1994):

$$J_{\text{pump}} = V_{\text{pump}} \frac{[\text{Ca}^{2+}]}{K_{\text{pump}} + [\text{Ca}^{2+}]} \quad (6.17)$$

Calcium extrusion has maximum velocity $V_{\text{pump}} = ak_2^+P_m/v$ (in units concentration per unit time; P_m is the number of pump molecules in a unit area of membrane) and is a function of the calcium concentration with half maximum flux at $K_{\text{pump}} = (k_1^- + k_2^+)/k_1^+$ (in units of concentration).

Little firm data is available about the properties of these pumps, but use of the simple Michaelis–Menten approach minimises the number of parameters that must be estimated. Pump model parameters are typically chosen to fine-tune the calcium transients in cellular compartments (Schiegg *et al.*, 1995). Estimates of pump velocity for the calcium–ATPase pump in hippocampal pyramidal cell models range over several orders of magnitude from around 10^{-13} to $10^{-10} \text{ mol cm}^{-2} \text{ s}^{-1}$, with half maxima at around $1 \mu\text{M}$ (Zador *et al.*, 1990; Jaffe *et al.*, 1994; Schiegg *et al.*, 1995). A much higher velocity of nearly $10^{-7} \text{ mol cm}^{-2} \text{ s}^{-1}$ has been used in a Purkinje cell model (De Schutter and Smolen, 1998). The sodium–calcium exchanger will have higher values for V_{max} and K_{pump} than the calcium–ATPase pump (Schiegg *et al.*, 1995).

An example of the effect of such a pump is given in Figure 6.3 (dashed line), which shows the response of a model with calcium influx and with removal via a pump and a constant background leak flux:

$$\frac{d[\text{Ca}^{2+}]}{dt} = J_{\text{cc}} - J_{\text{pump}} - J_{\text{leak}}. \quad (6.18)$$

This model is well-matched by the simple decay model with a suitable time constant; the calcium transients of the two models are indistinguishable in Figure 6.3 (blue and dashed lines).

6.5 Calcium stores

Intracellular calcium can be sequestered into stores in such structures as the endoplasmic reticulum (ER), with release into the cytoplasm being mediated by second-messenger pathways. Stores can have large capacity, with estimates of $[\text{Ca}^{2+}]$ in stores ranging from $100 \mu\text{M}$ to 5 mM . Uptake and release of calcium from these stores can result in intracellular calcium waves, or oscillations, on the timescale of seconds (Smith, 2001; Schuster *et al.*, 2002).

Uptake and release mechanisms are modelled in a similar fashion to the transmembrane fluxes. However, rather than modelling explicitly the physical structure of stores, such as the ER, it can be assumed that they occupy a fractional volume, with associated surface area, within the spatial compartment in which calcium concentration is being calculated. For example, the volume may be assumed to be in the form of a long, thin cylinder, thus enabling the store membrane surface area to be calculated (De Schutter and Smolen, 1998).

6.5.1 Calcium uptake

Uptake into the stores is via a Ca^{2+} –ATPase pump in the smooth ER membrane (known as SERCA). It binds two calcium ions for each ATP molecule, and so can be described by Michaelis–Menten kinetics with a Hill coefficient

of 2 (Blackwell, 2005):

$$J_{\text{up}} = V_{\text{up}} \frac{[\text{Ca}^{2+}]^2}{K_{\text{up}}^2 + [\text{Ca}^{2+}]^2}. \quad (6.19)$$

Uptake is across the surface area of the ER membrane α_{ER} . A limitation of this approach is that the uptake flux does not depend on the intrastore calcium concentration, even though empty stores have a higher uptake rate (De Schutter and Smolen, 1998).

6.5.2 Calcium release

The ER membrane contains calcium channels that are activated by calcium itself, leading to calcium-induced calcium release (CICR). The two major classes of channel correspond to membrane-bound receptors that bind ryanodine, and to receptors that are activated by inositol 1,4,5-triphosphate (IP_3). These different types of receptor tend to be localised in different parts of the ER and consequently different parts of a neuron. For example, in Purkinje cell spines, CICR is largely mediated by IP_3 receptors, whereas in hippocampal CA1 pyramidal cell spines, ryanodine receptors dominate (Berridge, 1998).

The calcium flux through the ER membrane into the cytoplasm is given by:

$$J_{\text{rel}} = V_{\text{rel}} R([\text{Ca}^{2+}])([\text{Ca}^{2+}]_{\text{store}} - [\text{Ca}^{2+}]), \quad (6.20)$$

where $R([\text{Ca}^{2+}])$ is the fraction of calcium channels in the open state, which depends on the cytoplasmic calcium concentration itself. $[\text{Ca}^{2+}]_{\text{store}}$ is the concentration of free calcium in the store.

This formulation is equivalent to the equations used to describe current flow through voltage-gated channels, where calcium concentration takes the place of voltage. The function R has been described by the same sort of mathematical formulations as for the opening of voltage-gated channels, principally either by Markov kinetic schemes or by Hodgkin–Huxley-style gating particles. The simplest approach is to use a Hill function of cytoplasmic calcium:

$$R([\text{Ca}^{2+}]) = \frac{[\text{Ca}^{2+}]^n}{K_{\text{rel}}^n + [\text{Ca}^{2+}]^n} \quad (6.21)$$

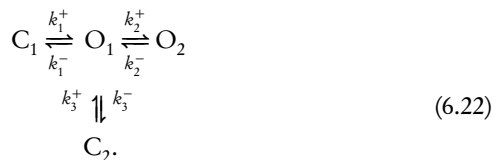
with a suitable Hill coefficient, n (Goldbeter *et al.*, 1990). Two problems with this model are that (1) CICR is not modulated instantaneously in concert with rapid changes in calcium (De Schutter and Smolen, 1998), so this steady state approach may not be accurate; and (2) it does not describe the IP_3 dependence of the IP_3 receptors. More complicated dynamic models for R are required.

Ryanodine receptor models

De Schutter and Smolen (1998) modify the Michaelis–Menten approach by assuming that the flux J_{rel} relaxes to the steady state value given by the Michaelis–Menten formulation for R , with a fixed time constant. In this way changes in cytoplasmic calcium due to, say, influx from outside the cell,

do not lead to instantaneous increases in calcium release from ryanodine-mediated stores. Also, they introduce a threshold so that the value of J_{rel} is set to zero below a certain cytoplasmic calcium concentration. This allows the store concentration, $[\text{Ca}^{2+}]_{\text{store}}$, to remain much higher than the cytoplasmic concentration, $[\text{Ca}^{2+}]$, which is the likely situation.

Other models use Markov kinetic schemes to capture the calcium dependence and dynamics of ryanodine receptor opening and slow inactivation, on the timescale of seconds. Keizer and Levine (1996) model the receptors assuming four states: two open states (O_1, O_2) and two closed states (C_1, C_2):



The forward rate coefficients k_1^+ and k_2^+ are dependent on the cytosolic calcium concentration, whereas the other rates are fixed. Increasing calcium drives the receptors more strongly into open states O_1 and O_2 . The open state O_1 can proceed slowly into closed state C_2 , providing the channel inactivation. Given a large population of receptors, we can interpret the states as indicating the fraction of available receptors in a given state. Thus the function R in our release flux Equation 6.20 is now:

$$R([\text{Ca}^{2+}]) = O_1 + O_2, \quad (6.23)$$

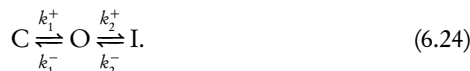
which is the fraction of receptors in an open state.

Tang and Othmer (1994) use a similar four-state kinetic scheme in which the inactivation step is also calcium dependent. Both models are phenomenological rather than directly trying to capture the states of the four subunits that make up a ryanodine receptor. As more becomes known about the receptors themselves, models based on the actual biophysics can be formulated.

IP₃ receptor models

Considerable attention has been paid to modelling IP₃-induced calcium release (De Young and Keizer, 1992; De Schutter and Smolen, 1998; Kuroda *et al.*, 2001; Schuster *et al.*, 2002; Fraiman and Dawson, 2004; Doi *et al.*, 2005) as it is likely to play a key role in intracellular calcium oscillations and long-term plasticity at synapses. The dynamics of the IP₃ receptors on the surface of a store are more complex than that of the ryanodine receptors. Firstly, in order to open, the receptors require binding of IP₃, as well as calcium. The receptor open probability exhibits a bell-shaped dependence on the intracellular calcium concentration and the receptors show a slow, calcium-dependent inactivation. As for the ryanodine receptor, the function R has been described by Markov kinetic schemes which capture various closed, open and inactivated states of the receptors, but also by phenomenological Hodgkin-Huxley-style equations for the open state.

A simple three-state kinetic scheme specifies that the receptors may be in a closed, open or inactivated state (Gin *et al.*, 2006):



The transition rate k_1^+ from closed to open depends on both IP_3 and calcium, and the rates k_1^- and k_2^+ out of the open state are calcium-dependent. Again treating the states as indicating the fraction of receptors in a given state, then the form of the function R to be used in Equation 6.20 is:

$$R(IP_3, [Ca^{2+}]) = O. \quad (6.25)$$

Doi *et al.* (2005) employ a more complex, seven-state kinetic model in which the receptors bind IP_3 and calcium sequentially to reach the open state. Binding of calcium alone leads to progressive entry into four inactivation states.

The process of rapid activation followed by inactivation is analogous to the voltage-dependent dynamics of sodium channels underlying action potential generation. Consequently, it is feasible to use Hodgkin-Huxley-style gating particles to describe these receptors. In this case the fraction of open receptors is a function of the state of activation and inactivation particles (Li and Rinzel, 1994; De Schutter and Smolen, 1998):

$$R(IP_3, [Ca^{2+}]) = m^3 b^3, \quad (6.26)$$

where the dynamics of m and b depend on the concentrations of IP_3 and intracellular calcium, rather than voltage.

All these models greatly simplify the actual dynamics of both ryanodine and IP_3 receptors. Other molecules may influence receptor sensitivity, such as cyclic ADP ribose for ryanodine receptors, and receptor opening may also be affected by intrastore calcium (Berridge, 1998; Berridge *et al.*, 2003).

6.6 | Calcium diffusion

So far we have considered our cellular compartment to contain a single pool of calcium in which the concentration is spatially homogeneous; a well-mixed pool. However, calcium concentrations close to a source may reach much higher values than for cellular regions far from the source. To capture such variations, it is necessary to model the transport of calcium through space by diffusion.

6.6.1 Two-pool model

An important requirement for many models of intracellular calcium is an accurate description of the calcium concentration immediately below the membrane. This is needed when modelling the electrical response of neuronal membrane containing calcium-activated potassium channels, which are likely to be activated only by a local calcium transient due to influx through nearby calcium channels. The simplest extension to our well-mixed model is to divide the compartment into two pools: a thin submembrane shell and

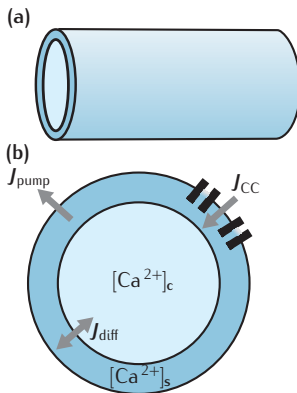


Fig. 6.4 Cylindrical compartment with a thin submembrane shell and a large central core.

the interior core (Figure 6.4). We need to add diffusion of calcium from the submembrane shell into the core to our existing models.

Due to Brownian motion of calcium molecules, there is an average drift of calcium from regions where there are many molecules to regions where there are fewer. In other words, calcium tends to flow down its concentration gradient; see Bormann *et al.* (2001), Koch (1999) and Section 2.2.2 for further details of this process. The resulting flux of calcium is given by Fick's first law (1855), which for a single spatial dimension x is (Equation 2.2):

$$J'_{\text{diff}} = -\alpha D_{\text{Ca}} \frac{d[\text{Ca}^{2+}]}{dx}, \quad (6.27)$$

where J'_{diff} is the rate of transfer of calcium ions across cross-sectional area α and D_{Ca} is the diffusion coefficient for calcium and has units of area per time. In what follows we consider the diffusional flux to be occurring between well-mixed pools of known volume. Dividing J'_{diff} by the pool volume will give the rate of change in concentration, or flux, of that pool, J_{diff} .

We consider only the diffusion of calcium along a single dimension x across known cross-sectional areas. In general, diffusion can occur in three dimensions and is properly described by a PDE that can be derived from Fick's first law (Koch, 1999). An overview of diffusion PDEs in single and multiple dimensions is given in Box 6.1.

In our two-pool model we need to calculate the flux due to diffusion between the submembrane shell and core compartment. To do this we make the simplest possible assumptions, resulting in a numerical scheme that approximates only crudely the underlying continuous diffusion PDE. The resulting model has limitations, which will become clear later. We assume that both pools are well-mixed, so that we can talk about the concentrations in the submembrane shell, $[\text{Ca}^{2+}]_s$, and the core, $[\text{Ca}^{2+}]_c$. The two compartments have volumes v_s and v_c , respectively, and diffusion takes place across the surface area α_{sc} of the cylindrical surface that separates them. These volumes and the surface area can be calculated from the length, diameter and thickness of the submembrane compartment.

A first order discrete version of Fick's first law gives the rate of change of calcium concentration in the cell core due to diffusion from the submembrane shell as:

$$J_{sc} = \frac{\alpha_{sc}}{v_c} D_{\text{Ca}} \frac{[\text{Ca}^{2+}]_s - [\text{Ca}^{2+}]_c}{\Delta_{sc}}, \quad (6.28)$$

where Δ_{sc} is the distance between the midpoints of the two compartments, which is the distance over which diffusion takes place. The flux from the core to the shell is in the opposite direction and is diluted into volume v_s . This results in our two-pool model being described by two coupled ODEs:

$$\begin{aligned} \frac{d[\text{Ca}^{2+}]_s}{dt} &= -D_{\text{Ca}} c_{sc} ([\text{Ca}^{2+}]_s - [\text{Ca}^{2+}]_c) + J_{cc} - J_{\text{pump}} - J_{\text{leak}} \\ \frac{d[\text{Ca}^{2+}]_c}{dt} &= D_{\text{Ca}} c_{cs} ([\text{Ca}^{2+}]_s - [\text{Ca}^{2+}]_c). \end{aligned} \quad (6.29)$$

Box 6.1 General diffusion

If we consider the flux of calcium into and out of an infinitesimally small volume over an infinitesimally small time period, from Equation 6.27 it can be shown that the rate of change in concentration over time and space is given by the PDE (Koch, 1999):

$$\frac{\partial[\text{Ca}^{2+}]}{\partial t} = D_{\text{Ca}} \frac{\partial^2[\text{Ca}^{2+}]}{\partial x^2}. \quad (\text{a})$$

This can easily be expanded to include diffusion in two or three dimensions. In Cartesian coordinates for three spatial dimensions:

$$\frac{\partial[\text{Ca}^{2+}]}{\partial t} = D_{\text{Ca}} \left(\frac{\partial^2[\text{Ca}^{2+}]}{\partial x^2} + \frac{\partial^2[\text{Ca}^{2+}]}{\partial y^2} + \frac{\partial^2[\text{Ca}^{2+}]}{\partial z^2} \right).$$

Particularly for the compartmental modelling of neurons, it is often useful to consider this equation with alternative coordinate systems. In cylindrical coordinates it becomes (Figure 6.8):

$$\frac{\partial[\text{Ca}^{2+}]}{\partial t} = D_{\text{Ca}} \left(\frac{\partial^2[\text{Ca}^{2+}]}{\partial r^2} + \frac{1}{r} \frac{\partial[\text{Ca}^{2+}]}{\partial r} + \frac{1}{r^2} \frac{\partial^2[\text{Ca}^{2+}]}{\partial \Theta^2} + \frac{\partial^2[\text{Ca}^{2+}]}{\partial x^2} \right)$$

for longitudinal distance x , radial distance r and axial rotation Θ .

As we are usually interested in axisymmetric radial diffusion within a compartment, or longitudinal diffusion between compartments, one dimension is sufficient for most purposes. It is only necessary to go to two or three dimensions if radial and longitudinal diffusion are being considered at the same time.

Longitudinal diffusion is handled in Cartesian coordinates by Equation (a), with x defining the longitudinal axis of the cylinder.

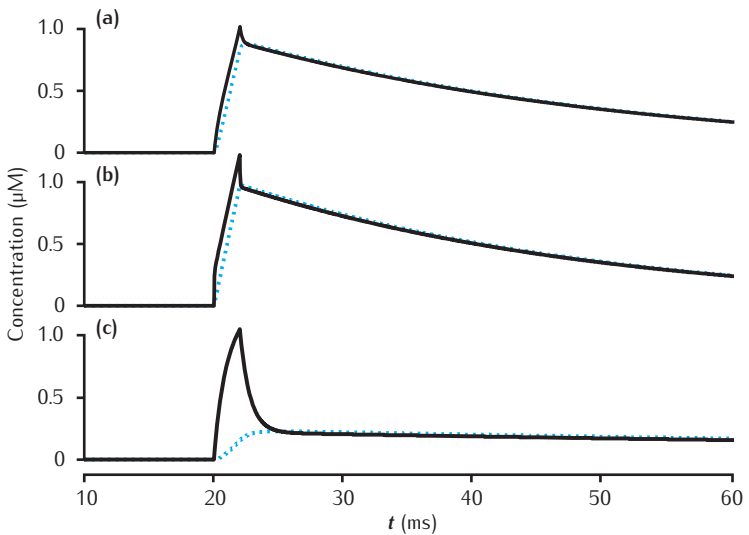
Radial diffusion is best handled in cylindrical coordinates. If we assume there is no concentration gradient in the Θ or x directions, the cylindrical diffusion equation reduces to:

$$\frac{\partial[\text{Ca}^{2+}]}{\partial t} = D_{\text{Ca}} \left(\frac{\partial^2[\text{Ca}^{2+}]}{\partial r^2} + \frac{1}{r} \frac{\partial[\text{Ca}^{2+}]}{\partial r} \right).$$

The coupling coefficient c_{sc} for movement from the shell to the core is $c_{sc} = a_{sc}/v_s \Delta_{sc}$, and that from the core to the shell is $c_{cs} = a_{sc}/v_c \Delta_{sc}$. Calcium may enter the submembrane shell through voltage-gated channels with flux J_{cc} . It is extruded across the membrane, with flux J_{pump} , in addition to diffusing into the cell core.

Example calcium transients from this model are shown in Figure 6.5. For a small compartment of 1 μm diameter, the shell and core concentrations are always similar, with a small peak in the submembrane concentration that is not mirrored in the core (Figure 6.5a). This peak is larger when the shell is very thin (0.01 μm ; Figure 6.5b). It might be acceptable to model this compartment very approximately as containing just a single pool of calcium. However, this is not possible when the compartment has a larger diameter of 4 μm (Figure 6.5c). In this case, calcium influx into the shell compartment is

Fig. 6.5 Calcium transients in the submembrane shell (black lines) and the compartment core (blue dashed lines) of a two-pool model that includes a membrane-bound pump and diffusion into the core. Initial concentration $C_{\text{Ca}0}$ is $0.05 \mu\text{M}$ throughout. Calcium current as in Figure 6.3. Compartment length is $1 \mu\text{m}$. (a) Compartment diameter is $1 \mu\text{m}$, shell thickness is $0.1 \mu\text{m}$; (b) Compartment diameter is $1 \mu\text{m}$, shell thickness is $0.01 \mu\text{m}$; (c) Compartment diameter is $4 \mu\text{m}$, shell thickness is $0.1 \mu\text{m}$. Diffusion: $D_{\text{Ca}} = 2.3 \times 10^{-6} \text{ cm}^2 \text{ s}^{-1}$; Pump: $V_{\text{pump}} = 10^{-11} \text{ mol cm}^{-2} \text{ s}^{-1}$, $K_{\text{pump}} = 10 \mu\text{M}$, $J_{\text{leak}} = V_{\text{pump}} * C_{\text{Ca}0} / (K_{\text{pump}} + C_{\text{Ca}0})$.



more rapid than diffusion from the shell to the core, resulting in a very large peak in the submembrane calcium concentration, which is then brought into equilibrium with the core concentration by diffusion. The core concentration never reaches levels near that of the submembrane shell as the calcium influx is diluted in the large compartmental volume.

Typically, calcium influx through voltage- or ligand-gated channels may be more rapid than the dispersal of calcium by diffusion. Hence the calcium concentration in the cellular compartment in which an influx occurs will reach a peak before diffusion, and other dispersion mechanisms, such as pumps, begin to restore the resting calcium level. This peak will be determined by the compartment volume. Thus the identical influx of calcium will cause a greater increase in concentration in a smaller compartment. Therefore, compartment sizes must be chosen with reference to the range of calcium influence that is being modelled; for example, the average distance of calcium-activated potassium channels from the voltage-gated calcium channels through which the necessary calcium enters.

6.6.2 Three-pool model

In certain situations it is necessary to subdivide the submembrane compartment further. For example, with calcium-activated potassium channels, a complication arises in that different types of such channel are apparently activated by different pools of calcium. The I_C current (Section 5.6) switches on rapidly due to calcium influx. Hence the underlying ion channels presumably are colocated with calcium channels, whereas the I_{AHP} current (Section 5.6) is much more slowly activated, probably due to these potassium channels being located further from the calcium channels. Multiple submembrane pools can be accommodated relatively simply, as proposed by Borg-Graham (1999).

In a way that does not complicate the model greatly, the submembrane shell is divided into two pools. The first pool (*local*: volume v_l) corresponds to a collection of membrane domains that are near calcium channels, while

the second pool (*submembrane*: volume v_s) consists of the remaining submembrane space that is further from the calcium channels (Figure 6.6). Calcium influx is directly into the local pool, with diffusion acting to move calcium into the submembrane pool. We define the volume of the local pool to correspond to some small fraction α_l ($\approx 0.001\%$) of the membrane surface area. For a thin submembrane shell the two volumes are approximately:

$$v_l = \alpha_l a_s \Delta_s, \quad v_s = (1 - \alpha_l) a_s \Delta_s, \quad (6.30)$$

where a_s is the surface area and Δ_s is the thickness of the submembrane shell.

We have only defined a volume for the local pool, but not a specific geometry. Diffusion between the local and submembrane pools must occur across an effective diffusive surface area. Without an explicit geometry for the local pool, we define the surface area between the pools as $a_{ls} = \alpha_l a_s \Delta_s$, with interdigititation coefficient α_{ls} per unit length; usually set to 1.

Diffusion also takes place between the submembrane volume v_s and the cell core v_c , but not, we assume, between the local pool and cell core. This occurs across the surface area separating the submembrane pool from the cell core, $a_{sc} = (1 - \alpha_l) a_s$.

The complete model is described by the following system of ODEs:

$$\begin{aligned} \frac{d[Ca^{2+}]_l}{dt} &= -D_{Ca} c_{sl} ([Ca^{2+}]_l - [Ca^{2+}]_s) + J_{cc} \\ \frac{d[Ca^{2+}]_s}{dt} &= D_{Ca} c_{ls} ([Ca^{2+}]_l - [Ca^{2+}]_s) \\ &\quad - D_{Ca} c_{cs} ([Ca^{2+}]_s - [Ca^{2+}]_c) - J_{pump} - J_{leak} \\ \frac{d[Ca^{2+}]_c}{dt} &= D_{Ca} c_{sc} ([Ca^{2+}]_s - [Ca^{2+}]_c). \end{aligned} \quad (6.31)$$

The local pool corresponds to the surface membrane containing calcium channels, so calcium influx J_{cc} is directly into the local pool. The submembrane shell contains the remaining surface membrane in which membrane-bound pumps exist to restore resting calcium levels, J_{pump} . The diffusive coupling coefficients are again of the form $c_{ij} = a_{ij}/v_j \Delta_{ij}$, where a_{ij} is the effective area between volumes i and j , v_j is the volume into which calcium is diluted and Δ_{ij} is the distance between the source and destination volumes.

An example of the calcium transients in all three pools is shown in Figure 6.7. The transients in the submembrane (Figure 6.7b) and the core (Figure 6.7c) pools match those of the two-pool model. However, the calcium concentration in the local pool (Figure 6.7a) is very rapid and reaches a much higher level. Thus the colocalised potassium channels are driven by a very different calcium transient from that seen in an average submembrane shell.

6.6.3 Radial diffusion

The assumption in the two- and three-pool models that the large central core of the cellular compartment is well-mixed may be reasonable for small compartments, but could be highly inaccurate for larger diameters. It may be necessary to divide the entire intracellular space into a number of thin shells, with diffusion of calcium taking place between shells, in the same

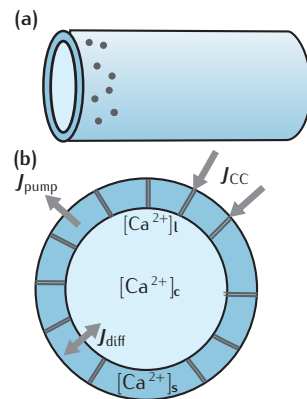


Fig. 6.6 Three-pool model of intracellular calcium. The grey dots on the surface and thin lines across the submembrane shell represent the local pool of the membrane surrounding calcium channels.

Fig. 6.7 Calcium transients in (a) the potassium channel colocalised pool, (b) the larger submembrane shell, (c) the compartment core in a three-pool model. Note that in (a) the concentration is plotted on a different scale. Compartment 1 μm in diameter with 0.1 μm thick submembrane shell; colocalised membrane occupies 0.001% of the total membrane surface area. Calcium influx into the colocalised pool. Calcium current, diffusion and membrane-bound pump parameters as in Figure 6.5.

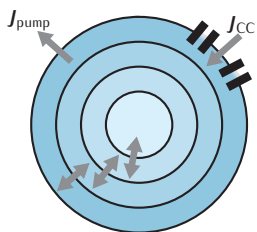
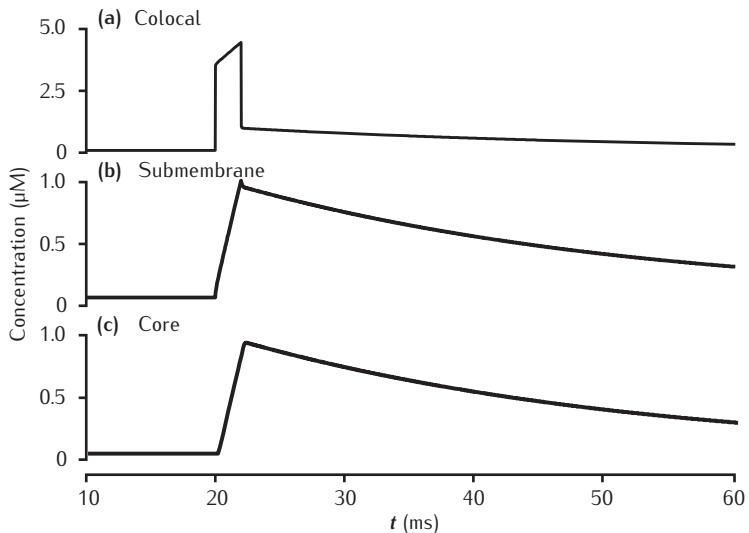


Fig. 6.8 Multiple shells for modelling radial diffusion of intracellular calcium.

way that we have so far considered diffusion from the submembrane shell into the core (Figure 6.8). This will then capture radial intracellular gradients in calcium, and also improve the accuracy of the submembrane calcium transient due to more accurate modelling of diffusion of incoming calcium away from the submembrane region.

Examples of submembrane calcium transients for different total numbers of shells, but with the same submembrane shell thickness, are shown in Figure 6.9. The remaining shells equally divide up the compartment interior. Our previous simple model containing only the submembrane shell and the cell core provides a reasonably accurate solution for both submembrane and core concentrations for a small dendritic compartment of 1 μm diameter (not shown). However, if the diameter is increased to 4 μm , at least four shells are required to model accurately the dynamics of diffusion of calcium into the interior, with a small improvement being gained by using 11 shells (Figure 6.9).

In particular, the submembrane concentration is exaggerated in the two-pool model as in this case diffusion into the interior is slow due to the gradient being calculated over the entire distance of 2 μm from the membrane to the compartment centre. With more shells, calcium is calculated as diffusing down a steeper gradient from the membrane to the centre of the nearest interior shell, a distance of 0.48 μm with 4 shells and 0.2 μm with 11 shells.

As the submembrane concentration is often the most critical to model accurately, a reasonable number of shells is required here, even if the concentration in only the submembrane shell is used by other model components, such as calcium-activated potassium channels. A good rule of thumb is that interior shells should all have the same thickness, Δr , which is twice the thickness of the submembrane shell. The innermost core shell should have diameter Δr (Carnevale and Hines, 2006). Our 11-shell model implements this criterion for the 4 μm diameter compartment with a 0.1 μm thick submembrane shell. However, this may lead to an excessive number of shells for large compartments with a thin submembrane shell. As shown here, smaller

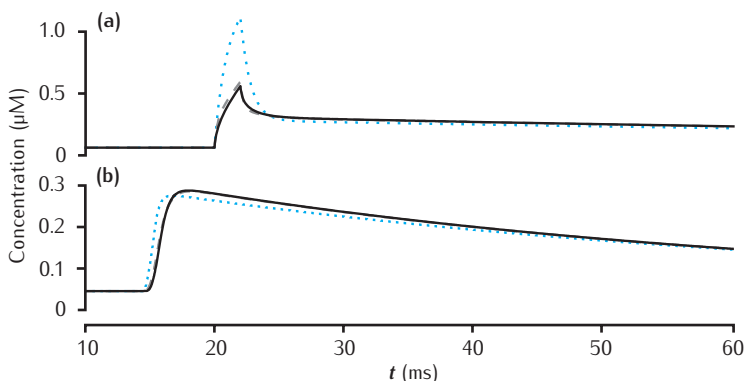


Fig. 6.9 Calcium transients in the (a) submembrane shell and (b) cell core (central shell) for different total numbers of shells. Black line: 11 shells. Grey dashed line: 4 shells. Blue dotted line: 2 shells. Diameter is 4 μm and the submembrane shell is 0.1 μm thick. Other shells equally subdivide the remaining compartment radius. All other model parameters are as in Figure 6.5.

numbers of shells may still provide good solutions. It is not possible to prescribe the optimum choice of shell thickness in any given situation, and so some testing with different numbers of shells is recommended.

6.6.4 Longitudinal diffusion

In addition to radial diffusion of calcium from the membrane to the compartment core, calcium may also diffuse longitudinally along a section of dendrite (Figure 6.10). Diffusion into a cylindrical compartment i from neighbouring compartments k and j is given by:

$$\frac{d[\text{Ca}^{2+}]_j}{dt} = D_{\text{Ca}} c_{ij} ([\text{Ca}^{2+}]_i - [\text{Ca}^{2+}]_j) + D_{\text{Ca}} c_{jk} ([\text{Ca}^{2+}]_k - [\text{Ca}^{2+}]_j). \quad (6.32)$$

The diffusional coupling coefficients are again of the form $c_{ij} = a_{ij}/v_j \Delta_{ij}$, where a_{ij} is the effective diffusional area between spaces i and j , v_j is the volume of the space into which calcium flows and Δ_{ij} is the distance between the source and destination volumes.

Figure 6.11 shows examples of calcium gradients along the length of a dendrite. In these examples, a 10 μm long segment of dendrite is divided into ten 1 μm long compartments, each of which contains four radial shells. Longitudinal diffusion is calculated along the length for each of these shells, in parallel with radial diffusion between the shells. The submembrane calcium concentration drops rapidly with distance from the calcium source, which is 0.5 μm along the dendrite. For a dendrite of 1 μm diameter, peak calcium is only 34% of the amplitude in the source compartment at a distance of 1.5 μm along the dendrite, which is 1 μm from the source. For a 4 μm diameter dendrite, the peak 1.5 μm along is only 24% of the source amplitude. However, the longitudinal diffusion clearly shapes the submembrane calcium transient in the source compartment. In Figure 6.11, compare the solid black lines with the dotted blue lines from the model without longitudinal diffusion. The peak concentration is reduced and the time course of calcium decay is significantly faster. Thus it may be necessary to include longitudinal diffusion to accurately capture the calcium transient resulting from a local calcium influx.

Under certain assumptions it is possible to calculate a space constant for diffusion that is equivalent to the electrical space constant for voltage (Box 6.4). Typically the space constant of diffusion is much shorter than

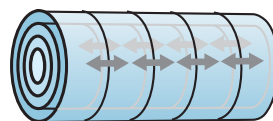
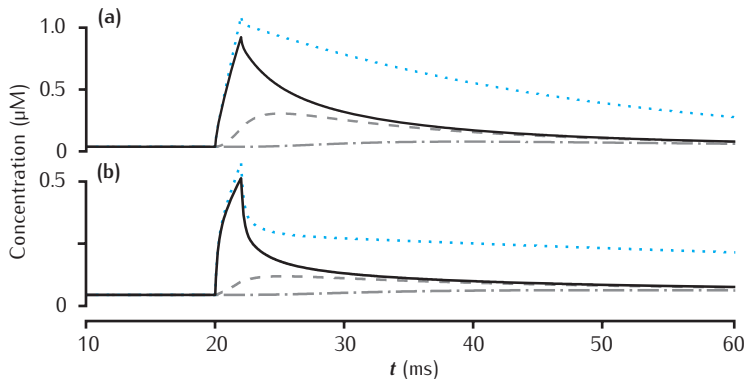


Fig. 6.10 Longitudinal diffusion of intracellular calcium between compartments along the length of a neurite.

Fig. 6.11 Longitudinal diffusion along a 10 μm length of dendrite. Plots show calcium transients in the 0.1 μm thick submembrane shell at different positions along the dendrite. Solid black line: 0.5 μm ; dashed: 1.5 μm ; dot-dashed: 4.5 μm . (a) Diameter is 1 μm . (b) Diameter is 4 μm . Calcium influx occurs in the first 1 μm length of dendrite only. Each of ten 1 μm long compartments contains four radial shells. Blue dotted line: calcium transient with only radial (and not longitudinal) diffusion in the first 1 μm long compartment. All other model parameters as in Figure 6.5.



the electrical space constant, and decreases with decreasing diameter. Thus diffusion along very thin cables, such as the neck of a spine, around 0.1 μm in diameter, is often ignored in models. However, as illustrated in Figure 6.11, longitudinal diffusion will influence local calcium transients in cables of the thickness of typical dendrites and axons (of the order of 1 μm).

6.6.5 Numerical calculation of diffusion

The numerical solution of diffusion equations is a complex subject, the full details of which are beyond the scope of this book. A brief outline of numerical integration techniques is given in Appendix B.1. Though this outline uses the membrane voltage equation as an example, this equation has the same form as the equation for the 1D diffusion of calcium. Details of the diffusional coupling coefficients that arise in various geometries of interest is given in Box 6.2. More detailed treatments of the numerical solution of the diffusion equation, including how it can be done in multiple dimensions, are to be found in De Schutter and Smolen (1998), Bormann *et al.* (2001) and Smith (2001).

6.6.6 Electrodiffusion and electrogenesis

Throughout this chapter we have been dealing with mechanisms that lead to the movement of ions, in this case calcium. Such movement generates electrical currents and, in turn, is affected by electrical fields (Chapter 2). Both of these effects have been neglected in our treatment of calcium fluxes. In the treatment of the electrical properties of a neuron, typically the actual movement of ions and resulting concentration gradients are ignored in calculating electrical current flow.

In many instances it is reasonable to neglect the effects of potential gradients when dealing with calcium concentrations, and concentration gradients when dealing with electrical currents (De Schutter and Smolen, 1998). However, it is possible to include these effects in our models explicitly, and this is sometimes important. For example, electrical currents due to ionic pumps can be significant. In Box 6.3 we consider the electrodiffusion of ions. It should be noted that including the effects of electrodiffusion in a model adds significantly to the computational load, as well as to the model complexity.

Box 6.2 | Diffusion coupling coefficients

The diffusional coupling coefficient from cellular compartment i to compartment j is:

$$c_{ij} = \frac{a_{ij}}{v_j \Delta_{ij}},$$

where a_{ij} is the surface area between compartments i and j , v_j is the volume of compartment j , and Δ_{ij} is the distance between the compartment centre points. These coefficients depend on the geometry being modelled and can take quite simple forms.

For axisymmetric radial diffusion into a cylinder of length Δx , consider two adjacent shells, both of thickness Δr , with the surface between them, the inner surface of shell i and the outer surface of cell j , having radius r . Then the surface area between the shells is $a_{ij} = 2\pi r \Delta x$. The volume of shell j is $v_j = \pi r^2 \Delta x - \pi(r - \Delta r)^2 \Delta x = \pi \Delta r (2r - \Delta r) \Delta x$. This results in the coupling coefficient:

$$c_{ij} = \frac{2r}{\Delta r^2 (2r - \Delta r)}.$$

For longitudinal diffusion along a cylinder of uniform radius r , the cross-sectional area between two compartments is always $a = \pi r^2$. If each compartment has length Δx , then the compartment volume is $v = a \Delta x$ and the coupling coefficient between any two compartments is:

$$c = \frac{a}{a \Delta x \cdot \Delta x} = \frac{1}{\Delta x^2}.$$

6.7 | Calcium buffering

Calcium interacts with a variety of other molecules in the intracellular space. These molecules act as buffers to the free diffusion of calcium and can strongly affect the spatial and temporal characteristics of the free calcium concentration. Endogenous neuronal calcium buffers include calmodulin, calbindin and parvalbumin (Koch, 1999; Smith, 2001; Berridge *et al.*, 2003). Visualising intracellular calcium requires the addition of a fluorescent dye to a neuron, such as Fura-2. Such dyes bind calcium and are thus calcium buffers that also strongly affect the level of free calcium. Models of intracellular calcium based on fluorescent dye measurements of calcium transients need to account for this buffering effect. Other exogenous buffers include EGTA (ethylene glycol tetraacetic acid) and BAPTA (bis(aminophenoxy)ethanetetraacetic acid). Explicitly modelling these buffers is necessary for comparison of models with experiments in which such buffers are used.

The second order interaction of calcium and a buffer, B, in a single, well-mixed pool is given by the kinetic scheme:



Box 6.3 | Electrodiffusion

Ions move down both their potential gradient and their concentration gradient. Changes in ionic concentrations in intracellular compartments also affect the local membrane potential. Therefore, electrical currents and ionic concentrations are intimately linked and ideally should be treated simultaneously. The effects of electrodiffusion have been treated in detail by Qian and Sejnowski (1989); see also useful discussions in De Schutter and Smolen (1998) and Koch (1999).

Consider longitudinal movement only of calcium along a cylindrical section of neurite. The calcium concentration as a function of time and space is properly derived from the Nernst–Planck equation (Koch, 1999), resulting in:

$$\frac{\partial[\text{Ca}^{2+}]}{\partial t} = D_{\text{Ca}} \frac{\partial^2[\text{Ca}^{2+}]}{\partial x^2} + D_{\text{Ca}} \frac{z_{\text{Ca}} F}{RT} \frac{\partial}{\partial x} \left([\text{Ca}^{2+}] \frac{\partial V}{\partial x} \right) - J_{\text{pump}} - J_{\text{leak}},$$

where now the simple diffusion of calcium along the cylinder (Box 6.1) is augmented by drift down the potential gradient (the second term on the right-hand side) and by the transmembrane flux, $J_{\text{pump}} + J_{\text{leak}}$, due to voltage-gated ion channels and pumps (De Schutter and Smolen, 1998).

To solve this equation we need an expression for the membrane potential V as a function of local ionic concentrations. Each ionic species, including calcium, contributes an amount of electrical charge, depending on its concentration. The local membrane potential is determined by the total charge contributed by all ionic species X_i (Qian and Sejnowski, 1989):

$$V(x, t) = V_{\text{rest}} + \frac{rF}{2C_m} \sum_i z_i ([X_i](x, t) - [X_i]_{\text{rest}})$$

for neurite cylindrical radius r , membrane capacitance C_m , ionic valence z_i and ionic concentrations $[X_i]$. For a typical intraneuronal environment, which ionic species should be included in this sum is debatable (De Schutter and Smolen, 1998).

Electrodiffusion can be implemented as a straightforward extension to standard compartmental modelling (Qian and Sejnowski, 1989), but it is computationally highly expensive. Concentration changes, particularly of calcium, can be large in small neural structures, such as spines (Box 2.3). Thus, it is important to use the GHK equation (Section 2.4) for computing transmembrane currents. However, given the small space constant of diffusion, implementation of the full electrodiffusion model may not be necessary (De Schutter and Smolen, 1998).

in which a single calcium ion binds with a single molecule of free buffer to produce calcium-bound buffer, CaB , with association and dissociation rate coefficients k^+ and k^- , respectively. This is the most basic buffering scheme. Common buffers, such as calmodulin, may contain multiple calcium binding sites, and so are better described by higher order reaction schemes (Koch, 1999), but accurate estimates of all rate coefficients in such schemes are not

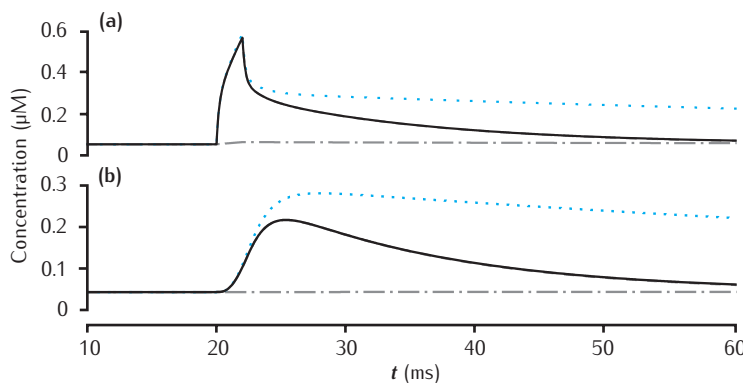


Fig. 6.12 Calcium transients in (a) the $0.1\text{ }\mu\text{m}$ thick submembrane shell and (b) the cell core of a single dendritic compartment of $4\text{ }\mu\text{m}$ diameter with four radial shells. Slow buffer with initial concentration $50\text{ }\mu\text{M}$, forward rate $k^+ = 1.5\text{ }\mu\text{Ms}^{-1}$ and backward rate $k^- = 0.3\text{ s}^{-1}$. Blue dotted line: unbuffered calcium transient. Grey dashed line (hidden by solid line): excess (EBA) buffer approximation. Grey dash-dotted line: rapid (RBA) buffer approximation. Binding ratio $\kappa = 250$. All other model parameters as in Figure 6.5.

readily available. In the following treatment we consider only this basic second order interaction.

Our intracellular model for calcium concentration now needs a term to account for the reaction with buffer. In addition, the model needs to account for the free, $[B]$, and bound, $[\text{CaB}]$, buffer concentrations. For a particular well-mixed cellular compartment this leads to the system of coupled ODEs:

$$\begin{aligned}\frac{d[\text{Ca}^{2+}]}{dt} &= -k^+[\text{Ca}^{2+}][B] + k^-[\text{CaB}] + J_{\text{Ca}} \\ \frac{d[B]}{dt} &= -k^+[\text{Ca}^{2+}][B] + k^-[\text{CaB}] + J_{\text{diffB}} \\ \frac{d[\text{CaB}]}{dt} &= k^+[\text{Ca}^{2+}][B] - k^-[\text{CaB}] + J_{\text{diffCaB}}.\end{aligned}\quad (6.34)$$

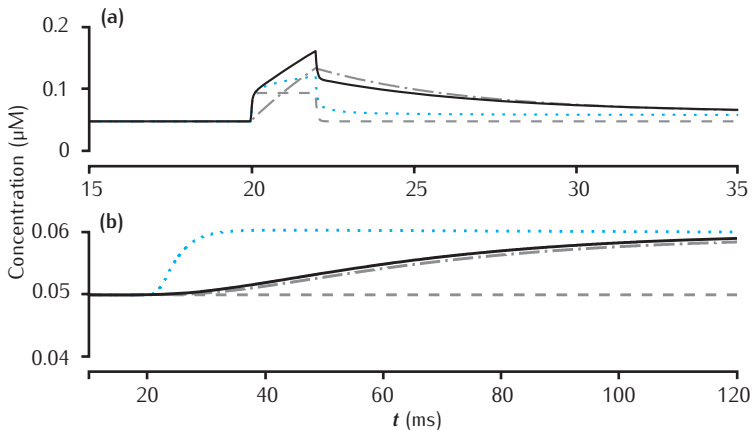
The calcium flux J_{Ca} lumps together all the possible sources and sinks for calcium, including diffusion between compartments. Both free and bound buffer may also diffuse with fluxes J_{diffB} and J_{diffCaB} , respectively. However, it is often assumed that free and bound buffer have the same diffusion coefficient D_{buf} , which is reasonable if the buffer molecules are much larger than calcium. This model can be easily extended to include multiple buffers with different characteristics. The cytoplasm may contain both fixed ($D_{\text{buf}} = 0$) and mobile ($D_{\text{buf}} \neq 0$) buffers.

The effect of buffers on calcium gradients can be drastic, depending on the buffer concentration and its binding rate. Figures 6.12 and 6.13 show the effects of both fixed and mobile buffers with slow and fast binding rates, respectively. The buffer is present in $50\text{ }\mu\text{M}$ concentration and the slow buffer has a higher affinity, with dissociation constant $K_B = k^-/k^+ = 0.2\text{ }\mu\text{M}$, than the fast buffer, with $K_B = 2\text{ }\mu\text{M}$.

The slow buffer reduces the calcium transient marginally in the submembrane shell and more significantly in the cell core. It also speeds up the return to resting levels, compared to the unbuffered case (Figure 6.12, blue dotted line). This situation is well captured by the excess buffer approximation, detailed in Section 6.7.1.

The fast buffer drastically reduces the peak amplitude and sharpens the submembrane calcium transient. However, now the return to equilibrium throughout the cell compartment is greatly slowed. The initial calcium

Fig. 6.13 Calcium transients in (a) the $0.1\text{ }\mu\text{m}$ thick submembrane shell and (b) the cell core of a single dendritic compartment of $4\text{ }\mu\text{m}$ diameter with four radial shells. Fast buffer with initial concentration $50\text{ }\mu\text{M}$, forward rate $k^+ = 500\text{ }\mu\text{Ms}^{-1}$ and backward rate $k^- = 1000\text{ s}^{-1}$. Black solid line: fixed buffer. Blue dotted line: mobile buffer with diffusion rate $D_{\text{buf}} = 1 \times 10^{-6}\text{ cm}^2\text{ s}^{-1}$. Grey dashed line: excess (EBA) approximation. Grey dash-dotted line: rapid (RBA) buffer approximation. Binding ratio $\kappa = 25$. All other model parameters as in Figure 6.5.



influx is largely absorbed by the submembrane buffer. The slow equilibration throughout the compartment and return to resting calcium levels is dictated by the time course of unbinding of calcium from the buffer. The mobility of the buffer has little effect when the buffer is slow (not shown), but increases the apparent diffusion rate of calcium when binding is fast, resulting in a faster rise in calcium in the core compartment (Figure 6.13, blue dotted line). These fast buffer effects can be derived mathematically by considering a rapid buffer approximation, as described in Section 6.7.2.

Full modelling of buffering, which might include a number of different buffers and buffers with multiple binding sites, may involve a large number of differential equations per compartment. Some specific assumptions about buffers can result in greatly simplified models of buffering that require modifications only to the ODE for calcium and do not require explicit ODEs for buffer concentrations at all. Two important simplifications are the excess buffer approximation (EBA) and the rapid buffer approximation (RBA).

6.7.1 Excess buffer approximation

An approximation that may be valid for endogenous buffers and often is valid for exogenous buffers is that the buffer is in excess and cannot be saturated by incoming calcium (Smith, 2001). In the steady state, when there is no influx of calcium, then the concentrations of free calcium and unbound buffer will reach resting levels, with:

$$[B]_{\text{res}} = \frac{K_B[B]_{\text{tot}}}{K_B + [Ca^{2+}]_{\text{res}}}, \quad [CaB]_{\text{res}} = \frac{[Ca^{2+}]_{\text{res}}[B]_{\text{tot}}}{K_B + [Ca^{2+}]_{\text{res}}}, \quad (6.35)$$

where the dissociation constant $K_B = k^-/k^+$, and $[B]_{\text{tot}} = [B] + [CaB]$.

The EBA assumes that both $[B]$ and $[CaB]$ are constant, with values $[B]_{\text{res}}$ and $[CaB]_{\text{res}}$, even during calcium influx. Substituting these values into the first ODE in Equation 6.34 gives:

$$\frac{d[Ca^{2+}]}{dt} = -k^+[Ca^{2+}][B]_{\text{res}} + k^-[CaB]_{\text{res}} + J_{Ca}. \quad (6.36)$$

From Equation 6.35, it can be shown that $k^-[\text{CaB}]_{\text{res}} = k^+[\text{Ca}^{2+}]_{\text{res}}[\text{B}]_{\text{res}}$. Substituting this into Equation 6.36 gives:

$$\frac{d[\text{Ca}^{2+}]}{dt} = -k^+[\text{B}]_{\text{res}}([\text{Ca}^{2+}] - [\text{Ca}^{2+}]_{\text{res}}) + J_{\text{Ca}}. \quad (6.37)$$

This is the same as the simple calcium decay model (Equation 6.15) with $\tau_{\text{dec}} = 1/(k^+[\text{B}]_{\text{res}})$, and so this simpler model can be used.

Figure 6.12, in which the slow buffer is in excess, illustrates that this approximation can capture well the time course of the initial calcium transient as it enters a cellular compartment and binds to the buffer. However, it cannot capture the complex dynamics of calcium binding and unbinding from the buffer interacting with diffusion between cellular compartments, which is prominent with the fast buffer (Figure 6.13).

6.7.2 Rapid buffer approximation

A complementary approximation is that the buffering of calcium is so fast that the calcium and buffer concentrations are essentially always in equilibrium with each other, so that:

$$[\text{B}] = \frac{K_B[\text{B}]_{\text{tot}}}{K_B + [\text{Ca}^{2+}]}, \quad [\text{CaB}] = \frac{[\text{Ca}^{2+}][\text{B}]_{\text{tot}}}{K_B + [\text{Ca}^{2+}]} \quad (6.38)$$

Calculating the differential of bound calcium with respect to free calcium gives the **calcium binding ratio**, κ :

$$\kappa = \frac{d[\text{CaB}]}{d[\text{Ca}^{2+}]} = \frac{K_B[\text{B}]_{\text{tot}}}{(K_B + [\text{Ca}^{2+}])^2}, \quad (6.39)$$

which indicates how much calcium entering a cellular compartment becomes bound to the buffer. If calcium concentrations are much less than the dissociation constant K_B this ratio is approximately $\kappa \approx [\text{B}]_{\text{tot}}/K_B$.

In neuronal cells, the binding ratio κ is typically large, on the order of 20 or more, indicating that 95% or more of the calcium is bound to intracellular buffers. For the examples in Figures 6.12 and 6.13, for the slow buffer $\kappa = 250$ and for the fast buffer $\kappa = 25$.

For a fixed buffer, where $D_{\text{buf}} = 0$ and hence $J_{\text{diffB}} = 0$ and $J_{\text{diffCaB}} = 0$:

$$\frac{d[\text{Ca}^{2+}]}{dt} + \frac{d[\text{CaB}]}{dt} = J_{\text{Ca}}. \quad (6.40)$$

Using Equation 6.39 we can write:

$$\frac{d[\text{CaB}]}{dt} = \frac{d[\text{CaB}]}{d[\text{Ca}^{2+}]} \frac{d[\text{Ca}^{2+}]}{dt} = \kappa \frac{d[\text{Ca}^{2+}]}{dt}. \quad (6.41)$$

Putting this into Equation 6.40 leads to:

$$\frac{d[\text{Ca}^{2+}]}{dt} = \frac{J_{\text{Ca}}}{1 + \kappa}. \quad (6.42)$$

The binding ratio κ describes how rapid buffering attenuates the influence of calcium influx J_{Ca} on the free calcium concentration. The calcium influx includes the diffusion of free calcium between cellular compartments,

and so the effective diffusion coefficient of free calcium is reduced to:

$$D_{\text{eff}} = \frac{D_{\text{Ca}}}{1 + \kappa}. \quad (6.43)$$

If the buffer can also diffuse, then it can be shown that this effective diffusion coefficient becomes approximately (Wagner and Keizer, 1994; Zador and Koch, 1994; De Schutter and Smolen, 1998; Koch, 1999; Smith, 2001):

$$D_{\text{eff}} = \frac{D_{\text{Ca}} + \kappa D_{\text{buf}}}{1 + \kappa}. \quad (6.44)$$

Even if the buffer diffuses more slowly than calcium ($D_{\text{buf}} < D_{\text{Ca}}$), which is likely as the buffers are generally much larger molecules, the effective diffusion of calcium is increased by the movement of calcium bound to buffer molecules.

Figure 6.13 shows that the RBA can capture something of the fast submembrane transient and follows well the slow cell core concentration. It fails to capture the dynamics of calcium with a slow buffer, drastically overestimating the effect of the buffer (Figure 6.12).

Use of the RBA allows the definition of space and time constants for the calcium concentration in the presence of diffusion and buffering, in analogy to the electrical space and time constants. Details of these definitions are given in Box 6.4.

6.7.3 Calcium indicator dyes

Experimental data concerning calcium levels in cellular compartments come from fluorescence measurements using calcium indicator dyes in tissue slice preparations. A model that seeks to match such results needs to include the binding of calcium to the indicator dye and how this affects the fluorescence of the dye. The rapid buffer approximation provides a simple model which can be used to extract information about peak calcium changes and endogenous buffer capacity from the imaging data.

Having matched the *in vitro* experimental results, the dye can be removed from the model. Now the model can be used to determine free calcium transients in response to a stimulus for the *in vivo* situation. This is ultimately the most interesting and explanatory use of a model, providing predictions about situations that cannot be explored experimentally.

Fluorescence measurements from calcium indicator dyes are taken at either one or two wavelengths, and at different temporal and spatial resolutions, depending on the dye and imaging equipment being used. We consider how to interpret a single wavelength fluorescence measurement, following the treatment of Maravall *et al.* (2000).

It is assumed that the fluorescence f is related linearly to the free calcium indicator dye concentration $[F]$ and the calcium-bound dye concentration $[CaF]$ via:

$$f = S_F[F] + S_{FCa}[CaF] = S_F[F]_{\text{tot}} + (S_{FCa} - S_F)[CaF], \quad (6.45)$$

where the total dye concentration is $[F]_{\text{tot}} = [F] + [CaF]$ and the coefficients S_F and S_{FCa} specify the contribution from the dye's unbound and

Box 6.4 | Space and time constants of diffusion

Longitudinal diffusion of calcium along a cylinder in the presence of a buffer is given by:

$$\frac{\partial[\text{Ca}^{2+}]}{\partial t} = D_{\text{Ca}} \frac{\partial^2[\text{Ca}^{2+}]}{\partial x^2} - k^+[\text{Ca}^{2+}][\text{B}] + k^-[\text{CaB}] + J_{\text{Ca}}.$$

If the RBA is assumed to hold, then the effect of the buffer is to alter the apparent diffusion rate of calcium, simplifying the expression for buffered diffusion of calcium to:

$$\frac{\partial[\text{Ca}^{2+}]}{\partial t} = D_{\text{eff}} \frac{\partial^2[\text{Ca}^{2+}]}{\partial x^2} + J_{\text{Ca}}.$$

Substituting in the effective diffusion rate given by Equation 6.44 and rearranging yields:

$$(1 + \kappa) \frac{\partial[\text{Ca}^{2+}]}{\partial t} = (D_{\text{Ca}} + \kappa D_{\text{buf}}) \frac{\partial^2[\text{Ca}^{2+}]}{\partial x^2} + J_{\text{Ca}}. \quad (\text{a})$$

We now assume that the extra calcium flux J_{Ca} is provided by a steady calcium current, $J_{\text{CC}} = -aI_{\text{Ca}}/2Fv = -2I_{\text{Ca}}/4Fr$, and a non-saturated pump, $J_{\text{pump}} = aV_{\text{max}}[\text{Ca}^{2+}]/vK_{\text{pump}} = 2P_m[\text{Ca}^{2+}]/r$, both across the surface area of the cylinder, which has radius r . Substituting these into Equation (a) and rearranging slightly leads to an equation that is identical in form to the voltage equation (Zador and Koch, 1994; Koch, 1999):

$$\frac{r(1 + \kappa)}{2} \frac{\partial[\text{Ca}^{2+}]}{\partial t} = \frac{r(D_{\text{Ca}} + \kappa D_{\text{buf}})}{2} \frac{\partial^2[\text{Ca}^{2+}]}{\partial x^2} - P_m[\text{Ca}^{2+}] - \frac{I_{\text{Ca}}}{2F}.$$

By analogy to the electrical space and time constants, the response of this system to a steady calcium current I_{Ca} in an infinite cylinder is an exponentially decaying calcium concentration with space constant:

$$\lambda_{\text{Ca}} = \sqrt{\frac{r(D_{\text{Ca}} + \kappa D_{\text{buf}})}{2P_m}}$$

and time constant:

$$\tau_{\text{Ca}} = \frac{r(1 + \kappa)}{2P_m}.$$

Both space and time constants are functions of the radius r . While the time constant may be on the same order as the electrical time constant, depending on the diameter, the space constant is typically a thousand times smaller than the electrical space constant (De Schutter and Smolen, 1998; Koch, 1999).

bound forms, respectively. The fluorescent intensity of saturated dye (i.e. maximally bound by calcium so that $[F]$ can be neglected compared to $[\text{CaF}]$) is $f_{\text{max}} = S_{\text{FCa}}[\text{F}]_{\text{tot}}$. The intensity in minimal calcium ($[\text{CaF}]$ neglected compared to $[F]$) is $f_{\text{min}} = S_{\text{F}}[\text{F}]_{\text{tot}}$.

Assuming that the RBA holds, following Equation 6.38 the concentration of calcium-bound dye is:

$$[\text{CaF}] = \frac{[\text{Ca}^{2+}][\text{F}]_{\text{tot}}}{K_{\text{F}} + [\text{Ca}^{2+}]} \quad (6.46)$$

with dissociation constant K_{F} . Given this approximation and the expressions for f , f_{max} and f_{min} above, the free calcium concentration can be derived as:

$$[\text{Ca}^{2+}] = K_{\text{F}} \frac{f - f_{\text{min}}}{f_{\text{max}} - f}. \quad (6.47)$$

In practice, it is difficult to measure f_{min} as calcium cannot be entirely removed from the experimental tissue slice preparation. Instead, this formulation is recast by introducing a new parameter, the dynamic range, $R_f = f_{\text{max}}/f_{\text{min}}$, of the indicator (Maravall *et al.*, 2000). Substituting this into Equation 6.47 and dividing top and bottom by f_{max} gives:

$$[\text{Ca}^{2+}] = K_{\text{F}} \frac{f/f_{\text{max}} - 1/R_f}{1 - f/f_{\text{max}}}. \quad (6.48)$$

If R_f is large, as it is for dyes such as Fluo-3 and Fluo-4, then $1/R_f$ is much smaller than f/f_{max} and does not much influence the calculated value of $[\text{Ca}^{2+}]$. So reasonable estimates of $[\text{Ca}^{2+}]$ can be obtained by estimating f_{max} *in situ* and using calibrated values of R_f and K_{F} .

Rather than trying to estimate the free calcium concentration, $[\text{Ca}^{2+}]$, more robust measurements of changes in calcium from resting conditions, $\Delta[\text{Ca}^{2+}] = [\text{Ca}^{2+}] - [\text{Ca}^{2+}]_{\text{res}}$, can be made. Now we make use of the change in fluorescence over the resting baseline, $\Delta f/f = (f - f_{\text{res}})/f_{\text{res}}$, which has the maximum value, $\Delta f_{\text{max}}/f = (f_{\text{max}} - f_{\text{res}})/f_{\text{res}}$. Using Equation 6.48 to give expressions for $[\text{Ca}^{2+}]$ and $[\text{Ca}^{2+}]_{\text{res}}$, substituting in $\Delta f/f$ and rearranging eventually leads to:

$$\Delta[\text{Ca}^{2+}] = K_{\text{F}} \left(1 - \frac{1}{R_f}\right) \frac{\left(\frac{\Delta f_{\text{max}}}{f_{\text{res}}} + 1\right) \Delta f}{\left(\frac{\Delta f_{\text{max}}}{f_{\text{res}}} - \frac{\Delta f}{f_{\text{res}}}\right) \Delta f_{\text{max}}}. \quad (6.49)$$

By substituting $\Delta f_{\text{max}}/f_{\text{res}}$ into Equation 6.48 for $[\text{Ca}^{2+}]_{\text{res}}$ and rearranging, resting calcium can be estimated as:

$$[\text{Ca}^{2+}]_{\text{res}} = K_{\text{F}} \left[\frac{\left(1 - \frac{1}{R_f}\right)}{\frac{\Delta f_{\text{max}}}{f_{\text{res}}}} - \frac{1}{R_f} \right]. \quad (6.50)$$

Estimates of endogenous buffer capacity can also be made by measuring calcium changes resulting from a known stimulus in different concentrations of indicator dye (Maravall *et al.*, 2000). If both the dye and the endogenous buffers are assumed to be fast, then:

$$\Delta[\text{Ca}^{2+}] = [\text{Ca}^{2+}]_{\text{peak}} - [\text{Ca}^{2+}]_{\text{res}} = \frac{\Delta[\text{Ca}^{2+}]_{\text{tot}}}{(1 + \kappa_{\text{B}} + \kappa_{\text{F}})}, \quad (6.51)$$

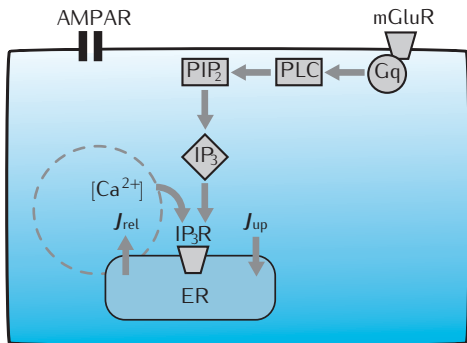


Fig. 6.14 Signalling pathway from glutamate to IP_3 production, leading to calcium release from intracellular stores in the ER.

where κ_B (κ_F) is the endogenous (dye) buffer capacity (calcium binding ratio). Given that $\Delta[\text{Ca}^{2+}]_{\text{tot}}$ is the same in each experiment, then the x -axis intercept of a straight-line fit to a plot of κ_F versus $1/\Delta[\text{Ca}^{2+}]$ will yield an estimate of κ_B .

6.8 | Complex intracellular signalling pathways

Up to this point we have concentrated on modelling intracellular calcium, but the methods apply to modelling general intracellular signalling pathways. In this section we consider the sorts of models that have been attempted for neuronal systems.

The deterministic modelling of well-mixed systems has been used to investigate the dynamics of a wide range of intracellular signalling cascades found in neurons (Bhalla and Iyengar, 1999), and particularly the temporal properties of the complex pathways underpinning long-term synaptic plasticity (Ajay and Bhalla, 2005). A major aspect is the quantitative determination of postsynaptic calcium transients resulting from particular synaptic stimulation protocols. Once this is achieved, the signalling pathways leading to changes in synaptic strength, of which arguably calcium is the key component, can be modelled. These pathways mediate such aspects as the phosphorylation state and the number of membrane-bound neurotransmitter receptors in the postsynaptic density (PSD).

6.8.1 Calcium transients

As we have seen, the calcium transient in a cellular compartment, such as a spine head, is the result of interaction between calcium fluxes through ion channels, extrusion of calcium by membrane-bound molecular pumps, binding of calcium by buffers and diffusion. An extra component is the production of IP_3 (Figure 6.14) which, together with calcium, leads to calcium release from internal stores by activation of IP_3 receptors in the ER membrane (Section 6.5.2). IP_3 is produced via a molecular cascade that begins with glutamate that is released in the synaptic cleft binding to membrane-bound metabotropic glutamate receptors (mGluRs). Activated mGluRs catalyse the activation of the Gq variety of G protein, which, in turn, activates phospholipase C (PLC). PLC then catalyses the production of IP_3 from the membrane phospholipid PIP₂ (Bhalla and Iyengar, 1999; Blackwell, 2005;

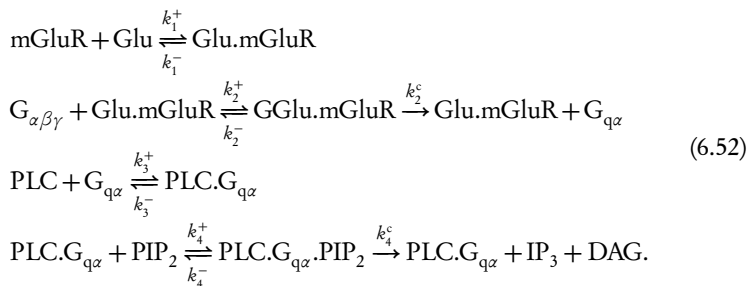
Box 6.5 | ODE model of IP₃ production

Under the assumptions that the spine head is well-mixed and that all molecular species are present in abundance, the signalling system for IP₃ production can be modelled as the set of ODEs:

$$\begin{aligned}\frac{d[\text{Glu.mGluR}]}{dt} &= k_1^+[\text{mGluR}][\text{Glu}] - k_1^-[\text{Glu.mGluR}] \\ \frac{d[\text{GGlu.mGluR}]}{dt} &= k_2^+[\text{Glu.mGluR}][\text{G}_{\alpha\beta\gamma}] - (k_2^- + k_2^c)[\text{GGlu.mGluR}] \\ \frac{d[\text{G}_{q\alpha}]}{dt} &= k_2^c[\text{GGlu.mGluR}] \\ \frac{d[\text{PLC.G}_{q\alpha}]}{dt} &= k_3^+[\text{PLC}][\text{G}_{q\alpha}] - k_3^-[\text{PLC.G}_{q\alpha}] \\ \frac{d[\text{PLC.G}_{q\alpha}.PIP_2]}{dt} &= k_4^+[\text{PLC.G}_{q\alpha}][PIP_2] - (k_4^- + k_4^c)[\text{PLC.G}_{q\alpha}.PIP_2] \\ \frac{d[IP_3]}{dt} &= k_4^c[\text{PLC.G}_{q\alpha}.PIP_2].\end{aligned}$$

One simplification would be to replace the equations relating to the enzymatic reactions with their steady state fluxes (Section 6.1), provided this is justified by the reaction rates (Blackwell, 2005). Note that equations for the concentrations of the remaining species should also be included, but could take the form of algebraic relationships, rather than ODEs, under the assumption of a closed system.

Doi *et al.*, 2005):



Including all complexes, this system contains 12 molecular species and requires the specification of ten reaction rates. A complete model would also include the return to the resting state once the glutamate transient is over, by the degradation of IP₃ and inactivation of the G protein. The implementation of this model as a set of differential equations is detailed in Box 6.5.

These pathways can be combined with a model for the IP₃ receptors in the ER membrane (Section 6.5.2) to complete the path from glutamate in the synaptic cleft to calcium release from intracellular stores (Figure 6.14). Doi *et al.* (2005) have modelled this complete system in detail, including a seven-state model of IP₃ receptors, to investigate the magnitude and time course of calcium transients in an individual Purkinje cell spine head following climbing fibre and parallel fibre activation. This single-compartment spine head

model describes 21 different molecular species and contains 53 variables and 96 parameters. This relatively large-scale signalling pathway model leads to long computer simulation times. Yet it is still a small model compared to the complete set of signalling pathways in a cell. Computationally, quantitative modelling of signalling pathways in this way may be limited to around 200 different molecular species (Bhalla, 2004a). It is still impractical to model pathways at this level of detail over the full spatial extent of a neuron. Doi *et al.* (2005) were modelling just a single spine head, and it would be computationally prohibitive to incorporate this into a detailed compartmental model of a Purkinje cell, including a full complement of thousands of spines.

6.8.2 Synaptic plasticity: LTP/LTD

A large number of modelling studies, at varying levels of detail, have aimed to relate calcium transients at glutamatergic synapses with changes in synaptic strength through phosphorylation of AMPA receptors (AMPARs) or insertion of new receptors (Ajay and Bhalla, 2005). In one detailed study, Kuroda *et al.* (2001) modelled the signalling pathways that drive phosphorylation of AMPARs in Purkinje cell spines. This process leads to a decrease in synaptic strength (LTD) through the internalisation of the AMPARs. This model contains 28 molecular species involved in 30 protein–protein interactions and 25 enzymatic reactions.

Other models, such as those of Bhalla and Iyengar (1999) and Castellani *et al.* (2005), consider the pathways leading to phosphorylation of particular AMPAR subunits found in hippocampal pyramidal cell spines, which results in an increase in synaptic strength (LTP) through an increase in receptor channel conductance. This increase is counteracted by competing pathways that dephosphorylate the subunits, resulting in LTD.

Hayer and Bhalla (2005) model the process of AMPAR recycling by which long-lasting changes in synaptic strength are implemented and maintained. They consider the stability of this process given the stochasticity due to the actual small numbers of molecules involved.

A particular challenge is to reconcile all these models with the wealth of data on LTP/LTD induction under different stimulation protocols, ranging from pairs of pre- and postsynaptic spikes, to trains of stimuli at different frequencies repeated over extensive periods of time. Models that greatly simplify the signalling pathways, but consequently have far fewer parameters, typically have been used to fit specific sets of LTP/LTD data (Abarbanel *et al.*, 2003; Castellani *et al.*, 2005; Rubin *et al.*, 2005; Badoual *et al.*, 2006). Examples are given in Section 7.5.

6.8.3 Beyond mass action in well-mixed systems

The two basic assumptions of the models presented, namely that the cellular compartment is well-mixed and that all molecular species are present in abundance, are both likely to be false for many situations of interest, including synaptic plasticity in spine heads. As already considered for calcium, gradients of diffusion can be modelled by subdividing a cellular compartment into smaller compartments between which molecules diffuse. This allows heterogeneous concentration profiles across the entire spatial system.

Long-lasting changes in synaptic strength have become known as **long-term potentiation (LTP)** for an increase in strength, and **long-term depression (LTD)** for a decrease (Section 7.5). The molecular mechanisms underpinning these changes are many and varied, of which AMPAR phosphorylation is one.

It should be noted that calmodulin, a molecule we have previously described as a calcium buffer (Section 6.7), plays an active role in these signalling pathways, particularly in its calcium-bound form. Thus it acts not simply as a buffer that shapes the free calcium transient, but as a calcium sensor that detects the magnitude and time course of a calcium transient and stimulates reactions accordingly (Burgoyne, 2007).

On the other hand, modelling a small number of molecules requires completely different modelling strategies that take into account the precise number of molecules present in a cellular compartment. Changes in the number of a molecular species will happen stochastically due to reaction with other molecules and diffusion through space.

Further techniques for stochastic and spatial modelling are introduced in Sections 6.9 and 6.10.

6.8.4 Parameter estimation

Formulating models of intracellular mechanisms relies on information about protein–protein interactions, plus the likely form of chemical reactions (Bhalla, 1998, 2001). This determines the kinetic equations for the model and thus enables the resulting set of mathematical equations (mostly ODEs) to be solved. In addition, information is required about reaction rates and initial molecular concentrations. Much of this information will come from experiments in systems other than the one being modelled. In the worst case, much information will be unavailable; in particular, good estimates for reaction rates. Where values are not known they must be assigned on the basis of reasonable heuristics or via parameter optimisation. Bhalla provides an excellent introduction to the availability and use of existing experimental data (Bhalla, 1998, 2001). Details of various online resources are given in Appendix A.2. Doi *et al.* (2005) give full details of where they obtained parameter values. They could not find values for 36 of their 96 parameters in the literature. In this situation the model was completed using a sensible parameter estimation strategy.

In binding reactions, such as:



the dissociation constant $K_d = k^-/k^+$, and possibly the time constant of the reaction, may be available. If it is assumed that one of the two species A and B is present in excess, say B, then the reaction is approximately first order (depends only on the concentration of A) and the time constant of A being converted to AB is:

$$\tau = \frac{1}{k^+ [B]_{\text{tot}} + k^-}. \quad (6.54)$$

If the concentration $[B]_{\text{tot}}$ is known for the experiment in which the time constant was measured, then this expression plus that for K_d allows determination of the forward and backward rate coefficients, k^+ and k^- .

For enzymatic reactions, such as:



values for $K_m = (k^- + k^c)/k^+$ and $V_{\text{max}} = k^c [E]_{\text{tot}}$ may be available. If the full enzymatic reaction is to be modelled, rather than the steady state Michaelis–Menten flux from substrate to product (Equation 6.11), then at least one rate will have to be assumed. The forward rate k^c can be determined from V_{max} , given a known enzyme concentration, but either k^+ or

k_1^- needs to be assumed to allow determination of the other from the value for K_m . Kuroda *et al.* (2001) assume that k_1^- is 2–20 times greater than k^c , on the basis that k_1^- is greater than k^c in many such reactions. Bhalla typically uses a scaling of four ($k_1^- = 4k^c$), having discovered that many models are highly insensitive to the exact ratio of k_1^- to k^c (Bhalla, 1998, 2001).

Parameter optimisation

After as many parameters as possible have been assigned values from experimental estimates, it still remains to determine values for all other parameters in a sensible fashion. Most likely this will be done by trying to minimise the difference between the model output and experimental data for the temporal concentration profiles of at least a few of the molecular species involved in the model. This may be attempted in a simple heuristic fashion (Doi *et al.*, 2005), which is acceptable if the number of unknown parameters is reasonably small and only a qualitative fit to experimental data is required. Otherwise, mathematical optimisation techniques that will adjust parameter values to minimise the error between the model output and the data should be used (Arisi *et al.*, 2006). Further details of parameter optimisation procedures are given in Section 4.5.

Further confidence in the model can be obtained by carrying out a thorough sensitivity analysis to determine the consequences of the choices made for parameter values. Doi *et al.* (2005) varied each parameter value over two orders of magnitude, while keeping all other values fixed, and compared the model outputs with a known experimental result that was not used during parameter estimation. This procedure indicates which particular model components (and hopefully their biochemical equivalents!) most strongly determine the system output.

6.9 | Stochastic models

So far we have considered models that calculate the temporal and spatial evolution of the concentration of molecular species. Concentration is a continuous quantity that represents the average number of molecules of a given species per unit volume. The actual number of molecules in a volume is an integer that is greater than or equal to zero. Chemical reactions take place between individual molecules in a stochastic fashion determined by their random movements in space and their subsequent interactions. The smooth changes in concentration predicted by mass action kinetics (Section 6.2.1) as two molecular species react to create a third product species masks the reality of fluctuating numbers of all three species, even at apparent equilibrium. For small numbers of molecules these fluctuations can be large relative to the mean. This may be crucial for a bistable system that in reality may randomly switch from one state to another when mass action kinetics would predict that the system is stable in a particular state.

If we are modelling low concentrations of molecules in small volumes, e.g. calcium in a spine head, then the number of molecules of a particular species may be very small (tens or less). The assumption of the law of

The **Monte Carlo simulation** approach is used for systems that contain a random element that precludes the direct calculation of desired quantities. Values for random variables, such as the next reaction time of molecular species, are obtained by sampling from their probability distributions. The system simulation is run many times with different outcomes, due to the random sampling. A quantitative average outcome may be calculated from the aggregation of many simulations.

mass action is then unreasonable and a different approach is required which takes into account the actual number of molecules present, rather than their concentration. Individual molecules undergo reactions and we may treat the reaction kinetics as describing the probability that a particular reaction, or state transition, may take place within a given time interval.

The time-evolution of such a system is then described by the so-called **master equation** (Gillespie, 1977) which specifies the probability distribution of the state of the system at any time, $P(X_1, \dots, X_N; t)$ where the state of the system is given by the number X_i of molecules of each of N species S_i . While generally it is possible to write down the master equation for a given system, it usually turns out to be intractable to solve both analytically and numerically (Gillespie, 1977). Instead, **Monte Carlo simulation** techniques can be used to simulate how the system state changes over time. Each new simulation will produce a different time evolution of the state due to the stochastic nature of reactions occurring. We now outline these techniques.

6.9.1 Exact methods

Gillespie (1977) developed a Monte Carlo scheme, called the **Stochastic Simulation Algorithm** (SSA), that produces trajectories that are provably drawn from the distribution described by the master equation, but no explicit knowledge of the master equation is required. Such schemes are known as exact stochastic methods. The approach is to use random numbers to determine:

- (1) at what time in the future the next reaction occurs; and
- (2) which reaction happens next.

Suppose our system contains N molecular species S_i and there are M reaction pathways R_j between the species. For example, a system with five species and two reaction pathways might be:



The reaction constants c_j are related to, but not identical with the reaction rates k_j in the deterministic, concentration-based description of such a system (Gillespie, 1977). If our system is spatially homogeneous, contained in a space with volume v , and is in thermal equilibrium, then $c_j \Delta t$ is the average probability that a particular combination of reactant molecules will react according to reaction pathway R_j in the next infinitesimal time interval Δt , e.g. one molecule of S_1 reacts with one molecule of S_2 to form one molecule of S_3 .

To determine which reaction happens next and when, we need an expression for the reaction probability density function $P(\tau, \mu)$. Given that the number of molecules of each reaction species (system state) at time t is (X_1, \dots, X_N) , $P(\tau, \mu) \Delta t$ is the probability that the next reaction will be R_μ and it will occur an infinitesimally short time after $t + \tau$.

Firstly, the probability that reaction R_μ will occur in the next infinitesimal time interval is $a_\mu \Delta t = b_\mu c_\mu \Delta t$ where b_μ is the number of distinct R_μ molecular reactant combinations in the current state (e.g. $b_1 = X_1 X_2$ where

X_1 and X_2 are the current number of molecules of S_1 and S_2 , respectively, in our example system). Then:

$$P(\tau, \mu)\Delta t = P_0(\tau)a_\mu\Delta t, \quad (6.57)$$

where $P_0(\tau)$ is the probability that no reaction occurs in the time interval $(t, t + \tau)$. It can be deduced that this probability is exponentially distributed and is given by:

$$P_0(\tau) = \exp\left(-\sum_{j=1}^M a_j \tau\right) = \exp(-a_0 \tau). \quad (6.58)$$

This gives us what we need to implement an algorithm for Monte Carlo simulation of state trajectories. A step-by-step approach is given in Box 6.6. The procedure is straightforward to implement in a computer simulation and produces stochastic time evolutions of the chemical system with exact reaction times. It is computationally fast, but has the drawback for modelling complex intracellular signalling pathways that computation time scales linearly with the number of reaction pathways M , as do deterministic, concentration-based models. This is not a problem for the simple examples we have given here, but can easily be if modelling a system that contains, say, proteins with multiple states due to, e.g. conformational changes, with each state reacting in slightly different ways. Such systems can contain millions of reaction pathways (Firth and Bray, 2001). Computation also scales linearly with the volume of the system, as the larger the volume the more molecules there are, and hence reactions take place more frequently. Various techniques have been employed to make the implementation of stochastic methods as efficient as possible (Gibson and Bruck, 2000; Gillespie, 1977, 2001).

A number of computer software packages for simulating intracellular signalling pathways incorporate both exact and approximate stochastic methods. Details can be found in Appendix A.1.2.

6.9.2 Approximate methods

An alternative approach, which is closer in principle to the numerical solution of deterministic models, is to calculate the system's time evolution on a per time-step basis. Such an approach provides only an approximation of the master equation as its accuracy depends on the size of time-step used, Δt . One advantage is that it allows the formulation of adaptive methods that switch between stochastic and deterministic solutions (Vasudeva and Bhalla, 2004). We now outline such an adaptive method.

A per time-step algorithm follows straightforwardly from the exact method (Vasudeva and Bhalla, 2004). We calculate the probability that a particular reaction R_μ takes place in a finite (but small) time interval, $(t, t + \Delta t)$. This is given as 1 minus the probability that the reaction does not take place:

$$P_\mu(\Delta t) = 1 - \exp(-a_\mu \Delta t). \quad (6.59)$$

For Δt sufficiently small, a useful approximation provides:

$$P_\mu(\Delta t) \approx 1 - (1 - a_\mu \Delta t) = a_\mu \Delta t. \quad (6.60)$$

The algorithm proceeds by testing for the occurrence of each of the M reactions and adjusting the molecular counts accordingly, on each time-step. The occurrence of a reaction is tested by generating a uniform random number

Box 6.6 | Stochastic Simulation Algorithm

A Monte Carlo simulation of Gillespie's exact method proceeds in the following way:

Step 0 Initialisation. Specify the M reaction constants c_j and the N initial molecular counts X_i . Set time t to zero.

Step 1 Calculate the M reaction probabilities given the current state of the system, $a_j = h_j c_j$, where h_j depends on the molecular counts of each reaction species.

Step 2 Generate a random number r_τ from a uniform distribution on the interval $[0,1]$. Use this number to calculate the time of the next reaction:

$$\tau = (1/a_0) \ln(1/r_\tau).$$

This is the same as drawing from the probability density function $P_\tau = a_0 \exp(-a_0 \tau)$, where a_0 is the sum of the M values, a_j .

Step 3 Generate another random number r_μ from the same uniform distribution and use this to calculate which reaction R_μ happens at time τ by selecting μ to be the integer for which:

$$\frac{1}{a_0} \sum_{j=1}^{\mu-1} a_j < r_\mu \leq \frac{1}{a_0} \sum_{j=1}^\mu a_j.$$

This is the same as drawing from the probability density function $P_\mu = a_\mu / a_0$

Step 4 Increase time t by τ and adjust the molecular counts X_i in accordance with the occurrence of reaction R_μ . For our example system 6.56, if R_1 occurred, X_1 and X_2 would be decremented by 1 and X_3 would be incremented by 1 to adjust the counts for species S_1 , S_2 and S_3 , respectively.

Step 5 Return to Step 1.

r_μ from the unit interval and then testing if $r_\mu < P_\mu$. If the test is true then it is assumed that a single instance of reaction R_μ has taken place in interval $(t, t + \Delta t)$.

Comparisons of deterministic (mass action) modelling with stochastic modelling of the simple reaction of a substrate S_1 going reversibly to a product S_2 are shown in Figure 6.15. When there are initially only ten molecules of S_1 , each simulation of the stochastic evolution of molecules of S_1 to molecules of S_2 produces large fluctuations in the amounts of S_1 and S_2 , even in the final steady state. Thus the mass action model does not capture the true and continuing dynamics of this system. The fluctuations in S_1 and S_2 could have profound consequences for their ability to take part in further downstream reactions. The deterministic and stochastic models are indistinguishable when there are initially 1000 molecules of S_1 (Figure 6.15a, f).

6.9.3 Molecule-based methods

A limitation of all these approaches is that the identity of individual molecules is not included, only the species to which they belong. Thus it

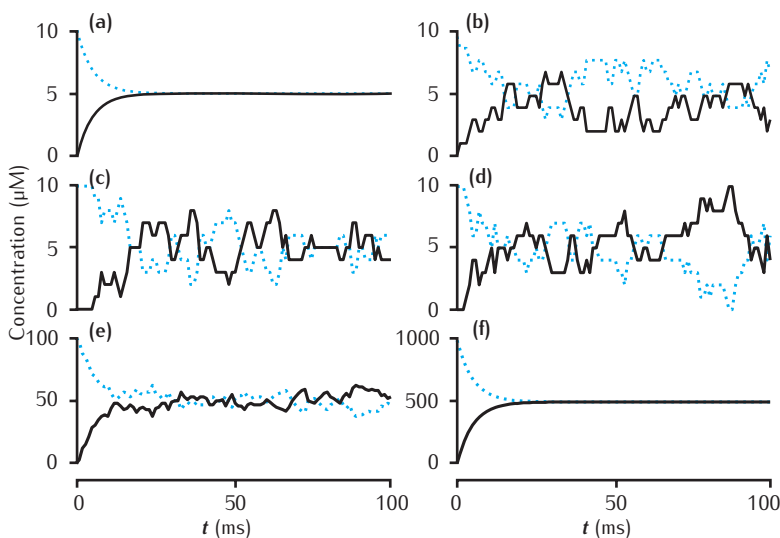


Fig. 6.15 Simulations of simple reversible reaction of S_1 (blue, dotted lines) being converted to S_2 (black, solid lines). Forward rate $k_f = 0.1$; backward rate $k_b = 0.1$. (a) Mass action model with $[S_1]_0 = 10 \mu\text{M}$; Stochastic model with initially (b)–(d) 10 molecules, (e) 100 molecules, and (f) 1000 molecules of S_1 .

is not possible to track over time, say, the different conformational states of a particular molecule. It is possible, though potentially computationally expensive, to carry out Monte Carlo simulations of a system of individual molecules, rather than just the number of each molecular species. This is the approach implemented in the StochSim simulation package (Firth and Bray, 2001; Le Nov  re and Shimizu, 2001). The system consists of individually identified molecules in the volume of interest (but without any particular spatial location). Molecules may have flags attached indicating, for example, their phosphorylation or conformational state. In brief, in each small timestep Δt , two molecules are selected at random, and they either react or not according to a pre-computed probability (for those two types of molecule and their current states). Calculation is very fast, but scales with the number of molecules in the system, which can be very large. Nonetheless, it may still be faster than the exact methods when the number of reaction pathways is also very large. Further details are given in Firth and Bray (2001).

6.9.4 Adaptive stochastic-deterministic methods

As highlighted above, the computation time for stochastic methods increases with the number of molecules in the system. However, as this number increases, the solution obtained approaches that of the deterministic concentration-based models. Neurons incorporate both large (cell bodies) and small (spine heads) volumes, and chemical signals, such as calcium concentrations, can change rapidly by an order of magnitude or more.

Efficient modelling of intracellular signalling within a neuron may be achieved by a combination of stochastic and deterministic methods, with automatic switching between methods when required. Such adaptive stochastic-deterministic methods are the subject of ongoing research, but one approach is as follows (Vasudeva and Bhalla, 2004). Consider the reaction:



A deterministic solution can be written in terms of the number of each molecular species, where the number is treated as a continuous variable:

$$\frac{dX_1}{dt} = -c_1 X_1 X_2, \quad (6.62)$$

where X_1 (X_2) is the number of molecules of species S_1 (S_2). If a simple Euler integration scheme (see Appendix B) with time-step Δt is used to solve this equation numerically, the change in the number of molecules of S_1 in a single time-step is given by:

$$\Delta X_1 = -c_1 X_1 X_2 \Delta t = -P_{S_1}, \quad (6.63)$$

where we call P_{S_1} the propensity for species S_1 to react. This equation can be used to update deterministically the number of molecules of S_1 at each time-step.

If we divide X_1 by the volume v in which the molecules are diluted, this is then a particular implementation of a concentration-based ODE model. However, in this formulation it is clear that when X_1 is small, say less than 10, it is a rather crude approximation to the real system. For example, does $X_1 = 1.4$ mean there are actually one or two molecules of S_1 present?

When P_{S_1} is significantly less than 1, it is equivalent to the probability that a molecule of S_1 reacts, used in the per time-step stochastic method outlined above, and could be used in this way. But P_{S_1} may also be much greater than 1, indicating that more than one molecule of S_1 may react in a single time-step. In this case we cannot treat P_{S_1} as a probability and it is more reasonable to update X_1 deterministically according to Equation 6.63. These considerations lead naturally to an algorithm that updates X_1 either stochastically or deterministically, depending on the magnitude of P_{S_1} :

If $P_{S_1} < P_{\text{thresh}}$ use a stochastic update for X_1 with probability P_{S_1} , otherwise use the deterministic update, Equation 6.63.

The threshold P_{thresh} should be much less than 1, e.g. 0.2.

This adaptive algorithm must also include a scheme for switching between continuous and discrete values for the ‘number’ of molecules for each species (Vasudeva and Bhalla, 2004). One scheme for going from a continuous to an integer number is to round up or down probabilistically depending on how far the real number is from the lower and upper integers. This can eliminate bias that might be introduced by deterministic rounding to the nearest integer (Vasudeva and Bhalla, 2004).

In our example above, the situation could arise in which species S_1 is in abundance (X_1 is large) but there are only a small number of molecules of S_2 . This could result in a large propensity P_{S_1} suggesting a deterministic update of the molecular numbers. However, for accuracy, X_2 , the number of molecules of S_2 , should really be updated stochastically. Thus, in addition to checking the propensity against a threshold value, molecular counts should also be checked against a minimum, X_{\min} (e.g. 100), below which they should be updated stochastically. A more complicated update is now required as a large propensity cannot be treated simply as a probability measure.

Noting that P_{S_1} is also the propensity for a molecule of S_2 to react, if P_{S_1} is greater than 1, then it is divided into integer and fractional parts; e.g.

$P_{S_1} = 1.25$ is split into $P_{\text{int}} = 1$ and $P_{\text{frac}} = 0.25$. These parts are used in the update rule (Vasudeva and Bhalla, 2004):

Choose a random number r uniformly from the interval $[0, 1]$.

If $r < P_{\text{frac}}$ then $\Delta X_2 = -P_{\text{int}} - 1$,
otherwise $\Delta X_2 = -P_{\text{int}}$.

For example, suppose $X_1 = 540$, $X_2 = 9$ and $P_{S_1} = 1.25$. Then X_1 would be decremented by 1.25, but 75% of the time X_2 would be decremented by 1, and 25% of the time by 2 (but ensuring that X_2 does not go below 0).

6.10 Spatial modelling

Much of the modelling of complex signalling pathways has been carried out under the assumption of a well-mixed system. This might be reasonable if considering the interactions in a spine head, but spatial inhomogeneities are likely over, say, a section of dendrite with many spines. The extension to a system in which at least some of the molecular species are subject to diffusion follows straightforwardly from the consideration of diffusible calcium and associated buffers, detailed above, when mass action kinetics can be assumed. The equations describing changes in molecular species that are mobile will include diffusive terms and constitute a reaction–diffusion system.

In situations in which deterministic calculations of mass action kinetics and diffusion are not appropriate, then movement of individual molecules, as well as their reaction, must be considered. Bulk diffusion is derived from the average movement of molecules subject to Brownian motion and thus undertaking random walks in space (Koch, 1999; Bormann *et al.*, 2001).

Movement of molecules can be approximated by restricting movement to diffusion between well-mixed pools across an intervening boundary (Bhalla, 2004b, c; Blackwell, 2006). This can be represented simply by another reaction pathway in which the ‘reaction’ is the movement of a molecule from one pool to another. This is the approach described earlier for the simple deterministic model of calcium in which it may diffuse from a submembrane shell to the cell core. The only ‘movement’ then is across the barrier between two cellular compartments, and not within each compartment. Consider two cellular compartments, labelled 1 and 2, with volumes v_1 and v_2 , separated by a distance Δx , with a boundary cross-sectional area a . Diffusion of molecular species A between these compartments can be described by the reaction pathway:



with rates $c_1 = aD_A/v_1\Delta x$ and $c_2 = aD_A/v_2\Delta x$ where D_A is the diffusion coefficient for A (Bhalla, 2004b). The adaptive algorithm described above can be employed such that the change in the number of molecules of A in compartment 1 over some small time-step Δt is given by:

$$\Delta X_1 = (-c_1 X_1 + c_2 X_2) \Delta t. \quad (6.65)$$

An alternative approach is to consider the probability that a molecule may leave a cellular compartment due to its Brownian motion. If such a

molecule may only move along a single dimension x and the compartment has length Δx , then the probability that a molecule of A will leave the compartment in a short time interval Δt is (Blackwell, 2006):

$$P_A = 2D_A \frac{\Delta t}{(\Delta x)^2}. \quad (6.66)$$

Of all the molecules of A that leave the compartment, half will move forwards and half will move backwards. The remaining molecules of A will not leave the compartment. By a single sampling of the corresponding trinomial distribution it is possible to determine the number of molecules of A moving forwards, backwards or not moving at all (Blackwell, 2006). This approach can readily be extended to movement in two or three dimensions.

Other approaches consider the specific location in space of particular molecules. Limited spatial location has been incorporated into the StochSim simulator (Appendix A.1.2) by allowing certain molecular species to be located in a 2D sheet with particular nearest-neighbour geometries. This could be used to model, say, an array of membrane-bound receptors (Firth and Bray, 2001; Le Novére and Shimizu, 2001). In analogy with cellular automata, these molecules may only interact with their nearest neighbours.

A more general approach is to simulate the movement and interaction of individual molecules through 3D space. Brownian motion of molecules can be specified as a probability distribution of the direction and distance a molecule may move in a fixed time-step. Such probability distributions are used in Monte Carlo simulations which adjust the position in space of diffusing molecules in a probabilistic fashion at each time-step. No discrete spatial grid is required as each molecule may occupy any possible 3D position. In principle, reactions between diffusing molecules could also be taken into account, but calculating collisions between individual molecules is computationally extremely intensive. Instead, computer simulators such as MCELL (Appendix A.1.2) only allow reactions between diffusing molecules and specified 2D surfaces corresponding to neuronal membrane that contain receptor molecules in defined patches. The simulation thus only needs to determine if the movement of a diffusing molecule would intersect with such a patch of membrane. However, advances in optimisation techniques for such simulations mean that completely arbitrary spatial geometries for membrane surface can be used, such as anatomically reconstructed synaptic clefts (Stiles and Bartol, 2001; Coggan *et al.*, 2005; Sosinsky *et al.*, 2005).

6.11 | Summary

A model that recreates typical neuronal electrical behaviour may well need to include intracellular signalling pathways, particularly those involving calcium. In this chapter we have detailed how the intracellular calcium concentration can be modelled. This involves mathematical descriptions for the variety of sources and sinks for calcium in a cellular compartment. These include voltage-gated calcium channels, membrane-bound pumps, calcium buffers and diffusion.

The techniques for modelling calcium are quite general and provide the tools for modelling other reaction-diffusion systems and intracellular signalling pathways. Examples of complex pathways of particular relevance to neuronal behaviour, such as synaptic plasticity, are discussed.

Consideration is given to whether it is reasonable to model cellular compartments as comprising well-mixed systems in which molecular species are present in sufficient abundance that mass action kinetics apply. In this situation, reaction schemes are modelled as systems of coupled ODEs that describe molecular concentrations. In small neuronal compartments, such as spine heads, even species such as calcium may only be present in a few tens of molecules or less. To model this situation requires stochastic models describing the movement and interaction of individual molecules.

Chapter 7

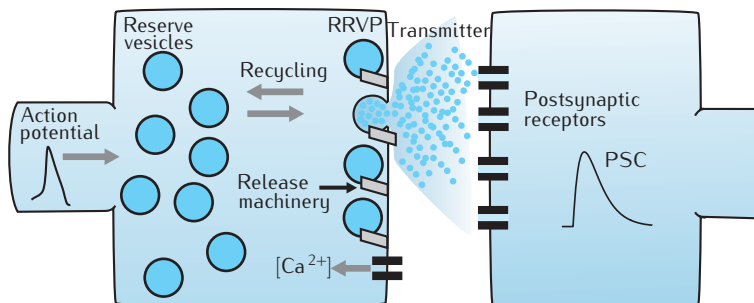
The synapse

This chapter covers a spectrum of models for both chemical and electrical synapses. Different levels of detail are delineated in terms of model complexity and suitability for different situations. These range from empirical models of voltage waveforms to more detailed kinetic schemes, and to complex stochastic models, including vesicle recycling and release. Simple static models that produce the same postsynaptic response for every presynaptic action potential are compared with more realistic models incorporating short-term dynamics that produce facilitation and depression of the postsynaptic response. Different postsynaptic receptor mediated excitatory and inhibitory chemical synapses are described. Electrical connections formed by gap junctions are considered.

7.1 | Synaptic input

So far we have considered neuronal inputs in the form of electrical stimulation via an electrode, as in an electrophysiological experiment. Many neuronal modelling endeavours start by trying to reproduce the electrical activity seen in particular experiments. However, once a model is established on the basis of such experimental data, it is often desired to explore the model in settings that are not reproducible in an experiment. For example, how does the complex model neuron respond to patterns of synaptic input? How does a model network of neurons function? What sort of activity patterns can a network produce? These questions, and many others besides, require us to be able to model synaptic input. We discuss chemical synapses in most detail as they are the principal mediators of targeted neuronal communication. Electrical synapses are discussed in Section 7.7.

The **chemical synapse** is a complex signal transduction device that produces a postsynaptic response when an action potential arrives at the presynaptic terminal. A schematic of the fundamental components of a chemical synapse is shown in Figure 7.1. We describe models of chemical synapses based on the conceptual view that a synapse consists of one or more active zones that contain a presynaptic readily releasable vesicle pool (RRVP)



which, on release, may activate a corresponding pool of postsynaptic receptors (Walmsley *et al.*, 1998). The RRP is replenished from a large reserve pool. The reality is likely to be more complex than this, with vesicles in the RRP possibly consisting of a number of subpools, each in different states of readiness (Thomson, 2000b). Recycling of vesicles may also involve a number of distinguishable reserve pools (Thomson, 2000b; Rizzoli and Betz, 2005).

A model of such a synapse could itself be very complex. The first step in creating a synapse model is identifying the scientific question we wish to address. This will affect the level of detail that needs to be included. Very different models will be used if our aim is to investigate the dynamics of a neural network involving thousands of synapses compared to exploring the influence of transmitter diffusion on the time course of a miniature **excitatory postsynaptic current (EPSC)**. In this chapter, we outline the wide range of mathematical descriptions that can be used to model both chemical and electrical synapses. We start with the simplest models that capture the essence of the postsynaptic electrical response, before including gradually increasing levels of detail.

Fig. 7.1 Schematic of a chemical synapse. In this example, the presynaptic terminal consists of a single active zone containing a RRP which is replenished from a single reserve pool. A presynaptic action potential leads to calcium entry through voltage-gated calcium channels which may result in a vesicle in the RRP fusing with the presynaptic membrane and releasing neurotransmitter into the synaptic cleft. Neurotransmitter diffuses in the cleft and binds with postsynaptic receptors which then open, inducing a postsynaptic current (PSC).

The abbreviation **IPSC**, standing for **inhibitory postsynaptic current**, is also used.

7.2 | The postsynaptic response

The aim of a synapse model is to describe accurately the postsynaptic response generated by the arrival of an action potential at a presynaptic terminal. We assume that the response of interest is electrical, but it could equally be chemical, such as an influx of calcium or the triggering of a second-messenger cascade. For an electrical response, the fundamental quantity to be modelled is the time course of the postsynaptic receptor conductance. This can be captured by simple phenomenological waveforms, or by more complex kinetic schemes that are analogous to the models of membrane-bound ion channels discussed in Chapter 5.

7.2.1 Simple conductance waveforms

The electrical current that results from the release of a unit amount of neurotransmitter at time t_s is, for $t \geq t_s$:

$$I_{\text{syn}}(t) = g_{\text{syn}}(t)(V(t) - E_{\text{syn}}), \quad (7.1)$$

where the effect of transmitter binding to and opening postsynaptic receptors is a conductance change, $g_{\text{syn}}(t)$, in the postsynaptic membrane. $V(t)$ is

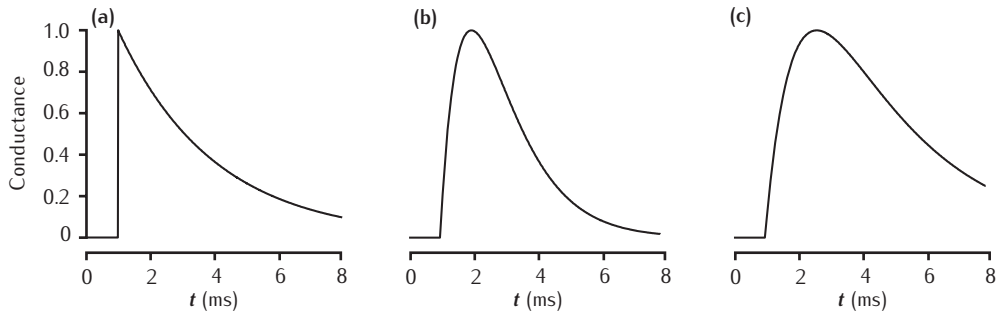


Fig. 7.2 Three waveforms for synaptic conductance: (a) single exponential decay with $\tau = 3$ ms, (b) alpha function with $\tau = 1$ ms, and (c) dual exponential with $\tau_1 = 3$ ms and $\tau_2 = 1$ ms. Response to a single presynaptic action potential arriving at time = 1 ms. All conductances are scaled to a maximum of 1 (arbitrary units).

the voltage across the postsynaptic membrane and E_{syn} is the reversal potential of the ion channels that mediate the synaptic current. Simple waveforms are used to describe the time course of the synaptic conductance, $g_{\text{syn}}(t)$, for the time after the arrival of a presynaptic spike, $t \geq t_s$. Three commonly used waveform equations are illustrated in Figure 7.2, in the following order, (a) single exponential decay, (b) alpha function (Rall, 1967) and (c) dual exponential function:

$$g_{\text{syn}}(t) = \bar{g}_{\text{syn}} \exp\left(-\frac{t - t_s}{\tau}\right) \quad (7.2)$$

$$g_{\text{syn}}(t) = \bar{g}_{\text{syn}} \frac{t - t_s}{\tau} \exp\left(-\frac{t - t_s}{\tau}\right) \quad (7.3)$$

$$g_{\text{syn}}(t) = \bar{g}_{\text{syn}} \frac{\tau_1 \tau_2}{\tau_1 - \tau_2} \left(\exp\left(-\frac{t - t_s}{\tau_1}\right) - \exp\left(-\frac{t - t_s}{\tau_2}\right) \right). \quad (7.4)$$

The alpha and dual exponential waveforms are more realistic representations of the conductance change at a typical synapse, and good fits of Equation 7.1 using these functions for $g_{\text{syn}}(t)$ can often be obtained to recorded synaptic currents. The dual exponential is needed when the rise and fall times must be set independently.

Response to a train of action potentials

If it is required to model the synaptic response to a series of transmitter releases due to the arrival of a stream of action potentials at the presynaptic terminal, then the synaptic conductance is given by the sum of the effects of the individual waveforms resulting from each release. For example, if the alpha function is used, for the time following the arrival of the n th spike ($t > t_n$):

$$g_{\text{syn}}(t) = \sum_{i=1}^n \bar{g}_{\text{syn}} \frac{t - t_i}{\tau} \exp\left(-\frac{t - t_i}{\tau}\right), \quad (7.5)$$

where the time of arrival of each spike i is t_i . An example of the response to a train of releases is shown in Figure 7.3.

A single neuron may receive thousands of inputs. Efficient numerical calculation of synaptic conductance is often crucial. In a large-scale network model, calculation of synaptic input may be the limiting factor in the speed of simulation. The three conductance waveforms considered are all solutions of the impulse response of a damped oscillator, which is given by the second

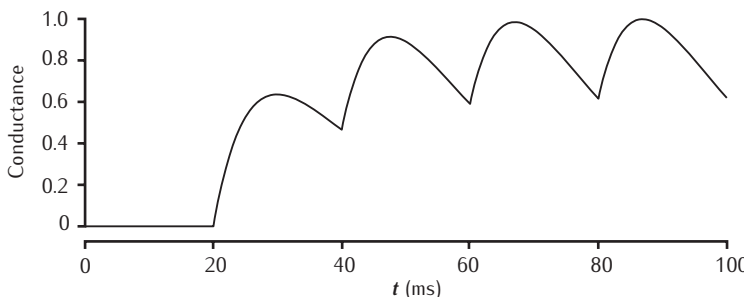


Fig. 7.3 Alpha function conductance with $\tau = 10\text{ ms}$ responding to action potentials occurring at 20, 40, 60 and 80 ms. Conductance is scaled to a maximum of 1 (arbitrary units).

order ODE for the synaptic conductance:

$$\tau_1 \tau_2 \frac{d^2 g}{dt^2} + (\tau_1 + \tau_2) \frac{dg}{dt} + g = \bar{g}_{\text{syn}} x(t). \quad (7.6)$$

The function $x(t)$ represents the contribution from the stream of transmitter releases. It results in an increment in the conductance by \bar{g}_{syn} if a release occurs at time t . The conductance $g(t)$ takes the single exponential form when $\tau_1 = 0$ and the alpha function form when $\tau_1 = \tau_2 = \tau$.

This ODE can be integrated using a suitable numerical integration routine to give the synaptic conductance over time (Protopapas *et al.*, 1998) in a way that does not require storing spike times or the impulse response waveform, both of which are required for solving Equation 7.5. A method for handling Equation 7.5 directly that does not require storing spike times and is potentially faster and more accurate than numerically integrating the impulse response is proposed in Srinivasan and Chiel (1993).

Voltage dependence of response

These simple waveforms describe a synaptic conductance that is independent of the state of the postsynaptic cell. Certain receptor types are influenced by membrane voltage and molecular concentrations. For example, NMDA receptors are both voltage-sensitive and are affected by the level of extracellular magnesium (Ascher and Nowak, 1988; Jahr and Stevens, 1990a, b). The basic waveforms can be extended to capture these sort of dependencies (Zador *et al.*, 1990; Mel, 1993):

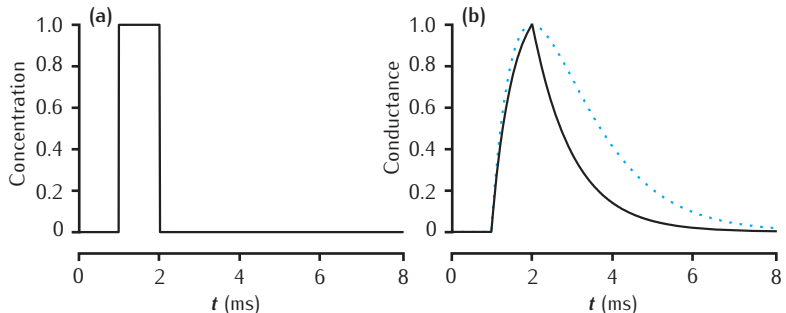
$$g_{\text{NMDA}}(t) = \bar{g}_{\text{syn}} \frac{\exp(-(t - t_s)/\tau_1) - \exp(-(t - t_s)/\tau_2)}{(1 + \mu [\text{Mg}^{2+}] \exp(-\gamma V))}, \quad (7.7)$$

where μ and γ set the magnesium and voltage dependencies, respectively. In this model the magnesium concentration $[\text{Mg}^{2+}]$ is usually set at a pre-determined, constant level, e.g. 1 mM. The voltage V is the postsynaptic membrane potential, which will vary with time.

7.2.2 Kinetic schemes

A significant limitation of the simple waveform description of synaptic conductance is that it does not capture the actual behaviour seen at many synapses when trains of action potentials arrive. A new release of neurotransmitter soon after a previous release should not be expected to contribute as much to the postsynaptic conductance due to saturation of postsynaptic

Fig. 7.4 Response of the simple two-gate kinetic receptor model to a single pulse of neurotransmitter of amplitude 1 mM and duration 1 ms. Rates are $\alpha = 1 \text{ mM}^{-1} \text{ ms}^{-1}$ and $\beta = 1 \text{ ms}^{-1}$. Conductance waveform scaled to an amplitude of 1 and compared with an alpha function with $\tau = 1 \text{ ms}$ (dotted line).



receptors by previously released transmitter and the fact that some receptors will already be open. Certain receptor types also exhibit desensitisation that prevents them (re)opening for a period after transmitter-binding, in the same way that the sodium channels underlying the action potential inactivate. To capture these phenomena successfully, kinetic – or Markov – models (Section 5.5) can be used. Here we outline this approach. More detailed treatments can be found in the work of Destexhe *et al.* (1994b, 1998).

Basic model

The simplest kinetic model is a two-state scheme in which receptors can be either closed, C, or open, O, and the transition between states depends on transmitter concentration, [T], in the synaptic cleft:



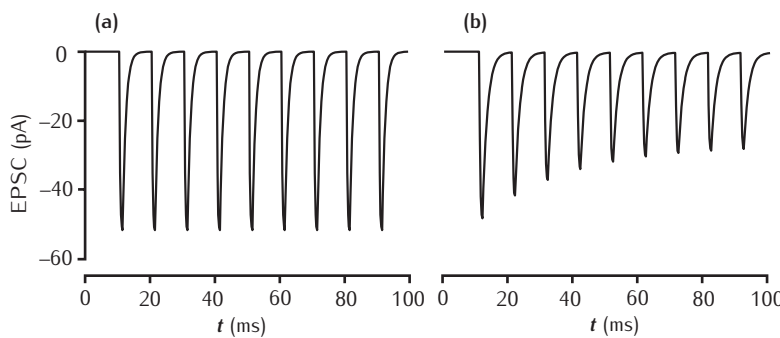
where α and β are voltage-independent forward and backward rate constants. For a pool of receptors, states C and O can range from 0 to 1, and describe the fraction of receptors in the closed and open states, respectively. The synaptic conductance is:

$$g_{\text{syn}}(t) = \bar{g}_{\text{syn}} O(t). \quad (7.9)$$

A complication of this model compared to the simple conductance waveforms discussed above is the need to describe the time course of transmitter concentration in the synaptic cleft. One approach is to assume that each release results in an impulse of transmitter of a given amplitude, T_{\max} , and fixed duration. This enables easy calculation of synaptic conductance with the two-state model (Box 7.1). An example response to such a pulse of transmitter is shown in Figure 7.4. The response of this scheme to a train of pulses at 100 Hz is shown in Figure 7.5a. However, more complex transmitter pulses may be needed, as discussed below.

The neurotransmitter transient

The neurotransmitter concentration transient in the synaptic cleft following release of a vesicle is characterised typically by a fast rise time followed by a decay that may exhibit one or two time constants, due to transmitter uptake and diffusion of transmitter out of the cleft (Clements *et al.*, 1992; Destexhe *et al.*, 1998; Walmsley *et al.*, 1998). This can be described by the same sort of



mathematical waveforms, e.g. alpha function, used to model the postsynaptic conductance itself (Section 7.2.1). However, a simple square-wave pulse for the neurotransmitter transient is often a reasonable approximation for use with a kinetic model of the postsynaptic conductance (Destexhe *et al.*, 1994a, 1998), as illustrated above.

For many synapses, or at least individual active zones, it is highly likely that, at most, a single vesicle is released per presynaptic action potential (Redman, 1990; Thomson, 2000b). This makes the use of simple phenomenological waveforms for the transmitter transient both easy and sensible. However, some synapses can exhibit multivesicular release at a single active zone (Wadiche and Jahr, 2001). The transmitter transients due to each vesicle released must then be summed to obtain the complete transient seen by the postsynaptic receptor pool. This is perhaps most easily done when a continuous function, such as the alpha function, is used for the individual transient, with the resulting calculations being the same as those required for

Fig. 7.5 Postsynaptic current in response to 100 Hz stimulation from (a) two-gate kinetic receptor model, $\alpha = 4 \text{ mM}^{-1} \text{ ms}^{-1}$, $\beta = 1 \text{ ms}^{-1}$; (b) five-gate desensitising model, $R_b = 13 \text{ mM}^{-1} \text{ ms}^{-1}$, $R_{u1} = 0.3 \text{ ms}^{-1}$, $R_{u2} = 200 \text{ ms}^{-1}$, $R_d = 10 \text{ ms}^{-1}$, $R_r = 0.02 \text{ ms}^{-1}$, $R_o = 100 \text{ ms}^{-1}$, $R_c = 1 \text{ ms}^{-1}$. Each presynaptic action potential is assumed to result in the release of a vesicle of neurotransmitter, giving a square-wave transmitter pulse amplitude of 1 mM and duration of 1 ms. The current is calculated as $I_{\text{syn}}(t) = g_{\text{syn}}(t)(V(t) - E_{\text{syn}})$. $E_{\text{syn}} = 0 \text{ mV}$ and the cell is clamped at -65 mV . The value of $g_{\text{syn}}(t)$ approaches 0.8 nS on the first pulse.

Box 7.1 Solving the two-state model

The basic two-state kinetic scheme (Equation 7.8), is equivalent to an ODE in which the rate of change of O is equal to the fraction converted from state C minus the fraction converted from O to C:

$$\frac{dO}{dt} = \alpha[T](1 - O) - \beta O,$$

where $O + C = 1$.

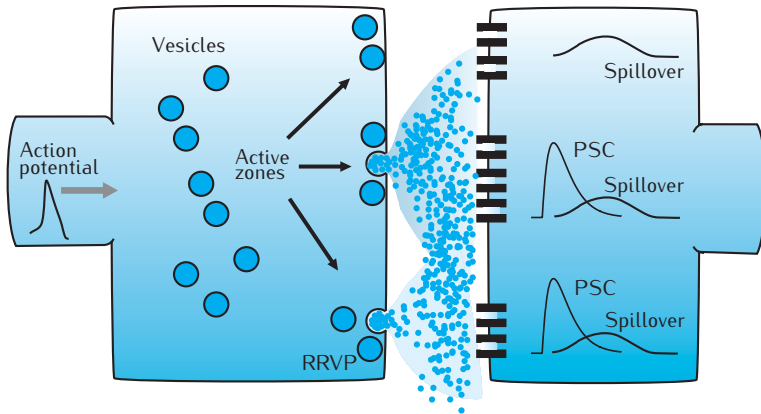
If the neurotransmitter transient is modelled as a square-wave pulse with amplitude T_{\max} then this ODE can be solved both for the duration of the transient, Equation a, and for the period when there is no neurotransmitter, Equation b. This leads to the numerical update scheme (Destexhe *et al.*, 1994a, 1998):

$$O_{t+1} = O_\infty + (O_t - O_\infty) \exp\left(\frac{-\Delta t}{\tau_O}\right) \quad \text{if } [T] > 0 \quad (\text{a})$$

$$O_{t+1} = O_t \exp(-\beta \Delta t) \quad \text{if } [T] = 0 \quad (\text{b})$$

for time-step Δt . In the presence of neurotransmitter the fraction of open receptors approaches $O_\infty = \alpha T_{\max}/(\alpha T_{\max} + \beta)$ with time constant $\tau_O = 1/(\alpha T_{\max} + \beta)$.

Fig. 7.6 Schematic of a chemical synapse with multiple active zones. Single vesicles are releasing at the lower two active zones, resulting in spillover of neurotransmitter between zones.



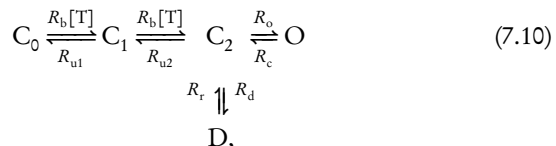
generating the postsynaptic conductance due to a train of action potentials (Section 7.2.1).

A further complication is spillover of transmitter from neighbouring active zones. To compensate for this requires consideration of the spatial arrangement of active zones and the likely contribution of spillover due to diffusion (Destexhe and Sejnowski, 1995; Barbour and Häusser, 1997). This can be described by a delayed, and smaller, amplitude transmitter transient that also must be summed together with all other transients at a particular active zone. A synapse containing multiple active zones with spillover of neurotransmitter between zones is illustrated in Figure 7.6.

More detailed models

Postsynaptic conductances often exhibit more complex dynamics than can be captured by the simple scheme used above. EPSCs may contain fast and slow components, and may decline in amplitude on successive presynaptic pulses due to desensitisation of the postsynaptic receptors. These factors can be captured in kinetic schemes by adding further closed and open states, as well as desensitised states (Destexhe *et al.*, 1994b, 1998).

A basic five-gate kinetic scheme that includes receptor desensitisation is:



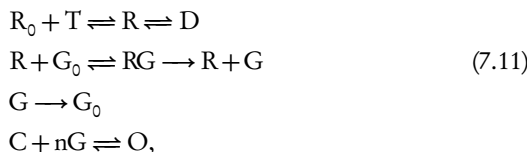
where the binding of two transmitter molecules is required for opening, and fully bound receptors can desensitise (state D) before opening. An example of how such a scheme may be translated into an equivalent set of ODEs is given in Section 5.5.1. The response of this scheme to 100 Hz stimulation, obtained by numerically integrating the equivalent ODEs, is shown in Figure 7.5b. The EPSC amplitude declines on successive stimuli due to receptor desensitisation.

Variations on this scheme have been used to describe AMPA, NMDA and γ -aminobutyric acid (GABA_A) receptor responses (Destexhe *et al.*, 1994b, 1998). More complex schemes include more closed, open and desensitised states to match the experimental time course of postsynaptic current

responses to applied and evoked neurotransmitter pulses. Transition rates may be constant, sensitive to ligands such as neurotransmitter or neuromodulators, or voltage-sensitive.

Models of metabotropic receptors

The kinetic schemes discussed above are suitable for modelling the response of ionotropic receptors in which the current-carrying ion channels are directly gated by the neurotransmitter. Other receptors, such as GABA_B, are metabotropic receptors that gate remote ion channels through second messenger pathways. Kinetic schemes can also be used to describe this type of biochemical system. For example, the GABA_B response has been modelled as (Destexhe and Sejnowski, 1995; Destexhe *et al.*, 1998):



where the receptors enter activated, R, and desensitised, D, states when bound by transmitter, T. G-protein enters an activated state, G, catalysed by R, which then proceeds to open the ion channels.

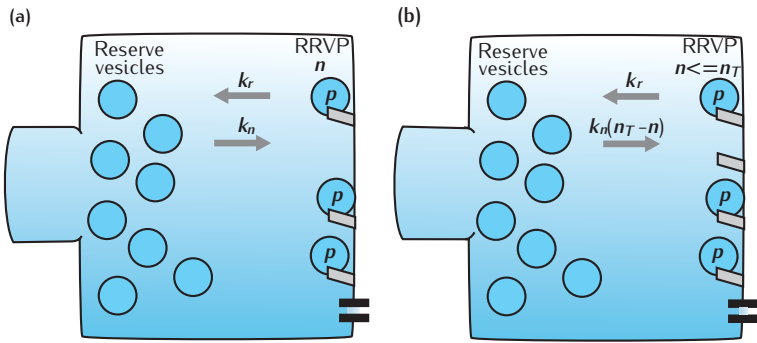
7.3 Presynaptic neurotransmitter release

Any postsynaptic response is dependent upon neurotransmitter being released from the presynaptic terminal. In turn, this depends on the availability of releasable vesicles of neurotransmitter and the likelihood of such a vesicle releasing due to a presynaptic action potential. A complete model of synaptic transmission needs to include terms describing the release of neurotransmitter.

The simplest such model, which is commonly used when simulating neural networks, is to assume that a single vesicle releases its quantum of neurotransmitter for each action potential that arrives at a presynaptic terminal, as in Figure 7.3. In practice, this is rarely a good model for synaptic transmission at any chemical synapse. A better description is that the average release is given by np where n is the number of releasable vesicles and p is the probability that any one vesicle will release (Box 1.2). Both n and p may vary with time, resulting in either facilitation or depression of release, and hence the postsynaptic response. Such short-term synaptic plasticity operates on the timescale of milliseconds to seconds and comes in a variety of forms with distinct molecular mechanisms, largely controlled by presynaptic calcium levels (Magleby, 1987; Zucker, 1989, 1999; Thomson, 2000a, b; Zucker and Regehr, 2002).

We consider how to model n and p . We present relatively simple models that describe a single active zone with a RRP that is replenished from a single reserve pool. Two classes of model are described, one in which an active zone contains an unlimited number of release sites and another which has a limited number of release sites (Figure 7.7).

Fig. 7.7 Two models of vesicle recycling and release at an active zone: (a) vesicle-state model in which the number of vesicles in the RRP is limited only by vesicle recycling and release rates; (b) release-site model in which there is a limited number of release sites. n is the number of vesicles available for release; p is the release probability of a vesicle; k_n is the arrival rate from the reserve pool; k_r is the return rate to the reserve pool.



7.3.1 Vesicle release

Firstly we consider models for p , the probability that a vesicle will be released. There is a direct relationship between p and presynaptic calcium levels. Release probability is determined by the calcium influx through one, or very few, voltage-gated calcium channels close to a release site, with p varying according to a power (usually 3–4) of the calcium concentration (Zucker and Fogelson, 1986; Redman, 1990; Thomson, 2000b). Most release occurs in synchrony with the arrival of a presynaptic action potential, which results in a rapid influx of calcium. Residual calcium levels between action potentials can result in spontaneous asynchronous release and may enhance release on subsequent action potentials (Zucker, 1999; Thomson, 2000a, b).

Complex models can be conceived that include explicitly the voltage waveform of the action potential, the accompanying calcium current through voltage-gated calcium channels, the associated change in intracellular calcium concentration, and then calcium-activated signalling pathways that eventually result in transmitter release. Unless it is the release process itself that is the subject of study, this level of detail is unnecessary. Here we use simpler approaches which describe the vesicle release probability as a direct function of a stereotypical action potential or the resultant calcium transient.

Phenomenological model of facilitation

At many synapses, trains of presynaptic action potentials cause the release probability to increase in response to the arrival of successive spikes, due to residual calcium priming the release mechanism (Del Castillo and Katz, 1954b; Katz and Miledi, 1968; Zucker, 1974; Thomson, 2000a, b). Release probability returns to baseline with a time constant of around 50–300 ms (Thomson, 2000a).

A simple phenomenological model that can capture the amplitude and time course of experimentally observed facilitation (Tsodyks *et al.*, 1998) increments the probability of release p by an amount $\Delta p(1-p)$ at each action potential, with p decaying back to baseline p_0 with a fixed time constant τ_f :

$$\frac{dp}{dt} = -\frac{(p - p_0)}{\tau_f} + \sum_s \Delta p(1-p)\delta(t - t_s), \quad (7.12)$$

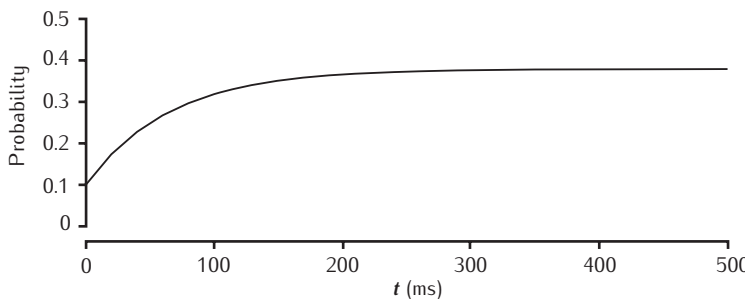


Fig. 7.8 Facilitation of release probability in the basic phenomenological model. Stimulation at 50 Hz with $p_0 = 0.1$, $\Delta p = 0.1$ and $\tau_f = 100$ ms.

where the **Dirac delta function** $\delta(t - t_s)$ results in the incremental increase in p at each spike time t_s . Only the times of presynaptic action potentials t_s appear explicitly in the model. The resultant calcium influx implicitly determines p , but is not explicitly modelled.

In between spikes, the solution of Equation 7.12 gives that p decays exponentially towards p_0 . For an interspike interval of Δt , p will return towards p_0 by the fractional amount, $1 - \exp(-\Delta t/\tau_f)$, from its value immediately following the previous action potential. This leads to an expression for the probability of release at the n th spike in terms of the probability at the $(n-1)$ th spike:

$$p_n = p_{n-1}^+ + (1 - \exp(-\Delta t/\tau_f))(p_0 - p_{n-1}^+) \quad (7.13)$$

where

$$p_{n-1}^+ = p_{n-1} + \Delta p(1 - p_{n-1}) \quad (7.14)$$

is the release probability attained just following the previous action potential due to facilitation. For a stream of spikes at a constant rate, the release probability reaches a steady state value per spike of:

$$p_\infty = \frac{p_0(1 - \exp(-\Delta t/\tau_f)) + \Delta p \exp(-\Delta t/\tau_f)}{1 - (1 - \Delta p)\exp(-\Delta t/\tau_f)}. \quad (7.15)$$

An example of facilitation in release is shown in Figure 7.8. Though p is calculated as a continuous function of time, the model is only used to determine the release probability of a vesicle at the time of arrival of each presynaptic action potential.

In this model there is no attempt made to provide a causal mechanism for the facilitation of release. Other slightly more complex models have attempted to relate the magnitude and time course of facilitation explicitly to calcium entry (Dittman *et al.*, 2000; Trommershäuser *et al.*, 2003).

The **Dirac delta function** is a useful mathematical function defined as:

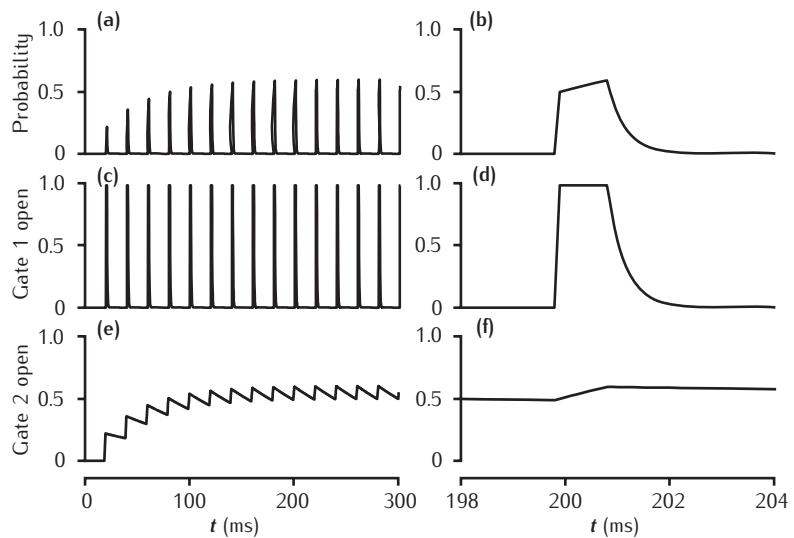
$$\begin{aligned} \delta(x) &= 0 \text{ for } x \neq 0 \\ \int_{-\infty}^{\infty} \delta(x) dx &= 1. \end{aligned}$$

In other words, the delta function is zero for all values of x except at $x = 0$ where it has an infinitely large value, and the area underneath this value is one unit.

Kinetic gating scheme

A different approach to modelling p attempts to represent the interaction between calcium and the release machinery by using a kinetic scheme driven by an explicit calcium concentration to capture the time course of release, in the same way that such schemes driven by the neurotransmitter transient can be used to describe the postsynaptic conductance change (Section 7.2.2).

Fig. 7.9 Facilitation of transmitter release in a kinetic two-gate model. Left-hand column shows stimulation at 50 Hz. Right-hand column shows release and gating transients at the tenth pulse. Fast gate: $k_1^+ = 200 \text{ mM}^{-1} \text{ ms}^{-1}$, $k_1^- = 3 \text{ ms}^{-1}$; slow gate: $k_2^+ = 0.25 \text{ mM}^{-1} \text{ ms}^{-1}$, $k_2^- = 0.01 \text{ ms}^{-1}$; square-wave $[\text{Ca}^{2+}]_r$ pulse: 1 mM amplitude, 1 ms duration.



A basic scheme (Bertram *et al.*, 1996) specifies p as the product of the proportions of open states of a number N (typically 2–4) of different gates:

$$p(t) = O_1(t) \times O_2(t) \dots \times O_N(t), \quad (7.16)$$

where $O_j(t)$ is the proportion of open states of gate j , which is determined by the local calcium concentration at the release site:



This requires a model of the calcium transient, $[\text{Ca}^{2+}]_r$, seen by the release site in response to the arrival of a presynaptic action potential. For many purposes a simple stereotypical waveform, such as a brief square-wave pulse, is sufficient. This model is mathematically identical to the simple kinetic scheme for postsynaptic conductance considered earlier (Section 7.2.2). More complex models of the effect of the local calcium concentration, that include the accumulation of residual calcium, may also be used.

An example of the time course of $p(t) = O_1 O_2$ resulting from a two-gate model, with one fast gate and one slow gate, is shown in Figure 7.9. Fast gates determine the total release probability attained for each action potential. They will close completely between action potentials. Slower gates may remain partially open between action potentials and gradually summate to achieve higher open states on successive action potentials. This results in facilitation of the probability of release obtained on successive action potentials.

This model is actually specifying the average rate of vesicle release as a function of time, rather than the probability that a vesicle will release. This rate can be turned into a probability that a vesicle will release by determining the area under the curve p in the interval $[t, t + \Delta t]$, for some small time interval Δt . This gives the probability p^* that a vesicle will release during

that interval. A crude, but useful approximation is:

$$p^* = p(t)\Delta t. \quad (7.18)$$

In principle, this form of model can describe both release due to presynaptic action potentials and spontaneous release between action potentials. However, with this gating scheme it is usual that at least one gate will close completely between action potentials, reducing r , and hence p , to zero, as illustrated in Figure 7.9. Note that release due to an action potential is spread realistically over a short time interval (right-hand column of Figure 7.9).

Other factors

These basic models of release can be extended to include other factors that affect the release probability, such as changes in the calcium transient due to calcium channel inactivation (Forsythe *et al.*, 1998) or activation of presynaptic metabotropic glutamate receptors (mGluRs). For example, mGluR activation has been modelled as a decrease by a small amount Δp_b in the baseline release probability p_b following each action potential (Billups *et al.*, 2005):

$$\frac{dp_b}{dt} = \frac{p_0 - p_b}{\tau_b} - \sum_s \Delta p_b \cdot p_b \delta(t - t_s). \quad (7.19)$$

This baseline recovers slowly with time constant τ_b , which is on the order of several seconds, to the initial release probability p_0 . Baseline release p_b is used in place of p_0 in Equation 7.12 when determining the spike-related release probability p .

7.3.2 Vesicle availability

The second part of the presynaptic model concerns the number n of vesicles available for release at any particular time, i.e. the size of the RRP. The average size of this pool is determined by the average rate of vesicle release and the rate at which the pool is replenished from reserve pools and vesicle recycling. Depletion of this pool has long been identified as a major component of synaptic depression (Liley and North, 1953; Del Castillo and Katz, 1954b; Elmqvist and Quastel, 1965; Betz, 1970; Kusano and Landau, 1975; Thomson, 2000b).

Continuous models

A basic model considers the RRP, V_p , to be replenished at rate k_n from a single reserve pool, V_r , containing n_r vesicles. The n vesicles in the RRP may spontaneously return to the reserve pool at rate k_r . Exocytosis (vesicle release) occurs at rate p , which typically reaches a brief maximum following arrival of a presynaptic action potential. This is described by the kinetic scheme:



This is an example of a **vesicle-state model** (Gingrich and Byrne, 1985; Heinemann *et al.*, 1993; Weis *et al.*, 1999), as vesicles may be either in

reserve, release-ready or released, and the size of the RRPV is not limited (Figure 7.7a).

For simplicity, we assume that the number of vesicles in the RRPV and reserve pool is sufficiently large that we can treat n and n_r as real numbers, representing the average number of vesicles. This is reasonable for large synapses, such as the neuromuscular junction and giant calyceal synapses in the auditory system. It could also represent the average over many trials at a single central synapse, or the average over many synapses onto a single cell. The kinetic scheme (Equation 7.20) is then equivalent to the ODE:

$$\frac{dn}{dt} = k_n n_r - k_r n - np. \quad (7.21)$$

A further simplification is to assume that the reserve pool is so large that n_r is effectively constant over the stimulation period. The model then reduces to:

$$\frac{dn}{dt} = k_n^* - k_r n - np, \quad (7.22)$$

with constant replenishment rate $k_n^* = k_n n_r$.

If no action potentials arrive at the synapse, such that $p(t) = 0$ for all t , the size of the RRPV reaches a steady state value of:

$$n_\infty = k_n^* / k_r. \quad (7.23)$$

If a vesicle release takes place with constant probability p_s on the arrival of each presynaptic action potential, the rate of vesicle release is then:

$$p(t) = p_s \delta(t - t_s) \quad (7.24)$$

for a spike arriving at time t_s , with $p(t) = 0$ for $t \neq t_s$. For action potentials arriving with a constant frequency f , the release rate averaged over time is:

$$p(t) = f p_s. \quad (7.25)$$

Substituting this value into Equation 7.22 and setting the rate of change in n to be zero, the inclusion of the synaptic stimulation rate f results in the steady state RRPV size being decreased to:

$$n_\infty = \frac{k_n^*}{k_r + f p_s} \quad (7.26)$$

compared to the resting size (Equation 7.23). Increasing stimulation frequency f depletes the RRPV further, since n_∞ decreases as f increases, resulting in a depression of the steady state postsynaptic response, which is proportional to $n_\infty p$.

A typical example from this model is illustrated, in combination with the phenomenological facilitation model for release probability p (Equation 7.12), in Figure 7.10 (left-hand column, solid lines).

An alternative formulation of the np active zone model assumes that the number of release sites in an active zone is physically limited to a maximum size, n_{\max} (Figure 7.7b). This **release-site model** (Vere-Jones, 1966; Dittman and Regehr, 1998; Weis *et al.*, 1999; Matveev and Wang, 2000) has different steady state and dynamic characteristics from the vesicle-state model. Each

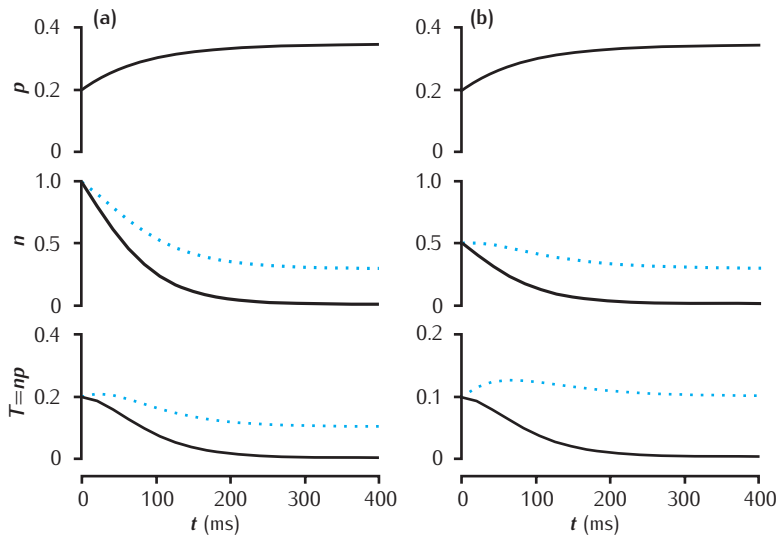


Fig. 7.10 Facilitation and depression in deterministic models of short-term synaptic dynamics. Phenomenological model of facilitation: $p_0 = 0.2$; $\Delta p = 0.05$; $\tau_f = 100$ ms.
(a) Vesicle-state model:
 $k_n^* = k_r = 0.2 \text{ s}^{-1}$.
(b) Release-site model: $n_T = 1$;
 $k_n = k_r = 0.2 \text{ s}^{-1}$. Solid lines:
 $n_s = 0$; dotted lines: $n_s = 0.1$.
Synapse stimulated at 50 Hz.

release site can either contain a vesicle (state V_p) or be empty (state V_e). A site may lose its vesicle through transmitter release, or via spontaneous undocking and removal to the reserve pool. An empty site can be refilled from the reserve pool. The state of a release site is described by the kinetic scheme:



where $k_r^* = p + k_r$ is the sum of the rate of vesicle release and the rate of spontaneous removal of vesicles to the reserve pool. Empty sites become filled with release-ready vesicles from an effectively infinite reserve pool at rate k_n . Given a total of n_{\max} release sites, the size of the RRP over time is described by the ODE:

$$\frac{dn}{dt} = k_n(n_{\max} - n) - k_r^* n. \quad (7.28)$$

In the absence of presynaptic activity ($p(t) = 0$), the size of the RRP reaches a steady state of:

$$n_\infty = \frac{k_n n_{\max}}{k_n + k_r}, \quad (7.29)$$

which is equal to n_{\max} if vesicles do not spontaneously undock, so that $k_r = 0$.

For stimulation with constant frequency f , the steady state decreases to:

$$n_\infty = \frac{k_n n_{\max}}{k_n + k_r + f p_s}. \quad (7.30)$$

An example for this model is shown in Figure 7.10 (right-hand column, solid lines). Note that if n is significantly less than n_{\max} , the term:

$$k_n(n_{\max} - n) \approx k_n n_{\max} = k_n^* \quad (7.31)$$

is constant, and this model is now equivalent to the vesicle-state model.

So far we have assumed that the refilling rate k_n of the RRPV is constant. The reality is likely to be rather more complex, with k_n being a direct or indirect function of the presynaptic calcium concentration (Gingrich and Byrne, 1985; Weis *et al.*, 1999; Dittman *et al.*, 2000; Trommershäuser *et al.*, 2003). In particular, the rate of filling of the RRPV may be dependent on presynaptic activity. At the neuromuscular junction (Worden *et al.*, 1997) and the calyx of Held (Wong *et al.*, 2003), recorded postsynaptic responses are well-fitted to the model if it is assumed that a fraction, or number, of new vesicles n_s are added to the RRPV following each presynaptic action potential.

For a regular stimulation frequency f , the release-site model is now:

$$\frac{dn}{dt} = k_n(n_{\max} - n) - k_r n + (n_s(n_{\max} - n) - n p_s) f. \quad (7.32)$$

The vesicle-state model, in which there is no hard limit to the size of the RRPV, now becomes:

$$\frac{dn}{dt} = k_n^* - k_r n + (n_s - n p_s) f. \quad (7.33)$$

The effect of n_s on the model responses is shown in Figure 7.10 (dotted lines). The activity-dependent recovery of the RRPV increases the steady state size of the RRPV for both models. For high-frequency stimulation of the vesicle-state model the size of the RRPV approaches the steady value:

$$n_\infty = \frac{k_n^* + f n_s}{k_r + f p_s} \approx n_s / p_s. \quad (7.34)$$

This steady state may be less than (depletion) or greater than (facilitation) the steady state RRPV size in the absence of activity (k_n^*/k_r), depending on the level of activity-dependent replenishment (n_s).

Many variations and extensions to these model components are possible, including one or more finite-sized reserve pools which may deplete, and more complex models of vesicle recycling and refilling of the RRPV.

Stochastic models

In the models discussed so far, we have been treating the number of presynaptic vesicles as a continuous variable representing an average over several spatially distributed synapses that are synchronously active, or over a number of trials at a single synapse (Tsodyks and Markram, 1997; Markram *et al.*, 1998; Dittman *et al.*, 2000). It is also possible to treat n as a count of the number of vesicles in the RRPV, with release of each vesicle being stochastic with probability p (Vere-Jones, 1966; Matveev and Wang, 2000; Fuhrmann *et al.*, 2002). This latter case is computationally more expensive, but represents more realistically the result of a single trial at typical central synapses for which the number of vesicles available for release at any time is limited, and failures of release can be common. This treatment also allows determination of the variation in synaptic response on a trial-by-trial basis.

Instead of treating kinetic models for the size of the RRPV, n , as being equivalent to continuous ODEs, they can be turned into discrete stochastic models by treating n as an integer representing the exact number of vesicles

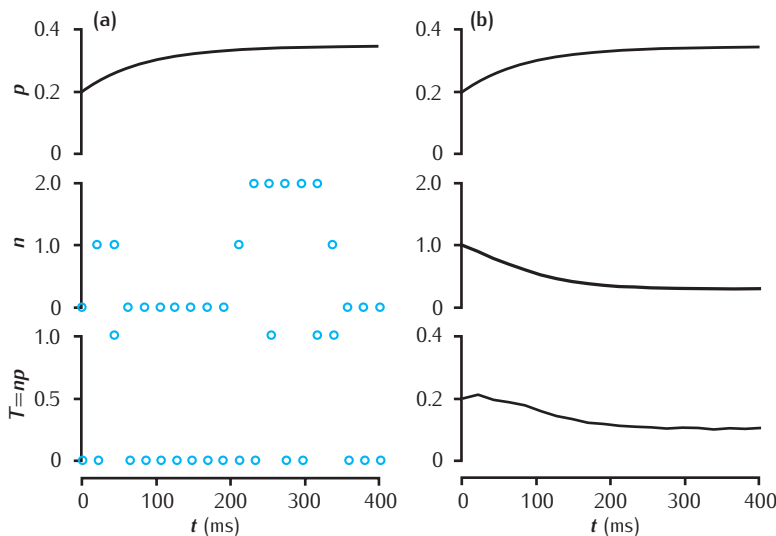


Fig. 7.11 Stochastic vesicle-state model of short-term dynamics at a single synaptic active zone. (a) A single simulation run, showing the release probability p , the actual number of releasable vesicles n (initially 1) and neurotransmitter release T . (b) Average values of these variables, taken over 10 000 trials. Phenomenological model of facilitation: $p_0 = 0.2$; $\Delta p = 0.05$; $\tau_f = 100$ ms. Vesicle-state model: $k_n^* = k_r = 0.2 \text{ s}^{-1}$; $n_s = 0.1$. Synapse stimulated at 50 Hz.

currently in the RRVP. The rates of vesicle recycling, k_n and k_r , and release p determine the probability that a new vesicle will enter or leave the RRVP in some small time interval Δt .

Computer simulation of this type of model is carried out using Monte Carlo techniques. An algorithm is detailed in Box 7.2. A single simulation is equivalent to a single experimental trial at a real synapse. Results from multiple simulations can be averaged to give equivalent results to the deterministic ODE models. Single and average responses from a stochastic version of the vesicle-state model are shown in Figure 7.11. The average response matches the output of the deterministic model.

7.4 | Complete synaptic models

A complete model of a synapse relates the arrival of the presynaptic action potential with a postsynaptic response. We have described a number of approaches to modelling the pre- and postsynaptic mechanisms involved. These different approaches may be mixed and matched to produce a complete model which contains sufficient detail for the purpose. If the synaptic model is used in a large neural network involving thousands of synapses, the simplest synaptic model will be sufficient. More complex models will be desirable and necessary if we wish to examine the short-term dynamics of a particular input pathway onto a single cell.

A distinguishing feature of complete models is whether the postsynaptic mechanism is driven by: (1) the time of arrival of a presynaptic spike; (2) the average amount of transmitter released due to a presynaptic spike; or (3) the transmitter transient due to the precise number of vesicles released by a spike.

The kinetic schemes for the postsynaptic conductance are driven by an explicit neurotransmitter transient. These postsynaptic models can be

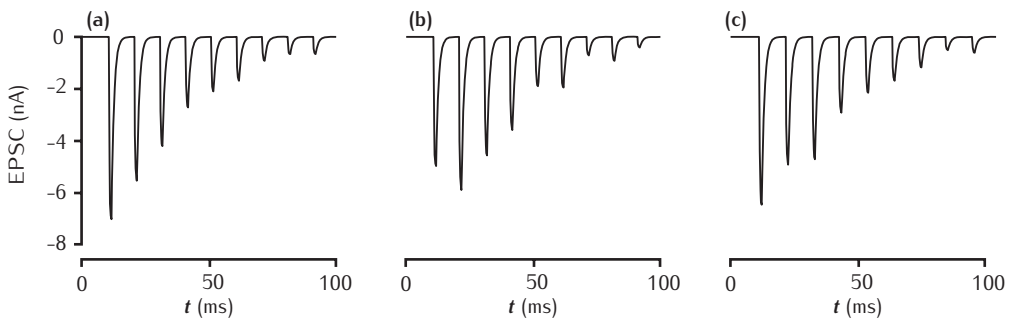


Fig. 7.12 Three distinct trials of a complete synapse model with 500 independent active zones. Each active zone uses the stochastic vesicle-state model of short-term synaptic dynamics combined with the two-gate kinetic model of AMPA receptors. Phenomenological model of facilitation: $p_0 = 0.2$; $\Delta p = 0.05$; $\tau_f = 100$ ms. Vesicle-state model: $k_n^* = k_r = 0.2 \text{ s}^{-1}$; $n_s = 0$. Two-gate kinetic receptor model: $\alpha = 4 \text{ mM}^{-1} \text{ ms}^{-1}$, $\beta = 1 \text{ ms}^{-1}$. $E_{\text{syn}} = 0$ mV, with postsynaptic cell clamped at -65 mV. Synapse stimulated at 100 Hz.

coupled with the presynaptic models of the RRP, n , and release probability p by producing a transmitter transient due to release, $T = np$. If releases due to a single presynaptic spike are assumed to be synchronous, then the parameter T can be used as a scaling factor for the amplitude of a pre-defined transmitter waveform, assuming interspike intervals are sufficiently large that successive waveforms will not overlap. If release is asynchronous, or transmitter waveforms from successive spikes overlap in time, then the transmitter transients due to individual releases will need to be summed to give the transmitter concentration over time.

Figure 7.12 shows the output of an example model based on the giant calyx of Held (Wong *et al.*, 2003) that combines the stochastic version of

Box 7.2 | Simulating a stochastic synapse model

Monte Carlo simulations of a model can be carried out using a per time-step method, as outlined previously for general kinetic schemes (Section 6.9.2). The algorithm is as follows.

- (1) Time is divided into sufficiently small intervals of duration Δt , so that the probability of a vesicle entering or leaving the RRP during Δt is significantly less than 1.
- (2) During each small time interval Δt , the arrival of a new vesicle from the reserve pool has probability p_a :

$$\begin{aligned} \text{vesicle-state model: } p_a &= 1 - \exp(-k_n^* \Delta t) \approx k_n^* \Delta t \\ \text{release-site model: } p_a &\approx k_n(n_{\max} - n) \Delta t. \end{aligned}$$

Arrivals are generated by testing whether a random number selected uniformly in the interval $[0,1]$ is less than or equal to p_a . If it is, n is incremented by 1.

- (3) Similarly, spontaneous undocking of a vesicle from the RRP is tested by selecting n random numbers uniformly from the interval $[0,1]$ and decrementing n by one for each number that is less than or equal to $k_r \Delta t$.
- (4) If a presynaptic action potential occurs in a particular time interval Δt , then each of the remaining n vesicles is tested for release against release probability p_s , a release occurring if a uniform random number in the interval $[0,1]$ is less than or equal to p_s .

the vesicle-state model for vesicle recycling and release (Figure 7.11) with a simple two-gate kinetic scheme for the AMPA receptor response (Figure 7.5). This shows the summed EPSCs due to 500 independent active zones which contain on average a single releasable vesicle. Note the trial-to-trial variation due to stochastic release and the interplay between facilitation of release and depletion of available vesicles.

If the trial-to-trial variation in the postsynaptic response is of interest, in addition to using a stochastic model for vesicle recycling and release, variations in **quantal amplitude**, which is the variance in postsynaptic conductance on release of a single vesicle of neurotransmitter, can be included. This is done by introducing variation into the amplitude of the neurotransmitter transient due to a single vesicle, or variation in the maximum conductance that may result (Fuhrmann *et al.*, 2002).

7.5 Long-lasting synaptic plasticity

The models detailed above incorporate aspects of short-term plasticity at synapses, such as variability in the availability of releasable vesicles and the probability of their release. Learning and memory in the brain is hypothesised to be at least partly mediated by longer-lasting changes in synaptic strength, known as **long-term potentiation (LTP)** and **long-term depression (LTD)**. While short-term plasticity largely involves presynaptic mechanisms, longer-lasting changes are mediated by increases or decreases in the magnitude of the postsynaptic response to released neurotransmitter.

Models of LTP/LTD seek to map a functional relationship between pre- and postsynaptic activity and changes in the maximum conductance produced by the postsynaptic receptor pool, typically AMPARs and NMDA receptors. The biology is revealing complex processes that lead to changes in the state and number of receptor molecules (Ajay and Bhalla, 2005). As outlined in the previous chapter (Section 6.8.2), these processes involve calcium-mediated intracellular signalling pathways. Detailed models of such pathways are being developed. However, for use in network models of learning and memory, it is necessary to create computationally simple models of LTP/LTD that capture the essence of these processes, while leaving out the detail. In particular, a current challenge is to find the simplest model that accounts for experimental data on **spike-timing-dependent plasticity (STDP)**. This data indicates that the precise timing of pre- and postsynaptic signals determines the magnitude and direction of change of the synaptic conductance (Levy and Steward, 1983; Markram *et al.*, 1997; Bi and Poo, 1998). The presynaptic signal is the arrival time of an action potential, and the postsynaptic signal is a **back-propagating action potential (BPAP)** or a synaptic calcium transient.

There are many mathematical formulations of an STDP rule. A simple one accounts for the change in synaptic strength resulting from a single pre- and postsynaptic spike pair. Suppose that a spike occurs in postsynaptic neuron j at time t^{post} , and one occurs in presynaptic neuron i at time t^{pre} . Defining the time between these spikes as $\Delta t = t^{\text{post}} - t^{\text{pre}}$, an expression

The first experimental evidence for long-lasting, activity-dependent changes in synaptic strength were obtained by Bliss and Lømo (1973). By inducing strong firing, or **tetanus**, in the granule cells of the dentate fascia of the hippocampus, Bliss and Lømo found that the amplitude of the signal due to granule cell synaptic currents remained larger after the tetanus, for hours or even days thereafter, leading to the term **long-term potentiation**. It soon became apparent that long-lasting decreases in synaptic strength could also occur in certain circumstances (Lynch *et al.*, 1977; Levy and Steward, 1979). The disparate forms of decreasing strength are known as **long-term depression**.

In addition to tetanic stimulation, it has been found that the relative timing of the presynaptic and the postsynaptic spikes affects the direction of synaptic plasticity. A synapse is more likely to be strengthened if the presynaptic neuron fires within approximately 50 milliseconds before the postsynaptic neuron; conversely, if it fires shortly after the postsynaptic neuron then the synapse is weakened. This phenomenon is referred to as **spike-timing-dependent plasticity** and is found in both developing (Zhang *et al.*, 1998) and adult synapses (Markram *et al.*, 1997; Bi and Poo, 1998).

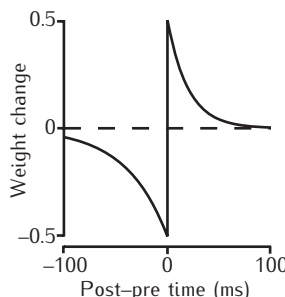


Fig. 7.13 Example STDP weight change curves. The weight is increased if the postsynaptic spike occurs at the time of, or later than, the presynaptic spike; otherwise the weight is decreased. The magnitude of the weight change decreases with the time interval between the pre- and postsynaptic spikes. No change occurs if the spikes are too far apart in time.

for the change in synaptic strength, or weight, w_{ij} is (Song *et al.*, 2000; van Rossum *et al.*, 2000):

$$\begin{aligned}\Delta w_{ij} &= A^{\text{LTP}} \exp(-\Delta t/\tau^{\text{LTP}}) && \text{if } \Delta t \geq 0 \\ \Delta w_{ij} &= -A^{\text{LTD}} \exp(\Delta t/\tau^{\text{LTD}}) && \text{if } \Delta t < 0.\end{aligned}\quad (7.35)$$

These weight change curves are illustrated in Figure 7.13. The parameters A^{LTP} , A^{LTD} , τ^{LTP} and τ^{LTD} can be determined experimentally. The data of Bi and Poo (1998) are well fit with $\tau^{\text{LTP}} = 17$ ms and $\tau^{\text{LTD}} = 34$ ms (van Rossum *et al.*, 2000). The magnitude of LTP, A^{LTP} , often is greater than that of LTD, but it is small for synapses that are already strong. In a synaptic model, the weight w_{ij} could be used as a scaling factor for the maximum postsynaptic receptor conductance, \bar{g}_{syn} (Section 7.2).

More complex models attempt to account for data from stimulation protocols that include triplets or more physiological patterns of spikes (Abarbanel *et al.*, 2003; Castellani *et al.*, 2005; Rubin *et al.*, 2005; Badoual *et al.*, 2006). The simplest such model is a generalisation of the simple spike pair model (Equation 7.35) that treats the weight change as the linear sum of changes due to individual spike pairs within a sequence of pre- and postsynaptic spikes (Badoual *et al.*, 2006). It relates the sequence of spike times to the rate of change in synaptic strength w_{ij} between presynaptic neuron i and postsynaptic neuron j , via the equation:

$$\frac{dw_{ij}}{dt} = \sum_k A^{\text{LTP}} \exp(-(t - \tilde{t}^{\text{pre}})/\tau^{\text{LTP}}) \delta(t - t_k^{\text{post}}) - \sum_l A^{\text{LTD}} \exp(-(t - \tilde{t}^{\text{post}})/\tau^{\text{LTD}}) \delta(t - t_l^{\text{pre}}).\quad (7.36)$$

The sum k is over all postsynaptic spikes, occurring at times t_k^{post} , and the sum l is over all presynaptic spikes. On occurrence of a postsynaptic spike, the weight is increased as an exponentially decaying function of the immediately preceding presynaptic spike time \tilde{t}^{pre} . Similarly, the weight is decreased when a presynaptic spike occurs, as an exponentially decaying function of the immediately preceding postsynaptic spike time \tilde{t}^{post} .

In reality, weight changes to general pre- and postsynaptic spike trains do not seem to be simple linear sums of the changes expected from individual spike pairs (Froemke and Dan, 2002). Further phenomenological components can be added to this simple model to incorporate effects such as weight saturation and spike triplet interactions, for example (Badoual *et al.*, 2006):

$$\begin{aligned}\frac{dw_{ij}}{dt} = \epsilon_i \epsilon_j \left[(w^{\text{LTP}} - w_{ij}) \sum_k A^{\text{LTP}} \exp(-(t - \tilde{t}^{\text{pre}})/\tau^{\text{LTP}}) \delta(t - t_k^{\text{post}}) \right. \\ \left. - (w_{ij} - w^{\text{LTD}}) \sum_l A^{\text{LTD}} \exp(-(t - \tilde{t}^{\text{post}})/\tau^{\text{LTD}}) \delta(t - t_l^{\text{pre}}) \right].\quad (7.37)\end{aligned}$$

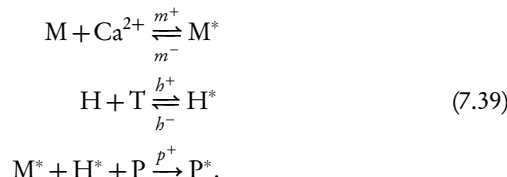
Previous spiking history seems to suppress the magnitude of change for the current spike pair (Froemke and Dan, 2002), and this is captured by two ‘suppression’ factors, $\epsilon_i = 1 - \exp(-(t_i - t_{i-1})/\tau_i^s)$ and $\epsilon_j = 1 - \exp(-(t_j - t_{j-1})/\tau_j^s)$, which are decaying functions of the time interval between the

previous and current spikes in pre- and postsynaptic neurons i and j , respectively. Weights are now limited to be within the range $w^{\text{LTD}} \leq w_{ij} \leq w^{\text{LTP}}$.

Rather than pre- and postsynaptic spike times, the major determinant of long-term synaptic changes is the postsynaptic calcium levels resulting from pre- and postsynaptic activity via calcium entry through NMDA- and voltage-gated calcium channels (Ajay and Bhalla, 2005). Both the magnitude and time course of calcium transients determine the sign and magnitude of synaptic weight changes. Badoual *et al.* (2006) present a simple, phenomenological intracellular signalling scheme to model the mapping from calcium to weight changes. An enzyme, K, mediates LTP in its activated form, K^* , which results from binding with calcium:



The LTD enzyme, P, is activated by two other enzymes, M and H, that are activated by calcium, and neurotransmitter, T, respectively:



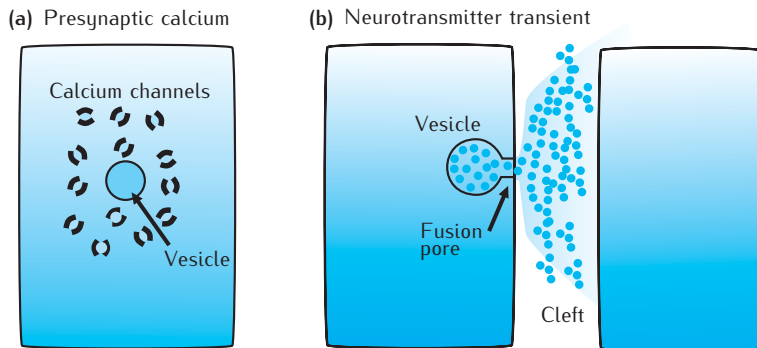
The percentage increase in synaptic weight (maximum conductance) is proportional to K^* and the percentage decrease is proportional to P^* , with the total weight change being the difference between these changes. This model specifies that the sign and magnitude of a weight change is determined by the peak amplitude of a calcium transient. It captures the basic phenomena that lower levels of calcium result in LTD, whereas higher levels result in LTP. More biophysically realistic, but computationally more complex models, that attempt to capture the relationship between postsynaptic calcium transients and changes in synaptic strength, are considered in Section 6.8.2.

7.6 | Detailed modelling of synaptic components

We have concentrated on models that describe synaptic input for use in either detailed compartmental models of single neurons or in neural networks. Modelling can also be used to gain greater understanding of the components of synaptic transmission, such as the relationship between presynaptic calcium concentrations and vesicle recycling and release (Zucker and Fogelson, 1986; Yamada and Zucker, 1992; Bennett *et al.*, 2000a, b), or the spatial and temporal profile of neurotransmitter in the synaptic cleft (Destexhe and Sejnowski, 1995; Barbour and Häusser, 1997; Rao-Miroznik *et al.*, 1998; Smart and McCammon, 1998; Franks *et al.*, 2002; Coggan *et al.*, 2005; Sosinsky *et al.*, 2005). This is illustrated in Figure 7.14.

Such studies typically require modelling molecular diffusion in either two or three dimensions. This can be done using the deterministic and

Fig. 7.14 (a) Spatial distribution of voltage-gated calcium channels with respect to location of a docked vesicle.
 (b) Spatial and temporal profile of neurotransmitter in the synaptic cleft on release of a vesicle.



stochastic approaches outlined in Chapter 6 in the context of modelling intracellular signalling pathways. Deterministic models calculate molecular concentrations in spatial compartments and the average diffusion between compartments (Zucker and Fogelson, 1986; Yamada and Zucker, 1992; Destexhe and Sejnowski, 1995; Barbour and Häusser, 1997; Rao-Miroznik *et al.*, 1998; Smart and McCammon, 1998). Stochastic models track the movement and reaction state of individual molecules (Bennett *et al.*, 2000a, b; Franks *et al.*, 2002). Increasingly, spatial finite element schemes based on 3D reconstructions of synaptic morphology are being employed (Coggan *et al.*, 2005; Sosinsky *et al.*, 2005). The simulation package MCELL (Stiles and Bartol, 2001) is specifically designed for implementing stochastic models based on realistic morphologies (Appendix A.1.2).

7.7 | Gap junctions

Though first identified in invertebrate and vertebrate motor systems (Furshpan and Potter, 1959; Auerbach and Bennett, 1969), it is now recognised that many neurons, including those in the mammalian central nervous system (Connors and Long, 2004), may be connected by purely electrical synapses known as **gap junctions**. These electrical connections are typically dendrite-to-dendrite or axon-to-axon and are formed by channel proteins that span the membranes of both connected cells (Figure 7.15a). These channels are permeable to ions and other small molecules, and allow rapid, but attenuated and slowed exchange of membrane voltage changes between cells (Bennett and Zukin, 2004). Gap junctions between cells of the same type usually are bidirectional, but junctions between cells of different types often show strong rectification, with depolarisations being transferred preferentially in one direction and hyperpolarisations in the other. This is due to the different cells contributing different protein subunits at either side of the junction (Marder, 2009; Phelan *et al.*, 2009). Gap junction conductance can also be modulated by various G protein-coupled receptors, leading to long-lasting changes in coupling strength as the result of neuronal activity (Bennett and Zukin, 2004), equivalent to the long-lasting changes seen at chemical synapses.

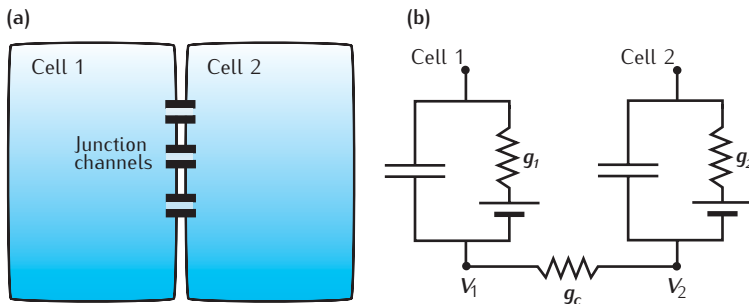


Fig. 7.15 (a) Schematic of a gap junction connection between two apposed neurites (dendrites or axons), with (b) the equivalent electrical circuit.

A simple gap junction model assumes a particular fixed, symmetric permeability of the gap junction channels. Thus the electrical current through a gap junction is modelled as being strictly ohmic, with a coupling conductance g_c . The current flowing into each neuron is proportional to the voltage difference between the two neurons at the point of connection (Figure 7.15b):

$$\begin{aligned} I_1 &= g_c(V_2 - V_1) \\ I_2 &= g_c(V_1 - V_2). \end{aligned} \quad (7.40)$$

An example of the effect of a gap junction between two axons is shown in Figure 7.16. The gap junction is half-way along the two axons, and an action potential is initiated at the start of one axon. If the gap junction is sufficiently strong then the action potential in the first axon can initiate an action potential in the second axon, which then propagates in both directions along this axon.

Even this simple connection between two neurons can lead to complex effects. The response of one neuron to the voltage change in the other can be quite asymmetric between neurons, despite a symmetric coupling conductance, if the two neurons have different cellular resistances (or, equivalently, conductances). For the circuit shown in Figure 7.15b, consider current being injected into cell 1 so that it is held at voltage V_1 , relative to its resting membrane potential. Kirchhoff's law for current flow stipulates that the current flowing into point V_2 must equal the current flowing out, so that:

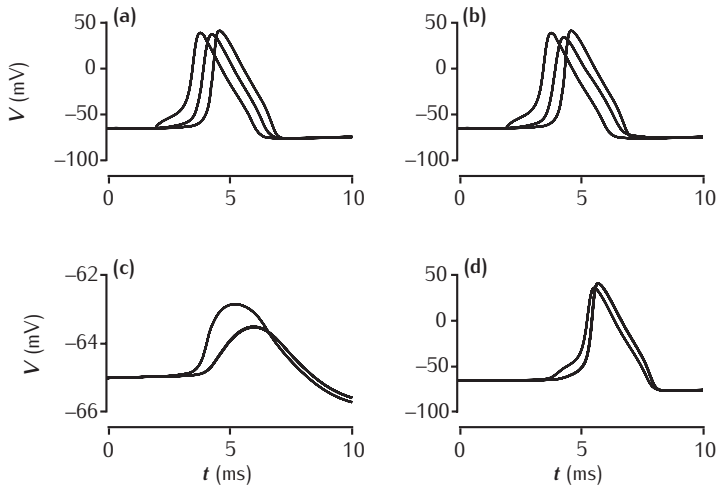
$$(V_1 - V_2)g_c = V_2g_c. \quad (7.41)$$

Rearranging this equation gives a coupling coefficient that describes the relative voltage seen in cell 2 for a given voltage in cell 1:

$$\frac{V_2}{V_1} = \frac{g_c}{g_2 + g_c}. \quad (7.42)$$

Clearly, V_2 is always less than V_1 , and the attenuation will be only small if the conductance of cell 2 is low (the cell has a high input resistance), relative to the coupling conductance. Similarly, if cell 2 is held at V_2 , then the

Fig. 7.16 Simulated action potential travelling along two axons that are joined by a gap junction half-way along their length. Membrane potentials are recorded at the start, middle and end of the axons. (a, b) Axon in which an action potential is initiated by a current injection into one end. (c) Other axon, with a 1 nS gap junction. (d) Other axon, with a 10 nS gap junction. Axons are 100 µm long, 2 µm in diameter with standard Hodgkin–Huxley sodium, potassium and leak channels.



attenuation in V_1 is given by:

$$\frac{V_1}{V_2} = \frac{g_c}{g_1 + g_c}. \quad (7.43)$$

If $g_1 \neq g_2$, then the attenuation across the gap junction is not symmetric for voltage changes in cell 1 or cell 2.

The above derivation of coupling attenuation assumes that the cellular conductances are fixed. However, changes in membrane potential are often accompanied by, or result from, changes in membrane conductance due to the opening or closing of ion channels. This can result in a fixed, symmetric coupling also being somewhat rectifying, with hyperpolarisations being less attenuated than depolarisations, due to the decrease in cellular membrane resistance associated with depolarisations. This is a different form of rectification than that resulting from an asymmetric subunit structure of the gap junction proteins.

7.8 | Summary

The chemical synapse is a very complex device. Consequently, a wide range of mathematical models of this type of synapse can be developed. When embarking on developing such a model it is essential that the questions for which answers will be sought by the use of the model are clearly delineated.

In this chapter we have presented various models for chemical synapses, ranging from the purely phenomenological to models more closely tied to the biophysics of vesicle recycling and release and neurotransmitter gating of postsynaptic receptors. Along the way we have highlighted when different types of model may be appropriate and useful.

Many of the modelling techniques are the same as those seen in the previous two chapters. In particular, the use of kinetic reaction schemes and their equivalent ODEs. Stochastic algorithms have been used when the ODE approach is not reasonable, such as for the recycling and release of small numbers of vesicles at an active zone.

Finally, we considered how subcomponents of the chemical synapse can also be illuminated by mathematical modelling. Reaction–diffusion systems at the ODE and stochastic levels are of importance here to investigate presynaptic calcium transients and the neurotransmitter transient in the synaptic cleft.

Mention was also made of modelling electrical gap junctions, which are simpler in operation than chemical synapses, but can result in highly asymmetric voltage changes between coupled cells.

Chapter 8

Simplified models of neurons

In this chapter a range of models with fewer details than in previous chapters is considered. These simplified neuron models are particularly useful for incorporating into networks since they are computationally more efficient, and sometimes they can be analysed mathematically. **Reduced compartmental models** can be derived from large compartmental models by lumping together compartments. Additionally, the number of gating variables can be reduced while retaining much of the dynamical flavour of a model. These approaches make it easier to analyse the function of the model using the mathematics of dynamical systems. In the yet simpler **integrate-and-fire** model, there are no gating variables, action potentials being produced when the membrane potential crosses a threshold. At the simplest end of the spectrum, **rate-based models** communicate via firing rates rather than individual spikes.

Up until this point, the focus has been on adding details to our neuron models. In this chapter we take the apparently paradoxical step of throwing away a lot of what is known about neurons. Given all the painstaking work that goes into building detailed models of neurons, why do this? There are at least two reasons:

- (1) We wish to explain how a complicated neural model works by stripping it down to its bare essentials. This gives an explanatory model in which the core mechanisms have been exposed and so are easier to understand.
- (2) We wish to understand the behaviour of a network of neurons. We can use a descriptive model to describe the essential function of the neurons in question. These are faster to simulate than compartmental neurons and may allow mathematical analysis of the network.

The programme of simplification in this chapter begins with multi-compartmental models. By reducing the number of compartments and reducing the number of state variables, models such as the two-compartment Pinsky-Rinzel model of a hippocampal pyramidal cell (Pinsky and Rinzel, 1994) can be derived. Despite having only two compartments, this model can exhibit a wide range of firing behaviour, and using it gives insights into the function of hippocampal pyramidal cells. A further reduction in the number

of compartments, to one, and a reduction of the number of state variables to two leads to models such as the FitzHugh–Nagumo model (FitzHugh, 1961; Nagumo *et al.*, 1962) or the Morris–Lecar model (Morris and Lecar, 1981). These models can be analysed using the mathematics of dynamical systems (Appendix B.2), and the behaviour of the system can be visualised straightforwardly. Analysis using these concepts helps explain what properties of a model lead to model behaviours such as Type I or Type II firing, as defined in Section 5.4.1. However, knowledge of dynamical systems analysis is not essential for understanding the rest of this chapter.

The next level of simplification discussed is to take away another state variable, leaving only the membrane potential. In order to produce spikes, this model neuron can have a spike-generating mechanism added to produce the venerable integrate-and-fire model (Lapicque, 1907; Hill, 1936; Knight, 1972). This model can be used as a simple description of neurons in large networks. These networks can often be analysed mathematically, helping to explain properties that arise out of the network. One example discussed is the effect of noise on transmission of signals through a network. The chapter also covers a number of variants of integrate-and-fire neurons, which can improve their fit to data.

Finally, we remove even the spikes, to give firing-rate models, which generate and receive firing rates rather than spike times. These models are appropriate for applications in which precise firing times are not very important to the network behaviour.

As discussed by other authors (e.g. Herz *et al.*, 2006), there are a number of factors to be taken into consideration when deciding upon what type and degree of simplification is appropriate:

The level of explanation: The elements of the model need to correspond to the physical elements being described. For example, a model incorporating models of the appropriate types of ion channels is needed in order to predict what happens to a neuron when a particular neuromodulator is released or a particular type of channel is blocked. However, if we can characterise the behaviour of the manipulated neurons, we could construct a simple functional model of them which would allow the behaviour of a network of such neurons to be predicted.

The data available: A complex model tends to contain more parameters. If there is not a great deal of data available, it may not be possible to constrain all these parameters; see, for example, the discussion of Markov models in Chapter 5.

The desired type of analysis: Very simple models allow mathematical analysis of networks, giving insight into mechanisms of network behaviour.

Computational resources: Simpler models are faster to simulate than more complex models. This is particularly a consideration when large networks of neurons are being simulated. However, as the speed of computers increases, lack of computational resources will become less of a consideration.

8.1 | Reduced compartmental models

This section considers two approaches to reducing the number of variables in compartmental models of neurons. The first approach is to reduce the number of compartments. The method due to Rall (1964) for reducing the number of compartments in a model by lumping compartments together into equivalent cylinders has already been discussed in Section 4.3.3. However, beyond this there are few hard-and-fast principles governing *when* it is appropriate to reduce the number of compartments, and by how much. We therefore proceed by example, citing cases in which neuron models with varying numbers of compartments have been employed. In particular, we discuss Pinsky and Rinzel's (1994) two-compartmental model of a hippocampal pyramidal cell in some depth. This model has been used widely, and our discussion illustrates how a simplified model can be used to understand the behaviour of models that correspond to real neurons more exactly.

The second approach is to reduce the number of state variables. This can be achieved by changing the equations governing the membrane potential so that the number of differential equations describing the system is reduced. There are a number of models in the literature with two state variables, and we focus on the model developed by Morris and Lecar (1981).

8.1.1 Models with more than two compartments

It is worth noting that reducing the number of compartments is not always appropriate. For example, cells whose neurites are much longer than the length constant (Section 2.9.1) must be split into hundreds or thousands of compartments in order to address questions regarding the spatio-temporal behaviour of the membrane potential throughout the neuron. For example, in their model of a Purkinje cell, De Schutter and Bower (1994a) used 1600 compartments to ensure that the passive electrotonic length of each compartment was less than 0.05 of the length constant. This level of detail allowed the response to *in vitro* current injection and inputs from realistic distributions of synaptic inputs to be simulated (De Schutter and Bower, 1994b). The prediction from the simulations that inhibitory inputs have more influence over spike timing than excitatory inputs was later confirmed by experiments (Jaeger and Bower, 1999).

An early example of a reduced model is the model of mitral cells in the olfactory bulb, due to Rall and Shepherd (1968). The model mitral cell comprised one somatic compartment with two ionic conductances, sufficient to create an action potential, and 5–10 dendritic compartments. Extracellular potentials were read out of the model, and compared to readings from extracellular electrodes in the olfactory bulb. The differences between the model and experimental results allowed Rall and Shepherd to infer the existence of dendro-dendritic synapses between mitral cells and granule cells. The existence of these synapses was confirmed subsequently by electron micrograph studies (Rall *et al.*, 1966).

Hippocampal CA1 and CA3 pyramidal cells have been modelled with varying numbers of compartments, ranging from over 1500 compartments in a model of a CA1 cell designed to investigate back-propagating

In an introduction to the papers in a retrospective collection of Rall's work (Segev *et al.*, 1995), Shepherd explains that there was a delay in writing up the model and so the experimental work (Rall *et al.*, 1966) was published two years before the modelling work (Rall and Shepherd, 1968).

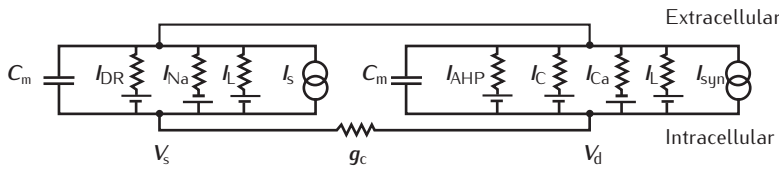


Fig. 8.1 Circuit diagram of the Pinsky–Rinzel model.

action potentials (Golding *et al.*, 2001; accession number 64167 in the modelling archive ModelDB) through models with a few hundred compartments (Poirazi *et al.*, 2003) or 64 compartments (Traub *et al.*, 1994), designed to investigate synaptic integration in single cells, down to models with 19 compartments (Traub *et al.*, 1991), which were able to reproduce experimentally recorded fast bursting, and were used in simulations of oscillations in the CA3 network (Traub *et al.*, 1992).

An example of where a relatively small and simple compartmental model has been used to good effect is in the analysis by Agmon-Snir *et al.* (1998) of coincidence-detection cells in the auditory brainstem. These cells have two dendritic trees emerging from the soma, and each tree receives synapses from one ear. By modelling these dendrites as passive cables, they showed that using these model cells produces better coincidence detection than a one-compartment cell. In addition, in the model there is an optimal length for the dendrites, which depends on the frequency of the inputs received by the cell. This mirrors the relationship between dendrite length and input frequency found in chicks (Smith and Rubel, 1979).

8.1.2 Two compartments: the Pinsky–Rinzel model

Pinsky and Rinzel (1994) used the ionic conductances of a 19-compartment reduced model of a CA3 cell developed by Traub *et al.* (1991) for their two-compartment model of the same cell type (Figure 8.1). The model, the equations for which are presented in Box 8.1, contains a soma and a dendrite compartment. The soma compartment contains sodium and potassium delayed rectifier currents (I_{Na} and I_{DR}). The dendrite contains a voltage-dependent calcium current I_{Ca} and a voltage-dependent potassium AHP current I_{AHP} , as well as a calcium-dependent potassium C current I_C . The proportion p of the membrane area occupied by the soma and the strength of the coupling conductance g_c between the soma and dendrite can be varied.

Despite the small number of compartments, the model can reproduce a variety of realistic activity patterns in response to somatic current injection or dendritic synaptic input. Figure 8.2 shows the behaviour of the somatic and dendritic membrane potential, the dendritic calcium concentration and the I_{AHP} activation variable q for three different combinations of somatic injection current I_s and the soma–dendrite coupling conductance g_c .

In the first combination (Figure 8.2a) the coupling conductance and the somatic injection current are relatively low. During the one second of stimulation, the neuron appears to produce four spikes (middle), giving a firing frequency of around 4 Hz. At a higher resolution (left), each spike can actually be seen to be a **burst** of action potentials. The first spike of the burst is initiated in the soma, and then spreads to the dendrite. The soma repolarises, but current from the dendrite is not able to flow quickly back to the

Box 8.1 | The Pinsky–Rinzel equations

The membrane equations for the two compartments in Figure 8.1 are:

$$\begin{aligned} C_m \frac{dV_s}{dt} &= -\bar{g}_L(V_s - E_L) - g_{Na}(V_s - E_{Na}) - g_{DR}(V_s - E_K) \\ &\quad + \frac{g_c}{p}(V_d - V_s) + \frac{I_s}{p} \\ C_m \frac{dV_d}{dt} &= -\bar{g}_L(V_d - E_L) - g_{Ca}(V_d - E_{Ca}) - g_{AHP}(V_d - E_K) - g_c(V_d - E_K) \\ &\quad + \frac{g_c}{1-p}(V_s - V_d) + \frac{I_{syn}}{1-p}. \end{aligned}$$

$C_m = 3 \mu F \text{ cm}^{-2}$ is the membrane capacitance; p is the proportion of the membrane area taken up by the soma ($p = 0.5$ in the simulations shown in Figure 8.2); g_c is the coupling conductance; I_s is the somatic injection current and I_{syn} is the dendritic synaptic current, set to zero in this chapter.

Other voltage-dependent conductances are modelled using the Hodgkin–Huxley formalism with differential equations for the state variables h , n , s , c and q . The state variable m has a very fast time constant τ_m so its value is well approximated by its steady state value m_∞ . To make the equations more legible we define the following quantities: $V_1 = V + 46.9$, $V_2 = V + 19.9$, $V_3 = V + 24.9$, $V_4 = V + 40$, $V_5 = V + 20$, $V_6 = V + 8.9$, $V_7 = V + 53.5$, $V_8 = V + 50$. The equations for the conductances and rate coefficients are:

$$\begin{aligned} g_{Na} &= \bar{g}_{Na} m_\infty^2 h & \alpha_m &= -\frac{0.32V_1}{\exp(-V_1/4)-1} & \beta_m &= \frac{0.28V_2}{\exp(V_2/5)-1} \\ & & \alpha_h &= 0.128 \exp\left(\frac{-43-V}{18}\right) & \beta_h &= \frac{4}{1+\exp(-V_5/5)} \\ g_{DR} &= \bar{g}_{DR} n & \alpha_n &= -\frac{0.016V_3}{\exp(-V_3/5)-1} & \beta_n &= 0.25 \exp\left(\frac{-V_4}{40}\right) \\ g_{Ca} &= \bar{g}_{Ca} s^2 & \alpha_s &= \frac{1.6}{1+\exp(-0.072(V-5))} & \beta_s &= \frac{0.02V_6}{\exp(V_6/5)-1} \\ g_c &= \bar{g}_c c \chi([Ca^{2+}]) & \alpha_c &= 0.0527 \left(\exp\left(\frac{V_8}{11}\right) - \exp\left(\frac{V_7}{27}\right) \right) & \text{for } V \leq -10 & \\ & & \alpha_c &= 2 \exp(-V_7/27) & & \text{for } V > -10 \\ & & \beta_c &= 2 \exp(-V_7/27) - \alpha_c & & \text{for } V \leq -10 \\ & & \beta_c &= 0 & & \text{for } V > -10 \\ & & & \chi([Ca^{2+}]) &= \min\left([Ca^{2+}]/250, 1\right) & \\ g_{AHP} &= \bar{g}_{AHP} q & \alpha_q &= \min(0.00002[Ca^{2+}], 0.01) & \beta_q &= 0.001 \end{aligned}$$

The calcium concentration is determined by the first order ODE:

$$\frac{d[Ca^{2+}]}{dt} = -0.13I_{Ca} - 0.075[Ca^{2+}].$$

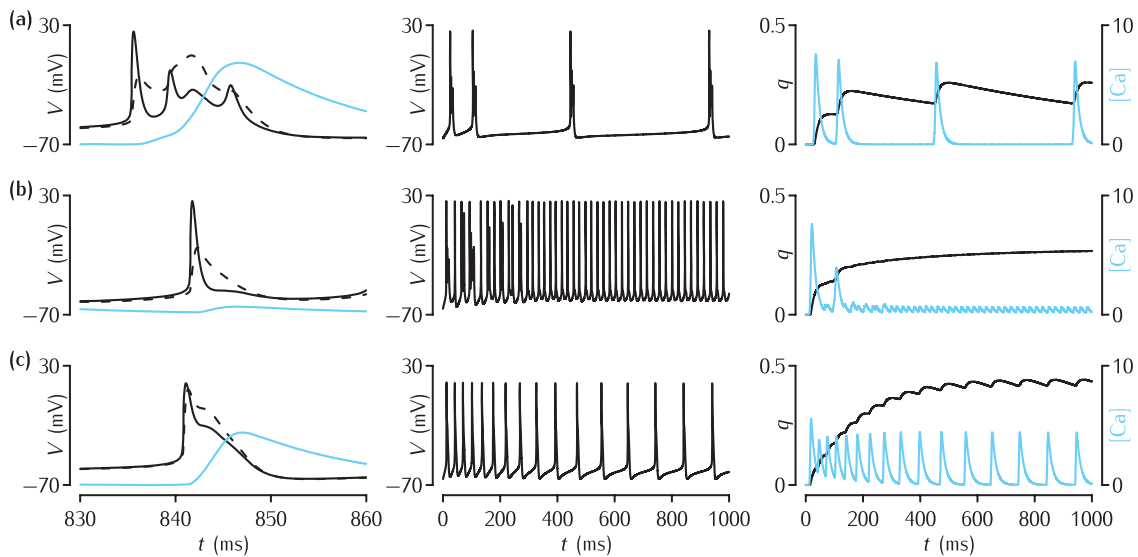
The maximum conductances in mS cm^{-2} are:

$$\bar{g}_L = 0.1 \quad \bar{g}_{Na} = 30 \quad \bar{g}_{DR} = 15 \quad \bar{g}_{Ca} = 10 \quad \bar{g}_{AHP} = 0.8 \quad \bar{g}_C = 15.$$

The reversal potentials are:

$$E_{Na} = 60 \text{ mV} \quad E_K = -75 \text{ mV} \quad E_{Ca} = 80 \text{ mV}.$$

In the equations presented here V has been shifted by -60 mV compared to the equations in Pinsky and Rinzel (1994), so that V refers to the actual membrane potential rather than the deflection from the resting potential.



soma due to the small coupling conductance. This means that there is then a significant voltage difference between the dendrite and the soma, so current flows back into the soma from the dendrite, triggering another spike. This second spike allows the dendrite to remain depolarised, thus causing the calcium current to flow and leading to a prolonged depolarisation of the dendrite. This long calcium spike activates the calcium-dependent potassium current I_{C} , which then causes both dendrite and soma to hyperpolarise and ends the calcium spike. The calcium influx also increases the activation of I_{AHP} (right-hand plot in Figure 8.2a), which, with its slow time constant, keeps the cell hyperpolarised for hundreds of milliseconds and determines the interburst interval.

In the second parameter combination, when the level of somatic current injection is higher, conventional action potentials result (Figure 8.2b, left). This is because the more frequent action potentials lead to a higher level of activation of I_{AHP} at the start of each action potential, thus causing the dendrite to be more hyperpolarised, preventing current flowing back from the dendrite and initiating another spike in the soma. There is also much less calcium influx into the dendrite, due to it being generally more hyperpolarised. The rate at which these spikes are fired, 44 Hz, is much higher than the rate at which the bursts are fired.

In the third parameter combination, there is the same level of current injection as in the second combination, but a higher coupling conductance. Single spikes are produced, but with a long afterdepolarising shoulder (Figure 8.2c, left) and the firing rate of 16 Hz is between the firing rates found in the other two combinations. The larger coupling conductance makes it much easier for current to flow between the soma and the dendrite. This means that the calcium spike in the dendrite is initiated before the soma has had time to repolarise. Thus the sodium current does not have a chance to deinactivate, so there is no second somatic spike, caused by electrotonic spread from the dendritic calcium spike. The firing rate adapts as the overall level of I_{AHP} activation increases (Figure 8.2c, right).

Fig. 8.2 Behaviour of the Pinsky–Rinzel model for different values of the coupling parameter g_c and the level of somatic current injection I_s . In each subfigure, the left-hand column shows the detail of the somatic membrane potential (solid line), the dendritic membrane potential (dashed line) and the calcium concentration (blue line) in a period of 30 ms around a burst or action potential. The middle column shows the behaviour of the membrane potential over 1000 ms. The right-hand column shows the behaviour of q , the I_{AHP} activation variable, and the calcium concentration over the period of 1000 ms. The values of I_s in mA cm^{-2} and g_c in mS cm^{-2} in each row are: (a) 0.15, 2.1; (b) 0.50, 2.1; (c) 0.50, 10.5.

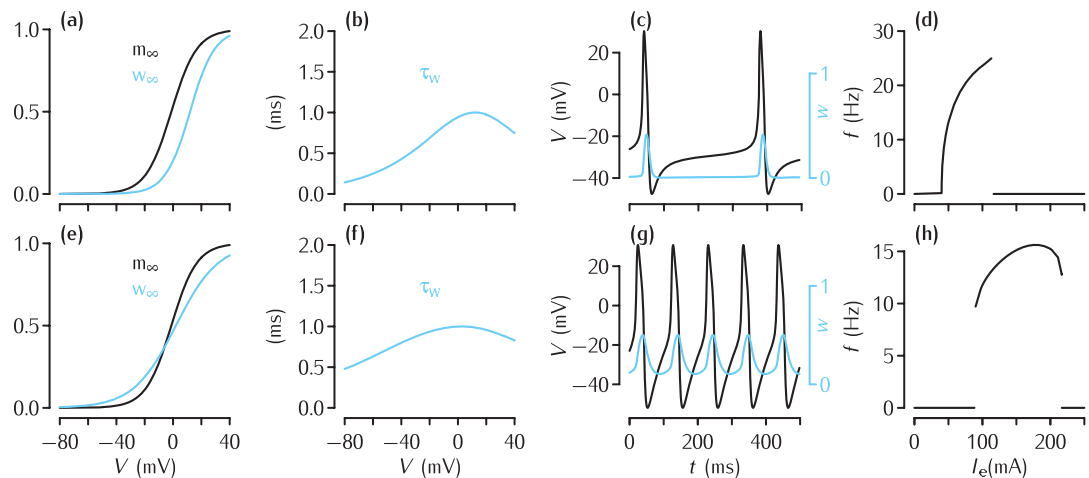


Fig. 8.3 The Morris–Lecar model with a set of parameters giving Type I firing behaviour (a–d) and a set giving Type II behaviour (e–h). (a,e) The steady state of the Ca^{2+} activation variable m_∞ (black) and the steady state of the K^+ activation variable w_∞ (blue) as functions of voltage. (b,f) The time constant for τ_w (blue). There is no time constant for the m state variable, as it responds instantaneously to changes in voltage. (c,g) The time course of the membrane potential V and potassium activation variable w just above the firing threshold for each set of parameters. In (c) the injected current is $I_e = 40.3 \text{ mA cm}^{-2}$, and the action potentials are being fired at 2.95 Hz; arbitrarily low frequencies are possible with slightly less current. In (g) the injected current is $I_e = 89.9 \text{ mA cm}^{-2}$, and the action potentials are being fired at 9.70 Hz; significantly lower frequencies are not possible. (d,h) The f - I curves. In (d), the f - I curve is of Type I since the transition from not firing to firing is continuous, whereas the curve in (h) is Type II because of the discontinuous jump in firing frequency at the onset of firing.

These behaviours, and other features investigated by Pinsky and Rinzel (1994) such as f - I curves, mirror the behaviour of the more complicated Traub *et al.* (1991) model. The simpler formulation of the Pinsky–Rinzel model allows for a greater understanding of the essential mechanisms at work in the more complex model, and in real neurons. A slightly simpler version of the model, though still with two compartments, has been dissected using the phase plane techniques described in Appendix B.2 (Booth and Rinzel, 1995).

The small size of the Pinsky–Rinzel model means that it is faster to simulate than the Traub *et al.* (1991) model, which is especially important when carrying out network simulations. Moreover, Pinsky and Rinzel (1994) demonstrated that a network of Pinsky–Rinzel neurons connected by excitatory synapses has similar properties, such as synchronous bursting, to a similar network of Traub neurons.

8.1.3 Single-compartment reduced models

The HH model of a patch of membrane explains the generation of action potentials well. However, because it contains one differential equation for each of the state variables V , m , n and h , it is hard to understand the interactions between the variables. Various authors have proposed sets of equations that have only two state variables – voltage and another state variable – which can recreate a number of properties of the HH model, most crucially the genesis of action potentials. Some well-known models are the FitzHugh–Nagumo model (FitzHugh, 1961; Nagumo *et al.*, 1962), the Kepler *et al.* (1992) model and the Morris–Lecar model (Morris and Lecar, 1981).

Since the Morris–Lecar model allows for the clearest application of dynamical systems theory (Appendix B.2), we describe it here. The model was developed to describe the barnacle giant muscle fibre, but the model has been applied to other systems, such as lobster stomatogastric ganglion neurons (Skinner *et al.*, 1993) and mammalian spinal sensory neurons (Prescott *et al.*, 2008). The model contains calcium, potassium and leak conductances. Both active conductances are non-inactivating and so they can be described by one state variable. A further reduction in state variables is made by

Box 8.2 | Morris–Lecar equations

I_e is the injected current;

I_i is the ionic current, comprising fast Ca^{2+} , slow K^+ and leak;

m_∞ is the Ca^{2+} activation variable;

w is the K^+ activation variable;

w_∞ is the steady state K^+ activation;

τ_w is the K^+ activation time constant;

ϕ is the temperature/time scaling.

$$C_m \frac{dV}{dt} = -I_i(V, w) + I_e$$

$$\frac{dw}{dt} = \frac{w_\infty(V) - w}{\tau_w(V)}$$

$$I_i(V, w) = \bar{g}_{\text{Ca}} m_\infty(V)(V - E_{\text{Ca}}) + \bar{g}_K w(V - E_K) + g_L(V - E_L)$$

$$m_\infty(V) = 0.5(1 + \tanh((V - V_1)/V_2))$$

$$w_\infty(V) = 0.5(1 + \tanh((V - V_3)/V_4))$$

$$\tau_w(V) = \phi / \cosh((V - V_3)/(2V_4)).$$

Parameters:

$$C_m = 20 \mu\text{F cm}^{-2} \quad E_{\text{Ca}} = 120 \text{ mV} \quad \bar{g}_{\text{Ca}} = 47.7 \text{ mS cm}^{-2}$$

$$\phi = 0.04 \quad E_K = -84 \text{ mV} \quad \bar{g}_K = 20.0 \text{ mS cm}^{-2}$$

$$E_L = -60 \text{ mV} \quad g_L = 0.3 \text{ mS cm}^{-2}$$

Type I parameters: $V_1 = -1.2 \text{ mV}$, $V_2 = 18.0 \text{ mV}$, $V_3 = 12.0 \text{ mV}$, $V_4 = 17.4 \text{ mV}$.

Type II parameters: $V_1 = -1.2 \text{ mV}$, $V_2 = 18.0 \text{ mV}$, $V_3 = 2.0 \text{ mV}$, $V_4 = 30.0 \text{ mV}$.

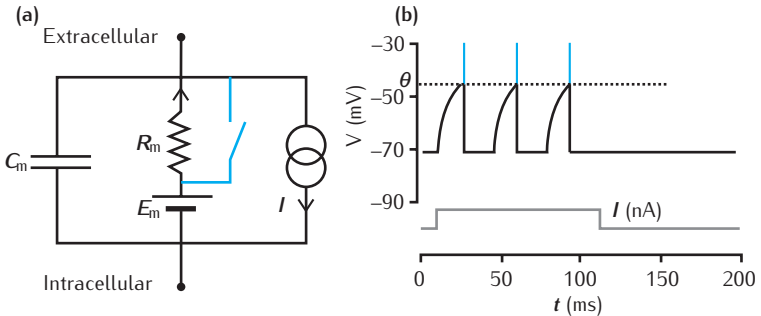
assuming that the calcium conductance responds instantaneously to voltage. There are thus two state variables: the membrane potential V and the potassium state variable w . The parameters V_1 , V_2 , V_3 and V_4 determine the half activation voltage and slope of the activation curves for the calcium and potassium conductances. Activation curves and time constants of the calcium and potassium currents for two different settings of the parameters are shown in Figure 8.3.

Both settings lead to trains of action potentials being produced in response to current injection (Figure 8.3c, g). The first setting of the parameters (Figure 8.3a, b) leads to Type I firing behaviour in the f - I curve (Figure 8.3d). The second set (Figure 8.3e, f) leads to Type II firing behaviour (Figure 8.3h). The full set of equations describing the Morris–Lecar model are given in Box 8.2.

Dynamical systems analysis can be used to characterise the different types of behaviour of the Morris–Lecar model, which depend on the amount of current injected and on the values of the parameters V_1 – V_4 (Box 8.2). The state of this system is characterised by the values of the variables V and w . It may become stable or unstable with both V and w varying periodically through time. The types of stability possible, the conditions when they occur and for what parameter settings there are transitions between states can

As described in Section 5.4.1, Hodgkin (1948) identified two types of neuron, distinguished by their f - I curves. In Type I neurons, the firing rate is zero below a threshold level of injected current and as the current is increased past the threshold, the firing rate starts to increase continuously from zero. In Type II neurons, the firing rate is also zero below the threshold current, but then jumps discontinuously as the current is increased past the threshold.

Fig. 8.4 The IF model. (a) The circuit diagram of the model. This is based on an RC circuit (Figure 2.14). When the membrane potential reaches a threshold voltage θ , the neuron is considered to have fired a spike and the switch, in blue on the circuit diagram, closes. This short circuits the membrane resistance, bringing the membrane potential back to the resting membrane potential E_m . (b) Response of the IF circuit to superthreshold current injection. The membrane potential approaches a fixed value exponentially, but before doing so, it hits the threshold, producing a spike (represented by the blue line). The membrane potential is then reset to the resting membrane potential, and after a refractory period, the switch opens, allowing the membrane potential to rise again.



be calculated and visualised. The properties of this model are explored in detail in Appendix B.2, as an illustration of the application of dynamical systems theory. Rinzel and Ermentrout (1998) consider the Morris-Lecar neuron in more detail and go on to analyse reduced neuronal models with three states, which can give rise to bursting and the aperiodic, apparently random behaviour that is referred to as chaos.

8.2 | Integrate-and-fire neurons

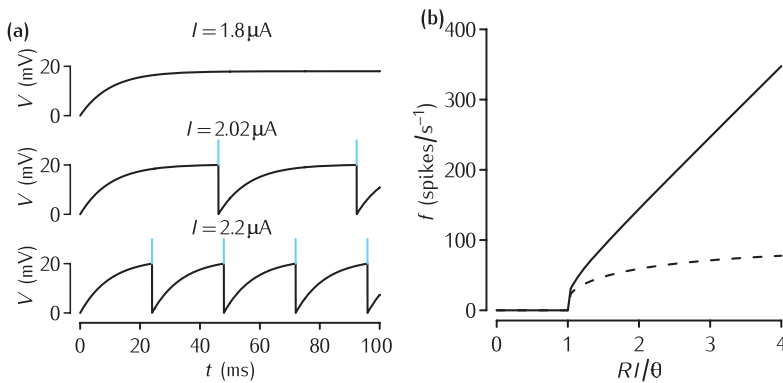
In the neuron models discussed so far, spiking behaviour is described using two or more coupled non-linear differential equations. This allows a detailed understanding of how action potentials and more complex spiking behaviours (such as bursting, Section 8.1.2) arise. Despite the complexity inherent in the generation of action potentials, in many cases their time course and the conditions required for their initiation can be characterised quite straightforwardly. When the membrane potential reaches a certain threshold, a spike is initiated. After an axonal propagation delay, this causes neurotransmitter release from synapses.

This characterisation is used in the **integrate-and-fire** neuron and the **spike-response** model neuron, the two classes of spiking neuron models to be discussed in this chapter. The differential equations that describe them are not coupled and therefore they are faster to simulate than even the simplified models discussed earlier in this chapter. This makes them especially useful for simulating large networks.

8.2.1 Basic integrate-and-fire neurons

The **integrate-and-fire model** is probably the oldest of the simplified models and may predate even the HH model. It captures the notion of the membrane being charged by currents flowing into it and, upon the membrane potential exceeding a threshold, firing an action potential and discharging. There are several variants of the model, in most of which the various components of the model have been added to reproduce the neuronal behaviour rather than for biological verisimilitude at the level of channel dynamics. The model can be thought of as an RC circuit used to model the passive patch of membrane (Figure 2.14), with a spike generation and reset mechanism added. In the circuit diagram shown in Figure 8.4a, the reset mechanism

According to Brunel and van Rossum (2007), whilst the integrate-and-fire model is often attributed to Lapicque (1907), models of this type were only analysed later (Hill, 1936) and the term was first used by Knight (1972).



is represented by a switch, which is closed when the membrane potential reaches a specified threshold level. It then short-circuits the membrane resistance, bringing the membrane potential back to rest. After a refractory period, the switch opens, allowing the membrane to charge again. This is illustrated in the response of the membrane potential to current injection shown in Figure 8.4b.

When the voltage is below this threshold, its value is determined by the equation for an RC circuit:

$$C_m \frac{dV}{dt} = -\frac{V - E_m}{R_m} + I, \quad (8.1)$$

where C_m is the membrane capacitance, R_m is the membrane resistance and I is the total current flowing into the cell, which could come from an electrode or from other synapses. This use of I is in distinction to Chapter 2, where I was the membrane current. This equation is often written in terms of the membrane time constant τ_m which, as in Chapter 2, is the product of R_m and C_m :

$$\tau_m \frac{dV}{dt} = -V + E_m + R_m I. \quad (8.2)$$

When the membrane potential V reaches the threshold, denoted by θ , the neuron fires a spike and the membrane potential V is reset to E_m .

Figure 8.5a shows the behaviour of an integrate-and-fire neuron when different levels of current are injected. Solving for V in Equation 8.2, with small currents, the membrane potential increases from zero and follows an exponential time course, saturating at $R_m I$:

$$V = E_m + R_m I (1 - \exp(-t/\tau_m)). \quad (8.3)$$

However, if $R_m I$ is bigger than the threshold θ , the voltage will cross the threshold at some point in time. The greater the current, the sooner this will happen. The membrane potential then resets to zero and the process repeats.

For above-threshold constant input, the integrate-and-fire neuron fires at a constant frequency. The dependence of frequency on current in a basic integrate-and-fire model is shown in the solid f - I curve in Figure 8.5b. There is no firing ($f = 0$) when the current is below threshold, and the firing

Fig. 8.5 Response of integrate-and-fire neurons to current injection. The parameters are $R_m = 10 \text{ k}\Omega$, $C_m = 1 \mu\text{F}$, $\theta = 20 \text{ mV}$ and $E_m = 0 \text{ mV}$, and the membrane time constant is $\tau_m = R_m C_m = 10 \text{ ms}$. (a) Time course of the membrane potential in response to differing levels of current injection. The current of $1.8 \mu\text{A}$ causes the membrane potential to increase, but does not take it to the firing threshold of 20 mV . For a level of current injection, $2.02 \mu\text{A}$, that is just above the threshold, the neuron spikes when the membrane potential reaches the threshold of 20 mV . The membrane potential is then reset to rest instantly and the membrane starts charging again. For a higher level of current injection, $2.2 \mu\text{A}$, the same process is repeated more frequently. (b) Integrate-and-fire neuron f - I curves. The solid line shows the f - I curve for an integrate-and-fire neuron without an absolute refractory period. The dashed line shows the f - I curve for an integrate-and-fire neuron with an absolute refractory period of 10 ms .

In integrate-and-fire models, the leak battery is often omitted from the circuit. The only effect this has is to make the resting membrane potential 0 mV rather than E_m ; this does not affect the dynamics of the membrane potential.

frequency increases as the current increases. The firing frequency just above the threshold is very close to zero, making the basic integrate-and-fire neuron a Type I model (Section 5.4.1).

The f - I curve of integrate-and-fire neurons

A simple example of the analysis that is possible for integrate-and-fire neurons is to calculate their f - I curve (Stein, 1965; Knight, 1972). For a given level of current injection starting at time $t = 0$, at the time T_s a spike occurs, when the membrane potential is equal to θ . By substituting $V = \theta$ and $t = T_s$ in Equation 8.3 and rearranging the equation, the time to the spike T_s is:

$$T_s = -\tau_m \ln \left(1 - \frac{\theta}{R_m I} \right). \quad (8.4)$$

When a spike occurs and $R_m I$ exceeds θ , the argument of this logarithmic function is between zero and one. This makes the logarithm negative which, combined with the negative sign in front of τ_m in Equation 8.4, makes the time to the spike positive, as it should be. As the current increases, the $\theta/R_m I$ term gets smaller, and the argument of the logarithm approaches one, making the logarithm smaller. Thus the time to spike is shorter for greater input currents, as expected.

The interval between consecutive spikes during constant current injection is the sum of the time to the spike and the absolute refractory period, $T_s + \tau_r$. The frequency f is the reciprocal of this interval:

$$f(I) = \frac{1}{\tau_r + T_s} = \frac{1}{\tau_r - \tau_m \ln(1 - \theta/(R_m I))}. \quad (8.5)$$

The solid curve in Figure 8.5b depicts the f - I curve when there is no refractory period ($\tau_r = 0$). Above a threshold level of current, the firing frequency increases with current, with no upper bound. The dashed curve in Figure 8.5b shows an f - I curve of an integrate-and-fire neuron with an absolute refractory period of 10 ms. The firing frequency increases more gradually with current, approaching a maximum rate of 100 Hz.

8.2.2 Synaptic input to integrate-and-fire neurons

Simple integrate-and-fire neurons bear at least a passing resemblance to many types of real neurons: given enough steady state input current they fire repeatedly, and the greater the input current, the faster the firing rate. This suggests that the integrate-and-fire model may give insightful results when presented with more complex, biologically motivated types of input, such as multiple synaptic inputs.

A simple way of describing the time course of a synaptic input is as a decaying exponential, which was introduced in Section 7.2.1:

$$g_{\text{syn}}(t) = \begin{cases} \bar{g}_{\text{syn}} \exp\left(-\frac{t-t_s}{\tau_{\text{syn}}}\right) & \text{for } t \geq t_s \\ 0 & \text{for } t < t_s, \end{cases} \quad (8.6)$$

where t_s is the time at which the synapse is activated, \bar{g}_{syn} is the maximum conductance of the synapse and $g_{\text{syn}}(t)$ is zero when t is less than t_s . The current passed through the synapse is:

$$I_{\text{syn}}(t) = g_{\text{syn}}(t)(V(t) - E_{\text{syn}}), \quad (8.7)$$

where E_{syn} is the reversal potential for the synapse under consideration. This current can be plugged into an integrate-and-fire neuron by including the synaptic current I_{syn} in the total current I .

To make the model easier to analyse and faster to simulate, **current-based synapses** can be used. In these synapses it is the time course of the synaptic current, rather than conductance, that is prescribed; for example, by a decaying exponential current:

$$I_{\text{syn}}(t) = \begin{cases} \bar{I}_{\text{syn}} \exp\left(-\frac{t-t_s}{\tau_{\text{syn}}}\right) & \text{for } t \geq t_s \\ 0 & \text{for } t < t_s, \end{cases} \quad (8.8)$$

where \bar{I}_{syn} is the maximum current. There is no dependence of the current on the membrane potential; compare this with Equation 8.7, where the membrane potential V changes over time. This decaying exponential time course for $t > t_s$ can be generated by the following differential equation:

$$\tau_{\text{syn}} \frac{dI_{\text{syn}}}{dt} = -I_{\text{syn}}, \quad (8.9)$$

with I_{syn} set to \bar{I}_{syn} at $t = t_s$. This equation will be useful when the integrate-and-fire neurons are simplified to rate-based neurons in Section 8.5.

For typical excitatory synapses, current-based synapses provide a reasonable approximation to conductance-based synapses. Implicit in Equation 8.8 is that \bar{I}_{syn} is the product of the conductance \bar{g}_{syn} and a constant driving force. If the resting potential is -70 mV , the firing threshold is -50 mV and, as in the case of AMPA synapses, the synaptic reversal potential is around 0 mV , then the driving force, $V(t) - E_{\text{syn}}$, ranges between -70 mV and -50 mV . As this is not a huge variation in percentage terms, this assumption is valid.

Inhibitory synapses are not so well approximated by current-based synapses since the reversal potential of inhibitory synapses is often close to the resting potential. In a conductance-based inhibitory synapse, the current may be outward if the membrane potential is above the reversal potential, or inward if it is below. In an inhibitory current-based synapse, the current may only be outward. This can also lead to unrealistically low membrane potentials. Nevertheless, current-based inhibitory synapses can be useful models, as they do capture the notion that inhibitory synapses prevent the neuron from firing.

The effect of a current-based synapse with a decaying exponential current (Equation 8.8) on the membrane potential can be calculated. The result (Figure 7.2c) is a dual exponential with a decay time constant equal to the membrane time constant τ_m and a rise time that depends on the decay time

Box 8.3 Approximating short PSCs by delta functions

The decaying exponential current in Equation 8.8 can be approximated by a delta function (Section 7.3.1):

$$I_{\text{syn}}(t) = \bar{Q}_{\text{syn}} \delta(t - t_s),$$

where \bar{Q}_{syn} is the total charge delivered by the synapse. To see this, note that the charge delivered by a decaying exponential synapse with finite τ_{syn} would be $\bar{Q}_{\text{syn}} = \bar{I}_{\text{syn}} \tau_{\text{syn}}$. Thus the current can be written

$$I_{\text{syn}}(t) = \begin{cases} \bar{Q}_{\text{syn}} \left[\frac{1}{\tau_{\text{syn}}} \exp\left(-\frac{t-t_s}{\tau_{\text{syn}}}\right) \right] & \text{for } t \geq t_s \\ 0 & \text{for } t < t_s. \end{cases}$$

As τ_{syn} approaches zero, the term in square brackets becomes very close to zero, apart from at $t = t_s$, where it has the very large value $1/\tau_{\text{syn}}$. This is approximately a delta function.

constant of the synaptic current input τ_{syn} :

$$V(t) = \begin{cases} R_m \bar{I}_{\text{syn}} \frac{\tau_{\text{syn}}}{\tau_m - \tau_{\text{syn}}} \left(\exp\left(-\frac{t-t_s}{\tau_m}\right) - \exp\left(-\frac{t-t_s}{\tau_{\text{syn}}}\right) \right) & \text{for } t \geq t_s \\ 0 & \text{for } t < t_s. \end{cases} \quad (8.10)$$

The same waveform is sometimes used to model synaptic conductances (Section 7.2.1).

The simplest approximation to synaptic input is to make the EPSCs or IPSCs infinitesimally short and infinitely sharp by reducing the synaptic time constant τ_{syn} towards zero. In this case the voltage response approximates a simple decaying exponential:

$$V(t) = \begin{cases} \frac{R_m \bar{Q}_{\text{syn}}}{\tau_m} \exp\left(-\frac{t-t_s}{\tau_m}\right) & \text{for } t \geq t_s \\ 0 & \text{for } t < t_s, \end{cases} \quad (8.11)$$

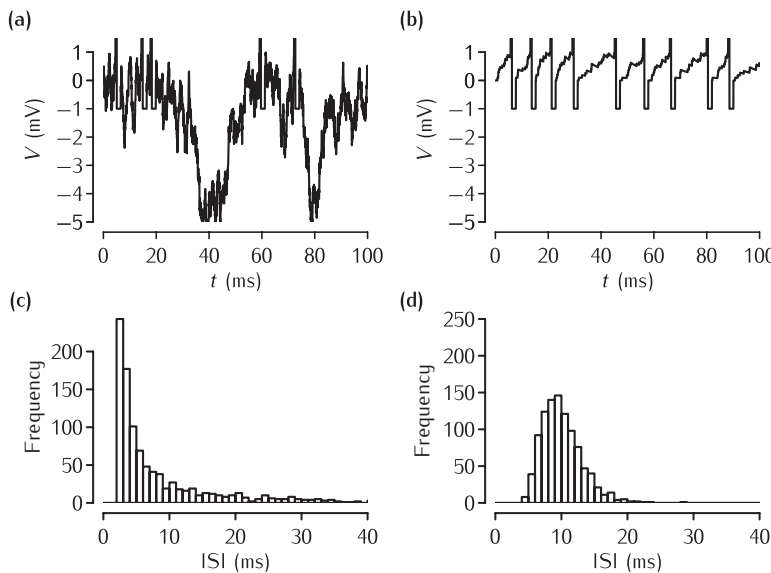
where $\bar{Q}_{\text{syn}} = \bar{I}_{\text{syn}} \tau_{\text{syn}}$ is the total charge contained in the very short burst of current. In order to simulate this, the quantity $R_m \bar{Q}_{\text{syn}}/\tau_m$ is added to the membrane potential of the integrate-and-fire neuron at time t_s ; no differential equation for I_{syn} is required. Infinitesimally short EPSCs or IPSCs can be denoted conveniently using delta functions (Box 8.3).

8.2.3 Applications of integrate-and-fire neurons

Understanding the variability of neuronal firing

There are many sources of random input to neurons, such as the spontaneous release of vesicles at synapses, or the arrival of photons at low light levels. Equally, many types of neurons appear to have a random component to their firing patterns. An important question is therefore the relationship between the variability of inputs to neurons and the variability of their outputs.

Integrate-and-fire neurons have played an important role in understanding this relationship. The **Stein model** (Figure 8.6) comprises an



integrate-and-fire neuron that receives infinitesimally short input pulses from a number of excitatory and inhibitory neurons whose random firing is generated by a Poisson process (Box 8.4 and Appendix B.3). The input causes the membrane potential to fluctuate, sometimes causing it to cross the threshold (Figure 8.6a).

The pattern of firing of the neuron depends strongly on the frequency and size of the excitatory and inhibitory inputs. For example, in Figure 8.6a, where the amount of excitatory and inhibitory input is finely balanced, the time course of the membrane potential and its pattern of firing times appears to be very irregular. In contrast, when there are a smaller number of excitatory inputs present, but no inhibition, the neuron can fire at the same rate, but much more regularly (Figure 8.6b).

The regularity of the spike train can be summarised in **interspike interval (ISI) histograms** (Figures 8.6c, d). Both neurons are firing at the same average rate, yet the ISI histograms look quite different. The neuron with excitation and inhibition – which fires more irregularly – has an ISI that appears to be exponentially distributed, with a large number of very short intervals and a long tail of longer intervals. In contrast, the neuron that appears to fire more regularly has ISIs that appear to be distributed according to a skewed normal distribution centred on 10 ms.

The ISI histograms can be summarised still further, by extracting the **coefficient of variation** (CV), defined as the standard deviation of the ISIs divided by their mean. A regularly spiking neuron would have a CV of 0, since there is no variance in the ISIs, whereas a Poisson process has a CV of 1. The CV of a neuron receiving a mix of excitation and inhibition (Figure 8.6a, c) is 1.26, whereas the more regularly firing neuron (Figure 8.6b, d) has a CV of 0.30.

A variant of the Stein model was used by Shadlen and Newsome (1994, 1995, 1998) in their debate with Softky and Koch (1993) about whether specialised cellular mechanisms are required to account for the randomness in

Fig. 8.6 (a) The Stein (1965) model with balanced excitation and inhibition. The time course of the voltage over 100 ms of an integrate-and-fire neuron that receives inputs from 300 excitatory synapses and 150 inhibitory synapses. Each synapse receives Poisson spike trains at a mean frequency of 100 Hz. The threshold is set arbitrarily to 1 mV, the membrane time constant of the neuron is 10 ms, and there is a refractory period of 2 ms. Each excitatory input has a magnitude of 0.1 of the threshold, and each inhibitory input has double the strength of an excitatory input. Given the numbers of excitatory and inhibitory inputs, the expected levels of excitation and inhibition are therefore balanced. (b) The time course of a neuron receiving 18 excitatory synapses of the same magnitude as in (a). The output firing rate of the neuron is roughly 100 Hz, about the same as the neuron in (a), but the spikes appear to be more regularly spaced. (c) An ISI histogram of the spike times from a sample of 10 s of the firing of the neuron in (a). (d) An ISI histogram for the neuron shown in (b).

Box 8.4 | Poisson processes

A **Poisson process** generates a sequence of discrete events randomly at times t_1, t_2, \dots . Radioactive decay of atoms or the production of spikes are both examples of sequences of discrete events that could be modelled using a Poisson process.

In a Poisson process, the probability of an event occurring in a short period Δt is $\lambda\Delta t$, where λ is the rate at which events are expected to occur and where Δt is small enough that $\lambda\Delta t$ is much less than 1.

The expected distribution of times between events is an exponential of the form $\lambda e^{-\lambda t}$, just like the open and closed time distributions of a state of a stochastic channel (Figure 5.15b).

The probability $P(k)$ of k events happening in a time period of T is given by the **Poisson distribution** (Appendix B.3):

$$P(k) = \frac{e^{-\lambda T} (\lambda T)^k}{k!}.$$

The expected number of events (the mean) in the interval T is λT , and the variance in the number of events is also λT .

Since the probability of an event occurring is independent of the time since the last event, the Poisson process has the Markov property (Section 5.7).

the firing times of neocortical cells. The model showed that a mixture of random excitatory and random inhibitory input to simple integrate-and-fire neurons with membrane time constants of around 10 ms could produce the kind of irregular spike train observed in the neocortex. Shadlen and Newsome (1994) argued that this meant that some of the elements of a much more complex compartmental model of cortical neurons (Softky and Koch, 1993) were not needed to produce realistic firing patterns. In the simulations with the more complex model, only excitatory inputs had been presented to the cell, so in order to achieve the very noisy output patterns, the model had to have various conductance terms added to it to reduce the membrane time constant and therefore produce noisier output. Had Softky and Koch (1993) also used inhibitory inputs, then the extra conductance terms may not have been necessary.

Under certain circumstances, the simplicity of the integrate-and-fire model allows the mean firing rate to be derived mathematically as a function of the arrival rates of the inputs, the threshold, the membrane time constant and the refractory period (Stein, 1965; Tuckwell, 1988; Amit and Brunel, 1997b). Suppose an integrate-and-fire neuron receives spikes generated by a Poisson process at a rate v_E through an excitatory synapse of strength w_E and Poisson-generated spikes at a rate v_I through a synapse of strength w_I . The first step is to consider what would happen to the membrane were there no threshold. From a starting value of $V(0)$ at $t = 0$, the membrane potential would drift towards a mean value μ , but would wander around this value by an amount quantified by the variance σ^2 . The calculations presented in Box 8.5 show that μ and σ depend on the weights, input

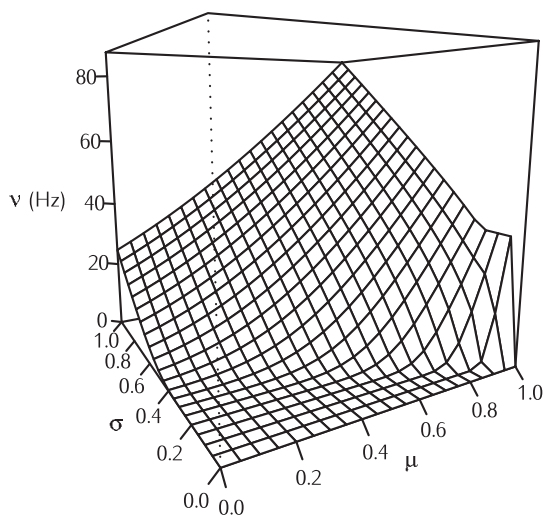


Fig. 8.7 Mean firing frequency v of the Stein model as a function of the mean μ and standard deviation σ of the membrane potential evoked by Poisson spike trains. Parameters: threshold $\theta = 1$, refractory period $\tau_r = 0\text{ ms}$ and membrane time constant $\tau_m = 10\text{ ms}$.

firing rates and membrane time constant:

$$\mu = \tau_m(w_E v_E - w_I v_I) \quad \text{and} \quad \sigma^2 = \frac{\tau_m}{2}(w_E^2 v_E + w_I^2 v_I). \quad (8.12)$$

If the mean value μ is of the order of at least σ below the threshold, the neuron will not fire very often, and it is possible to derive an expression for the mean firing frequency in terms of μ and σ . This dependence is shown in Figure 8.7. For low levels of noise (σ small) the dependence of the firing frequency on the mean input is similar to the dependence on current injection (Figure 8.5b). As the level of noise increases, the firing rate curve is smoothed out so that the effective threshold of the neuron is reduced.

Network and plasticity models

Integrate-and-fire neurons are useful in understanding basic properties of large networks of neurons. An example of such a network model is covered in Section 9.3. The effects of synaptic plasticity can be built into these models to make large scale models of memory (Amit and Brunel, 1997b). Even one integrate-and-fire neuron with a mixture of excitatory and inhibitory inputs may capture enough of the input–output relations of more complex cells to make it a substrate for models of spike-timing dependent synaptic plasticity (Song *et al.*, 2000; van Rossum *et al.*, 2000).

8.3 Making integrate-and-fire neurons more realistic

The basic integrate-and-fire model described so far is able to model regularly firing cells with Type I characteristics, but cannot produce behaviours such as Type II firing, firing rate adaptation or bursting, all of which are observed in many real neurons in response to current injection. This section outlines a number of modifications that can be made to the basic integrate-and-fire

Box 8.5 Analysis of the Stein model

The goal of this analysis is to compute the expected firing rate of an integrate-and-fire neuron that receives spikes generated by a Poisson process at a rate v_E through an excitatory synapse of strength w_E and Poisson-generated spikes at a rate v_I through a synapse of strength w_I . The equation for the membrane potential is:

$$\frac{dV}{dt} = -\frac{V(t)}{\tau} + w_E \sum_k \delta(t - t_E^k) - w_I \sum_k \delta(t - t_I^k),$$

where t_E^k are the times of spikes from excitatory neurons and t_I^k are the times of spikes from inhibitory neurons. $\delta(t)$ is the delta function defined in Section 7.3.1 and τ is the membrane time constant.

Following Tuckwell (1988), the first step is to consider what would happen to the membrane were there no threshold. From a starting value of $V(0)$ at $t = 0$, the membrane potential would drift towards a mean value μ , but would wander around this value by an amount quantified by the variance σ^2 . To calculate μ and σ^2 , the following substitution is made:

$$Y(t) = e^{t/\tau} V(t).$$

This allows us to write:

$$\frac{dY}{dt} = \frac{e^{t/\tau}}{\tau} V(t) + e^{t/\tau} \frac{dV}{dt} = e^{t/\tau} \left(w_E \sum_k \delta(t - t_E^k) - w_I \sum_k \delta(t - t_I^k) \right).$$

This equation is integrated to give the time course of $Y(t)$:

$$Y(t) = Y(0) + \int_0^t e^{t'/\tau} \left(w_E \sum_k \delta(t - t_E^k) - w_I \sum_k \delta(t - t_I^k) \right) dt'.$$

Since the expected number of excitatory and inhibitory spikes in the time dt are $v_E dt$ and $v_I dt$, the expected value of $Y(t)$, $\langle Y(t) \rangle$, can be written:

$$\langle Y(t) \rangle = Y(0) + \int_0^t e^{t'/\tau} (w_E v_E - w_I v_I) dt' = Y(0) + \mu(e^{t/\tau} - 1),$$

where the steady state mean depolarisation is $\mu = \tau(w_E v_E - w_I v_I)$. Similarly, the variance of the number of excitatory and inhibitory events is $v_E dt$ and $v_I dt$, making the total variance of $Y(t)$:

$$\text{Var}(Y(t)) = \int_0^t e^{2t'} (w_E^2 v_E + w_I^2 v_I) dt' = \sigma^2 (e^{2t/\tau} - 1),$$

where the steady state variance is $\sigma^2 = (\tau/2)(w_E^2 v_E - w_I^2 v_I)$.

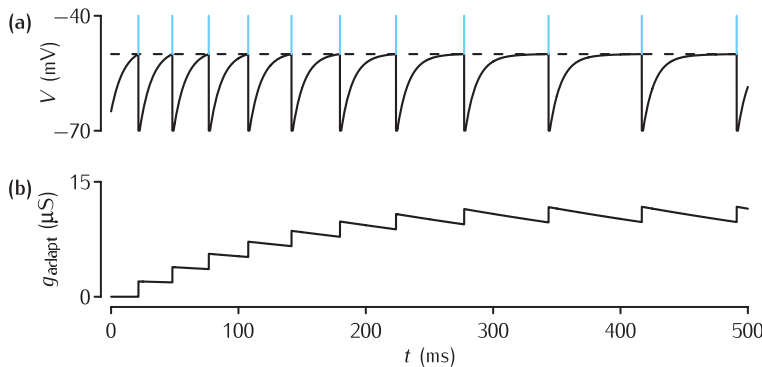
Converting back to voltage, this gives:

$$\langle V(t) \rangle = V(0)e^{-t/\tau} + \mu(1 - e^{-t/\tau}) \quad \text{and} \quad \text{Var}(V(t)) = \sigma^2(1 - e^{-2t/\tau}).$$

When the mean depolarisation μ is below the threshold θ , it is possible to derive an expression for the average firing rate in terms of μ and σ (Tuckwell, 1988; Amit and Brunel, 1997b):

$$f(\mu, \sigma) = \left(\tau_r + \tau \int_{-\mu/\sigma}^{(\theta-\mu)/\sigma} \sqrt{\pi} \exp(u^2) (1 + \text{erf } u) \right)^{-1}.$$

This is the expression plotted in Figure 8.7. $\text{erf } u$ is the error function, defined in Box 2.7.



model so that it can reproduce a wider repertoire of intrinsic neuronal firing patterns.

8.3.1 Adaptation

In many types of neuron, the firing rate in response to a sustained current injection decreases throughout the spike train. The standard integrate-and-fire models described so far cannot exhibit this behaviour. However, it is possible to incorporate this behaviour into integrate-and-fire models by incorporating an extra conductance I_{adapt} that depends on the neuronal spiking (Koch, 1999; Latham *et al.*, 2000). Whenever the neuron spikes, the adaptive conductance g_{adapt} is incremented by an amount Δg_{adapt} and otherwise it decays with a time constant of τ_{adapt} :

$$\frac{dg_{\text{adapt}}}{dt} = -\frac{g_{\text{adapt}}}{\tau_{\text{adapt}}} \quad \text{and} \quad I_{\text{adapt}} = g_{\text{adapt}}(V - E_m). \quad (8.13)$$

Figure 8.8 shows the response to a constant level of current injection of an integrate-and-fire neuron incorporating such an adapting conductance. It can be seen (Figure 8.8a) that the ISIs increase over time until, after about 10 ms, they are constant. The reason for this slowing down is the gradual build-up of the adapting conductance seen in Figure 8.8b.

A related approach is to make the threshold a variable that depends on the time since the neuron last spiked (Geisler and Goldberg, 1966). One possible function is a decaying exponential function:

$$\theta(t) = \theta_0 + \theta_1 \exp((t - t_s)/\tau_r), \quad (8.14)$$

where t_s is the time since the neuron spiked and τ_r is a refractory time constant.

8.3.2 Quadratic integrate-and-fire model

One advantage of the basic integrate-and-fire neuron is its faster speed of simulation compared to a model which generates spikes using realistic conductances. However, this speed of simulation comes at the expense of a poor fit to the ionic current in a spiking neuron when the membrane potential is close to the threshold. In a standard, linear integrate-and-fire neuron, the closer the membrane potential is to the threshold, the greater the outward ionic current (Figure 8.9a). In contrast, in a model with active conductances, in the neighbourhood of the threshold, the current goes from being outward

Fig. 8.8 Response of an adapting integrate-and-fire neuron to a constant level of current injection. (a) The time course of the membrane potential (black) and the spikes resulting from crossing the threshold of -50 mV (blue). (b) The time course of the adaptation conductance, g_{adapt} . The basic integrate-and-fire parameters are $R_m = 10\text{ k}\Omega$, $C_m = 1\text{ }\mu\text{F}$, $\theta = -50\text{ mV}$ and $E_m = -70\text{ mV}$, and the membrane time constant is $\tau_m = R_m C_m = 10\text{ ms}$. The adaptation parameters are: $\tau_{\text{adapt}} = 10\text{ ms}$ and $\Delta g_{\text{adapt}} = 2\text{ }\mu\text{S}$. The level of current injection is $2.2\text{ }\mu\text{A}$.

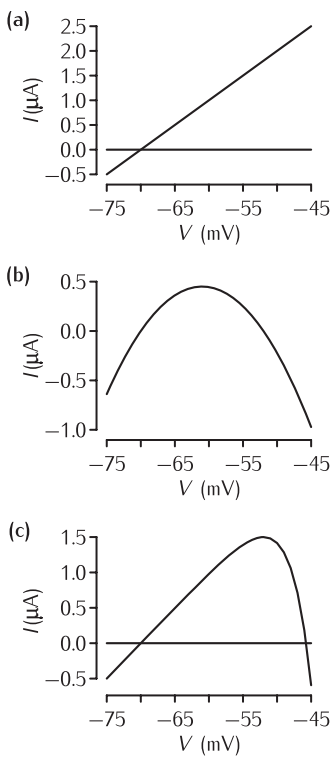


Fig. 8.9 I - V curves for linear and non-linear integrate-and-fire models. (a) I - V curve for the linear integrate-and-fire model with $E_m = -70$ mV and $R_m = 10$ k Ω . (b) I - V curve for the quadratic integrate-and-fire model (Equation 8.15). E_m and R_m as for linear integrate-and-fire; $V_{\text{thresh}} = -52$ mV. (c) I - V curve for the exponential integrate-and-fire model (Equation 8.16). E_m and R_m as for linear integrate-and-fire; $V_T = -52$ mV, $\Delta_T = 3$ mV.

to inward. A hybrid model, which models the ionic current close to the threshold better than the linear integrate-and-fire neuron, is the **quadratic integrate-and-fire neuron** (Hansel and Mato, 2000; Latham *et al.*, 2000). It replaces the $(V - E_m)/R_m$ term in the integrate-and-fire neuron (Equation 8.1) with a quadratic function of V , that is zero both at the resting potential E_m and the threshold V_{thresh} :

$$C_m \frac{dV}{dt} = -\frac{(V - E_m)(V_{\text{thresh}} - V)}{R_m(V_{\text{thresh}} - E_m)} + I. \quad (8.15)$$

The I - V characteristic of this ionic current is plotted in Figure 8.9b. When the membrane potential exceeds the threshold V_{thresh} , this quadratic term becomes positive, causing the neuron to depolarise still further. At a preset value of the membrane potential θ , the membrane potential is reset to the voltage V_{reset} , which can differ from the resting membrane potential. Adaptation currents can also be added to the quadratic integrate-and-fire neuron (Latham *et al.*, 2000).

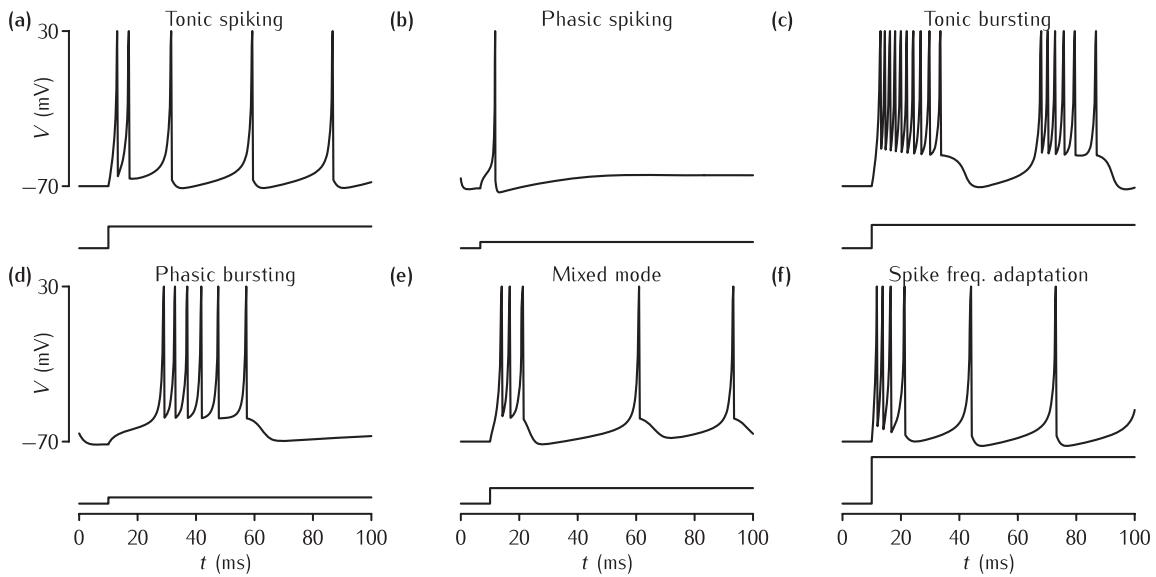
8.3.3 Exponential integrate-and-fire model

Another non-linear variation on the standard integrate-and-fire neuron is the **exponential integrate-and-fire neuron** (Fourcaud-Trocmé *et al.*, 2003). Its form is similar to a linear integrate-and-fire neuron, except that there is an additional current that depends on the exponential of the voltage:

$$C_m \frac{dV}{dt} = -\left(\frac{V - E_m}{R_m} - \frac{\Delta_T}{R_m} \exp\left(\frac{V - V_T}{\Delta_T}\right) \right) + I, \quad (8.16)$$

where V_T is a threshold voltage and Δ_T is a spike slope factor that determines the sharpness of spike initiation. The I - V characteristic of the ionic current is plotted in Figure 8.9c. As with the quadratic neuron, the current is zero very close to E_m , rises to a maximum at $V = V_T$, and then falls, going below zero. If the neuron is initialised with a membrane potential below the upper crossover point, the membrane potential decays back to the resting membrane potential E_m . However, if the membrane potential is above the crossover point, the membrane starts to depolarise further, leading to a sharp increase in voltage, similar to the start of an action potential in the HH model. There is also a threshold θ , which is greater than V_T , at which the membrane potential is reset to V_{reset} .

The curve differs from the quadratic curve in that it is asymmetrical, and has a larger linear region around E_m . Also, the exponential dependence of the additional current matches the lower part of the sodium activation curve better than the quadratic form, suggesting that this is likely to be a more accurate simplification of neurons with fast sodium currents than the quadratic neuron. The exponential integrate-and-fire neuron behaves in a similar way to the quadratic integrate-and-fire neuron. However, differences in the behaviour of the two types of neuron are apparent during fast-spiking behaviour, as the quadratic integrate-and-fire neuron tends to take longer to produce a spike (Fourcaud-Trocmé *et al.*, 2003).



8.3.4 The Izhikevich model

Model neurons that produce a wide range of realistic behaviours can be constructed by adding a recovery variable to the quadratic integrate-and-fire model. One example of this type of model is the **Izhikevich model** (Izhikevich, 2003; Izhikevich and Edelman, 2008), defined by the following equations:

$$\begin{aligned} \frac{dV}{dt} &= k(V - E_m)(V - V_{\text{thresh}}) - u + I \\ \frac{du}{dt} &= a(b(V - E_m) - u) \end{aligned} \quad (8.17)$$

if $V \geq 30 \text{ mV}$, then $\begin{cases} V \text{ is reset to } c \\ u \text{ is reset to } u + d, \end{cases}$

where u is the recovery variable, meant to represent the difference between all inward and outward voltage-gated currents, and k , a , b , c and d are parameters. As with other integrate-and-fire models, the various terms used in the equation specifying the model are justified primarily because they reproduce firing behaviour rather than arising directly from the behaviour of ion channels. Figure 8.10 illustrates a number of the behaviours that the model can exhibit for various settings of the parameters and various current injection protocols (Izhikevich, 2004). This model is efficient to simulate as part of a network, and can be implemented using Euler integration (Appendix B.1.1). For an example of a very large-scale network implemented using these neurons, see Izhikevich and Edelman (2008).

8.3.5 Fitting spiking neuron models to data

A common method of comparing neuron models with real neurons is to inject a noisy current into the soma, or simulated soma, and record the membrane potential or just the times of spikes. The same current is then

Fig. 8.10 The Izhikevich model.

A number of classes of waveforms can be produced using various settings of the parameters a , b , c and d . In all plots,

$k = 0.04 \text{ V s}^{-1}$, $E_m = -70 \text{ mV}$ and $V_{\text{thresh}} = -55 \text{ mV}$.

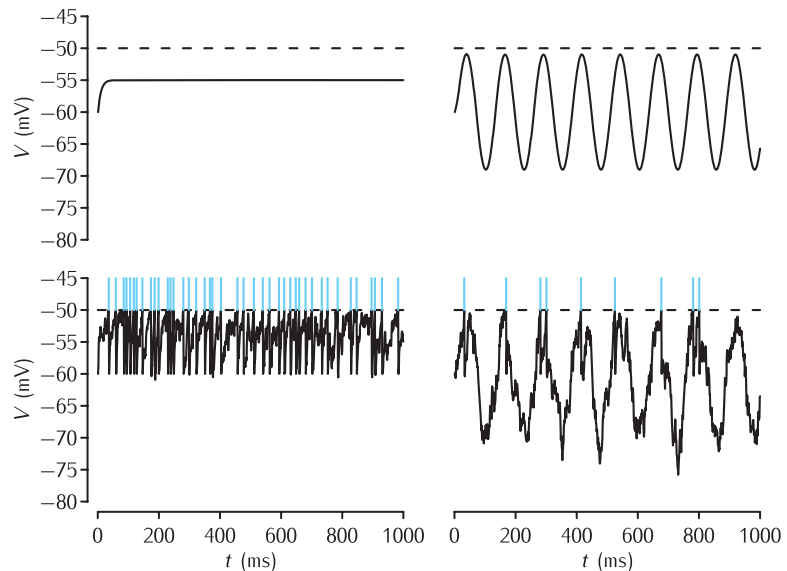
Parameters for each subplot, with units omitted for clarity:

(a) $a = 0.02$, $b = 0.2$, $c = -65$, $d = 6$ (b) $a = 0.02$, $b = 0.25$, $c = -65$, $d = 6$ (c) $a = 0.02$, $b = 0.2$, $c = -50$, $d = 2$

(d) $a = 0.02$, $b = 0.25$, $c = -55$, $d = 0.05$ (e) $a = 0.02$, $b = 0.2$, $c = -55$, $d = 4$ (f) $a = 0.01$, $b = 0.2$, $c = -65$, $d = 8$.

Current steps are shown below each voltage trace, and are all to the same scale; the step in (f) has a height of 30 V s^{-1} . Figure adapted from Izhikevich (2004) and generated by code derived from that available at www.izhikevich.com.

Fig. 8.11 The effects of noise in integrate-and-fire neurons. The upper traces show the membrane potential of a noiseless integrate-and-fire neuron presented with either a constant current injection (left) or a sinusoidally varying current (right), neither of which is strong enough to take the neuron to threshold. The lower traces show the membrane potential (black line) and spike times (blue strokes) produced in response to the same inputs by a noisy integrate-and-fire neuron described by Equation 8.18 with $\sigma = 1 \text{ mV}$. In the case of constant input, the integrate-and-fire neuron fires, albeit irregularly. In the case of the sinusoidal input, the noise is sufficient to cause the neuron to fire at some of the peaks of the oscillations. This is an example of stochastic resonance. In all simulations: $E_m = -60 \text{ mV}$, $\tau_m = 10 \text{ ms}$ and $\theta = -50 \text{ mV}$. The time-step $\Delta t = 1 \text{ ms}$.



injected into the model neuron and its parameters are tuned until its membrane potential time course, or spike times, resemble the real data as closely as possible. In order to quantify the goodness of fit of a model with the data, metrics have to be defined – for example, the fraction of spikes in the model that occur within 2 ms of spikes from the real neuron. The same procedure can be used when comparing two different model neurons.

One example of this type of work, and how it is undertaken, is provided by Jolivet *et al.* (2004). This task has also been a subject of the Quantitative Single-Neuron Modelling Competition organised by Gerstner and colleagues (Jolivet *et al.*, 2008). At the time of writing, an adaptive form of the exponential integrate-and-fire neuron (Section 8.3.3) is in the most accurate class of models in the competition.

8.3.6 Incorporating noise into integrate-and-fire neurons

In Chapter 5 it was seen that membrane currents are noisy due to the random opening and closing of channels. This can be modelled as **diffusive noise** in integrate-and-fire neurons by adding a stochastic term to the membrane equation. Although it is possible to express diffusive noise in the formal mathematical framework of stochastic differential equations, for the purpose of running simulations, it is sufficient to understand the noise in the context of a simulation using forward Euler integration:

$$V(t + \Delta t) = V(t) + \frac{1}{\tau_m} ((E_m - V(t) + R_m I(t)) \Delta t + \sigma \Delta W(t)), \quad (8.18)$$

where Δt is the time-step, $\Delta W(t)$ is a random variable drawn from a Gaussian distribution with a mean of zero and a variance of Δt , and σ parameterises the level of noise. The firing and membrane potential reset are the same as in a conventional integrate-and-fire neuron. Figure 8.11 shows an example of the evolution of the membrane potential through time and the firing pattern of a noisy integrate-and-fire neuron subjected to either constant or periodic inputs. With the constant current input, the noisy inputs

More generally, ΔW can be drawn from any **Wiener process**, a class of stochastic processes of which Brownian motion is one example. See Tuckwell (1988) or Gardiner (1985) for more on the theory of Wiener processes.

$W(t)$ allow the neuron to fire even when the mean input $I(t)$ would not be enough to cause a deterministic neuron with the same threshold to fire. Thus the f - I curves presented in Section 8.2 are not a good description of the firing of this neuron. However, it is possible to derive analytically curves that describe the mean firing rate for an input current with a given mean and standard deviation (Tuckwell, 1988; Amit and Tsodyks, 1991a). As discussed by Tuckwell (1988) and Gerstner and Kistler (2002), this type of noise can also be used to model the total input from large numbers of randomly spiking neurons (Section 8.2.3).

With constant current input, in comparison with the deterministic integrate-and-fire neuron, the firing of the noisy neuron is irregular. However, when presented with a sub-threshold periodic stimulus, noise can be used to allow the neuron to fire at the peak of the periodic stimulus. This phenomenon, whereby noise effectively uncovers an underlying periodic stimulus, is known as **stochastic resonance** (Benzi *et al.*, 1981) and has been demonstrated in the crayfish mechanosensory system (Douglas *et al.*, 1993).

In the noisy neurons just introduced, the noise is introduced in the equation for the integration of the input currents to give the membrane potential. An alternative method of introducing noise to this diffusive noise or noisy integration is to have deterministic integration but a noisy threshold (Gerstner and Kistler, 2002), or **escape noise**. This is implemented by producing spikes with a probability that depends on the membrane potential. It can be useful in mathematical analysis of noisy integrate-and-fire neurons. With an appropriate choice of firing probability function, it can be mapped approximately onto the diffusive noise model (Gerstner and Kistler, 2002).

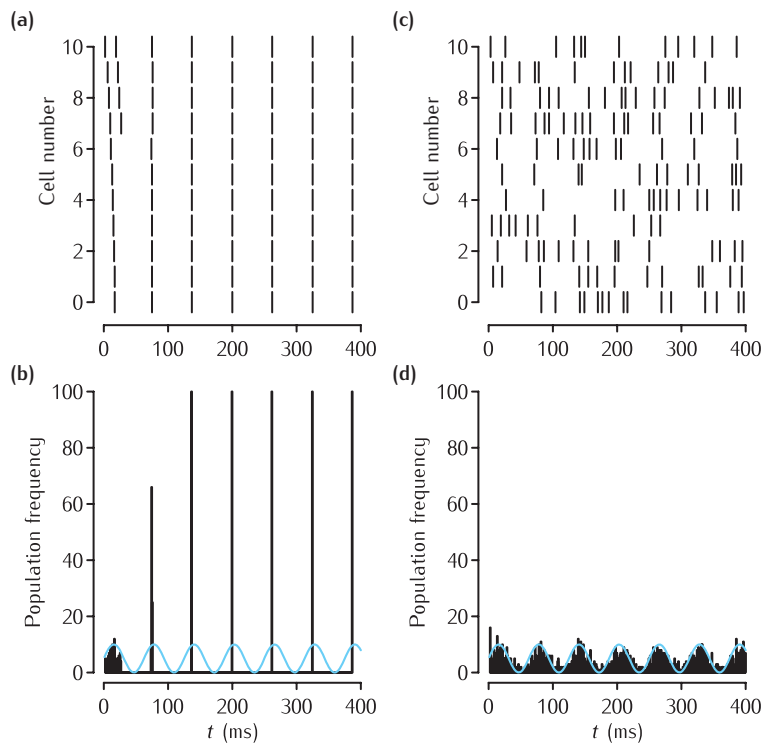
8.3.7 Applications of noisy integrate-and-fire neurons

An important application of noisy integrate-and-fire neurons is to investigate how effective populations of neurons are at transmitting time-varying or transient inputs. This is particularly motivated by the early stages of sensory systems, in which, although the firing patterns of individual cells may not be tightly coupled to the stimulus, the overall firing frequency of the population can be tightly coupled to the input.

For example, Hospedales *et al.* (2008) have used integrate-and-fire neurons to investigate how noise might affect the response fidelity of medial vestibular neurons, which are involved in the vestibulo-ocular reflex. They set up a model population of medial vestibular neurons, each of which fires persistently due to a constant pacemaker component of the input current $I(t)$. At the start of the simulation, each cell is initialised with a different membrane potential. In a population of cells where there is no diffusive noise, this initialisation means that each cell will be at a different point or phase in its regular cycle of firing and then being reset. If there is no additional input to the cells, they will continue firing out of phase with each other.

However, when a sinusoidal component is added to the signal, the cells tend to fire at the peak of the cycle. This leads to the firing times of the population of cells becoming synchronised over successive cycles of the sinusoidal input component (Figure 8.12a). When a population of 100 such

Fig. 8.12 Signal transmission in deterministic and noisy integrate-and-fire neurons. In each simulation a 16 Hz sinusoidal signal was injected into an integrate-and-fire neuron. (a) The spike times in 11 different deterministic neurons, whose membrane potentials at $t = 0$ range between -60 mV and -50 mV . Initially, the neurons fire asynchronously, but after two cycles of the input, the firing is synchronous. This is reflected in the firing histogram shown in (b), which results from a total of 100 neurons, only 11 of which are shown in (a). (c–d) The same simulations but with noise added to the neurons. The spikes are now much more asynchronous, and the population firing rate is a much more faithful representation of the input current, shown as a blue line. Parameters: $\tau_m = 20\text{ ms}$, $E_m = -60$, $\theta = -50\text{ mV}$, $R_m = 100\text{ M}\Omega$, $I(t) = I_0 + I_1 \sin(2\pi 16t)$, $I_0 = 0.1\text{ nA}$, $I_1 = 0.1\text{ nA}$. In (c–d), $\sigma = 40\text{ mV}$.



cells is considered, the instantaneous population firing rate has sharp peaks, locked to a particular point in the cycle. In contrast, when some diffusive noise is added to the neuron, the firing times of the neurons become desynchronised (Figure 8.12c). This leads to the population firing rate being a more accurate, albeit noisy, reproduction of the input current (Figure 8.12d).

The simplicity of integrate-and-fire neurons has allowed this type of question to be investigated analytically. Knight (1972) used elegant mathematical methods to show that a population of leaky integrate-and-fire neurons will tend to synchronise with a suprathreshold, periodically varying input stimulus. In addition, noise in the system tends to desynchronise cells, leading to the population activity of the neurons being more informative about the underlying input stimulus. The timing precision of the first spike in response to a transient increase in input current has been investigated by van Rossum (2001) and the propagation of firing rates through layers has also been studied (van Rossum *et al.*, 2002).

8.4 | Spike-response model neurons

An alternative but related approach to the integrate-and-fire neuron model is the **spike-response model** neuron. These model neurons lend themselves to certain types of mathematical analysis, but for simulations, integrate-and-fire neurons are more efficient (Gerstner and Kistler, 2002). For a comprehensive treatment of spike-response model neurons, see Gerstner and Kistler (2002).

A key element of the spike response model is the **impulse response** of the neuron being modelled; that is, the voltage response to a very short burst

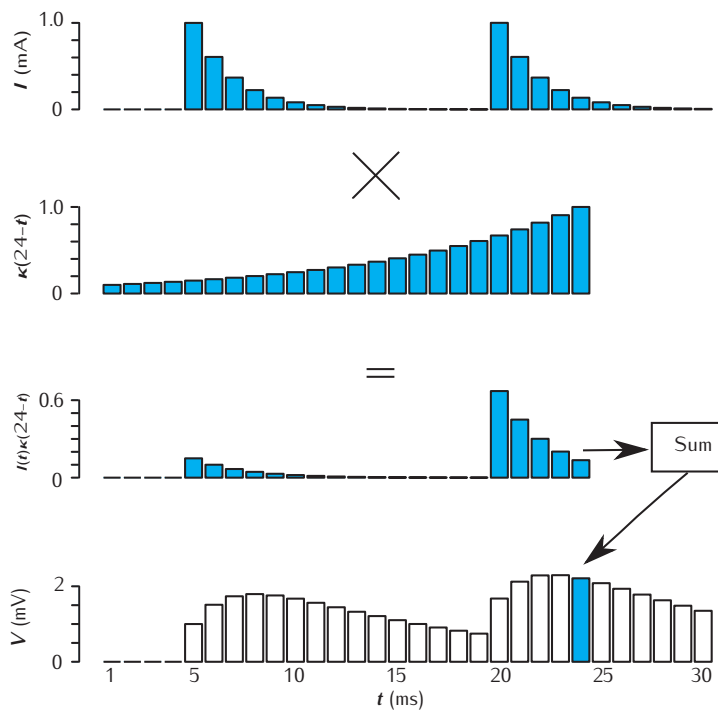


Fig. 8.13 Demonstration of a spike-response model neuron. At the top, the input current to a neuron is shown. To calculate the voltage at a particular time, for example, $t = 24$, the impulse response function (second panel down) is shifted so that it is aligned with $t = 24$. This shows how much influence the input current at times leading up to $t = 24$ has on the output voltage at time $t = 24$. Each element of this is multiplied by the corresponding element of the current to produce the weighted current input shown in the third panel down. The contributions from all times are then summed to produce the voltage at $t = 24$, which is highlighted by the blue bar in the fourth panel. The unshaded bars in this figure were produced by the same procedure, but with the impulse response in the second panel down shifted appropriately.

of input current. It is assumed that the amount of charge injected in the impulse is small, so the membrane potential remains well below firing threshold. In the case of an integrate-and-fire neuron, the impulse response is a decaying exponential. For most cells it will tend to be a heavily damped oscillation. However, in the spike-response model, in principle it can be any function that is zero for $t < 0$, so that an impulse can only affect the membrane potential *after* it has arrived. In what follows, the impulse response function will be denoted by $\kappa(t)$. For example, the decaying exponential impulse response in a membrane with a membrane time constant τ is:

$$\kappa(t) = \exp(-t/\tau). \quad (8.19)$$

This is often referred to as the **impulse response kernel**.

When the impulse response of a neuron is measured, the time course of the voltage is sampled at time points separated by Δt , the inverse of the sampling frequency. The times of the samples are $t_i = i\Delta t$, where the index $i = 0, 1, 2, \dots$. The impulse response is then effectively a vector where element $\kappa(t_i)$ corresponds to the continuous impulse response at t_i . If a neuron's impulse response is known, it can be used to predict its sub-threshold voltage response to current input from either synapses or electrodes. This is achieved by calculating the convolution of the time course of the input current with the neuron's impulse response:

$$V(t_i) = E_m + \sum_{j=0}^i \kappa(t_i - t_j) I(t_j). \quad (8.20)$$

This is shown graphically in Figure 8.13.

The **impulse response** is also known as the **Green's function**. In the context of a convolution (Equation 8.20) it is also known as the **convolution kernel** or **kernel** for short.

The convolution of two discrete functions $A(t_i)$ and $B(t_j)$ is:

$$\sum_j A(t_i - t_j)B(t_j).$$

If $B(t_j)$ is zero everywhere except for $B(0) = 1$, then the result of the convolution operation is A . The convolution of two continuous functions $A(t)$ and $B(t)$ is defined analogously:

$$\int A(t - t')B(t')dt'.$$

Two-dimensional convolution is defined in Section 10.5.

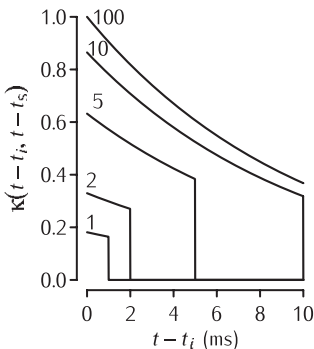


Fig. 8.14 Typical spike-dependent impulse responses, or kernels, plotted at various times after the spike. The kernel is defined by $\kappa(t - t_i, t - t_s) = (1 - \exp(-(t - t_s)/\tau_s)) \exp(-(t - t_i)/\tau)$, where τ is the membrane time constant and τ_s is the refractory time constant. The kernel is zero for inputs that occur before a spike. The value of the kernel is plotted against $t - t_i$, for various periods $t - t_s$ since the spike, as indicated by the number next to each curve.

The **convolution** of the impulse response with the input current describes the sub-threshold response only. Spikes are modelled in a similar way to the integrate-and-fire model, by adding a threshold θ . When the membrane potential rises past this threshold, a spike is produced. The spike affects the time course of the membrane potential in two ways:

Integration of current. During a spike the membrane conductance is high, so the memory of any input currents before the spike effectively leaks away, meaning that current inputs before the last spike have virtually no influence on the membrane potential. The conductance is still higher than at rest during the refractory period (Section 3.3.1), making the impulse response of the neuron to injected current dependent on the time since the spike. An input will tend to evoke a smaller voltage response right after a spike. The impulse response of the neuron must therefore depend on the time since the last spike, as well as the time since the current injection.

Spike response. Since the voltage waveform of spikes is usually highly stereotyped, the membrane potential during the spike can be modelled by adding the voltage waveform of a typical spike and any afterhyperpolarisation or afterdepolarisation that follows it during the refractory period. This waveform is given the mathematical symbol $\eta(t_k)$ and is also called the **spike response kernel**.

To incorporate the effect of the action potential on the integration of current, an impulse response kernel κ with two arguments can be used. The first argument is the time since the input current and the second argument is the time since the spike. With the addition of the spike response kernel η , the resulting membrane potential is given by:

$$V(t_i) = E_m + \sum_{j=0}^i \kappa(t_j - t_i, t_i - t_s) I(t_j) + \eta(t_i - t_s), \quad (8.21)$$

where t_s is the time of the last spike, and the impulse response kernel now depends on the time since the last spike, $t_i - t_s$. An example spike-time-dependent impulse kernel is shown in Figure 8.14. The effect of this kernel is that inputs that occur before a spike are ignored altogether, and the effect of inputs that arrive shortly after a spike is less than the effect of those that arrive after a longer period has elapsed.

8.5 Rate-based models

In some neural systems, such as the fly visual system, the timing of individual spikes has been shown to encode information about stimuli (Rieke *et al.*, 1997). Other examples include: the tendency of spikes in the auditory nerve to be locked to a particular phase of the cycle of a sinusoidal tone (Anderson *et al.*, 1971); the representation of odours by spatio-temporal patterns of spikes in the locust antennal lobe (Laurent, 1996); and the phase of the theta rhythm at which hippocampal place cells fire encoding how far a rat is through the place field (O'Keefe and Recce, 1993). Despite the importance

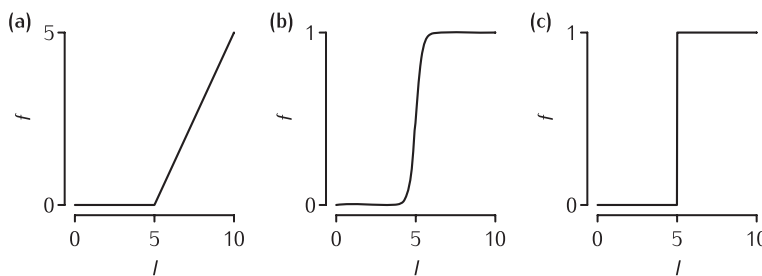


Fig. 8.15 Forms of f - I curves for rate-based neurons.
(a) Piecewise linear function (Equation 8.22) with threshold $\theta = 5$ and slope $k = 1$.
(b) Sigmoid function (Equation 8.23) with $\theta = 5$ and slope $k = 5$. **(c)** Step function (Equation 8.24) with $\theta = 5$.

of single spikes in some systems, in many systems the average firing rate of a single neuron, determined by counting spikes in a time window, or the population firing rate of a group of neurons conveys a considerable amount of information. This observation goes back to Adrian's study of frog cutaneous receptors, in which he found that the firing frequency was proportional to the intensity of the stimulus (Adrian, 1928). It is therefore sometimes reasonable to simplify neural models further still by considering only the firing rate, and not the production of individual spikes.

When injected with a steady current I , an integrate-and-fire neuron fires at a steady rate f that depends on the input current. By contrast, in firing rate models a characteristic function $f(I)$ converts synaptic current into a firing rate directly, bypassing the integration of current and the threshold. The function $f(I)$ does not have to be the same as the one computed for the integrate-and-fire model (Equation 8.5), though it should usually be positive; negative firing rates are not physiological. Common examples of this function are piecewise linear functions (Figure 8.15a):

$$f(I) = \begin{cases} 0 & \text{for } I < \theta \\ kI & \text{for } I \geq \theta, \end{cases} \quad (8.22)$$

or a sigmoid function (Figure 8.15b):

$$f(I) = \frac{\bar{f}}{1 + \exp(-k(I - \theta))}, \quad (8.23)$$

where \bar{f} is the maximum firing rate, θ is a threshold and k controls the slope of the f - I curve. For large values of k , the sigmoid curve approximates to a step function (Figure 8.15c):

$$f(I) = \begin{cases} 0 & \text{for } I < \theta \\ 1 & \text{for } I \geq \theta. \end{cases} \quad (8.24)$$

Neurons where f is a step function are sometimes referred to as **McCulloch-Pitts neurons**, in recognition of the pioneering work of McCulloch and Pitts (1943), who regarded the neurons as logical elements and showed that networks of such neurons could be constructed that would implement logical functions.

8.5.1 Application in feedforward networks

This type of rate-based model has extensive applications to **artificial neural network** models. As a bridge to Chapter 9, where networks are described

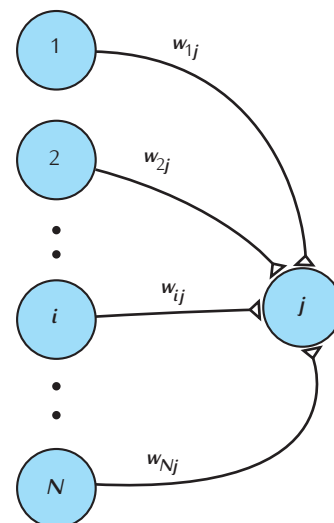


Fig. 8.16 A feedforward network. There are N input neurons on the left-hand side, which connect onto an output neuron j on the right-hand side. Each connection has a synaptic weight w_{ij} .

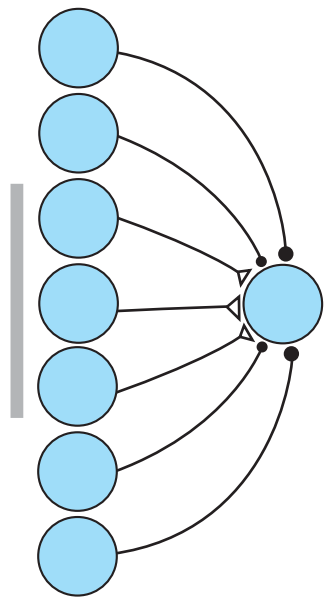


Fig. 8.17 Example of how neurons responsive to on-centre stimuli can be constructed. The neurons on the left represent neurons responsive to neighbouring areas of visual space. The neurons in the centre connect to the output neuron on the right via excitatory synapses (open triangles), but the neurons at the edge connect via inhibitory synapses (filled circles). Stimuli such as the bar (far left), for which the visual neurons in the middle are most excited, will elicit the maximal response from the neuron.

extensively, here we describe some of the simplest forms of network involving connections between neurons designated as inputs and neurons designated as outputs. The first example is the **feedforward network**. The synaptic current in an output neuron is derived from the firing rates of the input neurons to which it is connected and the appropriate synaptic conductances; there are no loops which allow feedback.

If each input neuron, labelled with the subscript i (Figure 8.16), fires at a constant rate, the current flowing into an output cell, labelled j , will also be constant:

$$I_j = \sum_i w_{ij} f_i, \quad f_j = f(I_j), \quad (8.25)$$

where the **weight** w_{ij} describes the strength of the connection from input neuron i to output neuron j .

A simple example of a feedforward network model is involved in the connections that underlie receptive fields (Figure 8.17). Suppose that our input neurons represent retinal ganglion cells at different locations on the retina, then with appropriate connections, output cells can be constructed that have on-off characteristics such as on-off cells in the Lateral Geniculate Nucleus (LGN).

When coupled with rules for changing the synaptic strengths, or weights, which are dependent on the activity of the presynaptic and the postsynaptic neurons, networks of rate-based neurons can carry out the task of heteroassociation; that is, learning associations between pairs of activity patterns. These feedforward heteroassociative networks (Marr, 1969; Willshaw *et al.*, 1969) are described in more detail in Section 9.2. Notably, Marr's (1969) theory of cerebellar function had great impact amongst cerebellar physiologists, despite his use of such simple model neurons.

8.5.2 Time-varying inputs to feedforward networks

If the inputs to the network vary in time, Equation 8.25 can still be used for a feedforward network. However, for quickly changing inputs, it would not give very realistic results, since the rate of change of the output follows the rate of changes in the inputs instantaneously, whereas it would be expected that changes in the output firing rates should lag changes in the input firing rates. To make the model more realistic, we can adapt the differential equation used to convert spikes into decaying exponential currents (Equation 8.9) by feeding in firing rates of other neurons instead of spikes:

$$\tau_{\text{syn}} \frac{dI_j}{dt} = -I_j + \sum_i w_{ij} f_i, \quad f_j = f(I_j). \quad (8.26)$$

Although this equation is rate-based, it can give a good approximation of a network comprising integrate-and-fire neurons (Amit and Tsodyks, 1991a). Broadly speaking, the total number of spikes that would be expected to be received within a millisecond by a postsynaptic neuron has to be large – say of the order of tens or hundreds. If this is the case, the fluctuations in the numbers of spikes arriving within a millisecond should be low, and the function $f(I_j)$ can be approximated by the f - I curve for integrate-and-fire neurons (Equation 8.5), or by an f - I curve for integrate-and-fire neurons

with diffusive noise (Section 8.3.6). Under different simplifying assumptions, other forms of rate-based models with slightly different equations can be derived (Dayan and Abbott, 2001).

8.5.3 Application in recurrent networks

The more complicated Equation 8.26 can also be used to model recurrent networks, where there may be a connection back from neuron j to neuron i (Figure 8.18). Two examples of the types of computation that recurrent networks of rate-based neurons can perform are input integration and autoassociative memory.

Input integration is seen in premotor neurons in the medial vestibular nucleus in the brainstem (Seung, 1996). These cells receive information about eye velocity, but their firing rate is related to eye position. They thus implement the mathematical operation of integration. The function of these neurons has been modelled (e.g. Cannon *et al.*, 1983; Seung, 1996) using a network of simple linear rate-based neurons, (Figure 8.19). The weight matrix is set up so that the firing rate of the network can integrate input information that represents velocity to produce a position output. Using insights from this network of simple neurons, a network can be constructed comprising more realistic conductance-based neurons, so that the network of more complex neurons performs the same function as the network of simpler neurons (Seung *et al.*, 2000). Dayan and Abbott (2001) discuss this example in much more mathematical detail.

Recurrent networks can be used to carry out the task of autoassociation, which is storing a pattern so that upon presentation of part of a previously stored memory pattern, the remainder of the same pattern can be retrieved. As with heteroassociative networks, patterns in these autoassociative networks are stored by setting the synaptic weights using a learning rule which depends on the activity of pre- and postsynaptic neurons (Little, 1974; Hopfield, 1982, 1984; Tsodyks and Feigelman, 1988). Rather than using the differential equation (Equation 8.26), the activity of recurrent networks is often updated in discrete time-steps. This may be a **synchronous update**, in which at each time-step the activity of all of the units is updated on the basis of the activity of the previous time-step. Alternatively, **asynchronous update** may be used, in which at each time-step a randomly chosen unit is updated. Hertz *et al.* (1991) provides a fuller discussion of the advantages and disadvantages of each method. In Chapter 9 recurrent memory networks comprising synchronously updated rate-based neurons are described in more detail.

8.5.4 Limitations of rate-based models

While rate-based models can be a reasonable representation of neuronal activity and processing in a number of areas of the nervous system, and can have great explanatory power, given their small number of parameters, by definition they cannot be used to investigate whether individual spikes are relevant for neural encoding, processing and the dynamics of networks.

One example is the response of populations of neurons receiving a common input. In Equation 8.26 for the evolution of the total synaptic current as a function of the firing rates, a sharp increase in firing rates will lead to

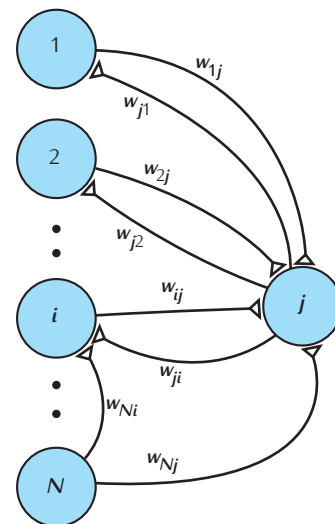


Fig. 8.18 A network with recurrent connections. The network is similar to the feedforward network shown in Figure 8.16, except that here there are some feedback connections, creating loops.

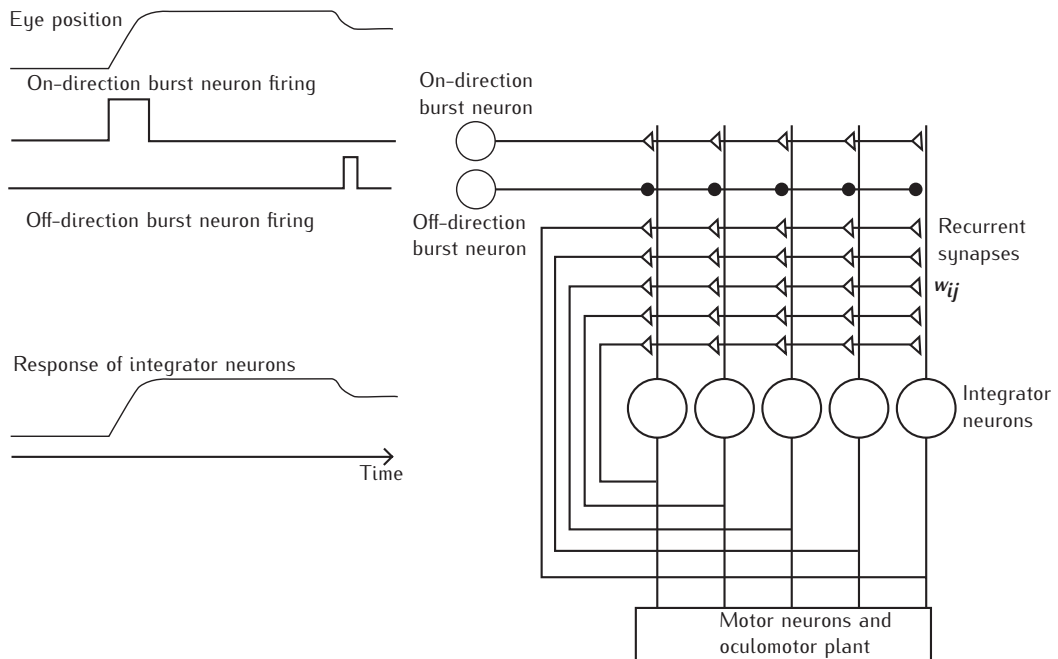


Fig. 8.19 A network that models the function of medial vestibular nucleus neurons. The actual eye position is shown at the top left. The network receives inputs from eye velocity neurons, the on-direction burst neuron and the off-direction burst neuron. The network integrates these inputs to give a firing rate response in the integrator neurons that mirrors the eye position response. In order for this to work correctly, the recurrent weights w_{ij} need to be tuned correctly. Figure after Seung *et al.* (2000).

the synaptic current increasing, after a time lag. As the output firing rate depends on the synaptic current, the increase in the output firing rate also lags behind the increase in the input firing rates.

We might assume that this finding could also be applied to a population of spiking neurons which receive common input. If the cells are quiescent before the increase in firing rates, this is indeed the case. However, if there is sufficient input to cause the neurons to be tonically firing before the increase in input, and if the firing of the neurons is asynchronous, the population firing rate can follow the input firing rate with virtually no lag (Knight, 1972; Gerstner, 2000).

8.6 | Summary

This chapter has described how details can be progressively removed from complex models of neurons to produce simpler model neurons. From the large variety of models that have been devised, we have chosen to concentrate on three broad categories of neuron model.

- (1) Models where the spike generation is due to a system of differential equations that include an equation for the membrane potential and equations for voltage-dependent conductances. The parameter space of models of this form with few variables can be explored thoroughly and they are amenable to insightful mathematical analysis.
- (2) Models where action potentials are imposed when the membrane potential crosses a threshold. Such models are good for mimicking the behaviour of neurons, especially for inclusion in a network, and they are also mathematically analysable.

- (3) Models where not even action potentials are considered, but rather the firing rate of the neuron is the critical variable. Whilst many details are lost here, it is possible to construct simple networks with such neural models that give insights into complex computations.

The choice of model depends on the level of the explanation, the data available, whether the model should be analysable mathematically and the computational resources to hand. A fruitful approach can be to use models at different levels of complexity. Intuitions for the system can be gained from simple models, and these intuitions can then be tested in more complex models.

Including neurons in networks has only been touched on in this chapter. Issues arising from modelling networks are dealt with more fully in Chapter 9.

Chapter 9

Networks of neurons

In their implementation of Marr's influential theory of cerebellar cortex as a learning machine (Marr, 1969), Tyrrell and Willshaw (1992) constructed a simulation model of all the circuitry associated with a single Purkinje cell. With the limited computing resources available at the time, they did this by modelling each 3D layer of cells and connections in a 2D plane. To build the model they had to guess many parameter values about the geometry as these were not available. Their simulation results agreed broadly with the analysis carried out by Marr.

An essential component of the art of modelling is to carry out appropriate simplifications. This is particularly important when modelling networks of neurons. Generally, it is not possible to represent each neuron of the real system in the model, and so many design questions have to be asked. The principal questions concern the number of neurons in the model network, how each neuron should be modelled and how the neurons should interact. To illustrate how these questions are addressed, different types of model are described. These range from a series of network models of associative memory, in which both neurons and synapses are represented as simple binary or multistate devices, two different models of thalamocortical interactions, in which the neurons are represented either as multi-compartmental neurons or as spiking neurons, and multi-compartmental models of the basal ganglia and their use in understanding Parkinson's disease. The advantages and disadvantages of these different types of model are discussed.

Two severe limitations prevent the modeller from constructing a model of a neural system in which each nerve cell is represented directly by a counterpart model neuron. One limitation is that there are so many neurons in the neural system that having a full-scale model is computationally infeasible. The second limitation is that usually only incomplete data is available about the functional and structural properties of the neurons, how they are arranged in space and how they interconnect.

The design issues that are most commonly addressed concern the numbers and types of model neurons and the topology of how they connect with each other. Another crucially important issue is how the cells are situated in 3D space. Since the embedding of network models in space is not normally attempted, this issue has not often been discussed, with some notable exceptions. An early attempt is the simulation model of Marr's theory of **cerebellar cortex** (Marr, 1969; Tyrrell and Willshaw, 1992). In Section 9.1 we consider these design issues.

The most common properties that are investigated in network models of the nervous system are the patterns of firing within the array of neurons and how such patterns are modified through specific synaptic learning rules. In this chapter, we examine these two properties in a variety of network

models in which the neurons are modelled to differing levels of detail. We start by looking at very simple networks where both neurons and synapses are modelled as two-state devices. In these networks most emphasis has been on the effects of synaptic modification. Accordingly, in Section 9.2 we describe three different approaches to constructing generic models of network associative memory in which the neuron is treated as a two-state device and the modifiable synapse as a simple binary or linear device. We show that one advantage of extreme simplification is that analytical results for how these networks can be used most efficiently can be obtained and the capacity of the system can be calculated.

For networks of more complex neurons, it is important to characterise their firing patterns before associative storage can be assessed. In Section 9.3 we examine an integrate-and-fire network model of a cortical column, and we explore associative storage and retrieval in this network. In Section 9.4 we look at network models of more complex, multi-compartmental model neurons, again looking at how associative memory can be embedded in them.

Section 9.5 contains three examples of modelling of thalamocortical connections using model neurons of different complexity. These large-scale network models are used to examine network phenomena such as oscillatory neural activity as recorded in electroencephalograms (EEGs).

Finally, we look at a clinically related application, in which the emphasis is on the patterns of activity under normal and abnormal conditions. In Section 9.6 we discuss how to model the effects of deep brain stimulation of the subthalamic nucleus in the basal ganglia, now used successfully for the relief of Parkinson's disease. We describe a multi-compartmental network model of the subthalamic nucleus and related structures and discuss the validation and predictions made from the model.

9.1 | Network design and construction

In the preceding chapters we have seen that the construction of the model of a single neuron involves a vast range of choices concerning how to model components such as cell morphology, ion channels and synaptic contacts. Each choice involves a compromise over the level of biological detail to include. How to make useful simplifications is an important part of the modelling process.

The same is true if we want to build a network of neurons. A major decision is to choose at which level of detail to model the individual neurons. For a large-scale network with thousands, or hundreds of thousands of neurons, this may require using the simplified models introduced in the previous chapter. Other issues also arise with network models. How should we handle communication between neurons? Do we need to model axons and the propagation of action potentials along them? Do we need to model short-term dynamics and stochastic neurotransmitter release at synapses? Our network is almost certainly going to be smaller than real size in terms of the numbers of neurons. In which case, how should we scale the numbers of

Some neurobiological systems contain a small number of neurons enabling neurons to be represented one-to-one in the model. For examples see Abbott and Marder (1998).

neurons of different classes in the network? Finally, do we need to consider the location of neurons in space? In this section we explore possible answers to these questions.

9.1.1 Connecting neurons together

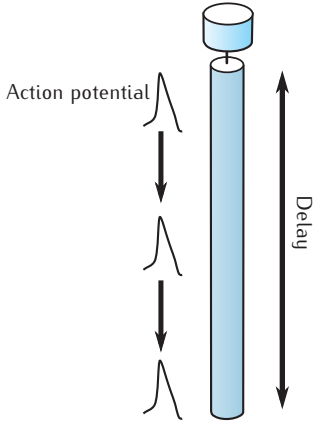


Fig. 9.1 An action potential is initiated in the axon initial segment and propagates along the axon. This can be modelled as a delay line, which specifies the time taken for the action potential to travel the length of the axon. The action potential itself is not modelled.

Networks of neurons are formed predominantly through neurons connecting together via chemical synapses formed between axonal terminals from efferent neurons and the postsynaptic membrane of receiving neurons. The signal that passes from the efferent to receiving neuron is the action potential. A possibility for modelling these connection pathways is to include in each cell model a compartmental model of its axon along which action potentials propagate. This is computationally very expensive and arguably unnecessary. Action potentials are stereotypical and the information content of signals passing from one neuron to another is carried by the times of action potentials arriving at synapses, rather than the precise voltage waveform of the action potential.

Consequently, the approach that is almost uniformly applied is to treat the signal that passes from one neuron to another to be the presence or absence of an action potential. Then the connection from one neuron to another is modelled as a **delay line** (Figure 9.1). The voltage in the soma or axon initial segment of the efferent cell is monitored continuously. If the voltage goes over a defined threshold (e.g. 0 mV), this signals the occurrence of an action potential. The delay line then signals this occurrence to the synaptic contact on the receiving neuron at a defined time later, corresponding to the expected transmission time of the action potential along the real axon. This approach is not only vastly cheaper computationally than compartmental modelling of axons, but it is also easily implemented on parallel computers, as only spike times need to be sent between processors (Brette *et al.*, 2007; Hines and Carnevale, 2008).

There are circumstances where it is necessary to model the detail of action potential propagation along axons. The delay line model assumes that action potential propagation is entirely reliable and is not modulated along the length of the axon. The possibility of action potential failure at branch points or due to presynaptic inhibition are ignored. These effects have been explored using compartmental models of isolated axons (Parnas and Segev, 1979; Segev, 1990; Manor *et al.*, 1991a, b; Graham and Redman, 1994; Walmley *et al.*, 1995). They could certainly be expected to influence network dynamics and thus raise the challenge of modelling action potential propagation in a network model.

9.1.2 Scaling neuronal numbers

Many networks of interest contain thousands or even millions of neurons, which it is often not feasible to model. It is then necessary to model a scaled-down version of the actual network. This involves scaling both the numbers of neurons and the number of synapses between neurons.

Suppose our network is going to be one-tenth the size of the brain nucleus we are modelling. This nucleus contains three cell types – a principal excitatory neuron that makes up 80% of the cell population, and two types of inhibitory interneuron, each constituting about 10% of the

population. The obvious way to scale neuronal numbers is to retain the relative proportions of cells of different types (80:10:10) in our one-tenth-sized model. Provided this results in reasonable numbers of cells of each type in the model, then this could be an appropriate choice. What may constitute a reasonable number of cells is discussed below.

The principal use of the model is likely to be to study the population response of the excitatory cells. For this to be an accurate reflection of physiology, it is important that the excitatory and inhibitory synaptic input onto these cells represents realistic population activities. In our model network, inhibition from each population of inhibitory interneuron should be as close as possible to that experienced by a real excitatory neuron *in vivo*. Given that we have fewer interneurons in our model network than exist *in vivo*, there are two ways of achieving this:

- (1) Scale up the maximum synaptic conductance of each connection from an inhibitory interneuron onto an excitatory cell by a factor of ten, in this example.
- (2) Create ten times the number of synaptic contacts from each interneuron onto each excitatory cell than exist *in vivo*.

Neither approach is perfect. Scaling the synaptic conductances may give an equivalent magnitude of inhibition. However, this will be applied as a few large conductance changes at isolated points on the excitatory cell. As discussed in more detail in Section 9.3.3, the resulting voltage changes and integration with excitatory inputs will be distorted. Creating more synaptic contacts from each interneuron will result in a realistic spatial distribution of inhibitory inputs, but spikes arriving at these inputs may have unnatural correlations since groups of them are more likely to derive from the same interneuron. Unless it is actually possible to include physiological numbers of interneurons in the network model, one of these compromises is required. The same considerations apply to the inputs from excitatory neurons.

If it is likely that different sized network models will be tested, it is very useful to fix the number of afferent inputs that a given cell receives from the population of cells of each type in the model. For example, the number of inhibitory inputs that each excitatory cell receives from each of two populations of inhibitory interneurons should remain fixed regardless of the actual number of each cell type in the model. When the number of cells is changed, a cell of a particular type will provide fewer or more synaptic contacts onto a target cell, but the target cell will always have the same number of synaptic inputs from the efferent cell population (Orbán *et al.*, 2006).

Another effect of scaling the numbers of neurons is that the small populations of interneurons may be scaled to the point of having only one or a few cells representing these populations in the model. In this case the population activity in the model of these interneurons may be a serious distortion of the activity *in vivo*. Real activity may involve thousands of asynchronously firing cells, with the instantaneous population activity providing a good estimate of some modulating driving force, such as slowly changing sensory input (Section 8.2.2; Knight, 1972; Hospedales *et al.*, 2008). The small population in the model may only provide a poor representation of the modulating input.

If this is the case, then it may be possible to scale each population of cells differently. If the excitatory cells are not strongly recurrently connected, then only a relatively small number of these cells are required in the model to allow a good study of their network activity (Orbán *et al.*, 2006). This then allows relatively larger populations of interneurons to be modelled so that both their population activity and their inhibitory effect on the excitatory cells are much more physiological. This approach was taken by Orbán *et al.* (2006) in a model of the CA1 area of hippocampus, where recurrent connections between pyramidal cells are sparse. Their network model of theta activity contained a small number (15–30) of detailed 256-compartment pyramidal cells, but with populations of up to 200 basket and 90 oriens lacunosum-moleculare cells, each cell modelled by a single compartment.

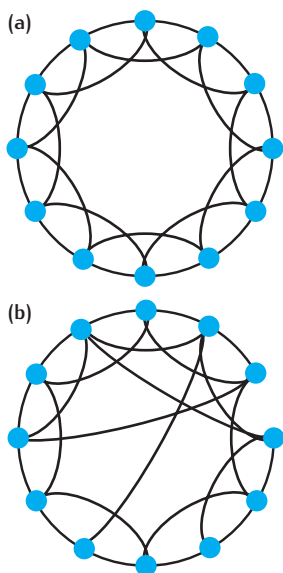


Fig. 9.2 (a) Local connectivity in which a neuron connects only to near neighbours.
 (b) Small-world connectivity in which some of the local connections are replaced by longer-range connections.

9.1.3 Positioning neurons in space

Real neurons have a particular location within a brain nucleus, and connectivity patterns between neurons are often distance-dependent. To capture these patterns it may be necessary to place our model neurons in virtual space.

For, say, a cortical column or other small part of a brain area, it may be reasonable to assume that connectivity is completely uniform (e.g. every neuron connects to every other neuron) or that there is a fixed probability that one neuron makes contact with another neuron. In this case the precise spatial location of a neuron is not relevant and can be ignored.

In general, though, we will need to lay our cells out in some 1D, 2D or 3D arrangement that reflects the physiological layout. Typically this is done with a regular spacing between cells. Then, when forming connections between cells, the probability that an efferent cell forms a connection onto a target cell can be a function of the distance between them. This function is often an exponential or Gaussian function so that the probability of connection decreases with distance (Figure 9.2a). This reflects the basic connection arrangement in many brain nuclei. More complex connection strategies can easily be implemented. So-called **small-world networks** (Watts and Strogatz, 1998; Netoff *et al.*, 2004; Földy *et al.*, 2005) can be generated by first creating a network with only local connections between cells (a cell connects to a few of its nearest neighbours) and then randomly reassigning a small proportion of the connections to be much longer-range connections (Figure 9.2b).

One problem to deal with is that of edge effects, in which cells at the edge of our spatial layout receive fewer connections than interior cells. This could be overcome by assuming the spatial arrangement actually wraps around, so that a cell at the end of the line is assumed to be a neighbour of the cell at the opposite end of the line (Netoff *et al.*, 2004; Wang *et al.*, 2004; Földy *et al.*, 2005; Santhakumar *et al.*, 2005), i.e. the line is actually a circle (Figure 9.2). A more biological solution might be to have a sufficiently large model network that the cells at the boundaries can be ignored.

9.1.4 Variability in cell properties

The vast majority of neuronal network models contain populations of cells with completely uniform properties, including morphology and membrane

physiology. This does not reflect the variation seen within biological neurons and can lead to artifacts in network behaviour due to uniformity in cellular responses to synaptic input. A better approach is to introduce variance into one or more cellular properties, including membrane resistance, resting membrane potential and ion channel densities. Experimental estimates of these parameters may be available that indicate the magnitude of variance in a biological population. Variations in electrophysiological responses may indicate variability in membrane ion channel densities (Aradi and Soltesz, 2002).

Alternatively, some variation can be introduced into a population of otherwise identical cell models by either starting a simulation with different initial conditions for each cell; e.g. different starting membrane potentials, or providing a different background stimulus, in the form of a small depolarising or hyperpolarising current injection, to each cell (Orbán *et al.*, 2006).

Computational models and experiments have shown that signal integration in cells and collective network behaviour is strongly influenced by variability in individual cell characteristics (Aradi and Soltesz, 2002; Aradi *et al.*, 2004). Another consideration is the relative proportion of cells of different types within the network. Classification of cell types is an art form that is still evolving (Somogyi and Klausberger, 2005; Markram, 2006). Thus the number of cell populations and their relative sizes may be free variables in the network model. Simulations have shown that networks containing the same cell types, but in different proportions, can show significantly different behaviour (Földy *et al.*, 2003, 2005).

9.1.5 New network quantities

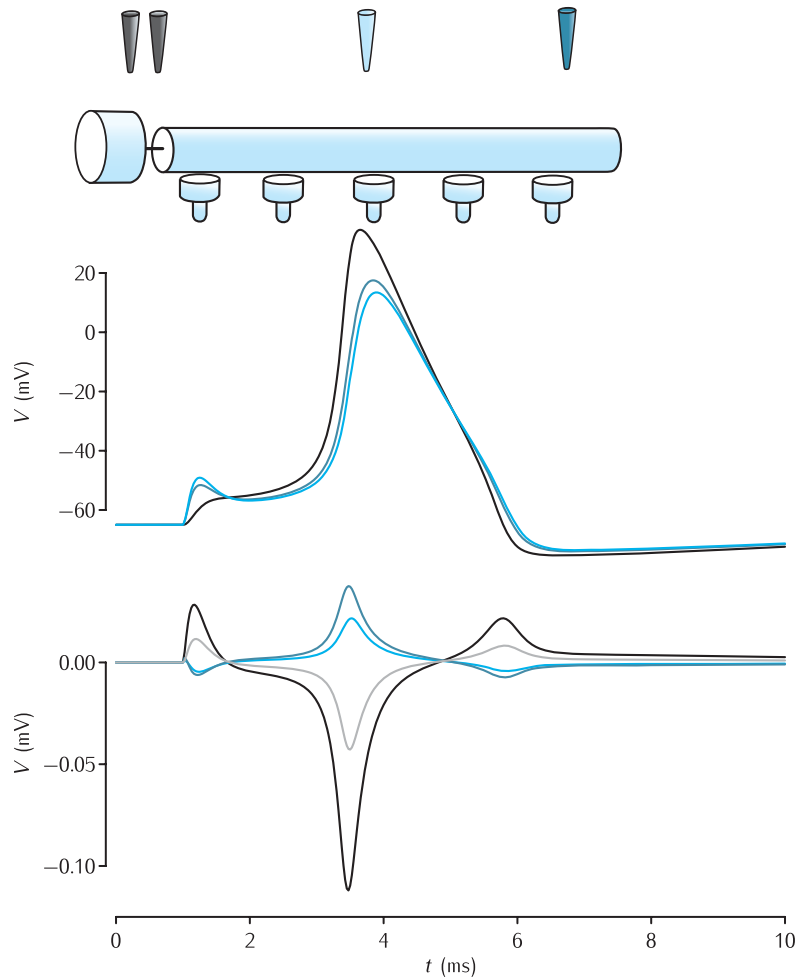
Modelling a network of spatially located neurons, as opposed to a single, isolated neuron, allows for the possibility of modelling new signals in addition to cellular voltages. These include pseudo EEGs and **extracellular field potentials**. A basic field potential equation is (Rall, 1962; Protopapas *et al.*, 1998; Bédard *et al.*, 2004):

$$\Phi(x, y, z, t) = \frac{1}{4\pi\sigma} \sum_{i=1}^n \frac{I_i(t)}{d_i}, \quad (9.1)$$

where Φ is the field potential at a particular recording site (x, y, z) , and each of the n current sources I_i is a distance d_i from the recording site. The conductivity of brain tissue is assumed to have a uniform value, σ , throughout. For a network of spatially located compartmental cell models, according to Equation 9.1, the current sources correspond to the membrane current in each compartment in each cell. Figure 9.3 gives example traces of the extracellular membrane potential calculated in this way in the vicinity of a schematic compartmental neuron model.

There are two principal limitations to using Equation 9.1. The first is that uniform extracellular conductance is an approximation to reality, and the second is that the extracellular medium has capacitive properties as well as conductive ones (Ranck, 1963; Bédard *et al.*, 2004). In general, the problem

Fig. 9.3 Simulation of extracellular field potentials. Extracellular electrodes (black, grey, blue and dark-blue) are placed close to a ball-and-stick model neuron with an active soma and synapses on its dendrite. The soma is 40 μm long and 40 μm in diameter. The single dendritic cable is 200 μm long and 4 μm in diameter. The top traces show intracellular recordings when the synapses are activated enough to cause an action potential to be fired. Traces are from the soma (black), halfway down the dendrite (blue) and in the distal dendrite (dark-blue). The initial synaptic stimulation can be seen in the dendritic traces. The lower traces show the extracellular recordings corresponding to the electrodes of the same colour. During the synaptic stimulation, the dendrites act as a sink of extracellular current and the soma acts as a source. This can be seen in the negative deflection of the extracellular potential in medial and distal dendrites and the positive deflection of the extracellular potential close to the soma. During the action potential, the soma is a sink of current and the dendrites are current sources; this is reflected in the large negative deflection of the extracellular potential close to the soma and the smaller deflections of the extracellular potential near the dendrites. As the neuron repolarises, the roles of the soma and dendrites are again reversed.

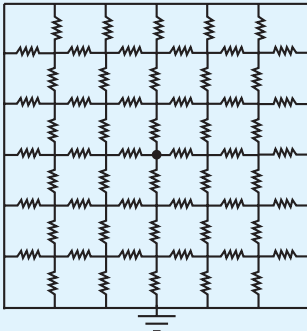


of inhomogeneous media can be addressed using a finite-element model of the extracellular medium (Box 9.1). The second problem can be addressed by deriving a version of Equation 9.1 that incorporates capacitance (Bédard *et al.*, 2004). With capacitive properties included, the extracellular potential has its own time-dependent dynamics. The response to a periodic membrane current signal of a particular frequency can be computed. High-frequency signals are expected to attenuate more than low ones, meaning that the action potentials, which are very sharp and hence contain a lot of high-frequency components, will be highly attenuated at relatively small distances from the neuron. Fourier analysis can be used to predict the response to any particular time-varying signal (Bédard *et al.*, 2004).

Extracellular spatial concentration gradients of neuromodulators and volume transmitters, such as nitric oxide, can also be modelled using diffusion equations (Philippides *et al.*, 2000, 2005) or reaction-diffusion equations (Feng *et al.*, 2005b).

Box 9.1 Finite-element models of electric fields

The voltage spread in brain tissue due to an extracellular electrode can be modelled in a similar way to that described already for compartmental models of neurons. The extracellular space is modelled as a uniform conductance through which current flows, represented as a network of resistors:



The electrode is the black disc and the return current to the electrode passes through the rim of the network. Here there is no capacitance, so the current balance equation for each internal node with no electrode is:

$$0 = \sum_{j \in \mathcal{N}_i} \frac{V_j - V_i}{R_{ij}},$$

where \mathcal{N}_i is the set of nodes connected to node i . For the node containing the electrode, the zero on the left-hand side of the equation is replaced with the electrode current. For the nodes on the boundary, V_i is set to 0 mV, the potential of the return electrode. These equations can be formulated as a matrix equation and the steady state potentials can be computed (Butson and McIntyre, 2005).

In this example, there is no capacitance, and hence no dynamics, as there are no terms involving dV_i/dt . Capacitance can be incorporated in the model by replacing the real-valued resistance with a complex-valued impedance, in which the imaginary component represents capacitance. The amplitude and phase of the voltage at each node in response to an oscillating electrode current of any frequency can then be computed. Using Fourier analysis, this can be used to compute the response of each node to a periodic, time-varying electrode current (Butson and McIntyre, 2005).

In place of the regular square mesh used here, an irregular mesh may be used, in which the regions in which the voltage varies most have a finer mesh (Butson and McIntyre, 2005). Meshes can span 2D or 3D space. Software packages such as CALCULIX (<http://www.calculix.de>) are able to carry out finite-element analysis.

9.2 Schematic networks: the associative memory

The first concrete example of a network to be studied in this chapter is the associative network model mentioned in Section 8.5.1. The network can

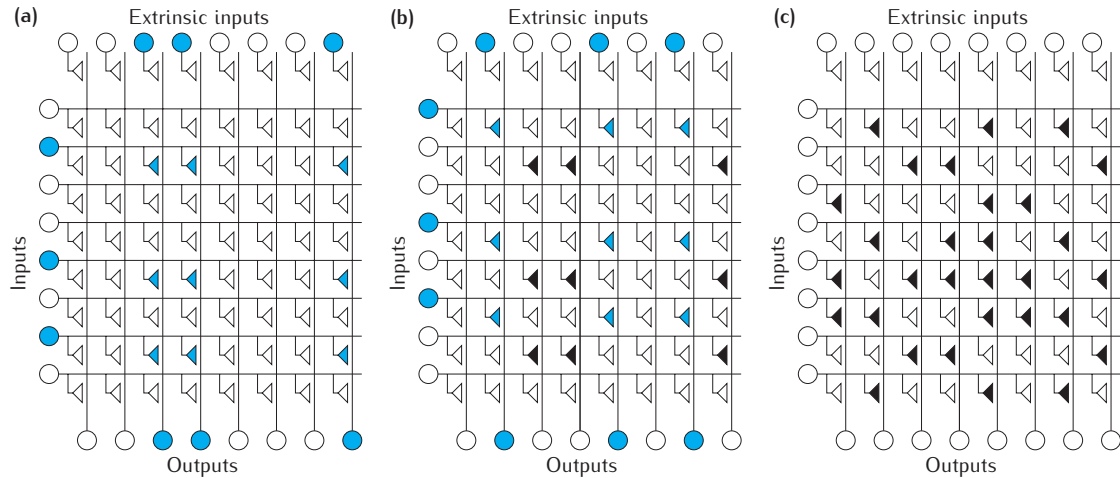


Fig. 9.4 The Associative Net, an associative memory model with binary weights. There is an input layer, an output layer and strong extrinsic inputs to each output neuron. Synapses are denoted by triangles. They can be either unpotentiated (unfilled) or potentiated (filled).

(a) Storage of the first association in the network. The input and output patterns are shown as patterns of empty and filled circles. The synapses which are potentiated by this association are indicated by filled synapses; all the other synapses are unpotentiated.

(b) Storage of a second association. The original set of potentiated synapses remain (black synapses), but more synapses corresponding to the input and output patterns are potentiated (blue synapses).

(c) After several associations have been stored in the network and more synapses have been potentiated.

exist in feedforward and recurrent forms, but common to both is the idea of storing and recalling patterns of activity, each of which might represent a stimulus or an event. In the case of the feedforward network, the task is **heteroassociation**; that is, to associate two different patterns of activity with each other. An example of an association (Marr, 1970) might be a monkey observing a rotten branch (input) and the finding that the branch breaks upon the monkey swinging on it (output). This association may be learnt by experience, and afterwards the monkey will associate rotten branches with falling. The recurrent network's task is to store patterns so that each stored pattern can be recalled upon presentation of a fragment of it. For example, seeing part of a familiar face might be sufficient to evoke a memory of the entire face. Effectively, this is associating a pattern with itself, so the task is called **autoassociation**.

The architecture of the network is similar to various neuroanatomical structures; associative networks similar to the ones described here form part of Marr's theories of the cerebellum (Marr, 1969), the neocortex (Marr, 1970) and the hippocampus (Marr, 1971). The structure of the feedforward network is similar to the arrangement of connections in the perforant path from the entorhinal cortex to the granule cells of the dentate gyrus in the hippocampus, and the structure of the recurrent network is similar to hippocampal area CA3 (McNaughton and Morris, 1987).

In this section, feedforward and recurrent associative networks with binary-valued synapses and binary-valued input and output patterns are described. Whilst these networks contain very simple elements, they are a good starting point for understanding how a network of neurons can perform a function. Later sections of the chapter will demonstrate that the function carried out by these simple networks can be performed by spiking neuron network models whose connections have been set up using similar principles.

9.2.1 The feedforward associative network

The feedforward associative network model, called the **Associative Net**, introduced by Willshaw *et al.* (1969), comprises two layers of neurons: an input

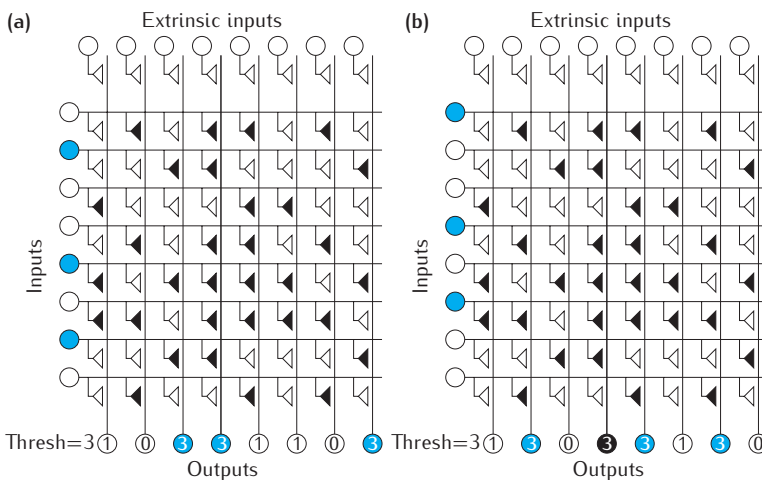


Fig. 9.5 Recall in the Associative Net. (a) Recall of the first association stored in Figure 9.4. The depolarisation is shown in each output neuron. If the depolarisation reaches the threshold of 3, the neuron is active (blue shading). All the correct neurons are activated. (b) Recall of the second pattern stored. All the correct output neurons are activated, but there is also one output neuron (indicated by black shading) that is activated erroneously. This is because the synapses from the active inputs to this neuron have been potentiated by other associations.

layer containing N_A neurons, and an output layer containing N_B neurons. Every neuron in the input layer is connected to every neuron in the output layer and so the connections can be visualised in matrix form (Figure 9.4). Each neuron can be either active (1) or inactive (0), and an **association** is represented by a pair of patterns of 0s and 1s across the input and output layers. In what follows, a fixed number M_A neurons, randomly chosen from the total of N_A neurons, is active in any one input pattern together with a fixed number M_B in any output pattern, chosen similarly.

The task of the network is to store associations through selected synapses, which can exist in one of two states. During the training phase of the network, it is assumed that input patterns are presented at the same time as strong extrinsic inputs coerce the output neurons into firing in the corresponding output pattern. This means that some synapses are potentiated through the firing of both the presynaptic and postsynaptic neurons. According to the **Hebbian** prescription (Box 9.3), these are the conditions under which synapses are strengthened, and so the strength of each of these potentiated synapses is set to 1, being indicated in the matrix (Figure 9.4) by a filled synapse. This is repeated for the storage of further associations.

To retrieve the output pattern that was stored alongside an input pattern, the input pattern is presented to the network. For each output neuron, the dendritic sum is calculated, which is the number of active input neurons which are presynaptic to potentiated synapses on the output neuron. The dendritic sum is then compared to the threshold, which is set to be equal to M_A . If the sum is equal to the threshold, then the output neuron is considered to be active. It can be seen from the example in Figure 9.5a that associations can be retrieved successfully.

As more memories are stored in the matrix, the number of potentiated synapses increases. It is therefore possible that output cells may be activated when they should not be, because, by chance, M_A synapses from active input neurons have been potentiated (Figure 9.5b). This spurious activity might correspond to faulty recall of a memory. Because of the simplicity of the network, it is possible to compute how the amount of spurious activity will vary as a function of the number of input and output cells and the number

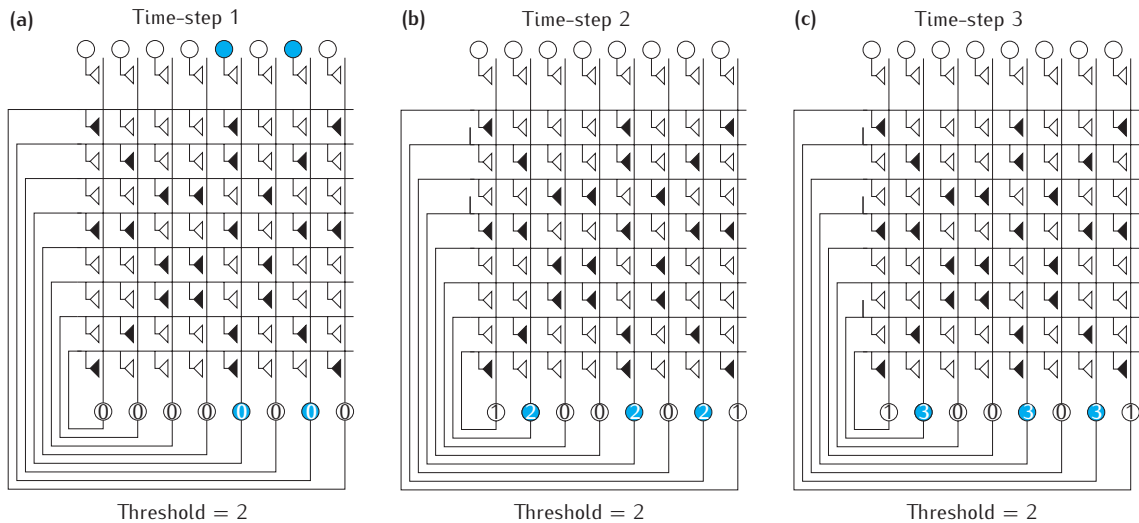


Fig. 9.6 Demonstration of pattern completion in the recurrent associative network. (a) At the first time-step, two out of three neurons which were active in a previously stored pattern are active in the pattern presented as cue to the extrinsic inputs. This causes the corresponding output neurons to fire. (b) At the second time-step, the activity is fed round to the recurrent inputs (indicated by spikes on the input lines). This gives two units of activation at all of the neurons in the pattern. Given that the threshold is set to two, this causes all neurons in the pattern to fire. (c) At the third time-step, the activity from all three neurons is fed back to the recurrent inputs. This causes three units of depolarisation on each neuron and, in this case, no spurious neurons are activated.

of neurons that are active in the input and output patterns. This leads to an estimate of the ultimate capacity of the system. Under optimal conditions, the network is used with very high efficiency (Box 9.2).

By setting a criterion for the frequency of errors that can be tolerated, it is possible to determine how many patterns can be stored in a network.

The calculations in Box 9.2 show that capacity (the number of associations stored reliably) increases as the proportion of neurons that are active in a pattern decreases. This is because the more synapses are potentiated, the more errors are likely to be made; learning a pattern with a low proportion of active neurons leads to a smaller fraction of the synapses in the network being potentiated than learning a pattern with a higher proportion of activated neurons.

9.2.2 The recurrent associative network

We now consider a network similar to the one studied by Gardner-Medwin (1976) in which the connections from a layer of associative input neurons are replaced by recurrent collaterals from the output neurons (Figure 9.6). Extrinsic inputs are still responsible for activating the output cells during training, but the presynaptic and postsynaptic patterns are now identical and so the resulting weight matrix is symmetric. The process of recall is now progressive, occurring over multiple time-steps. This allows the network to perform **pattern completion**; that is, recall of an entire pattern when presented with a fragment of it.

The demonstration in Figure 9.6 makes it clear that in order for pattern completion to work, the threshold has to be lower than the number of neurons that are active in the fragment of the pattern which is presented. The lower the threshold, the more powerful the network is as a pattern completion device. However, with a lower threshold, the amount of spurious activity increases. There is therefore the risk that the spurious activity may lead to more spurious activity. In turn, this may lead to a greater number of spurious activations, with the result that the network ends up in an

Box 9.2 Capacity of the Associative Net

Simple analysis (Willshaw *et al.*, 1969) reveals the conditions under which the system can be used optimally, when the network can be used with high efficiency compared with a random access store with no associative capability. Under these conditions, patterns are coded sparsely; i.e. each pattern is represented by activity in a relatively small number of neurons.

If M_A of the N_A input neurons and M_B of the N_B extrinsic input neurons are active in the storage of an association (both sets of active neurons being chosen randomly), then the probability of a synapse having the associated input and extrinsic neurons active is $f_A f_B$ where $f_A = M_A/N_A$ and $f_B = M_B/N_B$ are the fractions of neurons that are active in input and extrinsic input patterns, respectively.

We determine the proportion of synapses p that have been potentiated in the storage of R associations by calculating the probability that a synapse has never been potentiated in the storage of any association:

$$1 - p = (1 - f_A f_B)^R.$$

Assuming $f_A f_B \ll 1$ and after rearrangement, this can be rewritten as:

$$R = -\log_e(1 - p)/(f_A f_B). \quad (\text{a})$$

During retrieval, an input pattern which activates M_A input neurons is presented. Some of the $N_B - M_B$ output neurons which should be silent in recall may be activated because of erroneous activation of synapses in the storage of other associations. This occurs with probability p^{M_A} and so the mean number of erroneous responses per pattern retrieved is:

$$\epsilon = (N_B - M_B)p^{M_A}.$$

A limit of good recall is at $\epsilon = 1$. A safer limit (Willshaw *et al.*, 1969) is:

$$N_B p^{M_A} = 1,$$

from which it follows that:

$$M_A = -\log_2 N_B / \log_2 p. \quad (\text{b})$$

The efficiency of retrieval E is the ratio of the number of bits in the R patterns retrieved to the number of binary storage registers available. Assuming perfect retrieval, this is:

$$E = R \log_2(C_{M_B}^{N_B})/(N_A N_B),$$

where $C_{M_B}^{N_B}$ is the number of possible combinations of M_B out of N_B elements.

Approximating $\log_2(C_{M_B}^{N_B})$ as $M_B \log_2 N_B$ leads to:

$$E = R M_B \log_2 N_B / (N_A N_B).$$

Substituting for f_A, f_B , R and $\log_2 N_B$ using Equations (a) and (b):

$$E = \log_2 p \log_e(1 - p).$$

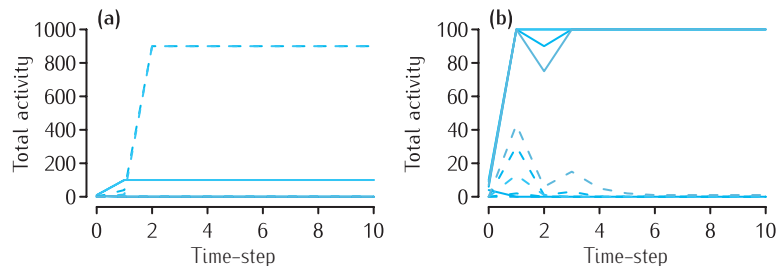
E has a maximum value of $\log_e 2$ (69%) when $p = 0.5$. Under these conditions:

$$R = \log_e 2 / (f_A f_B) \quad M_A = \log_2 N_B.$$

This analysis demonstrates that when working under optimal conditions the network is extremely efficient, sparse coding is required and the number of associations stored reliably scales in proportion to the ratio $N_A N_B / M_A M_B$.

Fig. 9.7 The effects of threshold and inhibition on pattern completion in the recurrent associative network. (a) One hundred patterns were learnt in a network of 1000 neurons, with 100 neurons active per pattern. The threshold was set at nine units, and then recall was tested in the network by presenting 10% of the active neurons of five different patterns. The graph shows the number of correctly active neurons (solid lines) and the number of spuriously active units (dashed lines) at each point in time of each of the five simulations. In most simulations, while the number of correctly active units is 100, the number of spuriously active units rises up to the maximum value of 900. (b) Recall was tested in exactly the same way on the same network, but with a threshold $\theta = 0.5$ and an inhibition parameter $\gamma = 0.9$. After at most five time-steps, the network settles to a state where there is the full complement of correct units and no or very few spurious ones.

The step function $\Theta(x)$ has a value of 1 if the value of x is greater than 1 and 0 otherwise (Figure 8.15c).



uninformative state in which all neurons are active. This is demonstrated in Figure 9.7a, in which the threshold (nine units) is just below the number of neurons activated initially (ten active neurons selected from patterns containing 100 active neurons). All the correct neurons are active after the first update, but the number of spuriously active neurons in the network increases to its maximum within two updates.

To counteract this problem, inhibitory neurons can be added to the network. The level of inhibition in the network is assumed to be proportional to the number of output neurons which become activated. When only part of a pattern is presented, the activity, and thus the level of inhibition, is low. It is therefore straightforward to activate the low-threshold neurons. However, on the second pass, when more neurons are active, the inhibition is proportionally larger, making it harder to recruit extra neurons to fire.

This principle is demonstrated by the set of simulations summarised in Figure 9.7b. The equation governing the network is:

$$x_j(t+1) = \Theta \left(\sum_i w_{ij} x_i(t) - \gamma \sum_i x_i(t) - \theta \right), \quad (9.2)$$

where $x_j(t)$ is the activity (0 or 1) of neuron j at time-step t , θ is the threshold and γ is the global inhibition parameter. The function $\Theta(\cdot)$ is the step function. The threshold is set to $\theta = 0.5$ and the inhibition $\gamma = 0.9$. Thus, if the network were in a full recall state, with 100 active neurons, it would receive 90 units of inhibition. As with the network in which there is no inhibition and the threshold is just below the number of neurons activated ($\gamma = 0$, $\theta = 9$, Figure 9.7a), recall is tested by presenting patterns in which ten of the original 100 active neurons are active. With these settings, the network can reach a recall state in which all the correct neurons are active and there are no or few spurious firings.

The recall states of a recurrent network are referred to as **attractors** because, given a starting configuration of the network sufficiently close to a recall state, the configuration will be attracted towards the recall state. This is made particularly explicit by Hopfield's innovation of the **energy function** (Hopfield, 1982). Any individual configuration of networks of this type can be assigned an energy. Recall states (or attractors) of the network are minima within this energy landscape, and the process by which the state moves towards the attractor is called **attractor dynamics**.

9.2.3 Variations on associative networks

Incompletely connected networks

Despite the simplicity of the associative network model, examination of its properties demonstrates that network models with very simple elements can give important insights into how networks comprising more complex elements might behave. The simple associative network model has demonstrated how a network might recall a pattern; the importance of the sparseness of memory patterns; and the importance of how the threshold and level of inhibition are set.

The original analysis has been extended in several directions to allow for the examination of more realistic cases. Buckingham (1991) examined threshold setting strategies for heteroassociative recall of noisy cues. Gardner-Medwin (1976) was amongst the first to investigate the biologically more plausible situation where the network is incompletely connected; i.e. a synapse between two neurons exists with only a certain probability. This means that the number of synapses activated for a given input varies, and requires a lowering of the threshold in order to maintain firing. Buckingham and Willshaw (1993) and Graham and Willshaw (1995) examined efficient threshold setting strategies for heteroassociative recall of noisy cues in incompletely connected heteroassociative networks. Motivated by properties of real synapses in hippocampal area CA3, the effect of stochastic transmission and variations to the update dynamics have been investigated (Bennett *et al.*, 1994; Graham and Willshaw, 1999).

Linear associative networks

A large volume of research has been devoted to analysing networks in which the weights have continuous rather than binary values, though the activity states of the model neurons are still binary. One issue has been how each synapse should be modified in response to the activity in the two neurons forming the synapse; the issue of the best synaptic **learning rule** has been much discussed (Box 9.3). Typically, synapses can be depressed as well as potentiated. In this case the optimal learning rule can be calculated (Dayan and Willshaw, 1991), which is the covariance rule (Sejnowski, 1977). A key finding is that, regardless of whether the update is synchronous (Little, 1974) or asynchronous (Hopfield, 1984; Amit *et al.*, 1985; Amit, 1989), the capacity of the network can scale with the size of the network. This scaling occurs only when the learning rule is tuned to the fraction of neurons that are active in any one pattern being present, so that the *average* change in weights caused by learning a pattern is zero (Sejnowski, 1977; Palm, 1988; Dayan and Willshaw, 1991). This principle can be summarised as ‘What goes up must come down’ and suggests that one role of long-term depression is to optimise storage capacity (Dayan and Willshaw, 1991). Networks in which the synapses have several discrete conductance levels have also been studied (Amit and Fusi, 1994).

Palimpsests

All the networks described so far are only able to learn a finite number of memories before recall becomes impossible. It is possible to construct networks which can always learn new memories by virtue of forgetting old

Box 9.3 | Synaptic learning rules for networks

In his well-known book, *The Organization of Behavior*, Hebb (1949) postulated: 'When an axon of cell A is near enough to excite cell B or repeatedly or consistently take part in firing it, some growth or metabolic change takes place in one or both cells such that A's efficiency, as one of the cells firing B, is increased.' From this has arisen the notion of **Hebbian plasticity**: that the activity patterns in the presynaptic and the postsynaptic neurons jointly determine the amount by which the synapse is modified. The mantra 'cells that fire together wire together' is often heard. The concept of Hebbian plasticity was given weight by the discovery of long-term potentiation (Bliss and Lømo, 1973; Chapter 7). Seung *et al.* (2000) provides a retrospective view of Hebb's book and the work leading from it.

Hebbian rule. A very simple form of a Hebbian rule is that a synapse is strengthened according to the product of the input (presynaptic) and training (postsynaptic) activities of the appropriate neuron, here interpreted as spiking rates. For an input activity I and a training (postsynaptic) activity T , with α as a constant of proportionality, the change in weight W is:

$$\Delta W = \alpha IT.$$

Synapses are never weakened and so ultimately any model using this learning rule will explode as all synapses become large and positive.

BCM rule. Based on experimental work on the development of ocular dominance in cortex, Bienenstock *et al.* (1982) developed the **BCM rule**. They supplemented the basic Hebbian equation with a threshold on the postsynaptic activity to allow both strengthening and weakening of synapses:

$$\Delta W = \alpha IT(T - \theta_T).$$

With a fixed threshold θ_T the rule would cause instabilities. Varying it according to the postsynaptic firing rate can implement competition between synapses on the same postsynaptic cell. Strengthening a synapse on a particular postsynaptic neuron leads to an enhanced postsynaptic firing rate and therefore a higher threshold, which then decreases the chance that other synapses on the same neuron will be strengthened.

Covariance rule. An earlier proposed rule (Sejnowski, 1977) provides a threshold on both presynaptic and postsynaptic activity. Synapses are strengthened when the difference of the input activity from its mean value has the same sign as the deviation of the training activity from its mean, and weakened otherwise. If the respective mean values of input and training signals are $\langle I \rangle$ and $\langle T \rangle$, the change in weight W is:

$$\Delta W = \alpha(I - \langle I \rangle)(T - \langle T \rangle).$$

In the special case when input and training activities are binary valued and there are fixed probabilities that the input and training neurons are active during storage, Dayan and Willshaw (1991) showed that the covariance rule is the optimal linear rule. When both input and training neurons are equally likely to be in the '0' or the '1' state, this reduces to the familiar Hopfield rule (Hopfield, 1984).

ones. This can be achieved in networks with binary weights by random de potentiation of synapses (Willshaw, 1971; Amit and Fusi, 1994), and is achieved in networks with continuous weights by various methods (Nadal *et al.*, 1986; Parisi, 1986; Sterratt and Willshaw, 2008). In networks with binary weights, a histogram of the time for which the synapse stays in the potentiated or unpotentiated state, similar to the histogram of channel open times (Section 5.7), can be plotted, and it has an exponential form. In the context of binary synapses, synaptic states with different levels of stability have been considered (Fusi *et al.*, 2005). Transitions between these states are stochastic and on multiple timescales, leading to histograms exhibiting a long-tailed power law dependence ($1/t^\mu$ with $\mu > 1$) rather than an exponential one. This mirrors the distribution of ages of exhibited memories measured in psychological experiments (Rubin and Wenzel, 1996).

Networks in which old memories are overwritten by new ones are often referred to as **palimpsests**, by analogy to the ancient and medieval practice of scraping away an existing text from vellum or papyrus in order to make way for new text. A faint impression remains of the original text, which can be deciphered using modern archaeological techniques.

Associative memory in networks of graded neurons

Associative networks can also be implemented as networks of graded firing rate neurons (Amit and Tsodyks, 1991b). In this case the neuronal dynamics follow a first order differential equation (Section 8.5.2) and the firing rate is based on the *f-I* curve of noisy integrate-and-fire neurons. The cells in this simulation can show a wide range of firing rates.

The approach is also related to that of Treves (1990), who investigated networks comprising rate-based neurons with piecewise-linear *f-I* curves (Figure 8.15), rather than the binary neurons used in previous models. This type of network can store patterns in which the activity in the neurons is graded, rather than being binary. Roudi and Treves (2006) extended the analysis by comparing associative networks with threshold-linear, binary or smoothly saturating rate-based neurons.

9.2.4 Feedforward artificial neural networks

In Section 8.5.1 some simple feedforward networks were described. The computational power of feedforward neural networks has been analysed extensively by researchers in the field of **artificial neural networks**. In this field the primary emphasis is on designing networks containing many nerve-cell-like elements that carry out useful tasks, such as pattern recognition. Feedforward networks which are made up of input neurons and output neurons and the connections between them have limited computational power and the addition of intermediate, so-called hidden, neurons increases their power and applicability. One example of how this type of network has been applied to neuroscience is to understand how neurons learn coordinate transformations in analysing the responses of cells in the posterior parietal cortex, which have receptive fields that depend on the position of the eyes. Zipser and Andersen (1988) showed how a network with a hidden layer with inputs that represent the location of an object on the retina and the direction of a head coordinate transformation could learn to transform the position of the object to be relative to the head, rather than the retina. The algorithm used to set up the connections between neurons was the widely used **back propagation algorithm** (Rumelhart *et al.*, 1986a). Box 9.4 gives a very brief overview of artificial neural networks and describes this algorithm.

Box 9.4 Artificial neural networks

In the simplest neural network model, a neuron's behaviour is characterised by a single number, representing its activity or firing rate, and the effect of one neuron on another through a synapse is characterised by another number, the synaptic weight. By gradual adjustment of its weights, a neural network can be trained to associate specific activity patterns across its input neurons with similar patterns across its output neurons from examples presented to it.

A simple **Perceptron** (Rosenblatt, 1958) has a set of input neurons and a single output neuron to which all input neurons are connected. The output y is a non-linear function f of the weighted sum of the inputs:

$$y = f\left(\sum_i w_i x_i\right).$$

In its simplest form, the function f is a step function with a threshold θ . The task is to associate a set of input vectors x^μ with a set of classifications y^μ , which could be 0 or 1. Using the simple Perceptron, only those sets of patterns which are linearly separable can be classified correctly. As an example, input patterns across three input neurons can be plotted in 3D space and the two classes are linearly separable if they can be separated by a plane. When the patterns are linearly inseparable, use of the Widrow–Hoff (1960), or Delta rule sets the weights to give the minimum number of classification errors. In the training phase, at each presentation of an input–output pattern, each weight w_i in the network is changed according to the product of its input activity x_i^μ with the classification error at this stage of training; i.e. the difference between the desired output y^μ and the actual output y for the input x^μ :

$$\Delta w_i = \epsilon x_i^\mu (y^\mu - y); \quad \Delta \theta = \epsilon (y^\mu - y),$$

where ϵ is a small learning rate. After a number of presentations of the training patterns, the weights of the network settle to values which make the network perform the classification optimally. Block (1962) and Minsky and Papert (1969) proved that when the patterns are linearly separable, stepwise adjustment of the weight values will always lead to the correct classification.

Whilst this is the optimal learning rule for training the network, there is little evidence from biology that a synapse can detect the difference between the actual and desired output activity. The Perceptron is thus an example of an artificial neural network. This is in contrast to the networks studied in the main text, whose relation to biology is closer.

The back propagation algorithm is a significant extension of the Perceptron algorithm which enables arbitrary associations between inputs and outputs to be learnt in a feedforward network, provided that a sufficient number of hidden units are interspersed between inputs and outputs. In this algorithm, the errors made by the hidden units after presentation of any one input during training are calculated recursively from the errors made by the neurons to which the hidden units project; hence 'back propagation'. There is a vast literature on the subject of artificial neural networks and the

Box 9.4 (*continued*)

back propagation algorithm, addressing such issues as the speed of training, the ability of networks to generalise to respond appropriately to unseen inputs, their biological plausibility and application to real-life classification and prediction problems (Minsky and Papert, 1969; Hinton and Anderson, 1981; McClelland *et al.*, 1986; Rumelhart *et al.*, 1986b; Hertz *et al.*, 1991; Bishop, 1995). Hertz *et al.* (1991) provide a thorough introduction to artificial neural networks and Cowan and Sharp (1988) provide a historical overview of the development of neural networks.

9.3 Networks of simplified spiking neurons

The network introduced in the previous section demonstrates how memories might be encoded in synaptic strengths, and shows – amongst other things – the importance of setting the level of inhibition so as to prevent activity exploding. However, the neuron model underlying the network was extremely simple, and we might question whether more complicated neurons could support memory storage.

This section presents an approach taken to address this question by Amit and Brunel (1997b), who embedded recurrent associative memory networks in a network of excitatory and inhibitory integrate-and-fire neurons. As just described, memories can be stored by altering the strengths of the connections between the excitatory neurons. The network is intended to represent a cortical column, the motivation being recordings from cells in monkey temporal cortex (Miyashita, 1988). These cells fire at elevated rates for a number of seconds after a familiar visual stimulus has been presented briefly – suggestive of the attractor dynamics exhibited by the recurrent memory networks described earlier. In addition, in the absence of any stimulus, cells fire at a low background rate, and the cells in a column are thought to receive a constant background barrage of spikes from other cortical columns.

Amit and Brunel's modelling of this data proceeded in two stages. Firstly, a recurrently connected network of excitatory and inhibitory neurons was set up which could reproduce roughly the experimentally-recorded firing statistics in the absence of a stimulus. In order to set the parameters of this network, an extension of the analysis which had been applied to the Stein model (Section 8.2.3) was helpful. This analysis also informed the process of scaling down the size of the realistic network to a manageable size. The second stage was to embed memories in the network by modifying the synaptic weights according to a Hebbian learning rule.

9.3.1 Recurrent network of integrate-and-fire neurons without learning

The network constructed by Amit and Brunel (1997b) comprises N_E excitatory and N_I inhibitory neurons. The membrane potential V_j of each cell

In contrast to earlier equations for the membrane potential in this book, neither the membrane capacitance nor the membrane resistance appears in Equation 9.3. The reason for this is that the membrane resistance or capacitance scale all of the weights, and so the effect of changing the resistance or the capacitance can be achieved by scaling the weights. However, the equation appears to be dimensionally incorrect; the units of current do not match the units of voltage divided by time. This can be resolved by treating the current as though it had units of $V\text{s}^{-1}$.

evolves in time according to:

$$\frac{dV_j}{dt} = -\frac{V_j}{\tau_j} + I_j^{\text{rec}} + I_j^{\text{ext}}, \quad (9.3)$$

where τ_j is the membrane time constant of the neuron, I_j^{rec} is the contribution to the current from recurrent collaterals and I_j^{ext} is the contribution from external input to the cell. When the neuron reaches the threshold θ , it emits a spike; the time of the k th spike produced by neuron j is denoted t_j^k . After firing, the neuron is reset to $V_{\text{reset}} = 10\text{mV}$ and there is a refractory period of $\tau_0 = 2\text{ms}$. The membrane time constant has the same value τ_E for all excitatory neurons and τ_I for all inhibitory neurons.

The recurrent input to the cell comes from all of the other excitatory and inhibitory cells in the network. The recurrent input received by neuron j at time t is:

$$I_j^{\text{rec}}(t) = \sum_{i \in E, k} c_{ij} w_{ij} \delta(t - \tau_{ij} - t_i^k) - \sum_{i \in I, k} c_{ij} w_{ij} \delta(t - \tau_{ij} - t_i^k). \quad (9.4)$$

The relationship between presynaptic neuron i and postsynaptic neuron j is specified by three quantities. c_{ij} is a random binary variable denoting whether a connection exists. If it does, w_{ij} is the weight of connection and τ_{ij} is the propagation delay from i to j . The first summation is over all the spikes (numbered k) of all the neurons i in the excitatory (E) group of neurons; the second summation is over all spikes from all inhibitory (I) neurons. δ indicates a delta function, defined in Section 7.3.1. The strength of the connection w_{ij} is drawn randomly from a Gaussian distribution with a mean which depends on the classes of the two neurons it connects (w_{EE} for excitatory-to-excitatory synapses, w_{IE} for excitatory-to-inhibitory synapses and so on) and a standard deviation of Δ times the mean. The delays τ_{ij} are drawn from a uniform distribution between 0.5 ms and 1.5 ms.

The input from external columns is assumed to come from neurons firing in other cortical columns. The times of spikes $t_j^{\text{ext},k}$ arriving at neuron j are generated by an independent Poisson process at a rate $cN_E v_E^{\text{ext}}$, where v_E^{ext} is the mean firing rate of cells in the external columns. The increase in membrane potential is set to be the same as the mean weight onto other excitatory or inhibitory neurons:

$$I_j^{\text{ext}} = \begin{cases} w_{EE} \sum_k \delta(t - t_j^{\text{ext},k}), & j \in E \\ w_{IE} \sum_k \delta(t - t_j^{\text{ext},k}), & j \in I. \end{cases} \quad (9.5)$$

The parameters of the network are set up so that v_E^{ext} is similar to the actual mean firing rate v_E of the excitatory neurons modelled in the cortical column. Thus the mean external input is similar to the input the column receives from local excitatory cells.

Figure 9.8 shows the results of an event-based simulation (Box 9.7) of the network (Amit and Brunel, 1997b) that we carried out. There were $N_E = 6000$ excitatory and $N_I = 1500$ inhibitory neurons, where the probability of

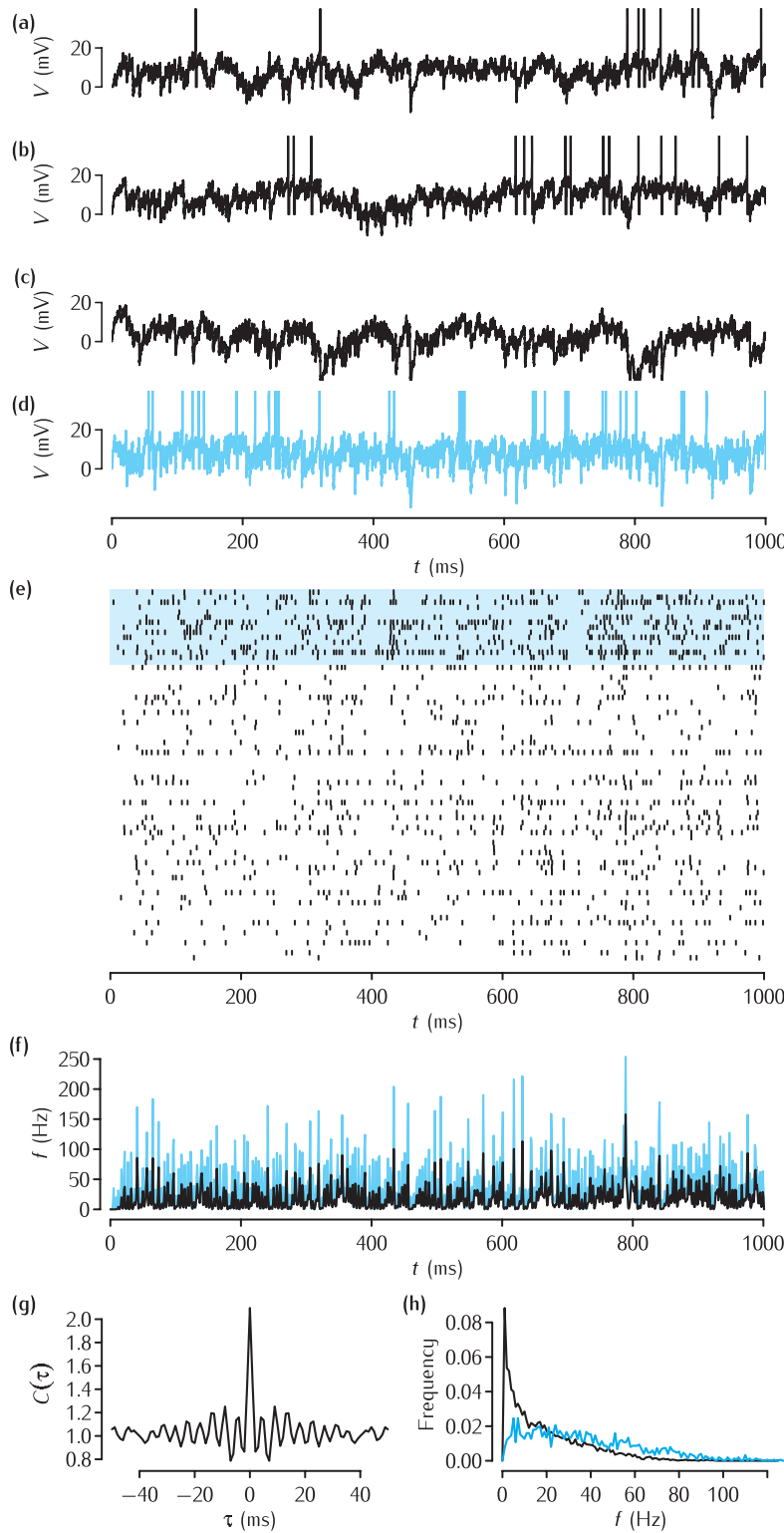


Fig. 9.8 Our simulations of a network of recurrently connected excitatory and inhibitory neurons using Equations 9.3, 9.4 and 9.5, after Amit and Brunel (1997b). **(a–c)** The time courses of the membrane potential of three excitatory neurons. **(d)** The time course of one inhibitory neuron. **(e)** A spike raster of 60 excitatory neurons (lower traces) and 15 inhibitory neurons (upper traces, highlighted in blue). **(f)** Population firing rates of the excitatory (black) and inhibitory neurons (blue). **(g)** Average autocorrelation of spikes from excitatory neurons. **(h)** Histogram of average firing rates of excitatory neurons (black) and inhibitory neurons (blue). Parameter values: $\theta = 20 \text{ mV}$, $V_{\text{reset}} = 10 \text{ mV}$, $\tau_E = 10 \text{ ms}$, $\tau_I = 5 \text{ ms}$, $w_{EE} = 0.21 \text{ V s}^{-1}$, $w_{EI} = 0.63 \text{ V s}^{-1}$, $w_{IE} = 0.35 \text{ V s}^{-1}$, $w_{II} = 1.05 \text{ V s}^{-1}$, $\Delta = 0.1$, τ_{ij} is drawn uniformly from the range $[0.5, 1.5] \text{ ms}$ and $v_E^{\text{ext}} = 13 \text{ Hz}$.

a connection existing ($c_{ij} = 1$) is 0.2. In Figure 9.8a–c the membrane potentials of three excitatory neurons are shown. Two of the neurons fire irregularly at different time-averaged rates, whilst the third is completely silent. In Figure 9.8d the activity of an inhibitory neuron is shown. This appears similar to the activity of the excitatory neurons. Figure 9.8e shows a spike raster of 60 of the excitatory neurons and 15 of the inhibitory neurons (highlighted). Whilst the firing times are random, there are events in which a large number of neurons fire. This can be seen more clearly by computing some statistics of the spike trains (Box 9.5). In the plots of the excitatory and inhibitory population firing rates (Figure 9.8f), there is an irregular oscillation in the overall activity levels. In order to quantify this, the cross-correlation of the population firing rates can be computed (Figure 9.8g). The histogram of time-averaged firing rates is shown in Figure 9.8h. The number of excitatory neurons firing at a particular frequency follows a roughly exponential distribution, whilst the distribution of inhibitory firing rates is flatter.

9.3.2 Insights from the Stein model

So far, the behaviour of the network has been described with only one set of parameters. In order to set these parameters, Amit and Brunel (1997a, b) analysed the network under some simplifying assumptions:

- (1) Each neuron receives a large number of spikes within its integration period.
- (2) The increase in membrane potential due to an incoming spike is small compared to the threshold.
- (3) The firing times of the excitatory and inhibitory neurons are independent, although the firing rates may not be.

This analysis, summarised in Box 9.6, is an extension of the analysis of the Stein model, which was encountered in Section 8.2.3.

A number of constraints on the parameters emerge from the analysis:

- Inhibition has to be sufficiently strong relative to excitation for the stable state to exist, but it does not have to be finely tuned.
- Up to a point, the faster the inhibition, the less inhibition is required.
- For a given ratio of the inhibitory and excitatory input to neurons, the weights from excitatory cells must be sufficiently large compared to the threshold.

In fact, the simulations shown in Figure 9.8 demonstrate that the firing times are correlated, and so the assumptions of the analysis are not fulfilled strictly. However, the correlations are sufficiently small that the results of the analysis are good enough for the parameters of the network to be set so that there is a stable level of activity. More recent analysis, which uses the tools of statistical physics, can address non-stationary firing rates (Buice and Cowan, 2009).

9.3.3 Scaling

The Amit and Brunel (1997b) model network is supposed to represent a cortical column, with around 10^5 neurons. They simulated a number of networks of various sizes. Of these, the network presented here, which is the

Box 9.5 | Spike statistics

In order to make sense of spike trains recorded from multiple neurons, a number of statistics can be employed. A prerequisite for computing the statistics is to bin the spike times by computing $S_i(t)$, the number of spikes produced by neuron i in the interval $[t, t + \Delta t]$. The width of a bin Δt is typically on the order of a millisecond.

The **instantaneous population firing rate** in a pool of N neurons is defined as:

$$v(t) = \frac{1}{N\Delta t} \sum_{i=1}^N S_i(t).$$

At the end of a simulation of duration T , the **temporally averaged firing rate** of a neuron can be computed:

$$v_i = \frac{1}{T} \sum_{k=0}^{T/\Delta t - 1} S_i(k\Delta t).$$

The **autocorrelation** is a temporally averaged quantity defined as:

$$C_i(\tau) = \frac{1}{T - \tau} \sum_{k=0}^{(T-\tau)/\Delta t - 1} S_i(k\Delta t) S_i(k\Delta t + \tau).$$

The autocorrelation indicates how well the instantaneous firing of a neuron correlates with its firing at a time τ later. For a Poisson spike train with rate v , the autocorrelation is expected to have a peak value v at τ and is expected to be $v\Delta t$ elsewhere. Autocorrelations sometimes have sidebands, which indicate periodic activity.

The **cross-correlation** is similar to the autocorrelation, except that it indicates how the instantaneous firing of one neuron i is related to the firing of another neuron j at a time τ later:

$$C_{ij}(\tau) = \frac{1}{T - \tau} \sum_{k=0}^{(T-\tau)/\Delta t - 1} S_i(k\Delta t) S_j(k\Delta t + \tau).$$

Correlated activity between neurons is revealed as a peak, which may not lie at $\tau = 0$.

Amit and Brunel (1997b) used an average cross-correlation, defined between excitatory and inhibitory neurons as:

$$\bar{C}_{EI}(\tau) = \frac{1}{T - \tau} \sum_{k=0}^{(T-\tau)/\Delta t - 1} v_E(k\Delta t) v_I(k\Delta t + \tau),$$

where $v_E(t)$ and $v_I(t)$ are the instantaneous population rates for the excitatory and inhibitory neurons.

For more detailed introductions to spike train statistics, see texts such as Dayan and Abbott (2001), Koch (1999), Gabbiani and Koch (1998) and Rieke *et al.* (1997).

Box 9.6 Analysis of excitatory–inhibitory networks

Amit and Brunel's (1997b) analysis of an excitatory–inhibitory network is an extension of the analysis of the Stein model, which was outlined in Box 8.5. It is supposed that the network reaches a state in which each neuron fires in a random manner that can be described by Poisson statistics. The mean firing rate of the excitatory neurons v_E is a function of the mean μ_E and variance σ_E^2 of the membrane potential in excitatory neurons:

$$v_E = f(\mu_E, \sigma_E) \text{ and } v_I = f(\mu_I, \sigma_I). \quad (\text{a})$$

Figure 8.7 shows a typical form of f . Similarly, the mean firing rate of the inhibitory neurons v_I depends on the mean μ_I and variance σ_I^2 of the membrane potential in the inhibitory neurons.

Using the same reasoning as in Box 8.5, but with the excitatory and inhibitory incoming spike rates being $cN_E(v_E + v_E^{\text{ext}})$ and $cN_I v_I$, respectively, the means and variances of the membrane potential of the excitatory and inhibitory neurons can be written down:

$$\begin{aligned} \mu_E &= \tau_E(w_{EE}cN_E(v_E + v_E^{\text{ext}}) - w_{EI}cN_I v_I) \\ \sigma_E^2 &= \frac{\tau_E}{2}(w_{EE}^2cN_E(v_E + v_E^{\text{ext}}) + w_{EI}^2cN_I v_I) \\ \mu_I &= \tau_I(w_{IE}cN_E(v_E + v_E^{\text{ext}}) - w_{II}cN_I v_I) \\ \sigma_I^2 &= \frac{\tau_I}{2}(w_{IE}^2cN_E(v_E + v_E^{\text{ext}}) + w_{II}^2cN_I v_I). \end{aligned} \quad (\text{b})$$

The set of equations (a) and (b) forms a closed system of equations in the four variables μ_E , μ_I , σ_E and σ_I . A solution can be found numerically and analysed for stability (Box B.2).

Equations (b) for the means and variances show that changing the size of the system by changing N_E and N_I changes the means and variances, and is therefore expected to change the behaviour of the network. The equations also demonstrate that this can be compensated for by scaling the connection probability c so that cN_E and cN_I remain constant. In contrast, the mean weights cannot be used to compensate for changes in the size of the system. For example, the mean can be kept constant by scaling w_{EE} so that $N_E w_{EE}$ remains constant. However, this implies that $N_E w_{EE}^2$ changes, and so the variances change.

A contrast to this analysis of an excitatory–inhibitory network of noisy spiking neurons is Wilson and Cowan's (1972) well-known analysis of a network of noiseless rate-based neurons. Their analysis culminates in a pair of coupled ODEs for the population firing rates:

$$\begin{aligned} \tau_E dv_E/dt &= -v_E + (1 - rv_E)f(w_{EE}v_E - w_{EI}v_I + v_E^{\text{ext}}) \\ \tau_I dv_I/dt &= -v_I + (1 - rv_I)f(w_{IE}v_E - w_{II}v_I + v_I^{\text{ext}}), \end{aligned}$$

where r is a refractory period and f is a firing rate function of current alone (Chapter 8). The system can exhibit steady state and oscillating (limit cycle) behaviour, and can be analysed using dynamical systems theory (Appendix B.2).

one we simulated (Figure 9.8), has only 7500 neurons, smaller by a factor of 13.3. Simulating this network demonstrates a number of the principles underlying the design of models that were laid out in Section 9.1.2:

- (1) The fraction of excitatory and inhibitory cells in the scaled-down network is the same as in the original, 80% and 20%, respectively.
- (2) The probability c of two neurons being connected has been scaled up by a factor of 4 so as to compensate partly for the smaller number of inputs.
- (3) The spontaneous firing rates have been scaled up from around 1–5 Hz *in vivo* to around 13 Hz.

Taken together, this means that the expected number of spikes impinging on an excitatory or inhibitory neuron in one second should be roughly the same as the number of spikes arriving in one second at a neuron of the same type in the full network (Box 9.6). A large number of spikes arriving within the period of the membrane time constant is necessary for the analysis of the network (Section 9.3.2) to be valid.

To a first approximation, scaling up the connectivity c to compensate for the reduction in network size should cause no change in the network behaviour. However, the connection probability cannot be greater than 1, so the scope for increasing c is limited. For example, if the connectivity in the full network is 5%, the maximum factor by which the connectivity can be increased is 20. In contrast, scaling the synaptic weights w_{ij} would be expected to change the network behaviour, as demonstrated in Box 9.6.

In order to increase the firing rates, the function that converts the mean and variance of the depolarisation into a firing rate has to be altered, or the mean weights (w_{EE} , w_{EI} , w_{IE} and w_{II}) need to be modified. Thus scaling the firing rates does change the network behaviour. However, there is no reason to suppose that a large network with realistic firing rates could not be constructed.

Despite the attempt to maintain the fundamental characteristics of the network in the scaled-down version, the size of the network does have an effect on its behaviour. The larger the network, the smaller the magnitude of the oscillations in activity, as shown by the height of the peak of the cross-correlation function. Plotting the height of the cross-correlation against network size suggests that, for infinitely large networks, the cross-correlation function would be flat (Amit and Brunel, 1997b). Since this is one of the assumptions of the analysis, this suggests that the analysis would be precise in the case of an infinitely large network. With very small networks, chance correlations can cause large fluctuations, which throw the network into a persistent state of rapid firing.

9.3.4 Associative memory in a simplified spiking network

To embed memories in the network, Amit and Brunel (1997b) used a stochastic learning rule. They assumed that a sequence of binary-valued patterns was presented to each of the excitatory neurons of the network, and that only the connections between pairs of excitatory neurons were modifiable. Whenever the pre- and postsynaptic neurons on either side of a connection were both active, the connection between them was set to a potentiated value with a fixed probability. Whenever only one of the pre- or postsynaptic

Box 9.7 Event-based simulation

Conventional methods for solving the time course of variables described by coupled differential equations involve splitting up time into discrete chunks of length Δt . These methods can be applied to spiking neuron models, but the precision with which the time of a spike can be specified is limited by the length of Δt .

In **event-based simulation** methods, rather than simulating every time-step of the simulation, each step in the simulation corresponds to the production or reception of a spike. For the entire network there is a queue of event times which are expected to occur in the future. At each step, the earliest event on the list is considered. If this is a spike production event in neuron i , events tagged with the identity j of receiving neurons are added to the queue to occur at time $t + \tau_{ij}$, where τ_{ij} is the delay from i to j . If the event is a spike being received at neuron j , the time at which neuron j is next expected to fire is recomputed. For certain classes of synaptic potential in current-based neurons, this can be done with arbitrary precision that is limited only by the floating-point accuracy of the computer.

In some simulations of networks of integrate-and-fire neurons, there are significant differences between the level of synchronisation observed in event-based and time-step methods, even when the time-step is 0.01 ms, two orders of magnitude faster than the rise time of EPSCs (Hansel *et al.*, 1998).

While event-based methods are more precise than time-step methods, the logic behind them and their implementation are quite intricate, and depends on the class of neuron. Event-based methods exist for integrate-and-fire models with various types of current-based synapses, and many of these methods are incorporated in simulators such as NEURON (Carnevale and Hines, 2006; van Elburg and van Ooyen, 2009). Event-based simulation methods for conductance-based neurons have also been developed (Brette, 2006; Rudolph and Destexhe, 2006) but, again, the type of conductance time courses they can simulate is limited.

A selection of learning rules for networks of simpler model neurons is described in Box 9.3.

neurons was active, the connection was set to a depressed level. Connections which had been potentiated or depressed were not eligible for further modification. The result is a synaptic matrix which was then imposed on the network of integrate-and-fire neurons.

Figure 9.9 shows spike rasters of excitatory and inhibitory neurons in the model network. Initially, in the prestimulus period, both the inhibitory and excitatory neurons are spontaneously active. In the stimulus period, current is fed to excitatory neurons that were active in a previously stored pattern. Excitatory neurons which were active in this pattern, a sample of which is shown in the five top neurons in the raster in Figure 9.9a, fire at rates that are higher than their spontaneous rates. In the delay period, after the stimulus is removed, the excitatory neurons in the pattern continue firing, albeit at a lower rate than during the stimulus period. This delay period can persist for a number of seconds, though it is vulnerable to particularly large oscillations

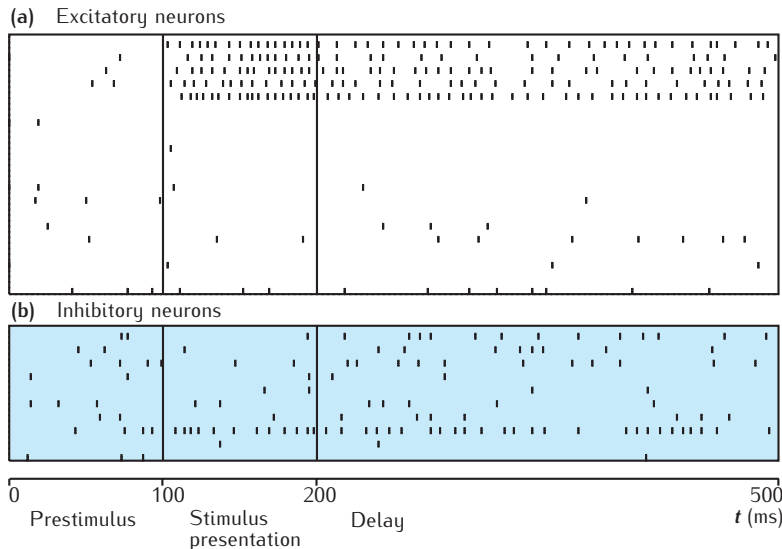


Fig. 9.9 Recalling a memory embedded in a network of integrate-and-fire neurons.

(a) Spike rasters from 20 excitatory neurons, including five active in a recalled pattern.
 (b) Spike rasters of ten inhibitory neurons. From Amit and Brunel (1997b). Reprinted by permission of the publisher (Taylor & Francis Group, <http://www.informaworld.com>).

in the global activity of the network. This demonstrates that the associative network described in the previous section can be implemented in a network of integrate-and-fire neurons.

9.4 | Networks of conductance-based neurons

Computational models of networks of spiking neurons have played a key role in helping our understanding of the activity properties of neurons embedded in different brain nuclei. Two major, and somewhat competing, network effects have been studied. The first is how networks of coupled excitatory and inhibitory neurons can maintain irregular firing patterns, as recorded in the cortex. One such study has been described in the previous section. The flip-side to this is that such networks have a strong tendency to exhibit more regular, rhythmic firing. Prominent **field oscillations** at a range of frequencies, from a few hertz to hundreds of hertz, have been recorded in different brain areas in different behavioural states for the animal. Computational models provide considerable insight into how these rhythms may arise in different networks. Network models have been used to explore how different frequencies arise and how oscillations may be coherent over spatially distributed cell populations (Traub *et al.*, 1999, 2004, 2005; Bartos *et al.*, 2007). A detailed example will be considered in Section 9.5. Synaptic and intrinsic cell time constants are important, as is the structure of recurrent excitatory and feedback inhibitory loops (Traub *et al.*, 2004; Bartos *et al.*, 2007). Spatial coherence may involve gap junctions that can quickly entrain the firing of groups of cells (Traub *et al.*, 2004; Bartos *et al.*, 2007).

One such rhythm is the **gamma oscillation**, ranging in frequency from around 30 Hz to 70 Hz, recorded in many areas in mammalian neocortex and the hippocampus. In simple terms, such a rhythm is the natural consequence of the time course of GABA_A-mediated feedback inhibition within

a recurrent network of excitatory cells that also drive a population of inhibitory interneurons that feed back inhibition onto those cells. This is precisely the arrangement seen in the Amit and Brunel network model discussed above. Irregular firing in that network arises from the delicate balancing of excitation and inhibition. If inhibition is dominant, then the network becomes an oscillator. The gamma oscillation has been given central importance as a possible substrate for information coding. The basic idea is that a pattern of information is defined by neurons that fire on the same oscillation cycle (Singer, 1993; Lisman and Idiart, 1995).

Above, we saw that patterns in an associative memory of spiking neurons can be defined as a group of neurons firing at an elevated rate, compared to the background firing rate of the network (Figure 9.9). An alternative is that a pattern corresponds to those neurons that spike together on a particular gamma cycle. This is an example of a temporal code, rather than a rate code. In this scenario a new pattern can be recalled potentially every 25 ms or so (Lisman and Idiart, 1995). Different patterns being recalled on each gamma cycle may constitute a meaningful pattern sequence. For example, the route ahead through an environment, where each pattern represents a location.

To demonstrate network rhythms and their role in associative memory, we consider a recurrent network of excitatory cells that also includes feedback inhibition. Based on the model of Sommer and Wennekers (2000, 2001), our model network contains 100 excitatory cells that are modelled using the Pinsky–Rinzel two-compartment model of a hippocampal CA3 pyramidal cell, introduced in Chapter 8. In such a small network we allow these cells to be connected in an all-to-all manner. In addition, each cell forms an inhibitory connection with all other cells. This provides a level of inhibition that is proportional to the level of excitatory activity in the network. This could be, and would be in a biological network, mediated by an explicit population of inhibitory cells, but for computational simplicity these are omitted. This network model is considerably smaller in size and simpler in structure than the model of Amit and Brunel. This is allowable precisely because we are modelling an oscillating network in which the principal neurons are firing more or less in synchrony. This is easily achieved with small groups of neurons, whereas the asynchrony required by Amit and Brunel requires a large degree of heterogeneity, which is lost in small networks. The simplification of not modelling the inhibitory interneurons introduces a very specific assumption about the connectivity and subsequent activity levels within a feedback inhibitory loop. Recent models that include explicit interneurons demonstrate that memory recall is rather robust to the precise form of this feedback inhibition (Hunter *et al.*, 2009).

The final ingredient of our model is a structured weight matrix that defines the autoassociative storage of binary patterns, as described earlier for the schematic autoassociative memory network (Section 9.2.2). Here, each pattern consists of ten active cells out of the population of 100. Fifty patterns are generated by random selection of the ten cells in each pattern. They are stored in the weight matrix by the binary Hebbian learning scheme described earlier. This binary matrix is used to define the final connectivity between the excitatory cells – an entry of 1 in the matrix means the excitatory connection between these cells is retained, whereas an entry of 0 means

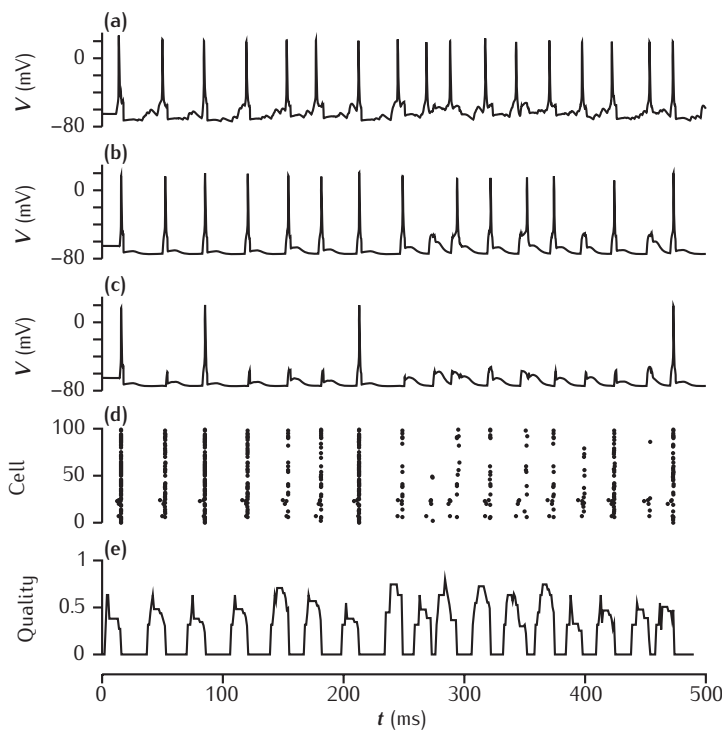


Fig. 9.10 Network simulation based on the model of Sommer and Wennekers (2001). The top three traces are the time courses of the membrane potential of three excitatory neurons. (a) A cue cell. (b) A pattern cell. (c) A non-pattern cell. (d) A spike raster of the 100 excitatory neurons. (e) The recall quality over time, with a sliding 10 ms time window.

the connection is removed. Note that the matrix is symmetric, so if cell i is connected to cell j , then cell j is also connected to cell i .

We test recall of a stored pattern by providing external stimulation to a subset of the cells in a particular pattern, so that they become active. Network activity is then monitored to see if the remaining cells of the pattern subsequently become active, and whether any non-pattern (spurious) cells also become active. Fifty patterns is a lot to store for this size of memory network, and errors in the form of spurious activity can be expected during pattern recall. The quality of recall is measured continuously by forming a binary vector defined by all cells that are active (fire action potentials) within the given time window (10 ms) and then calculating the **scalar product** of this vector against the stored pattern vector, normalised to the length of the recalled vector. A value of 1 results if the pattern is recalled perfectly; otherwise the quality is less than 1 (some pattern cells do not become active or some spurious cells are active).

In the example shown in Figure 9.10, the model pyramidal cells are connected by conductance-based excitatory synapses that have an instantaneous rise time and a decay time of 2 ms for the conductance, and a reversal potential of 0 mV, equivalent to the characteristics of AMPA-receptor-mediated synapses. The inhibitory synapses have an instantaneous conductance rise time, but a decay time of 7 ms and a reversal potential of -75 mV, equivalent to GABA_A-receptor-mediated synapses. The excitatory connection weight (maximum AMPA conductance) is 6 nS and the inhibitory connection weight (maximum GABA_A conductance) is 2 nS, with a 2 ms connection delay for all connections. An external stimulus consisting of a

continuous 500 Hz Poisson-distributed spike train (representing the convergence of many presynaptic cells) is applied to four cells from one of the stored patterns, to act as a recall cue.

The cued activity results in barrages of network activity roughly every 25 ms (within the gamma frequency range), with each barrage consisting of the cued cells, many of the remaining pattern cells and some spurious (non-pattern) cells. Close examination of each barrage reveals that the cued cells fire first, followed by the pattern cells, then the spurious cells. Hence, during a barrage, the recall quality rises in stages to a peak before falling back. Thus not only which cells fire on a gamma cycle, but their phase of firing also contains information about the stored pattern. If the strength of inhibition is reduced (not shown), many more spurious cells fire, but late in a gamma cycle, and in addition the cue and pattern cells start to fire in bursts, providing another distinguishing feature of the pattern. This bursting is an intrinsic characteristic of CA3 pyramidal cells, captured by the Pinsky–Rinzel model.

9.5 | Large-scale thalamocortical models

We continue these examples with models of **thalamocortical systems**, one of the greatest challenges for computational neuroscience in trying to understand the function of the mammalian brain. We begin with the work of Traub *et al.* (2005) on constructing a detailed model of a cortical column and its interaction with the thalamus. We then introduce the **Blue Brain project** (Markram, 2006) and the approaches that it is taking to generate as accurate a model as possible of a single cortical column. Finally, we look at an example of modelling a complete thalamocortical system (Izhikevich and Edelman, 2008).

9.5.1 Modelling a cortical column

Traub *et al.* (2005) provide a primer for constructing large-scale models of mammalian brain areas, giving precise detail on the cell models and network connectivity, and the model design decisions taken based on experimental data and computational feasibility. The opening two paragraphs of the paper set forth the motivations and difficulties of such a study with great clarity:

The greatest scientific challenge, perhaps, in all of brain research is how to understand the cooperative behaviour of large numbers of neurons. Such cooperative behaviour is necessary for sensory processing and motor control, planning, and in the case of humans, at least, for thought and language. Yet it is a truism to observe that single neurons are complicated little machines, as well as to observe that not all neurons are alike – far from it; and finally to observe that the connectional anatomy and synaptology of complex networks, in the cortex for example, have been studied long and hard, and yet are far from worked out. Any model, even of a small bit of cortex, is subject to difficulties and hazards: limited data, large numbers of parameters, criticisms that models with complexity comparable to the modelled system cannot be scientifically useful, the expense and

slowness of the necessary computations, and serious uncertainties as to how a complex model can be compared with experiment and shown to be predictive.

The above difficulties and hazards are too real to be dismissed readily. In our opinion, the only way to proceed is through a state of denial that any of the difficulties need be fatal. The reader must then judge whether the results, preliminary as they must be, help our understanding.

Working in this ‘state of denial’, Traub *et al.* have built a large-scale model of a single-column thalamocortical network made up of 3560 multi-compartmental neurons. Their aim is to increase our understanding of the neural network mechanisms underpinning relatively simple phenomena, such as pharmacologically-induced network oscillations. While the model is large-scale in a modelling sense, it is still rather small and very simplified compared to real thalamocortical networks. Consequently, in the opinion of its authors, it is more suited to studying phenomena involving strong correlations between activity in neural populations, so that network behaviour is identifiable by observation of a small number of cells. The model simulations provide predictions concerning the physiology of network oscillations such as persistent gamma and epileptogenesis. Here, we give an overview of the structure of this model and how it was designed.

The Traub thalamocortical model

The model effectively encompasses a single cortical column and its connectivity with the thalamus (Traub *et al.*, 2005). Space is defined only in the direction of cortical depth, reflecting the layered structure of the cortex. This dimension is required for calculating extracellular field potentials at different cortical depths. Lateral distance is assumed to be insignificant when constructing network connectivity.

Cell types

The model network contains 3560 neurons, of which 19% are GABAergic, in line with experimental estimates. The individual cell populations are:

superficial (layer two/three): 1000 regular spiking and 50 fast rhythmic bursting pyramidal cells; 90 basket cells; 90 axoaxonic cells; 90 low threshold spiking interneurons

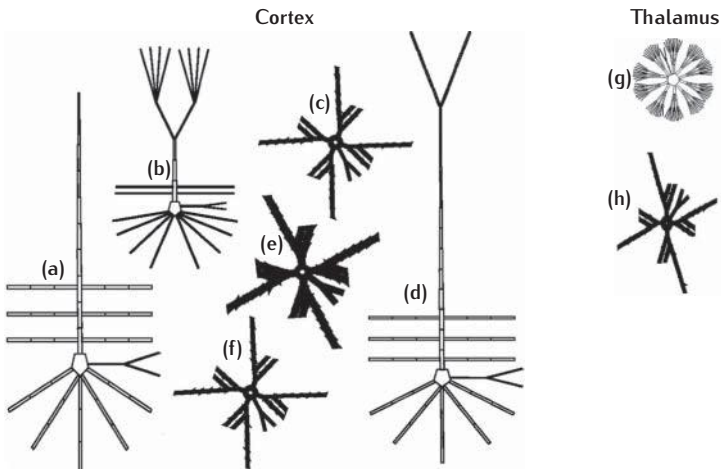
layer four: 240 spiny stellate cells

deep (layer five/six): layer five tufted pyramidal cells: 800 intrinsically bursting and 200 regular spiking; 500 layer six non-tufted regular spiking pyramidal cells; 100 basket cells; 100 axoaxonic cells; 100 low threshold spiking interneurons

thalamus: 100 thalamocortical relay cells; 100 nucleus reticularis thalamic cells.

Population sizes are not known with any certainty and so these sizes represent estimates of the relative number of different cell types. Many identified cell types are missing. The included types are those specifically known from experiments to be involved in the network phenomena investigated with the model.

Fig. 9.11 Morphological structure of the different cell types in the Traub model.
(a) Layer six non-tufted pyramidal cells (regular spiking),
(b) layer two/three pyramidal cells (regular spiking, fast rhythmic bursting), **(c)** superficial interneurons (basket cells and axoaxonic cells, low-threshold spiking), **(d)** layer five tufted pyramidal cells (intrinsically bursting, regular spiking), **(e)** layer four spiny stellate, **(f)** deep interneurons, **(g)** nucleus reticularis thalamic, **(h)** thalamocortical relay.
Adapted from Traub *et al.* (2005), with permission from The American Physiological Society.



Model cell structure

Each cell type is defined by a multi-compartmental model with a particular stylised anatomical structure that captures the principal dendrites with between 50 and 137 compartments (Figure 9.11). All model cells of a particular type have exactly the same anatomy. The number of compartments was deemed sufficient, on the basis of numerous computer simulations, to reproduce detailed neuronal firing behaviours, given spatially distributed ion channels and synapses. In particular, the compartmental structures are sufficiently detailed to allow for:

- differences in electogenesis between soma, axon and dendrites;
- action potential initiation in the axon and back propagation into the dendrites;
- dendritic calcium spikes and bursts.

An identical set of ion channels is used across all cell types, and consists of: fast, inactivating sodium; persistent sodium; delayed rectifier, slow AHP, A, C, K2 and M types of potassium channel; low- and high-threshold calcium; and the anomalous rectifier h channel. Some small differences in ion channel kinetics across cell type are included. Spatial distributions of these channels are cell-type specific and combine with the anatomy and differing channel kinetics to give the varied spiking behaviours across cell types. All cells within a population are identical, except for possible variation in injected bias currents that, to some extent, accounts for variations in morphology and ion channel density within cells of the same type.

Network connectivity

Network connectivity includes both chemical synapses and gap junctions. Connectivity is specified by the number of connections received by a cell of type *post* from a cell of type *pre*. For each *post* cell, *pre* cells are selected randomly until the required number of connections is made. A single *pre* cell can make more than one contact onto a single *post* cell. This connectivity scheme aims to match the probability of connection between cells of a

given type found in cortex. It does not match the total number of synapses a given target cell has as there are no connections from cells outside the single cortical column being modelled, and not all cells within the column are included.

Contact numbers are derived as far as possible from experimental estimates, which are crude at best. Such estimates are derived typically from the probability of finding connected cells for paired recordings in slice preparations (Thomson and Deuchars, 1997). Probabilities are affected by tissue slice thickness, since many axons and dendrites are lost from a slice. Estimates based on identifying synaptic contacts in an anatomical reconstruction of a cell can give good estimates of the number of excitatory or inhibitory synapses onto a cell, but the source cells are unknown.

Synaptic strengths, in the form of unitary AMPA, NMDA and GABA_A synaptic conductances, are largely unknown. Initial values were set from typical physiological estimates, then the conductances were tuned on the basis of many trial simulations that were matched against voltage recordings from different cell types in experimentally analogous situations. Ion channel distributions in the individual cell models were also tuned in this way. Once set, synaptic conductances were not altered by either short- or long-term plasticity during simulations.

Connection delays were assumed to be negligible within the cortical column and the thalamus, but were set uniformly to be 1 ms for connections from thalamus to cortex and 5 ms from cortex to thalamus, as axonal conduction velocity is known to be slower in this direction.

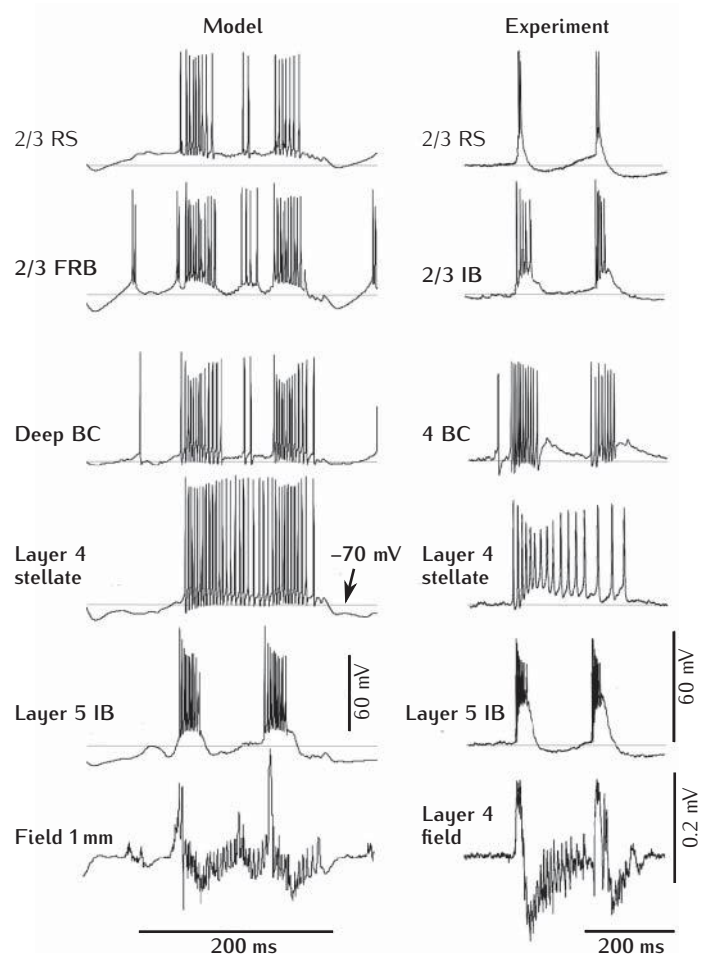
A particular feature of the model, which is to an extent predictive, is the existence of dendrodendritic and axoaxonic gap junctions between particular cell types.

Model outcomes

The model network was configured to approximate a variety of experimental slice preparations via scaling of synaptic conductances and application of bias currents to mimic the effects of the bath application of drugs that were ion channel blockers or neuromodulators. Simulations of the model allowed the recording of electrical activity in identified cells, as well as the determination of population activity, presented in the form of a calculated extracellular field potential at different cortical depths.

The model makes predictions about the physiology underlying network oscillatory states, including persistent gamma oscillations, sleep spindles and different epileptic states. An example of epileptiform double bursts in most cortical neurons in a disinhibited model network, compared with experimental data recorded *in vitro* from rat auditory cortex, is shown in Figure 9.12. A key conclusion is that electrical connections between defined neural types make significant contributions to these network states. Another important factor is the presence of strong recurrent interactions between layer four spiny stellate cells. These conclusions await further direct experimental evidence for their confirmation. Known network behaviours that are not reproducible by the model are also noted in the paper (Traub *et al.*, 2005).

Fig. 9.12 Epileptiform double bursts in most cortical neurons in a disinhibited model network (left column) and a rat auditory cortex slice preparation (right column). RS: regular spiking; FRB: fast rhythmic bursting; IB: intrinsically bursting; BC: basket cells. Adapted from Traub *et al.* (2005), with permission from The American Psychological Society.



The Blue Brain project

The Traub model (Traub *et al.*, 2005), in common with all existing computational models of brain nuclei, has limited detail in terms of all the network components, including: cell types; cell anatomy and physiology; and network connectivity. The Blue Brain project (Markram, 2006) is designed to overcome all these limitations both by obtaining the relevant experimental data and developing computational techniques that will allow the construction and simulation of an accurate cortical column model.

An important contribution of this project will be computational tools allowing the positioning in 3D space of anatomically accurate compartmental cell models, and the consequent determination of network connectivity through ascertaining the likelihood of physical contacts between neurites (dendrites and axons) from different cells, as shown in Figure 3 of Markram (2006).

9.5.2 Modelling a large-scale thalamocortical system

To go beyond modelling a single cortical column requires the ability to simulate a very large number of neurons, which currently requires the use of

simplified cell models. This is the approach taken by Izhikevich and Edelman (2008) to model thalamocortical interaction over an entire mammalian brain. Simulations with 1 000 000 neurons were carried out. An implementation of a variant of the model with 10^{11} neurons, equivalent to the number in a human brain, was also reported.

The main simplification that allows modelling on this scale is the use of integrate-and-fire cell models shown in Chapter 8. Here, the Izhikevich cell model that was described in Section 8.3 is used, which can be tuned to match the firing characteristics of many different cell types. It is also used in a multi-compartmental version in which multiple integrate-and-fire compartments are coupled with a fixed conductance. This allows for the spatial distribution of synaptic input, but does not capture heterogeneity in electrical properties across the neurites of a cell.

The large-scale patterns of interconnectivity in the model are derived from **diffusion tensor imaging** (DTI) data obtained from **magnetic resonance imaging** (MRI) of humans. The small-scale connectivity and the layered structure of cortex is derived from anatomical data from cats. Individual cell types and their firing properties are based on data from rats. So, whilst it is still a long way from an accurate model of a human brain, the approach offers hope that such a large-scale model is feasible.

This model allows the examination of spontaneous network oscillations and how they may vary and propagate across the cortex. Differences in phase and power of oscillations in the delta, alpha and gamma frequency bands are seen (Izhikevich and Edelman, 2008). Given that the cortical microcircuit is identical everywhere in this model, the diversity in rhythms must arise from differences in the long-range connectivity between cortical areas. Also, it is demonstrated that the addition of a single spike in a single neuron can lead to significant changes in activity throughout the cortex over the course of about one second.

9.6 Modelling the neurophysiology of deep brain stimulation

The **basal ganglia** are a collection of subcortical nuclei consisting of the striatum, the external and internal segments of the globus pallidus, the subthalamic nucleus and the substantia nigra. In **Parkinson's disease**, loss of dopamine cells in the substantia nigra leads to significant structural and functional changes in the striatum (Day *et al.*, 2006). The resulting perturbation in the patterns and types of striatal activity propagates through the basal ganglia and is likely to play a primary role in the symptoms of Parkinson's disease (Albin *et al.*, 1989).

Deep brain stimulation (DBS) is currently the primary surgical treatment for Parkinson's disease and is now in use as a therapeutic treatment. In DBS, a stimulating electrode is placed chronically in the basal ganglia and a subcutaneously located signal generator unit provides current to the electrode. The most common anatomical target for the electrode is the subthalamic nucleus (STN), although other basal ganglia nuclei can be targeted.

High-frequency electrical stimulation of the STN can significantly improve motor symptoms in patients.

Despite its success and widespread use, the mechanisms by which DBS leads to clinical benefits are still debated. As ablation of the same target nuclei have similar clinical benefits, this motivated the initial hypothesis that DBS leads to a similar suppression of neural activity (Filho *et al.*, 2001). Neuropathological evidence for this is divided. The glutamatergic STN projection neurons can easily discharge well above the stimulation frequencies of 100–150 Hz used clinically (Kita *et al.*, 1983). In addition, elevations of extracellular glutamate levels in the substantia nigra and other nuclei targeted by the STN projection neurons have been measured during high-frequency stimulation (Windels *et al.*, 2000). Directly recording the physiological effects of the DBS stimulation within the STN is experimentally difficult due to interference of the stimulating electrode.

It is vital to understand the mechanisms by which DBS achieves its clinical benefits if the procedure is to be effectively optimised and further developed. DBS operates at the network level, affecting large numbers of neural processes within range of the stimulating contacts on the electrode. However, measuring the effects of the stimulation close to the stimulating electrode is difficult. The development of a model combining accurate physiology of the neurons and processes, together with a physical model of DBS stimulation can provide unique insight into its underlying mechanisms. In this section we review a detailed network level model of DBS within the basal ganglia (Miocinovic *et al.*, 2006).

9.6.1 Modelling deep brain stimulation

A model of the action of DBS needs to encompass all of the key neural systems influenced by the stimulating electrode. Which parts of the basal ganglia are affected, and the effectiveness of the therapy, depends critically on the placement of the stimulating electrode. Therefore, determining the electrode location accurately is the first step. Electrophysiological models of the neural elements must then be defined. This includes populations of entire neurons, axon tracks/bundles and terminating axons and boutons targeting cells within the vicinity of the electrode. In addition, an accurate model of the electrode itself and the electric field it generates within neural tissue during stimulation must be defined (Box 9.1).

Putting this together, a model of DBS with the aim of elucidating its electrophysiological effects requires the following components:

- (1) An accurate 3D model of basal ganglia anatomy, including the location of the DBS electrode from a therapeutically effective placement.
- (2) A model of the electrode and the electric field it generates within neural tissue (Box 9.1).
- (3) Models of the neurons that lie within the influence of this electric field, including their channel composition and how this influences their electrical responses.
- (4) A model of axons and axon tracts.
- (5) Models of terminating boutons and synaptic release under the influence of the electric field during high-frequency stimulation.

In this example, we show how Miocinovic *et al.* (2006) bring together distinct models of the DBS electrode and its field effect on axons (McIntyre *et al.*, 2004) and models of the STN projection neurons (Gillies and Willshaw, 2006), together with new data from animal models of Parkinson's disease and high-frequency stimulation (Hashimoto *et al.*, 2003).

The virtual basal ganglia

Primate models of Parkinson's disease have provided an invaluable research tool in understanding the underlying pathophysiology. Single injections of 1-methyl-4-phenyl-1,2,3,6-tetrahydropyridine (MPTP) through the internal carotid artery leads to contralateral bradykinesia and rigidity, two cardinal symptoms of Parkinson's disease. This primate model has recently provided a framework in which to examine the key parameters in DBS (Hashimoto *et al.*, 2003). Scaled clinical DBS electrodes implanted in Parkinsonian macaques has provided a valuable tool for investigating its underlying mechanisms.

As the position of the stimulating electrode plays a critical role in the effectiveness of the treatment, determining the location of neural processes with respect to the stimulating electrode is a critical part of the computational model. Three-dimensional reconstruction from histological slices of the brain of the Parkinsonian macaque provides the trajectory of the electrode in relation to key basal ganglia nuclei. Figure 9.13 illustrates a 3D reconstruction of a single macaque brain and the relative position of the clinically effective stimulating electrode.

A significant proportion of STN projection neurons is likely to be influenced by the stimulating electrode. The positions of the neurons and their axons must be accurately specified to estimate the extent of this influence. Three-dimensional reconstruction of macaque STN projection neurons that target the pallidum show that their axons course dorsally along the ventral border of the thalamus or ventrally along the lateral border of the STN (Sato *et al.*, 2000). Anatomical models of a single reconstructed STN neuron morphology can be adapted to create two additional populations whose pallidal projections follow these paths (Figure 9.13a). This provides three anatomical types of STN neurons that may be influenced differentially by the electrode.

The axons of the **globus pallidus** internal segment (GPi) cross the internal capsule dorsal to the STN. This tract is called the lenticular fasciculus and is also modelled due to its proximity to the stimulating electrode. These fibres course along the dorsal border of the STN before targeting the thalamus (Figure 9.13b).

Finally, the internal capsule lies directly along the lateral border of the STN. Clinical DBS can lead to evoked motor responses resulting from activation of corticospinal fibres in this tract. Consequently, corticospinal fibres are also modelled running lateral to the STN (Figure 9.13c).

Each of the five reconstructed pathways (three populations of subthalamic-pallidal axon paths, the lenticular fasciculus and the corticospinal fibres of the **internal capsule**) were replicated by being placed at randomly chosen positions within their respective anatomical boundaries. The model STN neuron morphologies were duplicated randomly within the STN to create a population of projection neurons. This created an

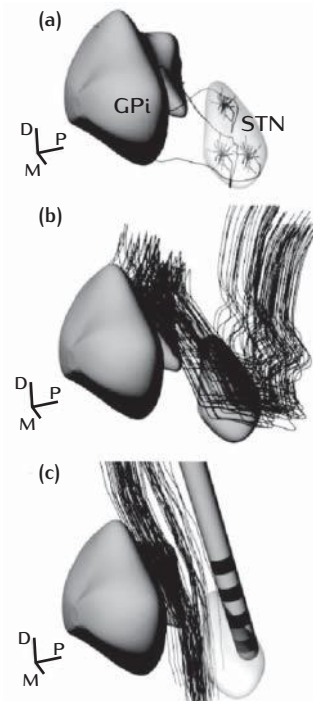


Fig. 9.13 Arrangement in 3D of neurons, axons and the DBS electrode. (a) STN projection neurons with three axonal geometries located in the STN and with axons extending towards the GPi. (b) GPi fibres from the lenticular fasciculus en route to the ventral thalamus. (c) Corticospinal fibres in the internal capsule, and the DBS electrode. Adapted from Miocinovic *et al.* (2006), with permission from The American Physiological Society.

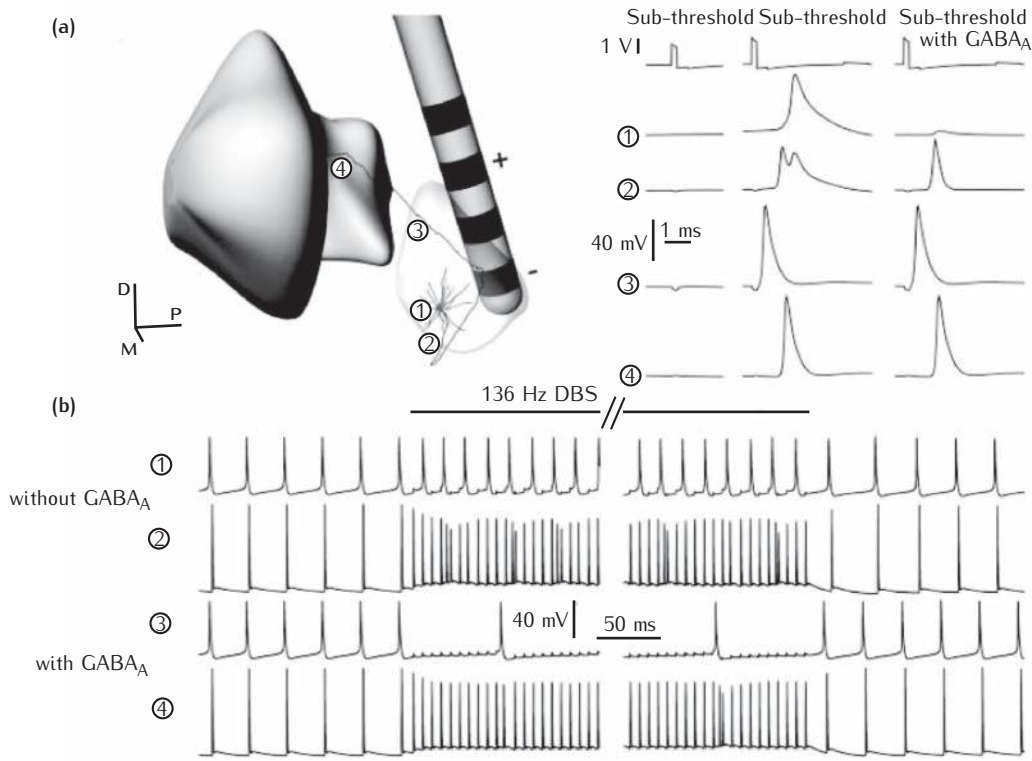


Fig. 9.14 3D simulation of DBS. (a) A DBS electrode is shown next to a model of an STN neuron. The DBS electrode induces an extracellular electric field (not shown) which stimulates the STN neuron, leading it to fire when the DBS electrode pulse is super-threshold. The traces at the right indicate the simulated membrane potential measured from the corresponding positions of the STN neuron shown in the figure, when the DBS pulse is either sub-threshold or super-threshold, and when there is GABAergic input to the soma. (b) Simulated STN activity in response to high-frequency DBS stimulation with and without GABAergic input. Adapted from Miocinovic *et al.* (2006), with permission from The American Physiological Society.

anatomical model of neural processes within the vicinity of the DBS electrode. After the random placement, any processes or neurons and dendritic fields that significantly intersected with the electrode itself were removed from the model (effectively eliminating ‘damaged’ cells or axons). In total, a sample of 150 STN projection neurons, 80 axons of the lenticular fasciculus and 70 corticospinal fibres of the internal capsule were included in the anatomical model.

Network compartmental models

A compartmental modelling approach was used to specify the physiological properties of the neurons in the network. Compartmental models have the advantage of being able to describe accurately the wide range of neural physiology observed in STN projection neurons (Gillies and Willshaw, 2006). However, the disadvantages of using compartmental models in networks include the enormous numbers of parameters involved and the computational resources required. This can significantly restrict the numbers of neurons that can be simulated. The most common approach to dealing with the large numbers of parameters is to use published models of neurons, the code for which may be available in databases such as ModelDB (Appendix A.2.1). These models are then replicated to create network populations.

The compartmental model of the STN projection neuron was adapted from the model due to Gillies and Willshaw (2006) (Figure 9.14). The original model was based on rat STN projection neuron anatomy and

physiology. Adaptation of the model to the reconstructed macaque STN morphology was made via adjustments to the maximum channel conductances, leaving the underlying channel kinetic properties unchanged. In particular, the model conductances were re-tuned to reproduce the physiological characteristics observed in macaque STN neurons in the Parkinsonian state.

The myelinated axon compartmental models of McIntyre *et al.* (2002) were adapted to model the axons of the STN neurons, the lenticular fasciculus and the corticospinal fibres of the internal capsule. As only the pallidal axons of the lenticular fasciculus were modelled, and not their originating neural body, tonic firing patterns characteristic of neurons of the GPi were induced in these fibres using simulated current injection at the axon origin.

The influence of high-frequency stimulation-induced trans-synaptic conductances on STN neuron activity was also investigated in the simulations. STN neurons receive a GABAergic input from the pallidum that primarily terminates proximally (Smith *et al.*, 1990). GABA_A synaptic conductances were added to the somatic compartment of the STN model. The effects of high-frequency stimulation-induced trans-synaptic conductances were modelled via synchronous activation of these conductances in each STN neuron in response to stimulation pulse onset.

Modelling the DBS electrode

To model the DBS electrode and the surrounding extracellular space, Miocinovic *et al.* (2006) used a 3D finite-element model (Box 9.1). The extracellular conductivity was assumed to be homogeneous, although a later study (Miocinovic *et al.*, 2009) used anisotropic conductivities inferred from diffusion tensor imaging studies. The simulated dimensions were intended to represent those of a DBS electrode for a human, scaled down for a monkey. The electrode shaft was modelled as an insulator, and each of the four contacts as a conductor (Figure 9.14). For bipolar stimulation the potential at two of the four contacts had to be specified. The stimulus waveforms were biphasic square voltage pulses which were modified to take account of the effects of electrode capacitance.

9.6.2 Results

The performance of the model was assessed by calculating the levels of tonic activation during clinically effective and clinically ineffective STN DBS for these three populations:

- (1) fibres of passage from the CST
- (2) STN projection neurons
- (3) fibres of passage of neurons from the GPi.

In the modelling studies the neurons were stimulated and electrodes were positioned as for the two Parkinsonian macaques used in this study. This enabled direct comparisons to be made between the model findings and the single unit recordings made in the macaques.

Simulation results

Activation levels of simulated corticospinal fibres were small, as found experimentally by measuring muscular contraction. This indicated that the voltage spread in the tissue around the electrode was predicted accurately by the finite-element model.

Activity in both STN projection neurons (Figure 9.14) and GPi fibres of passage was found to be important in the context of STN DBS. The simulations showed that under simulated STN DBS conditions both STN neurons and GPi fibres were activated and there were statistically significant differences between clinically effective and clinically ineffective levels of activity. There was little effect of frequency, although it is known that DBS at frequencies greater than 100 Hz is more beneficial and at frequencies less than 50 Hz is sometimes less beneficial (Rizzone *et al.*, 2001). The results obtained from simulation studies did not change markedly when different variants of the STN model neuron were used. This seemed to be due to the fact that action potential propagation is initiated in the myelinated axon rather than the cell body (McIntyre *et al.*, 2004).

Electrophysiological recordings

The responses of both GPi neurons and STN neurons to STN DBS were measured using single unit recordings. By looking at the effects of moving the electrode 0.25 mm from its original position in different directions it was found that electrode placement was crucial. For example, for clinically effective stimulation, the activation of STN varied by between 18% and 42% compared to the levels with the electrode at its original position and between 6% and 16% for GPi fibres. There were differences between the two macaques in the rates of firing of GPi neurons, and these differences were predicted from the model.

Whereas in the simulations, STN activity was assessed at the distal end of the axon, microelectrode recordings in the STN pick up primarily somatic output. Therefore, recordings were also made in the STN axon. Activation was heavily dependent on the positioning of the electrode. With the stimulating electrode placed far away from the STN cell, the soma could become inhibited through the stimulation of the inhibitory inputs to the soma; with the stimulating electrode very close so that the axon was excited directly, axonal firing was dominated by this stimulation.

9.6.3 Predictions and limitations

Predictions

The main finding of this joint modelling/experimental study was that the model predicted that during STN DBS there can be activation of both STN projection neurons and GPi fibres of passage, and this was borne out by the experimental results. The relative proportion of activity in these two neuron types was highly dependent on electrode position. Indications from the experiments on the macaques are that for clinical benefit, approximately one-half of the STN should be active. Activation of GPi fibres is also beneficial, but large-scale activation may not be necessary.

Limitations

The model of STN used was as comprehensive a model as possible of the prime actors in DBS of the basal ganglia, but substantial simplifications had to be made. One major simplification was that the influence of afferent activity through cortical axons was not considered. There is recent evidence that direct stimulation of these axons can cause therapeutic effects (Dejean *et al.*, 2009; Gradinaru *et al.*, 2009) and these effects should be included in future models. Use of optogenetic technology in a freely moving Parkinsonian rat (Gradinaru *et al.*, 2009) offers a promising avenue for the direct monitoring of the individual components of basal ganglia circuitry.

Many of the parameter values describing biophysical properties came from rat STN neurons (Gillies and Willshaw, 2006) and so they do not necessarily apply to macaques. In addition, the simulated time courses of activation onset were very rapid, whereas the effects of DBS evolve over a much longer timescale. Two other limitations were that it was difficult to estimate the tissue conductivity in 3D, which was needed in modelling the effects of the electrode; and only the most likely candidates for involvement in STN DBS – STN projection neurons and GPi fibres – were considered, although there are other, much less likely, candidates.

Despite these qualifications, this is the first demonstration of an accurate simulation model for STN DBS, with important conclusions about the action of STN DBS being made. Constructing this model has revealed many issues, such as the need for an accurate model for electrode placement and stimulation that, when resolved, will enable this model to be used as part of a combined experimental/computational approach to obtaining a better understanding of the action and benefits of STN DBS.

9.7 | Summary

Constructing a model network of neurons requires decisions at every stage of model design, starting with choosing an appropriate level of description for the individual neurons within the network. Relative numbers of neurons within different subpopulations and how these neurons interconnect must also be specified. Here we have outlined the issues involved and provided guidelines for making appropriate choices.

A number of example network models have been described to illustrate both the construction of model networks as well as their intent and worth. Associative memory networks can be built from rate-based or spiking neurons. In simple models, mathematical analysis can be used to determine memory capacity and efficiency. With spiking neurons, firing patterns must be identified with abstract patterns of information. For example, firing rates or firing times may both provide a means of correspondence.

While the ultimate aim of network models may be to help us to understand the cognitive functions of neural subsystems, a realistic first step is to use models to shed light on the complex neural firing patterns recorded from

biological neural networks. Neural population activity often exhibits characteristic oscillations of different frequencies. Building relatively moderate-scale network models, but with detailed cell types and connectivity, provides powerful indicators of the mechanisms underlying the generation of oscillations. Network models can also be invaluable in helping to understand experimental and therapeutic setups involving an interaction between neural tissue and electrodes or other external sources of stimulation. An example of this is using models to explore the effects of DBS in the basal ganglia is described. Such models will hopefully aid in specifying the placement and stimulus characteristics of the electrodes to provide most therapeutic benefit.

Chapter 10

The development of the nervous system

So far we have been discussing how to model accurately the electrical and chemical properties of nerve cells and how these cells interact within the networks of cells forming the nervous system. The existence of the correct structure is essential for the proper functioning of the nervous system, and in this chapter we discuss modelling work that addresses the development of the structure of the nervous system. Existing models of developmental processes are usually designed to test a particular theory for neural development and so are not of such wide application as, for example, the HH model of nerve impulse propagation. We discuss several examples of specific models of neural development, at the levels of individual nerve cells and ensembles of nerve cells.

10.1 The scope of developmental computational neuroscience

Modelling of the development of the nervous system has been intense, but largely restricted to the development of the features of neurons and networks of neurons in specific cases. This means that computational theories of, for example, **neural precursors**, or **stem cells**, are not considered, although they could be. A long-established field of research, the elegant mathematical treatment of **morphogenetic fields**, providing possible mechanisms by which continuous gradients of molecules called **morphogens** can be read out to specify regions of the brain in early development (Turing, 1952; Meinhardt, 1983; Murray, 1993), is conventionally regarded as the province of theoretical biology rather than of developmental computational neuroscience.

There are very few well-accepted theories for how the machinery of development operates at the level of detail needed to construct a useful computational simulator, as has been done for compartmental modelling with simulators such as NEURON and GENESIS (Appendix A.1). Most researchers who use computational models for neural development construct a special-purpose simulator with the primary aim of testing out their own particular theory. Some available simulators that cover reasonably broad classes of

developmental problems, and are extensible to new problems, are listed in Appendix A.1.4.

In this chapter we describe computational modelling in two of the research areas which are popular amongst computational neuroscientists working on development: at the single neuron level and at the level of ensembles of neurons. We review models for the development of neuronal morphology (Section 10.2) and physiology (Section 10.3); the development of the spatial arrangement of nerve cells within a neural structure (Section 10.4); the development of the pattern of connections between nerve and muscle (Section 10.6) and between retina and optic tectum or superior colliculus (Section 10.7). We discuss a number of different types of model, which have been chosen to illustrate the types of questions that have been addressed, the ways in which they have been cast into a form suitable for computer simulation and their scope of applicability.

10.1.1 Background

The development of the nervous system occurs after a complex series of developmental steps, many of which are common to the development of very different multicellular organisms.

The fertilised egg goes through a series of cell divisions and rearrangements, ultimately forming several layers of cells. The layers give rise to the various organs of the body, including the nervous system. Amongst the stages of development are:

Cell division. A large collection of cells is generated from the fertilised egg.

Gastrulation. These cells are rearranged into three layers. The inner layer (**endoderm**) forms the gut and associated organs, the middle layer (**mesoderm**) forms muscle, cartilage and bone, as well as the **notochord**, the precursor of the vertebral column; the outer layer (**ectoderm**) forms the **epidermis**, the outer layer of the body, and the **neural plate** from which the nervous system develops.

Neurulation. Lying along the dorsal surface of the embryo, the edges of the neural plate fuse together to form the **neural tube**. At the same time, so-called **neural crest** cells migrate from epidermis to mesoderm to form the peripheral nervous system.

Development of the nervous system. In vertebrates, the rostral end of the neural tube enlarges to form the three primary vesicles of the brain, the remainder of the neural tube giving rise to the spinal cord. The retina also develops from the neural tube and the other sensory organs are formed from thickenings of the ectoderm. Formation of the individual structures of the brain involves a combination of accumulation of a large population of nerve cells through cell division, the migration of these cells, a significant amount of cell death and the formation and rearrangement of nerve connections.

There are many standard texts describing development, amongst them being those by Gilbert (1997) and Wolpert *et al.* (2002). There are very few texts specifically on neural development, modern exceptions being those by Sanes *et al.* (2000), Price and Willshaw (2000) and Price *et al.* (2011).

Several developmental neuroscience problems have been addressed extensively by computational neuroscientists, and a good recent review can be found in van Ooyen (2003). In chronological order of development, amongst the typical research problems investigated are:

The development of neuronal morphology. The development of specific shapes of nerve cells, with respect specifically to the complex dendrites (Section 10.2.1).

How nerve cells know where to go. Mechanisms for the positioning of individual cells within a population of nerve cells (Section 10.4.2) and mechanisms for how axons are guided to their target cells (Goodhill and Urbach, 2003).

The development of patterns of nerve connections. Two cases that have been studied intensely are:

- Development of the characteristic pattern of neuromuscular innervation in which each muscle fibre develops contact with a single axonal branch (Section 10.6).
- The development of retinotopically ordered maps of connections in vertebrates (Section 10.7).

Features. The development of functional properties of nerve cells (Hubel and Wiesel, 1963; Hubel and Wiesel, 1977; Churchland and Sejnowski, 1992).

- How individual nerve cells in visual cortex come to respond to specific types of visual stimuli, such as bars of light arranged at a particular position, stimulating a particular eye, or at a specific orientation in the visual field.

10.2 | Development of nerve cell morphology

The first example to be considered is the development of the characteristic shapes of neurons.

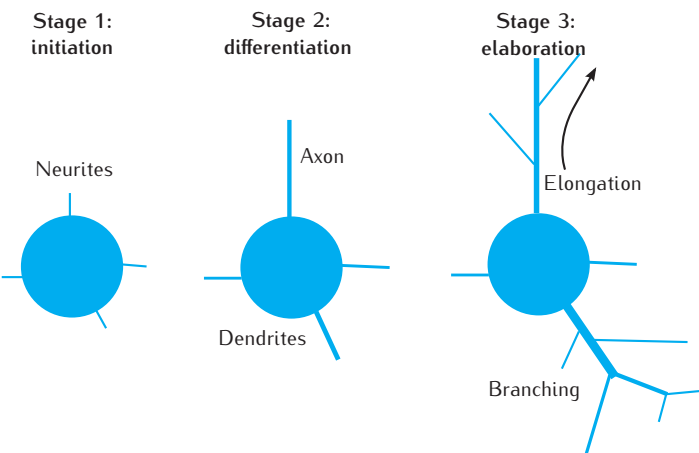
10.2.1 Development of morphology

From birth to adulthood a neuron changes from being a typically round cell into a complex branched structure of dendrites and an axon, which have distinct properties and functions. The cell's morphological development can be characterised into a number of stages (Figure 10.1):

- (1) neurite initiation
- (2) neurite differentiation and elongation
- (3) neurite (axon and dendrites) elaboration
 - elongation and branching
 - axon pathfinding
 - dendrite space filling.

As an example of the use of mathematical modelling and computer simulation to study nerve cell development, we consider models of the morphological development of dendrites, in stage 3. A comprehensive overview of modelling the various stages of nerve cell development can be found in

Fig. 10.1 Three stages of neurite development:
 (1) initiation, (2) differentiation into an axon and dendrites,
 (3) elaboration, including elongation and branching.



van Ooyen (2003). A summary of different modelling approaches and their technical considerations is provided in Graham and van Ooyen (2006).

When modelling the electrical properties of neurons, the aim is usually to reproduce recordings of membrane voltage over time, typically from a single spatial location, such as the cell body or known location in a dendrite. Membrane resistance and capacitance, and embedded ion channels are the determinants of the voltage response, and form the basic components of a model. To formulate a model of neurite development, the first question to ask is: which particular aspects of neurite morphology do we seek to reproduce in our model? It has to be decided exactly what data are to be reproduced and what underlying mechanisms may be assumed. Hillman (1979) defined seven fundamental parameters that characterise the morphology of neurites. These are listed in Box 10.1 and illustrated in Figure 10.2.

A model of dendritic development may seek to reproduce all or only some of these quantities, depending on the purpose of the model. Cell staining techniques enable values for these quantities to be collected from particular dendrites. Increasingly, databases of digitised stained cells are being made available publicly (Cannon *et al.*, 1998; Ascoli *et al.*, 2001; Ascoli, 2006). Software for extracting relevant morphological parameters is also available, such as L-Measure. The website NeuroMorpho.org is a curated inventory of digitally reconstructed neurons. As discussed in Chapter 4, modellers must be aware that experimental error will strongly affect this data, particularly segment diameters in thin, tapering dendrites (Ascoli *et al.*, 2001; Ascoli, 2002). Significant differences as reported from different laboratories can exist between the characteristics of digitised cells of the same type (Scorcioni *et al.*, 2004; Szilágyi and De Schutter, 2004).

10.2.2 Reconstruction of cell morphology

One purpose of neurite modelling may be to produce many examples of morphologically distinct neurons of a particular type for use in neural network models; or for determining whether differences in morphology can account for the variations in cell properties, such as input resistance (Winslow *et al.*, 1999). Here the aim is to generate morphologically realistic neurons of a particular age (usually adult), rather than follow the time course of

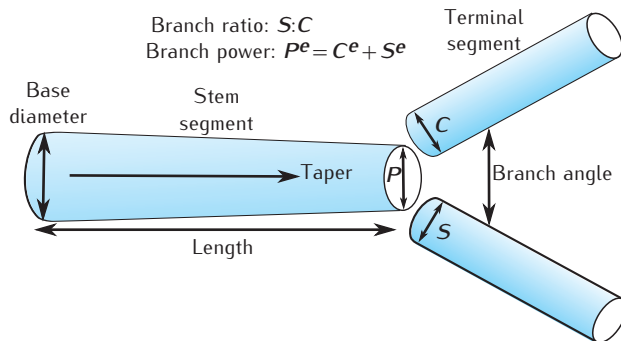


Fig. 10.2 Hillman's fundamental parameters of neurite morphology. This is based on the reasonable assumption that all branches are bifurcations, in which a parent branch has two daughter branches, referred to as the child and the sibling. P : parent branch diameter; C : child branch diameter; S : sibling branch diameter; e : branch power relationship.

development. Segment lengths and diameters are required for compartmental modelling of a neuron. Embedding in 3D space may be required for constructing network models in which the connectivity patterns between spatially distributed cells are important.

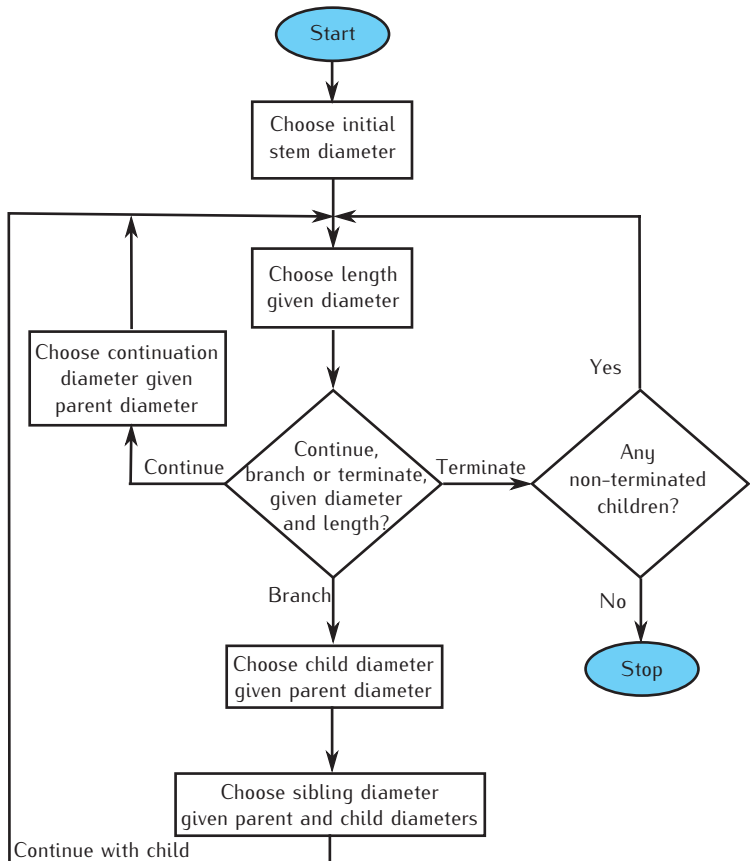
Such **reconstruction algorithms** (van Pelt and Uylings, 1999) can be based upon experimental distributions for Hillman's fundamental parameters, collected from particular types of neurite. These algorithms create neurites of statistically similar morphologies by appropriate sampling from the experimental distributions (Hillman, 1979; Burke *et al.*, 1992; Ascoli, 2002; Burke and Marks, 2002; Donohue *et al.*, 2002). The outcome is the specification of the diameter and length of each unbranched segment of neurite and whether each segment terminates or ends in a branch point leading to a bifurcation.

Histograms of segment diameters and lengths are collected from experimental tracings of real neurites. These histograms are then fitted with univariate (single variable) and multivariate (multiple variable) distributions; for example, the bivariate diameter and length distribution describes the probability that a neurite segment will have a particular diameter and length; similarly, the trivariate distribution of parent and two daughter diameters at branch points describes the probability that the parent and its daughter segments will have particular individual diameters. This has usually been done by fitting various parametric probability distributions, such as uniform, normal or gamma (Appendix B.3), to the data (Ascoli, 2002). An arguably better

Box 10.1 | Fundamental shape parameters of the neurite

- (1) stem branch diameters, P : parent; C : child; S : sibling;
- (2) terminal branch diameters;
- (3) branch lengths;
- (4) branch taper: ratio of branch diameter at its root to the diameter at its distal end;
- (5) branch ratio between diameters of daughter branches, $S:C$;
- (6) branch power e , relating the diameter of the parent to its daughters, $P^e = C^e + S^e$;
- (7) branch angle between sibling branches.

Fig. 10.3 Example reconstruction algorithm. Probability distributions for segment lengths, diameters and the likelihood of branching or termination are sampled to construct a neurite topology.



alternative is to use non-parametric **kernel density estimation** (KDE) techniques (Lindsay *et al.*, 2007; Torben-Nielsen *et al.*, 2008). An introduction to basic probability distribution fitting and estimation methods, including KDE, is given in Appendix B.3.3.

The reconstruction algorithms proceed by making assumptions about the dependencies between parameters, on the basis of the experimental distributions. A usual starting point is to use the diameter of a segment to constrain the choice of length and probability of termination or bifurcation. An example algorithm is given in Figure 10.3. This works by sampling an initial segment diameter. Then for each iteration, the segment is either increased in length by some fixed amount, terminated or branched to form two daughter segments (Lindsay *et al.*, 2007). The probabilities for continuation, termination or branching all depend on the current length and diameter, and the forms of these probability functions have to be supplied to the algorithm. A taper rate may be specified, such that the diameter changes (usually decreases) with length (Burke *et al.*, 1992; Burke and Marks, 2002; Donohue *et al.*, 2002). When a bifurcation takes place, the daughter diameters are selected from distributions that relate parent to daughter diameters, and daughter diameters to each other. The final outcome is a **dendrogram** that specifies dendrite topology. This can be used in the specification of a compartmental model of the neuron. Each run of the stochastic algorithm

will produce a slightly different dendrogram. Example dendograms from such multiple runs are shown in Figure 10.4.

The ability of an algorithm to reproduce real neurites can be tested by comparing the distributions of parameters between real and model neurites. Of particular interest are those parameters that emerge from the reconstruction process, such as the number of terminals, the path lengths to those terminals and the total length of the neurite. Simple algorithms may reproduce some but not all of the features of the neurites being modelled (Donohue *et al.*, 2002; Donohue and Ascoli, 2005). It is common for extra probability functions to be used to increase the match to data, such as one which specifies a reduction in branching probability with path distance from the cell body (Ascoli, 2002).

Alternative algorithms to the diameter-dependent example given here consider branching to be a function of distance, branch order (number of branch points between a segment and the cell body) and the expected number of terminal segments for the dendrite (Kliemann, 1987; Carriquiry *et al.*, 1991; Uemura *et al.*, 1995; Winslow *et al.*, 1999; Burke and Marks, 2002; Samsonovich and Ascoli, 2005a, b). A variety of temporal and spatial effects are likely to influence neurite outgrowth, including interaction with signalling molecules and other neurites in the external environment. Such factors may underpin these different dependencies, but are not modelled explicitly.

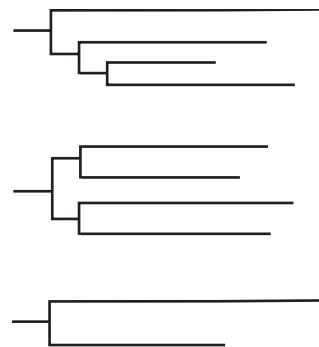


Fig. 10.4 Example dendograms produced by separate runs of a particular reconstruction algorithm. These show the topology (connectivity structure) and diameters of neurite segments. Note that the vertical lines only illustrate connectivity and do not form part of the neurite.

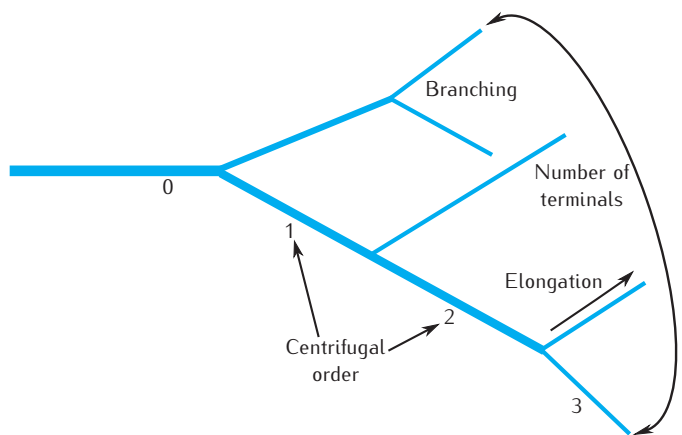
Embedding in 3D space

Reconstructing dendritic orientation in 3D space has been the subject of some modelling work (Ascoli, 2002; Burke and Marks, 2002). Realistic branch angles can be obtained by assuming a principle of volume minimisation at a bifurcation point (Tamori, 1993; Cherniak *et al.*, 1999, 2002). Orientation of dendritic branches can be described by a **tropism** rule in which branches have a strong tendency to grow straight and away from the cell body (Samsonovich and Ascoli, 2003).

10.2.3 Modelling cell growth

Reconstruction algorithms do not capture the developmental process, and simply reconstruct a neurite at a particular point in time. Models of development seek to capture how neuritic morphology evolves with time. Such **growth algorithms** (van Pelt and Uylings, 1999) may still be statistical, but now need to specify how the distributions of the fundamental parameters change over time. Basic models describe the elongation rate and branching rate of neurite segments, and how these rates may change with time and tree growth. Essentially, two approaches have been followed. The first tries to formulate the simplest possible description of the elongation and branching rates that generates trees with realistic morphology (Berry and Bradley, 1976; van Pelt and Verwer, 1983; Ireland *et al.*, 1985; Horsfield *et al.*, 1987; Nowakowski *et al.*, 1992; van Pelt and Uylings, 1999). The parameters of such models may indicate dependencies of these rates on developmental time or tree outgrowth, without identifying particular biophysical causes. The second approach tries to describe branching and elongation rates as functions

Fig. 10.5 The BESTL growth algorithm. A terminal segment's branching probability depends on its centrifugal order and the number of terminals in the tree. Terminal segment elongation rates may differ between the initial branching phase and a final, elongation-only phase.



of identifiable biophysical parameters (Hely *et al.*, 2001; Kiddie *et al.*, 2005). We look at examples of both approaches.

An example of the first approach that captures successfully much of the growth dynamics of a wide variety of dendrite types is the **BESTL algorithm** (van Pelt and Uylings, 1999; van Pelt *et al.*, 2001, 2003). This algorithm aims to reproduce the branching structure and segment lengths of dendrites (Figure 10.5). It does not consider diameters, though a Rall-type rule can be used to add diameters to segments (Section 4.3.3). Only terminal segments are assumed to lengthen and branch, with branching events resulting in bifurcations. Segment branching and elongation are handled as independent processes specified by a branching rate and an elongation rate.

The branching rate of each terminal segment j is (van Pelt *et al.*, 2003):

$$p_j(t) = D(t)C(t)2^{-S\gamma_j}n(t)^{-E} \quad (10.1)$$

where

$$C(t) = n(t)/\sum_{j=1}^{n(t)} 2^{-S\gamma_j} \quad (10.2)$$

$D(t)$ is the basic branching rate at time t

$C(t)$ is a normalising factor

$n(t)$ is the number of terminal segments

γ_j is the centrifugal order of terminal segment j (Figure 10.5)

S is a constant determining the dependence of branching on centrifugal order

E is a constant determining the dependence of branching on the number of terminals.

Elongation is handled independently of branching. Following a branching event, the algorithm proceeds by giving each daughter branch an initial, short length and an elongation rate, both drawn from gamma distributions (van Pelt *et al.*, 2003). Elongation may continue after branching has ceased, with developmental time being divided into an initial branching phase followed by an elongation-only phase. Elongation rates in the latter phase may be different from the branching phase (van Pelt and Uylings, 1999).

A discrete-time version of this algorithm is summarised in Box 10.2. The basic branching rate is calculated as $D(t) = B/T$ for a constant branching

Box 10.2 | The BESTL algorithm

Divide developmental time T into N time bins. For each time bin Δt_i ($i = 1$ to N):

- (1) During the initial branching phase:
 - (a) For each terminal j calculate the probability of branching within the time interval t_i to $t_i + \Delta t_i$ from Equation 10.1:
$$p_j(t_i)\Delta t_i.$$
 - (b) If branching occurs, add new daughter branches with given initial lengths and elongation rates drawn from gamma distributions.
 - (c) Lengthen all terminal branches according to their branching-phase elongation rate, l_b : $\Delta l = l_b\Delta t_i$.
- (2) During the final elongation phase, lengthen all terminal branches according to their elongation-only-phase elongation rate, l_e : $\Delta l = l_e\Delta t_i$.

parameter B over developmental time T . Example dendograms taken at increasing time points during a single run of the algorithm are shown in Figure 10.6.

The small number of parameters in the model enables parameter values to be optimised over experimental data sets. This is done largely using data from adult dendrites. The algorithm is run many times to produce distributions of the number of terminals, their centrifugal order and intermediate and terminal segment lengths. Model parameters B , S , E and terminal elongation rates are then adjusted using, say, the method of maximum likelihood estimation (Appendix B.3.3) to optimise these distributions against equivalent experimental data, usually to match the mean and standard deviation (van Pelt *et al.*, 1997; van Pelt and Uylings, 1999; van Pelt *et al.*, 2001, 2003). In this case the model predicts the temporal evolution of tree development. Where data from immature dendrites is available, this can also be used in the optimisation process (van Pelt *et al.*, 2003). Since the model tracks development over time, it is possible to use the model to make predictions about the effect of interventions during the growth process, such as pruning of particular branches (van Pelt, 1997).

Diameters must be added to the resultant dendograms to get neurite models that may be used in compartmental modelling. This can be done using a power law rule inspired by Rall, that relates a parent segment diameter to its two daughter diameters via branch power e (Figure 10.2). A new terminal segment is given a diameter drawn from a suitable distribution, and the branch power e at each bifurcation also is chosen from a distribution of values (van Pelt and Uylings, 1999). Then all segment diameters are updated recursively following a branching event, starting with intermediate segments whose daughters are both terminals. The diameter of a parent segment is then $P = (C^e + S^e)^{1/e}$, for diameters C , S for child and sibling. For a suitable distribution of e , a reasonable fit may be obtained to real diameter distributions for a number of types of dendrite (van Pelt and Uylings, 1999).

The relation between time bins and real developmental time may not be linear; i.e. the duration of each time bin might correspond to a different period of real time (van Pelt and Uylings, 2002; van Pelt *et al.*, 2003).

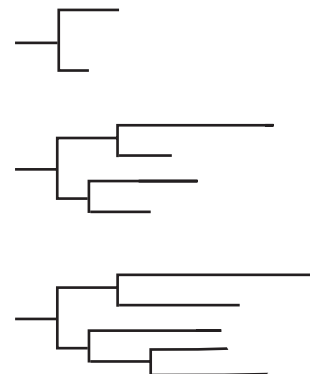
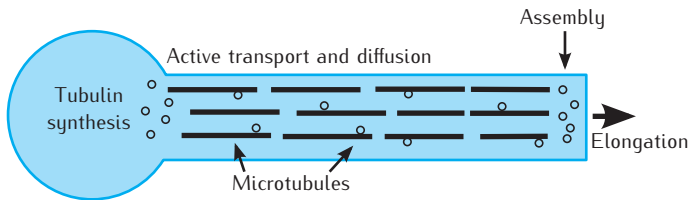


Fig. 10.6 Dendograms for a developing neurite, produced at increasing time points during a single run of the BESTL algorithm.

Fig. 10.7 Development of the intracellular cytoskeleton of a neurite, determined by transport of tubulin and assembly of microtubules.



10.2.4 Biophysical models of cell growth

An alternative approach to a statistical growth algorithm for modelling neurite development is one based on the known biophysics of neurite outgrowth. Such an algorithm may be more complex than a statistical algorithm like BESTL, and consequently it may be harder to optimise its parameters against known data. However, it gives a more direct handle on the key biochemical processes that underpin neuronal development. Biophysically based models have been used to study all of the different developmental phases outlined above. The common style is to model the production and transport of key growth-determining molecules through both intracellular and extracellular space, with molecular interactions taking place at specific spatial locations, such as in a growth cone. The modelling techniques are clearly similar to those we have considered for modelling intracellular signalling pathways and synaptic short-term dynamics (Chapters 6 and 7). However, in this case, space plays a prominent role and the physical structures being modelled change shape over time. This introduces extra numerical complexity into setting up and solving these models.

Intracellular models

The simplest approach involves modelling the production and transport (by diffusion and active transport) of molecules within a 1D intracellular space, as illustrated in Figure 10.7. The multidimensional extracellular space is assumed to be homogeneous and therefore can be ignored as its effects are represented intrinsically within elongation and branching rates, and other model parameters. The single intracellular dimension is the longitudinal axis of a neurite, with all molecular concentrations assumed to be uniform in the radial direction. The only complication arises from the assumption that neurite outgrowth – both elongation and branching – is dependent on molecular concentration, which will change as the cellular spaces change in volume. Care must be taken to ensure conservation of mass in all numerical calculations with such a model.

A basic example of this approach considers the production and transport of the protein **tubulin** along a growing neurite (Figure 10.7). Free tubulin has concentration $c(x, t)$ at a point x along the neurite at time t . Tubulin molecules move by active transport (α) and diffusion (D), and degrade with rate g (van Veen and van Pelt, 1994; Miller and Samuels, 1997; McLean and Graham, 2004; Graham *et al.*, 2006). In the cell body ($x = 0$) synthesis of tubulin occurs at a fixed rate $\epsilon_0 c_0$. At the distal end of the neurite ($x = l$) assembly of tubulin onto **microtubules** occurs at rate $\epsilon_1 c$, and spontaneous disassembly with rate ζ_1 . These processes are summarised by the following

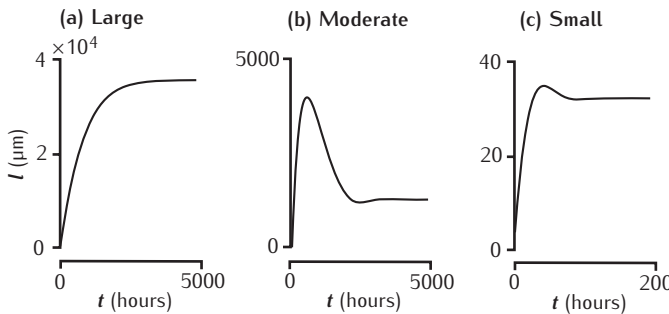


Fig. 10.8 Elongation of a model neurite over time in three growth modes (McLean and Graham, 2004; Graham *et al.*, 2006). Achieved steady state lengths are stable in each case, but there is a prominent overshoot and retraction before reaching steady state in the moderate growth mode.

equations for how the tubulin concentration $c(x, t)$ changes over time and space:

$$\frac{\partial c}{\partial t} + \alpha \frac{\partial c}{\partial x} = D \frac{\partial^2 c}{\partial x^2} - gc \quad (10.3)$$

$$-\frac{\partial c}{\partial x} = \epsilon_0 c_0 \quad \text{at } x = 0, \quad (10.3)$$

$$-\frac{\partial c}{\partial x} = \epsilon_l c - \zeta_l \quad \text{at } x = l. \quad (10.4)$$

Equations 10.3 and 10.4 describe the boundary conditions for the neurite in terms of the flux of tubulin into the neurite due to synthesis in the cell body (Equation 10.3) and its flux into microtubules at the growing end of the neurite (Equation 10.4).

This model has been used to investigate the dynamics of neurite outgrowth by specifying the elongation rate of the neurite as a function of the net microtubule assembly rate:

$$\frac{dl}{dt} = k\epsilon_l c(l, t) - k\zeta_l, \quad (10.5)$$

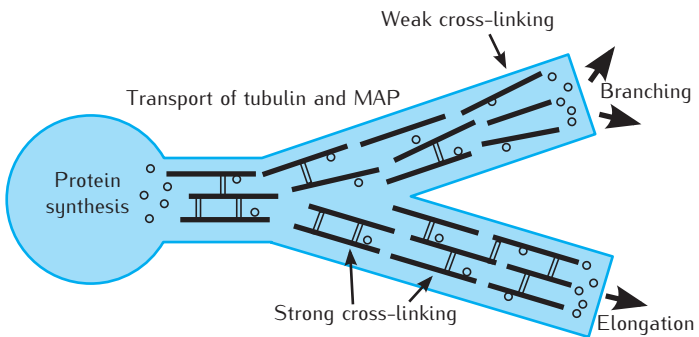
where the scaling factor k converts microtubule assembly and disassembly into a change in the length of the neurite (McLean and Graham, 2004; Graham *et al.*, 2006). Three growth modes are evident in this model (Figure 10.8). Growth to long lengths is determined by active transport of tubulin to the growing tip. In contrast, growth to short lengths is dominated by diffusion. Moderate lengths are achieved by a balance of active transport and diffusion.

An alternative model assumes that, rather than determining the elongation rate, the tubulin concentration at a neurite tip determines the branching rate $p(t)$ of the terminal:

$$p(t) = D(t)c(l, t). \quad (10.6)$$

This is on the basis that branching is more likely, the higher the rate at which microtubules are being assembled to provide the scaffold for new branches (van Pelt *et al.*, 2003; Graham and van Ooyen, 2004). As with the elongation model, branching rates are sensitive to tubulin synthesis and transport

Fig. 10.9 Development of the intracellular microtubule cytoskeleton of a neurite. Phosphorylated MAP results in weak cross-linking of microtubule bundles and a consequent higher likelihood of branching. Strong cross-linking, when MAP is dephosphorylated, promotes elongation.



rates. A close match to the BESTL model can be achieved with biophysical transport rates.

A natural extension to these models is to try to describe both elongation and branching as simultaneous functions of tubulin concentration and other factors affecting microtubule assembly. One approach introduces microtubule stability as a function of the phosphorylation state of **microtubule associated proteins**, or **MAPs** (Hely *et al.*, 2001; Kiddie *et al.*, 2005). The premise is that phosphorylated MAP loses its microtubule cross-linking ability, destabilising microtubule bundles and promoting branching. This necessitates modelling the production and transport of the MAPs and the influx and diffusion of calcium (Figure 10.9). The local calcium concentration determines the phosphorylation state of the MAPs. This phosphorylation process could be modelled in more or less detail using the techniques for modelling intracellular signalling pathways described in Chapter 6. Model results indicate that neurite tree topology is a strong function of the binding rate of MAP to microtubules and the phosphorylation rate of MAP (Hely *et al.*, 2001; Kiddie *et al.*, 2005).

Extracellular models

When the extracellular space is not homogeneous, it must be modelled explicitly. Often, this is done in terms of a 2D flat plane, rather than in 3D (Li *et al.*, 1992, 1995; van Veen and van Pelt, 1992; Hentschel and van Ooyen, 1999; Aeschlimann and Tettoni, 2001; Maskery *et al.*, 2004; Feng *et al.*, 2005a; Krottje and van Ooyen, 2007). Physical and chemical cues may be located at specific locations in this environment, influencing directional guidance and branching of neurite growth cones (Figure 10.10). The spatial location of each growth cone needs to be specified and tracked over time. The neurite itself is assumed not to occupy any volume so that only growth cone locations need to be calculated. The visco-elastic properties of the growth cone and trailing neurite may be included (van Veen and van Pelt, 1992; Li *et al.*, 1994, 1995; Aeschlimann and Tettoni, 2001). Extracellular chemical gradients are calculated on a spatial grid, given source locations and rates of diffusion (Hentschel and van Ooyen, 1999; Krottje and van Ooyen, 2007). The numerical solution of these models may use finite-element techniques (Appendix B.1).

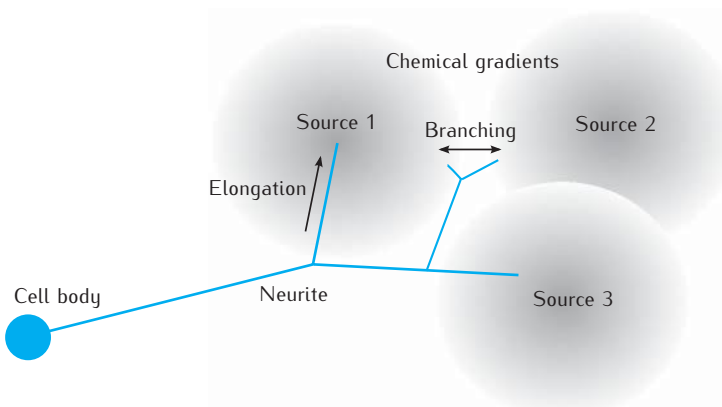


Fig. 10.10 Neurite outgrowth in an external environment containing three sources of a diffusible attractive chemical.

10.3 | Development of cell physiology

Relatively little modelling work has been concerned with the development of the membrane properties of neurons. In parallel with morphological development, ion channel distributions in the membrane also develop to give a neuron particular electrical properties. Experiments are gradually revealing the changes in neuronal electrical excitability at different stages of development, and the key role played by calcium influx (Spitzer *et al.*, 2002).

One early model considered the development of the classic electrical signal, the action potential (Bell, 1992). The model used a rule for changing the maximal sodium conductance that sought to minimise voltage fluctuations between local patches of membrane. Once an action potential was established in one patch, then the sodium channel density in the neighbouring membrane changed so as to also generate an action potential and so minimise the difference in voltage between adjacent patches.

It is also now apparent that homoeostatic principles that allow a neuron to maintain a similar electrophysiological responsiveness in the face of a changing environment are underpinned by changes in ion channel expression and distribution (Davis, 2006; Marder and Goaillard, 2006). Thus the developmental rules that result in the initial specification of ion channel distributions may still operate in the adult neuron to allow the neuron to adapt to changing circumstances and to cope with ion channel turnover. Modelling work has been carried out on **homoeostasis** (Abbott *et al.*, 2003), and this is likely to be relevant to development as well.

Typical models of homoeostasis adapt spatial ion channel densities according to a rule which is dependent on a signal that indicates the present response state of the neuron. This signal may be the intracellular calcium concentration, averaged over particular spatial and temporal scales (Siegel *et al.*, 1994; Liu *et al.*, 1998; Abbott *et al.*, 2003). A possible rule is of the form (Liu *et al.*, 1998; Abbott *et al.*, 2003):

$$\tau \frac{d\bar{g}_i}{dt} = \sum_a B_{ia} (\bar{S}_a - S_a) \bar{g}_i, \quad (10.7)$$

where the maximum conductance \bar{g}_i over a particular ion channel species i is adjusted with time constant τ in proportion B_{ia} to the offset of a number of signal sensors S_a from their setpoint values \bar{S}_a .

This rule has been used in a model of a stomatogastric ganglion neuron to maintain particular firing rate patterns in the face of environmental perturbations (Liu *et al.*, 1998). Three sensors that reacted to fast (millisecond), moderate (ten milliseconds) and slow (seconds) changes in submembrane calcium concentration were sufficient to detect changes in average firing rate and spiking patterns, from regular spiking to bursting. Suitable choices of sensor setpoints and conductance alteration per sensor B_{ia} resulted in neurons that were highly robust in their firing patterns.

Homoeostasis operates over longer timescales (hours or days) than the typical electrophysiological response that is reproduced in a compartmental model. Thus, potentially much longer simulations are needed. Simulation times can be minimised by making relatively rapid changes in ion channel densities in response to a signal averaged over a short period of activity. This assumes that the averaging is sufficient to give an accurate description of the state of the neuron and that it is not necessary to model the precise time course of the adaptation. The only constraint is that adaptation should be slower than signal detection. Liu *et al.* (1998) were able make conductance updates with a time constant of $\tau = 5$ seconds.

Other work has explored the possibility that developmental rules driving ion channel distributions may act to maximise information transfer between patterns of synaptic input and the cell output (Stemmler and Koch, 1999). The idea is that a cell's electrical excitability may be matched to the range of synaptic input it receives so that its output firing rate encodes an input. This contrasts with homoeostatic principles which operate to maintain a firing rate in the face of changing inputs.

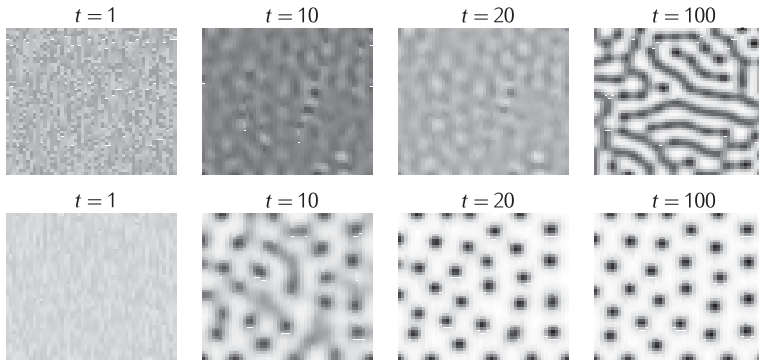
10.4 | Development of nerve cell patterning

There are two types of spatial patterns that develop within populations of nerve cells. In this section we discuss the patterns formed by the spatial arrangement of the nerve cells within a population. In Sections 10.5–10.7 we describe the development of connectivity patterns.

10.4.1 Development of pattern in morphogenesis

We approach the notion of pattern in a population of cells by discussing the emergence of pattern in morphogenesis, at stages long before the nervous system emerges. A body of mathematics has been developed to analyse morphogenesis and it is also applicable to the neurobiological questions we are considering.

A simple example of a biological pattern is where there is a systematic variation of some identifiable feature over a 2D biological structure or field. Well-known biological examples are the patterns on sea shells or butterfly



wings and the distribution of melanocytes over animal skins, such as the pattern of zebra stripes (Meinhardt, 1983; Murray, 1993).

The construction of models for the development of biological pattern has a long history. Turing (1952) was probably the first to compute the types of pattern that can be formed by a set of hypothetical molecules, or morphogens, that react with each other and diffuse over the substrate, or field, usually assumed to be 2D. The term **reaction-diffusion** is often used to describe this type of interaction. The mathematical principles underlying reaction-diffusion (Edelstein-Keshet, 1988; Murray, 1993) are used widely in modelling the emergence of pattern in neural development.

The basic requirements for the generation of spatial pattern in this way are that there must be (1) at least two different morphogens; (2) different rates of diffusion for the different morphogens; (3) specific interactions between the morphogens.

One case that is often considered is that of two morphogens which interact according to non-linear dynamics. Without any spatial effects, this interaction can be described by the following two coupled equations for how the morphogens, U and V , vary over time:

$$\frac{dU}{dt} = R_1(U, V), \quad (10.8)$$

$$\frac{dV}{dt} = R_2(U, V), \quad (10.9)$$

where R_1 and R_2 are non-linear functions which control the rates of production of U and V .

When the morphogens vary over 2D space as well as time, the two relevant equations are:

$$\frac{\partial U}{\partial t} = R_1(U, V) + D_1 \frac{\partial^2 U}{\partial x^2} + D_1 \frac{\partial^2 U}{\partial y^2}, \quad (10.10)$$

$$\frac{\partial V}{\partial t} = R_2(U, V) + D_2 \frac{\partial^2 V}{\partial x^2} + D_2 \frac{\partial^2 V}{\partial y^2}. \quad (10.11)$$

D_1 and D_2 are the diffusion coefficients controlling the rate of spread of the morphogens over the surface.

One specific choice for the functions R_1 and R_2 , which control the production of the two morphogens U and V , is given in the **Gierer-Meinhardt**

Fig. 10.11 Two numerical simulations of the Gierer-Meinhardt model. Each row of plots shows the development over time of patterns generated using the Gierer-Meinhardt Equations 10.12 and 10.13, which have been discretised on a 50×50 pixel grid. The starting conditions are randomised, and the patterns are allowed to develop over time until a steady state is reached. In the top row, stripe-like patterns emerge. Parameter values are: $\rho = 1.0$, $\rho_1 = 1 \times 10^{-5}$, $\rho_2 = 1 \times 10^{-4}$, $\mu_1 = 1.0$, $\mu_2 = 1.0$, $D_1 = 0.06$ and $D_2 = 0.4$. In the bottom row, employing different parameter values leads to a pattern of spots emerging. Parameter values are as for the top row except that the diffusion constants are $D_1 = 0.12$ and $D_2 = 1.6$. Simulations generated using a modified version of code written by Soetaert *et al.* (2010).

Miura and Maini (2004) give an introduction to Turing's model (1952) of pattern formation with the aim of motivating non-mathematicians to carry out their own simulations of the model.

model (Gierer and Meinhardt, 1972; Meinhardt, 1983):

$$\partial U / \partial t = \rho U^2 / V - \mu_1 U + \rho_1 + D_1 \partial^2 U / \partial x^2 + D_1 \partial^2 U / \partial y^2, \quad (10.12)$$

$$\partial V / \partial t = \rho U^2 - \mu_2 V + \rho_2 + D_2 \partial^2 V / \partial x^2 + D_2 \partial^2 V / \partial y^2. \quad (10.13)$$

Morphogen U is an activator as it promotes the synthesis of itself and V ; morphogen V is an inhibitor as it inhibits its own growth and ultimately limits the growth of U (Equations 10.12 and 10.13). Numerical simulations of this model with two sets of parameters are shown in Figure 10.11. Provided the parameter values in these equations satisfy certain conditions, stable spatial patterns of morphogen will emerge from almost uniform initial distributions of morphogen.

The mathematics of this type of scheme to develop periodic patterns has been explored widely and the results applied to the generation of many different types of periodic pattern, such as the pattern of cilia on the surface of a frog embryo, the bristles on the cuticle of the bug *Rhodnius* or of the spacing of leaves (Meinhardt, 1983). One crucial finding from this analysis is that the values of the fixed parameters compared to the size of the field determine the periodicity of the patterns found. Murray (1993) observed that in a developing system morphogenetic fields will change size and so the ratios of parameter values to field size change over time. He suggested that to generate many of the different types of patterns of animal coat marking seen, the reaction-diffusion mechanisms could be switched on at different stages of development, allowing patterns of different periodicity to be formed.

A simple way of modelling the production of a mosaic uses a random number generator to place cells on a 2D surface, one by one. Before each new cell is added in, a check is made as to whether its position is within the prespecified exclusion zone of any cells already present. If it is, the random number generator is used to find a new random position for the cell until a position is found which is sufficiently distant from all existing cells.

10.4.2 Development of pattern within a set of nerve cells

Nerve cells are arranged in many different types of pattern. In the mammalian system, perhaps the most remarkable is the 3D arrangements of nerve cells of six different types and their processes in the mammalian cerebellum (Eccles *et al.*, 1967). One particular type of cell pattern that has been analysed quantitatively is the pattern of nerve cells of particular types over the retina (Cook and Chalupa, 2000). For example, ganglion cells of each particular type are distributed over the surface of the vertebrate retina to form regular patterns, which have been called **mosaics**. From analysis of the spatial autocorrelation of these types of pattern, it has been suggested that the way these retinal mosaics are formed is consistent with each new cell being put down at a random position subject to a minimum spacing between any two cells (Galli-Resta *et al.*, 1997). **Production of mosaics** in this way can be modelled mathematically.

In order to test the applicability of this phenomenological model, attributes of the mathematical distributions can be measured and compared with what is found experimentally. The minimum spacing rule has been found to reproduce successfully the distribution of several mosaics, including rat cholinergic amacrine cells (Galli-Resta *et al.*, 1997; Figure 10.12) and nicotin-adenin-dinucleotide phosphate-diaphorase (NADPH-d)-active retinal ganglion cells in chick (Cellerino *et al.*, 2000).

Construction of a model at this level is useful but does not shed any light as to mechanism. In order to understand how in the retina an

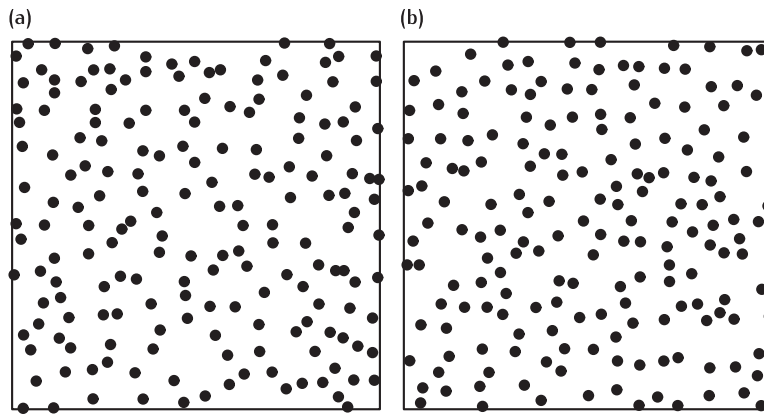


Fig. 10.12 Real and simulated distributions of retinal neurons. (a) Positions of rat cholinergic amacrine bodies (Resta *et al.*, 2005). Each cell is drawn with a 10 μm diameter and the field of view is 400 $\mu\text{m} \times 400 \mu\text{m}$. (b) Simulation of the observed field in panel (a). Here, the minimal distance exclusion zone was drawn from a normal distribution with mean = 22 μm , standard deviation = 6 μm . Reproduced by permission of Stephen Eglen.

irregular spatial distribution of undifferentiated cells is transformed into a regular distribution of differentiated cells, the idea of **lateral inhibition** has been invoked. In one approach, the Delta and Notch molecules are used in a type of reaction–diffusion scheme to impart primary or secondary fate to an ensemble of differentiating cells. Various authors have modelled this phenomenon and we adopt the formulation due to Eglen and Willshaw (2002), who applied the model of Delta–Notch signalling developed by Collier *et al.* (1996). This is a discrete rather than continuous problem, which is formulated in terms of the levels D_i and N_i of the two molecules in a typical cell i . The amount of these two quantities in a cell is used to express whether it is acquiring primary (D) or secondary (N) fate. Those differentiating cells which have primary fate develop into mature cells; for example, retinal ganglion cells of a particular class. The reaction equations are:

$$\frac{dD_i}{dt} = -D_i + g(N_i), \quad (10.14)$$

$$\frac{dN_i}{dt} = -N_i + f(\bar{D}_i) \quad (10.15)$$

$$\text{with } f(x) = x^2/(A + x^2) \quad \text{and} \quad g(x) = 1/(1 + Bx^2).$$

A and B are constants and \bar{D}_i is the average value of D computed over the neighbours of cell i . The neighbours of a cell are found using the Voronoi tesselation (Okabe *et al.*, 1992).

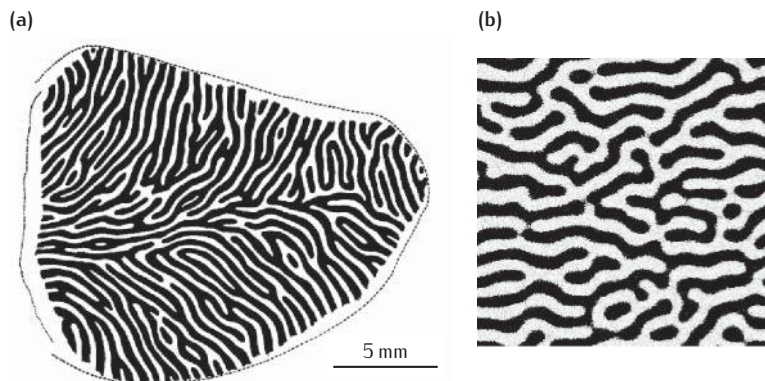
In this form of Equations 10.14 and 10.15, the quantities N_i and D_i are dimensionless. The functions f and g are chosen to be monotonically increasing and monotonically decreasing, respectively. This means that higher levels of D in a cell lead to higher levels of N in its neighbours, which leads to lower levels of D in these cells (Equation 10.15). Consequently, the values of D and N in neighbouring cells tend to go to opposite extremes. The result is that if a particular cell has primary fate (high D), the neighbouring cells will have secondary fate (high N). In this way, a mechanism of lateral inhibition is introduced, ensuring that cells are regularly spaced out over the retinal surface.

The purpose of this work was to investigate whether this mechanism of lateral inhibition would be sufficient to generate mosaic patterns with

The term lateral inhibition is used widely in neurobiology to describe situations where the activity in one nerve cell can diminish the activity in its neighbours. Usually ‘activity’ means the electrical activity of a nerve cell but more generally this can also refer to the amount of particular signalling molecule present in a cell.

Fig. 10.13 Comparison of anatomical and simulation patterns of ocular dominance.

(a) Ocular dominance pattern in monkey visual cortex (Hubel and Wiesel, 1977). (b) Simulated pattern. Figure in (a) reproduced with permission from The Royal Society; figure in (b) reproduced with permission from Nick Swindale.



the required regularity or whether an additional mechanism, in this case cell death, was needed (Eglen and Willshaw, 2002). Computer simulations were carried out to assess whether the regularity in an initially irregular distribution of cells could be improved by this method of assigning primary and secondary fate to cells.

In the simulations, the set of equations defined by Equations 10.14 and 10.15 was iterated until the values of D and N had stabilised in all cells. A cell i acquired primary fate if D_i exceeded 0.9, which was taken to be sufficiently close to its maximum value of 1; otherwise it was said to have acquired secondary fate.

It was found that lateral inhibition will make the distribution of primary fate cells more regular than in the initial irregular distribution, but is insufficient to produce mosaics to the required degree of regularity. A combination of lateral inhibition and cell death working together would suffice but the resulting pattern will depend on the precise type of cell death assumed in the model.

10.5 Development of patterns of ocular dominance

The patterns of connectivity between sets of cells are a property of the connections themselves rather than the cells. One early model for the development of pattern within the connections is due to Swindale (1980), who developed a model based on the concepts of reaction–diffusion (Section 10.4.1) for the development of patterns of **ocular dominance** in visual cortex. In layer IVc, the binocularly innervated part of mammalian visual cortex, individual nerve cells become driven preferentially by a particular eye. The distribution of ocular dominance over the cortex that is formed resembles a pattern of zebra stripes (Hubel *et al.*, 1977; Hubel and Wiesel, 1977; LeVay *et al.*, 1980; Figure 10.13a).

Swindale (1980) developed a high-level model for the production of these patterns. He supposed that at each point in layer IVc, assumed to be a 2D surface, the growth of the synapses, via the lateral geniculate nucleus, from the axons originating from the right and left eyes were influenced by other

synapses from other positions on the 2D surface. Synapses from the same eye which terminated on the cortex a short distance away exerted a positive effect and those further away a negative effect. The influences from synapses from the opposite eye were reversed.

These assumptions enabled him to formulate a set of equations for the development of the synaptic densities $n_L(x, y, t)$ and $n_R(x, y, t)$ at any position (x, y) on the cortical surface. The function $w_{RL}(x - x', y - y')$ specifies the influence on a synapse at position (x, y) from an axon originating from the right eye by a synapse at position (x', y') from an axon originating from the left eye. The functions w_{RL} , w_{RR} and w_{LL} are similar functions for the other types of possible between-eye and within-eye interactions. The rates of change of n_L and n_R are:

$$\frac{dn_L}{dt} = (n_L * w_{LL} + n_R * w_{LR})h(n_L), \quad (10.16)$$

$$\frac{dn_R}{dt} = (n_R * w_{RR} + n_L * w_{RL})h(n_R). \quad (10.17)$$

The asterisk denotes spatial convolution, and the terms in the equations involving convolution provide for the effect of interactions between synapses depending on distance.

A function $h(n)$ is used to keep the values of n_L and n_R between bounds. A suitable form for $h(n)$ which keeps n between 0 and a maximum value N is:

$$h(n_L) = n_L(N - n_L), \quad (10.18)$$

$$h(n_R) = n_R(N - n_R). \quad (10.19)$$

One special case that was considered is where, for all positions (x, y) on the surface, the sums of the left-eye and right-eye synapses are kept constant:

$$n_L + n_R = N. \quad (10.20)$$

One case that Swindale explored analytically was where the functions w_{LL} and w_{RR} describing the within-eye interactions are chosen to be excitatory at short range and inhibitory at long range (the **Mexican hat function**) and the between-eye interactions w_{LR} and w_{RL} are inverted Mexican hat functions (Figure 10.14). He examined the special case when the sum rule (Equation 10.20) is applied to the total synaptic density. In this case, the two identical within-eye functions are the exact negatives of the two identical between-eye functions. By looking at the Fourier components of the patterns of left-eye and right-eye synapses that emerge, he proved that, from an initial state in which the left-eye synapses and the right-eye synapses are randomly distributed, the cortical surface becomes partitioned amongst the left- and right-eye synapses to form a branching pattern of ocular dominance stripes, which has the features of the patterns seen experimentally (Figure 10.13b). The width of the stripes is controlled by the spread of the interaction functions. He was then able to account for several findings in the experimental literature. For example, the fact that monocular deprivation leads to the stripe width of the synapses from the deprived eye shrinking in favour of the width of the undeprived eye synapses is

The **convolution** of two functions $A(x, y)$ and $B(x, y)$ is:

$$\iint A(x', y')B(x - x', y - y')dx'dy'.$$

The convolution can be thought of as the function that results when the spatial filter B is applied to the function A .

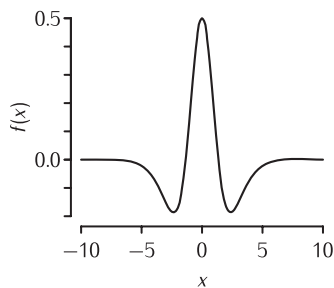


Fig. 10.14 A Mexican hat function. This is described by a function $f(x)$ that is formed by subtracting one Gaussian function from another with different parameter values: $f(x) = \exp(-x^2/2) - 0.5\exp(-(x/2)^2/2)$.

explicable if it is assumed that the monocular deprivation causes reductions in the short-range interactions both in within-eye and between-eye densities (Hubel *et al.*, 1977). While Swindale could provide a mathematical description of the formation of ocular dominance stripes together with a number of specific predictions, the physical basis of his model's components are not specified. In particular, his notion of a synaptic density is not tied to any measurable quantity. In addition, in discussing the monocular deprivation experiments, he does not propose a precise mechanism for the synaptic interaction function. In this case, he cites the explanation given by Hubel *et al.* (1977) that 'the deprived eye is presumed to lose its effectiveness locally'.

An earlier paper (von der Malsburg and Willshaw, 1976) gave a more specific model for the formation of ocular dominance stripes, which is held to be influenced by electrical neural activity. Synapses from the same eye are assumed to fire with correlated activity, and the activity from different eyes is anticorrelated; in addition, there are short-range excitatory connections and long-range inhibitory connections between cortical cells. Combining the effects of these separate mechanisms enables Swindale's four synaptic interaction functions to be implemented. In addition, a Hebbian synaptic modification rule (Box 9.3) enables individual cells to acquire a specific ocularity, leading to regular patterns of ocularity over the 2D cortical surface. In this model more assumptions are made about the properties of neurons and synapses than Swindale's, and therefore the model is less general. On the other hand, its specificity makes it easier to test experimentally.

10.6 Development of connections between nerve and muscle

To understand how the pattern of connections between nerve and muscle develops is another classic problem in developmental neurobiology that has been addressed through computational modelling. For reviews of the neurobiology see Jansen and Fladby (1990) and Sanes and Lichtman (1999), and for modelling approaches see van Ooyen (2001). Compared with the development of many other neural systems, this one is relatively simple, where both neuroanatomical and physiological information is known about the basic phenomenon in terms of how many nerve cells contact how many muscle fibres and how the pattern of neuromuscular connections changes over development. However, some very basic information is lacking and so the typical modelling approach has been to focus on working out what patterns of connection emerge in a model based on as yet untested assumptions.

Here, a set of closely related models is described to show how one set of modelling studies builds on previous work. Through this review we illustrate how models are constructed at different levels of detail and how different assumptions are necessary and are made use of in the models.

In vertebrate skeletal muscle, each muscle fibre is innervated along its length at a single region, the **endplate**. In adult muscle, each endplate receives innervation from a single motor neuron. In most cases there are more muscle

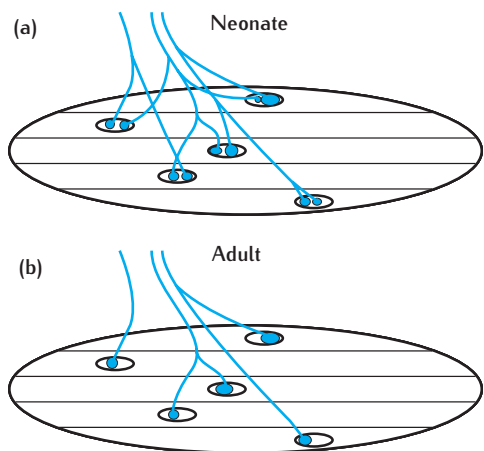


Fig. 10.15 Showing the transformation between the state of (a) superinnervation of individual fibres in neonatal skeletal muscle and (b) that of single innervation in adult muscle

fibres than motor neurons, and so the axon of each motor neuron branches profusely. In contrast, in neonatal muscle, each endplate is innervated by as many as 5–10 different motor neurons (Jansen and Fladby, 1990; Sanes and Lichtman, 1999; Figure 10.15). One basic question is how the transformation from superinnervation to single innervation of individual muscle fibres takes place. Since there is very little, if any, motor neuron death and little evidence for the making of new connections during this stage of development, it is generally held that axons withdraw contacts from individual muscle fibres until the state of single innervation is reached. This phenomenon is also seen in the development of connections between nerve cells such as in the superior cervical ganglion (Purves and Lichtman, 1980) and the cerebellar cortex (Crepel *et al.*, 1980).

Most modelling approaches are concerned with how contacts are withdrawn from the initial configuration of superinnervation to attain a pattern of single innervation. In all models, several crucial untested assumptions have to be made. The principal assumption is that there must be some physical property possessed by synapses, the amount of which determines whether a synapse will be withdrawn or will become stabilised. The strength of this property is assumed to vary between synapses and change during development. As will be described, another key assumption made is whether or not the physical property is in limited supply, as this will affect the type of interactions possible within the model.

This physical property could be related to the dimensions of the synapse, such as the area or volume of the synaptic contact, or the efficacy, measured by the depolarisation of the synaptic membrane by a given amount of transmitter. In the absence of any definitive answer, in most models the physical nature of this property is left unspecified; it is assumed that a scalar quantity, often called the **synaptic strength**, is assigned to each synapse. Synaptic strengths vary over time in a manner prescribed in the model. Synapses reaching a constant positive value are deemed to have been stabilised and those reaching zero strength to have been withdrawn. The problem for the computational modeller is to design a set of biologically plausible equations

for how synaptic strengths change over time that fit the known facts and lead to useful predictions.

10.6.1 Competition for a single presynaptic resource

Willshaw (1981) was the first to explore the idea mathematically that in the development of neuromuscular connections, axons compete with each other so as to maintain their synaptic strengths, the interactions being mediated through competition between the terminals at each endplate. He proposed a simple set of equations expressing this idea.

In this model, there are two opposing influences on a synaptic terminal. Following the suggestion of O'Brien *et al.* (1978), he assumed that each synapse emits into its endplate region an amount of a substance that degrades all synapses at that endplate. In addition, all synapses are being strengthened continuously, thereby counterbalancing the degradation in such a way that the total synaptic strength of all the synapses of each motor neuron is kept constant. These two effects are expressed in the following equation for the rate of change of the strength S_{nm} of the synapse of neuron n at endplate m , where the mean synaptic strengths is M_m :

$$\frac{dS_{nm}}{dt} = -\alpha M_m + \beta S_{nm}. \quad (10.21)$$

The relative strengths of these two opposing influences are expressed by the ratio of the factors α and β , which is determined by the constraint that the total amount of synaptic strength per motor neuron is kept constant. For neuron n this constraint is:

$$\sum_k (-\alpha M_m + \beta S_{nk}) = 0, \quad (10.22)$$

where the sum is over only those endplates with which axon n has a terminal.

It is straightforward to show that under the action of these two influences, any initial pattern of superinnervation is converted into a pattern in which just one synapse at each endplate has a positive synaptic strength and all the other synapses have zero strength, thus specifying a pattern of single innervation. Willshaw (1981) applied this model to some of the experimental results known at the time; for example, in the model, initially large **motor units** lose more connections than smaller ones, in agreement with experimental observation (Brown *et al.*, 1976).

This is a high-level model, relying on the assumptions of competition at an endplate through degradation and conservation of synaptic strength amongst motor neurons. There is some evidence for the first assumption. The second assumption of a rule for conserving a resource is attractive but there is little evidence for it. This is effectively a **sum rule**, often used in neural network theory. Normally such rules are introduced for computational necessity rather than biological realism. It remains a challenge to envisage how information about synaptic strengths on widely separate distal parts of the axon could be exchanged to enable the total strength of the synapses of each motor neuron to be kept constant. This is a problem for all models with presynaptic sum rules.

The **motor unit** is made up of a motor neuron and all the muscle fibres that it innervates. The size of the motor unit is the number of muscle fibres in it.

10.6.2 Competition for a single postsynaptic resource

A complementary model of competition was introduced by Gouzé *et al.* (1983). In this model, axons compete at the endplate directly for the finite amount of resource assigned to each muscle fibre. The rate equation for an individual terminal is now:

$$\frac{dS_{nm}}{dt} = K I_n \mu_m S_{nm}^\alpha, \quad (10.23)$$

where K and α are constants and I_n represents the electrical impulse activity in axon n . μ_m is the amount of resource available at muscle fibre m .

In this model a postsynaptic sum rule is imposed as it is assumed that the synapses are built out of the resource available at each muscle fibre, and the resource is limited. As synapses at a muscle fibre are built up, the amount of available resource decreases. Applying the conservation rule gives this expression for the rate of decrease of free resource μ_m :

$$\frac{d\mu_m}{dt} = - \left(\sum_j \frac{dS_{jm}}{dt} + d\mu_m \right), \quad (10.24)$$

where d is a small constant representing general degradation effects and, again, the sum is only over those axons which innervate endplate m .

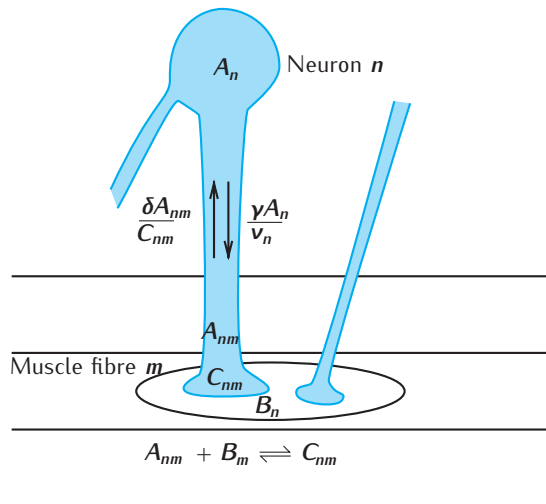
The value of the constant α in Equation 10.23 is assumed to be greater than 1. Therefore, the larger the strength of a synapse at any moment in time, the faster the resource is taken up by it, until the supply of resource is exhausted. Synapses are assumed to have small initial strengths, assigned randomly. Therefore, different synapses, having different initial strengths, will take up resources at different rates. Once all resources have been used up at an endplate, those synaptic strengths that have reached a prespecified value are regarded as stable and all others as having been withdrawn. This threshold value can be set so that only one synapse survives at each endplate. Through the term I_n , representing the rate of electrical activity, many activity-dependent effects can be modelled. This is an innovation that was not present in the model due to Willshaw (1981).

In this model the calculation of which synapse will survive at each muscle fibre is carried out independently. The conservation rule acts locally, at each endplate, and so does not require exchange of information between synapses from the same axon, over distance. However, there is a requirement for the total number of motor axons in the system to be communicated to each endplate. This is because the threshold value of synaptic strength at which synapses are regarded as stable depends on the number of motor neurons involved. The threshold has to be tuned when this number changes, to account for, for example, the emergence of single innervation after reducing the number of motor neurons by partial denervation of the motor nerve (Brown *et al.*, 1976; Betz *et al.*, 1980).

10.6.3 Competition for presynaptic and postsynaptic resources

Bennett and Robinson (1989) took a more biophysical approach by proposing a set of reactions for the production of what they called stabilising factor,

Fig. 10.16 Schematic diagram of the Dual Constraint model.



which plays the same role as synaptic strength. They suggested that there is a reversible binding between the presynaptic factor, A, originating in the motor neuron, and the postsynaptic factor, B, originating in the muscle fibre, to form the stabilising factor, C. The supply of both A and B is assumed to be limited; as more and more C is formed, A and B are used up.

The model described here is the extension by Rasmussen and Willshaw (1993) of Bennett and Robinson's (1989) formulation. The model is specified by a set of differential equations for the production of stabilising factor, C, from the locally available A and B; one molecule of A and one molecule of B makes one molecule of C (Figure 10.16).

In the equation for the production of the amount C_{nm} of stabilising factor at the terminal of axon n at the endplate of muscle m , the forward reaction is proportional to the product of the locally available amounts A_{nm} and B_m and the backward reaction is proportional to C_{nm} . Additionally, it is assumed that the forward rate is proportional to C_{nm} , which is a simple way of favouring the growth of synapses with high C_{nm} :

$$\frac{dC_{nm}}{dt} = \alpha A_{nm} B_m C_{nm} - \beta C_{nm}, \quad (10.25)$$

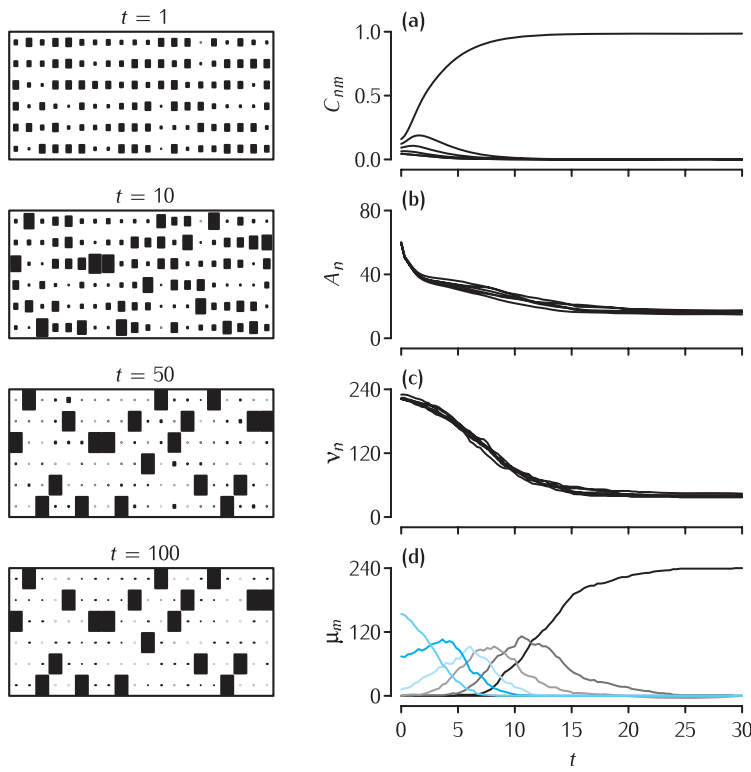
where α and β are constants. This is assumed to be a loss-free system, and so conservation relationships apply. The value of B_m , the amount of factor B available at endplate m , is determined by the condition that the initial amount B_0 is equal to the amount left in the muscle fibre plus the amount converted into factor C:

$$B_0 = B_m + \sum_j C_{jm}. \quad (10.26)$$

The value of A_{nm} , the amount of A available at the terminal of axon n at endplate m , is determined by the condition that the initial amount A_0 in neuron n equals the amount A_n that remains in the cell body plus the amount allocated to each of its terminals plus the amount converted into factor C:

$$A_0 = A_n + \sum_k A_{nk} + \sum_k C_{nk}. \quad (10.27)$$

Binding reactions of this type are described in Section 6.2.1



Since there are two constraints on this system, concerning the amounts of A and B available, Rasmussen and Willshaw (1993) called this the **Dual Constraint model** (DCM). Results of a simulation of DCM with $N = 6$ axons and $M = 240$ muscle fibres, typical values for the mouse lumbrical muscle, are shown in Figure 10.17.

Rasmussen and Willshaw (1993) gave an explicit mechanism for how the factor A is distributed to nerve terminals. Assuming that for each motor neuron the amount of factor A is distributed equally amongst its terminals gives rise to the differential equation:

$$\frac{dA_{nm}}{dt} = \gamma A_n / v_n - \delta A_{nm} / C_{nm}, \quad (10.28)$$

where γ and δ are constants and v_n is the number of axonal branches in neuron n .

In the original model (Bennett and Robinson, 1989), the total amount A_0 of factor A initially available was set equal to the total amount B_0 of factor B initially available. Rasmussen and Willshaw (1993) looked at the more general case when these quantities are not matched. By carrying out an analysis of the fluctuations of C_{nm} about the stable state, they showed that in the stable state all those synapses with a strength C_{nm} of less than $B_0/2$ will not survive.

This result is relevant to the debate over the significance of the phenomenon of **intrinsic withdrawal** (Fladby and Jansen, 1987). There is a lot of evidence that synapses compete at the endplate for sole

Fig. 10.17 The DCM applied to the mouse lumbrical muscle. Left-hand column shows the development through time of the pattern of connectivity as displayed in a connection matrix C_{nm} . The area of each square indicates the strength of that element of C_{nm} . For clarity, only 20 of the 240 endplates are shown. Right-hand column shows the development through time of four different quantities. (a) The value of C_{n1} , i.e. the strength of connections from each of the six axons competing for the first muscle fibre (Equation 10.25). (b) The value of the amount of available presynaptic resource A_n at each of the six axons (Figure 10.28). (c) The motor unit size v_n of each of the six axons. (d) The number of endplates μ which are singly or multiply innervated. The colour of the line indicates the level of multiple innervation, ranging from 1 (black) to 6 (blue). Parameters: $N = 6, M = 240, A_0 = 80, B_0 = 1, \alpha = 45, \beta = 0.4, \gamma = 3, \delta = 2$. Only terminals larger than $\theta = 0.01$ were considered as being viable. Terminals that were smaller than this value were regarded as not contributing to v_n and therefore did not receive a supply of A.

occupancy of the endplate. However, if competition for postsynaptic resources is the sole mechanism, endplates should never be denervated, as once single innervation is reached there will be nothing left for the surviving synapse to compete against and so it will not be eliminated. Since there is evidence for the emergence of denervated endplates, or intrinsic withdrawal, it has been argued that simple competition of this type does not operate. In the DCM, only synapses with at least a minimal amount $B_0/2$ of stabilising factor will survive. Since the reaction producing C involves the combination of one molecule of A with one of B, the maximum number of synapses that any given axon can make will be limited by the number of times that $B_0/2$ divides into A_0 . If the initial number of connections made by an axon is greater than this figure, $2A_0/B_0$, some of the synapses will be below critical strength and will then withdraw, with or without competition.

This model is a more biologically grounded model than the previous ones described, being expressed in terms of biological rate equations for the putative factors and not requiring information exchange over long distances to normalise synapses. It accounts for a wider range of phenomena as it addresses the finding of intrinsic withdrawal, but it does not address any activity-dependent effects.

10.6.4 Computation for resources generated at specific rates

An attempt to link the molecular factors directly to biology in a model for the withdrawal of superinnervation was reported in a third class of models due to van Ooyen and Willshaw (1999a, b, 2000). Here, the rather tight, and probably unrealistic, constraint that there is a fixed amount of resource which is shared amongst terminals is relaxed. The various factors that are assumed to build synapses are generated at specific rates and non-specific losses are built into the equations directly. This formalism is used widely in population biology, such as in models of consumer-resource systems (Yodzis, 1989).

Van Ooyen and Willshaw attempted to examine the situations under which patterns of innervation other than single innervation would result. One novel insight incorporated into this class of model was that neurotrophic signalling guides the formation and stabilisation of synaptic contacts and that neurotrophic factors may have positive feedback effects on synaptic growth through increasing the size of synapses (Garofalo *et al.*, 1992) or upregulating receptor density (Holtzmann *et al.*, 1992).

To aid comparison with the models already described, this new model is described using a formalism similar to that used for the DCM.

In this model the development of contacts from several different motor neurons to a single muscle fibre is analysed (Figure 10.18). Neurotrophin in an amount B , generated from muscle fibres, binds to receptors A_n , located on the presynaptic part of the terminal from neuron n . The strength of a synapse is represented by the amount C_n of bound receptor. For terminal n , the rate of production of bound receptor C_n follows standard reaction dynamics. The forward rate is proportional to the product A_nB of receptor A_n and locally available neurotrophin B . The backwards rate is proportional

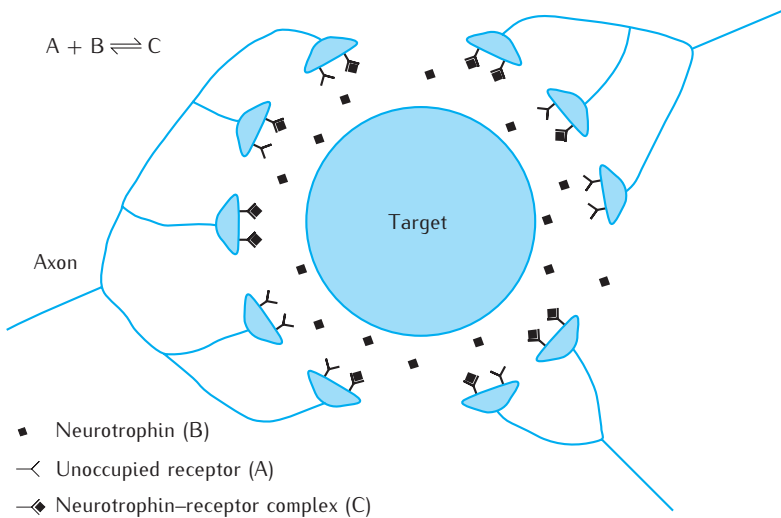


Fig. 10.18 Competitive model due to van Ooyen and Willshaw (1999a). Single target with three axons. Neurotrophin emitted by the target binds to the receptors on the axon terminals.

Reproduced with permission from The Royal Society.

to C_n . In addition, there is a non-specific loss term. This gives rise to the equation:

$$\frac{dC_n}{dt} = (\kappa_a A_n B - \kappa_d C_n) - \rho C_n, \quad (10.29)$$

where κ_a , κ_d and ρ are all constants.

Free receptor A_n in axon n is generated at variable rate ϕ_n . Some free receptor is lost on being converted to bound receptor and there are also non-specific losses:

$$\frac{dA_n}{dt} = \phi_n - (\kappa_a A_n B - \kappa_d C_n) - \gamma A_n, \quad (10.30)$$

where γ is a constant.

Neurotrophin B is produced at constant rate σ . Some neurotrophin is used up on binding to receptors and there are also non-specific losses:

$$\frac{dB}{dt} = \sigma - \delta B - \sum_k (\kappa_a A_k B - \kappa_d C_n), \quad (10.31)$$

where δ is a constant.

To represent in the model the finding that the density of receptor A_n can be upregulated by the amount of bound receptor (Holtzmann *et al.*, 1992), it was assumed that the rate of production ϕ_n is a function F of the density of bound receptor C_n . Since axonal growth takes place on a relatively slow timescale, with the time constant τ being of the order of days, this dependency is expressed by:

$$\tau \frac{d\phi_n}{dt} = F(C_n) - \phi_n. \quad (10.32)$$

At steady state, the functions F and ϕ_n are identical.

Since the precise form of the receptor growth function F is unknown, van Ooyen and Willshaw (1999a) investigated what pattern of innervation of a target cell would evolve for different types of upregulation function F .

When **steady state** is reached, ϕ_n changes no more and so $\frac{d\phi_n}{dt}$ equals 0. From Equation 10.32 it follows directly that $\phi_n = F(C_n)$.

They did this by examining the general class of function $F(C_n)$, defined as:

$$F(C_n) = \alpha_n C_n^p / (K_n^p + C_n^p). \quad (10.33)$$

K_n and α_n are constants for each neuron. By setting the parameter p to different values, van Ooyen and Willshaw (1999a) examined four qualitatively different cases which are motivated from biology (Figure 10.19):

- (1) $p = 0$. The value of the function $F(C_n)$ reduces to a constant; i.e. the rate of upregulation of receptor is assumed to be independent of the amount of bound receptor. In this case, there is no elimination of contacts and all the connections made initially survive (Figure 10.19a).
- (2) $p = 1$ and K_n is large, much greater than C_n . $F(C_n)$ now depends linearly on C_n over a large range. Elimination of axons occurs until single innervation is reached (Figure 10.19b).
- (3) $p = 1$ and K_n is smaller. F is a Michaelis-Menten function (Section 6.2.2). Elimination of contacts occurs and either single or multiple innervation results, depending on the precise values of the growth function (Figure 10.19c, d).
- (4) $p = 2$. In this case, $F(C_n)$ is a Hill function, a special case of the Michaelis-Menten function (Section 6.2.2). Unlike the other cases, where there is just one stable equilibrium pattern of innervation, here there are multiple possible stable states. Which equilibrium will be reached in any situation depends on the fixed parameter values and the initial values of ϕ_n (Figure 10.19e, f).

Examination of this model for the development of nerve connections by competition shows that using different assumptions for the nature of the competitive process leads to a model with different behaviours. This model involving the generation and consumption of neurotrophins is striking in that it provides a set of predictions which, in principle, are testable. Prominent amongst these is that different receptor upregulation functions lead to different patterns of connections; i.e. if the upregulation function is known then the pattern of connections can be predicted, and vice versa.

In a topographically ordered map of connections between two neural structures, the axons from one set of cell bodies make connections with the cells of another so that there is a geographical map of one structure on the other.

10.7 Development of retinotopic maps

Many **topographically ordered maps** of connections exist in the nervous system. Over the last 50 years, a variety of general theories and precise quantitative models for map formation have been advanced. The interest in this subject has increased dramatically over the last ten years owing to improvements in visualisation techniques and to new ways of investigating topographic map formation experimentally.

In all vertebrates, the axons from the retinal ganglion cells grow out to form the optic nerve (Figure 10.20). In non-mammalian vertebrates the main target structure of the retinal ganglion cell axons in the optic nerve is the **optic tectum**; in mammals the homologous target is the superior colliculus. The projection of axonal terminals on their target is in the form of a 2D map of the visual field, and hence the retina, onto the optic tectum or superior

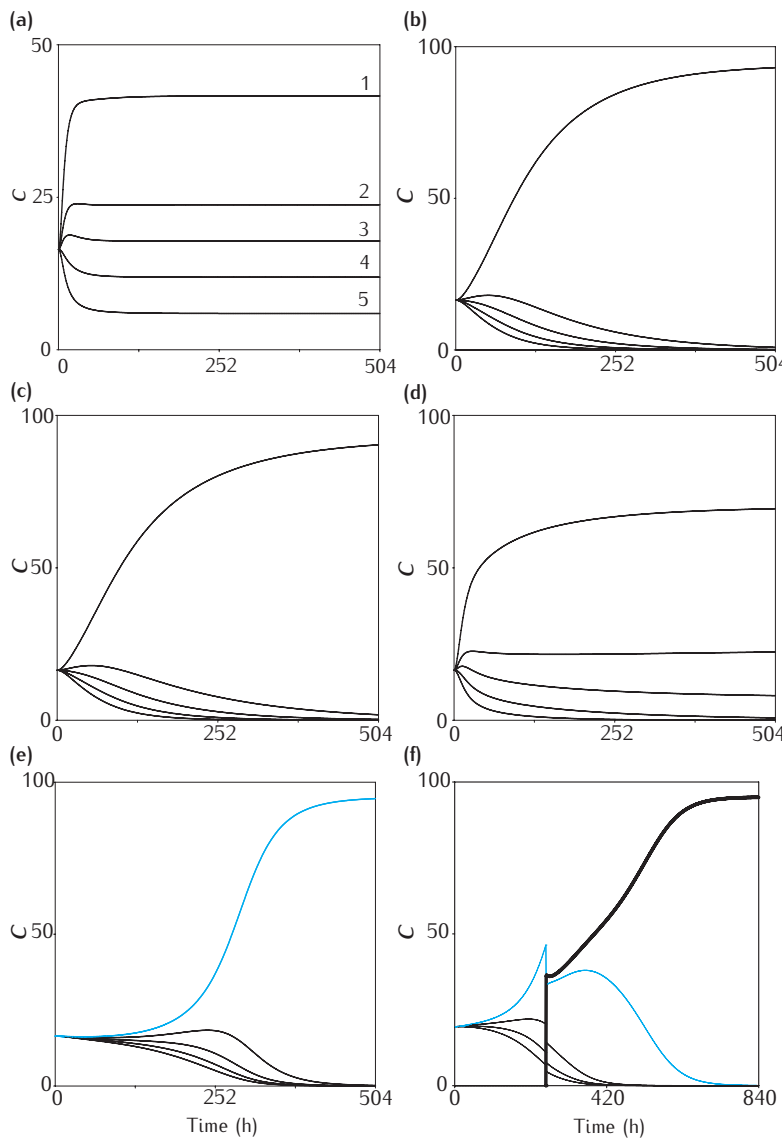


Fig. 10.19 Results from simulations of the model due to van Ooyen and Willshaw (1999a) for four different forms of the receptor upregulation function $F(C)$. The figures show how the concentration of bound receptor in different axonal terminals, taken as a measure of the terminal's ability to survive, vary over time. (a) $F(C)$ is constant: all the initial contacts survive. (b) $F(C)$ is effectively linear over a large range of C : contacts are eliminated until just one survives. (c-d) $F(C)$ is a Michaelis-Menten function. Either single innervation (c) or multiple innervation (d) results. (e-f) $F(C)$ is a Hill function. (e) Single innervation (blue line) results. (f) Shows that initial conditions influence the outcome. The simulation shown in (e) was stopped after 250 time-steps and an additional axon was introduced. The value of C for the axon that had survived in (e) (blue line) gradually went down to 0 and the survivor was the newly introduced axon. Figures from van Ooyen and Willshaw (1999a), where the parameter values are noted. Our (a) is Figure 3 of van Ooyen and Willshaw (1999a); (b) is 4a; (c) is 6c; (d) is 5b; (e) is 6a; (f) is 7c. Reproduced with permission from The Royal Society.

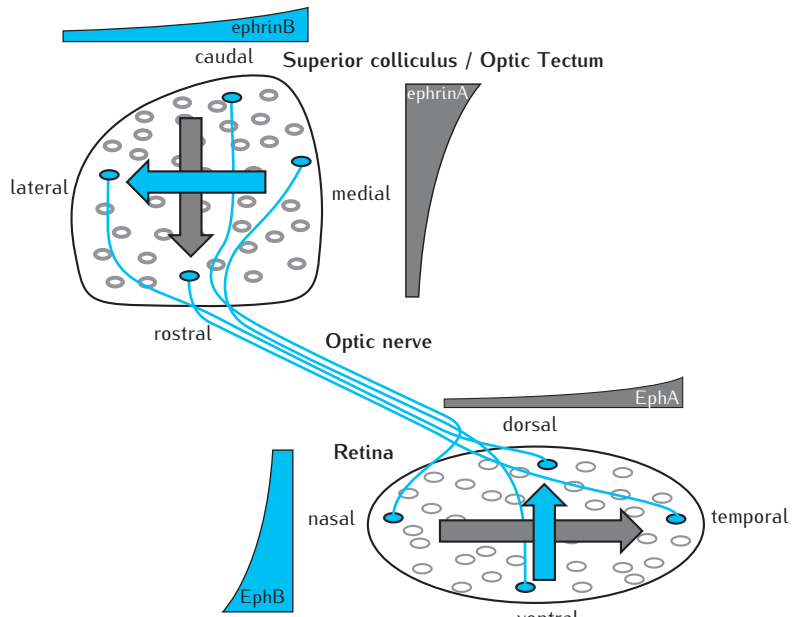
colliculus, in a fixed orientation. The fundamental question is how each axon finds its target site. The general modelling approach has been to develop a model to account for the production of ordered maps in normal animals and then to challenge the model to reproduce maps obtained in animals which have suffered disruption by surgical or genetic intervention.

10.7.1 Which data to model?

A systematic way of developing the ideal model is to establish the set of phenomena for which it is to account. The most important of these are:

Normal map: the development of an ordered 2D retinotopic map in a prespecified orientation (Figure 10.20).

Fig. 10.20 Retinotopic maps in the vertebrate visual system. Axons of the retinal ganglion cells (RGCs) form the optic nerve and travel to innervate the contralateral superior colliculus, or optic tectum. As the axons pass along the optic pathway to their targets, the topographic order initially present in the retina is largely destroyed, but it is recreated in the target region. The large arrows indicate the principal axes of the retina and the target region and their correspondence in the mature map. Each RGC contains EphA and EphB receptors. EphA receptor density increases smoothly from nasal to temporal retina and EphB density increases from dorsal to ventral retina. In the colliculus, the density of the ligand ephrinA increases from rostral to caudal and that of ephrinB from lateral to medial.



Connectivity plasticity: the fact that retinal axons can make connections with cells other than the ones that they would have contacted if part of a normal map. Early indications of this came from the expansion or contraction of ordered projections found in the **mismatch experiments** involving the regeneration of connections in adult fish (Figure 10.21b, c). For example, a surgically constructed half-retina eventually regenerates a map over the entire tectum, although normally it would be restricted to one half (Gaze and Sharma, 1970; Gaze and Keating, 1972; Sharma, 1972; Schmidt *et al.*, 1978). Connectivity flexibility is also seen in some species during early development. In the amphibians *Xenopus laevis* and *Rana*, as more and more retina and tectum becomes available during development, retinotectal connections are continually adjusted (Gaze *et al.*, 1974, 1979; Reh and Constantine-Paton, 1983). This class of behaviour is referred to as **systems-matching** (Gaze and Keating, 1972). Note that in the mouse, which has now become a popular experimental model, the retina and the colliculus do not change significantly in size whilst retinocollicular connections are being made and so connection plasticity might not be as important as in other species.

Maps formed in compound eyes: a set of studies (that have been largely ignored) on the properties of the experimentally induced **compound eye** projection in *Xenopus laevis* (Gaze *et al.*, 1963). Early in development, a half-eye rudiment is replaced surgically by another half-eye rudiment of different embryonic origin to form a *Xenopus* compound eye. Many different combinations of compound eye are possible, the most common ones being double nasal eyes (made from two nasal half rudiments), double temporal and double ventral eyes. In the adult, compound eyes are of normal size and appearance, apart from some abnormalities in pigmentation. A single optic nerve develops and

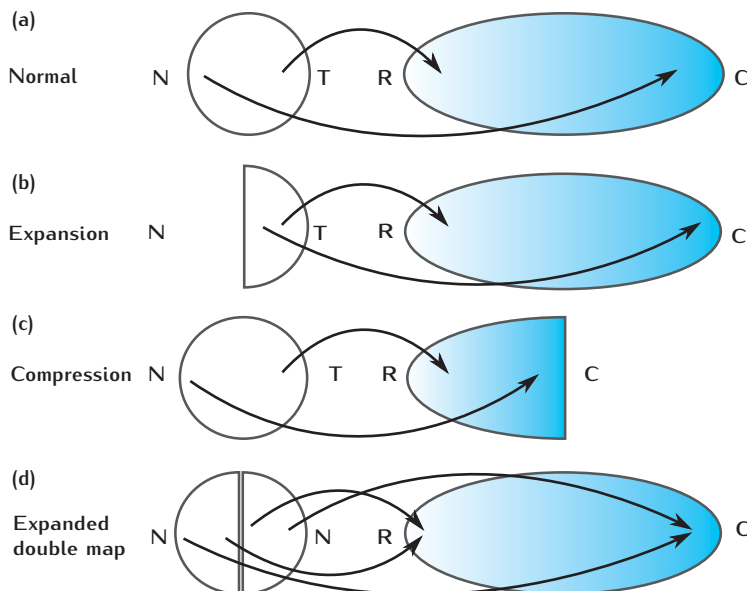


Fig. 10.21 Schematic showing the results of various experiments on the retinotectal system of non-mammalian vertebrates where the retina or tectum has been altered surgically.
(a) Normal projection showing that temporal retina (T) projects to rostral tectum (R), and nasal retina (T) projects to caudal tectum (C). **(b)** A half-retina expands its projection over the entire tectum. **(c)** A whole retina compresses its projection into a half-tectum. **(d)** A double nasal eye in *Xenopus* makes a double projection, with each of the two originally nasal poles of the retina projecting to caudal tectum and the vertical midline projecting rostrally.

innervates the contralateral tectum in the normal fashion. However, the projection made by a compound eye as assessed by extracellular recording is grossly abnormal. Each half-eye corresponding to the two half-eye rudiments which were brought together to make the compound eye projects in order across the entire optic tectum (Gaze *et al.*, 1963) instead of being localised to just one half of the tectum. When the two half rudiments are of matching origin, a double map results (Figure 10.21d). Depending on the type of compound eye made, the resulting ordered retinotectal maps may be completely continuous or may have lines of discontinuity within them.

Abnormal connectivity in genetically modified mice: over the last 40 years, several molecule types have been proposed that could guide axons to their sites of termination. However, there has been no strong candidate until the recent discovery of the existence of the **Eph receptor** and its ligand, **ephrin**, in graded form across the axes of retina and tectum/colliculus (Flanagan and Vanderhaeghen, 1998). These two molecules exist in two forms, A and B. Molecules of the A variant of the Ephs and ephrins could specify the order along one axis of the map, and molecules of the B variant the other axis (Figure 10.20). In normal maps, axons with high values of EphA terminate on target regions with low ephrinA and vice versa. In contrast, axons with high EphB terminate on regions with high ephrinB, and low EphB axons project to low ephrinB. Manipulation of the spatial distributions of Ephs and ephrins is now possible, giving rise to abnormal retinocollicular maps.

Knockout of ephrinAs: the knockout of some of the ephrinA molecules thought to label the rostrocaudal axis of the mouse colliculus results in axons terminating in abnormal positions. In some cases a small region of retina projects to more than one position on the colliculus (Feldheim *et al.*, 2000).

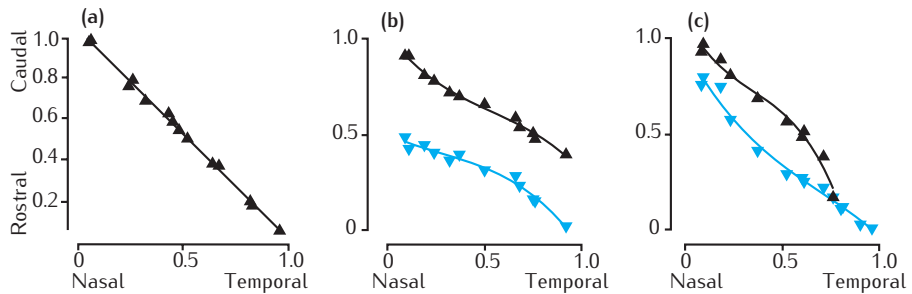


Fig. 10.22 The projection of nasotemporal retina onto rostrocaudal superior colliculus in EphA3 knockin mice compared with wild types. (a) Wild type projection. (b) Homozygous EphA3⁺⁺ knockin. (c) Heterozygous EphA3^{-/-} knockin. Black-filled triangles show projections from ganglion cells containing no EphA3; blue inverted triangles relate to EphA3 positive RGCs. From Willshaw (2006), redrawn from the results of retrograde tracing experiments (Brown *et al.*, 2000). Original data kindly provided by Greg Lemke.

Knockin of EphAs: an extra type of EphA receptor was introduced into 50% of the retinal ganglion cell population, distributed across the entire retina (Brown *et al.*, 2000). Each of the two populations of ganglion cells so defined makes its own map, one over rostral colliculus and one over caudal colliculus (Figure 10.22). The maps are correctly ordered over the rostrocaudal axis at least. Similar findings resulted when EphA knockin of this novel receptor type was combined with the knockout of an EphA receptor type normally present in the retina (Reber *et al.*, 2004).

10.7.2 Introduction to models for retinotopic map formation

The main classes of theories

Langley (1895), who carried out experiments on himself on the regeneration of peripheral nerve, was the first to propose a specific theory for the formation of nerve connections. He set the initial trend, which lasted until the 1970s, of using information from studies on regeneration to argue about development. The majority of theories were formulated between the 1940s and 1960s, and the main classes of mechanism discussed are:

- (1) **Fibre ordering:** that axons are guided to their target due to the ordering of nerve fibres within the pathway.
- (2) **Timing:** that during neurogenesis the earliest fibres reaching their target make contact with the earliest differentiating cells. This would assume a mechanism that converts positional information into temporal information.
- (3) **Chemoaffinity:** that there are biochemical labels amongst the retinal axons and their target cells that enable fibres and cells with matching labels to make connections.
- (4) **Neural activity:** that the patterns of electrical activity in neurons encode information enabling the appropriate contacts to be made.
- (5) **Competition:** that one of the signals guiding an axon to its targets arises from interactions with other axons.

Most quantitative models involve the implementation of one or more of these mechanisms in combination. We now describe some of these models, which we have classified according to the amount of detail within the model. Given that currently there is much interest in the Ephs and ephrins as the labels underlying chemoaffinity, all the models described contain a strong element of chemoaffinity. Detailed discussion of the entire variety of models,

including the important class of activity-based models, is given elsewhere (Prestige and Willshaw, 1975; Price and Willshaw, 2000; Goodhill and Xu, 2005; Goodhill, 2007).

The principal assumptions

It is useful to lay out the assumptions that are common to most models for the formation of retinotopic maps.

- (1) Most models are intended to apply once retinal axons have reached their target region, the optic tectum or the superior colliculus, where they are to make specific connections to form the ordered map.
- (2) The details of the 3D world in which axons have to find their targets are usually not represented in the model.
- (3) Some models are of connections forming between two 1D structures; some are for 2D structures interconnecting.
- (4) The numbers of cells in the two structures which are to interconnect are chosen to be large enough that a mapping of some precision can develop and are usually much smaller than in the real neural system.
- (5) The degree of connectivity between each retinal ganglion cell and each target cell is expressed in terms of some physical attribute of the contact between them, which is referred to as the synaptic strength of the connection.
- (6) The more detailed models are made up of a set of rules, usually expressed as a set of differential equations, for how each retinal axon develops contacts with a single cell or a set of target cells. To achieve this, the mathematical description of these models contains equations for calculating how the synaptic strengths change over time.
- (7) Most models contain elements of three basic mechanisms, which we refer to as mechanisms of chemoaffinity, activity-based interactions and competition. We now give more justification for the importance of these three building blocks.

10.7.3 Building blocks for retinotopic mapping models

Chemoaffinity

Sperry observed that after cutting the optic nerve in adult newt, rotating the eye and then allowing the retinotectal connections to regenerate, the animal's response to visual stimulation following restoration of visual function was not adapted to the eye rotation. For example, after a 180° eye rotation, the animal's response to stimulation of nasal retina was as if temporal retina of normal animals had been stimulated; the inference drawn was that each regenerating axon had found its original tectal partner. He proposed (Sperry, 1943, 1944, 1945) that there are preexisting sets of biochemical **markers** which label both retinal and tectal cells; and that the ordered pattern of connections observed during development is generated by the connecting together of each retinal cell with the tectal cell with the matching marker or label (Figure 10.23).

Activity-based interactions

Lettvin (cited in Chung, 1974) suggested that 'electrical activities in the optic nerve may be utilised by the nervous system in maintaining spatial contiguity between fibres'. From this general idea, a set of models has arisen

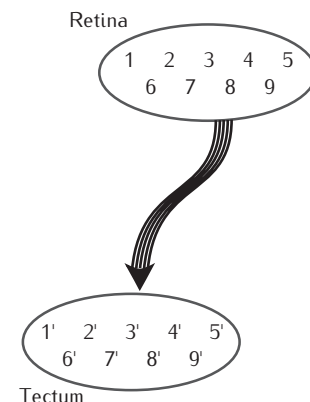


Fig. 10.23 The simplest form of the mechanism of chemoaffinity (Sperry, 1943, 1944, 1945) for the formation of specific retinotectal connections. Each retinal cell must carry a molecular label which identifies it uniquely. Each tectal cell must carry a similar identifying label. Each axon must be able to find and connect with the tectal cell carrying the corresponding label.

that is based on the concept that activity-based nearest-neighbour interactions amongst retinal and target cells lead to neighbouring retinal cells developing contacts preferentially with neighbouring target cells ('Cells that fire together wire together').

Such models require additional assumptions to be made, the fundamental ones being:

- At the time when connections are formed, the system is functional, in as far as there is activity in the retinal cells that excites, through already existing synapses, specific tectal/collicular cells.
- Cells that are neighbours in the retina or in the tectum/colliculus fire more strongly than non-neighbours. Usually it is assumed that there are short-range excitatory connections between retinal cells and tectal cells that mediate this. There is some evidence that the retina is spontaneously active and that the degree of correlation between the firing patterns at two points on the retina decreases with increasing distance between the points. Strongly correlated spontaneous activity has been demonstrated amongst ganglion cells in the adult at least (Rodieck, 1967; Arnett, 1978).
- Synapses between the more active retinal and tectal cells are strengthened preferentially. Usually a correlative mechanism is assumed of the types standardly invoked for models of synaptic plasticity in adults. Two examples are spike-time-dependent plasticity (Section 7.5) and plasticity of the simple Hebbian form (Box 9.3).

The action of an activity-based mechanism will ensure that the internal order of the map is established. The orientation of the overall map has to be specified in addition.

There is substantial evidence that electrical activity affects vertebrate connectivity. There is a lot of evidence about effects of electrical activity in the retinocortical pathway, but comparatively little about the effects on the organisation of the retinotectal or retinocollicular map. Retinal axons regenerating to the adult goldfish tectum either in the absence of neural activity through blockage of the sodium channels by TTX (Meyer, 1983; Schmidt and Edwards, 1983) or with the animal kept under stroboscopic illumination (Cook and Rankin, 1986), make less precise connections than controls. In mutant mice in which the $\beta 2$ subunit of the acetylcholine receptor has been deleted, compared to wild type the receptive fields of collicular neurons are elongated along the nasotemporal axis and the topography of the retinocollicular map is degraded only slightly (Mrsic-Flogel *et al.*, 2005).

Competition

In most models, except for the very simplest ones, a mechanism of competition is assumed to operate to constrain the strengths or distribution of the synapses formed in some way.

Sum rule. One way of expressing the idea of competition is to assume that the total strength of all the contacts made by each retinal cell is kept constant. In this case this means that the larger a particular synapse is, the smaller the other synapses made by that retinal cell will be; it could be said that target cells are competing to make contacts with each retinal cell. Normally a sum rule is represented by a mathematical

Although STDP is usually invoked in models of learning and memory, it also occurs in a developing system, the retinotectal system in *Xenopus laevis* (Zhang *et al.*, 1998).

equation embodying this rule rather than through a specific mechanism. An example of such a high-level rule was in the model for the elimination of superinnervation in developing muscle (Willshaw, 1981) described in Section 10.6.1. Sum rules are needed on computational grounds to prevent instability through runaway of synaptic strengths and are justified in general and intuitive terms rather than through the existence of a specific mechanism.

Constant innervation density. Another way to impose competition is through a mechanism keeping some measure of the density of contacts over the target structure at a constant level. This has been used as a mechanism for maintaining uniform innervation over the target structure; some authors have proposed it as a mechanism that overrides the assumed sets of fixed chemoaffinities so as to spread the connections from a surgically reduced retina over an intact tectum.

Homoeostatic plasticity. There is evidence that homoeostatic plasticity mechanisms adjust synaptic strengths to maintain stability of the system in terms of the mean levels of neural activity. Such mechanisms can promote competitive effects during activity-dependent development, and these are reviewed by Turrigiano and Nelson (2004). Homoeostasis is also described in Section 10.3, in the context of the development of physiological processes in the nerve cell.

10.7.4 Abstract models

The early models were formulated in terms of the properties that a satisfactory model should possess rather than specifying the computations to be performed for the required mappings to result.

Classic chemoaffinity. The original chemoaffinity theory is due to Sperry. In his earlier papers (Sperry, 1943, 1944, 1945) he assumed that retinal and tectal labels match together like locks and keys. In the later paper (Sperry, 1963), the labels were assumed to be molecules that exist in graded form across the retina or tectum, each molecule labelling a separate axis. No other information about how the labels would be matched together was given.

Plasticity through regulation. One problem with Sperry's original idea of chemoaffinity is that the model does not allow any flexibility of connection; i.e. retinal axon A will always connect with target cell A^* regardless of what other cells are present. To account for the expanded and contracted maps seen in the mismatch experiments, it was suggested that the surgical removal of cells triggers regulation or a reorganisation of labels in the surgically affected structure (Meyer and Sperry, 1973). For example, retinal hemiablation would cause the set of labels initially deployed over the remaining half-retina to become rescaled such that the set of labels possessed by a normal retina would now be spread across the half-retina. This would allow the half-retina to come to project in order across the entire tectum (Figure 10.21). The mechanism was called **regulation** by analogy with the similar findings in the field of morphogenesis, where a complete structure can regenerate from a partial structure (Weiss, 1939).

Sperry's model was formulated as a reaction to the **retrograde modulation** hypothesis of his supervisor (Weiss, 1937a, b), another example of an abstract model. According to retrograde modulation, growing nerve fibres make contact with their target at random. Different retinal cells send out electrical signals of different types, with each tectal cell tuned to respond to the signal which is characteristic of a different retinal location. In this way, specificity between individual retinal and tectal cells is accomplished. How a tectal cell is tuned to a particular retinal signal is the crucial question and therefore as a mechanism for map-making this hypothesis is incomplete.

Fig. 10.24 Sets of affinities between eight retinal cells and eight tectal cells displayed in matrix form for the two different types of chemoaffinity scheme identified by Prestige and Willshaw (1975). Each retinal cell is identified with a row, each tectal cell with a column and the individual entries represent affinities. (a) In a direct matching scheme, of type I, each retinal/tectal cell has highest affinity with one particular tectal/retinal cell and less affinity with others. (b) In a scheme of type II, each retinal/tectal cell has a graded affinity with all tectal/retinal cells. In their model, Prestige and Willshaw (1975) interpreted affinities as contact lifetimes.

Prestige and Willshaw (1975) expressed the differences between chemoaffinity mechanisms of type I and II in terms of matrices showing the affinities between any specific pair of cells. In their model, affinities were interpreted as lifetimes of individual retinotectal connections. Connections were assumed to be made at random. Once made, a connection would remain for the specified lifetime, which would be extended if during this time another contact was made between the same retinal and tectal cells.

1	8	7	6	5	4	3	2	1	1	2	3	4	5	6	7	8	
2	7	8	7	6	5	4	3	2	2	2	4	6	8	10	12	14	16
3	6	7	8	7	6	5	4	3	3	3	6	9	12	15	18	21	24
4	5	6	7	8	7	6	5	4	4	4	8	12	16	20	24	28	32
5	4	5	6	7	8	7	6	5	5	5	10	15	20	25	30	35	40
6	3	4	5	6	7	8	7	6	6	6	12	18	24	30	36	42	48
7	2	3	4	5	6	7	8	7	7	7	14	21	28	35	42	49	56
8	1	2	3	4	5	6	7	8	8	8	16	24	32	40	38	56	64
1 2 3 4 5 6 7 8								1 2 3 4 5 6 7 8									
Type I								Type II									

Plasticity through competition. An alternative explanation for the systems-matching of connections is that the labels do not change, and the flexibility in connectivity is possible through competition (Gaze and Keating, 1972). On this interpretation, retinal axons would compete for tectal space. For example, the axons from a normal retina innervating a surgically reduced tectum will be subject to high competitive pressure and squeeze in to innervate the tectum available; conversely, the terminals from axons from a half-retina innervating a normal tectum will have less competitive pressure and would therefore be spread out over the entire tectum. How a combination of chemoaffinity and competition could work required a computational model, as described below.

10.7.5 Computational models

The next class of models described contains those formulated in terms of a set of equations, or rules, describing the mechanisms formulated at the synaptic level that come into play to enable the required nerve connections to be established. These mechanisms are largely proposed by the modeller.

Type I and type II chemoaffinity

Prestige and Willshaw (1975) distinguished between two types of chemoaffinity schemes (Figure 10.24). According to schemes of type I, each retinal cell has the greatest affinity for a small group of tectal cells and less for all other cells; direct matching, as in the original formulation due to Sperry (1963). Cells that develop connections according to this scheme will make specific connections with no scope for flexibility. According to schemes of type II, all axons have high affinity for making connections at one end of the tectum and progressively less for tectal cells elsewhere. Conversely, tectal cells have high affinity for axons from one pole of the retina and less from others; there is graded affinity between the two sets of cells. Prestige and Willshaw (1975) explored computational models of type II where the affinities were fixed.

Simulations of a 1D retina connecting to a 1D tectum showed that ordered maps can be formed only when competition is introduced by limiting the number of contacts that each cell can make. This ensures an even spread of connections; without competition, the majority of the connections would

be made between the retinal and tectal cells of highest affinity. In order to produce systems-matching when the two systems are of different sizes, the additional assumption had to be made that the number of connections made by each cell can be altered. This is equivalent to introducing a form of regulation, even though the labels as such are not changed.

Energy-based approaches to chemoaffinity

Another type of computational approach, originated by Fraser (1981) and developed by others, including Gierer (1983), is to assume that signals from both axons and target cells generate an energy field for each axon, which gives rise to forces that guide it to its position of minimum energy.

Gierer (1983) pointed out that this formulation can be interpreted in different ways, giving fundamentally different implementations. If axons are assumed to search randomly until hitting the position of minimum energy, at which point they make contact, then this is an implementation of the proposal due to Sperry (1963); if they are assumed to be directed by the forces generated in the field to move down the direction of the maximal slope of the field, then their resting position is where opposing forces are in equilibrium. This latter idea is reflected exactly in the notion of gradients and countergradients, which is favoured by a number of contemporary neuroscientists; e.g. Marler *et al.* (2008).

A simple example given by Gierer (1983) of a 1D countergradient model is one where a molecule distributed as a single gradient over the retina is inhibited by a molecule from a similar gradient produced in the tectum. The tectal molecule is inhibited by the retinal molecule in a complementary fashion.

Consider an axon from retinal position u , where there is an amount $e^{-\alpha u}$ of the retinal molecule. At time t , the axon is at tectal position x , where there is an amount $e^{-\alpha x}$ of the tectal molecule, α being a constant. The energy p at position x and the consequent force $\frac{dp}{dx}$ acting on the axon are:

$$p(x) = e^{-\alpha u}/e^{-\alpha x} + e^{-\alpha x}/e^{-\alpha u}, \quad (10.34)$$

$$\frac{dp}{dx} = \alpha(e^{-\alpha u}/e^{-\alpha x} - e^{-\alpha x}/e^{-\alpha u}). \quad (10.35)$$

The axon moves under the influence of the force so as to reduce the value of p until it reaches its unique minimum value, which is at $x = u$. This means that each axon, with a different value of u , will find a termination at a different tectal coordinate x . Since the molecules are distributed in smooth gradients across the retina and tectum respectively, an ordered map will result.

Augmented energy-based model

The disadvantage of the mapping mechanism just described is that it is of the Prestige and Willshaw type I, and so cannot account for the systems-matching behaviour following removal of retinal or tectal tissue from adult fish. To remedy this, Gierer (1983) invoked a competitive mechanism designed to equalise the density of innervation by adding to the energy function (Equation 10.34) a term $r(x, t)$ which increases at a rate proportional

Box 10.3 Implementation of the Gierer (1983) model

The ability to reproduce a model is just as important as the ability to reproduce an experiment. The current trend for authors to publish the code which produced published results was not always the case. In order to reproduce model results, a close reading of the original paper is often required.

Throughout this book, we have endeavoured to reimplement simulations as much as possible. Here we describe in more detail than usual the exercise of implementing a model from the published details. We chose the Gierer (1983) model of development of connections from retina to tectum as specified by Equations 10.36 and 10.37.

Gierer (1983) showed that, after removal of 12 of the original 24 retinal axons, the surviving 12 retinal axons form an expanded map over 24 tectal positions. According to Gierer (1983: 85):

To allow for graded density distributions, each fibre unit is subdivided into 16 equal density units, and the position of each density unit is calculated separately. Density $\rho \dots$ is the number of density units per unit area of tectum. If from [Equation 10.36] $\Delta\rho/\Delta x$ is negative, the density unit is shifted one position to the right, if $\Delta\rho/\Delta x$ is positive, the unit is shifted to the left. The process is carried out for all positions and density units, and reiterated, the time of development being given as the number of iterations. In the computer simulation, retinal and tectal areas extended from $x = u = 0.15$ (position 1) to $x = u = 3.6$ (position 24) with $\alpha = 1 \dots$ and $\epsilon \dots$ was taken as 0.005.

To describe the locations in the tectum and retina, we created two arrays, x and u , with components $x_j = 0.15i$, $i = 1, \dots, 24$ and $u_i = 0.015j$, $j = 1, \dots, 12$. The 12×16 matrix L records the locations of each axon's 16 terminals ('density units'). Each element of L contains the index of the tectal location to which the terminal projects. Each element of the density array ρ_j , $j = 1, \dots, 24$, is computed by counting how many elements in L are equal to j .

We found it difficult to understand what is calculated at each update step. Is just one or all of the 192 density units updated? Is the value of r updated every time a unit is shifted to the left or right? Exactly how is the gradient computed? For example, when comparing the values of the ρ to the left and right of a unit, what happens if *both* are lower? After some experimentation, we settled on the following. A time-step $\Delta t = 1/(16 \times 12)$ is chosen. At each time-step, a density unit (i, k) is chosen at random. Its position j is read out from L_{ik} . The gradient is estimated as $\rho_{i,j+1} - \rho_{i,j-1}$, a slightly different expression being used at the edges. The shift of i from position j to $j+1$ or $j-1$ is made as described by Gierer (1983) and the values of L_{ik} and ρ_j and ρ_{j-1} or ρ_{j+1} are updated. r is then updated: $r_j(t + \Delta t) = r_j(t) + \epsilon\rho_j\Delta t$.

Our simulations are almost certainly different from Gierer's. However, our results agree reasonably well with his, though in our simulations, development occurs about twice as quickly (Figure 10.25).

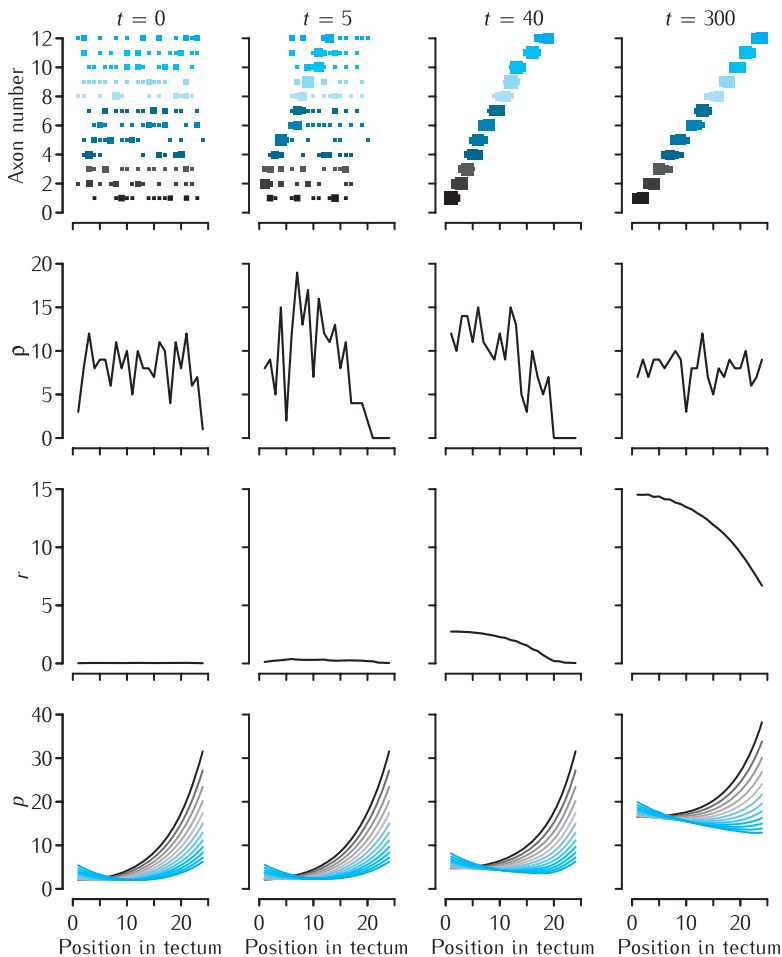


Fig. 10.25 Simulation of the establishment of connections in the mismatch experiments, after Gierer (1983). Each column shows the system at a different time. **Top row.** The projection of each of the 16 density units from each of 12 axons onto the 24 tectal positions. Each axon is colour coded, from axon 1 (black) to axon 12 (blue). The area of each square is proportional to the number of density units contributed by the axon to that tectal position. **Row 2.** The density of connections p at each tectal position. **Row 3.** The distribution of the accumulated density r over the tectum. **Row 4.** The value of the potential p at each tectal location for each of the 12 axons. The colour of the curve corresponds to the colours in the top row. At $t = 0$, the initial random state of the mapping with uniform density p over the tectum and r is uniformly zero. The minimum value of p for each axon is at the tectal position appropriate to a normal map. By $t = 5$, most of the axons fill the left-hand part of the tectum in a topographic fashion, the preferred positions of axons corresponding to the positions of the minima of potential p . By $t = 40$, prolonged occupancy of the axons in the left half of the tectum has caused the accumulated density r to increase in the left part of the tectum, decreasing towards the right. This causes the minima of the p curves to be shifted to the right, so that the optimal positions of axons are shifted to the right (top row). By $t = 300$ the process is essentially complete, with an ordered and expanded mapping from retina to tectum.

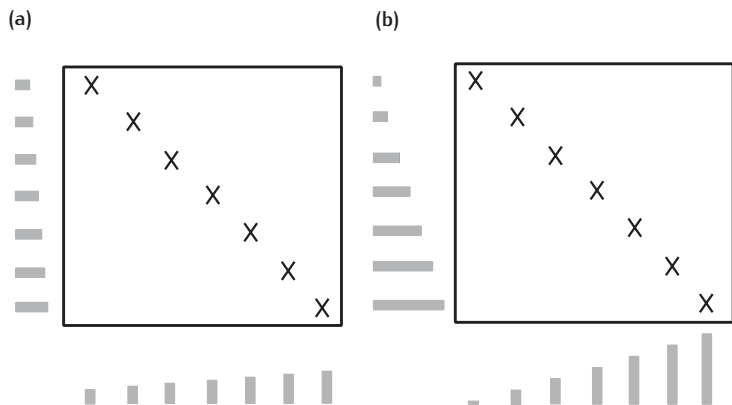
to the local density of terminals $\rho(x, t)$. The effect of this is to maintain a constant density of terminals over the entire tectum. With the constant ϵ specifying the rate of increase of p , Equation 10.34 for the energy p now becomes:

$$p(x, t) = e^{-\alpha u} / e^{-\alpha x} + e^{-\alpha x} / e^{-\alpha u} + r(x, t), \quad (10.36)$$

$$\frac{\partial r}{\partial t} = \epsilon \rho(x, t). \quad (10.37)$$

Consider the case of a surgically reduced half-retina reinnervating the goldfish optic tectum, where initially there is a map in the normal half of the tectum before expansion (Schmidt *et al.*, 1978). According to the augmented model (Gierer, 1983), an axon would be subject to a chemoaffinity force directing it to return to its normal position together with one that directs it into uninervated tectum. The compromise between these two forces allows the half retinal projection to be distributed over the entire tectum. The reason for this is that, with the axons returning initially to the positions they would occupy if part of a normal map, the distribution of accumulated synaptic density will always provide a force directing axons into the uninervated territory. Figure 10.25 gives representative results from our

Fig. 10.26 The principle behind the Marker Induction model. The connections made between the cells on the nasotemporal axis of the retina projecting to rostrocaudal axis of the tectum are shown schematically. By operation of the mechanism of induction, an ordered gradient of markers in the retina (grey bars laid out from left to right) is reproduced over the tectum (grey bars stacked vertically). Connections are made as indicated by crosses in the connectivity matrix where the length of the retinal bar matches the length of the tectal bar. (a) If the gradient is shallow then so is the tectal gradient. (b) If the retinal gradient is steeper then the tectal gradient is also steeper.



implementation of Gierer's (1983) model. Once synaptic density over the tectum has become uniform, at each time-step a constant value is added to the energy p (Equation 10.36) and so the two opposing forces will always remain in equilibrium. The simulations presented by Gierer (1983) were for maps in 1D. It is possible to extend this model to the formation of 2D maps.

Marker induction

If retinotectal connections are made by the matching together of labels, then the extended or compressed retinotectal projections seen in the mismatch experiments must represent evidence that the labels had changed. Schmidt *et al.* (1978) argued that either the labels in the retina or the labels in the tectum, or both, had changed. They carried out a set of ingenious experiments in adult goldfish in which half of one retina was removed. Subsequently, either the normal or the half-retina was forced to innervate the ipsilateral tectum that already carried a retinal projection. The nature of the tectal labels was inferred from knowledge of the retinal projection that it already carried. They concluded that in these experiments the surgically constructed half-retina always retained its original labels and the changes in labels were in the tectum; i.e. the changes were induced from the retina (Schmidt *et al.*, 1978).

Willshaw and von der Malsburg developed the idea that the establishment of retinotopic mapping can be thought of in terms of a mechanism that connects neighbouring retinal cells to neighbouring tectal cells. They proposed two ways in which such a mechanism could be implemented, either in electrical terms (Willshaw and von der Malsburg, 1976) or in molecular terms, which gave rise to a new type of chemoaffinity model, the **Marker Induction model** (von der Malsburg and Willshaw, 1977; Willshaw and von der Malsburg, 1979). This is a chemoaffinity model of type I, with the added feature that the tectal cells are labelled by the incoming fibres, the pattern of labels over the tectum determining and being determined by the growth of synapses between retinal fibres and tectal cells (Boxes 10.4 and 10.5).

According to the model, each tectal cell acquires, by induction through the synapses, the markers that are characteristic of the retinal cells that innervate it, at rates determined by the current strengths of these synapses.

Box 10.4 | The Marker Induction model

It is assumed that over the retina there are concentration gradients of a number of transportable substances, at least one for each spatial dimension. Each retinal location is identified uniquely by the blend of concentrations of the various substances, which thereby act as labels or markers. These substances are transported down the axons to the axonal terminals, where they are injected onto the tectal surface at a rate proportional both to their concentration and the strength of the synapse. They then spread out to label tectal cells. Each synapse between a retinal fibre and a tectal cell has a **strength**, specifying the rate of injection of markers from axon to cell. In addition, it has a **fitness**, which specifies the similarity between the marker blends carried by the retinal and tectal cells.

Synaptic strengths are governed by three rules, which are implemented in the underlying dynamics:

- (1) The strength of a synapse is proportional to its fitness. The greater the fitness (i.e. the more similar the marker blends of retinal and tectal cells), the greater the synaptic strength.
- (2) Competition is introduced by imposing the condition that the sum of the strengths of all of the synapses from each retinal cell is fixed; if some synapses are strengthened then others are weakened. This assures stability as no synapse can grow without bound.
- (3) Each axon forms new terminal branches nearby existing ones and branches with synapses whose strengths fall below a threshold value are removed.

There is also lateral transport of the markers in the tectum, ensuring that neighbouring tectal cells carry similar blends of markers. The synaptic strengths are changed according to the similarity between the respective retinal and tectal configurations of markers. As a result, each tectal cell develops synapses preferentially to those retinal cells innervating it and acquires the markers that are similar to those in these retinal cells. The result is a map of synaptic strengths that is locally continuous. Since the model specifies internal order only, there is no information about any particular map orientation. This has to be supplied separately and could be done either by biasing the initial pattern of innervation or by providing weak polarising gradients of markers in the tectum. With the addition of this second mechanism, a continuous map in the required orientation results, with a copy of the retinal markers becoming induced onto the tectum.

In this model the problem is solved of how a set of markers, or labels, in one structure can be reproduced in a second set in a way that is resistant to variations in the developmental programme for the individual structures. The model is able to account for the systems-matching sets of results (Gaze and Keating, 1972), as well as those on the reinnervation of optic tectum following graft translocation and rotation that suggest that in some, but not all, cases, different parts of the optic tectum have acquired specificities for

Box 10.5 Equations for the Marker Induction model

The model is defined by differential equations for how the amounts of tectal markers and the strengths of the retinotectal synapses change in response to the retinal markers induced through the axons innervating these cells. The equations given here are for the later version of the model, where Ephs and ephrins are assumed to be the retinal and tectal markers, respectively. For more details, see Willshaw (2006).

Definitions

- (1) Each retinal cell i contains amounts R_i^A and R_i^B , representing the densities of receptors EphA and EphB in that cell. The EphA and EphB receptor profiles are expressed as two orthogonal gradients of markers across the retina.
- (2) Each tectal cell j contains amounts T_j^A and T_j^B , representing the densities of ligands ephrinA and ephrinB in that cell.
- (3) The *synaptic strength* between retinal axon i and tectal cell j is S_{ij} .
- (4) The parameters α , β , γ and κ are constants.
- (5) The amounts of *induced marker* I_j^A , I_j^B are the sums of the total amounts of T_j^A and T_j^B available in the terminals of the axons impinging on tectal cell j , weighted by the appropriate synaptic strengths.

$$I_j^A \equiv \sum_k S_{kj} R_k^A / \sum_k S_{kj}, \quad I_j^B \equiv \sum_k S_{kj} R_k^B / \sum_k S_{kj}.$$

The tectal cells. In each tectal cell j , the rate at which tectal markers are produced depends on the total amount of induced marker.

The amount T_j^A changes until the product of T_j^A with the amount of induced marker I_j^A attains a constant value, here set at 1, subject to a condition that enforces spatial continuity through short-range interchange of markers between cells

$$\Delta T_j^A = \alpha(1 - I_j^A T_j^A) + \beta \nabla_m^2 T_j^A. \quad (a)$$

The Laplacian operator ∇_m^2 is calculated over the m nearest neighbours of cell j .

The amount T_j^B is changed until it is identical to the total amount of induced marker I_j^B .

$$\Delta T_j^B = \alpha(I_j^B - T_j^B) + \beta \nabla_m^2 T_j^B. \quad (b)$$

Determining the synaptic strengths. The strength of each synapse is set according to the similarity between the markers carried by the retinal cell and the tectal cell concerned. For any synapse (i, j) , the closer the product of R_i^A with T_j^A is to the preset level of 1, and the closer the value of R_i^B approaches that of T_j^B , the higher the similarity. Competition is introduced by normalising the total strength from each retinal cell to 1; a synaptic strength can be interpreted as the probability of a given retinal axon contacting a given tectal cell.

To calculate a measure of similarity Φ between the markers in retinal cell i and those in tectal cell j , first define the distance measure Ψ :

$$\Psi_{ij} \equiv (R_i^A T_j^A - 1)^2 + (R_i^B - T_j^B)^2.$$

Then define Φ as

$$\Phi_{ij} \equiv \exp(-\Psi_{ij}/2\kappa^2).$$

The change in synaptic strength ΔS_{ij} is

$$\Delta S_{ij} = (S_{ij} + \gamma \Phi_{ij}) / \sum_k (S_{ik} + \gamma \Phi_{ik}) - S_{ij}. \quad (c)$$

individual retinal fibres (Yoon, 1971, 1980; Levine and Jacobson, 1974; Jacobson and Levine, 1975; Hope *et al.*, 1976; Gaze and Hope, 1983). The existence of tectal specificities is the crucial difference between implementing the nearest-neighbour idea in molecular terms rather than electrical terms as in the neural activity model (Willshaw and von der Malsburg, 1976).

The Arrow model

Hope *et al.* (1976) proposed the **Arrow model**, according to which two axons terminating at neighbouring target locations are able to exchange positions if they are in the wrong relative position (Figure 10.27). A simple 1D analogy that was used to explain this model is that soldiers are required to line up in order of height by swapping positions with their neighbours. To do this they need to know which end of the line is to be the ‘high’ end and which the ‘low’ end. Whilst the computations that are to be carried out are specified in detail in the model, the way the model is implemented is not biologically realistic. There is a discrete number of target sites and contacts, which seems unbiological. In addition, the process of pairwise swapping over of connections may be a good summary description of a process of refinement of connections, but it is not clear whether this is possible without axons being tangled up. To account for the expansion and contraction of projections in the mismatch experiments, in the model the swapping over process is alternated with one of random exploration, so that all the available target structure is covered. Overton and Arbib (1982) made this model biologically more realistic and added a second influence which directed axons to their appropriate tectal position, thereby adding a direct matching chemoaffinity mechanism which accounts for results from a set of tectal graft translocation experiments which are inconsistent with the original Arrow model. A more biologically based model that represents a further refinement to this model is described below.

An advantage of the original Arrow model (Hope *et al.*, 1976) was that it was falsifiable. It predicts that the map produced by allowing optic nerve fibres to reinnervate the adult tectum after a portion of the tectum has been removed, rotated and then replaced will be normal except that the small portion of the map identified with the rotated part of the tectum will be rotated by a corresponding amount. However, since there is no information about absolute position on the tectum, if two parts of the tectum are interchanged without rotation, the model predicts a normal map. Hope *et al.* (1976) reported that the maps obtained after translocation do contain matching translocated portions, which falsifies their own model.

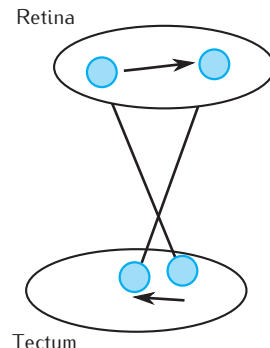


Fig. 10.27 Schematic of the Arrow model (Hope *et al.*, 1976). This is a procedure for checking that the two members of each pair of retinal axons that terminate close to one another are in the correct relative orientation. If they are not (as shown here), they swap positions. The algorithm selects pairs of axons that terminate near to one another at random, and continues until all pairs of neighbouring retinal axons are correctly aligned.

10.7.6 Eph/ephrin-based chemoaffinity models

The development of quantitative models for the establishment of ordered retinotectal or retinocollicular connections has received a new lease of life due to the use of the connectivity patterns found in mutant mice to test the models. There are now a number of models designed to incorporate information about the distribution of Ephs and ephrins across both retina and colliculus or tectum and their possible role as the labels of chemoaffinity in normal and transgenic animals.

The Servomechanism model

Honda (1998) developed a formalised version of a proposal originally due to Nakamoto *et al.* (1996), which he called the **Servomechanism** model. It was applied to the projection made in mice by axons from the nasotemporal axis of the retina to the rostrocaudal axis of the colliculus. It was intended to account for the findings that:

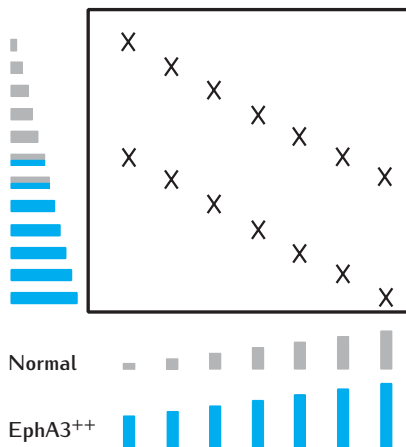
- (1) axons grow into the colliculus at the rostral pole and then move up towards their site of termination more caudally;
- (2) EphA receptors and ephrinA ligands are arranged in counter-gradients; that is, axons from the high end of the EphA gradient in the retina normally project to the cells at the low end of the ephrinA gradient in the colliculus and vice versa;
- (3) the interactions between EphA receptors and ephrinAs cause repulsion.

According to the model, all axons are subject to two guidance signals. One signal is the same for all axons and directs them towards posterior colliculus. A second signal acts in the opposite direction, the amount of signal being determined by the number of receptors bound by ligands. In the simplest case, if the axon has an amount R of receptor which binds to an amount L of ligand, the strength of the variable signal is the product RL . In the final stable state, when the mapping is set up, the constant force is counterbalanced by an equivalent amount of variable force. The same amount of variable signal results from either high receptor and low ligand, low receptor and high ligand, or a medium amount of both quantities. This would account for the ordered mapping observed.

This model is of type I, there being no flexibility of connection. In a later paper, Honda (2003) added a mechanism of interaxon competition to remedy this. This mechanism operates to maintain constant terminal density over the extent of the target. It is not clear whether the required flexibility of connections is attained. Once the terminal density becomes uniform, then this competitive mechanism will become ineffective and so axons will return to innervate the targets that they would do when part of a normal map. This paper (Honda, 2003) represents the first attempt to model the effects of knockin or knockout of the EphA receptors or the ephrinAs, which cause abnormal maps to be produced.

Augmented marker induction

Recently, Willshaw (2006) adapted the marker induction model (Willshaw and von der Malsburg, 1979). He used smooth gradients of EphA and EphB to label the two axes of the retina and similar smooth gradients of ephrinAs and ephrinBs to label the corresponding axes of the colliculus. Each synapse is strengthened according to how closely (1) the product of the amount of EphA in the axon with the amount of ephrinA in the collicular cell is to a preset level, and (2) the amount of EphB in the axon is to the amount of ephrinB in the collicular cell. Willshaw (2006) showed that the double maps formed in mutant mice in which half the retinal ganglion cells have an extra EphA receptor type (Brown *et al.*, 2000; Figure 10.22) are predicted from this



model (Figure 10.28). Predictions from this model that have yet to be tested are those in the family of double maps found by Reber *et al.* (2004), who extended the EphA knockin paradigm (Brown *et al.*, 2000) by combining knockin with knockout of EphA receptors. The distributions of the labels across the colliculus will be different from case to case and in each case will match those in the retina.

Enhanced Arrow model

Koulakov and Tsigankov (2004) proposed a probabilistic model whereby axons terminating on neighbouring target positions will swap locations according to a measure of an energy function which reflects the distance on the retina between their parent ganglion cells. The model was applied to the mapping of the nasotemporal axis of the retina to the rostrocaudal axis of the colliculus (Figure 10.22a).

In the 1D case, suppose that two axons labelled by receptor levels R_1 and R_2 terminate at neighbouring positions on the colliculus where the ligand levels are L_1 and L_2 . The probability that these two axons exchange their positions is calculated as:

$$P = 1/2 + \alpha(R_1 - R_2)(L_1 - L_2), \quad (10.38)$$

where α is a positive constant.

This means that exchange of axonal positions is likely when the difference between R_1 and R_2 has the same sign as the difference between L_1 and L_2 . This will force axons with high EphA to terminate in regions of low ephrinA, and vice versa.

The converse situation found in the mapping of the dorsoventral retinal axis to the mediolateral axis in the colliculus where an EphB gradient is matched directly with an ephrinB gradient can be achieved by reversing the plus sign in Equation 10.38.

Although expressed in a different language, effectively this model is a probabilistic version of the earlier class of Arrow models already described (Hope *et al.*, 1976; Overton and Arbib, 1982), with similarities also with the servomechanism idea (Nakamoto *et al.*, 1996; Honda, 1998). It is very similar

Fig. 10.28 Schematic showing how the Marker Induction model generates the double map seen in the EphA3 knockin experiments (Brown *et al.*, 2000). There are two gradients of marker distributed across the nasotemporal axis of the retina, one for the normal cells and one for the EphA3⁺⁺ cells. Grey indicates the amount of EphA in normal cells and blue the amount in the EphA3⁺⁺ cells. EphA3 positive cells are deemed to have had their EphA marker increased by a constant amount (Brown *et al.*, 2000). There is a single gradient of EphA3 in the axons distributed across the colliculus. Crosses in the matrix indicate where connections are made, where the amount of marker in the retina (horizontal axis) matches the amount in the colliculus (vertical axis). EphA3⁺⁺ cells project to the front of the colliculus and normal cells to the back, giving rise to a double representation of retina onto field. The marker induction model (Willshaw, 2006) would have also predicted that the projection on rostral colliculus is from the population of EphA3⁺⁺ cells, as found experimentally (Brown *et al.*, 2000).

to the Extended Branch Arrow model (Overton and Arbib, 1982), except for the way in which stochasticity is introduced and that the labels used have been identified as the EphA receptors and the ephrinA ligands. In all these Arrow models (Hope *et al.*, 1976; Overton and Arbib, 1982; Koulakov and Tsigankov, 2004) there is competition, introduced implicitly by imposing a fixed number of axons or axonal branches and collicular sites.

This model has been applied to the double maps produced in the EphA3 knockin experiments (Brown *et al.*, 2000). In the 1D model it was assumed that alternating retinal sites have the extra EphA receptor and so have elevated EphA levels. This means that axons from neighbouring retinal sites which are adjacent in the tectum are most likely to be interchanged, thus forming two separated maps as found in homozygous EphA3 knockins (Figure 10.22b). In heterozygous animals, the two maps fuse in rostral colliculus (Figure 10.22c). This finding was explained on the basis that the signal-to-noise ratio of the probabilistic fibre switching is lower in rostral colliculus because of lower EphA3 levels. The effect depends on the precise shapes of the Eph and ephrin profiles in retina and colliculus.

10.8 | Summary

In this chapter we have reviewed examples of modelling work in the exciting field of developmental neuroscience. So far, the modelling of neural development has proved to be a minority occupation amongst computational neuroscientists. One reason for this could be that, for many computational neuroscientists, the best-studied systems in developmental neuroscience, such as the development of single neuron morphology in cerebellum (McKay and Turner, 2005), of topographically ordered connections in the vertebrate retinotectal or retinocollicular system (Section 10.7) or of olfactory connections (Mombaerts, 2006) are straightforward examples of the instructions in the genome playing out during development. As a consequence, it may be thought that to understand these systems does not present such a challenge to computational neuroscientists compared with trying to understand the role played by the mammalian neocortex in perception or learning.

Another reason may be that, for many people within the field, the brain is the organ of computation and the field of computational neuroscience studies how the brain computes (Churchland and Sejnowski, 1992). The implicit assumption, derived in part from the fact that many computational neuroscientists were weaned on the study of artificial neural networks and parallel distributed processing (Rumelhart *et al.*, 1986b), is that the neurons are the computational elements and the currency of neural computation is the nerve impulse.

In this chapter we have made it clear that the signalling processes involved in neural development have both molecular and electrical components. In most developmental situations, whilst it is usually clear as to what should be modelled (e.g. how does the elimination of superinnervation occur?), it is less clear as to what the components of the underlying mechanisms are.

This means that it is possible to design different types of model for the same developmental phenomenon, each model embodying completely different types of assumed mechanism. Using examples from investigations of the development of the properties of single nerve cells and their connections, we have attempted to show the variety of models that have been devised, at different levels of abstraction, to address very specific questions.

Chapter 11

Farewell

This book has been about the principles of computational neuroscience as they stand at the time of writing. In some cases we have placed the modelling work that we described in its historical context when we felt this would be useful and interesting. We now make some brief comments about where the field of computational neuroscience came from and where it might be going.

11.1 The development of computational modelling in neuroscience

The field of computational modelling in neuroscience has been in existence for almost 100 years. During that time it has gone through several stages of development. From the 1930s, researchers in the field of **mathematical biophysics** conceived of mathematical and physical models of biophysical phenomena. In the more neural applications, there was work on how networks of nerve cells could store and retrieve information through the adaptive tuning of the thresholds of selected nerve cells (Shimbel, 1950), on linking psychophysical judgements with the underlying neural mechanisms (Landahl, 1939) and mathematical accounts of how nerve cells could act as logical elements and what the computational capabilities of a network of such elements were (McCulloch and Pitts, 1943). From the 1950s onwards there was interest in treating the brain as a uniform medium and calculating its modes of behaviour, such as the conditions under which it would support the propagation of waves of activity across it (Beurle, 1956). Much of this work laid the foundation for the field of artificial neural networks in the 1950s and 1960s. This field enjoyed a renaissance in the 1980s and is now regarded as part of machine learning. Cowan and Sharp (1988) give a historical account of this field.

From the 1950s, computational models that addressed much more specific questions were being developed. Different models were constructed at different levels of detail. One of the most famous of these is the model of the propagation of the nerve impulse (Hodgkin and Huxley, 1952d), the

subject of Chapter 3 of this book. The model of how the cerebellar cortex could function as a memory device (Marr, 1969) is much more high level; for example, the modifiable synapses in the model are represented as two-state devices. Notwithstanding, this model has been a source of inspiration for physiologists investigating how the cerebellar cortex might be used to learn to associate motor commands with actions.

The last 20 years have seen an ever-increasing involvement of computational modellers in the study of the nervous system. Most computational models are aimed at answering specific rather than general questions. They rely heavily on experimental data to constrain the model. Many experimental neuroscientists have collaborations with computational neuroscientists; all the premier neuroscience journals accept papers describing computational neuroscience modelling work that links to experimental results.

11.2 The future of computational neuroscience

What advances might be expected to take place over the next 20 years in computational modelling in neuroscience? These will be driven by advances in computer technology, advances in new measurement techniques in neuroscience and a growing acceptance of the utility of the modelling paradigm.

With the powerful computational resources now available, it is possible to run simulations of networks in which the numbers of model neurons and supporting cell types approach those in the full-size system. It is possible to simulate networks of at least tens of thousands of model neurons with the detail of a Hodgkin–Huxley neuron, or thousands of more detailed neurons. However, even assuming that the speed and storage capacity of computers will continue to increase at a rate approximating to **Moore's law** (Moore, 1965), detailed modelling of a single nerve cell at the molecular level will still be impossible. Given that a cell contains at least 10^{12} molecules, to simulate all the molecular interactions within a single cell for even a day would require at least 10^{23} of our most powerful computers (Noble, 2006).

The acceptance of modelling in all branches of biology is being helped by the newly emerging fields of **neuroinformatics** and **systems biology**.

Neuroinformatics describes the application of the quantitative sciences to the neurosciences. Definitions of the scope of neuroinformatics differ amongst communities. One useful definition is that neuroinformatics involves the development and uses of databases, software tools and computational modelling in the study of neuroscience.

Systems biology is the use of modelling techniques to understand specific biological systems at many different levels, a dynamic interaction being envisaged between the processes of modelling and the acquisition of experimental data. The prime example of systems biology is in the extensive research initiative to understand heart physiology (Noble, 2006). The availability of biological databases and powerful computing resources, and the rapid growth of models of cells, tissues and organs, has made it possible to study the function and dysfunction of the heart at many levels, from genes to the entire system.

The original formulation of **Moore's law** is that the power of a computer, expressed in terms of the number of components that can be placed on a computer chip, doubles every year. There have been various predictions about when the fundamental physical barriers will cause this law to break down. So far this has not happened, although it is now accepted that this law, and other similar laws, should be modified. Moore (1975) modified his statement to give a doubling every 18 months or two years.

Noble (2006) points out that computational neuroscience and systems biology share a common line of descent from Hodgkin and Huxley's work.

11.2.1 The importance of abstraction

Particularly within systems biology, there is a growing interest in constructing simulation models of the many complex molecular interactions within a single cell. This has highlighted the more general issue that, to make progress in the computational modelling of biological systems, abstraction of the elements of the system will be required. Without abstraction, the resulting models will be too complex to understand and it will not be feasible to carry out the desired computations even using the fastest computers that might be developed over the next 20 years. As discussed in earlier chapters in this book, the level at which the abstraction is carried out will depend on the question being asked. For example, to calculate how much information could be stored in an associative memory model, the precise dynamics of the synaptic modification rule may not be important. But to understand the time course of memory acquisition it probably will be. Brenner (2010) makes the case that in biological systems, the cell is the most important element, and so this is the desired level of abstraction.

11.2.2 Sharing data and models

As more and more use is being made of experimental data by modellers, the need is increasing for neuroscience data to be freely accessible. There have been various conflicting views on this. It is often difficult and time consuming to acquire experimental data, and so people can be reluctant to share their data. In addition, for some data sets, particularly of clinical origin, there are issues of confidentiality. On the other hand, it has been argued that data generated in projects funded by public bodies should be publicly available. Many funding bodies now actively promote the sharing of high-quality data. Most journals now require their authors to share their data, either directly on request or by placing the data in a publicly accessible database. It is more difficult for modellers to obtain unpublished data, but then the question of data quality will arise. With an increased quantity and complexity of neuroscience data being available, there will be an increased demand for new methods of data analysis and presentation. Resources of data and accompanying analytical tools are now being assembled for specific areas of neuroscience.

In parallel with the trend for sharing data, computational neuroscientists are starting to share computational models. Many people develop their own models and make them freely available. Communities now exist to support users of the simulation packages NEURON and GENESIS, and developers can contribute their models to freely accessible repositories.

However, there is still a significant amount of needless duplication. This could be solved by everyone contributing their model code to agreed standards. For this to be useful, effort has to be put into making the code portable and understandable. At present the culture does not reward peoples' efforts to do so. There are initiatives that attempt to define model standards; for example, the NeuroML initiative (www.neuroml.org) aims to develop an XML-based language for devising models of nerve cells and networks of nerve cells.

One example of a collaborative data-sharing initiative is CARMEN (Code Analysis, Repository and Modelling for E-Neuroscience, www.carmen.org). This enables the sharing and exploitation of neurophysiological data, primarily of recordings of neural activity.

In the same way that published experimental databases are required to be made openly accessible, journals might consider making available the code for any published modelling paper. Such a facility might also be useful to referees.

11.2.3 Applications of computational modelling

In this book we have concentrated on using computational modelling towards gaining an understanding of the function and development of the nervous system. We anticipate that the number of application areas will increase, and here we mention just three of them.

Close integration between model and theory. There are ways in which computational modelling and experiment can be used interactively. Computer models could be run so as to provide instant feedback during the course of experiments as to how the experimental conditions should be changed. The model simulation would need to take seconds or minutes, at most. Hence the complexity of the model will be constrained by the power of the computer on which it is running. At the more specific level, the technique of dynamic clamp (Figure 4.15 in Section 4.5.1) allows the electrophysiological properties of a neuron to be investigated by injecting current into it through electrodes, with the current being calculated as the output of a model which may take measurements, such as membrane voltage, as inputs (Destexhe and Bal, 2009). This approach can be used to simulate the action of a single synapse on the neuron, or the insertion of a new ionic channel current, for example.

The modelling of clinical interventions. Simulators such as NEURON and GENESIS are ideal for use in drug-discovery studies to understand, at the cellular and network level, the effects of the application of drugs to, say, block-specific ion channels (Aradi and Érdi, 2006). Systemic effects would be more difficult to predict as models at this level remain to be established. Another type of intervention is seen in the use of deep-brain stimulation (DBS) for treatment of neurological conditions. An example of computational modelling that holds out great promise is described in Section 9.6. Continuous electrical stimulation of the subthalamic nucleus of the basal ganglia is used for the relief of Parkinsonism. Our understanding of why DBS works and how to configure it optimally will be greatly enhanced once satisfactory computational models have been developed.

Brain-machine interaction and neural prostheses. Already there are clear demonstrations that brain-derived signals can be used to drive external devices, such as computer-screen cursors and robotic arms (Lebedev and Nicolelis, 2006). Signals include EEGs and spiking from small ensembles of neurons. Models that interpret these signals are typically artificial neural networks or other machine learning algorithms. In principle, spiking neural network models could be used, provided their simulation ran in real time. This is still a significant barrier. However, such models could accept spiking inputs directly from biological neurons and produce a spiking output that could be used to stimulate downstream neurons. Such technology will open up the promise of neural prostheses, in which computer models replace damaged brain nuclei or augment brain function.

11.3 | And finally...

In comparison with the enormous leap forward in computer power that has been seen over the past 50 years, the fundamental principles of modelling in computational neuroscience have developed slowly and steadily. The increase in computing power is a double-edged sword. Whilst computers make possible new types of modelling and analysis which were unimaginable in the past, they also carry the risk of distracting us from these fundamental principles. In contrast, we feel confident that the principles of computational neuroscience that we have described in this book will be valid in 50 years time. We hope that new generations of researchers working in the neurosciences will use our book to formulate their theories precisely, express their theories as computational models and validate them through computer simulation, analysis and experiment.

Appendix A

Resources

Here is a list of resources related to computational neuroscience modelling. Most of these are resources that, at the time of writing, are available as open source software, but we cannot say for how long they will continue to be available in this way. Please refer to our web site, compneuroprinciples.org, for more up-to-date information.

A.1 Simulators

If the solution of a computational model is the evolution of a quantity, such as membrane potential or ionic concentration, over time and space, it constitutes a simulation of the system under study. Often simulated quantities change continuously and deterministically, but sometimes quantities can move between discrete values stochastically to represent, for example, the release of a synaptic vesicle or the opening and closing of an ion channel.

The process of describing and implementing the simulations of complex biophysical processes efficiently is an art in itself. Fortunately, for many of the models described in this book, in particular, models of the electrical and chemical activity of neurons, and to an extent the models of networks, this problem has been solved. An abundance of mature computer simulation packages exists, and the problem is in choosing a package and learning to use it. Here, neural simulators are described following approximately the order in which simulation techniques are described in the book:

- (1) Compartmental models of neurons and ensembles of neurons.
- (2) Models of subcellular processes.
- (3) Models of simplified models and networks of simplified neurons.
- (4) Models of developmental processes.

A.1.1 Compartmental models of neurons and ensembles of neurons

The compartmental modelling formalism is so well defined that high-quality neural simulators have been built that provide high-level (graphical) and low-level (textual commands) tools for defining a compartmental model of a neuron. This involves specifying the cell morphology and its passive and active

membrane properties. Usually it is possible to add new models of ion channels and other cellular components. In these simulators, numerical solutions of the equations specifying the voltages across the neuronal compartments are solved automatically using the best available numerical methods.

Many simulators allow the use of different levels of model for neurons. They also allow the specification and efficient simulation of networks of neurons. Parallel implementations for clusters of workstations are also available and can provide near-linear speedups for simulating networks (Goddard and Hood, 1998; Migliore *et al.*, 2006; Hines and Carnevale, 2008). Parallelisation of compartmental models of individual neurons is more difficult, but recent results indicate that good speedups can be achieved with the appropriate cell subdivision between processes (Hines *et al.*, 2008).

The following popular neural simulators are available. A review of certain simulators and their computational strategies is to be found in Brette *et al.* (2007). Given the breadth of neural simulators, being able to translate a model easily from one simulation platform to another, or to be able to use simulators with different strengths in combination, are important problems for which solutions are being developed (Cannon *et al.*, 2007).

NEURON: Cell models and their simulation are specified with the HOC scripting language, or with GUI tools. The NMODL language allows for adding new components such as new ion channel models. A large user base and many example models are freely available through ModelDB (see below). Details can be found in Carnevale and Hines (2006) and Hines and Carnevale (1997). <http://www.neuron.yale.edu>.

GENESIS: GEneral NEural SImulation System (Bower and Beeman, 1998). Similar remit and functionality to NEURON. It also has a large user base and is undergoing continual development and improvement. <http://www.genesis-sim.org>.

In addition, there are a large number of other neural simulators with similar or more restricted functionality. In alphabetical order, examples include:

HHsim: HHsim is a graphical simulation of a section of excitable neuronal membrane using the Hodgkin–Huxley equations. It provides full access to the Hodgkin–Huxley parameters, membrane parameters, stimulus parameters and ion concentrations. <http://www.cs.cmu.edu/~dst/HHsim>.

neuroConstruct: neuroConstruct (Gleeson *et al.*, 2007) automates the generation of script files for other simulation platforms, principally NEURON and GENESIS. It provides a framework for creating networks of conductance-based neuronal models, visualising and analysing networks of cells in 3D, managing simulations and analysing network firing behaviour. It uses the target platform to actually run simulations. <http://www.neuroconstruct.org>.

NEURONC: NEURONC was originally developed to model the nerve cells in the vertebrate retina. It has been extended extensively over the years and is now a general-purpose simulator for modelling a large number of nerve cells, each with a large number of compartments.

It has 3D visualisation tools for displaying networks. <http://retina.anatomy.upenn.edu/~rob/neuronc.html>.

Nodus: Nodus is a user-friendly package for simulating compartmental models of single cells, or small networks. It runs only on Apple Macintosh computers. http://www.tnb.ua.ac.be/software/nodus/nodus_info.shtml.

PSICS: Parallel Stochastic Ion Channel Simulator is designed to carry out simulation of compartmental models containing stochastic ion channels represented by kinetic schemes. PSICS computes the behaviour of neurons, taking account of the stochastic nature of ion channel gating and the detailed positions of the channels themselves. It supports representation of ion channels as kinetic schemes involving one or more serial gating complexes. PSICS is intended to be complementary to existing tools, inhabiting the space between whole-cell deterministic models as implemented in NEURON and GENESIS, and subcellular stochastic diffusion models (see MCELL, STEPS and StochSim below). <http://www.psics.org>.

SNNAP: Simulator for Neural Networks and Action Potentials is a tool for rapid development and simulation of realistic models of single neurons and neural networks. It includes mathematical descriptions of ion currents and intracellular second-messengers and ions. In addition, current flow can be simulated in compartmental models of neurons. <http://snnap.uth.tmc.edu>.

Surf-Hippo: Surf-Hippo is used to investigate morphologically and biophysically detailed compartmental models of single neurons and networks of neurons. Surf-Hippo allows ready construction of cells and networks using built-in functions and various anatomical file formats (Neurolucida, NTS and others). Surf-Hippo is a public-domain package, written in Lisp, and runs under Unix and Linux. <http://www.neurophys.biomedicale.univ-paris5.fr/~graham/surf-hippo.html>.

XNBC: XNBC is a software tool for neurobiologists to analyse simulated neurons and neural networks. Most of the cell models are abstract, but Hodgkin-Huxley models are also included. <http://www.b3e.jussieu.fr/xnbc>.

A.1.2 Models of subcellular processes

There is an increasing number of software packages available for modelling the sort of reaction or reaction-diffusion systems that have arisen throughout this book. The popular neural system simulators, GENESIS and NEURON, are both capable of being extended to handle intracellular calcium dynamics and complex signalling pathways. The **systems biology** field has spawned a number of sophisticated software packages for simulating general intracellular processes. A number of these packages and their main features are described below.

Chemesis: An add-on package to GENESIS, Chemesis (Blackwell and Hellgren Kotaleski, 2002) provides similar functionality to Kinetikit (see below), with added components to handle diffusion

between well-mixed compartments, enabling the simulation of reaction-diffusion systems. Systems are constructed using the GENESIS scripting language. <http://www.gmu.edu/departments/krasnow/CENlab/chemesis.html>.

Copasi: COnplex PAthway SImulator (Hoops *et al.*, 2006) provides deterministic, stochastic and hybrid solutions for well-mixed reaction systems. Copasi includes tools for parameter estimation and optimisation. It is platform independent. <http://www.copasi.org>.

Ecell: Ecell is similar to Copasi. Model systems can be constructed either via a scripting language or graphically (Takahashi *et al.*, 2003). A sophisticated graphical user interface is provided for both model construction and simulation. <http://www.e-cell.org>.

GEPASI: GEPASI is for modelling biochemical systems. It translates the language of chemistry (reactions) to mathematics (matrices and differential equations) in a transparent way. It simulates the kinetics of systems of biochemical reactions and provides a number of tools to fit models to data, optimise any function of the model, perform metabolic control analysis and linear stability analysis. <http://www.gepasi.org>.

Kinetikit: Kinetikit is an add-on package to GENESIS and enables the simulation of well-mixed reaction systems, with deterministic, stochastic or adaptive deterministic-stochastic methods. Systems can be constructed graphically or via the GENESIS scripting language. <http://www.genesis-sim.org>.

MCELL: MCELL is a simulator aimed at modelling reaction-diffusion systems in 3D, at the level of individual molecules using stochastic algorithms for molecular diffusion and reaction (Stiles and Bartol, 2001). Reactions can only take place between freely diffusing molecules and membrane-bound receptors. Highly realistic spatial geometries are easily handled. <http://www.mcell.psc.edu>.

MOOSE: Multiscale Object-Oriented Simulation Environment is the base and numerical core for large, detailed simulations in computational neuroscience and systems biology. MOOSE spans the range from single molecules to subcellular networks, from single cells to neuronal networks, and to still larger systems. It is backwards-compatible with GENESIS, and forwards-compatible with Python and XML-based model definition standards like SBML and MorphML. <http://moose.sourceforge.net>.

NMODL: NMODL is a programming language for adding new components to NEURON. It enables the easy specification of reaction and diffusion systems, either through specification of the rate equations or the corresponding ODEs (Carnevale and Hines, 2006). In-built solution methods for deterministic systems are provided. Stochastic algorithms can be explicitly constructed from scratch using NMODL. <http://www.neuron.yale.edu>.

STEPS: STEPS is a package for exact stochastic simulation of reaction-diffusion systems in arbitrarily complex 3D geometries. It is implemented in Python and the core simulation algorithm is an

implementation of Gillespie's SSA (Box 6.6), extended to deal with diffusion of molecules over the elements of a 3D tetrahedral mesh. Though developed for simulating detailed models of neuronal signalling pathways in dendrites and around synapses, it can be used for studying any biochemical pathway in which spatial gradients and morphology play a role. <http://steps.sourceforge.net/STEPS/Home.html>.

StochSim: StochSim is aimed at stochastic modelling of individual molecules (Le Novére and Shimizu, 2001), and handles reactions between molecules in well-mixed compartments (no diffusion). Nearest-neighbour interactions between membrane-bound molecules are also possible. <http://www.pdn.cam.ac.uk/groups/comp-cell/StochSim.html>.

VCELL: Virtual CELL simulator (Schaff *et al.*, 1997) uses finite element methods to model deterministic reaction-diffusion systems in 3D. This enables detailed modelling of intracellular geometry and the concentration gradients of molecules through this space. It is provided as a Java application over the Internet by the National Resource for Cell Analysis and Modeling. <http://www.vcell.org>.

A.1.3 Models of simplified neurons and their networks

Many simulators exist that are aimed at simulating the interactions within (possibly large-scale) networks of neurons. In these simulators, the neurons are usually represented at a fairly abstract level, such as integrate-and-fire or rate-based neurons. Amongst these are:

BRIAN: BRIAN is a simulator for spiking neural networks of integrate-and-fire or small compartment Hodgkin-Huxley neurons. It is written in Python and runs on many platforms. <http://www.briansimulator.org>.

CATACOMB2: Components And Tools for Accessible COMputer Modelling in Biology. CATAcomb 2 is a workbench for developing biologically plausible network models to perform behavioural tasks in virtual environments. <http://www.compneuro.org/catacomb>.

Emergent: Formerly PDP++, Emergent is a comprehensive simulation environment for creating complex, sophisticated models of the brain and cognitive processes using neural network models. Networks use computing units as used in artificial neural networks, which can represent rate-based neurons. Emergent includes a full GUI environment for constructing networks and the input/output patterns for the networks to process, and many different analysis tools for understanding what the networks are doing. <http://grey.colorado.edu/emergent>.

FANN: Fast Artificial Neural Network Library for simulating multi-layer networks of artificial computing units. <http://leenissen.dk/fann>.

iqr: iqr is a simulator for large-scale neural systems. It provides an efficient graphical environment to design large-scale multi-level neuronal

systems that can control real-world devices – robots in the broader sense – in real-time. <http://www.iqr-sim.net>.

LENS: The Light, Efficient Network Simulator for running artificial neural network models. <http://tedlab.mit.edu/~dr/Lens/index.html>.

NEST: NEural Simulation Technology for large-scale biologically realistic (spiking) neuronal networks. Neural models are usually point neurons, such as integrate-and-fire. <http://www.nest-initiative.org>.

NSL: The Neural Simulation Language supports neural models having as a basic data structure neural layers with similar properties and similar connection patterns, where neurons are modelled as leaky integrators with connections subject to diverse learning rules. <http://www.neuralsimulationlanguage.org>.

PCSIM: Parallel neural Circuit SIMulator is a tool for simulating networks of millions of neurons and billions of synapses. Networks can be heterogeneous collections of different model spiking point neurons. <http://www.lsm.tugraz.at/pcsim>.

A.1.4 Models of neural development

Reflecting the diversity and speciality of models of neural development (Chapter 10), associated simulation software is equally diverse and often quite specialised. However, more general-purpose developmental neural simulators are emerging that can handle models ranging from single-cell morphological development to network formation. Major examples are listed here.

CX3D: CX3D is a Java-based simulation tool for modelling the development of large realistic neural networks in a physical 3D environment (Zubler and Douglas, 2009). Java classes define neuronal morphology and the intra- and extracellular environments. New algorithms for network development can be programmed using these classes. <http://www.ini.uzh.ch/projects/cx3d>.

NETMORPH: NETMORPH is a simulator for modelling the development of large networks of morphologically realistic neurons (Koene *et al.*, 2009). Morphogenesis is based on statistical algorithms for directional outgrowth and branching of growth cones. <http://netmorph.org>.

Topographica: Topographica is a software package for computational modelling of neural maps. The goal is to help researchers understand brain function at the level of the topographic maps that make up sensory and motor systems. <http://topographica.org/Home/index.html>.

A.2 Databases

There are many online repositories storing biological models and data. Some of the most relevant to neural modelling are listed here.

A.2.1 Neural models

Computer code for models of individual neurons and networks of neurons are increasingly being made available in public repositories.

GENESIS: The GENESIS site hosts a number of example models built and run in GENESIS. <http://www.genesis-sim.org/models>.

Izhikevich IF: Izhikevich has some very simple MATLAB implementations of his IF model, including network simulations, on his website at: <http://vesicle.nsi.edu/users/izhikevich/publications/spikes.htm>.

ModelDB: ModelDB is a well-supported repository for published neural models, hosted by Yale University. Most entries have been developed in the NEURON simulator, but other codes are also represented, including GENESIS, XPPAUT and others. <http://senselab.med.yale.edu/senselab/modedb>.

A.2.2 Cell morphologies

There are also repositories of morphological reconstructions of biological neurons that are suitable for use in modelling studies.

Claiborne Lab: Claiborne Lab is a database of reconstructed cells from hippocampus. <http://www.utsa.edu/claibornelab>.

Hippocampal Neuronal Morphology: Hippocampal Neuronal Morphology Duke-Southampton archive of reconstructed hippocampal cells. It comes with morphology editing and viewing software, Cvapp. <http://www.compneuro.org/CDROM/nmorph/cellArchive.html>.

NeuroMorpho: NeuroMorpho is a large database (over 5000 cells) of digitally reconstructed neurons. <http://NeuroMorpho.org>.

VNED: Virtual Neuromorphology Electronic Database is a collection of reconstructed cells and model-generated cells of many different types. <http://krasnow.gmu.edu/cn3/L-Neuron/database/index.html>.

A.2.3 Cell signalling models and data

Repositories of cell signalling pathway models are available. Certain data relevant to the specification of parameter values in such models are also available. Protein interaction databases are useful for developing signalling schemes. Typically, little reaction-rate data is available. Enzymatic kinetics are generally more readily available.

Biomodels.net: Biomodels.net has published cell signalling models for a variety of simulation environments. Links to associated data sources are provided. Models can be run online via the simulation environment JWS Online (<http://jjj.biochem.sun.ac.za/index.html>). <http://www.ebi.ac.uk/biomodels>.

BJP Guide to Receptors and Channels: The BJP Guide provides an overview of receptors and channels with bibliographies for each channel subfamily. <http://www.nature.com/bjp/journal/vgrac/ncurrent>.

DOQCS: The Database of Quantitative Cellular Signalling contains models of signalling pathways, largely built using GENESIS and Kinetikit. It includes reaction schemes, concentrations and rate constants. <http://doqcs.ncbs.res.in>.

IUPHAR databases: The IUPHAR Database of G-Protein-Coupled Receptors and the IUPHAR Database of Voltage-Gated and Ligand-Gated Ion Channels contain information about the gene sequences, structural and functional characteristics and pharmacology of ion channels. They are available from the database of the IUPHAR Committee on Receptor Nomenclature and Drug Classification. <http://www.iuphar-db.org>.

A.2.4 Data analysis tools

Colquhoun's analysis programs: A suite of programs, developed by David Colquhoun and coworkers (Colquhoun *et al.*, 1996), which analyse single-channel data to determine opening and closing times, and then find the maximum likelihood fit of the kinetic scheme to the open and close time distributions. <http://www.ucl.ac.uk/Pharmacology/dcpr95.html>.

QuB: QuB is an alternative suite of programs to the Colquhoun programs, which use a different algorithm (Qin *et al.*, 1996) to infer kinetic scheme parameters from single-channel data. <http://www.qub.buffalo.edu>.

A.3 General-purpose mathematical software

The software packages in the preceding lists are all geared to simulating or analysing specific systems, although some of the packages have other capabilities. However, there are many tasks, such as customised data analysis and graph plotting, or simulating particular systems of differential equations for which more general-purpose mathematical software is required. For ultimate flexibility and speed, programming languages such as C, C++ and FORTRAN can be employed, but the time and skills required to learn and develop in these languages can be prohibitive.

Here, we present an alphabetical list of general-purpose mathematical software that has the following characteristics:

- They can be used interactively, by typing in commands and/or using a graphical interface.
- Sequences of commands can be stored to file to create scripts, which can then be run as programs.
- They can all plot 2D and 3D graphs, and plot other data.

AUTO: The grandparent of packages such as XPPAUT, PyDSTool and MatCont (see below), AUTO is dedicated to generating bifurcation diagrams using numerical continuation. It has a command-line interface in Python, but is probably more easily accessed via one of the other packages. <http://indy.cs.concordia.ca/auto>.

MatCont: MatCont is a freely available MATLAB (see below) software package for analysing dynamical systems using numerical continuation to create bifurcation diagrams. <http://sourceforge.net/projects/matcont>.

MATLAB: MATLAB® is a commercially available software package designed for numerical computations and data visualisation in science and engineering. MathWorks sell many additional toolboxes, including ones for statistics. There are also many contributed packages available, including a number with neuroscience applications. The graphics are interactive. It is available for Linux, Windows and MacOS. MATLAB is included in this list because of its wide use, even though it is not open source. <http://www.mathworks.com>.

OCTAVE: GNU Octave is an open source software environment, primarily intended for numerical computations. Its language is mostly compatible with MATLAB. It includes routines for solving sets of coupled ODEs and optimisation. It is available for Linux, Windows and MacOS. <http://www.gnu.org/software/octave>.

PyDSTool: PyDSTool is a developing open source integrated simulation, modelling and analysis package for dynamical systems, based on the SciPy package (see below). As well as solving systems of ODEs, it can be used to create bifurcation diagrams using numerical continuation. <http://www.cam.cornell.edu/~rclewley/cgi-bin/moin.cgi>.

R: Officially known as the *R project for statistical computing*, R is an open source software environment designed for statistical computing and graphics, which can be used as a general-purpose mathematical tool. It includes optimisation functions, and there is a wide array of contributed packages, including for solving sets of coupled differential equations. While the graphics capabilities are impressive, it is not possible to use the mouse to interact with plots, e.g. zooming in to a region of the data, though efforts are underway to make this possible. It is available for UNIX platforms, Windows and MacOS. <http://www.r-project.org>.

SciPy: Short for ‘Scientific Tools for Python’, SciPy is an open source software environment for mathematics and science implemented in the Python programming language. SciPy provides many numerical routines including ones for optimisation. The graphics are interactive. It is available for Linux, Windows and MacOS. <http://www.scipy.org>.

XPPAUT: XPPAUT is a general equation solver (Ermentrout, 2002). It allows easy definition and numerical solution of the systems of ODEs that arise in compartmental modelling. It is particularly useful for simulating reduced neuronal models such as Morris–Lecar and Fitzhugh–Nagumo, and examining phase plane plots of cell dynamics. It can also be used to create bifurcation diagrams using numerical continuation. It is available for Linux, Windows and MacOS. <http://www.math.pitt.edu/~bard/xpp/xpp.html>.

Appendix B

Mathematical methods

B.1 Numerical integration methods

Most of the mathematical models presented in this book involve differential equations describing the evolution in time and space of quantities such as membrane potential or calcium concentration. The differential equations are usually too complex to allow an analytical solution that would enable the explicit calculation of a value of, say, voltage at any particular time point or spatial position. The alternative is to derive algebraic expressions that approximate the differential equations and allow the calculation of quantities at specific, predefined points in time and space. This is known as numerical integration. Methods for defining temporal and spatial grid points and formulating algebraic expressions involving these grid points from the continuous (in time and space) differential equations are known as **finite difference** and **finite element methods**.

It is not our intention here to provide full details of these numerical integration methods. Instead, we will outline some of the simplest methods to illustrate how they work. This includes the Crank–Nicholson method (Crank and Nicholson, 1947), which is widely used as a basis for solving the cable equation. Further details on these methods as applied to neural models can be found in Carnevale and Hines (2006) and Mascagni and Sherman (1998).

B.1.1 Ordinary differential equations

We consider an ODE for the rate of change of membrane voltage:

$$\frac{dV}{dt} = f(V, t) \quad (\text{B.1})$$

for some function f of voltage and time. A particular example is the equation that describes the response of a patch of passive membrane to an injected current (Equation 2.16):

$$C_m \frac{dV}{dt} = \frac{E_m - V}{R_m} + \frac{I_e}{a}. \quad (\text{B.2})$$

As we saw in Chapter 2, if we assume that at time 0 that $V = E_m$ and I_e is switched from 0 to a finite value at this time and then held constant, this equation has an analytical solution:

$$V = E_m + (R_m I_e / a) [1 - \exp(-t / R_m C_m)]. \quad (\text{B.3})$$

In general, an ODE cannot be solved analytically. We now consider how numerical approximations can be derived and solved for ODEs. We compute numerical solutions to Equation B.2 to illustrate how approximate and exact solutions can differ.

These numerical solutions are derived from algebraic equations that approximate the time derivative of the voltage. In combination with the function f , this enables the approximate calculation of the voltage at predefined time points. The **forward Euler method** estimates the time derivative at time t as the slope of the straight line passing through the points $(t, V(t))$ and $(t + \Delta t, V(t + \Delta t))$, for some small time-step Δt :

$$\frac{dV}{dt} \approx \frac{V(t + \Delta t) - V(t)}{\Delta t}. \quad (\text{B.4})$$

This is known as a **finite difference method**, because it is estimating a quantity, the rate of change of voltage, that changes continually with time, using a measured change over a small but finite time interval Δt . How accurate this estimation is depends on how fast the rate of change of V is at that time. It becomes more accurate the smaller Δt is. For practical purposes in which we wish to calculate V at very many time points over a long total period of time, we want to make Δt as large as possible without sacrificing too much accuracy. Substituting this expression into our original Equation B.1 gives:

$$\frac{V(t + \Delta t) - V(t)}{\Delta t} = f(V(t), t). \quad (\text{B.5})$$

Rearranging, we arrive at an expression that enables us to calculate the voltage at time point $t + \Delta t$, given the value of the voltage at time t :

$$V(t + \Delta t) = V(t) + f(V(t), t)\Delta t. \quad (\text{B.6})$$

Suppose we start at time 0 with a known voltage $V(0) \equiv V^0$. We can use this formula to calculate iteratively the voltage at future time points Δt , $2\Delta t$, $3\Delta t$ and so on. If $t = n\Delta t$ and we use the notation $V^n \equiv V(t)$ and $V^{n+1} \equiv V(t + \Delta t)$, then:

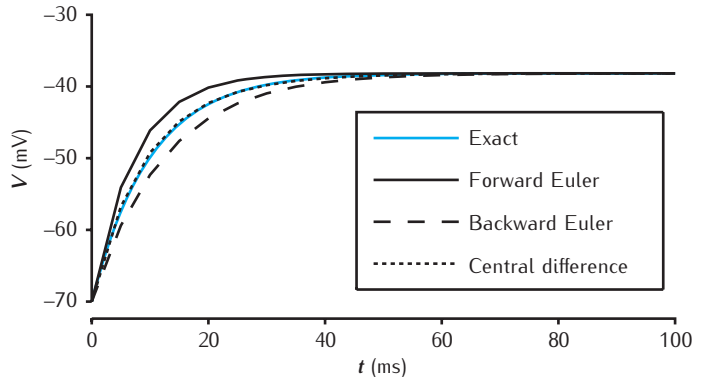
$$V^{n+1} = V^n + f(V^n, n\Delta t)\Delta t. \quad (\text{B.7})$$

For our example of the patch of passive membrane, this approximation is:

$$V^{n+1} = V^n + \frac{\Delta t}{C_m} \left(\frac{E_m - V^n}{R_m} + \frac{I_e^n}{a} \right). \quad (\text{B.8})$$

This approximation has first order accuracy in time, because the local error between the calculated value of V and its true value is proportional to the size of the time-step Δt . A comparison of this method with the exact solution for the voltage response to an injected current is shown in Figure B.1. A rather large value of 5ms for Δt is used to illustrate that this is only an

Fig. B.1 Comparison of finite difference approximations with the exact solution to current injection in passive membrane. The exact solution is plotted every 0.1 ms; the approximations use $\Delta t = 5$ ms.



approximation. If a time-step of less than 1 ms is used, then the approximation is virtually indistinguishable from the exact solution.

Other finite difference schemes can be more accurate for a given time-step and also more stable; the error grows but remains within finite bounds as the step size is increased. The **backward Euler method** is an example of a so-called implicit method that is also first order accurate in time, but is more stable than the forward Euler method. It results from using a past time point, rather than a future time point, in the approximation of the time derivative:

$$\frac{dV}{dt} \approx \frac{V(t) - V(t - \Delta t)}{\Delta t}. \quad (\text{B.9})$$

The full ODE is thus approximated as:

$$\frac{V(t) - V(t - \Delta t)}{\Delta t} = f(V(t), t). \quad (\text{B.10})$$

Shifting this to the same time points as the forward Euler method yields:

$$\frac{V(t + \Delta t) - V(t)}{\Delta t} = f(V(t + \Delta t), t + \Delta t). \quad (\text{B.11})$$

Now both left- and right-hand sides involve the unknown voltage at the time point $t + \Delta t$. Using the notation for iterative time points, for our example we have:

$$C_m \frac{V^{n+1} - V^n}{\Delta t} = \frac{E_m - V^{n+1}}{R_m} + \frac{I_e^{n+1}}{a}. \quad (\text{B.12})$$

Fortunately, as for the forward Euler expression, this can be rearranged to give an explicit, but now slightly different, equation for V^{n+1} :

$$V^{n+1} = \left[V^n + \frac{\Delta t}{C_m} \left(\frac{E_m}{R_m} + \frac{I_e^{n+1}}{a} \right) \right] / \left(1 + \frac{\Delta t}{R_m C_m} \right). \quad (\text{B.13})$$

For the same time-step, this method tends to underestimate the rate of change in voltage in our example (Figure B.1), whereas the forward Euler approximation overestimates it. Consequently, the backward Euler method produces an approximation that smoothly approaches and never overshoots the final steady state value of V . For large step sizes, the forward Euler method may produce values of V that are greater than the steady state,

leading to oscillations in V around this value. Such oscillations are not seen in the exact solution and are not desirable in a good approximation.

Note that in more complex models in which several related variables are being solved for, the backward Euler method will result in a set of equations that need to be solved simultaneously. Consequently, the backward Euler method is known as an **implicit method**. We will see this below for approximations to the cable equation. In contrast, with the forward Euler method, values at future time points of all variables can be calculated directly from values at known time points. The forward Euler method is an example of an **explicit method**.

A third method, which is both more accurate and stable than these Euler methods, is the **central difference** method, in which the time derivative is estimated from a future and a past value of the voltage:

$$\frac{dV}{dt} \approx \frac{V(t + \Delta t) - V(t - \Delta t)}{2\Delta t}. \quad (\text{B.14})$$

By examining the equations for the Euler methods, it should be clear that this method results by taking the average of the forward and backward Euler approximations. If we use the expression for the backward Euler method involving the future voltage, $V(t + \Delta t)$, then the ODE is approximated by:

$$\frac{V(t + \Delta t) - V(t)}{\Delta t} = \frac{1}{2} [f(V(t + \Delta t), t + \Delta t) + f(V(t), t)]. \quad (\text{B.15})$$

That is, we now take an average of the forward and backward Euler right-hand sides. For our example this leads to the expression:

$$C_m \frac{V^{n+1} - V^n}{\Delta t} = \frac{1}{2} \left(\frac{E_m - V^n}{R_m} + \frac{I_e^n}{a} + \frac{E_m - V^{n+1}}{R_m} + \frac{I_e^{n+1}}{a} \right). \quad (\text{B.16})$$

This can be rearranged to give an explicit expression for V^{n+1} . This approximation is accurate, even for the rather large time-step of 5 ms (Figure B.1). The central difference method is **second order** accurate in time because the error is proportional to the square of the step size Δt .

The choice of time-step depends critically on how rapidly the quantity of interest, such as membrane voltage, is changing. When simulating action potentials, a small time-step is required, on the order of 10–100 μs , to capture accurately the rapid rise and fall of the action potential. In between action potentials, however, a neuron may sit near its resting potential for a long period. During this time the small time-step is unnecessary. Variable time-step integration methods have been developed to account for just this sort of situation. The time-step is automatically increased when a variable is only changing slowly, and decreased when rapid changes begin. These methods can drastically decrease the computation time required and are available in certain neural simulators, such as NEURON (Carnevale and Hines, 2006).

B.1.2 Partial differential equations

These same methods can be used for the temporal discretisation of PDEs, but now the spatial dimension must also be discretised. Let us consider the cable equation (Section 2.9) for voltage spread along a neurite of uniform diameter d :

$$C_m \frac{\partial V}{\partial t} = \frac{E_m - V}{R_m} + \frac{d}{4R_a} \frac{\partial^2 V}{\partial x^2} + \frac{I_e(x)}{\pi d}. \quad (\text{B.17})$$

This involves the first derivative of V with respect to time, but the second derivative of V with respect to space. Consequently, a second order central difference method involving values at three different spatial grid points is required to discretise the spatial dimension:

$$\frac{\partial^2 V}{\partial x^2} \approx \frac{V(x + \Delta x) - 2V(x) + V(x - \Delta x)}{(\Delta x)^2} \quad (\text{B.18})$$

for a small spatial step Δx . If we use the notation that position x is the midpoint of compartment j , $x + \Delta x$ corresponds to compartment $j + 1$, $x - \Delta x$ to $j - 1$, and the length of each compartment is $l = \Delta x$, then this is identical to the compartmental structure introduced in Chapter 2. Using this notation and the above spatial discretisation, the forward Euler numerical approximation to the full cable equation is:

$$C_m \frac{V_j^{n+1} - V_j^n}{\Delta t} = \frac{E_m - V_j^n}{R_m} + \frac{d}{4R_a} \frac{V_{j+1}^n - 2V_j^n + V_{j-1}^n}{l^2} + \frac{I_{e,j}^n}{\pi d l}. \quad (\text{B.19})$$

To make clear the compartmental structure and enable all our equations to fit on one line so they are easy to read, now we will assume that the injected current is zero in compartment j , $I_{e,j}^n = 0$, so we can remove this term. We can rewrite Equation B.19 to indicate explicitly the current flow between compartments:

$$C_m \frac{V_j^{n+1} - V_j^n}{\Delta t} = \frac{E_m - V_j^n}{R_m} + \frac{c}{R_a} (V_{j+1}^n - V_j^n) + \frac{c}{R_a} (V_{j-1}^n - V_j^n), \quad (\text{B.20})$$

where we define a coupling coefficient c between compartments as the cross-sectional area between compartments divided by the surface area of a compartment multiplied by the length l between compartments:

$$c \equiv \frac{\pi d^2}{4} \frac{1}{\pi d l} = \frac{d}{4l^2}. \quad (\text{B.21})$$

Rearranging Equation B.20, we arrive at an expression for the voltage V_j^{n+1} in compartment j at time-step $n + 1$ as a function of the values of the voltage at the previous time-step n in compartment j and in its two neighbours, $j - 1$ and $j + 1$:

$$V_j^{n+1} = V_j^n + \frac{\Delta t}{C_m} \left(\frac{E_m - V_j^n}{R_m} + \frac{c}{R_a} (V_{j+1}^n - V_j^n) + \frac{c}{R_a} (V_{j-1}^n - V_j^n) \right). \quad (\text{B.22})$$

The backward Euler method uses the same spatial discretisation, but with values of V at time point $n + 1$ on the right-hand side:

$$C_m \frac{V_j^{n+1} - V_j^n}{\Delta t} = \frac{E_m - V_j^{n+1}}{R_m} + \frac{c}{R_a} (V_{j+1}^{n+1} - V_j^{n+1}) + \frac{c}{R_a} (V_{j-1}^{n+1} - V_j^{n+1}). \quad (\text{B.23})$$

To solve this, we rearrange it so that all unknown quantities are on the left-hand side and all known quantities are on the right:

$$-a V_{j-1}^{n+1} + b V_j^{n+1} - a V_{j-1}^{n+1} = V_j^n + \frac{\Delta t E_m}{C_m R_m}, \quad (\text{B.24})$$

where $a = \Delta t c / C_m R_a$ and $b = 1 + 2a + \Delta t / C_m R_m$. This gives a set of equations involving values of V at the new time $n + 1$, but at different spatial points along a cable, that must be solved simultaneously:

$$\mathbf{A}\mathbf{V}^{n+1} = \mathbf{B}, \quad (\text{B.25})$$

where \mathbf{A} is a tridiagonal matrix with entries, $A_{j,j} = b$, $A_{j,j-1} = A_{j,j+1} = -a$ and all other entries are zero. The entries in the vector \mathbf{B} are the right-hand side of Equation B.24.

A more stable and accurate method for this form of PDE is the Crank–Nicholson method (Crank and Nicholson, 1947), which uses central differences for both the temporal and spatial discretisations. As with the ODE, this results from taking the right-hand side to be the average of the forward and backward Euler approximations. As for the backward Euler method, this yields a system of equations involving values for voltage at the new time point in all compartments, which must be solved simultaneously.

Another aspect of calculating a solution to the cable equation is specifying the initial value of V at each spatial point and the boundary conditions that specify what happens at the end of the cable, where one of the grid points, $j + 1$ or $j - 1$, will not exist. When simulating a compartmental model of a neuron, the initial values are usually the resting membrane potentials, which may differ throughout a neuron due to differences in ionic currents. Sealed end boundary conditions are assumed to apply, meaning that the spatial derivative of V is zero at the end of each neurite. Specifying a value for the spatial derivative is known as a Neumann boundary condition. This can be easily incorporated into the discrete equations. Suppose our first spatial grid point is 0. The central difference formula for the spatial derivative at this point is:

$$\frac{\partial V(0)}{\partial x} \approx \frac{(V_1 - V_{-1})}{2\Delta x} = 0. \quad (\text{B.26})$$

This gives us $V_{-1} = V_1$, and we replace $V_1^n - 2V_0^n + V_{-1}^n$ with $2V_1^n - 2V_0^n$ for that compartmental equation.

Choosing an appropriate spatial step size for a neural model can be tricky. Possible approaches are dealt with in Chapter 4.

B.2 | Dynamical systems theory

In mathematics, any system of equations that describes how the state of a system changes through time is called a **dynamical system**. A simple example of a dynamical system is the movement of a pendulum, where the state can be described by one variable, the angle of the pendulum. A more complex example is the Lotka–Volterra model (Lotka, 1925; Volterra, 1926). As discussed in Chapter 1 (Figure 1.1), this model describes how two state variables – the numbers of predators and their prey – change over time. Almost all the neuron models encountered in this book are dynamical systems. The models which incorporate active channels have at least four state variables, and multi-compartmental models may have hundreds.

Dynamical systems of all sizes have a number of characteristic behaviours. The state variables may reach a stationary state, such as when a pendulum is at rest. The system may behave periodically; for example, a moving pendulum or the oscillating populations of predator and prey that can occur in the Lotka–Volterra model. There may be conditions under which **aperiodic**, or **chaotic** behaviour occurs. **Dynamical systems theory** is the area of applied mathematics that seeks to determine under what conditions the various types of behaviour are exhibited.

Box B.1 Morris–Lecar model

I_e is the injected current

I_i is the ionic current, comprising fast Ca^{2+} , slow K^+ and leak

m_∞ is the Ca^{2+} activation variable

w is the K^+ activation variable

w_∞ is the steady state K^+ activation

τ_w is the K^+ activation time constant

ϕ is the temperature/time scaling

$$C_m \frac{dV}{dt} = -I_i(V, w) + I_e$$

$$\frac{dw}{dt} = \frac{w_\infty(V) - w}{\tau_w(V)}$$

$$I_i(V, w) = \bar{g}_{\text{Ca}} m_\infty(V)(V - E_{\text{Ca}}) + \bar{g}_K w(V - E_K) + g_L(V - E_L)$$

$$m_\infty(V) = 0.5(1 + \tanh((V - V_1)/V_2))$$

$$w_\infty(V) = 0.5(1 + \tanh((V - V_3)/V_4))$$

$$\tau_w(V, w) = \phi / \cosh((V - V_3)/(2V_4))$$

Parameters:

$$C_m = 20 \mu\text{F cm}^{-2} \quad E_{\text{Ca}} = 120 \text{ mV} \quad \bar{g}_{\text{Ca}} = 47.7 \text{ mS cm}^{-2}$$

$$\phi = 0.04 \quad E_K = -84 \text{ mV} \quad \bar{g}_K = 20.0 \text{ mS cm}^{-2}$$

$$E_L = -60 \text{ mV} \quad g_L = 0.3 \text{ mS cm}^{-2}$$

Type I parameters: $V_1 = -1.2 \text{ mV}$, $V_2 = 18.0 \text{ mV}$, $V_3 = 12.0 \text{ mV}$, $V_4 = 17.4 \text{ mV}$

Type II parameters: $V_1 = -1.2 \text{ mV}$, $V_2 = 18.0 \text{ mV}$, $V_3 = 2.0 \text{ mV}$, $V_4 = 30.0 \text{ mV}$

This section aims to give a very brief and accessible introduction to concepts in dynamical systems theory, and to show its relevance to neuron models by applying it to the Morris–Lecar model (Box B.1), introduced in Section 8.1.3. Dynamical systems theory has been applied to other neuron models with two state variables; the Morris–Lecar model has been chosen because it is particularly useful for illuminating the mechanisms underlying Type I and Type II firing (Section 8.1.3).

There are many different kinds of dynamical systems, and so it is worth bearing in mind that the theory has applications beyond analysing individual neurons. Networks of neurons are dynamical systems, and it is possible to simplify them and formulate them in terms of coupled differential equations, allowing dynamical systems theory to be applied. A notable example is the **Wilson–Cowan oscillator**, the set of equations used by Wilson and Cowan (1972) to describe a network of coupled populations of excitatory and inhibitory neurons. A similar set of equations due to Amit and Brunel (1997a) is presented in Box 9.6. Wilson (1999) and Izhikevich (2007) provide many more examples of dynamical systems theory in the context of neuroscience.

In the interests of accessibility, there are no equations in the main text of this section. A minimal overview of the mathematics is given in Box B.2. The

Box B.2 | Stability analysis

Whether an equilibrium point is stable or unstable can be determined by considering small perturbations of the state variables from the equilibrium point. In general, the equations of a 2D system of differential equations can be written

$$\begin{aligned}\frac{dV}{dt} &= f(V, w) \\ \frac{dw}{dt} &= g(V, w),\end{aligned}$$

where $f(V, w)$ and $g(V, w)$ are given non-linear functions.

At an equilibrium point (V_0, w_0) , the two derivatives are equal to zero, so $f(V_0, w_0) = g(V_0, w_0) = 0$. At a point $(V_0 + \Delta V, w_0 + \Delta w)$ close to the equilibrium point, the Taylor expansion of $f(V, w)$ is:

$$f(V_0 + \Delta V, w_0 + \Delta w) \approx f(V_0, w_0) + \frac{\partial f}{\partial V} \Delta V + \frac{\partial f}{\partial w} \Delta w = \frac{\partial f}{\partial V} \Delta V + \frac{\partial f}{\partial w} \Delta w,$$

where $\partial f/\partial V$ and $\partial f/\partial w$ are evaluated at (V_0, w_0) . There is a similar Taylor expansion for $g(V, w)$, and using these expansions allows the differential equations to be linearised:

$$\frac{d\Delta V}{dt} \approx \frac{\partial f}{\partial V} \Delta V + \frac{\partial f}{\partial w} \Delta w \quad (\text{a})$$

$$\frac{d\Delta w}{dt} \approx \frac{\partial g}{\partial V} \Delta V + \frac{\partial g}{\partial w} \Delta w. \quad (\text{b})$$

The general solution of Equations (a) and (b) is:

$$\Delta V = Ae^{\lambda_1 t} + Be^{\lambda_2 t}$$

$$\Delta w = Ce^{\lambda_1 t} + De^{\lambda_2 t},$$

where A, B, C, D, λ_1 and λ_2 are constants. λ_1 and λ_2 are eigenvalues of the matrix:

$$\begin{pmatrix} \frac{\partial f}{\partial V} & \frac{\partial f}{\partial w} \\ \frac{\partial g}{\partial V} & \frac{\partial g}{\partial w} \end{pmatrix}.$$

This matrix is called the Jacobean matrix of Equations (a) and (b). The real parts, \Re , of the eigenvalues determine stability as follows:

$\Re(\lambda_1) < 0, \Re(\lambda_2) < 0$: stable equilibrium

$\Re(\lambda_1) > 0, \Re(\lambda_2) > 0$: unstable equilibrium

$\Re(\lambda_1) < 0, \Re(\lambda_2) > 0$ (or vice versa): saddle node.

Real parts also determine the speed towards or away from the equilibrium. Imaginary parts determine the speed at which the trajectory circles around the point. At a point where there are one or two eigenvalues with zero real parts, there is a bifurcation.

more mathematically minded may wish to consult Edelstein-Keshet (1988), who gives more details of the mathematics of bifurcations applied to biological problems, or Hale and Koçak (1991), who provide a more comprehensive and general treatment.

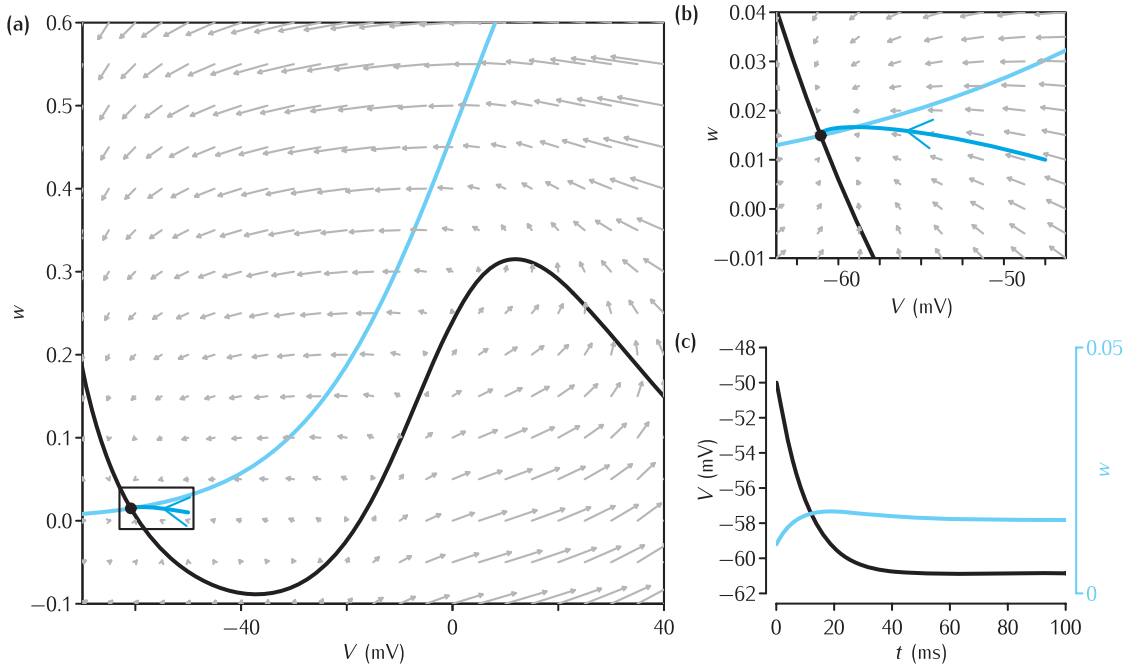


Fig. B.2 Phase plane analysis of Morris–Lecar neurons with Type II parameters and no injected current ($I_e = 0 \text{ mA cm}^{-2}$).

(a) The phase plane of the Morris–Lecar model. The dark blue line with an arrow on it shows a trajectory in the phase space, which ends at the stable node, denoted by the black solid circle. The solid black line is the V -nullcline and the light blue line is the w -nullcline. The rectangle highlights the portion of the phase plane that is shown in (b). This highlights the stable equilibrium point

$$V = -60.85 \text{ mV}, w = 0.014926.$$

(c) The time course of V (black line) and w (blue line) corresponding to the trajectory shown in (a). Note that V and w settle to steady values of -60.9 mV and 0.0149 , respectively, corresponding to their values at the equilibrium point in the phase plot.

B.2.1 The phase plane

The beauty of dynamical systems with two state variables is that they can be visualised using a plot called the **phase plane**. In a phase plane, each axis corresponds to one of the state variables – here V and w . Thus, each point in the phase plane represents a possible state (V, w) of the system. The word ‘phase’ is sometimes used instead of ‘state’, leading to the term ‘phase plane’. Figure B.2a shows the phase plane of the Morris–Lecar model with a set of parameters, $V_1 – V_4$, that give Type II behaviour (Box B.1, Figure 8.3), and with the injected current parameter set to zero, $I_e = 0 \text{ mA cm}^{-2}$. There are three types of information contained in this phase plane: a **trajectory** (the solid line with the arrow on it), an **equilibrium point** (solid circle at the end of the trajectory), arrows arranged in a grid indicating the **direction field** and two **nullclines** (the blue lines). Each type of information will now be described.

Trajectory and equilibrium point

The trajectory shows how the state of the system (V, w) changes as the system evolves through time. The trajectory shown in Figure B.2a corresponds to the time courses of V and w obtained by numerical solution of the Morris–Lecar equations shown in Figure B.2c. Given different initial conditions for V and w , the values of V and w at first change, but then move towards stable values V_0 and w_0 . In the phase plane this is drawn by taking the pair of values at each point in time and then plotting them against each other. It can be seen from the close-up in Figure B.2b that the trajectory ends at the pair of values (V_0, w_0) . This point is called the equilibrium

point, though it may also be referred to as a **node**, **steady state** or **singular point**.

Direction field

The direction field shows the direction in which the state of the system tends to move. It can be seen in the close up in Figure B.2b that the trajectory follows the flow suggested by the direction field. The x component of each arrow plotted in the direction field is proportional to the derivative dV/dt for the values of V and w upon which the arrow is anchored, and the y component of the arrow is proportional to dw/dt . Thus the direction of the arrow shows which direction the values of V and w will move in at that point in phase space, and the length of the arrow indicates how fast it will do so. The direction field gives a feel for the behaviour of the system, but to avoid clutter it is usually not plotted on phase planes.

Nullclines

Nullclines are defined as points where a derivative is zero. The blue line in Figure B.2a is the w -nullcline, which shows which combinations of w and V give $dw/dt = 0$. The black line is the V -nullcline, where $dV/dt = 0$. The nullclines intersect at the equilibrium point, because if the state of the system is at that point, it will not change as both derivatives are zero. In the case of the Morris-Lecar neuron, the w -nullcline is the same as the steady state activation curve for w (Figure 8.3e) since $dw/dt = 0$ when $w = w_\infty(V)$. The V -nullcline is obtained by setting the left-hand side of the equation for dV/dt in Box B.1 equal to zero and rearranging the resulting equation to obtain w in terms of V .

B.2.2 Stability and limit cycles

In the enlargement of the phase plane around the equilibrium point (Figure B.2b), the direction of the arrows suggests that, had the state of the system been started from any point close to the equilibrium point, the state of the system would be drawn inexorably towards the equilibrium point. This arrangement of arrows means that the equilibrium point is **stable**. Like a ball sitting at the bottom of a valley, if the state is moved slightly it will return to the point of zero gradient.

Figure B.3a shows how the phase plane changes when a constant current of $I_e = 0.15 \text{ mA cm}^{-2}$ is injected. The position of the w -nullcline is the same as in Figure B.2a, but the V -nullcline has been shifted upwards and to the right, and there is a corresponding change in the direction field. There is still only one intersection between the nullclines. This intersection is an equilibrium point, but in contrast to Figure B.2, it is **unstable**; this is denoted by an open circle rather than a solid one. The enlargement of the phase plane around the equilibrium point (Figure B.3b) shows the arrows of the direction field pointing away from the equilibrium point. Like a ball at the top of a hill, if the state is exactly on the equilibrium point it stays there. If the state is displaced even slightly from the equilibrium point, it will move away from the equilibrium point, just as the ball would start to roll down the hill if tapped.

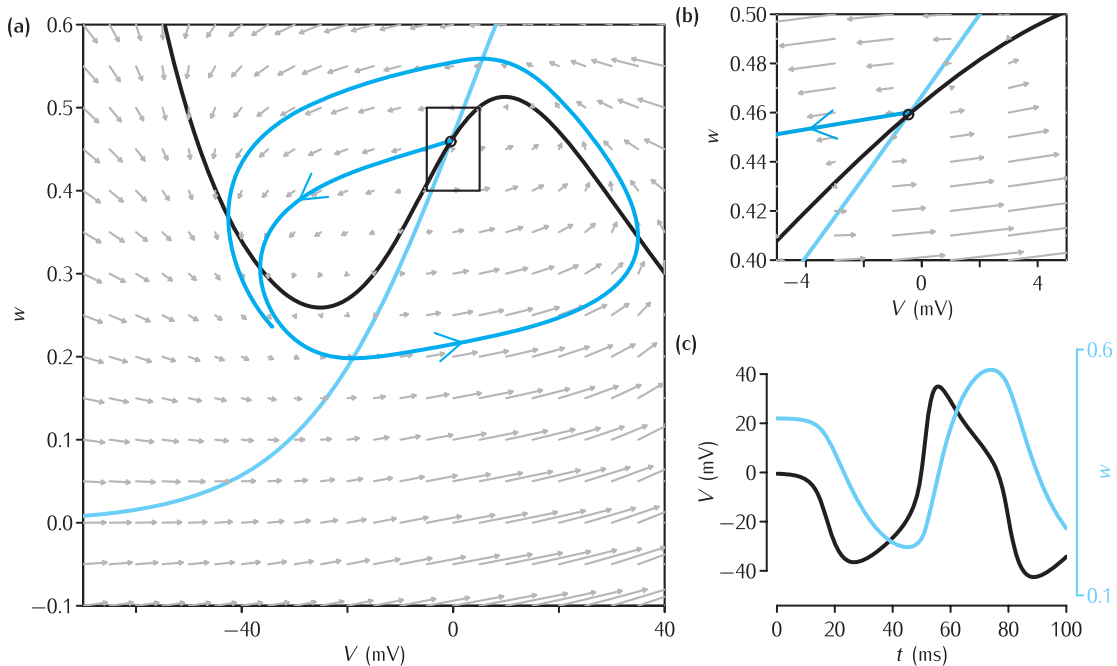


Fig. B.3 Phase plane analysis of Morris–Lecar neurons with Type II parameters with injected current ($I_e = 0.15 \text{ mA cm}^{-2}$). Panels (a–c) correspond to Figure B.2a–c. In this case the node is unstable rather than stable. This unstable node is denoted by an unfilled circle.

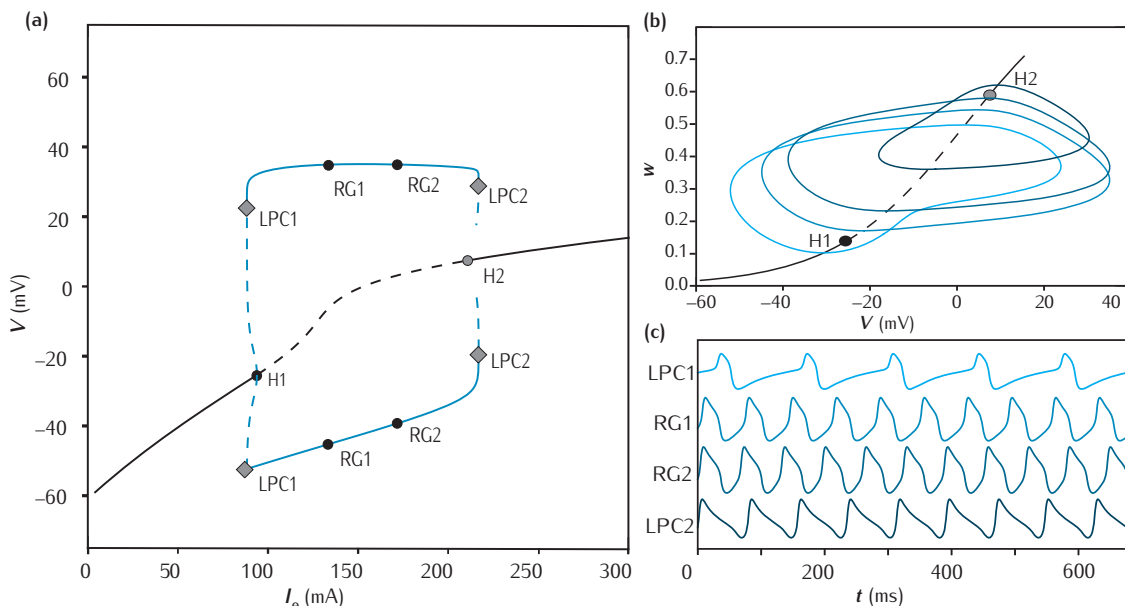
The trajectory plotted in Figure B.3a, b shows the state moving away from the equilibrium point. In this case, once the state has moved away from the equilibrium point, it never finds another such point. Instead, it starts to circle around the equilibrium point; this type of behaviour is called a **limit cycle**. Each loop of the state around the cycle corresponds to one period of oscillation. In neurons, each oscillation corresponds to an action potential and the recovery period (Figure B.3c).

Rather than plotting the direction field, it is possible to determine mathematically whether a given equilibrium point is stable or unstable (Box B.2). However, because of the non-linearity of the equations, it is generally not possible to compute the trajectory of the limit cycle analytically. However, for dynamical systems with two state variables, the **Poincaré–Bendixson theorem** (Hale and Koçak, 1991) sets out conditions under which limit cycles are guaranteed to exist.

B.2.3 Bifurcations

Suppose that the injected current starts out at zero, and is then increased very gradually. As this happens, the V -nullcline will gradually shift its position from that in Figure B.2 to that in Figure B.3. There will always be an equilibrium point where the nullclines intersect, and for low values of injected current it will be stable. However, for some threshold level of injected current, the equilibrium point will change abruptly from being stable to unstable. This abrupt change in behaviour is called a **bifurcation**. The parameter that is changed so as to induce the bifurcation, in this case the injected current I_e , is called the **bifurcation parameter**.

Bifurcations come in many varieties, depending on exactly how the equilibrium point moves from being stable to unstable. In this case, when the



bifurcation parameter passes through the bifurcation point, the behaviour of the system goes from being in equilibrium to being in a limit cycle with a non-zero frequency, making the f - I curve a Type II curve (Figure 8.3h).

A **bifurcation diagram** is a summary of the types of behaviour a system exhibits. The bifurcation diagram for the Morris–Lecar neuron with the parameters used so far is given in Figure B.4a. It has been generated by solving the Morris–Lecar equations using the method of **numerical continuation** (Krauskopf *et al.*, 2007), which is implemented in several software packages (Appendix A.3). The bifurcation parameter I_e is on the x -axis and one of the state variables, V , is on the y -axis.

Starting with values of I_e to the left of point H1 in Figure B.4a, the solid line shows the equilibrium value of V for a particular value of I_e . The point labelled H1 is a **bifurcation point**, at which the equilibrium point changes from being stable to unstable. The line continues as a dashed line to point H2, representing the value of V at the unstable equilibrium. Between H1 and H2, the only stable solution is the limit cycle, which is represented by the pair of solid lines between the bifurcation points LPC1 and LPC2. The heights of the lines show the maximum and minimum values of V during the limit cycle. At point H2 the equilibrium point becomes stable again. The points RG1 and RG2 have no significance other than to denote two examples of parameters between LPC1 and LPC2. Limit cycle trajectories for the points LPC1, RG1, RG2 and LPC2 are shown in the phase plane in Figure B.4b. Figure B.4c shows the corresponding time courses of V .

In the small range between LPC1 (at 88.2 mA cm^{-2}) and H1 (at 93.9 mA cm^{-2}) there are actually two stable solutions, the stable equilibrium and the limit cycle. There is also an unstable limit cycle, represented by the dashed lines between H1 and LPC1. The equilibrium solution can be reached by increasing the current slowly from below, and the limit cycle solution can

Fig. B.4 (a) Bifurcation diagram of the Morris–Lecar model with Type II parameters. The injected current I_e is on the x -axis and membrane potential is plotted on the y -axis. For $I_e < 93.8 \text{ mA cm}^{-2}$ or for $I_e > 212.0 \text{ mA cm}^{-2}$, the membrane potential settles to a steady value, which is represented by the single solid line. At intermediate values, the equilibrium indicated by the dashed line is unstable, and the system enters a limit cycle (oscillation). The maximum and minimum values of the oscillation are represented by the solid lines. (b) The stable equilibrium points (black lines) and sample limit cycles plotted in phase space. (c) The time course of the membrane potential corresponding to the limit cycles plotted in the phase space shown in (b).

Hopf bifurcations are also known as Andronov–Hopf bifurcations or Poincaré–Andronov–Hopf bifurcations.

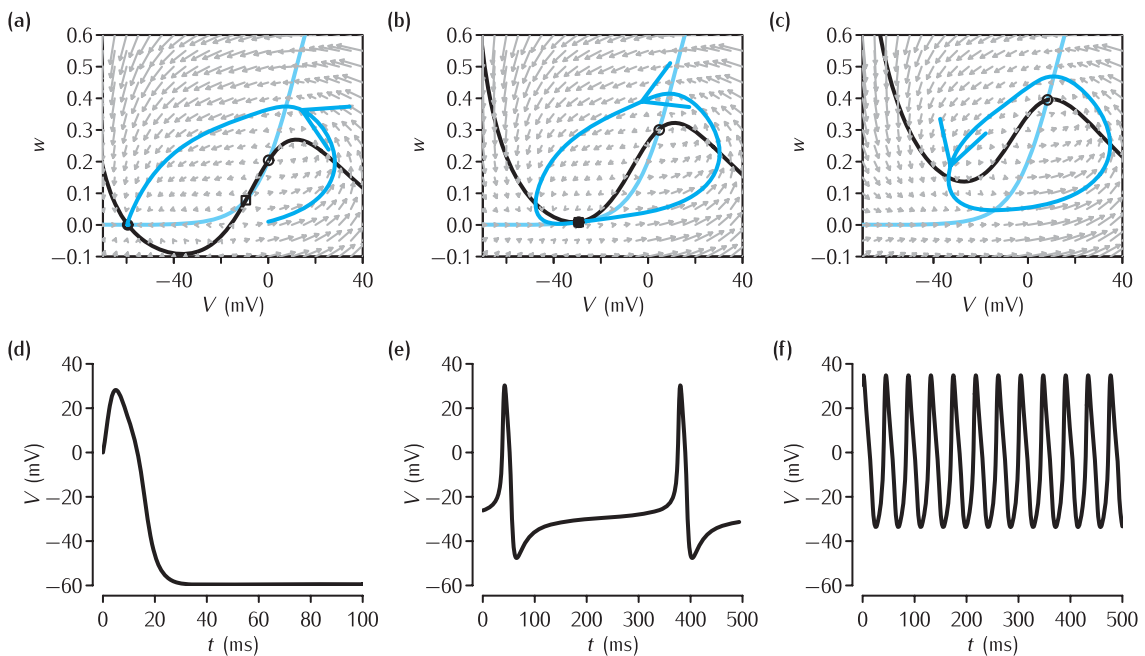


Fig. B.5 Dynamical systems analysis of Morris–Lecar neurons with Type I parameters (a–c) and corresponding trajectories of the membrane potential (d–f).

(a) With no applied current ($I_e = 0$), the system has one stable node (filled circle) at $V = -59.5 \text{ mV}$, $w = 2.70 \times 10^{-4}$ and an unstable node (unfilled circle) and a saddle point (unfilled square). (d) When the system state is started from an above threshold position, one action potential results. (b) The saddle node bifurcation when $I_e = 40.4 \text{ mA cm}^{-2}$, where the stable node and the saddle point merge, but the unstable node remains. A limit cycle trajectory emerges, though its frequency is very low (e). (c) A higher level of current injection ($I_e = 96.8 \text{ mA cm}^{-2}$). The saddle point and stable point have completely disappeared. There is one limit cycle, and its frequency is higher (f).

be reached by decreasing the current slowly from above. This type of multi-stability is known as **hysteresis**. Similarly, between H2 ($I_e = 212.0 \text{ mA cm}^{-2}$) and LPC2 (216.9 mA cm^{-2}) there is a stable equilibrium, a stable limit cycle and an unstable limit cycle.

In the dynamical systems literature, H1 is called a **supercritical Hopf bifurcation** and H2 is a **subcritical Hopf bifurcation**. According to the Poincaré–Andronov–Hopf theorem, the limit cycle that emerges at a Hopf bifurcation always has a non-zero frequency, which corresponds to the definition of Type II firing.

B.2.4 The saddle-node bifurcation

We now investigate the phase plane and bifurcation diagram of the Morris–Lecar neuron with the setting of the parameters $V_1 – V_4$ (Box B.1) that gives Type I firing behaviour. The only differences between these parameters are in the steady state activation curve for w , which is steeper and shifted to the right compared to the Type II set. This is reflected in the phase plane shown in Figure B.5a, in which there is no applied current. The V -nullcline is the same as the phase plane for Type II parameters with no injected current (Figure B.2a), but the w -nullcline is steeper, and shifted to the right. This has the effect of creating three intersections between the nullclines and so there are three equilibrium points.

A stability analysis shows that the left-most equilibrium point is stable and the right-most one is unstable. The equilibrium point in the middle, denoted by the open square, is a type of unstable equilibrium point called a **saddle node**. A saddle node is like the bottom of a dip in a mountain ridge: in either direction along the ridge, the gradient is upwards, but in either of the directions at right angles, the gradient is downwards. If the system state

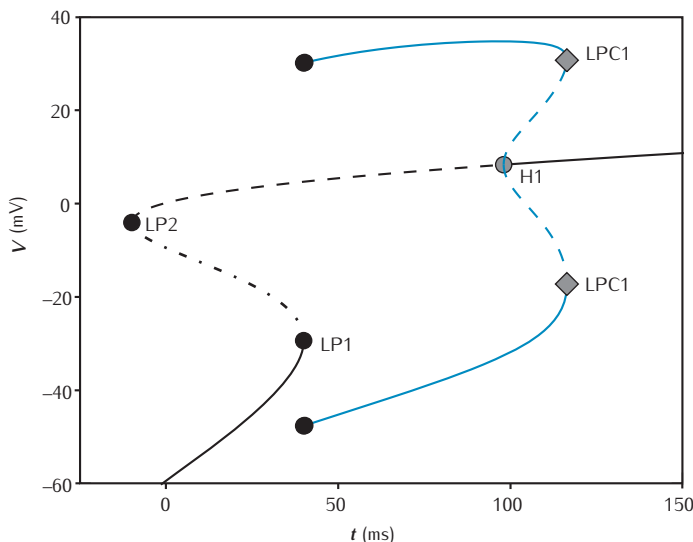


Fig. B.6 Bifurcation diagram of the Morris–Lecar model with Type I parameters. The axes are labelled as in Figure B.4. Solid black line denotes stable node, dashed line denotes unstable node and dash-dotted line denotes saddle point. The blue lines denote the maximum and minimum of a limit cycle. See text for full explanation.

lies on the saddle node, small perturbations from it would cause the state to return to the stable equilibrium point.

As more current is injected, the V -nullcline changes until the stable point and the saddle point merge, as shown in Figure B.5b, and then disappear, as shown in Figure B.5c. The type of bifurcation that occurs when the saddle node and the unstable equilibrium point merge is called a **saddle-node bifurcation**. At this point the V and w variables start to oscillate. However, in contrast with the Hopf bifurcation, the oscillation is of very low frequency when I_e is just above its value at the saddle-node bifurcation, and increases steadily above this value. This makes the Morris–Lecar neuron with the second set of parameters fire in a Type I fashion.

The bifurcation diagram of the Morris–Lecar model with Type I parameters is shown in Figure B.6. For the values of I_e between -9.95 mA cm^{-2} (LP2) and 40.0 mA cm^{-2} (LP1), there are three fixed points. The stable fixed point is shown by the solid line, the unstable fixed point by the dashed line and the saddle node by the dash-dotted line. Above LP1 (at $I_e = 40.0\text{ mA cm}^{-2}$), the saddle-node bifurcation, both the stable node and the saddle node disappear, leaving the unstable node and the stable limit cycle. The bifurcation point H1 (at $I_e = 98.1\text{ mA cm}^{-2}$) is a subcritical Hopf bifurcation. As with the type II neurons, the equilibrium point changes from being unstable to stable again. Between H1 and the bifurcation point LPC1 (at 116.4 mA cm^{-2}), both the equilibrium and limit cycle solutions are possible. Above LPC1, only the stable equilibrium point exists.

B.3 | Common probability distributions

Stochastic models in which certain model components include a probabilistic or random element have appeared frequently in this book. The opening and closing of ion channels (Chapter 5), molecular interactions in intracellular signalling pathways (Chapter 6), synaptic vesicle release and transmitter

Table B.1 Common continuous probability distributions

Distribution	Probability density function	Parameters
Uniform	$f(x) = \frac{1}{b-a}$, $x \in [a, b]$	Range a to b
Exponential	$f(x) = \lambda \exp(-\lambda x)$, $x \geq 0$	Rate $\lambda > 0$
Gaussian	$f(x) = \frac{1}{\sqrt{2\pi\sigma^2}} \exp\left(-\frac{(x-\mu)^2}{2\sigma^2}\right)$	Mean μ ; variance σ^2
Gamma	$f(x) = x^{k-1} \frac{\exp(-x/\theta)}{\theta^k \Gamma(k)}$, $x > 0$	Scale $\theta > 0$; shape $k > 0$ $\Gamma(k) = (k-1)!$ for integer k

diffusion (Chapter 7) can all be described in a probabilistic way. Quantities whose value is in some way random, be they model variables or parameters, or experimentally measured data, are described by **probability distributions** which assign a probability that a quantity will have a particular value or range of values. As a convenient point of reference, we describe here some common probability distributions that are relevant to the models discussed in this book.

B.3.1 Continuous random variables

Continuous random variables X may take any real value, the probabilities of which are described by their **probability distribution function**:

$$F(x) = P(X \leq x), -\infty < x < \infty \quad (\text{B.27})$$

and associated **probability density function** (PDF):

$$f(x) = \frac{dF(x)}{dx} \text{ with } \int_{-\infty}^{\infty} f(x) dx = 1. \quad (\text{B.28})$$

$F(x)$ is the probability that the random variable X has a value less than or equal to x . For an infinitesimal interval, $[x, x + \Delta x]$, then $f(x)\Delta x$ is the probability that X takes a value within this interval. For a finite interval, $[a, b]$, then

$$P(a \leq X \leq b) = \int_a^b f(x) dx. \quad (\text{B.29})$$

The PDFs of common distribution functions are listed in Table B.1 and illustrated in Figure B.7.

The generation of random numbers is central to Monte Carlo simulations of stochastic models. This, at least, involves drawing numbers from a **uniform distribution**. Other probability distributions can often be derived as transformations on the uniform distribution. Drawing a random number from a given distribution involves first drawing a uniform random number from a given range (typically from 0 to 1) and then transforming the number. Random number generators on computers are based on algorithms for producing uniform random numbers. Such computed numbers are only ever pseudo-random, and some algorithms are better than others. The benchmark

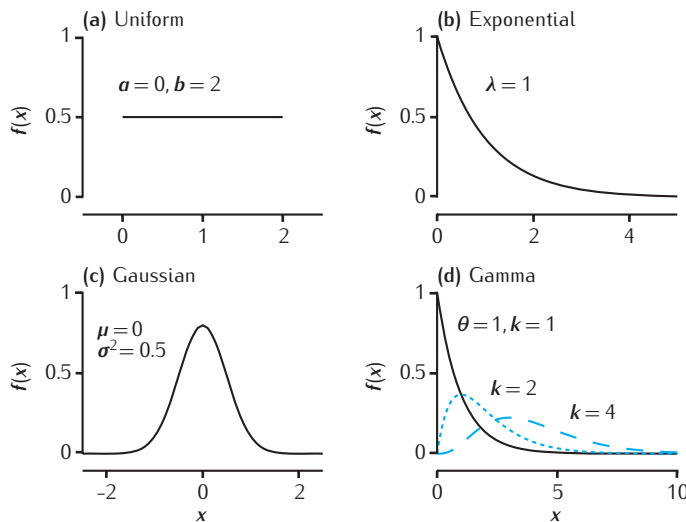


Fig. B.7 Examples of probability density functions for the common continuous probability distributions defined in Table B.1.

is the length of a random number sequence an algorithm can deliver before it starts to repeat the sequence.

The **exponential distribution** is at the heart of the SSA (Box 6.6) for simulating chemical reactions. If two chemical species are reacting at a constant rate, then the time between reaction events is described by the exponential distribution. This is intimately linked to the discrete Poisson distribution (see below) that describes the number of reaction events in a given time interval. Poisson and exponential distributions are also often good models for the number of spikes emitted by a neuron in a time interval, and their interspike intervals, respectively. The time of occurrence t of the next event in a Poisson process of rate λ , as drawn from an exponential distribution, can be calculated as $t = (1/\lambda)\ln(1/p)$, where p is a uniform random number on $[0,1]$.

Quantities in the natural world often conform to Gaussian (normal) distributions in which measured values are symmetrically clustered around a mean value. Adding variation to model parameters can be done by adding Gaussian noise, drawn from a **Gaussian distribution** with zero mean and a specified variance, to the mean parameter value. This might be used to introduce membrane potential noise through random variation in an injected current, or to create a population of cells of a given type with slightly different properties, such as variation in membrane resistance and capacitance.

Experimental data usually includes some random variation that can be captured by fitting a probability distribution to the data, rather than calculating just the mean value of the data. Gaussian distributions are often suitable, but some quantities exhibit skewed distributions that are not well fit by a Gaussian distribution. In Chapter 10, probabilistic reconstruction and growth models are based on, and try to match, the statistics of morphological data collected from real neuronal dendrites. Dendritic segment lengths are always greater than 0 and are clustered around a non-zero mean with typically a long tail towards long length values. Such a distribution is well fit by a **gamma distribution**, which can assume shapes ranging between the exponential and Gaussian distributions (Figure B.7).

Table B.2 Common discrete probability distributions

Distribution	Distribution function	Parameters
Binomial	$P(x) = \binom{n}{p} p^x (1-p)^{n-x}, \quad x = 0, 1, \dots, n$	Trials n ; probability of success $p \in [0, 1]$
Poisson	$P(x) = \frac{\lambda^x}{x!} \exp(-\lambda), \quad x = 0, 1, \dots$	Mean number $\lambda > 0$

B.3.2 Discrete random variables

Other stochastic processes only allow discrete, or positive integer, values. Examples from this book include the release of vesicles at a chemical synapse (Box 1.2 and Chapter 7). A synaptic active zone may contain n vesicles that are able to release with a probability p on the arrival of a presynaptic action potential. The number that do release is governed by either Poisson or binomial distributions. Spike trains emitted by neurons often exhibit variation in their interspike intervals such that the number of spikes occurring in some fixed time interval is described by a **Poisson distribution** (Chapter 8).

Discrete random variables can only assume a finite set of values with non-zero probability. The probability distribution of such a random variable X defines the probability $P(x)$ of every value x that X can have. Common examples are given in Table B.2 and illustrated in Figure B.8.

The **binomial distribution** describes the number of successes in n independent trials, with the probability of success of a trial being p . The Poisson distribution describes the number of (rare) events that occur in a given time period, or given spatial volume, given that the events occur at a fixed rate λ . It turns out that the Poisson distribution is a good approximation to the binomial distribution for large n and small p , with $\lambda = np$ (Figure B.8a, b). This can provide a computationally more efficient way of generating binomially distributed numbers, if these conditions hold.

B.3.3 Fitting distribution functions to data

At the heart of creating a stochastic model is the problem of defining suitable probability distributions for model quantities that are random variables. As with models of dendritic growth (Chapter 10), this may involve estimating the parameters of a given distribution from experimental data, to provide a **parametric model**. For example, we might decide that a given set of data is well approximated by a Gaussian distribution. In this case, we need to estimate the mean and variance of the data to specify this continuous distribution.

Maximum likelihood estimation

One common approach to this problem is the method of **maximum likelihood estimation** (MLE). Suppose we have a sample value x for a random variable X . Then we define the **likelihood** of the sample, $L \equiv L(x)$, as the probability, $p(x)$, if X is discrete, or the probability density, $f(x)$, if X is continuous. To take the Gaussian distribution as an example, the probability density is a function defined by two parameters, μ and σ^2

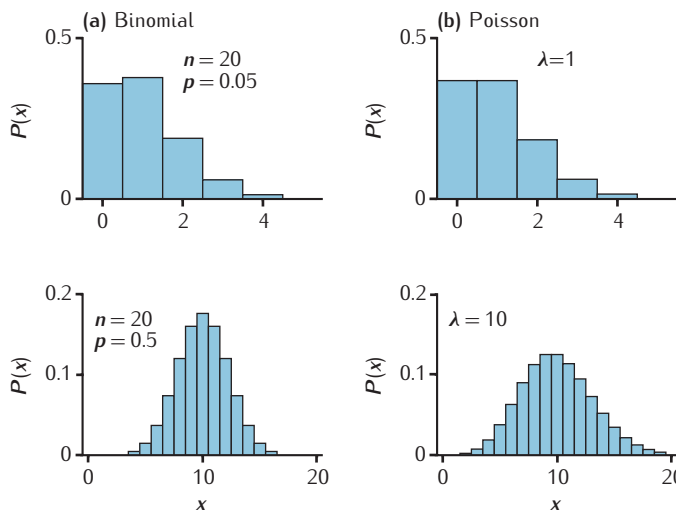


Fig. B.8 Examples of common discrete probability histograms for the distributions defined in Tables B.2.

(Table B.1). MLE seeks to find values of μ and σ^2 that maximise the likelihood of sample x . If we have n independent samples, x_1, \dots, x_n , then the likelihood of these samples is the joint probability density, $L = f(x_1, x_2, \dots, x_n) = f(x_1)f(x_2)\dots f(x_n)$ where:

$$f(x_i) = \frac{1}{\sqrt{2\pi\sigma^2}} \exp\left(-\frac{(x_i - \mu)^2}{2\sigma^2}\right). \quad (\text{B.30})$$

The likelihood is maximised with respect to the parameters when:

$$\frac{dL}{d\mu} = \frac{dL}{d\sigma^2} = 0. \quad (\text{B.31})$$

Given the functional form for $f(x)$, this is solved easily, yielding sample estimates for the mean and variance:

$$\hat{\mu} = \frac{1}{n} \sum_{i=1}^n x_i, \quad \hat{\sigma}^2 = \frac{1}{n} \sum_{i=1}^n (x_i - \hat{\mu})^2. \quad (\text{B.32})$$

This procedure can be carried out for any parameterised distribution function, though finding the solution may be more or less difficult than for the Gaussian distribution. Note that minimising the root-mean-squared-error between model output and experimental data is equivalent to carrying out MLE if we can assume that the experimental measurements are subject to independent Gaussian noise with a constant variance (Press *et al.*, 1987).

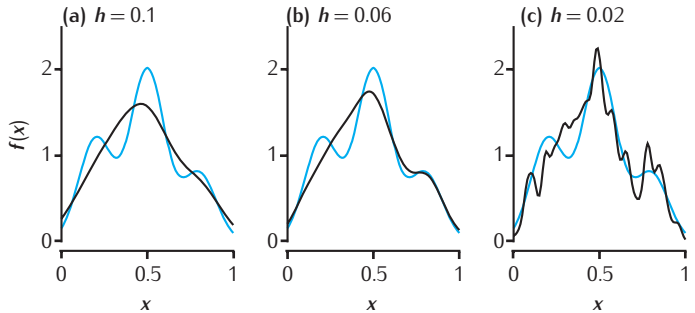
Note that a better, unbiased estimate of the sample variance is:

$$\hat{\sigma}^2 = \frac{1}{n-1} \sum_{i=1}^n (x_i - \hat{\mu})^2.$$

Non-parametric models

In general, a common distribution, such as Gaussian or gamma, may not provide a good fit to the data. In this case it is more appropriate not to make any assumptions about the shape of the underlying distribution and produce a **non-parametric model**. One approach to non-parametric modelling is **kernel density estimation (KDE)**. Suppose we have n measurements x_i ($i = 1, \dots, n$) of our random variable X . A KDE of the probability density

Fig. B.9 Example of kernel density estimation. Two hundred samples are drawn from a mixture of three Gaussian distributions: $\mu_1 = 0.2$, $\sigma_1 = 0.1$, $\mu_2 = 0.5$, $\sigma_2 = 0.1$, $\mu_3 = 0.8$, $\sigma_3 = 0.1$, with 30% of values drawn from the first distribution, 50% from the second and 20% from the third. Three KDEs are formed using Gaussian kernels and different values for the smoothing parameter h . The KDEs are shown in black and the true distribution in blue in each plot.



function is:

$$\hat{f}(x) = \frac{1}{nb} \sum_{i=1}^n K\left(\frac{x - x_i}{h}\right) \quad (\text{B.33})$$

for some **kernel function** K and bandwidth, or smoothing parameter, h . The kernel function is such that the estimated probability density at a point x is the sum of the known points x_i , with decreasing weight with increasing distance from x . A common choice of kernel function is the Gaussian probability density function, with h specifying the standard deviation of the Gaussian. This leads to:

$$\hat{f}(x) = \frac{1}{nb\sqrt{2\pi}} \sum_{i=1}^n \exp\left(-\frac{(x - x_i)^2}{2b^2}\right). \quad (\text{B.34})$$

Given the kernel function, this model has only the single smoothing parameter h that needs to be specified. An appropriate choice for h is vital; if h is too large then the kernel density model is rather smooth and may not capture well the underlying distribution of the data; conversely, if h is too small then the model will exhibit large variations that are specific to the particular data set on which the model is based (Figure B.9). Automatic bandwidth selection is a difficult process for which a variety of methods have been proposed. A simple rule of thumb that often works well is to assume that the data actually comes from a single Gaussian distribution, and then set:

$$h = 0.9S n^{-1/5} \quad (\text{B.35})$$

where S is the minimum of the estimated sample standard deviation σ and three-quarters of its interquartile range (Torben-Nielsen *et al.*, 2008).

B.4 Parameter estimation

Estimating values for model parameters is a crucial step in developing an accurate and informative model. Parameter estimation in stochastic models is discussed in Section B.3.3. Here we consider determining parameter values in deterministic models. Approaches to this problem have been discussed in Chapters 4 and 6. The step-by-step process of parameter estimation is outlined in Section 4.5. Here we provide a general, but not detailed, coverage of some popular algorithms used in deterministic parameter estimation. A useful review is also to be found in van Geit *et al.* (2008).

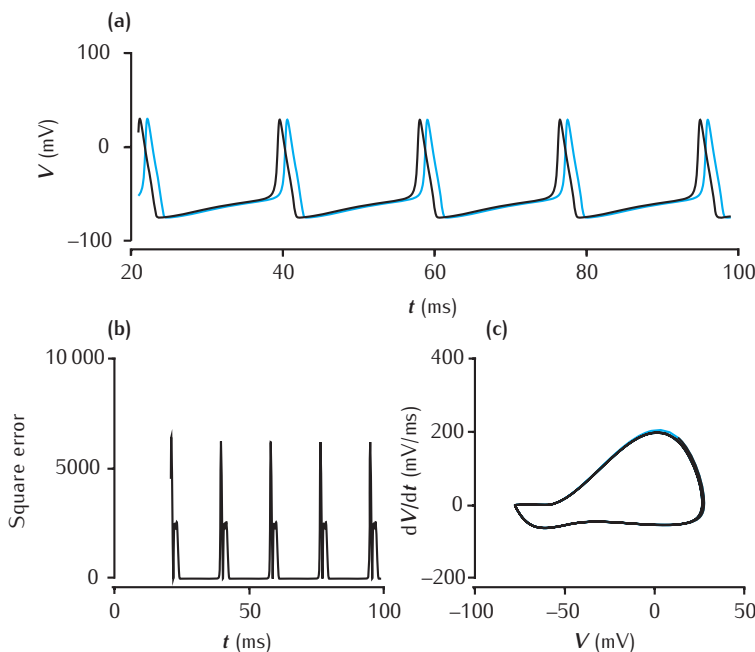


Fig. B.10 (a) Two action potential trains, slightly shifted in time. (b) The squared error between these two voltage traces can be large at specific time points. (c) The phase plot is identical in both cases.

B.4.1 Error measures

Parameter estimation requires some measure of how good the model is with a given set of parameter values. Such a measure may specify the fitness of the model or the error between the model and certain experimental data. Error measures are most commonly used, and the process of parameter estimation involves using an optimisation algorithm to determine a set of parameter values that minimises the error. The success of parameter estimation lies in both choosing a suitable error measure as well as an efficient optimisation algorithm.

Direct fitting

Error measures based on electrophysiological data may measure the direct error between, say, a recorded voltage trace at discrete time points over a given time period and the model's voltage output over the same time points. The total error is usually calculated as the square root of the sum-of-squared errors at each time point. It should be noted that such measures can be very sensitive to noise in the experimental data. For example, when trying to match a recorded action potential, any small time-base mismatch (phase shift) between the model and experimental traces can lead to very large errors (Figure B.10), even when the shape of the model action potential is a very close match to the experimental potential (van Geit *et al.*, 2008). This sensitivity can be removed by basing the error measure on a phase plot of V versus dV/dt instead (LeMasson and Maex, 2001; Achard and De Schutter, 2006; van Geit *et al.*, 2008). The phase plot captures details of the shape of the action potential, independently of its exact occurrence in time.

Feature-based fitting

Error measures can also be based on features derived from experimental recordings, such as action potential amplitude and width, cell resistance and capacitance, etc. Such features may be obtained by averaging over many sets of experimental data and so are much more robust to noise than parameter estimation of passive properties by direct fitting.

Particularly with feature-based fitting, it may be attempted to meet more than one criterion at the same time, with different criteria potentially being in conflict. Such multi-objective error measures usually weight each criterion, or feature, both to normalise all numerical values and to either equalise or bias the contribution of particular features to the error measure (Section 4.5).

B.4.2 Optimisation algorithms

Finding a good parameter set involves searching for parameter values that minimise our error measure. A complex error measure can have many troughs and peaks (Section 4.5). Troughs form local minima, which may fall well short of the best minimisation that can be achieved (Figure B.11). We require an algorithm that can find the bottom of a trough that is at least close to the deepest possible, i.e. results in the smallest possible error. This algorithm must be able to search the error surface and eventually settle on the bottom of a deep trough without getting prematurely stuck in an unnecessarily shallow trough. Suitable algorithms typically include a stochastic component in their search strategy that may result in an occasional increase in the error measure during searching, with the hope that a small error point will eventually, but not too slowly, be found. Suitable methods include simulated annealing and evolutionary algorithms. Different algorithms can be combined effectively to provide an initial wide-spread search followed by an efficient descent to the bottom of a large trough in the error surface.

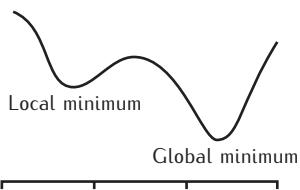


Fig. B.11 1D plot of an error surface showing one local and one global minimum.

Deterministic algorithms

Algorithms that use available information to compute a new set of parameter values that is always a better solution than the current set can often find a minimum very quickly. The down-side is that this is likely to be only a local minimum. Common algorithms make use of the local gradient of the error measure to determine the direction in which to explore (Figure B.12). They then find the minimum in that direction before determining a new direction to explore. If all directions result in an increase in the error, then a minimum has been found. Algorithms differ in the choice of the direction in which to search, given the local gradient.

The **steepest gradient descent** algorithm (Section 4.5) uses the intuitively appealing notion of searching for a minimum in the direction of maximally descending gradient. Successive search directions must be perpendicular to each other by virtue of the fact that the minimum in the previous direction has just been found. This can result in lots of small steps being taken to descend a long, narrow valley (Press *et al.*, 1987). A better alternative is **conjugate gradient descent** (Press *et al.*, 1987). It is possible, on the basis of local gradient information, to calculate a conjugate direction

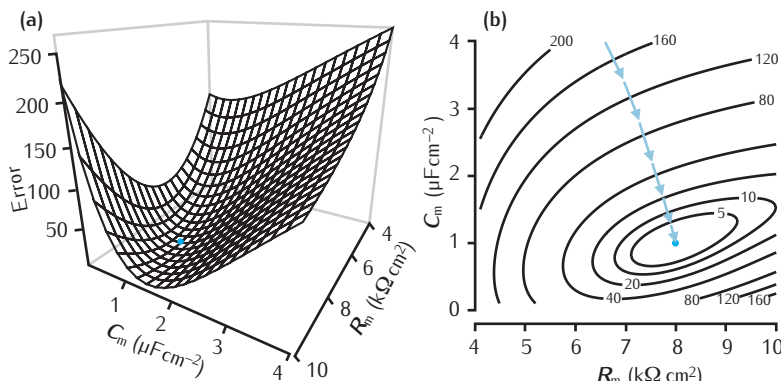


Fig. B.12 (a) An error surface generated from direct comparison of transients in a single compartment RC circuit model. For convenience of visualisation, the error surface is plotted over only two unknown variables, R_m and C_m . The minimum is indicated by a blue point ($C_m = 1 \mu\text{F cm}^{-3}$, $R_m = 8 \text{k}\Omega \text{cm}^2$). (b) A contour plot of the same surface demonstrating a single minimum. The arrows illustrate a gradient descent approach to finding the minimum.

of descent that does not ‘interfere’, at least with the previous direction, so that large steps can be taken in each new direction towards the minimum. Conjugate gradient descent is useful in parameter fitting of compartmental models with relatively few parameters (Bhalla and Bower, 1993; Vanier and Bower, 1999).

Typical error measures do not readily yield an explicit expression involving the parameters being optimised. Consequently, at each iteration the local gradient must be calculated numerically using many error measure evaluations at points around the current search point. To ensure the gradient descent is likely to find a useful minimum, a highly exploratory search, such as **brute force search**, can be used initially to narrow down the region of parameter space to be searched by gradient descent (Bhalla and Bower, 1993).

Another deterministic algorithm that does not require gradient calculations is the **downhill simplex** method (Press *et al.*, 1987; LeMasson and Maex, 2001). This involves selecting an initial set of N points in parameter space to define a ‘simplex’. Then the fitness of each point in the simplex is evaluated and the worst-performing point is moved towards the other points. Different algorithms vary in exactly how points are moved. In any case, the simplex contracts in space as a minimum is approached.

Stochastic algorithms

Stochastic algorithms combine exploiting local information with exploration of the search space. This exploration may involve moving into areas of worse fitness, but ultimately can result in a global minimum being found.

A popular algorithm that combines the exploitation of gradient descent and simplex methods with exploration is **simulated annealing** (Kirkpatrick *et al.*, 1983). The algorithm proceeds by probabilistically replacing the current solution with a new solution. The new candidate solution is usually chosen on the basis of some local information, which can be as simple as choosing a point randomly within a certain distance of the current solution. The probability that the new candidate y replaces the current solution x is calculated as a function of the *temperature* parameter T using a Boltzmann–Gibbs distribution (van Geit *et al.*, 2008):

$$P_{\text{repl}} = \begin{cases} 1 & \text{if } f(y) < f(x), \\ \exp[(f(x) - f(y))/cT] & \text{otherwise} \end{cases} \quad (\text{B.36})$$

where f is the error measure and c is a positive scaling constant. If the new candidate yields a lower error than the current solution, it replaces this solution. On the other hand, the candidate may still replace the current solution even if it has a higher error. In this case the probability of replacement depends on the temperature T . Initially, T is high, allowing exploration of the search space. As the algorithm proceeds, T is decreased, or ‘annealed’, leading to an increasingly deterministic choice of new candidates that reduce the error. Different annealing schedules can be used, such as exponential cooling, $T_k = \rho T_{k-1}$ on iteration k , with $0 < \rho < 1$. Simulated annealing often works well for optimising parameters in compartmental neural models (Vanier and Bower, 1999; Nowotny *et al.*, 2008).

An alternative is the family of **evolutionary algorithms**. This includes **genetic algorithms** (GA) (Holland, 1975) and **evolution strategies** (ES) (Achard and De Schutter, 2006; van Geit *et al.*, 2008). The essence of these algorithms is the evolution of a population of candidate solutions towards ever fitter solutions. This evolution includes reproduction, mutation and selection. The algorithms in the family differ in how candidate solutions are represented and precisely how evolution takes place. Both GA (Vanier and Bower, 1999) and ES (Achard and De Schutter, 2006) approaches are effective for neural model parameter optimisation. One advantage of ES is that it allows direct representation of real-valued parameters, whereas GA requires a binary encoding of parameter values.

References

- Abarbanel H. D. L., Gibb L., Huerta R. and Rabinovich M. I. (2003). Biophysical model of synaptic plasticity dynamics. *Biol. Cybern.* **89**, 214–226.
- Abbott L. and Marder E. (1998). Modeling small networks. In *Methods in Neuronal Modeling: From Ions to Networks*, 2nd edn, eds C. Koch and I. Segev (MIT Press, Cambridge, MA), chapter 10.
- Abbott L. F., Thoroughman K. A., Prinz A. A., Thirumalai V. and Marder E. (2003). Activity-dependent modification of intrinsic and synaptic conductances in neurons and rhythmic networks. In *Modeling Neural Development*, ed. A. van Ooyen (MIT Press, Cambridge, MA), pp. 151–166.
- Achard P. and De Schutter E. (2006). Complex parameter landscape for a complex neuron model. *PLoS Comput. Biol.* **2**, e94.
- Adrian E. D. (1928). *The Basis of Sensation: The Action of the Sense Organs* (Christophers, London).
- Aeschlimann M. and Tettoni L. (2001). Biophysical model of axonal pathfinding. *Neurocomputing* **38–40**, 87–92.
- Agmon-Snir H., Carr C. E. and Rinzel J. (1998). The role of dendrites in auditory coincidence detection. *Nature* **393**, 268–272.
- Ajay S. M. and Bhalla U.S. (2005). Synaptic plasticity in vitro and in silico: insights into an intracellular signaling maze. *Physiology (Bethesda)* **21**, 289–296.
- Albin R., Young A. and Penny J. (1989). Functional anatomy of basal ganglia disorders. *Trends Neurosci.* **12**, 366–375.
- Alexander S. P. H., Mathie A. and Peters J. A. (2008). Guide to receptors and channels (GRAC) 3rd edition. *Br. J. Pharmacol.* **153**, S1–S209.
- Amit D. J. (1989). *Modeling Brain Function: The World of Attractor Networks* (Cambridge University Press, Cambridge).
- Amit D. J. and Brunel N. (1997a). Model of global spontaneous activity and local structured activity during delay periods in the cerebral cortex. *Cereb. Cortex* **7**, 237–252.
- Amit D. J. and Brunel N. (1997b). Dynamics of a recurrent network of spiking neurons before and following learning. *Network Comp. Neural Syst.* **8**, 373–404.
- Amit D. J. and Fusi S. (1994). Learning in neural networks with material synapses. *Neural Comput.* **6**, 957–982.
- Amit D. J., Gutfreund H. and Sompolinsky H. (1985). Spin-glass models of neural networks. *Phys. Rev. A* **32**, 1007–1018.
- Amit D. J. and Tsodyks M. V. (1991a). Quantitative study of attractor neural network retrieving at low spike rates: I. substrate – spikes, rates and neuronal gain. *Network Comp. Neural Syst.* **2**, 259–273.
- Amit D. J. and Tsodyks M. V. (1991b). Quantitative study of attractor neural network retrieving at low spike rates: II. low-rate retrieval in symmetric networks. *Network Comp. Neural Syst.* **2**, 275–294.
- Anderson D. J., Rose J. E., Hind J. E. and Brugge J. F. (1971). Temporal position of discharges in single auditory nerve fibers within the cycle of a sine-wave stimulus: frequency and intensity effects. *J. Acoust. Soc. Am.* **49**, 1131–1139.
- Aradi I. and Érdi P. (2006). Computational neuropharmacology: dynamical approaches in drug discovery. *Trends Pharmacol. Sci.* **27**, 240–243.
- Aradi I. and Soltesz I. (2002). Modulation of network behaviour by changes in variance in interneuronal properties. *J. Physiol.* **538**, 227–251.

- Aradi I., Santhakumar V. and Soltesz I. (2004). Impact of heterogeneous perisomatic IPSC populations on pyramidal cell firing rates. *J. Neurophysiol.* **91**, 2849–2858.
- Arisi I., Cattaneo A. and Rosato V. (2006). Parameter estimate of signal transduction pathways. *BMC Neurosci.* **7** (Suppl 1), S6.
- Armstrong C. M. and Bezanilla F. (1973). Currents related to movement of the gating particles of the sodium channels. *Nature* **242**, 459–461.
- Arnett D. W. (1978). Statistical dependence between neighbouring retinal ganglion cells in goldfish. *Exp. Brain Res.* **32**, 49–53.
- Arrhenius S. (1889). Über die Reaktionsgeschwindigkeit bei der Inversion von Rohrzucker in Säuren. *Z. Phys. Chem.* **4**, 226–248.
- Ascher P. and Nowak L. (1988). The role of divalent cations in the N-methyl-D-aspartate responses of mouse central neurones in culture. *J. Physiol.* **399**, 247–266.
- Ascoli G. A. (2002). Neuroanatomical algorithms for dendritic modelling. *Network Comp. Neural Syst.* **13**, 247–260.
- Ascoli G. A. (2006). Mobilizing the base of neuroscience data: the case of neuronal morphologies. *Nat. Rev. Neurosci.* **7**, 318–324.
- Ascoli G. A., Krichmar J. L., Nasuto S. J. and Senft S. L. (2001). Generation, description and storage of dendritic morphology data. *Philos. Trans. R. Soc. Lond., B* **356** (1412), 1131–1145.
- Auer M. (2000). Three-dimensional electron cryo-microscopy as a powerful structural tool in molecular medicine. *J. Mol. Med.* **78**, 191–202.
- Auerbach A. A. and Bennett M. V. L. (1969). A rectifying electronic synapse in the central nervous system of a vertebrate. *J. Gen. Physiol.* **53**, 211–237.
- Badoval M., Zou Q., Davison A. P., Rudolph M., Bal T., Frégnac Y. and Destexhe A. (2006). Biophysical and phenomenological models of multiple spike interactions in spike-timing dependent plasticity. *Int. J. Neural Sys.* **16**, 79–97.
- Baker P. F., Hodgkin A. L. and Ridgway E. B. (1971). Depolarization and calcium entry in squid giant axons. *J. Physiol.* **218**, 709–755.
- Barbour B. and Häusser M. (1997). Intersynaptic diffusion of neurotransmitter. *Trends Neurosci.* **20**, 377–384.
- Bartos M., Vida I. and Jonas P. (2007). Synaptic mechanisms of synchronized gamma oscillations in inhibitory interneuron networks. *Nat. Rev. Neurosci.* **8**, 45–56.
- Bean B. P. (2007). The action potential in mammalian central neurons. *Nat. Rev. Neurosci.* **8**, 451–465.
- Bédard C., Kröger H. and Destexhe A. (2004). Modeling extracellular field potentials and the frequency-filtering properties of extracellular space. *Biophys. J.* **86**, 1829–1842.
- Bell A. J. (1992). Self-organisation in real neurons: anti-Hebb in ‘channel space’? In *Neural Information Processing Systems 4*, eds J. E. Moody, S. J. Hanson and R. P. Lippmann (Morgan Kaufmann, San Mateo, CA), pp. 35–42.
- Bennett M. R., Farnell L. and Gibson W. G. (2000a). The probability of quantal secretion near a single calcium channel of an active zone. *Biophys. J.* **78**, 2201–2221.
- Bennett M. R., Farnell L. and Gibson W. G. (2000b). The probability of quantal secretion within an array of calcium channels of an active zone. *Biophys. J.* **78**, 2222–2240.
- Bennett M. R., Gibson W. G. and Robinson J. (1994). Dynamics of the CA3 pyramidal neuron autoassociative memory network in the hippocampus. *Philos. Trans. R. Soc. Lond., B* **343**, 167–187.
- Bennett M. R. and Robinson J. (1989). Growth and elimination of nerve terminals at synaptic sites during polyneuronal innervation of muscle cells: a trophic hypothesis. *Proc. R. Soc. Lond., B* **235**, 299–320.

- Bennett M. V. L. and Zukin R. S. (2004). Electrical coupling and neuronal synchronization in the mammalian brain. *Neuron* **41**, 495–511.
- Benzi R., Sutera A. and Vulpiani A. (1981). The mechanism of stochastic resonance. *J. Phys. A Math. Gen.* **14**, L453–L457.
- Berridge M. J. (1998). Neuronal calcium signalling. *Neuron* **21**, 13–26.
- Berridge M. J., Bootman M. D. and Roderick H. L. (2003). Calcium signalling: dynamics, homeostasis and remodelling. *Nat. Rev. Mol. Cell Biol.* **4**, 517–529.
- Berry M. and Bradley P. M. (1976). The application of network analysis to the study of branching patterns of large dendritic trees. *Brain Res.* **109**, 111–132.
- Bertram R., Sherman A. and Stanley E. F. (1996). Single-domain/bound calcium hypothesis of transmitter release and facilitation. *J. Neurophysiol.* **75**, 1919–1931.
- Betz W. J. (1970). Depression of transmitter release at the neuromuscular junction of the frog. *J. Physiol.* **206**, 620–644.
- Betz W. J., Caldwell J. H. and Ribchester R. R. (1980). The effects of partial denervation at birth on the development of muscle fibres and motor units in rat lumbrical muscle. *J. Physiol.* **303**, 265–279.
- Beurle R. L. (1956). Properties of a mass of cells capable of regenerating pulses. *Philos. Trans. R. Soc. Lond., B* **240**, 55–94.
- Bezanilla F. and Armstrong C. M. (1977). Inactivation of the sodium channel: I. Sodium current experiments. *J. Gen. Physiol.* **70**, 549–566.
- Bhalla U. S. (1998). The network within: signaling pathways. In *The Book of GENESIS: Exploring Realistic Neural Models with the General Neural Simulation System*, 2nd edn, eds J. M. Bower and D. Beeman (Springer-Verlag, New York), pp. 169–192.
- Bhalla U. S. (2001). Modeling networks of signaling pathways. In *Computational Neuroscience: Realistic Modeling for Experimentalists*, ed. E. De Schutter (CRC Press, Boca Raton, FL), pp. 25–48.
- Bhalla U. S. (2004a). Models of cell signaling pathways. *Curr. Opin. Genet. Dev.* **14**, 375–381.
- Bhalla U. S. (2004b). Signaling in small subcellular volumes: I. Stochastic and diffusion effects on individual pathways. *Biophys. J.* **87**, 733–744.
- Bhalla U. S. (2004c). Signaling in small subcellular volumes: II. Stochastic and diffusion effects on synaptic network properties. *Biophys. J.* **87**, 745–753.
- Bhalla U. S. and Bower J. M. (1993). Exploring parameter space in detailed single neuron models: simulations of the mitral and granule cells of the olfactory bulb. *J. Neurophysiol.* **60**, 1948–1965.
- Bhalla U. S. and Iyengar R. (1999). Emergent properties of networks of biological signaling pathways. *Science* **283**, 381–387.
- Bi G. Q. and Poo M. M. (1998). Synaptic modifications in cultured hippocampal neurons: dependence on spike timing, synaptic strength, and postsynaptic cell type. *J. Neurosci.* **18**, 10464–10472.
- Bienenstock E. L., Cooper L. N. and Munro P. W. (1982). Theory for the development of neuron selectivity: orientation specificity and binocular interaction in visual cortex. *J. Neurosci.* **2**, 32–48.
- Billups B., Graham B. P., Wong A. Y. C. and Forsythe I. D. (2005). Unmasking group III metabotropic glutamate autoreceptor function at excitatory synapses in the rat CNS. *J. Physiol.* **565**, 885–896.
- Bishop C. M. (1995). *Neural Networks for Pattern Recognition* (Clarendon Press, Oxford).
- Blackwell K. T. (2005). Modeling calcium concentration and biochemical reactions. *Brains Minds Media* **1**, 224.

- Blackwell K. T. (2006). An efficient stochastic diffusion algorithm for modeling second messengers in dendrites and spines. *J. Neurosci. Methods* **157**, 142–153.
- Blackwell K. T. and Hellgren Kotaleski J. (2002). Modeling the dynamics of second messenger pathways. In *Neuroscience Databases: A Practical Guide*, ed. R. Kötter (Kluwer, Norwell, MA), chapter 5.
- Blaustein A. P. and Hodgkin A. L. (1969). The effect of cyanide on the efflux of calcium from squid axons. *J. Physiol.* **200**, 497–527.
- Bliss T. V. and Lømo T. (1973). Long-lasting potentiation of synaptic transmission in the dentate area of the anaesthetized rabbit following stimulation of the perforant path. *J. Physiol.* **232**, 331–356.
- Block H. D. (1962). The Perceptron: a model for brain functioning. *Rev. Mod. Phys.* **34**, 123–135.
- Bloomfield S. A., Hamos J. E. and Sherman S. M. (1987). Passive cable properties and morphological correlates in neurons of the lateral geniculate nucleus of the cat. *J. Physiol.* **383**, 653–668.
- Booth V. and Rinzel J. (1995). A minimal, compartmental model for a dendritic origin of bistability of motoneuron firing patterns. *J. Comput. Neurosci.* **2**, 299–312.
- Borg-Graham L. J. (1989). Modelling the somatic electrical response of hippocampal pyramidal neurons. Technical Report AI TR-1161, MIT AI Laboratory.
- Borg-Graham L. J. (1999). Interpretations of data and mechanisms for hippocampal pyramidal cell models. In *Cerebral Cortex, Volume 13: Models of Cortical Circuits*, eds P. S. Ulinski, E. G. Jones and A. Peters (Plenum Publishers, New York), pp. 19–138.
- Bormann G., Brosens F. and De Schutter E. (2001). Diffusion. In *Computational Modeling of Genetic and Biochemical Networks*, eds J. M. Bower and H. Bolouri (MIT Press, Cambridge, MA), pp. 189–224.
- Bower J. M. and Beeman D. (1998). *The Book of GENESIS: Exploring Realistic Neural Models with the General NEural SImulation System*, 2nd edn (Springer-Verlag, New York).
- Brenner S. (2010). Sequences and consequences. *Philos. Trans. R. Soc. Lond., B* **365**, 207–212.
- Brette R. (2006). Exact simulation of integrate-and-fire models with synaptic conductances. *Neural Comput.* **18**, 2004–2027.
- Brette R., Piwkowska Z., Monier C., Rudolph-Lilith M., Fournier J., Levy M., Frégnac Y., Bal T. and Destexhe A. (2008). High-resolution intracellular recordings using a real-time computational model of the electrode. *Neuron* **59**, 379–391.
- Brette R., Rudolph M., Carnevale T., Hines M., Beeman D., Bower J. M., Diesmann M., Morrison A., Goodman P. H., Harris Jr F. C., Zirpe M., Natschläger T., Pecevski D., Ermentrout B., Djurfeldt M., Lansner A., Rochel O., Vieville T., Muller E., Davison A. P., El Boustani S. and Destexhe A. (2007). Simulation of networks of spiking neurons: a review of tools and strategies. *J. Comput. Neurosci.* **23**, 349–398.
- Brown A., Yates P. A., Burrola P., Ortuno D., Vaidya A., Jessell T. M., Pfaff S. L., O’Leary D. D. and Lemke G. (2000). Topographic mapping from the retina to the midbrain is controlled by relative but not absolute levels of EphA receptor signalling. *Cell* **102**, 77–88.
- Brown A. M., Schwintz P. C. and Crill W. E. (1993). Voltage dependence and activation kinetics of pharmacologically defined components of the high-threshold calcium current in rat neocortical neurons. *J. Neurophysiol.* **70**, 1530–1543.

- Brown D. A. and Griffith W. H. (1983). Calcium-activated outward current in voltage-clamped hippocampal neurones of the guinea-pig. *J. Physiol.* **337**, 287–301.
- Brown M. C., Jansen J. K. S. and van Essen D. C. (1976). Polyneuronal innervation of skeletal muscle in new-born rats and its elimination during maturation. *J. Physiol.* **261**, 387–422.
- Brunel N. and van Rossum M. C. W. (2007). Lapicque's 1907 paper: from frogs to integrate-and-fire. *Biol. Cybern.* **97**, 337–339.
- Buckingham J. (1991). Delicate nets, faint recollections: a study of partially connected associative network memories. Ph. D. thesis, University of Edinburgh.
- Buckingham J. and Willshaw D. (1993). On setting unit thresholds in an incompletely connected associative net. *Network Comp. Neural Syst.* **4**, 441–459.
- Buice M. A. and Cowan J. D. (2009). Statistical mechanics of the neocortex. *Prog. Biophys. Mol. Biol.* **99**, 53–86.
- Burgoyne R. D. (2007). Neuronal calcium sensor proteins: generating diversity in neuronal Ca²⁺ signalling. *Nat. Rev. Neurosci.* **8**, 182–193.
- Burke R. E. and Marks W. B. (2002). Some approaches to quantitative dendritic morphology. In *Computational Neuroanatomy: Principles and Methods*, ed. G. A. Ascoli (The Humana Press Inc., Totowa, NJ), pp. 27–48.
- Burke R. E., Marks W. B. and Ulfhake B. (1992). A parsimonious description of motoneuron dendritic morphology using computer simulation. *J. Neurosci.* **12**, 2403–2416.
- Butson C. R. and McIntyre C. C. (2005). Tissue and electrode capacitance reduce neural activation volumes during deep brain stimulation. *Clin. Neurophysiol.* **116**, 2490–2500.
- Cannon R. C. and D'Alessandro G. (2006). The ion channel inverse problem: neuroinformatics meets biophysics. *PLoS Comput. Biol.* **2**, 862–868.
- Cannon R. C., Gewaltig M. O., Gleeson P., Bhalla U.S., Cornelis H., Hines M. L., Howell F. W., Muller E., Stiles J. R., Wils S. and De Schutter E. (2007). Interoperability of neuroscience modeling software: current status and future directions. *Neuroinformatics* **5**, 127–138.
- Cannon R. C., Turner D. A., Pyapali G. K. and Wheal H. V. (1998). An on-line archive of reconstructed hippocampal neurons. *J. Neurosci. Methods* **84**, 49–54.
- Cannon S., Robinson D. and Shamma S. (1983). A proposed neural network for the integrator of the oculomotor system. *Biol. Cybern.* **49**, 127–136.
- Carnevale N. T. and Hines M. L. (2006). *The NEURON Book* (Cambridge University Press, Cambridge).
- Carriquiry A. L., Ireland W. P., Kliemann W. and Uemura E. (1991). Statistical evaluation of dendritic growth models. *Bull. Math. Biol.* **53**, 579–589.
- Castellani G. C., Quinlan E. M., Bersani F., Cooper L. N. and Shouval H. Z. (2005). A model of bidirectional synaptic plasticity: from signaling network to channel conductance. *Learn. Mem.* **12**, 423–432.
- Catterall W. A., Dib-Hajj S., Meisler M. H. and Pietrobon D. (2008). Inherited neuronal ion channelopathies: new windows on complex neurological diseases. *J. Neurosci.* **28**, 11768–11777.
- Catterall W. A., Goldin A. L. and Waxman S. G. (2005a). International Union of Pharmacology. XLVII: nomenclature and structure-function relationships of voltage-gated sodium channels. *Pharmacol. Rev.* **57**, 397–409.
- Catterall W. A. and Gutman G. (2005). Introduction to the IUPHAR compendium of voltage-gated ion channels 2005. *Pharmacol. Rev.* **57**, 385.
- Catterall W. A., Perez-Reyes E., Snutch T. P. and Striessnig J. (2005b). International Union of Pharmacology. XLVIII: nomenclature and structure-function relationships of voltage-gated calcium channels. *Pharmacol. Rev.* **57**, 411–425.

- Cellerino A., Novelli E. and Galli-Resta L. (2000). Retinal ganglion cells with NADPH-diaphorase activity in the chick form a regular mosaic with a strong dorsoventral asymmetry that can be modeled by a minimal spacing rule. *Eur. J. Neurosci.* **12**, 613–620.
- Chalfie M., Tu Y., Euskirchen G., Ward W. W. and Prasher D. C. (1994). Green fluorescent protein as a marker for gene expression. *Science* **263**, 802–805.
- Cherniak C., Changizi M. and Kang D. W. (1999). Large-scale optimization of neuronal arbors. *Phys. Rev. E* **59**, 6001–6009.
- Cherniak C., Mokhtarzada Z. and Nodelman U. (2002). Optimal-wiring models of neuroanatomy. In *Computational Neuroanatomy: Principles and Methods*, ed. G. A. Ascoli (The Humana Press Inc., Totowa, NJ), pp. 71–82.
- Chow C. C. and White J. A. (1996). Spontaneous action potentials due to channel fluctuations. *Biophys. J.* **71**, 3013–3021.
- Chung S. H. (1974). In search of the rules for nerve connections. *Cell* **3**, 201–205.
- Churchland P. S. and Sejnowski T. J. (1992). *The Computational Brain* (MIT Press/Bradford Books, Cambridge, MA).
- Clapham D. E., Julius D., Montell C. and Schultz G. (2005). International Union of Pharmacology. XLIX: nomenclature and structure-function relationships of transient receptor potential channels. *Pharmacol. Rev.* **57**, 427–450.
- Clements J. D., Lester R. A., Tong G., Jahr C. E. and Westbrook G. L. (1992). The time course of glutamate in the synaptic cleft. *Science* **258**, 1498–1501.
- Clements J. D. and Redman S. J. (1989). Cable properties of cat spinal motoneurons measured by combining voltage clamp, current clamp and intracellular staining. *J. Physiol.* **409**, 63–87.
- Coggan J. S., Bartol T. M., Esquenazi E., Stiles J. R., Lamont S., Martone M. E., Berg D. K., Ellisman M. H. and Sejnowski T. J. (2005). Evidence for ectopic neurotransmission at a neuronal synapse. *Science* **309**, 446–451.
- Cole K. S. (1968). *Membranes, Ions, and Impulses: A Chapter of Classical Biophysics* (University of California Press, Berkeley).
- Collier J. E., Monk N. A. M., Maini P. K. and Lewis J. H. (1996). Pattern formation with lateral feedback: a mathematical model of Delta–Notch intracellular signalling. *J. Theor. Biol.* **183**, 429–446.
- Colquhoun D., Hawkes A. G. and Srodzinski K. (1996). Joint distributions of apparent open times and shut times of single ion channels and the maximum likelihood fitting of mechanisms. *Philos. Trans. R. Soc. Lond., A* **354**, 2555–2590.
- Connor J. A. and Stevens C. F. (1971a). Inward and delayed outward membrane currents in isolated neural somata under voltage clamp. *J. Physiol.* **213**, 1–19.
- Connor J. A. and Stevens C. F. (1971b). Prediction of repetitive firing behaviour from voltage clamp data on an isolated neurone soma. *J. Physiol.* **213**, 31–53.
- Connor J. A. and Stevens C. F. (1971c). Voltage clamp studies of a transient outward membrane current in gastropod neural somata. *J. Physiol.* **213**, 21–30.
- Connor J. A., Walter D. and McKown R. (1977). Neural repetitive firing: modifications of the Hodgkin–Huxley axon suggested by experimental results from crustacean axons. *Biophys. J.* **18**, 81–102.
- Connors B. W. and Long M. A. (2004). Electrical synapses in the mammalian brain. *Annu. Rev. Neurosci.* **27**, 393–418.
- Cook J. E. and Chalupa L. M. (2000). Retinal mosaics: new insights into an old concept. *Trends Neurosci.* **23**, 26–34.
- Cook J. E. and Rankin E. C. C. (1986). Impaired refinement of the regenerated retinotectal projection of the goldfish in stroboscopic light: a quantitative WGA-HRP study. *Exp. Brain Res.* **63**, 421–430.
- Coombs J. S., Curtis D. R. and Eccles J. C. (1956). Time courses of motoneuronal responses. *Nature* **178**, 1049–1050.

- Cowan J. D. and Sharp D. H. (1988). Neural nets. *Q. Rev. Biophys.* **21**, 365–427.
- Crank J. and Nicholson P. (1947). A practical method for numerical evaluation of solutions of partial differential equations of the heat-conduction type. *P. Camb. Philos. Soc.* **43**, 50–67.
- Crepel F., Delhaye-Bouchaud N., Guastavino J. M. and Sampaio I. (1980). Multiple innervation of cerebellar Purkinje cells by climbing fibres in staggerer mutant mouse. *Nature* **283**, 483–484.
- Cui J., Cox D. H. and Aldrich R. W. (1997). Intrinsic voltage dependence and Ca^{2+} regulation of *mslo* large conductance Ca^{2+} -activated K^+ channels. *J. Gen. Physiol.* **109**, 647–673.
- Davis G. W. (2006). Homeostatic control of neural activity: from phenomenology to molecular design. *Annu. Rev. Neurosci.* **29**, 307–323.
- Day M., Wang Z., Ding J., An X., Ingham C. A., Shering A. F., Wokosin D., Ilijic E., Sun Z., Sampson A. R., Mugnaini E., Deutch A. Y., Sesack S. R., Arbuthnott G. W. and Surmeier D. J. (2006). Selective elimination of glutamatergic synapses on striatopallidal neurons in Parkinson disease models. *Nat. Neurosci.* **9**, 251–259.
- Dayan P. and Abbott L. F. (2001). *Theoretical Neuroscience: Computational and Mathematical Modeling of Neural Systems* (MIT Press, Cambridge, MA).
- Dayan P. and Willshaw D. J. (1991). Optimising synaptic learning rules in linear associative memories. *Biol. Cybern.* **65**, 253–265.
- De Schutter E. and Bower J. M. (1994a). An active membrane model of the cerebellar Purkinje cell: I. Simulation of current clamps in slice. *J. Neurophysiol.* **71**, 375–400.
- De Schutter E. and Bower J. M. (1994b). An active membrane model of the cerebellar Purkinje cell: II. Simulation of synaptic responses. *J. Neurophysiol.* **71**, 401–419.
- De Schutter E. and Smolen P. (1998). Calcium dynamics in large neuronal models. In *Methods in Neuronal Modeling: From Ions to Networks*, 2nd edn, eds C. Koch and I. Segev (MIT Press, Cambridge, MA), pp. 211–250.
- De Young G. W. and Keizer J. (1992). A single-pool inositol 1,4,5-trisphosphate-receptor-based model for agonist-stimulated oscillations in Ca^{2+} concentration. *Proc. Nat. Acad. Sci. USA* **89**, 9895–9899.
- Dejean C., Hyland B. and Arbuthnott G. (2009). Cortical effects of subthalamic stimulation correlate with behavioral recovery from dopamine antagonist induced akinesia. *Cereb. Cortex* **19**, 1055–1063.
- Del Castillo J. and Katz B. (1954a). Quantal components of the end-plate potential. *J. Physiol.* **124**, 560–573.
- Del Castillo J. and Katz B. (1954b). Statistical factors involved in neuromuscular facilitation and depression. *J. Physiol.* **124**, 574–585.
- Destexhe A. and Bal T., eds (2009). *Dynamic-Clamp from Principles to Applications* (Springer-Verlag, New York).
- Destexhe A. and Huguenard J. R. (2000). Nonlinear thermodynamic models of voltage-dependent currents. *J. Comput. Neurosci.* **9**, 259–270.
- Destexhe A., Mainen Z. F. and Sejnowski T. J. (1994a). An efficient method for computing synaptic conductances based on a kinetic model of receptor binding. *Neural Comput.* **6**, 14–18.
- Destexhe A., Mainen Z. F. and Sejnowski T. J. (1994b). Synthesis of models for excitable membranes, synaptic transmission and neuromodulation using a common kinetic formalism. *J. Comput. Neurosci.* **1**, 195–230.
- Destexhe A., Mainen Z. F. and Sejnowski T. J. (1998). Kinetic models of synaptic transmission. In *Methods in Neuronal Modeling: From Ions to Networks*, 2nd edn, eds C. Koch and I. Segev (MIT Press, Cambridge, MA), pp. 1–25.

- Destexhe A. and Sejnowski T. J. (1995). G-protein activation kinetics and spill-over of GABA may account for differences between inhibitory synapses in the hippocampus and thalamus. *Proc. Nat. Acad. Sci. USA* **92**, 9515–9519.
- Dittman J. S., Kreitzer A. C. and Regehr W. G. (2000). Interplay between facilitation, depression, and residual calcium at three presynaptic terminals. *J. Neurosci.* **20**, 1374–1385.
- Dittman J. S. and Regehr W. G. (1998). Calcium dependence and recovery kinetics of presynaptic depression at the climbing fiber to Purkinje cell synapse. *J. Neurosci.* **18**, 6147–6162.
- Doi T., Kuroda S., Michikawa T. and Kawato M. (2005). Inositol 1,4,5-triphosphate-dependent Ca^{2+} threshold dynamics detect spike timing in cerebellar Purkinje cells. *J. Neurosci.* **25**, 950–961.
- Donohue D. E. and Ascoli G. A. (2005). Local diameter fully constrains dendritic size in basal but not apical trees of CA1 pyramidal neurons. *J. Comput. Neurosci.* **19**, 223–238.
- Donohue D. E., Scorcioni R. and Ascoli G. A. (2002). Generation and description of neuronal morphology using L-Neuron: a case study. In *Computational Neuroanatomy: Principles and Methods*, ed. G. A. Ascoli (The Humana Press Inc., Totowa, NJ), pp. 49–69.
- Douglas J. K., Wilkens L., Pantazelou E. and Moss F. (1993). Noise enhancement of the information transfer in crayfish mechanoreceptors by stochastic resonance. *Nature* **365**, 337–340.
- Doyle D. A., Morais Cabral J., Pfuetzner R. A., Kuo A., Gulbis J. M., Cohen S. L., Chait B. T. and MacKinnon R. (1998). The structure of the potassium channel: molecular basis of K^+ conduction and selectivity. *Science* **280**, 69–77.
- Eccles J. C., Ito M. and Szentagothai J. (1967). *The Cerebellum as a Neuronal Machine* (Springer-Verlag, Berlin).
- Economou M. N., Fernandez F. R. and White J. A. (2010). Dynamic clamp: alteration of response properties and creation of virtual realities in neurophysiology. *J. Neurosci.* **30**, 2407–2413.
- Edelstein-Keshet L. (1988). *Mathematical Models in Biology* (McGraw-Hill, Inc., New York).
- Eglen S. J. and Willshaw D. J. (2002). Influence on cell fate mechanisms upon retinal mosaic formation: a modelling study. *Development* **129**, 5399–5408.
- Einstein A. (1905). Über die von der molekularetheoretischen Theorie der Wärme geforderte Bewegung von in ruhenden Flüssigkeiten suspendierten Teilchen. *Ann. Phys. Leipzig* **17**, 549.
- Elmqvist D. and Quastel D. M. J. (1965). A quantitative study of end-plate potentials in isolated human muscle. *J. Physiol.* **178**, 505–529.
- Ermentrout B. (2002). *Simulating, Analyzing, and Animating Dynamical Systems: A Guide to XPPAUT for Researchers and Students* (SIAM, Philadelphia).
- Evers J. F., Schmitt S., Sibila M. and Duch C. (2005). Progress in functional neuroanatomy: precise automatic geometric reconstruction of neuronal morphology from confocal image stacks. *J. Neurophysiol.* **93**, 2331–2342.
- Eyring H. (1935). The activated complex in chemical reactions. *J. Chem. Phys.* **3**, 107–115.
- Feldheim D. A., Kim Y. I., Bergemann A. D., Frisén J., Barbacid M. and Flanagan J. G. (2000). Genetic analysis of ephrin-A2 and ephrin-A5 shows their requirement in multiple aspects of retinocollicular mapping. *Neuron* **25**, 563–574.
- Feng N., Ning G. and Zheng X. (2005a). A framework for simulating axon guidance. *Neurocomputing* **68**, 70–84.

- Feng N., Yang Y. and Zheng X. (2005b). Spatiotemporal neuronal signalling by nitric oxide: diffusion-reaction modeling and analysis. *Conf. Proc. IEEE Eng. Med. Biol. Soc.* **6**, 6085–6088.
- Fenwick E. M., Marty A. and Neher E. (1982). Sodium and calcium channels in bovine chromaffin cells. *J. Physiol.* **331**, 599–635.
- Fick A. (1855). Über Diffusion. *Ann. Phys. Chem.* **94**, 59–86.
- Filho O., Silva D., Souza H., Cavalcante J., Sousa J., Ferraz F., Silva L. and Santos L. (2001). Stereotactic subthalamic nucleus lesioning for the treatment of Parkinson's disease. *Stereotact. Funct. Neurosurg.* **77**, 79–86.
- Firth C. A. J. M. and Bray D. (2001). Stochastic simulation of cell signaling pathways. In *Computational Modeling of Genetic and Biochemical Networks*, eds J. M. Bower and H. Bolouri (MIT Press, Cambridge, MA), pp. 263–286.
- FitzHugh R. (1961). Impulses and physiological states in theoretical models of nerve membrane. *Biophys. J.* **1**, 445–466.
- Fladby T. and Jansen J. K. S. (1987). Postnatal loss of synaptic terminals in the partially denervated mouse soleus muscle. *Acta Physiol. Scand.* **129**, 239–246.
- Flanagan J. G. and Vanderhaeghen P. (1998). The ephrins and Eph receptors in neural development. *Annu. Rev. Neurosci.* **21**, 309–345.
- Földy C., Aradi I., Howard A. and Soltesz I. (2003). Diversity beyond variance: modulation of firing rates and network coherence by GABAergic subpopulations. *Eur. J. Neurosci.* **19**, 119–130.
- Földy C., Dyhrfjeld-Johnsen J. and Soltesz I. (2005). Structure of cortical microcircuit theory. *J. Physiol.* **562** (1), 47–54.
- Forsythe I. D., Tsujimoto T., Barnes-Davies M., Cuttle M. F. and Takahashi T. (1998). Inactivation of presynaptic calcium current contributes to synaptic depression at a fast central synapse. *Neuron* **20**, 797–807.
- Fourcaud-Trocmé N., Hansel D., van Vreeswijk C. and Brunel N. (2003). How spike generation mechanisms determine the neuronal response to fluctuating inputs. *J. Neurosci.* **23**, 11628–11640.
- Fox A. P., Nowycky M. C. and Tsien R. W. (1987). Kinetic and pharmacological properties distinguishing three types of calcium currents in chick sensory neurones. *J. Physiol.* **394**, 149–172.
- Fraiman D. and Dawson S. P. (2004). A model of the IP₃ receptor with a luminal calcium binding site: stochastic simulations and analysis. *Cell Calcium* **35**, 403–413.
- Franks K. M., Bartol T. M. and Sejnowski T. J. (2002). A Monte Carlo model reveals independent signaling at a central glutamatergic synapse. *Biophys. J.* **83**, 2333–2348.
- Fraser S. E. (1981). A different adhesion approach to the patterning of neural connections. *Dev. Biol.* **79**, 453–464.
- Froemke R. C. and Dan Y. (2002). Spike-timing-dependent synaptic modification induced by natural spike trains. *Nature* **416**, 433–438.
- Fuhrmann G., Segev I., Markram H. and Tsodyks M. (2002). Coding of temporal information by activity-dependent synapses. *J. Neurophysiol.* **87**, 140–148.
- Furshpan E. J. and Potter D. D. (1959). Transmission at the giant motor synapses of the crayfish. *J. Physiol.* **145**, 289–325.
- Fusi S., Drew P. J. and Abbott L. F. (2005). Cascade models of synaptically stored memories. *Neuron* **45**, 599–611.
- Gabbiani F. and Koch C. (1998). Principles of spike train analysis. In *Methods in Neuronal Modeling: From Ions to Networks*, 2nd edn, eds C. Koch and I. Segev (MIT Press, Cambridge, MA), pp. 313–360.
- Gabbiani F., Midgaard J. and Knöpfel T. (1994). Synaptic integration in a model of cerebellar granule cells. *J. Neurophysiol.* **72**, 999–1009.

- Galli-Resta L., Resta G., Tan S. S. and Reese B. E. (1997). Mosaics of Islet-1 expressing amacrine cells assembled by short range cellular interactions. *J. Neurosci.* **17**, 7831–7838.
- Gardiner C. W. (1985). *Handbook of Stochastic Methods* (Springer-Verlag, Berlin).
- Gardner-Medwin A. R. (1976). The recall of events through the learning of associations between their parts. *Proc. R. Soc. Lond., B* **194**, 375–402.
- Garofalo L., da Silva A. R. and Cuello C. (1992). Nerve growth factor induced synaptogenesis and hypertrophy of cortical cholinergic terminals. *Proc. Nat. Acad. Sci. USA* **89**, 2639–2643.
- Gaze R. M., Feldman J. D., Cooke J. and Chung S. H. (1979). The orientation of the visuo-tectal map in *Xenopus*: development aspects. *J. Embryol. Exp. Morphol.* **53**, 39–66.
- Gaze R. M. and Hope R. A. (1983). The visuotectal projection following translocation of grafts within an optic tectum in the goldfish. *J. Physiol.* **344**, 257.
- Gaze R. M., Jacobson M. and Székely G. (1963). The retinotectal projection in *Xenopus* with compound eyes. *J. Physiol.* **165**, 384–499.
- Gaze R. M. and Keating M. J. (1972). The visual system and ‘neuronal specificity’. *Nature* **237**, 375–378.
- Gaze R. M., Keating M. J. and Chung S. H. (1974). The evolution of the retinotectal map during development in *Xenopus*. *Proc. R. Soc. Lond., B* **185**, 301–330.
- Gaze R. M. and Sharma S. C. (1970). Axial differences in the reinnervation of the goldfish optic tectum by regenerating optic nerve fibres. *Exp. Brain Res.* **10**, 171–181.
- Geisler C. D. and Goldberg J. M. (1966). A stochastic model of the repetitive activity of neurons. *Biophys. J.* **6**, 53–69.
- Gentet L. J., Stuart G. J. and Clements J. D. (2000). Direct measurement of specific membrane capacitance in neurons. *Biophys. J.* **79**, 314–320.
- Gerstner W. (2000). Population dynamics of spiking neurons: fast transients, asynchronous states, and locking. *Neural Comput.* **12**, 43–89.
- Gerstner W. and Kistler W. (2002). *Spiking Neuron Models* (Cambridge University Press, Cambridge).
- Gibson M. A. and Bruck J. (2000). Efficient exact simulation of chemical systems with many species and many channels. *J. Phys. Chem. A* **104**, 1876–1889.
- Gierer A. (1983). Model for the retino-tectal projection. *Proc. R. Soc. Lond., B* **218**, 77–93.
- Gierer A. and Meinhardt H. (1972). A theory of biological pattern formation. *Kybernetik* **12**, 30–39.
- Gilbert S. F. (1997). *Developmental Biology*, 5th edn (Sinauer Associates, Inc., Sunderland, MA).
- Gillespie D. (1977). Exact stochastic simulation of coupled chemical reactions. *J. Phys. Chem.* **81**, 2340–2361.
- Gillespie D. (2001). Approximate accelerated stochastic simulation of chemically reacting systems. *J. Chem. Phys.* **115**, 1716–1733.
- Gillies A. and Willshaw D. (2006). Membrane channel interactions underlying rat subthalamic projection neuron rhythmic and bursting activity. *J. Neurophysiol.* **95**, 2352–2365.
- Gin E., Kirk V. and Sneyd J. (2006). A bifurcation analysis of calcium buffering. *J. Theor. Biol.* **242**, 1–15.
- Gingrich K. J. and Byrne J. H. (1985). Simulation of synaptic depression, post-tetanic potentiation, and presynaptic facilitation of synaptic potentials from sensory neurons mediating gill-withdrawal reflex in *Aplysia*. *J. Neurophysiol.* **53**, 652–669.

- Gleeson P., Steuber V. and Silver R. A. (2007). neuroConstruct: a tool for modeling networks of neurons in 3D space. *Neuron* **54**, 219–235.
- Goddard N. H. and Hood G. (1998). Large-scale simulation using Parallel GENESIS. In *The Book of GENESIS: Exploring Realistic Neural Models with the General NEural SImulation System*, eds J. M. Bower and D. Beeman 2nd edn (Springer-Verlag, New York), pp. 349–379.
- Goldbeter A., Dupont G. and Berridge M. J. (1990). Minimal model for signal-induced Ca^{2+} oscillations and for their frequency encoding through protein phosphorylation. *Proc. Nat. Acad. Sci. USA* **87**, 1461–1465.
- Golding N. L., Kath W. L. and Spruston N. (2001). Dichotomy of action-potential backpropagation in CA1 pyramidal neuron dendrites. *J. Neurophysiol.* **86**, 2998–3010.
- Goldman D. E. (1943). Potential, impedance, and rectification in membranes. *J. Gen. Physiol.* **27**, 37–60.
- Goldman L. and Schauf C. L. (1972). Inactivation of the sodium current in *Myxicola* giant axon. *J. Gen. Physiol.* **59**, 659–675.
- Goldman M. S., Golowasch J., Marder E. and Abbott L. F. (2001). Global structure, robustness, and modulation of neuronal models. *J. Neurosci.* **21**, 5229–5238.
- Goldstein S. A., Bayliss D. A., Kim D., Lesage F., Plant L. D. and Rajan S. (2005). International Union of Pharmacology. LV: nomenclature and molecular relationships of two-P potassium channels. *Pharmacol. Rev.* **57**, 527–540.
- Goodhill G. J. (2007). Contributions of theoretical modelling to the understanding of neural map development. *Neuron* **56**, 301–311.
- Goodhill G. J. and Urbach J. S. (2003). Axon guidance and gradient detection by growth cones. In *Modeling Neural Development*, ed. A. van Ooyen (MIT Press, Cambridge, MA), pp. 95–109.
- Goodhill G. J. and Xu J. (2005). The development of retinotectal maps: a review of models based on molecular gradients. *Network Comp. Neural Syst.* **16**, 5–34.
- Gouzé J. L., Lasry J. M. and Changeux J. P. (1983). Selective stabilization of muscle innervation during development: a mathematical model. *Biol. Cybern.* **46**, 207–215.
- Gradinari V., Mogri M., Thompson K. R., Henderson J. M. and Deisseroth K. (2009). Optical deconstruction of Parkinsonian neural circuitry. *Science* **324**, 354–359.
- Graham B. and Willshaw D. (1999). Probabilistic synaptic transmission in the associative net. *Neural Comput.* **11**, 117–137.
- Graham B. P., Lauchlan K. and McLean D. R. (2006). Dynamics of outgrowth in a continuum model of neurite elongation. *J. Comput. Neurosci.* **20**, 43–60.
- Graham B. P. and Redman S. J. (1994). A simulation of action potentials in synaptic boutons during presynaptic inhibition. *J. Neurophysiol.* **71**, 538–549.
- Graham B. P. and van Ooyen A. (2004). Transport limited effects in a model of dendritic branching. *J. Theor. Biol.* **230**, 421–432.
- Graham B. P. and van Ooyen A. (2006). Mathematical modelling and numerical simulation of the morphological development of neurons. *BMC Neurosci.* **7** (Suppl 1), S9.
- Graham B. P. and Willshaw D. J. (1995). Improving recall from an associative memory. *Biol. Cybern.* **72**, 337–346.
- Gutman G. A., Chandy K. G., Grissmer S., Lazdunski M., McKinnon D., Pardo L. A., Robertson G. A., Rudy B., Sanguinetti M. C., Stühmer W. and Wang X. (2005). International Union of Pharmacology. LIII: nomenclature and molecular relationships of voltage-gated potassium channels. *Pharmacol. Rev.* **57**, 473–508.

- Hagiwara S. and Saito N. (1959). Voltage-current relations in nerve cell membrane of *Onchidium verruculatum*. *J. Physiol.* **148**, 161–179.
- Hale J. K. and Koçak H. (1991). *Dynamics and Bifurcations* (Springer-Verlag, New York).
- Halliwell J. V. and Adams P. R. (1982). Voltage-clamp analysis of muscarinic excitation in hippocampal neurons. *Brain Res.* **250**, 71–92.
- Hamill O. P., Marty A., Neher E., Sakmann B. and Sigworth F. J. (1981). Improved patch-clamp techniques for high-resolution current recording from cells and cell-free membrane patches. *Pflügers Arch.* **391**, 85–100.
- Hansel D. and Mato G. (2000). Existence and stability of persistent states in large neuronal networks. *Phys. Rev. Lett.* **86**, 4175–4178.
- Hansel D., Mato G., Meunier C. and Neltner L. (1998). On numerical simulations of integrate-and-fire neural networks. *Neural Comput.* **10**, 467–483.
- Hashimoto T., Elder C., Okun M., Patrick S. and Vitek J. (2003). Stimulation of the subthalamic nucleus changes the firing pattern of pallidal neurons. *J. Neurosci.* **23**, 1916–1923.
- Hayer A. and Bhalla U. S. (2005). Molecular switches at the synapse emerge from receptor and kinase traffic. *PLoS Comput. Biol.* **1**, e20.
- Hebb D. O. (1949). *The Organization of Behavior* (Wiley, New York).
- Heinemann C. von Rüden, Chow R. H. and Neher E. (1993). A two-step model of secretion control in neuroendocrine cells. *Pflügers Arch.* **424**, 105–112.
- Heinemann S. H., Rettig J., Graack H. R. and Pongs O. (1996). Functional characterization of Kv channel beta-subunits from rat brain. *J. Physiol.* **493** (3), 625–633.
- Hely T. A., Graham B. P. and van Ooyen A. (2001). A computational model of dendrite elongation and branching based on MAP2 phosphorylation. *J. Theor. Biol.* **210**, 375–384.
- Hentschel H. G. E. and van Ooyen A. (1999). Models of axon guidance and bundling during development. *Proc. R. Soc. Lond., B* **266**, 2231–2238.
- Hertz J. A., Krogh A. S. and Palmer R. G. (1991). *Introduction to the Theory of Neural Computation* (Addison-Wesley, Reading, MA).
- Herz A. V., Gollisch T., Machens C. K. and Jaeger D. (2006). Modeling single-neuron dynamics and computations: a balance of detail and abstraction. *Science* **314**, 80–85.
- Hill A. V. (1936). Excitation and accommodation in nerve. *Proc. R. Soc. Lond., B* **119**, 305–355.
- Hill T. L. and Chen Y. D. (1972). On the theory of ion transport across the nerve membrane VI. Free energy and activation free energies of conformational change. *Proc. Nat. Acad. Sci. USA* **69**, 1723–1726.
- Hille B. (2001). *Ion Channels of Excitable Membranes* 3rd edn (Sinauer Associates, Sunderland, MA).
- Hillman D. E. (1979). Neuronal shape parameters and substructures as a basis of neuronal form. In *The Neurosciences: Fourth Study Program*, eds F. O. Schmitt and F. G. Worden (MIT Press, Cambridge, MA), pp. 477–498.
- Hines M. L. and Carnevale N. T. (1997). The NEURON simulation environment. *Neural Comput.* **9**, 1179–1209.
- Hines M. L. and Carnevale N. T. (2008). Translating network models to parallel hardware in NEURON. *J. Neurosci. Methods* **169**, 425–455.
- Hines M. L., Markram H. and Schuermann F. (2008). Fully implicit parallel simulation of single neurons. *J. Comput. Neurosci.* **25**, 439–448.
- Hinton G. E. and Anderson J. A., eds. (1981). *Parallel Models of Associative Memory* (Lawrence Erlbaum Associates, Hillsdale, NJ).

- Hirschberg B., Maylie J., Adelman J. P. and Marrion N. V. (1998). Gating of recombinant small-conductance Ca-activated K⁺ channels by calcium. *J. Gen. Physiol.* **111**, 565–581.
- Hodgkin A. L. (1948). The local electric changes associated with repetitive action in a non-medullated axon. *J. Physiol.* **107**, 165–181.
- Hodgkin A. L. (1964). *The Conduction of the Nervous Impulse* (Charles C Thomas, Springfield, IL).
- Hodgkin A. L. (1976). Chance and design in electrophysiology: an informal account of certain experiments on nerve carried out between 1934 and 1952. *J. Physiol.* **263**, 1–21.
- Hodgkin A. L. and Huxley A. F. (1952a). Currents carried by sodium and potassium ions through the membrane of the giant axon of *Loligo*. *J. Physiol.* **116**, 449–472.
- Hodgkin A. L. and Huxley A. F. (1952b). The components of membrane conductance in the giant axon of *Loligo*. *J. Physiol.* **116**, 473–496.
- Hodgkin A. L. and Huxley A. F. (1952c). The dual effect of membrane potential on sodium conductance in the giant axon of *Loligo*. *J. Physiol.* **116**, 497–506.
- Hodgkin A. L. and Huxley A. F. (1952d). A quantitative description of membrane current and its application to conduction and excitation in nerve. *J. Physiol.* **117**, 500–544.
- Hodgkin A. L., Huxley A. F. and Katz B. (1952). Measurement of current–voltage relations in the membrane of the giant axon of *Loligo*. *J. Physiol.* **116**, 424–448.
- Hodgkin A. L. and Katz B. (1949). The effect of sodium ions on the electrical activity of the giant axon of the squid. *J. Physiol.* **108**, 37–77.
- Hoffman D. A., Magee J. C., Colbert C. M. and Johnston D. (1997). K⁺ channel regulation of signal propagation in dendrites of hippocampal pyramidal neurons. *Nature* **387**, 869–875.
- Hofmann F., Biel M. and Kaupp B. U. (2005). International Union of Pharmacology. LI: nomenclature and structure–function relationships of cyclic nucleotide-regulated channels. *Pharmacol. Rev.* **57**, 455–462.
- Holland J. H., ed. (1975). *Adaptation in Natural and Artificial Systems: An Introductory Analysis with Applications to Biology, Control, and Artificial Intelligence* (University of Michigan Press, Ann Arbor, MI).
- Holmes W. R. and Rall W. (1992a). Electrotonic length estimates in neurons with dendritic tapering or somatic shunt. *J. Neurophysiol.* **68**, 1421–1437.
- Holmes W. R. and Rall W. (1992b). Electrotonic models of neuronal dendrites and single neuron computation. In *Single Neuron Computation*, eds T. McKenna, J. Davis and S. F. Zornetzer (Academic Press, Boston, MA), pp. 7–25.
- Holmes W. R. and Rall W. (1992c). Estimating the electrotonic structure of neurons with compartmental models. *J. Neurophysiol.* **68**, 1438–1452.
- Holmes W. R., Segev I. and Rall W. (1992). Interpretation of time constant and electrotonic length estimates in multicylinder or branched neuronal structures. *J. Neurophysiol.* **68**, 1401–1420.
- Holtzmann D. M., Li Y., Parada L. F., Kinsmann S., Chen C. K., Valletta J. S., Zhou J., Long J. B. and Mobley W. C. (1992). p140^{trk} mRNA marks NGF-responsive forebrain neurons: evidence that *trk* gene expression is induced by NGF. *Neuron* **9**, 465–478.
- Honda H. (1998). Topographic mapping in the retinotectal projection by means of complementary ligand and receptor gradients: a computer simulation study. *J. Theor. Biol.* **192**, 235–246.
- Honda H. (2003). Competition for retinal ganglion axons for targets under the servomechanism model explains abnormal retinocollicular projection of Eph receptor-overexpressing or ephrin-lacking mice. *J. Neurosci.* **23**, 10368–10377.

- Hoops S., Sahle S., Gauges R., Lee C., Pahle J., Simus N., Singhal M., Xu L., Mendes P. and Kummer U. (2006). COPASI – COmplex PAthway SImlator. *Bioinformatics* **22**, 3067–3074.
- Hope R. A., Hammond B. J. and Gaze R. M. (1976). The arrow model: retinotectal specificity and map formation in the goldfish visual system. *Proc. R. Soc. Lond., B* **194**, 447–466.
- Hopfield J. J. (1982). Neural networks and physical systems with emergent collective computational abilities. *Proc. Nat. Acad. Sci. USA* **79**, 2554–2558.
- Hopfield J. J. (1984). Neurons with graded response have collective computational properties like those of two-state neurons. *Proc. Nat. Acad. Sci. USA* **81**, 3088–3092.
- Horsfield K., Woldenberg M. J. and Bowes C. L. (1987). Sequential and synchronous growth models related to vertex analysis and branching ratios. *Bull. Math. Biol.* **49**, 413–430.
- Hospedales T. M., van Rossum M. C. W., Graham B. P. and Dutia M. B. (2008). Implications of noise and neural heterogeneity for vestibulo-ocular reflex fidelity. *Neural Comput.* **20**, 756–778.
- Hoyt R. C. (1963). The squid giant axon: mathematical models. *Biophys. J.* **3**, 399–431.
- Hoyt R. C. (1968). Sodium inactivation in nerve fibres. *Biophys. J.* **8**, 1074–1097.
- Hubel D. H. and Wiesel T. N. (1963). Receptive fields of cells in striate cortex of very young, visually inexperienced kittens. *J. Neurophysiol.* **26**, 994–1002.
- Hubel D. H. and Wiesel T. N. (1977). Functional architecture of macaque monkey visual cortex. *Proc. R. Soc. Lond., B* **1130**, 1–59.
- Hubel D. H., Wiesel T. N. and LeVay S. (1977). Plasticity of ocular dominance columns in monkey striate cortex. *Philos. Trans. R. Soc. Lond., B* **278**, 377–409.
- Huguenard J. R. and McCormick D. A. (1992). Simulation of the currents involved in rhythmic oscillations in thalamic relay neurons. *J. Neurophysiol.* **68**, 1373–1383.
- Hunter R., Cobb S. and Graham B. P. (2009). Improving associative memory in a network of spiking neurons. *Neural Network World* **19**, 447–470.
- Huys Q., Ahrens M. and Paninski L. (2006). Efficient estimation of detailed single-neuron models. *J. Neurophysiol.* **96**, 872–890.
- Ireland W., Heidel J. and Uemura E. (1985). A mathematical model for the growth of dendritic trees. *Neurosci. Lett.* **54**, 243–249.
- Irvine L. A., Jafri M. S. and Winslow R. L. (1999). Cardiac sodium channel Markov model with temperature dependence and recovery from inactivation. *Biophys. J.* **76**, 1868–1885.
- Izhikevich E. M. (2003). Simple model of spiking neurons. *IEEE Trans. Neural Netw.* **14**, 1569–1572.
- Izhikevich E. M. (2004). Which model to use for cortical spiking neurons? *IEEE Trans. Neural Netw.* **15**, 1063–1070.
- Izhikevich E. M. (2007). *Dynamical Systems in Neuroscience: The Geometry of Excitability and Bursting* (MIT Press, Cambridge, MA).
- Izhikevich E. M. and Edelman G. M. (2008). Large-scale model of mammalian thalamocortical systems. *Proc. Nat. Acad. Sci. USA* **105**, 3593–3598.
- Jacobson M. and Levine R. L. (1975). Plasticity in the adult frog brain: filling in the visual scotoma after excision or translocation of parts of the optic tectum. *Brain Res.* **88**, 339–345.
- Jaeger D. and Bower J. M. (1999). Synaptic control of spiking in cerebellar Purkinje cells: dynamic current clamp based on model conductances. *J. Neurosci.* **19**, 6090–6101.

- Jaffe D. B., Ross W. N., Lisman J. E., Lasser-Ross N., Miyakawa H. and Johnston D. (1994). A model for dendritic Ca^{2+} accumulation in hippocampal pyramidal neurons based on fluorescence imaging measurements. *J. Neurophysiol.* **71**, 1065–1077.
- Jahr C. E. and Stevens C. F. (1990a). A quantitative description of NMDA receptor-channel kinetic behavior. *J. Neurosci.* **10**, 1830–1837.
- Jahr C. E. and Stevens C. F. (1990b). Voltage dependence of NMDA-activated macroscopic conductances predicted by single-channel kinetics. *J. Neurosci.* **10**, 3178–3182.
- Jansen J. K. S. and Fladby T. (1990). The perinatal reorganization of the innervation of skeletal muscle in mammals. *Prog. Neurobiol.* **34**, 39–90.
- Jentsch T. J. (2000). Neuronal KCNQ potassium channels: physiology and role in disease. *Nat. Rev. Neurosci.* **1**, 21–30.
- Jentsch T. J., Neagoe I. and Scheel O. (2005). CLC chloride channels and transporters. *Curr. Opin. Neurobiol.* **15**, 319–325.
- Jiang Y., Lee A., Chen J., Ruta V., Cadene M., Chait B. T. and Mackinnon R. (2003). X-ray structure of a voltage-dependent K^+ channel. *Nature* **423**, 33–41.
- Johnston D. and Wu S. M. S. (1995). *Foundations of Cellular Neurophysiology* (MIT Press, Cambridge, MA).
- Jolivet R., Lewis T. J. and Gerstner W. (2004). Generalized integrate-and-fire models of neuronal activity approximate spike trains of a detailed model to a high degree of accuracy. *J. Neurophysiol.* **92**, 959–976.
- Jolivet R., Schürmann F., Berger T., Naud R., Gerstner W. and Roth A. (2008). The quantitative single-neuron modeling competition. *Biol. Cybern.* **99**, 417–426.
- Katz B. and Miledi R. (1968). The role of calcium in neuromuscular facilitation. *J. Physiol.* **195**, 481–492.
- Keizer J. and Levine L. (1996). Ryanodine receptor adaptation and Ca^{2+} -induced Ca^{2+} release-dependent Ca^{2+} oscillations. *Biophys. J.* **71**, 3477–3487.
- Kepler T. B., Abbott L. F. and Marder E. (1992). Reduction of conductance-based neuron models. *Biol. Cybern.* **66**, 381–387.
- Kiddie G., McLean D. R., van Ooyen A. and Graham B. P. (2005). Biologically plausible models of neurite outgrowth. *Prog. Brain Res.* **147**, 67–80.
- Kirkpatrick S., Gelatt C. D. and Vecchi M. P. (1983). Optimization by simulated annealing. *Science* **220**, 671–680.
- Kita H. and Armstrong W. (1991). A biotin-containing compound N-(2-aminoethyl) biotinamide for intracellular labeling and neuronal tracing studies: comparison with biocytin. *J. Neurosci. Methods* **37**, 141–150.
- Kita H., Chang H. and Kitai S. (1983). Pallidal inputs to the subthalamus: intracellular analysis. *Brain Res.* **264**, 255–265.
- Klee R., Ficker E. and Heinemann U. (1995). Comparison of voltage-dependent potassium currents. *J. Neurophysiol.* **74**, 1982–1995.
- Kliemann W. A. (1987). Stochastic dynamic model for the characterization of the geometric structure of dendritic processes. *Bull. Math. Biol.* **49**, 135–152.
- Knight B. W. (1972). Dynamics of encoding in a population of neurons. *J. Gen. Physiol.* **59**, 734–766.
- Koch C. (1999). *Biophysics of Computation: Information Processing in Single Neurons* (Oxford University Press, New York).
- Koene R. A., Tijms B., van Hees P., Postma F., de Ridder A., Ramakers G. J. A., van Pelt J. and van Ooyen A. (2009). NETMORPH: a framework for the stochastic generation of large scale neuronal networks with realistic neuron morphologies. *Neuroinformatics* **7**, 195–210.
- Köhling R. (2002). Voltage-gated sodium channels in epilepsy. *Epilepsia* **43**, 1278–1295.

- Koulakov A. A. and Tsigankov D. N. (2004). A stochastic model for retinocollicular map development. *BMC Neurosci.* **5**, 30–46.
- Krauskopf B., Osinga H. M. and Galán-Vioque J., eds (2007). *Numerical Continuation Methods for Dynamical Systems: Path Following and Boundary Value Problems* (Springer, Dordrecht).
- Krottje J. K. and van Ooyen A. (2007). A mathematical framework for modeling axon guidance. *Bull. Math. Biol.* **69**, 3–31.
- Kubo Y., Adelman J. P., Clapham D. E., Jan L. Y., Karschin A., Kurachi Y., Lazdunski M., Nichols C. G., Seino S. and Vandenberg C. A. (2005). International Union of Pharmacology. LIV: nomenclature and molecular relationships of inwardly rectifying potassium channels. *Pharmacol. Rev.* **57**, 509–526.
- Kuroda S., Schweighofer N. and Kawato M. (2001). Exploration of signal transduction pathways in cerebellar long-term depression by kinetic simulation. *J. Neurosci.* **21**, 5693–5702.
- Kusano K. and Landau E. M. (1975). Depression and recovery of transmission at the squid giant synapse. *J. Physiol.* **245**, 13–32.
- Landahl H. (1939). A contribution to the mathematical biophysics of psychophysical discrimination II. *Bull. Math. Biophys.* **1**, 159–176.
- Langley J. N. (1895). Note on regeneration of pre-ganglionic fibres of the sympathetic ganglion. *J. Physiol.* **18**, 280–284.
- Lapicque L. (1907). Recherches quantitatives sur l'excitation électrique des nerfs traitée comme une polarisation. *J. Physiol. Paris* **9**, 620–635.
- Larkman A. and Mason A. (1990). Correlations between morphology and electrophysiology of pyramidal neurons in slices of rat visual cortex: I. Establishment of cell classes. *J. Neurosci.* **10**, 1407–1414.
- Larkman A., Stratford K. and Jack J. (1991). Quantal analysis of excitatory synaptic action and depression in hippocampal slices. *Nature* **350**, 344–347.
- Latham P. E., Richmond B. J., Nelson P. G. and Nirenberg S. (2000). Intrinsic dynamics in neuronal networks: I. Theory. *J. Neurophysiol.* **83**, 808–827.
- Laurent G. (1996). Dynamical representation of odors by oscillating and evolving neural assemblies. *Trends Neurosci.* **19**, 489–496.
- Le Novère N. and Shimizu T. S. (2001). STOCHSIM: modelling of stochastic biomolecular processes. *Bioinformatics* **17**, 575–576.
- Lebedev M. A. and Nicolelis M. A. L. (2006). Brain-machine interfaces: past, present and future. *Trends Neurosci.* **29**, 536–546.
- LeMasson G. and Maex R. (2001). Introduction to equation solving and parameter fitting. In *Computational Neuroscience: Realistic Modeling for Experimentalists*, ed. E. De Schutter (CRC Press, Boca Raton, FL), pp. 1–23.
- LeVay S., Wiesel T. N. and Hubel D. H. (1980). The development of ocular dominance columns in normal and visually deprived monkeys. *J. Comp. Neurol.* **191**, 1–51.
- Levine R. L. and Jacobson M. (1974). Deployment of optic nerve fibers is determined by positional markers in the frog's tectum. *Exp. Neurol.* **43**, 527–538.
- Levy W. B. and Steward O. (1979). Synapses as associative memory elements in the hippocampal formation. *Brain Res.* **175**, 233–245.
- Levy W. B. and Steward O. (1983). Temporal contiguity requirements for long-term associative potentiation/depression in the hippocampus. *Neuroscience* **8**, 791–797.
- Li G. H., Qin C. D. and Li M. H. (1994). On the mechanisms of growth cone locomotion: modeling and computer simulation. *J. Theor. Biol.* **169**, 355–362.
- Li G. H., Qin C. D. and Wang L. W. (1995). Computer model of growth cone behavior and neuronal morphogenesis. *J. Theor. Biol.* **174**, 381–389.

- Li G. H., Qin C. D. and Wang Z. S. (1992). Neurite branching pattern formation: modeling and computer simulation. *J. Theor. Biol.* **157**, 463–486.
- Li W. C., Sofe S. R. and Roberts A. (2004). A direct comparison of whole cell patch and sharp electrodes by simultaneous recording from single spinal neurons in frog tadpoles. *J. Neurophysiol.* **92**, 380–386.
- Li Y. X. and Rinzel J. (1994). Equations for InsP₃ receptor-mediated [Ca²⁺]_i oscillations derived from a detailed kinetic model: a Hodgkin–Huxley like formalism. *J. Theor. Biol.* **166**, 461–473.
- Liley A. W. and North K. A. K. (1953). An electrical investigation of effects of repetitive stimulation on mammalian neuromuscular junction. *J. Neurophysiol.* **16**, 509–527.
- Lima P. A. and Marrion N. V. (2007). Mechanisms underlying activation of the slow AHP in rat hippocampal neurons. *Brain Res.* **1150**, 74–82.
- Lindsay K. A., Maxwell D. J., Rosenberg J. R. and Tucker G. (2007). A new approach to reconstruction models of dendritic branching patterns. *Math. Biosci.* **205**, 271–296.
- Lisman J. E. and Idiart M. A. P. (1995). Storage of 7 ± 2 short-term memories in oscillatory subcycles. *Science* **267**, 1512–1514.
- Little W. A. (1974). The existence of persistent states in the brain. *Math. Biosci.* **19**, 101–120.
- Liu Z., Golowasch J., Marder E. and Abbott L. F. (1998). A model neuron with activity-dependent conductances regulated by multiple calcium sensors. *J. Neurosci.* **18**, 2309–2320.
- Long S. B., Campbell E. B. and Mackinnon R. (2005). Crystal structure of a mammalian voltage-dependent shaker family K⁺ channel. *Science* **309**, 897–903.
- Lotka A. J. (1925). *Elements of Physical Biology* (Williams and Wilkins, Baltimore, MD).
- Lux H. D., Schubert P. and Kreutzberg G. W. (1970). Direct matching of morphological and electrophysiological data in the cat spinal motoneurons. In *Excitatory Synaptic Mechanisms*, eds P. Anderson and J. K. Janson (Universitetsforlaget, Oslo), pp. 189–198.
- Lynch G. S., Dunwiddie T. and Gribkoff V. (1977). Heterosynaptic depression: a postsynaptic correlate of long-term potentiation. *Nature* **266**, 737–739.
- Magee J. C. and Johnston D. (1995). Characterization of single voltage-gated Na⁺ and Ca²⁺ channels in apical dendrites of rat CA1 pyramidal neurons. *J. Physiol.* **487**, 67–90.
- Magistretti J. and Alonso A. (1999). Biophysical properties and slow voltage-dependent inactivation of a sustained sodium current in entorhinal cortex layer-II principal neurons: a whole-cell and single-channel study. *J. Gen. Physiol.* **114**, 491–509.
- Magistretti J., Castelli L., Forti L. and D'Angelo E. (2006). Kinetic and functional analysis of transient, persistent and resurgent sodium currents in rat cerebellar granule cells *in situ*: an electrophysiological and modelling study. *J. Physiol.* **573**, 83–106.
- Magleby K. L. (1987). Short-term changes in synaptic efficacy. In *Synaptic Function*, eds G. M. Edelman, L. E. Gall, W. Maxwell and W. M. Cowan (Wiley, New York), pp. 21–56.
- Major G. (1993). Solutions for transients in arbitrarily branching cables: III. Voltage clamp problems. *Biophys. J.* **65**, 469–491.
- Major G., Evans J. and Jack J. J. (1993a). Solutions for transients in arbitrarily branching cables: I. Voltage recording with a somatic shunt. *Biophys. J.* **65**, 423–449.

- Major G., Evans J. and Jack J. J. (1993b). Solutions for transients in arbitrarily branching cables: II. Voltage clamp theory. *Biophys. J.* **65**, 450–468.
- Major G. and Evans J. D. (1994). Solutions for transients in arbitrarily branching cables: IV. Nonuniform electrical parameters. *Biophys. J.* **66**, 615–638.
- Major G., Larkman A. U., Johas P., Sackmann B. and Jack J. J. (1994). Detailed passive cable models of whole-cell recorded CA3 pyramidal neurons in rat hippocampal slices. *J. Neurosci.* **14**, 4613–4638.
- Malthus T. R. (1798). *An Essay on the Principle of Population* (Oxford University Press, Oxford).
- Manor Y., Gonczarowski J. and Segev I. (1991a). Propagation of action potentials along complex axonal trees: model and implementation. *Biophys. J.* **60**, 1411–1423.
- Manor Y., Koch C. and Segev I. (1991b). Effect of geometrical irregularities on propagation delay in axonal trees. *Biophys. J.* **60**, 1424–1437.
- Maravall M., Mainen Z. F., Sabatini B. L. and Svoboda K. (2000). Estimating intracellular calcium concentrations and buffering without wavelength ratioing. *Biophys. J.* **78**, 2655–2667.
- Marder E. (2009). Electrical synapses: rectification demystified. *Curr. Biol.* **19**, R34–R35.
- Marder E. and Goaillard J. M. (2006). Variability, compensation and homeostasis in neuron and network function. *Nat. Rev. Neurosci.* **7**, 153–160.
- Marder E. and Prinz A. A. (2002). Modeling stability in neuron and network function: the role of activity in homeostasis. *Bioessays* **24**, 1145–1154.
- Markram H. (2006). The blue brain project. *Nat. Rev. Neurosci.* **7**, 153–160.
- Markram H., Gupta A., Uziel A., Wang Y. and Tsodyks M. (1998). Information processing with frequency-dependent synaptic connections. *Neurobiol. Learn. Mem.* **70**, 101–112.
- Markram H., Luebke J., Frotscher M. and Sakmann B. (1997). Regulation of synaptic efficacy by coincidence of postsynaptic APs and EPSPs. *Science* **275**, 213–215.
- Marler K. J. M., Becker-Barroso E., Martinez A., Llovera M., Wentzel C., Poopalasundaram S., Hindges R., Soriano E., Comella J. and Drescher U. (2008). A TrkB/ephrinA interaction controls retinal axon branching and synaptogenesis. *J. Neurosci.* **28**, 12700–12712.
- Marmont M. (1949). Studies on the axon membrane. *J. Cell. Comp. Physiol.* **34**, 351–382.
- Marr D. (1969). A theory of cerebellar cortex. *J. Physiol.* **202**, 437–470.
- Marr D. (1970). A theory for cerebral neocortex. *Proc. R. Soc. Lond., B* **176**, 161–234.
- Marr D. (1971). Simple memory: a theory for archicortex. *Philos. Trans. R. Soc. Lond., B* **262**, 23–81.
- Mascagni M. V. and Sherman A. S. (1998). Numerical methods for neuronal modeling. In *Methods in Neuronal Modeling: From Ions to Networks*, 2nd edn, eds C. Koch and I. Segev (MIT Press, Cambridge, MA), pp. 569–606.
- Maskery S., Buettner H. M. and Shinbrot T. (2004). Growth cone pathfinding: a competition between deterministic and stochastic events. *BMC Neurosci.* **5**, 22.
- Matveev V. and Wang X. J. (2000). Implications of all-or-none synaptic transmission and short-term depression beyond vesicle depletion: a computational study. *J. Neurosci.* **20**, 1575–1588.
- Maurice N., Mercer J., Chan C. S., Hernandez-Lopez S., Held J., Tkatch T. and Surmeier D. J. (2004). D₂ dopamine receptor-mediated modulation of voltage-dependent Na⁺ channels reduces autonomous activity in striatal cholinergic interneurons. *J. Neurosci.* **24**, 10289–10301.

- McClelland J. L., Rumelhart D. E. and the PDP Research Group, eds (1986). *Parallel Distributed Processing: Explorations in the Microstructure of Cognition. Volume 2: Psychological and Biological Models* (MIT Press, Cambridge, MA).
- McCulloch W. S. and Pitts W. (1943). A logical calculus of the ideas immanent in nervous activity. *Bull. Math. Biophys.* **5**, 115–133.
- McIntyre C., Grill W., Sherman D. and Thakor N. (2004). Cellular effects of deep brain stimulation: model-based analysis of activation and inhibition. *J. Neurophysiol.* **91**, 1457–1469.
- McIntyre C., Richardson A. and Grill W. (2002). Modelling the excitability of mammalian nerve cells: influence of afterpotentials on the recovery cycle. *J. Neurophysiol.* **87**, 995–1006.
- McKay B. E. and Turner R. W. (2005). Physiological and morphological development of the rat cerebellar Purkinje cell. *J. Physiol.* **567**, 829–850.
- McLean D. R. and Graham B. P. (2004). Mathematical formulation and analysis of a continuum model for tubulin-driven neurite elongation. *Proc. R. Soc. Lond., A* **460**, 2437–2456.
- McNaughton B. L. and Morris R. G. M. (1987). Hippocampal synaptic enhancement and information storage within a distributed memory system. *Trends Neurosci.* **10**, 408–415.
- Meinhardt H. (1983). *Models of Biological Pattern Formation*, 2nd edn (Academic Press, London).
- Mel B. W. (1993). Synaptic integration in an excitable dendritic tree. *J. Neurophysiol.* **70**, 1086–1101.
- Metz A. E., Spruston N. and Martina M. (2007). Dendritic D-type potassium currents inhibit the spike afterdepolarization in rat hippocampal CA1 pyramidal neurons. *J. Physiol.* **581**, 175–187.
- Meyer R. L. (1983). Tetrodotoxin inhibits the formation of refined retinotopography in goldfish. *Dev. Brain. Res.* **6**, 293–298.
- Meyer R. L. and Sperry R. W. (1973). Tests for neuroplasticity in the anuran retinotectal system. *Exp. Neurol.* **40**, 525–539.
- Michaelis L. and Menten M. L. (1913). Die Kinetik der Invertinwirkung. *Biochem. Z.* **49**, 333–369.
- Migliore M., Cannia C., Lytton W. W., Markram H. and Hines M. L. (2006). Parallel network simulations with NEURON. *J. Comput. Neurosci.* **21**, 119–129.
- Migliore M., Cook E. P., Jaffe D. B., Turner D. A. and Johnston D. (1995). Computer simulations of morphologically reconstructed CA3 hippocampal neurons. *J. Neurophysiol.* **73**, 1157–1168.
- Migliore M., Ferrante M. and Ascoli G. A. (2005). Signal propagation in oblique dendrites of CA1 pyramidal cells. *J. Neurophysiol.* **94**, 4145–4155.
- Migliore M. and Shepherd G. M. (2002). Emerging rules for the distributions of active dendritic conductances. *Nat. Rev. Neurosci.* **3**, 362–370.
- Miller K. E. and Samuels D. C. (1997). The axon as a metabolic compartment: protein degradation, transport and maximum length of an axon. *J. Theor. Biol.* **186**, 373–379.
- Minsky M. L. and Papert S. A. (1969). *Perceptrons* (MIT Press, Cambridge, MA).
- Miocinovic S., Lempka S. F., Russo G. S., Maks C. B., Buston C. R., Sakaie K. E., Vitek J. L. and McIntyre C. C. (2009). Experimental and theoretical characterization of the voltage distribution generated by deep brain stimulation. *Exp. Neurol.* **216**, 166–176.
- Miocinovic S., Parent M., Buston C., Hahn P., Russo G., Vitek J. and McIntyre C. (2006). Computational analysis of subthalamic nucleus and lenticular fasciculus activation during therapeutic deep brain stimulation. *J. Neurophysiol.* **96**, 1569–1580.

- Mishina M., Kuroasaki T., Tobimatsu T., Morimoto Y., Noda M., Yamamoto T., Terao M., Lindstrom J., Takahashi T., Kuno M. and Numa S. (1984). Expression of functional acetylcholine receptor from cloned cDNAs. *Nature* **307**, 604–608.
- Miura T. and Maini P. K. (2004). Periodic pattern formation in reaction–diffusion systems: an introduction for numerical simulation. *Anat. Sci. Int* **79**, 112–113.
- Miyashita Y. (1988). Neuronal correlate of visual associative long-term memory in the primate temporal cortex. *Nature* **335**, 817–820.
- Moczydlowski E. and Latorre R. (1983). Gating kinetics of Ca^{2+} -activated K^+ channels from rat muscle incorporated into planar lipid bilayers: evidence for two voltage-dependent Ca^{2+} binding reactions. *J. Gen. Physiol.* **82**, 511–542.
- Mombaerts P. (2006). Axonal wiring in the mouse olfactory system. *Annu. Rev. Cell Dev. Biol.* **22**, 713–737.
- Moore G. E. (1965). Cramming more components onto integrated circuits. *Electronics* **8**, 1–4.
- Moore G. E. (1975). Progress in digital integrated electronics. *1975 International Electronic Devices Meeting* **1**, 11–13.
- Morris C. and Lecar H. (1981). Voltage oscillations in the barnacle giant muscle fiber. *Biophys. J.* **35**, 193–213.
- Mrsic-Flogel T. D., Hofer S. B., Creutzfeldt C., Cloëz-Tayarani I., Changeux J. P., Bonhoeffer T. and Hübener M. (2005). Altered map of visual space in the superior colliculus of mice lacking early retinal waves. *J. Neurosci.* **25**, 6921–6928.
- Murray J. D. (1993). *Mathematical Biology*, 2nd edn (Springer-Verlag, Berlin, Heidelberg, New York).
- Nadal J. P., Toulouse G., Changeux J. P. and Dehaene S. (1986). Networks of formal neurons and memory palimpsests. *Europhys. Lett.* **1**, 535–542.
- Nagumo J., Arimoto S. and Yoshizawa S. (1962). An active pulse transmission line simulating nerve axon. *Proc. IRE* **50**, 2061–2070.
- Nakamoto M., Cheng H. J., Friedman G. C., McLaughlin T., Hansen M. J., Yoon C. H., O’Leary D. D. M. and Flanagan J. G. (1996). Topographically specific effects of ELF-1 on retinal axon guidance *in vitro* and retinal axon mapping *in vivo*. *Cell* **86**, 755–766.
- Narahashi T., Moore J. W. and Scott W. R. (1964). Tetrodotoxin blockage of sodium conductance increase in lobster giant axons. *J. Gen. Physiol.* **47**, 965–974.
- Neher E. and Sakmann B. (1976). Single-channel currents recorded from membrane of denervated frog muscle fibres. *Nature* **260**, 779–802.
- Nernst W. (1888). Zur Kinetik der Lösung befindlichen Körper: Theorie der Diffusion. *Z. Phys. Chem.* **2**, 613–637.
- Netoff T. I., Clewley R., Arno S., Keck T. and White J. A. (2004). Epilepsy in small-world networks. *J. Neurosci.* **24**, 8075–8083.
- Nilius B., Hess P., Lansman J. B. and Tsien R. W. (1985). A novel type of cardiac calcium channel in ventricular cells. *Nature* **316**, 443–446.
- Nitzan R., Segev I. and Yarom Y. (1990). Voltage behavior along the irregular dendritic structure of morphologically and physiologically characterized vagal motoneurons in the guinea pig. *J. Neurophysiol.* **63**, 333–346.
- Noble D. (2006). Systems biology and the heart. *Biosystems* **83**, 75–80.
- Nowakowski R. S., Hayes N. L. and Egger M. D. (1992). Competitive interactions during dendritic growth: a simple stochastic growth algorithm. *Brain Res.* **576**, 152–156.
- Nowotny T., Levi R. and Selverston A. I. (2008). Probing the dynamics of identified neurons with a data-driven modeling approach. *PLoS ONE* **3**, e2627.

- O'Brien R. A. D., Østberg A. J. C. and Vrbova G. (1978). Observations on the elimination of polyneural innervation in developing mammalian skeletal muscle. *J. Physiol.* **282**, 571–582.
- Okabe A., Boots B. and Sugihara K. (1992). *Spatial Tessellations: Concepts and Applications of Voronoi Diagrams* (Wiley, New York).
- O'Keefe J. and Recce M. L. (1993). Phase relationship between hippocampal place units and the EEG theta rhythm. *Hippocampus* **3**, 317–330.
- Orbán G., Kiss T. and Érdi P. (2006). Intrinsic and synaptic mechanisms determining the timing of neuron population activity during hippocampal theta oscillation. *J. Neurophysiol.* **96**, 2889–2904.
- Overton K. J. and Arbib M. A. (1982). The extended branch-arrow model of the formation of retino-tectal connections. *Biol. Cybern.* **45**, 157–175.
- Palm G. (1988). On the asymptotic information storage capacity of neural networks. In *Neural Computers*, eds R. Eckmiller and C. von der Malsburg (Springer-Verlag, New York), pp. 271–280.
- Parisi G. (1986). A memory which forgets. *J. Phys. A Math. Gen.* **19**, L617–L620.
- Park M. R., Kita H., Klee M. R. and Oomura Y. (1983). Bridge balance in intracellular recording: introduction of the phase-sensitive method. *J. Neurosci. Methods* **8**, 105–125.
- Parnas I. and Segev I. (1979). A mathematical model for conduction of action potentials along bifurcating axons. *J. Physiol.* **295**, 323–343.
- Patlak J. (1991). Molecular kinetics of voltage-dependent Na^+ channels. *Physiol. Rev.* **71**, 1047–1080.
- Phelan P., Goulding L. A., Tam J. L. Y., Allen M. J., Dawber R. J., Davies J. A. and Bacon J. P. (2009). Molecular mechanism of rectification at identified electrical synapses in the *Drosophila* giant fiber system. *Curr. Biol.* **18**, 1955–1960.
- Philippides A., Husbands P. and O'Shea M. (2000). Four-dimensional neuronal signaling by nitric oxide: a computational analysis. *J. Neurosci.* **20**, 1199–1207.
- Philippides A., Ott S. R., Husbands P., Lovick T. A. and O'Shea M. (2005). Modeling cooperative volume signaling in a plexus of nitric-oxide-synthase-expressing neurons. *J. Neurosci.* **25**, 6520–6532.
- Pinsky P. F. and Rinzel J. (1994). Intrinsic and network rhythmogenesis in a reduced Traub model for CA3 neurons. *J. Comput. Neurosci.* **1**, 39–60.
- Planck M. (1890). Über die Erregung von Electricität und Wärme in Electrolyten. *Ann. Phys. Chem. Neue Folge* **39**, 161–186.
- Poirazi P., Brannon T. and Mel B. W. (2003). Arithmetic of subthreshold synaptic summation in a model CA1 pyramidal cell. *Neuron* **37**, 977–987.
- Pollak E. and Talkner P. (2005). Reaction rate theory: what it was, where is it today, and where is it going? *Chaos* **15**, 26116.
- Prescott S. A., De Koninck Y. and Sejnowski T. J. (2008). Biophysical basis for three distinct dynamical mechanisms of action potential initiation. *PLoS Comput. Biol.* **4**, e1000198.
- Press W. H., Flannery B. P., Teukolsky S. A. and Vetterling W. T., eds (1987). *Numerical Recipes: The Art of Scientific Computing* (Cambridge University Press, Cambridge).
- Prestige M. C. and Willshaw D. J. (1975). On a role for competition in the formation of patterned neural connexions. *Proc. R. Soc. Lond., B* **190**, 77–98.
- Price D., Jarman A. P., Mason J. O. and Kind P. C. (2011). *Building Brains: An Introduction to Neural Development* (in press, Wiley-Blackwell).
- Price D. J. and Willshaw D. J. (2000). *Mechanisms of Cortical Development* (Oxford University Press, Oxford).

- Protopapas A. D., Vanier M. and Bower J. M. (1998). Simulating large networks of neurons. In *Methods in Neuronal Modeling: From Ions to Networks*, 2nd edn, eds C. Koch and I. Segev (MIT Press, Cambridge, MA), pp. 461–498.
- Purves D. (1981). *Microelectrode Methods for Intracellular Recording and Ionophoresis* (Academic Press, London).
- Purves D. and Lichtman J. W. (1980). Elimination of the synapses in the developing nervous system. *Science* **210**, 153–157.
- Qian N. and Sejnowski T. J. (1989). An electro-diffusion model for computing membrane potentials and ionic concentrations in branching dendrites, spines and axons. *Biol. Cybern.* **62**, 1–15.
- Qin F., Auerbach A. and Sachs F. (1996). Estimating single-channel kinetic parameters from idealized patch clamp data containing missed events. *Biophys. J.* **70**, 264–280.
- Rall W. (1957). Membrane time constant of motoneurons. *Science* **126**, 454.
- Rall W. (1962). Electrophysiology of a dendritic neuron model. *Biophys. J.* **2**, 145–167.
- Rall W. (1964). Theoretical significance of dendritic trees for neuronal input–output relations. In *Neural Theory and Modeling*, ed. R. F. Reiss (Stanford University Press, Palo Alto), pp. 73–97.
- Rall W. (1967). Distinguishing theoretical synaptic potentials computed for different somadendritic distributions of synaptic inputs. *J. Neurophysiol.* **30**, 1138–1168.
- Rall W. (1969). Time constants and electrotonic length of membrane cylinders and neurons. *Biophys. J.* **9**, 1438–1541.
- Rall W. (1977). Theoretical significance of dendritic trees for neuronal input–output relations. In *Handbook of Physiology: The Nervous System – Cellular Biology of Neurons* (American Physiological Society, Bethesda, MD), pp. 39–97.
- Rall W. (1990). Perspectives on neuron modeling. In *The Segmental Motor System*, eds M. D. Binder and L. M. Mendell (Oxford University Press, New York), pp. 129–149.
- Rall W., Burke R. E., Holmes W. R., Jack J. J., Redman S. J. and Segev I. (1992). Matching dendritic neuron models to experimental data. *Physiol. Rev.* **72**, 159–186.
- Rall W. and Shepherd G. M. (1968). Theoretical reconstruction of field potentials and dendrodendritic synaptic interactions in olfactory bulb. *J. Neurophysiol.* **31**, 884–915.
- Rall W., Shepherd G. M., Reese T. S. and Brightman M. W. (1966). Dendrodendritic synaptic pathway for inhibition in the olfactory bulb. *Exp. Neurol.* pp. 44–66.
- Ramón y Cajal S. (1911). *Histologie du Système Nerveux de l'Homme et des Vertébrés* (Maloine, Paris). English translation by P. Pasik and T. Pasik (1999). *Texture of the Nervous System of Man and the Vertebrates* (Springer, New York).
- Ran I., Quastel D. M. J., Mathers D. A. and Puil E. (2009). Fluctuation analysis of tetanic rundown (short-term depression) at a corticothalamic synapse. *Biophys. J.* **96**, 2505–2531.
- Ranck Jr J. B. (1963). Specific impedance of rabbit cerebral cortex. *Exp. Neurol.* **7**, 144–152.
- Rao-Miroznik R., Buchsbaum G. and Sterling P. (1998). Transmitter concentration at a three-dimensional synapse. *J. Neurophysiol.* **80**, 3163–3172.
- Rasmussen C. E. and Willshaw D. J. (1993). Presynaptic and postsynaptic competition in models for the development of neuromuscular connections. *Biol. Cybern.* **68**, 409–419.
- Reber M., Burrola P. and Lemke G. (2004). A relative signalling model for the formation of a topographic neural map. *Nature* **431**, 847–853.

- Redman S. J. (1990). Quantal analysis of synaptic potentials in neurons of the central nervous system. *Physiol. Rev.* **70**, 165–198.
- Reh T. A. and Constantine-Paton M. (1983). Retinal ganglion cell terminals change their projection sites during larval development of *Rana pipiens*. *J. Neurosci.* **4**, 442–457.
- Resta V., Novelli E., Di Virgilio F. and Galli-Resta L. (2005). Neuronal death induced by endogenous extracellular ATP in retinal cholinergic neuron density control. *Development* **132**, 2873–2882.
- Rieke F., Warland D., de Ruyter van Steveninck R. and Bialek W. (1997). *Spikes: Exploring the Neural Code* (MIT Press, Cambridge, MA).
- Rinzel J. and Ermentrout B. (1998). Analysis of neural excitability and oscillations. In *Methods in Neuronal Modeling: From Ions to Networks*, 2nd edn, eds C. Koch and I. Segev (MIT Press, Cambridge, MA), pp. 251–291.
- Rizzoli S. O. and Betz W. J. (2005). Synaptic vesicle pools. *Nat. Rev. Neurosci.* **6**, 57–69.
- Rizzzone M., Lanotte M., Bergamasco B., Tavella A., Torre E., Faccani G., Melcarne A. and Lopiano L. (2001). Deep brain stimulation of the subthalamic nucleus in Parkinson's disease: effects of variation in stimulation parameters. *J. Neurol. Neurosurg. Psychiatr.* **71**, 215–219.
- Rodieck R. W. (1967). Maintained activity of cat retinal ganglion cells. *J. Neurophysiol.* **30**, 1043–1071.
- Rodriguez A., Ehlenberger D. B., Dickstein D. L., Hof P. R. and Wearne S. L. (2008). Automated three-dimensional detection and shape classification of dendritic spines from fluorescence microscopy images. *PLoS ONE* **3**, e1997.
- Rodriguez B. M., Sigg D. and Bezanilla F. (1998). Voltage gating of *Shaker K⁺* channels: the effect of temperature on ionic and gating currents. *J. Gen. Physiol.* **112**, 223–242.
- Rosenblatt F. (1958). The perceptron: a probabilistic model for information storage and organization in the brain. *Psychol. Rev.* **65**, 386–408.
- Roudi Y. and Treves A. (2006). Localized activity profiles and storage capacity of rate-based autoassociative networks. *Phys. Rev. E* **73**, 61904.
- Roux B., Allen T., Bernèche S. and Im W. (2004). Theoretical and computational models of biological ion channels. *Q. Rev. Biophys.* **37**, 15–103.
- Rubin D. C. and Wenzel A. E. (1996). One hundred years of forgetting: a quantitative description of retention. *Psychol. Rev.* **103**, 734–760.
- Rubin J. E., Gerkin R. C., Bi G. Q. and Chow C. C. (2005). Calcium time course as a signal for spike-timing-dependent plasticity. *J. Neurophysiol.* **93**, 2600–2613.
- Rudolph M. and Destexhe A. (2006). Analytical integrate-and-fire neuron models with conductance-based dynamics for event-driven simulation strategies. *Neural Comput.* **18**, 2146–2210.
- Rumelhart D. E., Hinton G. E. and Williams R. J. (1986a). Learning representations by back-propagating errors. *Nature* **323**, 533–536.
- Rumelhart D. E., McClelland J. L. and the PDP Research Group, eds (1986b). *Parallel Distributed Processing: Explorations in the Microstructure of Cognition. Volume 1: Foundations* (MIT Press, Cambridge, MA).
- Sabatini B. L., Oertner T. G. and Svoboda K. (2002). The life cycle of Ca²⁺ ions in dendritic spines. *Neuron* **33**, 439–452.
- Sah P. and Faber E. S. (2002). Channels underlying neuronal calcium-activated potassium currents. *Prog. Neurobiol.* **66**, 345–353.
- Sah P., Gibb A. J. and Gage P. W. (1988). Potassium current activated by depolarization of dissociated neurons from adult guinea pig hippocampus. *J. Gen. Physiol.* **92**, 263–278.

- Sakmann B. and Neher E., eds (1995). *Single-channel Recording* 2nd edn (Plenum Press, New York).
- Samsonovich A. V. and Ascoli G. A. (2003). Statistical morphological analysis of hippocampal principal neurons indicates cell-specific repulsion of dendrites from their own cell. *J. Neurosci. Res.* **71**, 173–187.
- Samsonovich A. V. and Ascoli G. A. (2005a). Algorithmic description of hippocampal granule cell dendritic morphology. *Neurocomputing* **65–66**, 253–260.
- Samsonovich A. V. and Ascoli G. A. (2005b). Statistical determinants of dendritic morphology in hippocampal pyramidal neurons: a hidden Markov model. *Hippocampus* **15**, 166–183.
- Sanes D. H., Reh T. A. and Harris W. A. (2000). *Development of the Nervous System* (Academic Press, San Diego, CA).
- Sanes J. R. and Lichtman J. W. (1999). Development of the vertebrate neuromuscular junction. *Annu. Rev. Neurosci.* **22**, 389–342.
- Santhakumar V., Aradi I. and Soltész I. (2005). Role of mossy fiber sprouting and mossy cell loss in hyperexcitability: a network model of the dentate gyrus incorporating cell types axonal typography. *J. Neurophysiol.* **93**, 437–453.
- Sato F., Parent M., Lévesque M. and Parent A. (2000). Axonal branching pattern of neurons of the subthalamic nucleus in primates. *J. Comp. Neurol.* **424**, 142–152.
- Schaff J., Fink C. C., Slepchenko B., Carson J. H. and Loew L. M. (1997). A general computational framework for modeling cellular structure and function. *Biophys. J.* **73**, 1135–1146.
- Schiegg A., Gerstner W., Ritz R. and van Hemmen J. L. (1995). Intracellular Ca^{2+} stores can account for the time course of LTP induction: a model of Ca^{2+} dynamics in dendritic spines. *J. Neurophysiol.* **74**, 1046–1055.
- Schmidt J. T., Cicerone C. M. and Easter S. S. (1978). Expansion of the half retinal projection to the tectum in goldfish: an electrophysiological and anatomical study. *J. Comp. Neurol.* **177**, 257–278.
- Schmidt J. T. and Edwards D. L. (1983). Activity sharpens the map during the regeneration of the retinotectal projection in goldfish. *Brain Res.* **269**, 29–39.
- Schrempf H., Schmidt O., Kümmel R., Hinnah S., Müller D., Betzler M., Steinkamp T. and Wagner R. (1995). A prokaryotic potassium ion channel with two predicted transmembrane segments from *Streptomyces lividans*. *EMBO J.* **14**, 5170–5178.
- Schuster S., Marhl M. and Höfer T. (2002). Modelling of simple and complex calcium oscillations: from single-cell responses to intercellular signalling. *Eur. J. Biochem.* **269**, 1333–1355.
- Scorcioni R., Lazarewicz M. T. and Ascoli G. A. (2004). Quantitative morphometry of hippocampal pyramidal cells: differences between anatomical classes and reconstructing laboratories. *J. Comp. Neurol.* **473**, 177–193.
- Segev I. (1990). Computer study of presynaptic inhibition controlling the spread of action potentials into axonal terminals. *J. Neurophysiol.* **63**, 987–998.
- Segev I., Rinzel J. and Shepherd G., eds (1995). *The Theoretical Foundation of Dendritic Function: Selected Papers of Wilfrid Rall with Commentaries* (MIT Press, Cambridge, MA).
- Sejnowski T. J. (1977). Statistical constraints on synaptic plasticity. *J. Theor. Biol.* **69**, 385–389.
- Seung H. S. (1996). How the brain keeps the eyes still. *Proc. Nat. Acad. Sci. USA* **93**, 13339–13344.
- Seung H. S., Lee D. D., Reis B. Y. and Tank D. W. (2000). Stability of the memory of eye position in a recurrent network of conductance-based neurons. *Neuron* **26**, 259–271.

- Shadlen M. N. and Newsome W. T. (1994). Noise, neural codes and cortical organization. *Curr. Opin. Neurobiol.* **4**, 569–579.
- Shadlen M. N. and Newsome W. T. (1995). Is there a signal in the noise? *Curr. Opin. Neurobiol.* **5**, 248–250.
- Shadlen M. N. and Newsome W. T. (1998). The variable discharge of cortical neurons: implications for connectivity, computation, and information coding. *J. Neurosci.* **18**, 3870–3896.
- Sharma S. C. (1972). The retinal projection in adult goldfish: an experimental study. *Brain Res.* **39**, 213–223.
- Sharp A. A., O'Neil M. B., Abbott L. F. and Marder E. (1993). The dynamic clamp: artificial conductances in biological neurons. *Trends Neurosci.* **16**, 389–394.
- Shepherd G. M. (1996). The dendritic spine: a multifunctional integrative unit. *J. Neurophysiol.* **75**, 2197–2210.
- Shimbel A. (1950). Contributions to the mathematical biophysics of the central nervous system with special reference to learning. *Bull. Math. Biophys.* **12**, 241–275.
- Siegel M., Marder E. and Abbott L. F. (1994). Activity-dependent current distributions in model neurons. *Proc. Nat. Acad. Sci. USA* **91**, 11308–11312.
- Singer W. (1993). Synchronization of cortical activity and its putative role in information processing and learning. *Annu. Rev. Physiol.* **55**, 349–374.
- Skinner F. K., Turrigiano G. G. and Marder E. (1993). Frequency and burst duration in oscillating neurons and two-cell networks. *Biol. Cybern.* **69**, 375–383.
- Smart J. L. and McCammon J. A. (1998). Analysis of synaptic transmission in the neuromuscular junction using a continuum finite element model. *Biophys. J.* **75**, 1679–1688.
- Smith D. J. and Rubel E. W. (1979). Organization and development of brain stem auditory nuclei of the chicken: dendritic gradients in nucleus laminaris. *J. Comp. Neurol.* **186**, 213–239.
- Smith G. D. (2001). Modeling local and global calcium signals using reaction-diffusion equations. In *Computational Neuroscience: Realistic Modeling for Experimentalists*, ed. E. De Schutter (CRC Press, Boca Raton, FL), pp. 49–85.
- Smith Y., Bolam J. P. P. and Von Krosigk M. (1990). Topographical and synaptic organization of the GABA-containing pallidosubthalamic projection in the rat. *Eur. J. Neurosci.* **2**, 500–511.
- Soetaert K., Petzoldt T. and Setzer R. W. (2010). Solving differential equations in R: Package deSolve. *J. Stat. Softw.* **33**, 1–25.
- Softky W. R. and Koch C. (1993). The highly irregular firing of cortical cells is inconsistent with temporal integration of random EPSPs. *J. Neurosci.* **13**, 334–350.
- Sommer F. T. and Wennekers T. (2000). Modelling studies on the computational function of fast temporal structure in cortical circuit activity. *J. Physiol. Paris* **94**, 473–488.
- Sommer F. T. and Wennekers T. (2001). Associative memory in networks of spiking neurons. *Neural Netw.* **14**, 825–834.
- Somogyi P. and Klausberger T. (2005). Defined types of cortical interneurone structure space and spike timing in the hippocampus. *J. Physiol.* **562** (1), 9–26.
- Song S., Miller K. D. and Abbott L. F. (2000). Competitive Hebbian learning through spike-timing-dependent synaptic plasticity. *Nat. Neurosci.* **3**, 919–926.
- Sosinsky G. E., Deerinck T. J., Greco R., Buitenhuis C. H., Bartol T. M. and Ellisman M. H. (2005). Development of a model for microphysiological simulations: small nodes of Ranvier from peripheral nerves of mice reconstructed by electron tomography. *Neuroinformatics* **3**, 133–162.

- Sperry R. W. (1943). Visuomotor co-ordination in the newt (*Triturus viridescens*) after regeneration of the optic nerve. *J. Comp. Neurol.* **79**, 33–55.
- Sperry R. W. (1944). Optic nerve regeneration with return of vision in anurans. *J. Neurophysiol.* **7**, 57–69.
- Sperry R. W. (1945). Restoration of vision after crossing of optic nerves and after contralateral transplantation of the eye. *J. Neurophysiol.* **8**, 15–28.
- Sperry R. W. (1963). Chemoaffinity in the orderly growth of nerve fiber patterns and connections. *Proc. Nat. Acad. Sci. USA* **50**, 703–710.
- Spitzer N. C., Kingston P. A., Manning Jr T. J. and Conklin M. W. (2002). Outside and in: development of neuronal excitability. *Curr. Opin. Neurobiol.* **12**, 315–323.
- Srinivasan R. and Chiel H. J. (1993). Fast calculation of synaptic conductances. *Neural Comput.* **5**, 200–204.
- Stein R. B. (1965). A theoretical analysis of neuronal variability. *Biophys. J.* **5**, 173–194.
- Stemmler M. and Koch C. (1999). How voltage-dependent conductances can adapt to maximize the information encoded by neuronal firing rate. *Nat. Neurosci.* **2**, 521–527.
- Sterratt D. C. and Willshaw D. (2008). Inhomogeneities in heteroassociative memories with linear learning rules. *Neural Comput.* **20**, 311–344.
- Steuber V., Schutter E. D. and Jaeger D. (2004). Passive models of neurons in the deep cerebellar nuclei: the effect of reconstruction errors. *Neurocomputing* **58–60**, 563–568.
- Stevens C. F. (1978). Interactions between intrinsic membrane protein and electric field. *Biophys. J.* **22**, 295–306.
- Stiles J. R. and Bartol T. M. (2001). Monte Carlo methods for simulating realistic synaptic microphysiology using MCell. In *Computational Neuroscience: Realistic Modeling for Experimentalists*, ed. E. De Schutter (CRC Press, Boca Raton, FL), pp. 87–127.
- Stocker M. (2004). Ca^{2+} -activated K^+ channels: molecular determinants and function of the SK family. *Nat. Rev. Neurosci.* **5**, 758–770.
- Storm J. F. (1988). Temporal integration by a slowly inactivating K^+ current in hippocampal neurons. *Nature* **336**, 379–381.
- Strassberg A. F. and DeFelice L. J. (1993). Limitations of the Hodgkin-Huxley formalism: effects of single channel kinetics on transmembrane voltage dynamics. *Neural Comput.* **5**, 843–855.
- Stratford K., Mason A., Larkman A., Major G. and Jack J. J. B. (1989). The modelling of pyramidal neurons in the visual cortex. In *The Computing Neuron*, eds R. Durbin, C. Miall and G. Mitchison (Addison-Wesley, Wokingham), pp. 296–321.
- Stuart G. and Spruston N. (1998). Determinants of voltage attenuation in neocortical pyramidal neuron dendrites. *J. Neurosci.* **18**, 3501–3510.
- Sumikawa K., Houghton M., Emtage J. S., Richards B. M. and Barnard E. A. (1981). Active multi-subunit ACh receptor assembled by translation of heterologous mRNA in *Xenopus* oocytes. *Nature* **292**, 862–864.
- Swindale N. V. (1980). A model for the formation of ocular dominance stripes. *Proc. R. Soc. Lond., B* **208**, 243–264.
- Szilágyi T. and De Schutter E. (2004). Effects of variability in anatomical reconstruction techniques on models of synaptic integration by dendrites: a comparison of three Internet archives. *Eur. J. Neurosci.* **19**, 1257–1266.
- Takahashi K., Ishikawa N., Sadamoto Y., Sasamoto H., Ohta S., Shiozawa A., Miyoshi F., Naito Y., Nakayama Y. and Tomita M. (2003). E-Cell 2: multi-platform E-Cell simulation system. *Bioinformatics* **19**, 1727–1729.

- Tamori Y. (1993). Theory of dendritic morphology. *Phys. Rev. E* **48**, 3124–3129.
- Tang Y. and Othmer H. G. (1994). A model of calcium dynamics in cardiac myocytes based on the kinetics of ryanodine-sensitive calcium channels. *Biophys. J.* **67**, 2223–2235.
- Thomson A. M. (2000a). Facilitation, augmentation and potentiation at central synapses. *Trends Neurosci.* **23**, 305–312.
- Thomson A. M. (2000b). Molecular frequency filters at central synapses. *Prog. Neurobiol.* **62**, 159–196.
- Thomson A. M. and Deuchars J. (1997). Synaptic interactions in neocortical local circuits: dual intracellular recordings *in vitro*. *Cereb. Cortex* **7**, 510–522.
- Thurbon D., Lüscher H., Hofstetter T. and Redman S. J. (1998). Passive electrical properties of ventral horn neurons in rat spinal cord slices. *J. Neurophysiol.* **79**, 2485–2502.
- Tombola F., Pathak M. M. and Isacoff E. Y. (2006). How does voltage open an ion channel? *Annu. Rev. Cell Dev. Biol.* **22**, 23–52.
- Torben-Nielsen B., Vanderlooy S. and Postma E. O. (2008). Non-parametric algorithmic generation of neuronal morphologies. *Neuroinformatics* **6**, 257–277.
- Traub R. D., Bibbig A., LeBeau F. E. N., Buhl E. H. and Whittington M. (2004). Cellular mechanisms of neuronal population oscillations in the hippocampus *in vitro*. *Annu. Rev. Neurosci.* **27**, 247–278.
- Traub R. D., Contreras D., Cunningham M. O., Murray H., LeBeau F. E. N., Roopun A., Bibbig A., Wilent W. B., Higley M. J. and Whittington M. (2005). Single-column thalamocortical network model exhibiting gamma oscillations, sleep spindles, and epileptogenic bursts. *J. Neurophysiol.* **93**, 2194–2232.
- Traub R. D., Jefferys J. G., Miles R., Whittington M. A. and Tóth K. (1994). A branching dendritic model of a rodent CA3 pyramidal neurone. *J. Physiol.* **481**, 79–95.
- Traub R. D., Jefferys J. G. R. and Whittington M. A. (1999). *Fast Oscillations in Cortical Circuits* (MIT Press, Cambridge, MA).
- Traub R. D. and Llinás R. (1977). The spatial distribution of ionic conductances in normal and axotomized motoneurons. *Neuroscience* **2**, 829–850.
- Traub R. D., Miles R. and Buzsáki G. (1992). Computer simulation of carbachol-driven rhythmic population oscillations in the CA3 region of the *in vitro* rat hippocampus. *J. Physiol.* **451**, 653–672.
- Traub R. D., Wong R. K., Miles R. and Michelson H. (1991). A model of a CA3 hippocampal pyramidal neuron incorporating voltage-clamp data on intrinsic conductances. *J. Neurophysiol.* **66**, 635–650.
- Treves A. (1990). Threshold-linear formal neurons in auto-associative networks. *J. Phys. A Math. Gen.* **23**, 2631–2650.
- Trommershäuser J., Schneggenburger R., Zippelius A. and Neher E. (2003). Heterogeneous presynaptic release probabilities: functional relevance for short-term plasticity. *Biophys. J.* **84**, 1563–1579.
- Tsien R. W. and Noble D. (1969). A transition state theory approach to the kinetics of conductance changes in excitable membranes. *J. Membr. Biol.* **1**, 248–273.
- Tsodyks M. V. and Feigel'man M. V. (1988). The enhanced storage capacity in neural networks with low activity level. *Europhys. Lett.* **6**, 101–105.
- Tsodyks M. V. and Markram H. (1997). The neural code between neocortical pyramidal neurons depends on neurotransmitter release probability. *Proc. Natl. Acad. Sci. USA* **94**, 719–723.
- Tsodyks M. V., Pawelzik K. and Markram H. (1998). Neural networks with dynamic synapses. *Neural Comput.* **10**, 821–835.

- Tuckwell H. C. (1988). *Introduction to Theoretical Neurobiology: Volume 2, Nonlinear and Stochastic Theories* (Cambridge University Press, Cambridge).
- Turing A. M. (1952). The chemical basis of morphogenesis. *Philos. Trans. R. Soc. Lond., B* **237**, 37–72.
- Turrigiano G. G. and Nelson S. B. (2004). Homeostatic plasticity in the developing nervous system. *Nat. Rev. Neurosci.* **5**, 97–107.
- Tyrrell L. R. T. and Willshaw D. J. (1992). Cerebellar cortex: its simulation and the relevance of Marr's theory. *Philos. Trans. R. Soc. Lond., B* **336**, 239–257.
- Uemura E., Carriquiry A., Kliemann W. and Goodwin J. (1995). Mathematical modeling of dendritic growth in vitro. *Brain Res.* **671**, 187–194.
- van Elburg R. A. J. and van Ooyen A. (2009). Generalization of the event-based Carnevale–Hines integration scheme for integrate-and-fire models. *Neural Comput.* **21**, 1913–1930.
- van Geit W., De Schutter E. and Achard P. (2008). Automated neuron model optimization techniques: a review. *Biol. Cybern.* **99**, 241–251.
- van Ooyen A. (2001). Competition in the development of nerve connections: a review of models. *Network Comp. Neural Syst.* **12**, R1–R47.
- van Ooyen A., ed. (2003). *Modeling Neural Development* (MIT Press, Cambridge, MA).
- van Ooyen A. and Willshaw D. J. (1999a). Competition for neurotrophic factor in the development of nerve connections. *Proc. R. Soc. Lond., B* **266**, 883–892.
- van Ooyen A. and Willshaw D. J. (1999b). Poly- and mononeuronal innervation in a model for the development of neuromuscular connections. *J. Theor. Biol.* **196**, 495–511.
- van Ooyen A. and Willshaw D. J. (2000). Development of nerve connections under the control of neurotrophic factors: parallels with consumer-resource models in population biology. *J. Theor. Biol.* **206**, 195–210.
- van Pelt J. (1997). Effect of pruning on dendritic tree topology. *J. Theor. Biol.* **186**, 17–32.
- van Pelt J., Dityatev A. E. and Uylings H. B. M. (1997). Natural variability in the number of dendritic segments: model-based inferences about branching during neurite outgrowth. *J. Comp. Neurol.* **387**, 325–340.
- van Pelt J., Graham B. P. and Uylings H. B. M. (2003). Formation of dendritic branching patterns. In *Modeling Neural Development*, ed. A. van Ooyen (MIT Press, Cambridge, MA), pp. 75–94.
- van Pelt J. and Uylings H. B. M. (1999). Natural variability in the geometry of dendritic branching patterns. In *Modeling in the Neurosciences: From Ionic Channels to Neural Networks*, ed. R. R. Poznanski (Harwood Academic Amsterdam), pp. 79–108.
- van Pelt J. and Uylings H. B. M. (2002). Branching rates and growth functions in the outgrowth of dendritic branching patterns. *Network Comp. Neural Syst.* **13**, 261–281.
- van Pelt J., van Ooyen A. and Uylings H. B. M. (2001). Modeling dendritic geometry and the development of nerve connections. In *Computational Neuroscience: Realistic Modeling for Experimentalists*, ed. E. De Schutter (CRC Press, Boca Raton, FL), pp. 179–208.
- van Pelt J. and Verwer R. W. H. (1983). The exact probabilities of branching patterns under segmental and terminal growth hypotheses. *Bull. Math. Biol.* **45**, 269–285.
- van Rossum M. C. W. (2001). The transient precision of integrate and fire neurons: effect of background activity and noise. *J. Comput. Neurosci.* **10**, 303–311.
- van Rossum M. C. W., Bi G. Q. and Turrigiano G. G. (2000). Stable Hebbian learning from spike timing-dependent plasticity. *J. Neurosci.* **20**, 8812–8821.

- van Rossum M. C. W., Turrigiano G. G. and Nelson S. B. (2002). Fast propagation of firing rates through layered networks of noisy neurons. *J. Neurosci.* **22**, 1956–1966.
- van Veen M. and van Pelt J. (1992). A model for outgrowth of branching neurites. *J. Theor. Biol.* **159**, 1–23.
- van Veen M. and van Pelt J. (1994). Neuritic growth rate described by modeling microtubule dynamics. *Bull. Math. Biol.* **56**, 249–273.
- Vandenberg C. A. and Bezanilla F. (1991). A sodium channel gating model based on single channel, macroscopic ionic, and gating currents in the squid giant axon. *Biophys. J.* **60**, 1511–1533.
- Vanier M. and Bower J. (1999). A comparative survey of automated parameter-search methods for compartmental neural models. *J. Comput. Neurosci.* **7**, 149–171.
- Vasudeva K. and Bhalla U. S. (2004). Adaptive stochastic-deterministic chemical kinetic simulations. *Bioinformatics* **20**, 78–84.
- Vere-Jones D. (1966). Simple stochastic models for the release of quanta of transmitter from a nerve terminal. *Aust. J. Stat.* **8**, 53–63.
- Verhulst P. F. (1845). Recherches mathématiques sur la loi d'accroissement de la population. *Nouv. mém. de l'Academie Royale des Sci. et Belles-Lettres de Bruxelles* **18**, 1–41.
- Volterra V. (1926). Fluctuations in the abundance of a species considered mathematically. *Nature* **118**, 558–560.
- von der Malsburg C. and Willshaw D. J. (1976). A mechanism for producing continuous neural mappings: ocularity dominance stripes and ordered retino-tectal projections. *Exp. Brain Res. Suppl.* **1**, 463–469.
- von der Malsburg C. and Willshaw D. J. (1977). How to label nerve cells so that they can interconnect in an ordered fashion. *Proc. Nat. Acad. Sci. USA* **74**, 5176–5178.
- Wadiche J. I. and Jahr C. E. (2001). Multivesicular release at climbing fiber-Purkinje cell synapses. *Neuron* **32**, 301–313.
- Wagner J. and Keizer J. (1994). Effects of rapid buffers on Ca^{2+} diffusion and Ca^{2+} oscillations. *Biophys. J.* **67**, 447–456.
- Walmsley B., Alvarez F. J. and Fyffe R. E. W. (1998). Diversity of structure and function at mammalian central synapses. *Trends Neurosci.* **21**, 81–88.
- Walmsley B., Graham B. and Nicol M. (1995). A serial E-M and simulation study of presynaptic inhibition along a group Ia collateral in the spinal cord. *J. Neurophysiol.* **74**, 616–623.
- Wang J., Chen S., Nolan M. F. and Siegelbaum S. A. (2002). Activity-dependent regulation of HCN pacemaker channels by cyclic AMP: signaling through dynamic allosteric coupling. *Neuron* **36**, 451–461.
- Wang X. J., Tegnér J., Constantinidis C. and Goldman-Rakic P. S. (2004). Division of labor among distinct subtypes of inhibitory neurons in a cortical microcircuit of working memory. *Proc. Nat. Acad. Sci. USA* **101**, 1368–1373.
- Watts D. J. and Strogatz S. H. (1998). Collective dynamics of ‘small-world’ networks. *Nature* **393**, 440–442.
- Wearne S. L., Rodriguez A., Ehlenberger D., Rocher A. B., Henderson S. C. and Hof P. R. (2005). New techniques for imaging, digitization and analysis of three-dimensional neuronal morphology on multiple scales. *Neuroscience* **136**, 661–680.
- Wei A. D., Gutman G. A., Aldrich R., Chandy G. K., Grissmer S. and Wulff H. (2005). International Union of Pharmacology. LII: nomenclature and molecular relationships of calcium-activated potassium channels. *Pharmacol. Rev.* **57**, 463–472.
- Weis S., Schneggenburger R. and Neher E. (1999). Properties of a model of Ca^{2+} -dependent vesicle pool dynamics and short term synaptic depression. *Biophys. J.* **77**, 2418–2429.

- Weiss J. N. (1997). The Hill equation revisited: uses and misuses. *FASEB J.* **11**, 835–841.
- Weiss P. (1937a). Further experimental investigations on the phenomenon of homologous response in transplanted amphibian limbs: I. Functional observations. *J. Comp. Neurol.* **66**, 181–209.
- Weiss P. (1937b). Further experimental investigations on the phenomenon of homologous response in transplanted amphibian limbs: II. Nerve regeneration and the innervation of transplanted limbs. *J. Comp. Neurol.* **66**, 481–536.
- Weiss P. (1939). *Principles of Development* (Holt, New York).
- Widrow B. and Hoff M. E. (1960). Adaptive switching circuits. In *1960 IRE WESCON Convention Record* (IRE, New York), volume 4, pp. 96–104.
- Wigmore M. A. and Lacey M. G. (2000). A Kv3-like persistent, outwardly rectifying, Cs⁺-permeable, K⁺ current in rat subthalamic nucleus neurones. *J. Physiol.* **527**, 493–506.
- Willshaw D. (1971). Models of distributed associative memory. Ph.D. thesis, University of Edinburgh.
- Willshaw D. J. (1981). The establishment and the subsequent elimination of polyneuronal innervation of developing muscle: theoretical considerations. *Proc. R. Soc. Lond., B* **212**, 233–252.
- Willshaw D. J. (2006). Analysis of mouse EphA knockins and knockouts suggests that retinal axons programme target cells to form ordered retinotopic maps. *Development* **133**, 2705–2717.
- Willshaw D. J., Buneman O. P. and Longuet-Higgins H. C. (1969). Non-holographic associative memory. *Nature* **222**, 960–962.
- Willshaw D. J. and von der Malsburg C. (1976). How patterned neural connections can be set up by self-organization. *Proc. R. Soc. Lond., B* **194**, 431–445.
- Willshaw D. J. and von der Malsburg C. (1979). A marker induction mechanism for the establishment of ordered neural mappings: its application to the retinotectal problem. *Philos. Trans. R. Soc. Lond., B* **287**, 203–234.
- Wilson C. J. and Park M. R. (1989). Capacitance compensation and bridge balance adjustment in intracellular recording from dendritic neurons. *J. Neurosci. Methods* **27**, 51–75.
- Wilson H. R. (1999). *Spikes, Decisions and Actions: The Dynamical Foundations of Neuroscience* (Oxford University Press, New York).
- Wilson H. R. and Cowan J. D. (1972). Excitatory and inhibitory interactions in localized populations of model neurons. *Biophys. J.* **12**, 1–24.
- Windels F., Bruet N., Poupart N., Urbain N., Chouvet G., Feuerstein C. and Savasta M. (2000). Effects of high frequency stimulation of subthalamic nucleus on extracellular glutamate and GABA in substantia nigra and globus pallidus in the normal rat. *Eur. J. Neurosci.* **12**, 4141–4146.
- Winslow J. L., Jou S. F., Wang S. and Wojtowicz J. M. (1999). Signals in stochastically generated neurons. *J. Comput. Neurosci.* **6**, 5–26.
- Wolpert L., Beddington R., Jessell T., Lawrence P., Meyerowitz E. and Smith J. (2002). *Principles of Development*, 2nd edn (Oxford University Press, Oxford).
- Wong A. Y. C., Graham B. P., Billups B. and Forsythe I. D. (2003). Distinguishing between presynaptic and postsynaptic mechanisms of short term depression during action potential trains. *J. Neurosci.* **23**, 4868–4877.
- Woolf T. B., Shepherd G. M. and Greer C. A. (1991). Serial reconstruction of granule cell spines in the mammalian olfactory bulb. *Synapse* **7**, 181–192.
- Worden M. K., Bykhovskaya M. and Hackett J. T. (1997). Facilitation at the lobster neuromuscular junction: a stimulus-dependent mobilization model. *J. Neurophysiol.* **78**, 417–428.

- Wu C., Reilly J. F., Young W. G., Morrison J. H. and Bloom F. E. (2004). High-throughput morphometric analysis of individual neurons. *Cereb. Cortex* **14**, 543–554.
- Yamada W. M. and Zucker R. S. (1992). Time course of transmitter release calculated from simulations of a calcium diffusion model. *Biophys. J.* **61**, 671–682.
- Yamada W. M., Koch C. and Adams P. R. (1998). Multiple channels and calcium dynamics. In *Methods in Neuronal Modeling: From Ions to Networks*, 2nd edn, eds C. Koch and I. Segev (MIT Press, Cambridge, MA), pp. 93–133.
- Yodzis P. (1989). *Introduction to Theoretical Ecology* (Harper and Row, New York).
- Yoon M. (1971). Reorganization of retinotectal projection following surgical operations on the optic tectum in goldfish. *Exp. Neurol.* **33**, 395–411.
- Yoon M. G. (1980). Retention of the topographic addresses by reciprocally translated tectal re-implant in adult goldfish. *J. Physiol.* **308**, 197–215.
- Yu F. H., Yarov-Yarovoy V., Gutman G. A. and Catterall W. A. (2005). Overview of molecular relationships in the voltage-gated ion channel superfamily. *Pharmacol. Rev.* **57**, 387–395.
- Zador A. and Koch C. (1994). Linearized models of calcium dynamics: formal equivalence to the cable equation. *J. Neurosci.* **14**, 4705–4715.
- Zador A., Koch C. and Brown T. H. (1990). Biophysical model of a Hebbian synapse. *Proc. Nat. Acad. Sci. USA* **87**, 6718–6722.
- Zhang L. I., Tao H. W., Holt C. E., Harris W. A. and Poo M. M. (1998). A critical window for cooperation and competition among developing retinotectal synapses. *Nature* **395**, 37–44.
- Zipser D. and Andersen R. A. (1988). A back-propagation programmed network that simulates response properties of a subset of posterior parietal neurons. *Nature* **331**, 679–684.
- Zubler F. and Douglas R. (2009). A framework for modeling the growth and development of neurons and networks. *Front. Comput. Neurosci.* **3**, 25.
- Zucker R. S. (1974). Characteristics of crayfish neuromuscular facilitation and their calcium dependence. *J. Physiol.* **241**, 91–110.
- Zucker R. S. (1989). Short-term synaptic plasticity. *Annu. Rev. Neurosci.* **12**, 13–31.
- Zucker R. S. (1999). Calcium- and activity-dependent synaptic plasticity. *Curr. Opin. Neurobiol.* **9**, 305–313.
- Zucker R. S. and Fogelson A. L. (1986). Relationship between transmitter release and presynaptic calcium influx when calcium enters through discrete channels. *Proc. Nat. Acad. Sci. USA* **83**, 3032–3036.
- Zucker R. S. and Regehr W. G. (2002). Short-term synaptic plasticity. *Annu. Rev. Physiol.* **64**, 355–405.

Index

A bold font denotes a definition of the term. ‘f’ refers to a figure.

action potential, **47**
 back-propagating, **189**, **199**
 burst, **199**, **199–201**
 initiation via gap junctions, **193**
 postsynaptic response to, **172**,
 174–175
 propagating, **64**
 in reduced model, **202**
 and release of neurotransmitter,
 179–187
 simulated, **61–64**, **106**, **122**, **201f**, **201**
 space-clamped, **60–64**
 stochastic, **122**
activation, **51**
activation energy, **124**, **125**
active channel, *see* ion channels, active
active transport, **276**
active zone, **173f**, **177–179**, **180f**, **184**,
 187, **188f**, **194**
activity, *see* developmental models,
 activity-based
afterhyperpolarisation, **47**, **64**
 after burst, **115**
 due to calcium-dependent potassium
 channels, **115**
 modelling with SRM neurons, **220**
alpha function, **173–177**, **175f**, **176f**
AMPA receptor, **178**, **188f**, **189**, **207**, **253**,
 257
 phosphorylation of, **135**, **161**
 and synaptic plasticity, **161**
amperes, **20**
anatomical structures, *see* neuron
 morphology
anion, **14**, **22**
aperiodic behaviour, **204**, **333**
Arrhenius equation, **124**
Arrow model, **309**
artificial neural network, **221**, **241**, **242**,
 312
association, **235**
Associative Net, **234**
associative network, **233**
assumptions of theory, **1**
attractor, **238**
attractor dynamics, **238**
auditory cortex, **257**, **258f**
autoassociation, **223**, **234**

autoassociative network, **223**
autocorrelation, **247**
auxiliary subunits, *see* subunits
Avogadro’s number, **25**
axial current, **21**, **36**, **37**, **49**, **58**, **61**, **74**
axial resistance, **34**, **37**, **74**
 estimation from transients, **83–93**
axial resistivity, *see* axial resistance
axoaxonic cell, **255**
axon, *see* neurites
 see also squid giant axon
axon initial segment, **75**, **228**, **228f**

back-propagating action potential, *see*
 action potential, back-propagating
backpropagation algorithm, **241**, **242**
backward Euler method, *see* numerical
 integration methods
BAPTA, **151**
basal ganglia, **259**
basket cell, **230**, **255**
battery, **15**
BCM rule, **240**
BESTL algorithm, **274**, **275f**
 see also neurite growth algorithms
bifurcation, **335**, **338**, **338–341**
 saddle-node bifurcation, **340–341**, **341**
 subcritical Hopf bifurcation, **340**, **341**
 supercritical Hopf bifurcation, **340**
bifurcation diagram, **327**, **339**, **341**
bifurcation parameter, **338**
bifurcation point, **339**, **341**
binding ratio, *see* calcium binding ratio
binding reaction, **135**, **135–136**, **162**
binomial distribution, **344**
biocytin, **77**
Blue Brain project, **254**, **258**
boundary conditions, **38**, **80**, **333**
 Dirichlet, **38**
 killed end, **38**, **42–43**
 leaky end, **38**, **42–43**, **44**, **86**
 Neumann, **38**, **333**
 sealed end, **38**, **41**, **40–42**, **44**, **77**, **86**,
 333
 bouton, **75**, **76**, **260**
 BPAP, *see* action potential,
 back-propagating
 bridge balance, **91**

Brownian motion, **18**, **144**, **169**, **170**, **216**
buffering, **151–159**
 binding ratio, *see* calcium binding
 ratio
 effective diffusion coefficient, **155–156**
 endogenous, **151**, **154**, **158**
 endogenous buffer capacity, **156**, **158**
 excess buffer approximation, **154–155**
 exogenous, **151**, **154**
 fixed, **137**, **153–154**
 mobile, **137**, **153–154**
 of calcium, **161**
 rapid buffer approximation, **155–156**
bungarotoxin, **104**
burst firing, *see* action potential, burst

cable, **36**
 sealed end, *see* boundary conditions,
 sealed end
cable equation, **40**, **74**
 and input resistance in branching tree,
 86
derivation of, **41**
numerical integration of, **331**
steady state solutions, **40–44**
time-dependent solutions, **40–45**
calcium, **10**, **96**
 buffering of, **151–159**
 decay, **138–139**
 diffusion of, **143–150**
 fluxes, *see* flux
 release, **141–143**
 space constant of diffusion, **149**, **152**,
 157
 store, **140**
 time constant of diffusion, **157**
 uptake, **140–141**
calcium binding ratio, **155**
calcium channels, *see* calcium current
 vesicle release, **180**, **192f**
calcium conductance, **131**, **203**
calcium current, **109**, **138**, **173**
 inactivation, **183**
L-type, **102**, **104f**
N-type, **102**
R-type, **102**
 in Traub model, **256**
T-type, **101**, **102**, **104f**, **109**

- calcium indicator dye, 156–159
 calcium-activated potassium channel, *see* potassium current, calcium-activated
 calcium-ATPase pump, 139, 140
 calcium-induced calcium release, 141
 calmodulin, 151, 152, 161
 calyx of Held, 186, 188
 capacitance, 17
see also membrane capacitance
 capacitance compensation, 91
 capacitive current, 30, 34, 50
 capacitor, 15, 17
 CARMEN, 316
 Cartesian coordinates, 145
 cation, 14
 cDNA, *see* cloned DNA
 cell division, 268
 central difference, *see* numerical integration methods
 cerebellum, 282
Marr's theory of, 234
 channels, *see* ion channels
 chaos, 204, 333
 chemoaffinity, 298, 299, *see also* developmental models, chemoaffinity-based
type I, 302, 303, 306, 310
type II, 302
 CICR, *see* calcium-induced calcium release
 cloned DNA, 101, 104
 coefficient of variation, 209
 compartment, 36, 75, *see* isopotential assumption
 size, 76–77
 compartmental model, 58, 72
Pinsky-Rinzel model, 199
 reduced, 80, 106, 198
see also equivalent cylinder
 compartmental modelling, 72
 competition between synapses, 240
 in developmental models, 288–294, 298, 300–302
 computational modelling, 5
 future of, 315
 history of, 314–315
 rationale for, 5–7
 concentration gradient, 19
 maintenance of, 16
 conditioning pulse, 59
 conductance, 21, 29–30
see also membrane conductance
 connectivity pattern, 230, 230f
 local, 230f
 constant-field equations, *see* Goldman–Hodgkin–Katz current equation
 constraint satisfaction, 9
 consumer–resource system, 292
 continuation, *see* numerical continuation
 conventions
 membrane current, *see* membrane current, convention
 voltage, *see* membrane potential, convention
 convolution, 219, 220
 of functions of two variables, 285
 convolution kernel, *see* impulse response
 cortical column, 230, 243, 254
 cortical pyramidal neuron, *see* pyramidal cell
 corticospinal fibres, 261
 cosh, *see* hyperbolic functions
 coth, *see* hyperbolic functions
 covariance learning rule, 239
 cross-correlation, 246, 247, 249
 average, 247
 current, 20
see also ionic current; membrane current
 current clamp, 31
 current density, 20
 relationship to flux, 20
 current source, 15, 31
 current-based synapse, *see* synapses, current-based
 cyclic-nucleotide-gated channel family, 98, 101
 cylindrical coordinates, 145
 cytoplasm, 14
 deactivation, 51, 56, 62, 113
 deep brain stimulation, 259
 model of, 260–265
 deinactivation, 62
 Delaunay triangulation, 283
 delay line model of action potential propagation, 228
 delayed rectifier current, *see* potassium current, delayed rectifier
 delta function, *see* Dirac delta function
 Delta molecule, 283
 dendrites, *see* neurites
 dendritic spines, 79–80
 clearance of calcium from, 139
 diffusion along neck, 150
 ionic concentration in, 25
 model of calcium transients in, 160
 reconstruction of, 78
 dendritic trees, 75–76, 199
 equivalent cylinder, 80–82, 82
 input resistance of, 85
 synaptic inputs to, 39
see also neurite growth algorithms
 dendrogram, 272, 273
 depolarisation, 33, 47
 detailed balances, *see* microscopic reversibility
 development, 268–269
 of ion channel distributions, 279–280
 intrinsic withdrawal, 291–292
 of neurite morphology, 269–270
 of neuromuscular connections, 286–294
 of ocular dominance, 284–286
 of olfactory connections, 312
 of patterns in morphogenesis, 280–282
 of patterns in set of neurons, 282–284
 of retinotopic maps, 294–312
see also neurite growth algorithms
 developmental models, 269–312
 activity-based, 299–300
 chemoaffinity-based, 301–312
 differential equation, *see* ordinary differential equation; partial differential equation
 diffusion, 18, 18–19, 134, 137, 143, 232, 276
 approximated, 139
 of calcium during development, 278
 coupling coefficient, 145, 151, 193
 in derivation of GHK equations, 26–28
 in derivation of Nernst equation, 22–26
 longitudinal, 145, 149f, 150f, 149–150, 151, 157
 numerical calculation of, 150
 of growth factors extracellularly, 278
 of tubulin, 276
 radial, 145, 147–149, 151
 in three dimensions, 145
 three-pool model, 146–147
 in two dimensions, 145
 two-pool model, 143–146
see also reaction–diffusion system
 diffusion coefficient, 19, 29, 144, 153, 169, 281
see also buffering, effective diffusion coefficient
 diffusion tensor imaging, 259, 263

- diffusive noise, 216
 effect on response fidelity, 217–218
 effect on synchronisation, 218
 in integrate-and-fire neurons, 216–217, 223
- Dirac delta function, 181, 208, 212, 244
- direct fitting, *see* parameter estimation, of passive properties, direct fitting
- direction field, 336, 337–338
- dissociation constant, 135, 136, 139, 153–155, 158, 162
- dowhill simplex method, 349
see also parameter estimation
- drift velocity, 19
- driving force, 29, 50, 57, 69, 207, 229
- Dual Constraint model, 289–292, 290f, 291
- dual exponential function, 174f, 173–174, 207
- dynamic clamp, 91, 92f, 317
- dynamical system, 327, 333
- dynamical systems theory, 248, 333, 333–341
- EC_{50} , 116
- ectoderm, 268
- edge effect, 230
- effective valency of equivalent gating charge, 127, 129
- EGTA, 151
- eigenvalue, 335
- electric field, 17, 19–20
 constant field assumption, 29, 35
 of DBS electrode, 260–261, 262f
 in GHK equations, 26, 29
 movement of gating charges in, 126–128
 in Nernst equation, 22–23
 non-uniform, 130
- electrode current, 74
- electrodiffusion, 17, 20–21, 129, 150, 152
- electrogenesis, 150
- electrogenic pump, 16
see also ionic pump
- electromotive force, 17, 30, 58
- electron microscopy, 78, 79, 198
- electrotonic distance, 80, 81
- electrotonic length, 81, 81f, 82, 198
- endoderm, 268
- endoplasmic reticulum, 19, 140
- endplate, 286
 development of connections to, 286–292
- endplate potential, 6
- energy barrier, 125, 126f
- energy barrier model, *see* transition state theory
- energy function, 238
 in model of development of topography, 303, 311
see also error measure
- ensemble of recordings, 103, 104f
- enthalpy, 125, 127
- entropy, 125, 126, 128, 130
- enzymatic reaction, 136, 136–137, 162
see also Michaelis–Menten kinetics
- Eph receptor, 297, 297–298
 EphA, 296f, 297–298, 309–312
 EphA knockin, 311, 312
 EphB, 296f, 297, 310–312
- Eph/ephrin-based chemoaffinity models, 309–312
- ephrin ligand, 297, 297–298
 ephrinA, 297–298, 309–312
 ephrinA knockout, 297
 ephrinB, 297, 310–312
- epidermis, 268
- epileptic state, 257
- EPP, *see* endplate potential
- EPSC, *see* excitatory postsynaptic current
- EPSP, *see* excitatory postsynaptic potential
- equilibrium point, 336, 336–341
 saddle node, 335, 340, 341
 stable, 335, 337, 341
 unstable, 335, 337
- equilibrium potential, 23, 29, 30, 70, 107
 assumed to be constant, 133
 of calcium, 133
 leak, 106f
 potassium, 26, 57, 106
 sodium, 26, 69
- equivalent cylinder, 80, 81, 81f, 82, 198
- equivalent electrical circuit, 31, 72, 115
 of gap junction, 193
 in Hodgkin–Huxley model, 50f
 of spatially extended neurite, 36–37
 simplification of, 31–32
- ER, *see* endoplasmic reticulum
- error function, 45
- error measure, 87–90, 88, 94–95, 347–350
- error surface, 89, 89f, 348, 349f
- escape noise, 217
- event-based simulation, 250
- excitatory postsynaptic current, 39f, 178, 208
- approximation by Dirac delta function, 208
- excitatory postsynaptic potential, 36, 39, 78f, 80, 80f
- exocytosis, 183
- exponential distribution, 343
- extracellular field potential, 231, 232f, 257
- extracellular resistance, 36, 37
- Eyring equation, 126
- facilitation, 180–181
- farad, 17
- Faraday's constant, 19, 20, 25, 117, 129, 138
- feedback inhibition, 251–252
- feedforward network, 221f, 222, 223f, 234, 242
 time-varying inputs to, 222–223
- Fick's first law, 18f, 23, 26, 29, 144
- field oscillations, 251
- finite-difference method, 328, 329
see also numerical integration methods
- finite-element method, 192, 278, 323, 328
- finite-element model, 232, 263
- firing rate, 197
 adaptation, 213
 average, 221
 background, 252
 in BCM rule, 240
f–I curve, 106f
 homoeostasis, 280
 optimal encoding, 280
 population, 218, 218f, 221, 247, 248
 scaling, 249
- in Stein model, 209f, 210
- temporally averaged, 247
 transmission of in network, 223–224
see also rate-based models
- fitness measure, *see* error measure
- FitzHugh–Nagumo model, 197
- fixation procedures, 78
- fixed point, *see* equilibrium point
- fluctuations due to ion channels, 121–122
- fluorescent dye, 78, 139, 151
- flux, 18, 20
 calcium, 137–138
 calcium decay, 138–139
 calcium diffusion, 143–150
 calcium extrusion, 139–140
 calcium release, 141–143
 to calcium store, 140
 calcium uptake, 140–141

- saturation of, 35
 of tubulin, 277
 forward Euler method, *see* numerical integration methods
 free energy, *see* Gibbs free energy
 free parameters, 8, 93
 reduction in number of, 94
 see also parameter estimation
 G protein, 159, 160
 GABA_A receptor, 178, 251, 253, 257, 263
 GABA_B receptor, 179
 GABAergic synapses, 255, 262f, 263
 gamma distribution, 275, 343
 gamma oscillation, 251, 257
 role in associative memory, 251–254
 gap junction, 192, 192–194
 and action potential initiation, 193
 and network oscillations, 251
 in thalamocortical network, 256
 gas constant, 19, 117, 129
 gastrulation, 268
 gate, 52, 52–54, 99
 in model of vesicle release, 181–183
 gating charge, 99, 104, 126
 equivalent, 127, 127f, 129
 gating current, 68, 104f, 104, 104–105, 113, 123
 neglected in HH model, 68–69
 gating particle models, 105–110
 accuracy of, 97
 comparison with unrestricted kinetic schemes, 114–115
 equivalence with subclass of Markov models, 112
 implemented as kinetic scheme, 112–113
 gating particles, 52, 52–58
 activating, 52, 107
 correspondence with channel structure, 98
 inactivating, 56, 105, 107
 independence of, 68
 with more than two states, 129
 gating variable, 52, 56–61, 65, 69–70, 108, 108f, 111
 determining voltage-dependence of rate coefficients, 70
 see also state variable; gating particles
 Gaussian distribution, 343, 344
 in kernel density estimation, 345–346
 in maximum likelihood estimation, 344–345
 GENESIS simulator, 33, 316, 317, 320–322
 GHK current equation, *see* Goldman–Hodgkin–Katz current equation
 GHK voltage equation, *see* Goldman–Hodgkin–Katz voltage equation
 Gibbs free energy, 125, 126, 129
 Gierer–Meinhardt model, 282
 gigaseal, 100f, 103
 global minimum, 89f, 348f
 globus pallidus, 259, 261
 Goldman–Hodgkin–Katz current equation, 27, 26–30, 67
 validity of assumptions, 35–36
 Goldman–Hodgkin–Katz voltage equation, 28
 Golgi method, 78
 Green’s function, *see* impulse response
 growth algorithm, *see* neurite growth algorithms
 growth cone, 278
 half activation voltage, 109f, 129, 203
 effect of heterologous expression on, 114
 HCN, *see* hyperpolarisation-activated cyclic-nucleotide-gated channel family
 heat energy, *see* enthalpy
 Hebbian learning rule, 243, 252, 286
 in development of retinotopy, 300
 Hebbian plasticity, 235, 240
 heteroassociation, 222, 234
 heteroassociative network, 222, 223, 239
 see also Associative Net
 heterologous expression, 101, 104
 effect on channel parameters, 114
 heteromer, 98
 HH model, *see* Hodgkin–Huxley model
 Hill coefficient, 116, 137
 Hill function, 116f, 116, 137, 294
 hippocampus, 230, 234
 as associative network, 234
 LTP in, 189
 Marr’s theory of, 234
 oscillations in, 251
 place cells, 220
 see also pyramidal cell
 Hodgkin–Huxley formalism, 200
 approximations in, 66–69
 fitting to data, 69–70
 Hodgkin–Huxley model, 48, 50–59
 compared to model with A-type potassium currents, 105–106
 correspondence with channel structure, 98
 discrepancy with experiment, 113
 implemented as kinetic scheme, 119
 prediction of gating charges, 105
 simulations, 60–64
 with stochastic channels, 122
 homeostasis, 279
 of ion channel densities, 279–280
 of synaptic strengths, 301
 homomer, 98
 Hopf bifurcation, *see* bifurcation
 hyperbolic functions, 44
 hyperpolarisation, 33
 hyperpolarisation-activated current, 102
 hyperpolarisation-activated cyclic-nucleotide-gated channel family, 98
 hysteresis, 340
 I_h , *see* hyperpolarisation-activated current
 impulse response, 218, 218–220, 220f
 impulse response kernel, *see* impulse response
 inactivating channel, 98, 105
 inactivation, 56, 56–57, 102, 109, 109f, 110, 142
 of IP₃ receptors, 142–143
 quantification of, 59
 role in action potential, 62–64
 of ryanodine receptors, 142
 independence principle, 29, 51
 validity of, 35, 67
 inhibition, 209
 in associative network, 238
 balanced with excitation, 209f, 209–211
 role in controlling network activity, 243–251
 see also feedback inhibition; lateral inhibition
 inhibitory postsynaptic current, 208
 approximation with Dirac delta function, 208
 initial conditions, 61
 of Markov kinetic scheme, 119
 variation between cells in network, 231
 injected current, 34
 input impedance, 34

- input resistance, 34, 34–35, 40
 of cable with sealed end, 44
 of leaky cable, 44
 measurement of, 85
 of semi-infinite cable, 42
 integrate-and-fire neuron, 197, 204, 204–218
 exponential, 214f, 214, 216
 impulse response, 219
 Izhikevich model, 215
 in large network model, 259
 in network, 243–251
 quadratic, 214f, 214, 213–214
 intensive quantity, 31
 internal capsule, 261
 International Union of Pharmacology, 98
 interspike interval histogram, 209
 intracellular buffer, *see* buffering
 intracellular resistance, 36
 intracellular signalling pathway, *see* signalling pathways
 intrinsic withdrawal, *see* development, of neuromuscular connections
 inverse problem, 123
 inverse slope, 108, 129
 ion channel blocker, 257
see also TTX
 ion channel blockers, 103
 ion channel nomenclature
 ad hoc, 101
 clone, 100
 gene, 100
 ion channels, 15, 48
 active, 15
 approximated as passive, 31
 alternate splicing of channel DNA, 101–103
 complexity of models, 73
 densities, 74, 231
 diffusion of ions through, 18–19
 distribution over neurites, 93–94
 equivalent electromotive force due to combination of, 31
 estimating conductance of, 95
 expression of DNA, *see* heterologous expression
 genes, 99–100
 genetic families, 100–101
 incorporating models derived from diverse sources, 94
I–V characteristic, 67
 ligand-gated, 115–117
 modelling considerations, 131
 passive, 15
 saturation of flux, 35
 selectivity, 15, 36, 66
 structure of, 97–99
 temperature dependence of conductance, 66
 voltage-gated-like superfamily, 100
see also calcium current; gating charge; potassium current; rate coefficients; single-channel recording; sodium current; subunits
 ion substitution method, 51, 51f, 69
 ionic current, 32, 34, 49, 50, 74
see also calcium current; hyperpolarisation-activated current; leak current; sodium current; potassium current
 ionic pump, 15f, 16, 26, 137f, 138, 150
 calcium, 137
 high affinity, low capacity, 139
 low affinity, high capacity, 139
 ionotropic receptors, 179
 IP_3 , 141, 159
 degradation of, 160
 production of, 159, 160
 IP_3 receptor, 141, 159, 160
 model, 142–143
 IPSC, *see* inhibitory postsynaptic current
 ISI, *see* interspike interval histogram
 isopotential assumption, 76–77
 errors due to, 77
 of extracellular medium, 36–37
 of neurite, 36, 73, 75
see also space clamp
 IUPHAR, *see* International Union of Pharmacology
I–V characteristic, 21
 calcium, 35, 109
 instantaneous, 67
 quasi-ohmic, 30, 32, 34, 35, 37, 57, 67, 69
 steady state, 67
 Jacobean matrix, 335
 kernel, *see* impulse response
 kernel density estimation, 272, 345
 kernel function, 346
 killed end, *see* boundary conditions
 kinetic equation, 54
 kinetic schemes, 68, 110, 110–115
 fitting to data, 123–124
 and independent gating particles, 112–115
 second order, 151–153
 of synaptic receptors, 175–179
 for vesicle availability, 183–186
see also Markov models; signalling pathways; transition state theory
 Kirchhoff's current law, 32, 193
 knockin, *see* Eph receptor, EphA
 knockin
 knockout, *see* ephrin ligand, ephrinA knockout
 L-Measure, 270
 label, *see* markers
 lateral geniculate nucleus relay cell, 81
 lateral inhibition, 283, 283–284
 law of mass action, *see* mass action kinetics
 leak conductance, 50, 58, 123f, 202
 leak current, 50, 57–58
 leaky end, *see* boundary conditions
 learning rule, 223, 239, 239, 240
 length constant, 40, 43f, 44, 76, 77, 79, 81, 82, 198
see also space constant, electrical
 lenticular fasciculus, 261, 261f, 262, 263
 levels of analysis, 7
 levels of detail, 7
 light microscopy, 78
 likelihood, 344
 limit cycle, 248, 338, 337–341
 lipid bilayer, 14, 15, 15f
 local circuit, 61
 local circuit current, 58, 64
 local minima, 89–90, 348
 logistic function, 3
 logistic growth, 4f
 long-term depression, 134, 161, 189, 189–191, 239
 long-term potentiation, 134, 161, 189, 189–191, 240
 low threshold spiking interneuron, 255
 LTD, *see* long-term depression
 LTP, *see* long-term potentiation
 lumbrical muscle, 291
 macroscopic currents, 103
 macroscopic interpretation of kinetic scheme, 112
 magnetic resonance imaging, 259
 MAPs, *see* microtubule associated proteins
 Marker Induction model, 306, 306–309
 markers, 299
 Markov models, 97, 110, 110–115, 118–119

- comparison of ensemble and stochastic simulation, 121–123
 fitting to data, 326
 single-channel simulation, 119–120, 321
see also kinetic schemes; transition state theory
 Markov property, 118, 210
 mass action kinetics, 163
 comparison with stochastic kinetics, 166
 validity of, 161–164
 master equation, 164, 164–166
 mathematical biophysics, 314
 mathematical model, 2, 1–6
 maximum conductance, 52, 53, 55, 93
 estimation of, 94–95
 homoeostatic regulation of, 280
 regulation by LTP and LTD, 189
 of synapse, 189, 207
 temperature dependence of, 66
see also synaptic strength
 maximum likelihood estimation, 344, 344–345
 McCulloch–Pitts neurons, 221
 MCELL, 170, 192
 melanocytes, 281
 membrane action potential, *see* action potential, space-clamped
 membrane capacitance, 24, 30–36, 205
 charging and discharging during action potential, 64
 estimation from voltage transients, 83–93
 estimation of, 84
 and geometry, 75
 low-pass filtering, 76
 and stochastic simulation, 122
 variations in, 74
 membrane conductance, 32, 50, 194
 active, 50
 during action potential, 220
 fluctuations in, 121, 122
 passive, 50
see also calcium conductance; leak conductance; maximum conductance; potassium conductance; sodium conductance
 membrane current, 28, 32, 34, 37, 49, 50, 59f, 61, 205
 contribution to extracellular field potential, 231
 convention, 18
 noise in, 216
 membrane potential, 13, 34
 and capacitive current, 30
 behaviour in Morris–Lecar model, 202f
 behaviour in Pinsky–Rinzel model, 201f
 in cable, 39–44
 steady state behaviour, 40–43
 time-dependent behaviour, 43–44
 in compartmental model, 36–39
 convention, 18
 fluctuations in, 121–122, 209–211
 in integrate-and-fire model, 204–205
 origin of, 22–30
 in passive RC circuit, 32–35
 passive transients in, 84
 in SRM, 218–220
 in voltage clamp, 49
see also action potential; isopotential assumption; resting membrane potential
 membrane pump, *see* ionic pump
 membrane resistance, 33, 34, 39, 205
 estimation from voltage transients, 83–93
 variations in, 74
 membrane time constant, 33, 45, 46f, 91, 205, 207, 249
 MEPP, *see* miniature endplate potential
 mesoderm, 268
 messenger RNA, 104
 metabotropic glutamate receptor, 159, 183
 metabotropic receptors, 179
 Mexican hat function, 285
 Michaelis–Menten function, 137, 294
 Michaelis–Menten kinetics, 136, 137, 140
 modified, 141
 microscopic currents, 103, 110
 microscopic interpretation of kinetic scheme, 112
 microscopic reversibility, 130
 microtubule associated proteins, 278
 microtubules, 19, 276f, 276
 assembly of, 276–278
 miniature endplate potential, 6
 mismatch experiments, 296, 301, 305f, 306, 309
 molarity, 18
 Monte Carlo simulation, 164, 166, 170, 187, 188
 of individual molecules, 167
 importance of random numbers, 342
see also Stochastic Simulation Algorithm
 Moore’s law, 315
 morphogenesis, 280
 development of patterns in, 280–282
 morphogenetic fields, 267, 282
 morphogens, 267, 281
 morphology, *see* neuron morphology
 Morris–Lecar model, 197, 202f, 203, 334, 336, 341
 bifurcation diagram, 339f, 341f
 phase plane, 336f
 motor neuron, 80, 81, 84f
 charging time constant, 45
 development of connections from, 286–292
 motor units, 288
 mRNA, *see* messenger RNA
 mRNA transfection, *see* heterologous expression
 multi-compartmental modelling, *see* compartmental modelling
 multimer, 98
 mutant mice, 300, 309, 310
 neocortex, 312
 irregular spiking in, 210
 Marr’s theory of, 234
 oscillations in, 251
 Nernst equation, 23, 24, 26, 28, 133
 derivation of, 24
 Nernst potential, *see* equilibrium potential
 Nernst–Planck equation, 20, 23, 24, 129, 152
 network
 asynchronous update, 223
 excitatory-inhibitory, 243–246
 location of neurons in, 230
 recurrent, 243–246
 scaling, 228–230
 synchronous update, 223
 variability of cell properties, 230–231
 Neumann boundary condition, *see* boundary conditions
 neural crest, 268
 neural plate, 268
 neural precursors, 267
 neural tube, 268
 neurite growth algorithms, 273
 biophysical, 276–278
 statistical, 273–275

- neurites, 16
 fundamental shape parameters, 270, 271
 longitudinal movement of calcium in, 152
 passive
 cable equation, 39–44
 equivalent electrical circuit, 36–39
 neurobiotin, 77
 neuroinformatics, 315
 NeuroML, 316
 neuromuscular junction, 184, 186
 neuron morphology, 77–82, 270
 centrifugal order, 274, 274f, 275
 development of, 269–273
 reconstruction from images, 77–79
 representation by geometric objects, 75–76
 simplification, 80–82
 NEURON simulator, 33, 80, 250, 316, 317, 320–322, 325
 neurotransmitter, 175, 176f, 187, 191
 current response to, 173
 and ionotropic receptors, 179
 transient, 176–178
 neurotransmitter release, 6, 173f, 177f, 187f, 179–187, 204
 depression, 179, 183, 184
 facilitation, 179–181
 role of calcium in, 134
 spillover, 178f, 178
 neurotrophic factors, 292
 neurotrophic signalling, 292
 neurulation, 268
 NMDA receptor, 138, 175, 178, 191, 257
 node, *see* equilibrium point
 noise, 218f
 due to ion channels, 121–122
 effect on response fidelity, 217
 Gaussian, 343
 in recordings, 85, 87, 96f, 347, 348
 in simulated annealing, 89
 in threshold, 217
 see also diffusive noise; escape noise;
 variability of neuronal firing
 non-ohmic conductor, 21
 non-parametric kernel density
 estimation, *see* kernel density
 estimation
 non-parametric model, 345
 non-inactivating channel, 98, 109, 202
 normal distribution, *see* Gaussian
 distribution
 Notch molecule, 283
 notochord, 268
 nucleus reticularis thalamic cell, 255
 nullcline, 336f, 336, 337–338, 340–341
 numerical continuation, 326, 327, 339
 numerical integration methods, 328–333
 accuracy of, 329–331
 backward Euler, 330
 central difference, 331
 explicit method, 331
 first order, 328–331
 first order accuracy, 329
 forward Euler, 329
 implicit method, 331
 second order, 331
 second order accuracy, 331
 ocular dominance, 240, 284
 development of, 284–286
 ODE, *see* ordinary differential equation
 Ohm's law, 21f, 21, 27, 30, 37
 ohmic conductor, 21
 olfactory bulb model, 198
 optic tectum, 294, 296f
 reinnervation of, 305, 307
 optimisation algorithm, *see* parameter
 optimisation algorithms
 optogenetic technology, 265
 ordinary differential equation, 3, 32
 numerical integration, 328–331
 oriens lacunosum-moleculare cell, 230
 palimpsests, 241
 parallel distributed processing, 312
 parameter estimation, 87
 of active properties, 94–95
 of passive properties, 83–93
 direct fitting, 86, 85–87, 89
 of signalling pathways, 162–163
 uniqueness of estimates, 92–93
 parameter estimation, sensitivity
 analysis, 163
 parameter optimisation algorithms, 8, 89, 348
 brute force, 349
 conjugate gradient descent, 348
 deterministic, 348–349
 evolution strategies, 350
 evolutionary, 350
 genetic algorithms, 350
 gradient descent, 89, 348
 stochastic, 349–350
 parameter space, 8, 349
 parameters, 8
 see also free parameters
 parametric model, 344
 Parkinson's disease, 259, 261
 partial differential equation, 40
 numerical integration, 331–333
 passive channel, *see* ion channels, passive
 patch clamp technique, 100f, 103
 determining ion channel densities, 93
 see also whole-cell patch electrode
 pattern completion, 236f, 236, 238f
 PDE, *see* partial differential equation
 Perceptron, 242
 permeability, 15, 16, 23, 29, 68
 permittivity, 17
 phase, 335
 see also state variable
 phase plane, 336, 336–340
 phospholipase C, 159
 phosphorylation
 of AMPA receptors, 134, 161
 of MAPs, 278
 Pinsky–Rinzel model, *see*
 compartmental model
 PIP₂, 159
 Poincaré–Bendixson theorem, 338
 Poincaré–Andronov–Hopf bifurcation,
 see bifurcation
 Poisson distribution, 6, 210, 343, 344
 Poisson process, 118, 120, 209, 210, 343
 as spike generator, 210, 212, 244
 population biology, 292
 postsynaptic current, 173–175
 see also excitatory postsynaptic
 current; inhibitory postsynaptic
 current
 postsynaptic density, 159
 potassium channel
 Aeropyrum pernix, 99
 A-type, 114
 calcium dependent, 90
 KcsA, 99
 Shaker K_v1.2 voltage-gated, 99
 potassium conductance, 50, 51, 52f, 53,
 56, 62–64, 98, 105, 203
 A-type, 107
 calcium dependent, 131
 potassium current, 50, 51–56
 A-type, 70, 101, 102, 105, 105–106,
 109, 131
 AHP, 102
 C-type, 102
 calcium-activated, 115–117
 D-type, 102
 delayed rectifier, 48, 62, 102, 105
 fast rectifier, 102
 in Traub model, 256

- muscarinic, 102
 sAHP, 102
 potential difference, 17, 19f, 21
see also membrane potential
 potential energy, 17, 126
see also enthalpy
 predictions, 1
 primary fate, 283, 284
 principal subunits, *see* subunits
 probability density function, 164, 166, 342, 346
 probability distribution function, 342
 probability distribution of state of system, 164
 probability distributions, 341–344, 342
 continuous, 342–343
 discrete, 344
 and neuronal morphology, 271
 pump, *see* ionic pump
 Purkinje cell model, 140, 160, 161, 198, 226
 pyramidal cell, 79, 80f, 81, 105
 fast rhythmic bursting, 255
 layer five tufted, 255
 layer six non-tufted, 255
 models, 198–199
 Pinsky-Rinzel model, 199–202, 252
 regular spiking, 255
 Q_{10} temperature coefficient, 65
 quantal amplitude, 6, 189
 quantal analysis, 6
 quantal hypothesis, 6
 Quantitative Single-Neuron Modelling Competition, 216
 quasi-ohmic approximation to channel I – V characteristic, 35, 70
Rana, 296
 rate code, 252
 rate coefficients, 54, 112, 118, 119, 125
 in binding reaction, 135
 derivation from transition state theory, 124–130
 determining voltage-dependence of, 54–57
 effect of temperature on, 65–66
 in kinetic schemes, 112–113
 in thermodynamic models, 106–109
 rate law, 54
 rate-based models, 220–224, 241, 242
 rate-limiting factor, 108, 109, 129
 RC circuit, 32f, 32–35, 204
 behaviour of, 33–35
see also compartment; parameter estimation, passive properties
 reaction rate coefficient, *see* rate coefficients
 reaction-diffusion system, 134, 232, 281
 in development, 282–284
 simulators, 321
 readily releasable vesicle pool, 183–188
 receptor desensitisation, 176, 178
 reconstruction algorithm, 271, 272, 272f, 273, 273f
 recovery potential, 59
 rectification, 21f, 21, 27
 in gap junctions, 192
 inward, 27
 outward, 27
 refractory period, 63, 96, 204f, 205, 206
 absolute, 63, 205f, 206
 relative, 63
 regenerative property of action potentials, 47
 regulation of markers, 301
 release-site model, 180f, 184, 185f, 186, 188
 repolarisation, 33, 47, 62
 reserve pool, 173, 173f, 179, 180f, 183–188
 activity-dependent recovery, 186
 resistance, 21f, 21
see also axial resistance; extracellular resistance; input resistance; membrane resistance
 resistor, 15, 21
 resting membrane potential, 13
 in Hodgkin-Huxley model, 58
 origin of, 22–26
 variability in, 231
 retinal mosaics, 282, 283, 284
 production of, 282
 retinocollicular system, *see* development, of retinotopic maps
 retinotectal system, *see* development, of retinotopic maps
 retinotopic maps, *see* development, of retinotopic maps
 retrograde modulation, 301
 reversal potential, 27, 28, 31, 34, 36, 70
 potassium, 62
 sodium, 62
 of synapse, 174, 207
 ryanodine, 141
 ryanodine receptor, 142, 143
 model, 141–142
 S4 segment, 99, 99f
 saddle node, *see* equilibrium point
 saddle-node bifurcation, *see* bifurcation
 scalar product, 253
 sealed end, *see* boundary conditions
 second-messenger, 101, 115, 134, 137, 173, 179
 secondary fate, 283, 284
 selective permeability, 15
 sensitivity analysis, 8, 93, *see* parameter estimation, sensitivity analysis
 SERCA, *see* calcium-ATPase pump
 servomechanism model, 310
 sharp electrode, 90, 91
 shunt, 90, 91
 signal-to-noise ratio, 312
 signalling pathways, 134, 134–137, 159–163, 278
 calcium transients, 159–161
 LTP and LTD, 161
 parameter estimation, 162–163
 production of IP_3 , 159–160
 repositories of models, 325–326
 simple model of STDP, 191
 simulators of, 321–323
 spatial modelling, 169–170
 stochastic modelling, 163–169
 well-mixed assumption, 161–162, 169
 simulated annealing, 89, 349
see also parameter estimation
 single-channel recording, 96f, 97, 103
 singular point, *see* equilibrium point
 sinh, *see* hyperbolic functions
 sleep spindle, 257
 small-world networks, 230
 sodium conductance, 56, 56f, 57, 59, 62, 63, 68f, 279
 sodium current, 50, 56–57, 102
 persistent, 102
 in Traub model, 256
 sodium–calcium exchanger, 139, 140
 sodium–hydrogen exchanger, 16
 sodium–potassium exchanger, 15
 soma shunt conductance, 91, 93
 space clamp, 48, 49, 61
see also action potential, space-clamped
 space constant
 diffusion, 149
 electrical, 149

- specific axial resistance, *see* axial resistance
 specific membrane capacitance, *see* membrane capacitance
 spike response kernel, 220
 spike-response model neuron, 204, 218, 218–220, 219f
 spike-timing-dependent plasticity, 189, 189–191
 spines, *see* dendritic spines
 spiny stellate cell, 255, 257
 squid giant axon, 47–48
 concentrations of ions, 24
 gating current in, 104f
 in Hodgkin–Huxley model, 50–66
 permeability of membrane to ions, 28
 resting membrane potential of, 28
 SRM neuron, *see* spike-response model neuron
 SSA, *see* Stochastic Simulation Algorithm
 state variable, 111, 333–338
 reduction in number of, 196–197, 202
 see also gating variable
 STDP, *see* spike-timing-dependent plasticity
 steady state, *see* equilibrium point
 Stein model, 208, 243, 246, 248
 stem cells, 267
 step function, 221, 221f
 stochastic differential equations, 216
 stochastic resonance, 216f, 217
 Stochastic Simulation Algorithm, 164, 166
 stochastic synapse model, 188
 StochSim, 167, 170
 stomatogastric ganglion, 131, 202, 280
 subcritical Hopf bifurcation, *see* bifurcation
 subunits, 98
 auxiliary, 98, 102–104, 115
 principal, 98, 99, 99f, 103
 sum rule, 285, 288, 300
 postsynaptic, 289
 presynaptic, 288
 supercritical Hopf bifurcation, *see* bifurcation
 superinnervation, 287
 elimination of, 287–292
 superior cervical ganglion, 287
 superior colliculus, 294, 296f, 298f
 synapses, 172–195
 chemical, 172, 173f, 178f
 current-based, 207
 electrical, *see* gap junction
 in thalamocortical network, 256
 synaptic cleft, 170, 173f, 176, 191, 192f
 synaptic depression, *see* neurotransmitter release, depression
 synaptic strength, 287
 systems biology, 315, 321
 systems-matching, 296, 303
 temperature parameter, 90
 temporal code, 252
 test pulse, 59
 tetanus, 189
 Thévenin's theorem, 31
 thalamocortical relay cell, 255
 thalamocortical system, 254
 model of, 258–259
 thalamus, 254, 255, 261
 thermodynamic models, 97, 106–110, 124, 130
 derivation of, 129
 threshold, 60
 time constants of passive transients, 84–85
 voltage clamp, 85
 topographically ordered maps, 294
 TPC, *see* two-pore channels family
 trajectory, 335, 336, 336–338, 340f
 transient receptor potential channel family, 98, 101
 transition probabilities, 118–120, 123
 transition state, 126f
 transition state theory, 66, 108, 124, 125–126
 application to voltage-gated channels, 126–128
 transmembrane current, *see* membrane current
 1,4,5-triphosphate, *see* IP₃
 tropism, 273
 TRP, *see* transient receptor potential channel family
 TTX, 103, 105, 300
 tubulin, 276
 assembly of, 276–278
 transport, 276f
 two-pore channels family, 98
 Type I excitability, *see* Type I neuron
 Type I neuron, 106, 202f, 203, 206, 341
 Type II excitability, *see* Type II neuron
 Type II neuron, 106, 202f, 203, 340
 uniform distribution, 342
 universal gas constant, *see* gas constant
 valency, 19, 20
 variability of neuronal firing, 208–211
 vesicle availability, 183–187
 recycling, 180f, 183
 reserve pool, *see* reserve pool
 vesicle release, 180–187
 vesicle-state model, 183, 185f, 184–188, 187f, 188f
 voltage clamp, 48
 time constants, 85
 voltage-sensitive dye, 94
 weight, 222, 242
 see also synaptic strength
 well-mixed system, 135, 159
 see also signalling pathways
 whole-cell patch electrode, 90, 91
 Wiener process, 216
 Wilson–Cowan oscillator, 334
 X-ray crystallography, 97, 99
Xenopus laevis, 296
 compound eye, 296